

Research Fund for Coal and Steel  
INNOSEIS Project RFCS-02-2015

# **Innovative anti-seismic devices and systems**

2017

Edited by  
**Ioannis Vayas**



## **Innovative anti-seismic devices and systems**

**1<sup>st</sup> edition, 2017**

### **Published by:**

ECCS – European Convention for Constructional Steelwork

[publications@steelconstruct.com](mailto:publications@steelconstruct.com)

[www.steelconstruct.com](http://www.steelconstruct.com)

All rights reserved. No parts of this publication may be reproduced, stored in a retrieval system, or transmitted in any form or by any means, electronic, mechanical, photocopying, recording or otherwise, without the prior permission of the copyright owner

ECCS assumes no liability regarding the use for any application of the material and information contained in this publication.

**Copyright © 2017 ECCS** – European Convention for Constructional Steelwork

**ISBN:** 978-92-9147- 136-2

**Printed in** Sersilito, Empresa Grafica Lda.

**Legal deposit**

## PROLOG

Earthquakes take place since the Goddess Athena buried a Giant, Enceladus, during the Gigantomachy in the mountain of Etna in Sicily. Recent investigations confirmed that seismic activity is also due to other reasons, such as tectonic activity, besides volcanic outbursts, when Enceladus feels uncomfortable in Etna. From all natural hazards, earthquakes constitute the one causing the largest combined threat to life and property loss. However, although earthquakes cannot be avoided their catastrophic effects on the building environment can if proper concepts are followed.

Following the international needs, extensive research on seismic resistant structures has been carried out in Europe. A number of innovative systems based on energy dissipation and damping have been recently invented as the result of national and European research projects. The dissipative parts, where damage potentially concentrates are mostly small and dismountable to enable their easy replacement after strong earthquakes. However, these systems have not claimed a fair share of the steel construction market, as provisions for their design have not been included in the Eurocodes and only a few designers are confident enough to employ them. The INNOSEIS project, which has received funding from the Research Fund for Coal and Steel (RFCS) with the participation of 11 partners, aims to deal with this shortcoming. The target of the INNOSEIS project is on one side to disseminate knowledge on 12 innovative systems in order to reach a wider use in practical application and on the other side to offer the tools for formally promoting any new lateral-load resisting system to a code-approved status via a standardized performance-based methodology to determine reliable behaviour factors and confirm that the associated risk is within acceptable limits.

This Volume presents 12 innovative systems in the form of information brochures, out of which three (3) got the status of anti-seismic devices after fulfilling the requirements of the relevant European Standard EN 15129. The information brochures include description of the systems, experimental investigations, design rules, structural analyses and applications. The systems under discussion are dissipative connections, dissipative links, dissipative beam splices, replaceable shear links and shear panels, modified braces, self-centring devices as well as hysteretic devices, triangle or moon-shaped.

Besides this volume, other documents and actions such as preparation of design guidelines, establishment of a procedure to determine consistent behaviour factors, design of case studies and organization of seminars and workshops for disseminate

the material produced were prepared and carried out. More information on the project, its partners and activities are included in the site <http://innoseis.ntua.gr>, The material of this volume was jointly prepared by all partners of the project. Editor of this volume is the project Coordinator and leader of the relevant Work Package. The partners of INNOSEIS are as follows:

National Technical University of Athens (Coordinator)	Greece
Politehnica University of Timisoara	Romania
Politecnico di Milano	Italy
Universita di Napoli Federico II	Italy
Universita di Pisa	Italy
Rheinisch Westfälische Technische Hochschule Aachen	Germany
Instituto Superior Tecnico Lisbon	Portugal
University of Architecture, Civil Engineering and Geodesy	Bulgaria
Universiteit Hasselt	Belgium
Maurer Sohne Engineering GmbH&CO KG	Germany
ECCS–European Convention for Constructional Steelwork	Belgium



## AUTHORS

NATIONAL TECHNICAL UNIVERSITY OF ATHENS (NTUA)

Institute of Steel Structures

EL-15780 Athens, Greece

Chapters 1, 4

Authors: Ioannis Vayas, Pavlos Thanopoulos, Panagiotis Tsarpalis, Danai Dimakogianni

HASSELT UNIVERSITY

Construction Engineering Research Group

Campus Diepenbeek, Agoralaan building H, BE3590 Diepenbeek

Chapter 2

Authors: Jose Henriques, Herve Degee

RHEINISCH-WESTFAELISCHE TECHNISCHE HOCHSCHULE AACHEN (RWTH)

Institute of Steel Construction

52074 Aachen, Germany

Chapter 3

Authors: Benno Hoffmeister, Marius Pinkawa

POLITECNICO DI MILANO (POLIMI)

Department of Architecture, Built Environment and Construction Engineering Piazza Leonardo da Vinci, 32, 20133 Milan, Italy

Chapter 5

Authors: Carlo Andrea Castiglioni, Amin Alavi, Giovanni Brambilla

INSTITUTO SUPERIOR TÉCNICO (IST)

Department of Civil Engineering, Architecture and Georesources

Av. Rovisco Pais, 1049-001 Lisbon, Portugal

Chapter 6

Authors: Luís Calado, Jorge M. Proença, João Sio

POLITEHNICA UNIVERSITY OF TIMISOARA (UPT)

Steel Structures and Structural Mechanics department

Ioan Curea Street, no.1, Timisoara, Romania

Chapter 7, 8

Authors of Chapter 7: Adriana Chesoan, Aurel Stratan, Dan Dubina

Authors of Chapter 8: Calin Neagu, Florea Dinu, Dan Dubina

UNIVERSITET PO ARCHITEKTURA STROITELSTVO I GEODEZIJA (UACEG)

Department of Steel and Timber Structures

1 Hr. Smirnenski blvd. 1046 Sofia, Bulgaria

Chapter 9

Authors: Tzvetan Georgiev, Lora Raycheva, Dimo Zhelev, Nikolaj Rangelov

UNIVERSITY OF PISA (UNIP)

Department of Civil and Industrial Engineering

56122 Pisa, Italy

Chapter 10

Authors: Francesco Morelli, Agnese Natali, Walter Salvatore

MAURER SOHNE ENGINEERING GMBH & CO. KG (MSE)

Frankfurter Ring 193

80807 Munich, Germany

Chapter 11, 12

Author of Chapter 11: Christiane Butz

Authors of Chapter 12 : Valentina Renzi, Christiane Butz, Renzo Medeot

# CONTENTS

<b>PROLOG .....</b>	<b>I</b>
<b>AUTHORS .....</b>	<b>III</b>
<b>CONTENTS .....</b>	<b>V</b>
<b>1 INERD PIN CONNECTIONS .....</b>	<b>1</b>
1.1 INTRODUCTION .....	1
1.2 DESCRIPTION OF THE INERD PIN CONNETCION .....	1
1.3 LIMIT STATE MODELS .....	3
1.4 EXPERIMENTAL INVESTIGATIONS ON INERD PIN CONNECTIONS .....	6
1.5 DESIGN RULES .....	13
1.6 ANALYSES ON 2D BUILDING FRAMES .....	22
1.7 CONCLUSIONS .....	32
1.8 FIELD OF APPLICATION .....	33
1.9 PREVIOUS PUBLICATIONS .....	34
1.10 BIBLIOGRAPHIC REFERENCES .....	34
<b>2 INERD U CONNECTIONS .....</b>	<b>37</b>
2.1 INTRODUCTION .....	37
2.2 DESCRIPTION OF U-CONNECTION .....	37
2.3 LIMIT STATE MODELS .....	38
2.4 EXPERIMENTAL INVESTIGATIONS ON U-CONNECTIONS .....	39
2.5 SEISMIC DESIGN OF BUILDING FRAME .....	40
2.6 FIELD OF APPLICATION .....	46
2.7 BIBLIOGRAPHIC REFERENCES .....	46
<b>3 FUSEIS BEAM LINKS .....</b>	<b>49</b>
3.1 INTRODUCTION .....	49
3.2 DESCRIPTION OF FUSEIS BEAM LINK SYSTEM .....	49
3.3 LIMIT STATE MODELS .....	52
3.4 EXPERIMENTAL INVESTIGATIONS ON FUSEIS BEAM LINKS .....	53
3.5 DESIGN RULES .....	62
3.6 ANALYSES ON 2D BUILDING FRAMES .....	69
3.7 CONCLUSIONS .....	83
3.8 FIELD OF APPLICATION .....	84
3.9 PUBLICATIONS .....	84
3.10 BIBLIOGRAPHIC REFERENCES .....	85
<b>4 FUSEIS PIN LINKS .....</b>	<b>87</b>
4.1 INTRODUCTION .....	87
4.2 DESCRIPTION OF FUSEIS PIN LINKS SYSTEM .....	87
4.3 LIMIT STATE MODELS .....	90
4.4 EXPERIMENTAL INVESTIGATIONS ON FUSEIS PIN LINKS .....	91
4.5 DESIGN RULES .....	98
4.6 ANALYSES ON 2D BUILDING FRAMES .....	107
4.7 CONCLUSIONS .....	124
4.8 FIELD OF APPLICATION .....	124
4.9 PUBLICATIONS .....	125
4.10 BIBLIOGRAPHIC REFERENCES .....	125

<b>5</b>	<b>FUSEIS BOLTED BEAM SPLICES.....</b>	<b>127</b>
5.1	INTRODUCTION.....	127
5.2	DESCRIPTION OF THE FUSEIS BOLTED BEAM SPLICES .....	127
5.3	EXPERIMENTAL INVESTIGATIONS .....	129
5.4	ANALYTICAL MODELS .....	138
5.5	DESIGN RULES.....	140
5.6	ANALYSES AND DESIGN OF 2D FRAMES .....	150
5.7	FIELD OF APPLICATION.....	162
5.8	CONCLUSIONS.....	162
5.9	PUBLICATIONS.....	163
5.10	REFERENCES.....	163
<b>6</b>	<b>FUSEIS WELDED BEAM SPLICES .....</b>	<b>165</b>
6.1	INTRODUCTION.....	165
6.2	DESCRIPTION OF THE WELDED FUSEIS BEAM SPLICES .....	165
6.3	EXPERIMENTAL INVESTIGATIONS ON THE WELDED FUSEIS BEAM SPLICES.....	167
6.4	NUMERICAL MODELLING OF THE WELDED FUSEIS BEAM SPLICES.....	175
6.5	DESIGN GUIDELINES.....	176
6.6	ANALYSES ON A 3D BUILDING .....	184
6.7	CONCLUDING REMARKS .....	198
6.8	REFERENCES.....	199
6.9	ATTACHMENT A .....	201
<b>7</b>	<b>REPLACEABLE BOLTED LINK .....</b>	<b>203</b>
7.1	INTRODUCTION.....	203
7.2	DESCRIPTION OF REPLACEABLE BOLTED LINKS SYSTEM.....	203
7.3	EXPERIMENTAL INVESTIGATIONS ON REPLACEABLE BOLTED LINKS SYSTEM..	205
7.4	DESIGN RULES.....	210
7.5	ANALYSIS OF 2D BUILDING FRAMES.....	217
7.6	CONCLUSIONS.....	232
7.7	FIELD OF APPLICATION.....	233
7.8	PUBLICATIONS.....	233
7.9	BIBLIOGRAPHIC REFERENCES.....	234
<b>8</b>	<b>REPLACEABLE SHEAR PANEL.....</b>	<b>237</b>
8.1	INTRODUCTION.....	237
8.2	DESCRIPTION OF REPLACEABLE SHEAR PANELS .....	237
8.3	EXPERIMENTAL INVESTIGATIONS ON SHEAR PANELS.....	240
8.4	DESIGN RULES.....	247
8.5	ANALYSIS ON 2D BUILDING FRAMES .....	254
8.6	CONCLUSIONS.....	265
8.7	FIELD OF APPLICATION.....	266
8.8	PUBLICATIONS.....	266
8.9	BIBLIOGRAPHIC REFERENCES.....	266
<b>9</b>	<b>CONCENTRICALLY BRACED FRAME WITH MODIFIED BRACES (CBF-MB) .....</b>	<b>269</b>
9.1	INTRODUCTION.....	269
9.2	DESCRIPTION OF THE CBF-MB SYSTEM .....	269
9.3	ANALYTICAL MODELS .....	272

9.4	EXPERIMENTAL INVESTIGATIONS.....	274
9.5	DESIGN RULES .....	282
9.6	ANALYSES AND DESIGN OF 2D FRAMES .....	292
9.7	CONCLUSIONS .....	307
9.8	FIELD OF APPLICATION .....	308
9.9	PREVIOUS PUBLICATIONS.....	308
9.10	BIBLIOGRAPHIC REFERENCES .....	308
<b>10</b>	<b>STEEL SELF - CENTRING DEVICE.....</b>	<b>311</b>
10.1	INTRODUCTION .....	311
10.2	THE STEEL SELF-CENTERING DEVICE (SSCD) .....	314
10.3	MECHANICAL MODEL AND EXPERIMENTAL CHECK OF THE SSCD.....	318
10.4	APPLICATION TO THE DESIGN OF A COMMERCIAL BUILDING (A CASE STUDY)...	329
10.5	CONCLUSIONS .....	347
10.6	FIELD OF APPLICATION .....	348
10.7	PUBLICATIONS .....	348
10.8	BIBLIOGRAPHIC REFERENCES .....	348
<b>11</b>	<b>TRIANGLE STEEL HYSTERETIC DEVICE (TRSH).....</b>	<b>351</b>
11.1	INTRODUCTION .....	351
11.2	DESCRIPTION OF THE TRIANGULAR STEEL HYSTERETIC BRACING SYSTEM.....	351
11.3	ANALYTICAL MODEL .....	354
11.4	EXPERIMENTAL INVESTIGATIONS.....	359
11.5	DESIGN RULES .....	367
11.6	2D CASE-STUDY FRAME.....	373
11.7	CONCLUSIONS .....	381
11.8	FIELD OF APPLICATION .....	382
11.9	REFERENCES .....	382
<b>12</b>	<b>MOON-SHAPED STEEL HYSTERETIC DEVICE (MSSH) .....</b>	<b>383</b>
12.1	INTRODUCTION .....	383
12.2	DESCRIPTION OF THE MOON SHAPED STEEL HYSTERETIC DEVICE .....	383
12.3	STRUCTURAL MODELS .....	385
12.4	EXPERIMENTAL INVESTIGATIONS ON MSSH DEVICES .....	389
12.5	DESIGN RULES .....	395
12.6	ANALYSES OF A 2D BUILDING FRAME .....	401
12.7	CONCLUSIONS .....	410
12.8	FIELD OF APPLICATION .....	410
12.9	BIBLIOGRAPHIC REFERENCES .....	411



# 1 INERD PIN CONNECTIONS

## 1.1 INTRODUCTION

In the frame of the European Research Program of the Research Fund for Coal and Steel “Two Innovations for Earthquake Resistant Design” (Acronym: INERD), under contract number 7210-PR-316, two innovative dissipative connections were introduced, namely the U and pin connection, which is presented within this information brochure.

The INERD project contained extensive experimental, numerical and analytical investigations of the pin connection, and resulted in the drafting of a preliminary Design Guide, all of which are presented in the relevant Technical Reports and journal publications.

The object of this information brochure is to briefly describe the configuration of the INERD pin connection and to demonstrate the basic principles of its behaviour. Some typical experimental and analytical results are also presented, but emphasis is given to the modelling instructions and dimensioning rules that are needed for the analysis and design of structures containing the INERD pin connections. Also reference is made to a detailed case study, where these rules are applied.

## 1.2 DESCRIPTION OF THE INERD PIN CONNECTION

The INERD pin connection is used between the vertical brace of a building and its column, and can be realised with various layouts, like the ones shown in Fig. 1.1. It consists of two external plates, which are bolted or welded to the column flanges, and one or two internal plates, which are welded at the end of the brace. A pin, which can have a rectangular, rounded or circular cross section, passes through all the plates via appropriate-sized holes. The strong axis of the pin cross section can be parallel or perpendicular to the brace axis.

The initial design of the connection assumed one internal plate and a rectangular pin (Fig. 1.1a), but it was subsequently modified in order to include more layouts. During the INERD project, connections with two welded internal and two bolted external plates were investigated (Fig. 1.1b). The pins that were used were rectangular and rounded. Tests of the configuration with one internal plate took place in the frame of a national research project.

The connection behaves in a relatively simple way, which can be modelled with a beam that is subjected to 3- or 4-point bending. The element that acts as a beam is the pin, which is supported at the location of the external plates. The axial force of the brace is transferred through the internal plates to the corresponding points of the pin, and acts as one or two concentrated loads, depending on the number of internal plates. Since the resistance of the connection against axial force occurs through bending of the pin, it is independent of its direction. As a result, in order to distinguish

the two cases, it can be stated that “the plates of the INERD connection are in compression” when the brace is subjected to compression, and that “the plates of the INERD connection are in tension” in the opposite case.

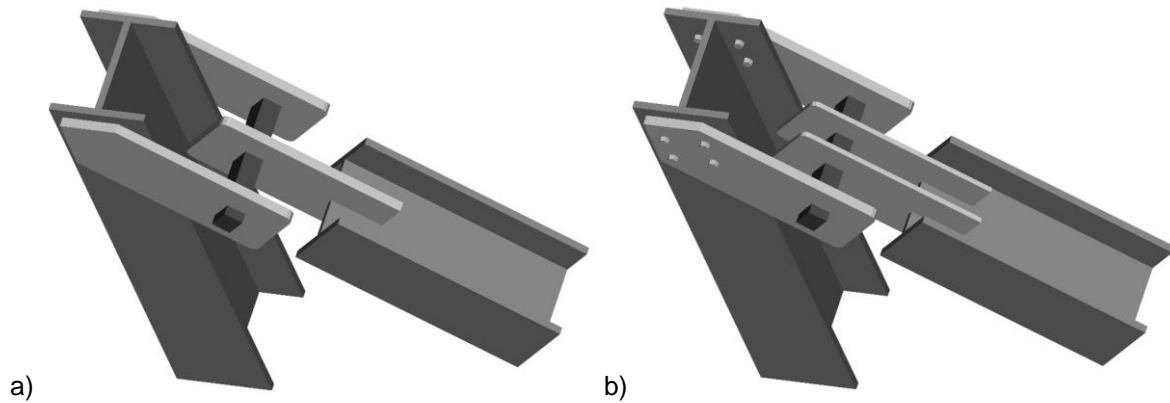


Fig. 1.1: Possible configurations of the INERD pin connection

The connection is designed in the Ultimate Limit State (ULS), excluding the seismic combinations, so that the pin will remain elastic. However, in case of the design earthquake, the braces are activated and subjected to significant axial forces, which results in the plastification of the pin, in order to dissipate the seismic energy. The resistance of the connection, including the anticipated overstrength, is designed to be lower than the brace resistance against buckling and, obviously, tension. As a result, the usual dissipation mechanism of a CBF, which is mainly due to the yielding of the tension diagonal, is not allowed to develop. Instead, the plastification is limited to the INERD connections, where plastic hinges are formed in the pin at the location of the plates. Due to the conversion of the axial force to bending of the pin, regardless of the force direction, the INERD connections behave in a similar manner for both the tension and compression diagonals.

The response of a typical INERD connection under tension is shown in Fig. 1.2. At the first stage of loading, the supports act as pinned, so the beam is simply supported (Fig. 1.2a) and the moment of the pin is concentrated in its middle (3- or 4-point bending). When the acting moment becomes equal to the plastic moment resistance of the pin, hinges are formed at the location of the internal plates and significant pin deformation takes place (Fig. 1.2b). As it was observed in the experimental investigation, the pin can facilitate very large displacements (of the order of magnitude of its height or even larger). As a result, at the second stage of loading, the end supports begin to act as fixed, resulting in the further increase of the connection resistance, until plastic hinges are formed also at the supports (Fig. 1.2c). At the final stage of loading, the pin resistance has been fully exploited, and the remaining stiffness of the connection, which is relatively low, is caused mainly due to strain hardening and the expansion of the plastic zones.



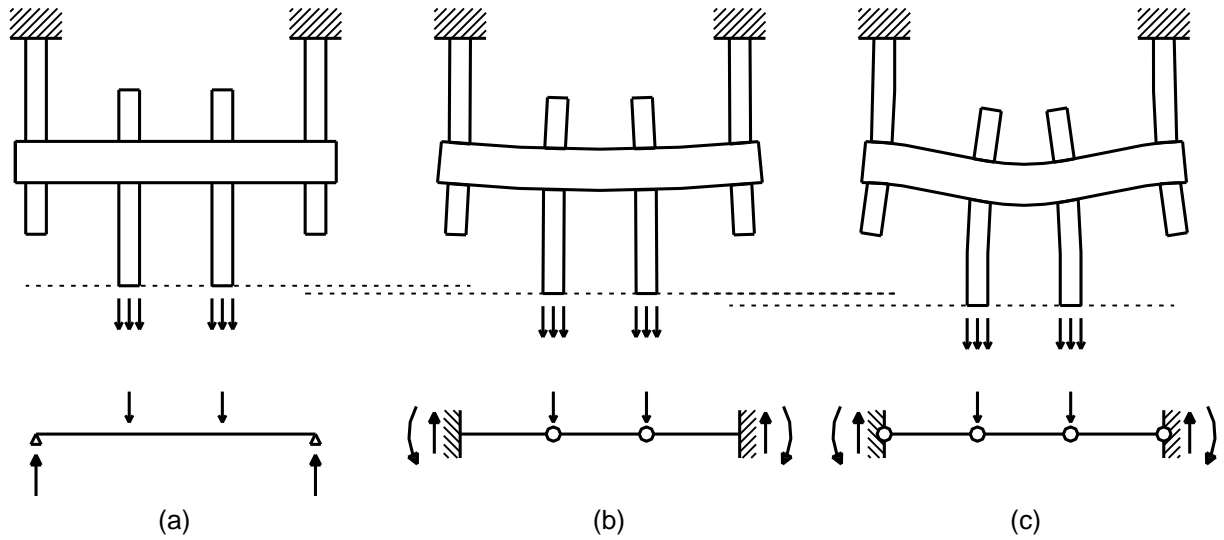


Fig. 1.2: Stages of loading of INERD pin connection and corresponding static model

It goes without saying that this simplified model of an ideal beam under bending is based on several assumptions, like ignoring shear/bending interaction and the lateral bending or relative rotation of the plates. Nevertheless, its accuracy is satisfactory for preliminary design and, mainly, it is a valuable key in order to demonstrate the basic characteristics and properties of the connection.

By varying the number of braced frames per direction, the configuration of the plates and the dimensions of the pins, the INERD pin system provides versatile possibilities for the efficient design of a seismic resistant steel structure.

### 1.3 LIMIT STATE MODELS

For the preliminary design of the INERD pin connections and the dimensioning of the test specimens a simplified beam model is introduced. This model is based on the assumption that the pin behaves like a beam, either simply-supported or fixed, depending on the stage of loading, with point loads at the location of the internal plates. The equivalent beam (Fig. 1.3a) models the behaviour of the connection with a tri-linear curve, as shown in Fig. 1.3b. The span  $d_{ext}$  of the beam is taken equal to the clear distance of the external plates. The axial force of the brace is modelled as two point loads that are applied at a distance  $a$  from the supports, which is equal to the clear distance between internal and external plates. It is noted that the term axial deformation or resistance of the connection describes a vector that is parallel to the brace axis.

As it is demonstrated in Fig. 1.3, the response of the connection can be modelled by two different static systems, the first for loading between points O and I, and the second for loading between points I and II. The former system corresponds to a simply-supported beam subjected to 4-point bending, meaning that the beam ends can rotate freely ( $K_{sup} = 0$ ). This system describes the response of the connection at

the initial stage of loading, until a plastic hinge is formed at the locations where the point loads are applied (point I at Fig. 1.3b). Subsequently, the axial deformation increases at a faster rate and the pin ends are fixed by the external plates ( $K_{sup} = \infty$ ), no longer allowing the free rotation. As a consequence, moments start to develop at the end supports, which are increased until plastic hinges are also formed at these points, a situation that corresponds to point II of Fig. 1.3b.

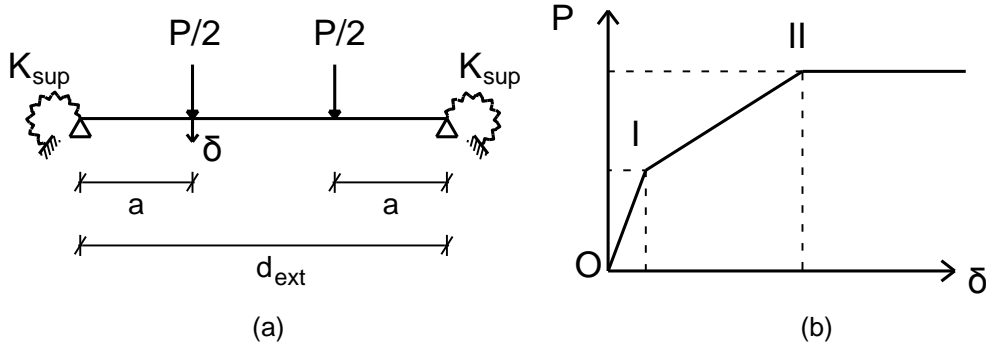
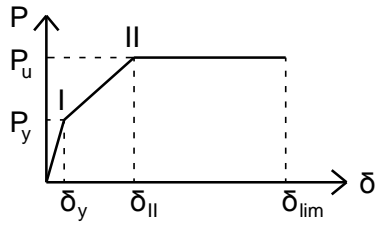
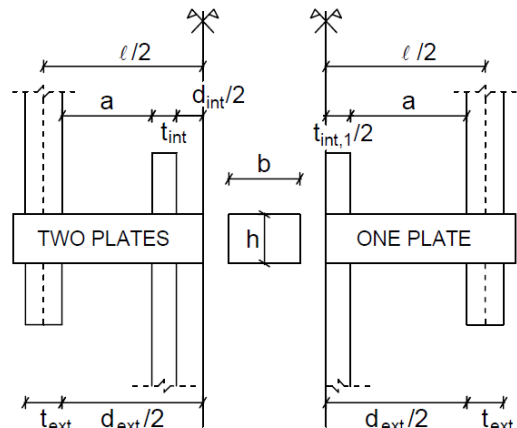
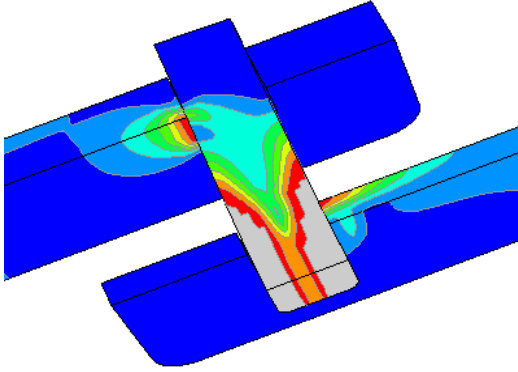
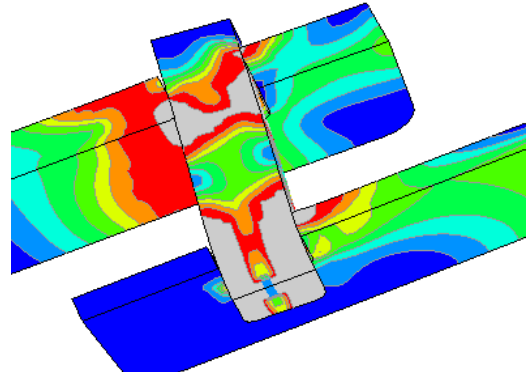


Fig. 1.3: Simplified analytical beam model: (a) equivalent static system and (b) tri-linear curve of axial force vs. deformation

The equations of the simplified analytical model are summarized in Table 1.1, where figures from FE analyses are also provided, in order to demonstrate the stress distribution at the stages of loading that correspond to points I and II. To ensure that this model provides accurate results, it is good practice to maintain some simple geometric limitations (e.g. minimum plate thickness and distance between plates), like the ones given in Table 1.3. In any case, it must be kept in mind that deviations from the results of the detailed model of §1.5.2 can be relatively large, so values taken from the simplified model should be considered as indicative, for the preliminary design of the connections.

**Table 1.1: Outline of simplified model of INERD pin connections [28]**

	Axial force	Axial deformation
Point I Yield “y”	$P_y = \frac{2 \cdot M_{pl}}{a/1.1}$	$\delta_y = 1.5 \cdot \frac{M_{pl}}{E \cdot I} \cdot \ell^2 \cdot \frac{a}{6} \cdot (3 - 4\alpha)$
Point II Ultimate “u”	$P_u = \frac{4 \cdot M_{pl}}{a/1.1}$	
Overstrength for capacity design	$1.3 \cdot P_u$	
Deformation capacity	$P_{lim} = P_u$	$\delta_{lim} = 0.8 \cdot a$
<p> <math>\ell</math> = axial distance between external plates  <math>a</math> = clear distance between external and internal plate  <math>\alpha = a / \ell</math>  <math>\approx 0.5</math> for one internal plate  <math>d_{ext}</math> = clear distance between external plates  <math>d_{int}</math> = clear distance between internal plates  <math>= 0</math> for one internal plate  <math>t_{ext}</math> = thickness of external plates  <math>t_{int}</math> = thickness of internal plates  <math>= \text{half the thickness for one internal plate}</math>  <math>E</math> = steel modulus of elasticity  <math>f_y</math> = steel yield stress  <math>I</math> = moment of inertia of pin cross section  <math>W_{pl}</math> = plastic modulus of pin cross section  <math>M_{pl}</math> = pin plastic moment resistance </p> <div style="display: flex; align-items: center;"> <div style="flex: 1;">  </div> <div style="flex: 1; padding-left: 20px;"> <p>For pins with rectangular cross section:</p> <math>W_{pl} = b \cdot h^2 / 4</math>  <math>I = b \cdot h^3 / 12</math>  <math>h, b</math> = pin height and width </div> </div>		
<div style="display: flex; justify-content: space-around;"> <div style="text-align: center;">  <p>Von Mises stresses at point I</p> </div> <div style="text-align: center;">  <p>Von Mises stresses at point II</p> </div> </div>		

## 1.4 EXPERIMENTAL INVESTIGATIONS ON INERD PIN CONNECTIONS

### 1.4.1 Experimental investigations on individual connections

#### 1.4.1.1 Test setup, description of specimens and loading history

The tests on the individual connections took place in IST Lisbon, and are described in detail in the Lisbon final report [12]. The specimens comprise four plates and a pin of rectangular or rounded cross section. The internal and external plates are connected together via much thicker plates, which substitute the column and brace, by providing stiff lateral support. At the same time, they connect the specimen with the equipment of the test setup, so that the load can be applied perpendicular to the axis of the pin. The test setup for the individual connections is shown in Fig. 1.4.

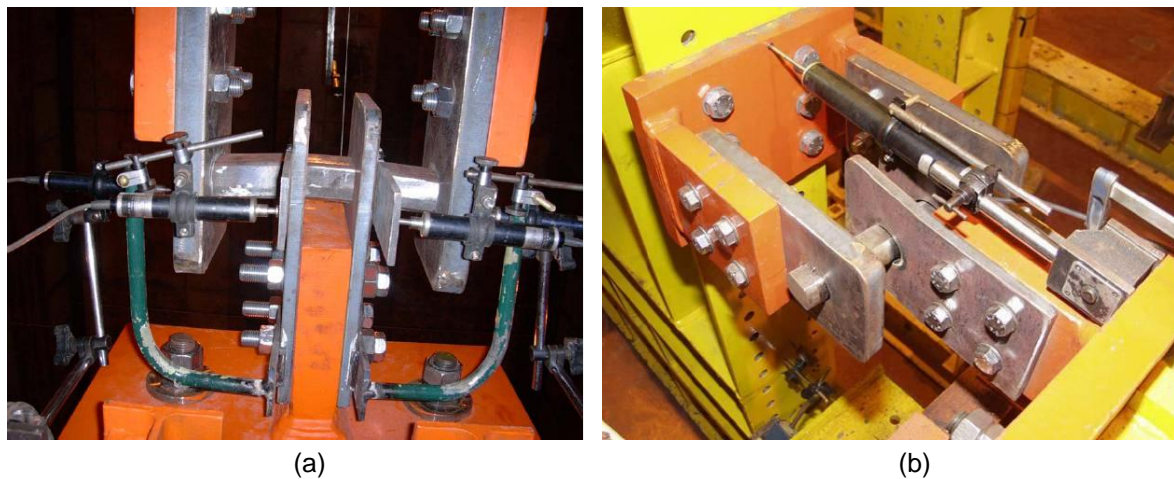


Fig. 1.4: Lisbon test setups for a pin of (a) rectangular and (b) rounded cross section

In total, four types of specimens were examined, for various combinations of the pin cross section and the distance of the internal plates, as shown in Table 1.2. The steel properties of the various parts were derived from material tests that were performed on coupons that were provided during the production of the various parts of the connection.

The specimens were subjected to three types of loading, always by controlling the applied displacement of the internal plates:

- Monotonic loading in compression.
- Cyclic loading with cycles of increasing magnitude according to the provisions of ECCS (European Convention for Constructional Steelwork) [20]. In particular, assuming a yield displacement equal to  $\delta_y$  (calculated analytically equal to 5 mm), this loading comprises a series of simple load cycles with magnitudes equal to  $\frac{1}{4}\delta_y$ ,  $\frac{1}{2}\delta_y$ ,  $\frac{3}{4}\delta_y$  and  $\delta_y$ , which are successively applied in both directions of loading. Afterwards, triple load cycles are applied for every multiple of the yield displacement ( $2\delta_y$ ,  $3\delta_y$ ,  $4\delta_y$  etc.) up until the failure of the specimen.

- Cyclic loading with cycles of constant amplitude. In particular, the rectangular pins were subjected to cycles of total width 30, 40, 50 and 60 mm, while cycles of 40 and 60 mm were applied to the rounded pins

Table 1.2: Specimen dimensions [mm]

<p><b>Type A</b></p> <p>180 350 30 240 30 15 70 15 320 41 51 50 87 40 50 70 70 70</p>	<p><b>Type B</b></p> <p>180 350 30 240 30 15 70 15 320 61 41 40 87.5 60 40 70 70 70</p>
<p><b>Type C</b></p> <p>180 350 30 240 30 15 50 15 320 41 51 50 87 40 50 80 50 80</p>	<p><b>Type D</b></p> <p>180 350 30 240 30 15 50 15 320 61 41 40 87.5 60 40 80 50 80</p>

#### 1.4.1.2 Results of monotonic tests

The pin connections showed a ductile behaviour with considerable load increase after going into the plastic region, which is caused due to strain hardening and the change of the bearing mechanism as explained in §1.3. The data that were recorded or calculated for all tests were the load-displacement history, the dissipated energy (total and plastic) and the connection stiffness. Indicative results are shown in Fig. 1.5.



Under cyclic loading, the pin connections exhibited excellent dissipative behaviour with wide hysteresis loops and significant resistance against low-cycle fatigue. It was found that the monotonic curve is practically identical to the skeleton curve of the cyclic loading. It was also observed that the loops showed significant pinching and that the resistance in compression is slightly larger than the resistance in tension, which can be justified by the lateral bending of the plates and the different bending stiffness they provide as supports.

The data that were recorded or calculated for all tests were the load-displacement history, the number of cycles until failure, the dissipated energy (total and per half-cycle) and the connection stiffness for each cycle. Indicative results are shown in Fig. 1.6.

From the constant amplitude tests (Fig. 1.7), best-fit and design S-N curves were derived in order to evaluate the pin behaviour under low-cycle fatigue, which proved to be very good, mainly due to the absence of welds or notches near the plastification zones.

## 1.4 EXPERIMENTAL INVESTIGATIONS ON INERD PIN CONNECTIONS

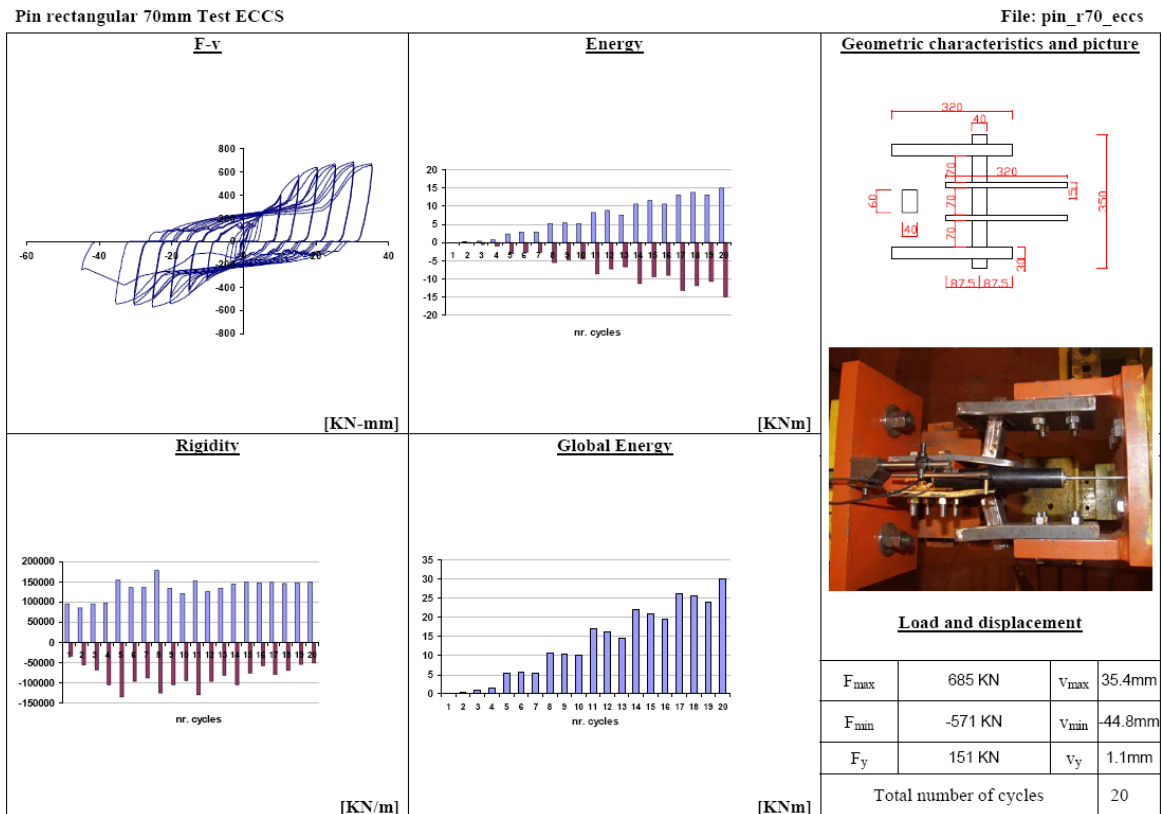
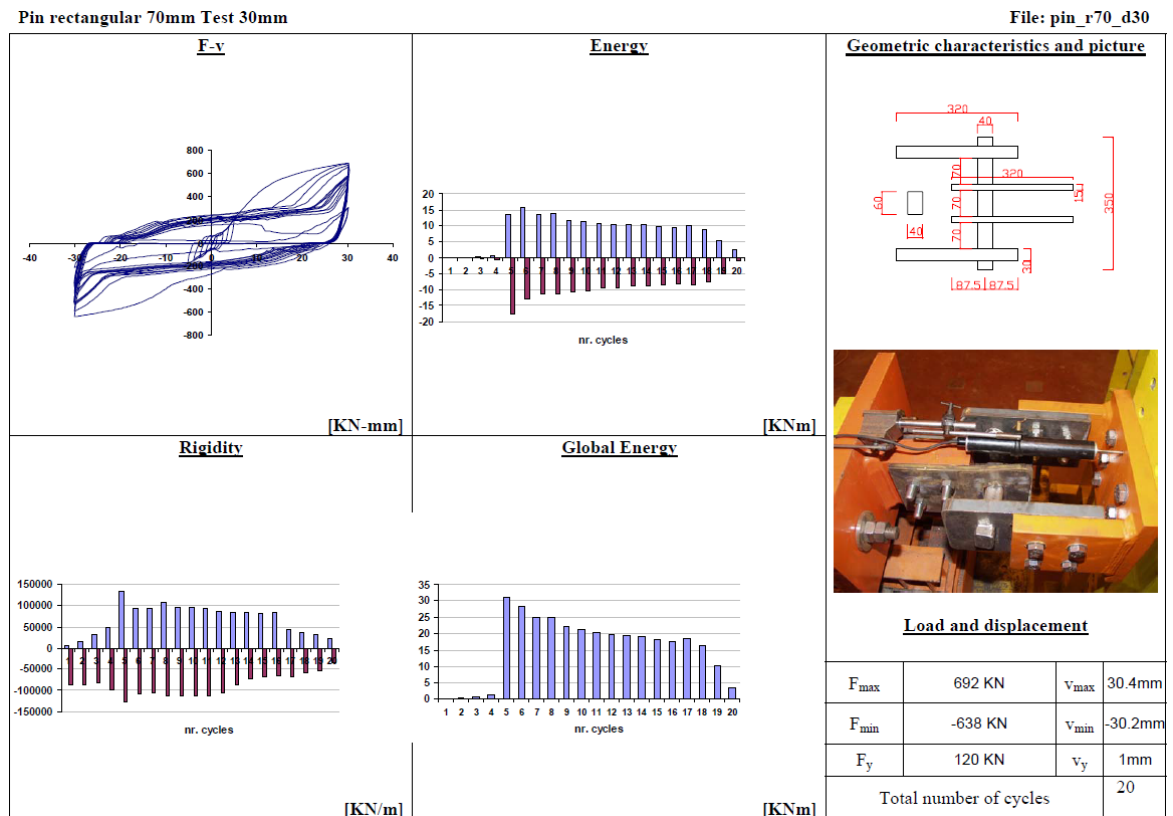


Fig. 1.6: Indicative results of ECCS loading – Specimen “TypeB”

Fig. 1.7: Indicative results of constant amplitude loading ( $\pm 30$ mm) – Specimen “TypeB”



### 1.4.2 Experimental investigations on overall frames

#### 1.4.2.1 Test setup, description of specimens and loading history

In addition to the tests on individual connections, full scale tests were performed on a frame containing INERD connections in order to better understand how the connections would behave as part of a more realistic structure. These tests took place in Politecnico di Milano, and are described in detail in the Milan final report [13]. The frame specimen had a height of 3.00 m and a width of 3.40 m (Fig. 1.8). The cross section of the columns was HEB 240, the beam HEB 200 and the braces HEB 160. The INERD pin connections were the same as the ones presented in Table 1.2.



Fig. 1.8: Milan test setup

The specimens were subjected to two types of loading, always by controlling the applied displacement at the top of the frame:

- Cyclic loading with cycles of increasing magnitude, according to the provisions of ECCS, as described in §1.4.1.1. The yield displacement  $\delta_y$  was analytically calculated equal to 6 mm. The initial cycles of loading (smaller than  $\delta_y$ ) were omitted for practical reasons.



## 1.4 EXPERIMENTAL INVESTIGATIONS ON INERD PIN CONNECTIONS

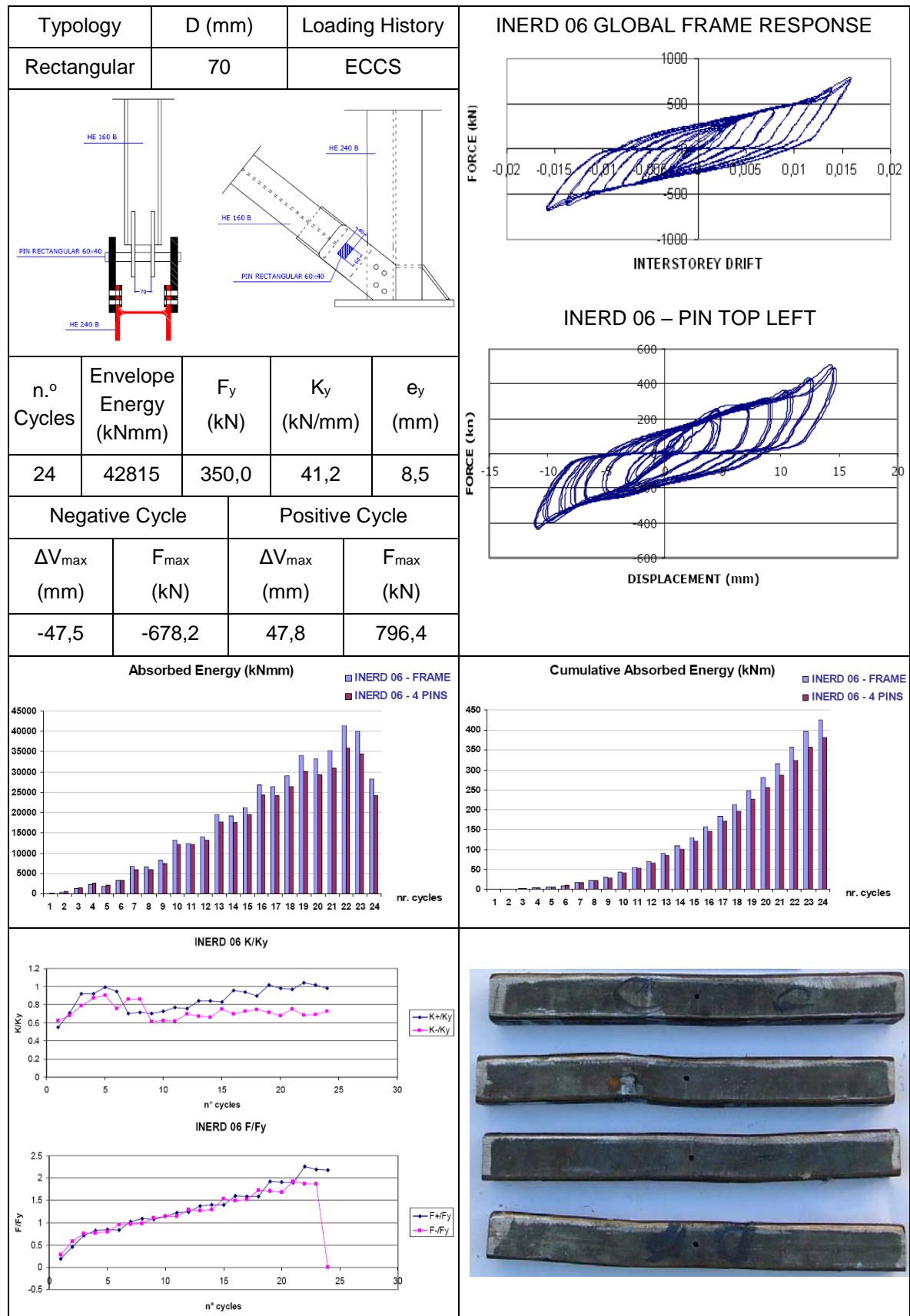


Fig. 1.9: Indicative results of ECCS cyclic loading (Milan) – Specimen “TypeB”

- Cyclic loading that corresponds to the response of a structure under a real earthquake. Specifically, the applied displacement corresponds to the response of the first storey of a typical six-storey building, as defined by nonlinear dynamic analysis. Due to the limitations of the equipment, the load was applied as quasi-static and not in real time.

#### 1.4.2.2 Test results

In the frame tests results, it was also observed that the pin connections exhibited excellent dissipative behaviour and it was confirmed that no problems were to be expected in the global behaviour of a frame containing such connections. The tests also verified that no local problems occurred in the connection e.g. due to the relative rotation and lateral deformation of the plates, slip or torsion of the pin etc.

Indicative results from the frame tests are shown in Fig. 1.9. The data that were recorded are similar as those of the individual connections. It is observed that the “positive” resistance, which corresponds to “pulling” the test frame, is slightly higher than the “negative” resistance, which corresponds to “pushing” the frame. Such a response is typical in experimental investigations since effects of out-of-plane deformations arise when the frame is pushed, while the test frame straightens when it is pulled.

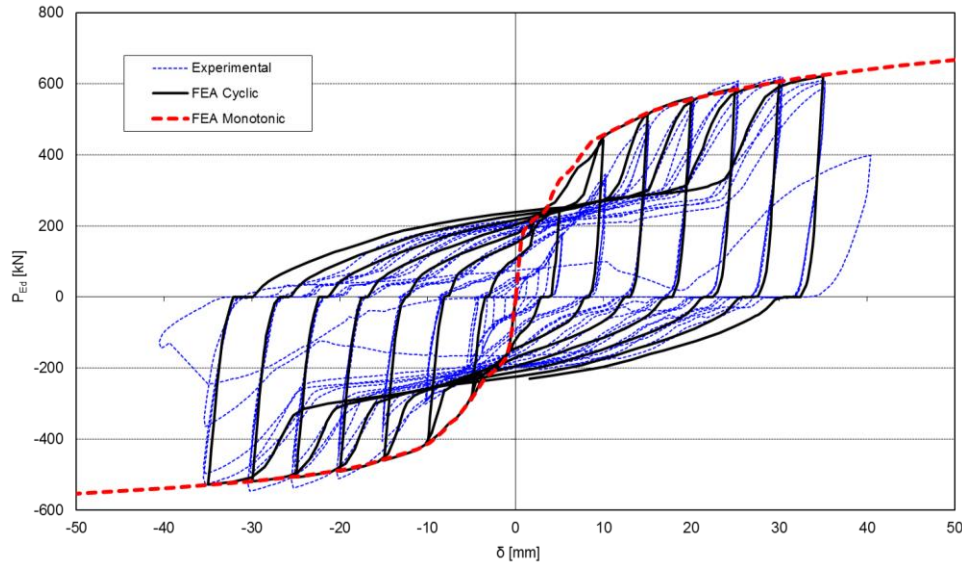


Fig. 1.10: Axial force  $P_{Ed}$  vs. axial deformation  $\delta$  – Comparison between experimental and FEA results for specimen “TypeD”

#### 1.4.3 Calibration of FE model

In Fig. 1.10 the response of the INERD connection from the test results is plotted vs. the results derived from FEM analysis. The material stress vs. strain law was defined in such a way that allowed for the inclusion of Bauschinger effects which proved to be important for cyclic loading. The axial force and deformation are positive when the braces are in compression.

It may be seen that the connection strength to positive loading (brace in compression) is higher than the relevant strength to negative loading (brace in tension), due to the different rotational stiffness of the external plates. Some pinching is observed due to ovalisation of the holes of the eye-bars, otherwise stable hysteretic loops are achieved. Similar satisfactory agreement between experimental and FEM results was observed for all types of tested connections. The analyses and the tests indicated that the monotonic curves represent skeleton curves of the cyclic ones, except at low deformations where they are stiffer than the latter. Based on this calibrated FE model, an extensive parametric numerical analysis was performed, to investigate various connection configurations.

## 1.5 DESIGN RULES

The conclusions from the analytical and numerical studies were summarized in a design guide for practical application. The design guide provides recommendations on the dimensioning of the INERD pin connections and the design of a frame containing such connections. The design methodology of this guide, is based on the provisions of EN 1993-1-1 [17] and EN 1998-1 [19]. Some clauses of EN 1998-1-1 were appropriately rearranged to cover the use of the dissipative connections. It also includes structural details and constructional recommendations.

### 1.5.1 Preliminary design and construction rules

For the preliminary sizing and dimensioning of the pins, the simplified limit state model presented in §1.3 and is summarized in Table 1.1, should be deployed. This fast and practical methodology can be used for the selection of the required number of braced bays, the cross section of the pins, the distance and dimensions of the plates, etc.

However, in order to determine the connection properties with increased accuracy and calculate the ductility and overstrength requirements of the frame, the detailed methodology of §1.5.2 must be implemented.

To ensure the more efficient response of the connections, the geometric requirements given in Table 5.1 should be satisfied. In this way, the validity of the design rules is guaranteed, as the dimensions of the connections are within the fields that were covered from the experimental and numerical investigations. In addition, the designer is protected from detailing flaws that could lead to inferior connection behaviour, e.g. by selecting thin, flexible plates.

**Table 1.3: Geometric requirements for INERD pin connections**

Shape of the pin cross section	$h \leq b \leq 2 \cdot h$
Minimum distance between plates	$a \geq h$
Thickness of external plates:	$t_{ext} \geq 0.75 \cdot h$
Thickness of internal plates:	$t_{int} \geq 0.5 \cdot t_{ext}$ for two plates $t_{int} \geq t_{ext}$ for one plate
Basic dimensions of an INERD pin connection: $b$ the width of the pin $h$ the height of the pin $t_{ext}$ the thickness of the external plate $t_{int}$ the thickness of the internal plate $d_{ext}$ the clear distance between the external plates $d_{int}$ the clear distance between the internal plates $a$ the clear distance between the internal and external plates	

Aiming to avoid excessive overstrength, the steel material of the dissipative pins shall have controlled properties. In accordance with EN 1998-1-1 [19] its yield strength must have a maximum value of:

$$f_{y,max} \leq 1.1 \cdot \gamma_{ov} \cdot f_y \quad \text{Eq. (1.1)}$$

where  $\gamma_{ov} = 1.25$  is the overstrength factor  
 $f_y$  is the nominal value of the yield strength

If the properties of the pin material are controlled and its maximal yield strength is guaranteed below that described by eq. (1.1), the overstrength factor can be reduced accordingly in order to achieve a more economical design.

### 1.5.2 Design for linear elastic analysis

The design rules are intended to ensure that yielding will occur in the pins of the INERD connections, prior to any yielding or buckling of any other elements. Therefore, the design of buildings with INERD pin connections is based on the assumption that mainly the pins will dissipate energy via the formation of plastic hinges. The following design methodology may be applied:

#### 1) Simulation

A building with INERD pin connections may be simulated with a common structural software with an elastic model. The connections can be modelled with zero-length linear springs whose constant can be defined as in Equations (1.2):

$$K_{pin} = \frac{32 \cdot E \cdot I}{l^3} \text{ for one plate} \quad \text{Eq. (1.2a)}$$

$$K_{pin} = \frac{8 \cdot E \cdot I}{a \cdot l^2 \cdot \alpha \cdot (3 - 4 \cdot \alpha)} \text{ for two plates} \quad \text{Eq. (1.2b)}$$

Since a frame with INERD connections is essentially a braced frame, the beam-to-column connections and column bases are formed as simple in order to achieve an economic design and to avoid other members from resisting seismic loads. The bases of all the columns of the building are also pinned.

## 2) Analysis

Static linear analysis is performed under dead and live loading and the members of the main frame are dimensioned according to the provisions of EN1993-1-1 [17] for the ULS and SLS combinations. The internal forces due to seismic loading are calculated with the conventional method of Multi-Modal Response Spectrum Analysis, where the number of modes of vibration considered in each direction is such that the sum of the effective mass is at least equal to 90% of the total mass. The design spectrum shall be defined with a maximum behaviour factor equal to 4 for High Ductility Class and 3 for Medium Ductility Class. In case an INERD connection is only used in one end of the brace, the behaviour factor should be reduced accordingly (3 for DCH and 2 for DCM).

## 3) Limitation of interstorey drift

For a seismic action with a larger probability of occurrence than the design earthquake, it is important to satisfy the damage limitation requirement. In this way, it is ensured that, for a seismic action with a lower return period, the non-structural elements of the building will not be seriously damaged and that the building will remain operational with no or minimal repairs.

In linear analysis, the displacements induced by the design seismic action  $d_s$  shall be calculated on the basis of the elastic deformations  $d_e$  of the structural system through the expression:

$$d_s = q \cdot d_e \quad \text{Eq. (1.3)}$$

In case the capacity ratios  $\Omega$  of the dissipative elements are low, the calculation of the design interstorey drift based on  $d_s$  is conservative, and a reduction factor  $q_\Omega$ , equal to the capacity ratio of the connections, may be employed as follows:

$$d_s = q \cdot q_\Omega \cdot d_e \quad \text{Eq. (1.4)}$$

The design interstorey drift of each storey  $d_r$  is defined as the difference of the average lateral displacements at the top and bottom of this storey, and must be limited according to EN1998-1. The limiting value depends on the type of the non-structural elements and the importance class of the building.

#### 4) Second order effects

The possible influence of second order effects shall be taken into account with the interstorey drift sensitivity coefficient  $\theta$  according to the provisions of EN1998-1. Coefficient  $\theta$  is calculated for both directions and each floor of the building:

$$\theta = \frac{P_{tot} \cdot d_r}{V_{tot} \cdot h_{story}} \quad \text{Eq. (1.5)}$$

where  $P_{tot}$  is the total gravity load at the storey under consideration  
 $V_{tot}$  is the total seismic storey shear

Alternatively, coefficient  $\theta$  may be calculated by a linear buckling analysis through the factor  $\alpha_{cr}$ , the factor by which the design loading has to be increased to cause elastic global instability. The analysis is carried out under the constant gravity loads of the seismic combination ( $1,0 \cdot G + 0,3 \cdot \phi \cdot Q$ ) and produces the buckling modes. The dominant modes of x and y directions are chosen and the correspondent  $\alpha_{cr}$  values are calculated as follows:

$$\alpha_{cr} = \frac{1}{\theta} = \frac{F_{cr}}{F_{Ed}} \quad \text{Eq. (1.6)}$$

where  $F_{cr}$  is the elastic critical buckling load for global instability mode based on initial elastic stiffness  
 $F_{Ed}$  is the design loading for the seismic combination

To take into consideration the inelastic displacements of the building,  $\alpha_{cr}$  shall be divided by the  $q$  factor:

$$\theta = \frac{q}{\alpha_{cr}} \quad \text{Eq. (1.7)}$$

The provisions of EN1998-1 state that if the interstorey drift sensitivity coefficient is limited to  $\theta \leq 0,1$ , the second order effects can be safely ignored. If  $0,1 < \theta < 0,2$ ,

second-order effects may approximately be taken into account by multiplying the relevant seismic action effects by a factor equal to  $1/(1-\theta)$ . If  $0.2 < \theta < 0.3$ , a more accurate second order analysis should be performed. Values of  $\theta > 0.3$  are not allowed.

## 5) Dissipative elements verifications

### a) Axial resistance

The resistance of the pin connections is calculated at the yield and ultimate points in order to design the structure against static and seismic loads. The curve of the axial force vs the axial deformation is practically tri-linear as shown in Fig. 1.11. The resistance against yield (Point I) is given as the minimum of two values, depending if the pin behaves primarily in bending or in shear:

$$P_{y,Rd} = \min \left\{ \frac{1.7 \cdot M_{pl}}{a_{red,I} \cdot \gamma_{py}} ; k_{pin} \cdot \frac{2 \cdot M_{pl}}{a \cdot \gamma_{py}} \right\} \quad \text{Eq. (1.8)}$$

where  $M_{pl} = W_{pl} \cdot f_y$  is the plastic moment resistance of the pin

$a_{red,I} = a - 0.5 \cdot h$  the reduced lever arm for point I

$k_{pin} = 1 + 0.1 \cdot \frac{b}{h}$  is the pin shape factor with  $1.1 \leq k_{pin} \leq 1.2$

$\gamma_{py} = 1.05$  safety factor for yield due to model uncertainty

The yield resistance of the connection must be larger than the axial force of the static and frequent seismic combinations.

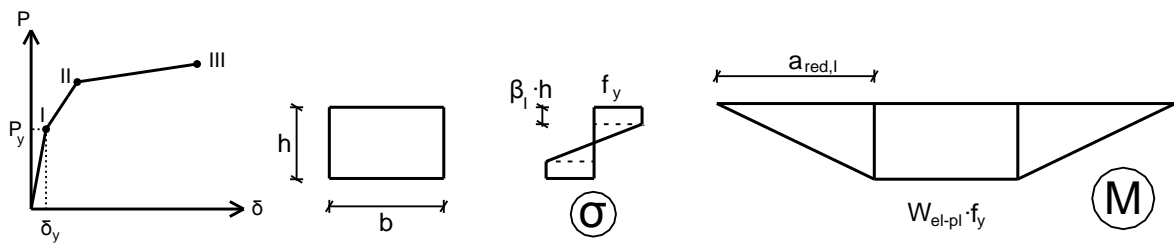


Fig. 1.11: Normal stresses of the pin and moment diagram at the point of first yield

For the calculation of the ultimate resistance of the connection, the reduced lever arm of point III is used:

$$a_{red,III} = a - h \quad \text{Eq. (1.9)}$$

For  $a_{red,III} \leq 0$  the pin behaves primarily in shear, although such a case is prevented by the geometrical restrictions of Table 5.1, as it is not recommended.

The ultimate resistance in this case is:

$$P_{u,Rd} = k_{pin} \cdot \frac{2 \cdot b \cdot h \cdot f_y}{\sqrt{3} \cdot \gamma_{pu}} \quad \text{Eq. (1.10)}$$

where  $\gamma_{pu} = 1.1$  safety factor for ultimate load due to model uncertainty

For  $a_{red,III} > 0$  the pin behaves in bending and shear (Fig. 1.12) and the ultimate resistance of the connection due to bending of the pin is given in equation (1.11a). The remaining capacity of the pin to undertake shear defines the ultimate resistance of the connection in shear, as defined in equation (1.11b). The factor  $\beta_{III}$  defines the percentage of the pin that has undergone significant plastic deformation on each side, with  $0 \leq \beta_{III} \leq 0.5$ . The ultimate resistance of the connection is found through an iterative process by changing factor  $\beta_{III}$ , so that the two values of equations (1.11a) and (1.11b) become equal.

$$P_{u,M,Rd} = k_{pin} \cdot \frac{4 \cdot M_u}{a_{red,III} \cdot \gamma_{pu}} \quad \text{Eq. (1.11a)}$$

$$P_{u,V,Rd} = k_{pin} \cdot \frac{2 \cdot b \cdot (1 - 2 \cdot \beta_{III}) \cdot h \cdot f_y}{\sqrt{3} \cdot \gamma_{pu}} \quad \text{Eq. (1.11b)}$$

where  $M_u = W_{u,pl} \cdot f_{mid}$  the ultimate plastic resistance of the pin  
 $f_{mid} = f_y + (f_u - f_y) \cdot \lambda_f / 2$  the maximum normal stress of the pin  
 $\lambda_f = \left( \frac{a - h}{2 \cdot h} \right)^2$  a factor for the influence of shear with  $0 \leq \lambda_f \leq 1$   
 $W_{u,pl} = b \cdot h^2 \cdot \left[ \beta_{III} - \beta_{III}^2 + \chi \cdot (0.5 - \beta_{III})^2 \right]$  the plastic modulus of the pin,  
 taking into account the reduction due to the shear stresses  
 $\chi = \sqrt{1 - (f_y / f_{mid})^2}$

The ultimate resistance of the connection must be larger than the axial force of the design seismic combinations, and is also used for the capacity design of connecting members.

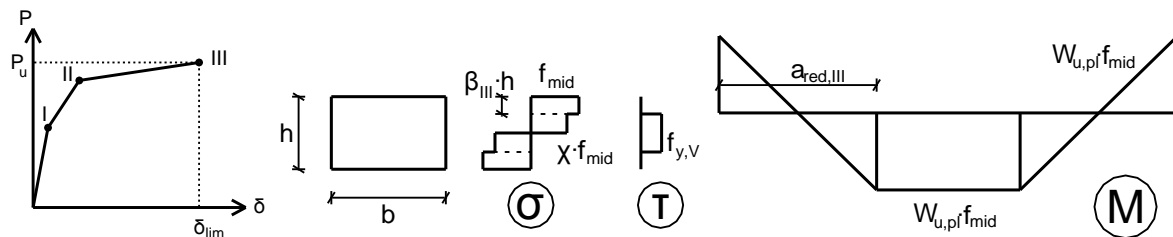


Fig. 1.12: Normal and shear stresses of the pin and moment diagram at the point of ultimate resistance



It was generally observed that the resistance of the pin connections under tension can be somewhat smaller than the one under compression. However, this effect is minimized by proper detailing and is not taken into account during the design. The axial resistance at point II can be taken as the average of the corresponding values at points I and III.

b) Global dissipative behaviour

An overstrength factor is defined for every pinned connection:

$$\Omega_i = \frac{P_{u,Rd,i}}{P_{Ed,i}} \quad \text{Eq. (1.12)}$$

In order to achieve a homogeneous global dissipative behaviour of the structure, it should be checked that the maximum overstrength ratio  $\Omega_{max}$  over the entire structure does not differ from the minimum value  $\Omega_{min}$  by more than 25%:

$$\frac{\Omega_{max}}{\Omega_{min}} \leq 1.25 \quad \text{Eq. (1.13)}$$

c) Axial deformations

The INERD pin connections must undertake significant deformations in order to dissipate energy, so it must be verified that they have adequate deformation capacity. This can be accomplished by limiting the interstorey drift:

$$d_r \leq \frac{1.6 \cdot a}{H \cdot \cos \varphi} \quad \text{Eq. (1.14)}$$

where  $H$  is the height of the storey under consideration  
 $\varphi$  is the angle of the brace with the horizontal line

It must be noted that if only one INERD connection is to be used on the ends of the braces, the limiting value of eq. (5.14) must be reduced by 50%.

6) Non-dissipative element verifications

The beams, columns and braces of the frame, as well as the non-dissipative elements of the connections (plates, bolts, welds etc.) shall be designed based on the capacity resistance of the pins, rather than the action calculated from the analysis, in order to ensure the energy dissipation and failure mechanisms.

a) The resistance  $R_d$  of welds or bolts of the INERD pin connection must satisfy the criterion:

$$R_d \geq 1.1 \cdot \gamma_{ov} \cdot P_{u,Rd} \quad \text{Eq. (1.15)}$$

where  $P_{u,Rd}$  is the ultimate resistance of the pin connection under consideration  
 $\gamma_{ov} = 1.25$  is the recommended overstrength factor

For bolted connections, High Strength Friction Bolts should be used (Categories B, C or E according to EN1993-1-8).

b) Diagonal members shall be verified to yielding and buckling assuming the exhaustion of the capacity of the pins at their ends:

$$N_{Ed} = \Omega_{\max} \cdot P_{u,Rd} \quad \text{Eq. (1.16)}$$

where  $\Omega_{\max}$  is the maximum value of all the pinned connections of the diagonals

c) Beams and columns connected to braces with flexible INERD connections should meet the following minimum resistance requirement:

$$N_{pl,Rd}(M_{Ed}) \geq N_{Ed,G} + 1.1 \cdot \gamma_{ov} \cdot \Omega_{\min} \cdot N_{Ed,E} \quad \text{Eq. (1.17)}$$

where  $N_{pl,Rd}(M_{Ed})$  is the axial design resistance of the frame member according to EN1993, taking into account the interaction with the bending moment  $M_{Ed}$   
 $N_{Ed,G}$  is the axial force of the frame member due to non-seismic actions of the seismic combinations  
 $N_{Ed,E}$  is the axial force of the frame member due to the seismic action of the seismic combinations  
 $\Omega_{\min}$  is the minimum value of all the pinned connections of the diagonals

### 1.5.3 Design for nonlinear analysis (Pushover)

The structural model used for elastic analysis shall be extended to include the response of structural elements beyond the elastic range and estimate expected plastic mechanisms and the distribution of damage through a pushover analysis.

Since the ductile elements are the INERD pin connections, the linear springs that describe them will be replaced by nonlinear springs whose properties were determined by the experimental results and the FE analyses. The recommended material law of the nonlinear springs is shown in Fig. 1.13. It should be noted that the curve can be conservative when compared to the monotonic test curves, without taking into account favourable effects like strain hardening, catenary action etc. In addition, three Performance Levels are defined on the curve, namely Immediate Occupancy (IO), Life Safety (LS) and Collapse Prevention (CP).

The values that are proposed in Fig. 1.13 refer to the response of the connection both under compression and tension, as it is assumed that the geometric requirements of Table 5.1 are satisfied, or that lateral bending of the plates is prevented via mechanical means.

Point	P	$\delta_{pl}$
A	0	0
B	$P_{yd}$	0
C	$P_{ud}$	$0.5 \cdot h$
D	$P_{ud}$	$a$
E	$0.5 \cdot P_{ud}$	$a$
F	$0.5 \cdot P_{ud}$	$1.5 \cdot a$
Acceptance criteria ( $\delta_{pl}$ )		
IO	$0.25 \cdot h$	
LS	$0.6 \cdot h$	
CP	$0.8 \cdot a$	

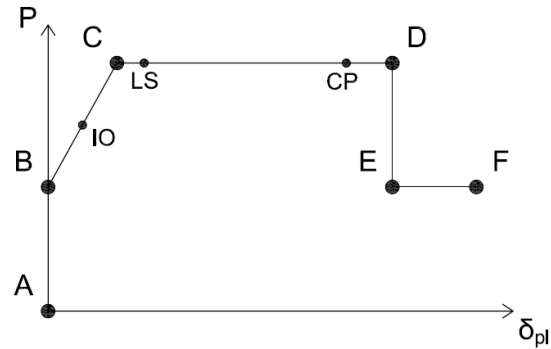


Fig. 1.13: Proposed nonlinear properties of the INERD pin connection spring

The hinge properties of the non-dissipative elements shall be calculated according to the provisions of relevant codes (e.g. FEMA-356). Since the frame is braced, all members are subjected primarily to axial forces. Therefore, columns and braces must have potential “hinges” that allow for yielding under tension and buckling under compression (combined with bending moment, if relevant). Alternatively, non-dissipative elements can be modelled without any hinges as long as it is verified that all acting forces and moments remain below the corresponding plastic resistance.

#### 1.5.4 Design for nonlinear dynamic analysis

The most accurate way to investigate the seismic response of a steel building with INERD pin connections is by performing a nonlinear dynamic analysis with an earthquake accelerogram. This type of analysis provides a detailed record of the global response of the structure, accumulated damage of the connections, maximum and residual interstorey drifts etc.

The nonlinear law that was used for the INERD connection springs for the static nonlinear analysis, described in §1.5.3, must be expanded in order to exhibit an adequate hysteretic behaviour. The proposed hysteretic law is shown in Fig. 1.14. It was defined in software OpenSees, with the parallel use of two hysteretic materials with different force-deformation laws and pinching properties, in order to accurately calibrate the hysteretic behaviour with the results of the cyclic tests.

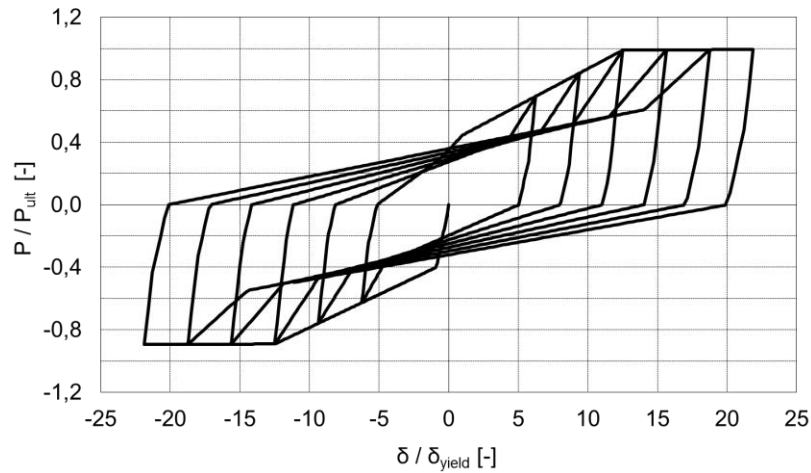


Fig. 1.14: Hysteretic behaviour of the INERD pin connection nonlinear spring

Significant axial deformations will develop within the connections as a result of the seismic response of the structure. From the history of the axial force and plastic deformation of the connection, the damage index for load cycles of variable amplitude can be determined with the Palmgren – Miner law of accumulated damage. The number of cycles to be sustained by the system is dictated by low-cycle fatigue considerations, which deal with the deformation and strain histories, rather than the stress histories which are more suitable for high-cycle fatigue. The drift ranges per cycle can be applied at the experimental fatigue curve that was derived during the Lisbon tests, in order to calculate the number of the correspondent cycles  $N$ .

## 1.6 ANALYSES ON 2D BUILDING FRAMES

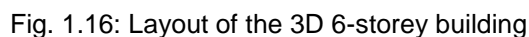
All the analytical models, the results from the experimental and numerical investigation and the proposed design rules, were verified through numerical analyses of 2D building frames with software OpenSees. The frames were part of a realistic 3D building, and were examined both with classic concentric braces and with braces with INERD pin connections. Initially the frames were designed through elastic analysis at ULS and SLS, including capacity design. Nonlinear static and dynamic analyses followed to investigate their response beyond the elastic range and confirm the proposed behaviour factor.

### 1.6.1 Description of examined building frames

#### 1.6.1.1 Geometry and assumptions

Three basic 2D frame configurations were thoroughly examined with static and dynamic nonlinear analyses, in addition to their design according to the Eurocodes, the Greek Seismic Code and the INERD pin design rules, where relevant. The frames had three, six and nine storeys, as shown in Fig. 1.15. In addition, an alternative 3D 6-storey building was examined as a case study (Fig. 1.16), in order

Steel quality is S355 and I-sections were used for all frame members, namely HEB for the columns, IPE for the beams and HEA for the braces. Realistic assumptions were made for the buckling lengths of all members under compression and/or bending. For each storey, a diaphragm was deployed between all the nodes, thus modelling the effect of the composite floor.



The braces had either full-strength bolted connections or INERD pin connections, whose characteristics were based on the buckling resistance of the diagonals or were derived after applying the proposed design rules. The cross sections of all members, as well as the connections vary along the height of the buildings, in order to ensure a homogeneous dissipative response as well as an economic design. The loads that were considered for the frames are summarized in Table 6.1.

**Table 1.4: Static and seismic loading of frames under investigation**

Gravity loads	
Dead load (excl. self-weight of steel)	6.0 kN/m <sup>2</sup>
Live load	3.0 kN/m <sup>2</sup> for the 2D frames 5.0 kN/m <sup>2</sup> for the 3D case study
Seismic loads (Greek National Code EAK2000)	
Ground type	B ( $T_B = 0.15$ ses, $T_C = 0.60$ sec)
Peak ground acceleration	$A = 0.24 \cdot g$ (seismic zone II)
Importance class	$\Sigma 2$ ( $\gamma_I = 1.0$ )
Behaviour factor	$q = 3$ for classic CBF $q = 4$ for INERD connections
Foundation coefficient	$\theta = 1.0$
Damping ratio	4% (steel bolted structures)
Seismic combination coefficient for the live loads	$\psi_2 = 0.30$

#### 1.6.1.2 Simulation

All members were modelled as linear beam or truss elements, unless otherwise stated. The frames that were examined have concentric braces and, therefore, all the beam-to-column connections and column bases are designed as simple connections. The frame beams were designed as steel elements, i.e. no composite action was taken into account.

The hysteretic behaviour of all dissipative elements (braces, INERD connections) was modelled in such a way, as to provide accurate results for linear and nonlinear, static or dynamic, analyses. The hysteretic law of the braces is shown in Fig. 1.17, while for the INERD connections (zero-length springs) it was explained in §1.5.4 and Fig. 1.14. For both cases, it was verified that the response in monotonic tension and compression is very accurate. For cyclic loading, the response is calibrated as best as possible with experimental results [7, 12].

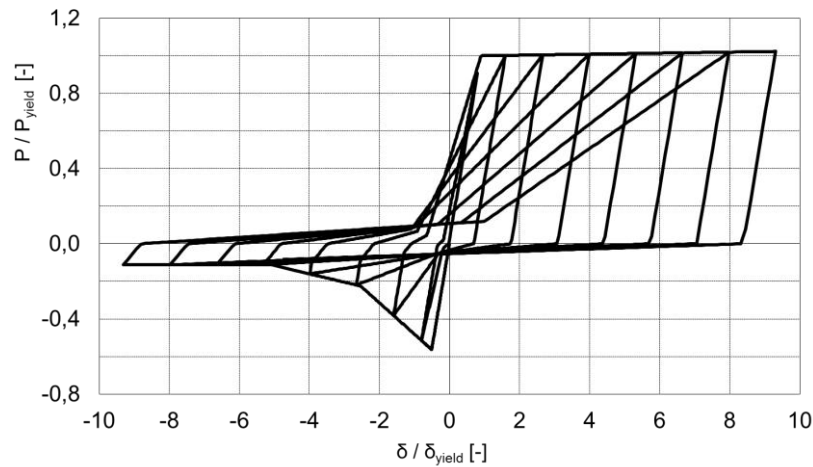


Fig. 1.17: Hysteretic behaviour of a typical brace

### 1.6.2 Linear and response spectrum analysis

The frames can be modelled by use of a common structural software and designed based on the provisions of the Eurocodes and the design rules of §1.5.2. In case it is not possible to model the three elements of the INERD brace (e.g. due to instabilities), it is possible to model it with one truss element. The stiffness of the combined element can be calculated by adding the stiffness of the three springs in series (two connections and a brace of length  $L_{br}$ ). The full design of the 3D building case study is demonstrated in detail in [28].

For the static loads, linear analysis can be performed, while the seismic loads are analysed with multi-modal response spectrum analysis. The results are not presented within. In Fig. 1.19, the fundamental eigen-period for the initial stiffness of every 2D frame is shown. The designation of each frame is “storeys” × “bays”, with the letter “d” used for frames with INERD connections, while no designation corresponds to the classic CBF.

### 1.6.3 Nonlinear static analyses (Pushover)

For the six 2D frames with classic CBF and INERD pin connections (marked “d”), pushover analyses were performed, with a triangular force distribution. The results are shown in Fig. 1.18, where the total base shear (expressed as a % of the total vertical load) is plotted as a function of the displacement at the top (expressed as a % of the total height of the building). The following observations can be made:

- The frames with classic CBF are stiffer than the frames with INERD pin connections. This is valid because of the influence of the compression diagonals. After the buckling of these diagonals, the frame quickly loses its stability.
- The frames with classic CBF have larger lateral resistance. This is also to be expected, as the resistance of the INERD pin connections is limited by the resistance against buckling of the diagonal. Therefore, the braces with the

INERD connections can resist a smaller base shear than the corresponding tension and compression diagonal.

- The frames with INERD pin connections show significant ductility when compared to the corresponding frames with full strength connections. The main reason for this, is the capacity of the dissipative connections to undertake large deformation without a drop in their resistance, while the braces are protected against buckling. This buckling of the compression diagonal that is allowed in the classic CBF, results in a rapid decrease of the lateral stiffness and increase of the load of the tension diagonal.

The latter observation can justify the selection of a higher behaviour factor  $q$  for the frames with INERD connections, in comparison to the classic CBF.

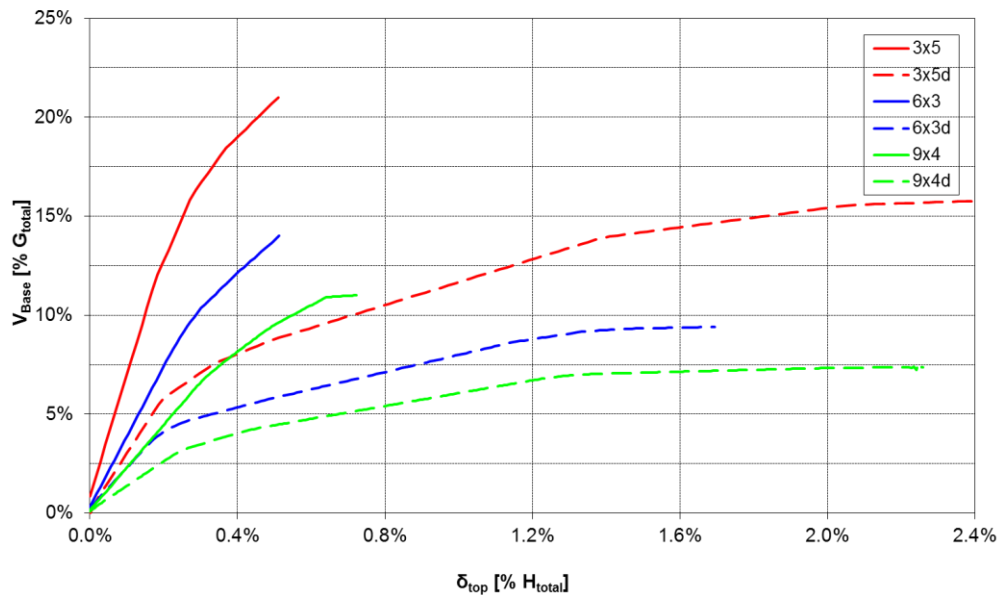


Fig. 1.18: Pushover curves of the frames with full-strength and INERD pin connections

#### 1.6.4 Nonlinear dynamic analyses (time-history)

The seismic response of the frames was investigated with nonlinear dynamic analyses under real seismic records, with the software OpenSees. Four natural and two artificial accelerograms with quite different characteristics were used. The scaled response spectrums of the earthquake records are shown in Fig. 1.19.



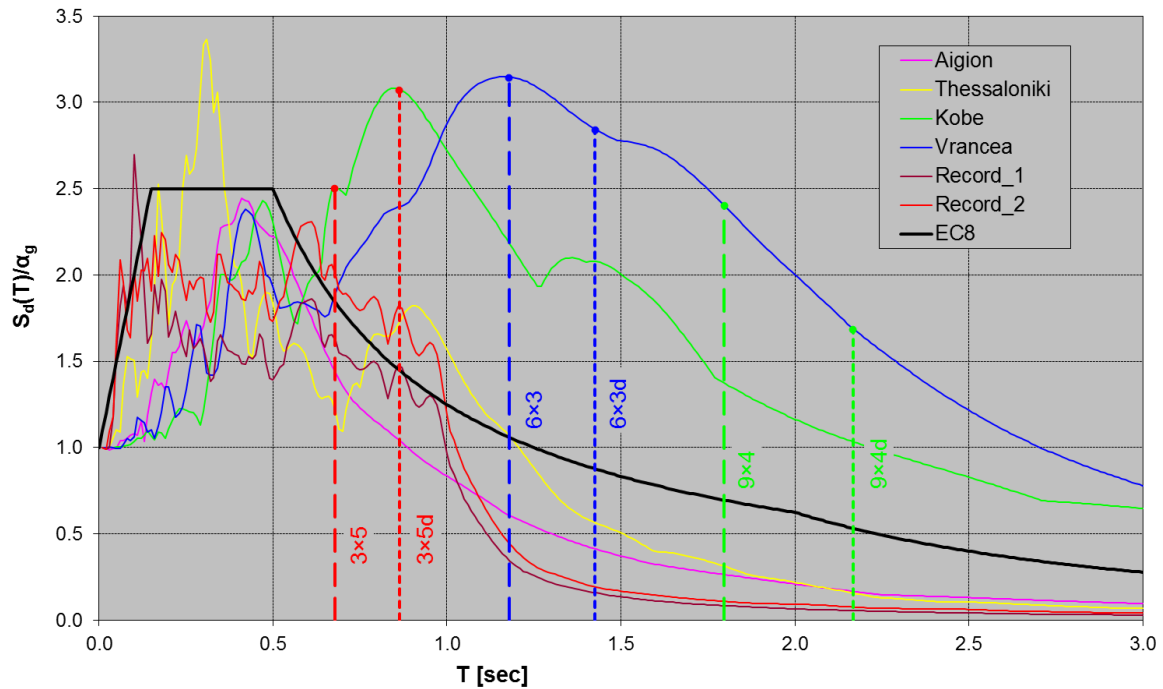


Fig. 1.19: Scaled response spectra of selected earthquakes

An incremental dynamic analysis was deployed in order to investigate the seismic response of the frames for increasing Peak Ground Accelerations (PGAs). The results for the interstorey drifts and the top displacement of the six 2D frames are shown in Fig. 1.20 and Fig. 1.21. Each point of the curve corresponds to the maximum value of a dynamic analysis. The following observations can be made:

- The records of Kobe and Vrancea activate different eigenperiods than the ones from the code spectrum. For this reason, the dynamic response of the frames for the Kobe and Vrancea records is significantly worse.
- The total displacement of all frames is acceptable for the design earthquake acceleration ( $2.35 \text{ m/sec}^2$ ). In addition, for the records excluding Kobe and Vrancea, the interstorey drifts of all stories are acceptable (below 2%).
- The interstorey drifts for frequent, smaller earthquakes, of about 50% of the design earthquake, are acceptable in order to avoid damage of the non-structural elements of the building (0.5-0.7%).
- For an extreme seismic event, of about 200% of the design earthquake, the frames with INERD connections exhibit smaller deformations.
- The use of INERD pin connections leads to a more stable and reliable behaviour due to the fact that the buckling of the braces is prevented.

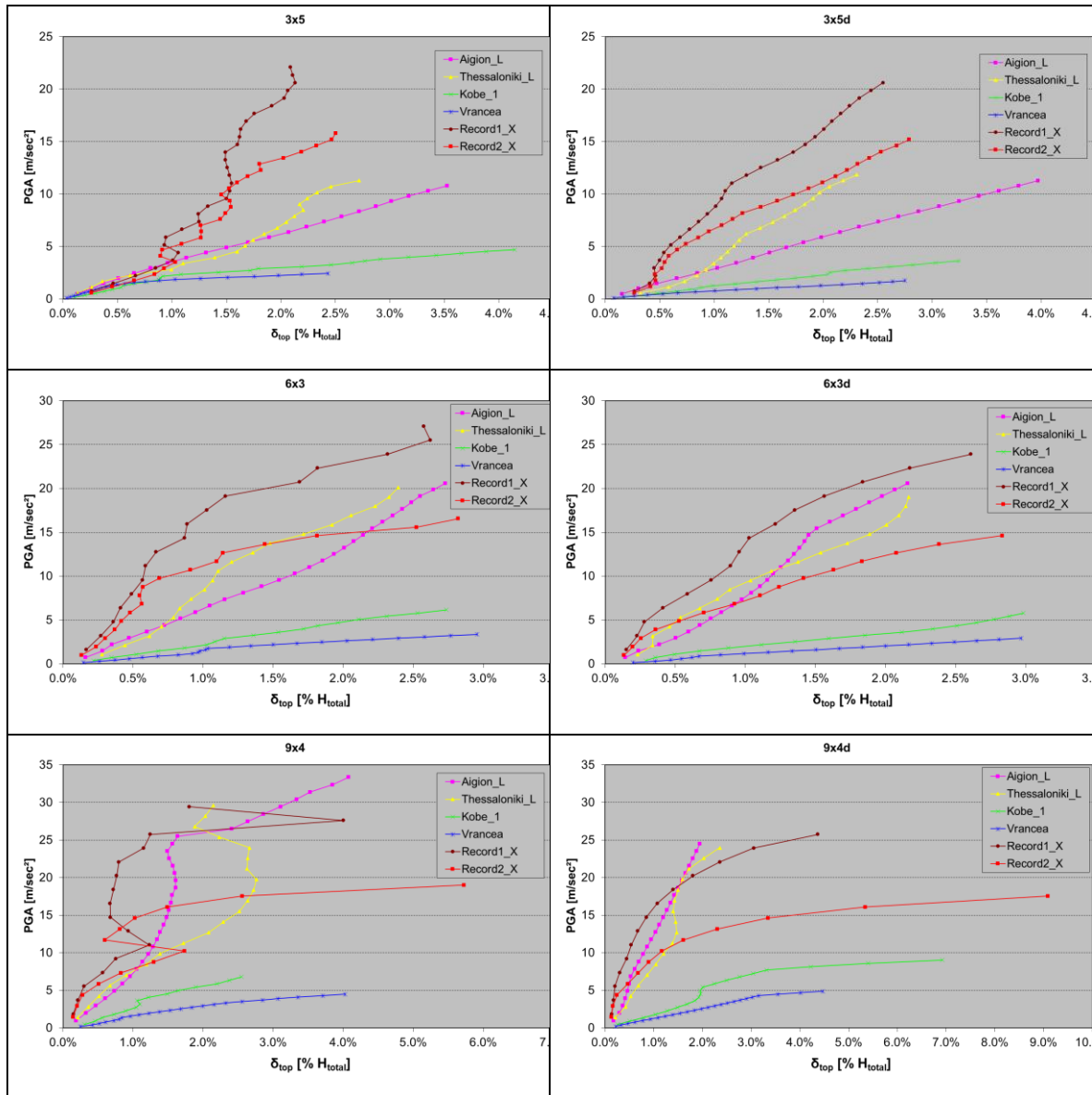


Fig. 1.20: Peak Ground Acceleration vs. total drift  $\delta_{top}$  as a % of total height of building

The results of the dynamic analyses prove the superior cyclic behaviour of the INERD pin connections. The classic braces buckle under compression, which leads to the “instant” transfer of the corresponding lateral load to the tension diagonals. This fact, combined with the rapid degradation of the hysteresis loop of the brace after a few significant cycles of loading can lead to very large deformations and somewhat unstable behaviour as the PGA increases.

On the other hand, the hysteresis loop of the INERD connections is quite stable and exhibits significant energy absorption even for large accelerations and many significant cycles of loading.

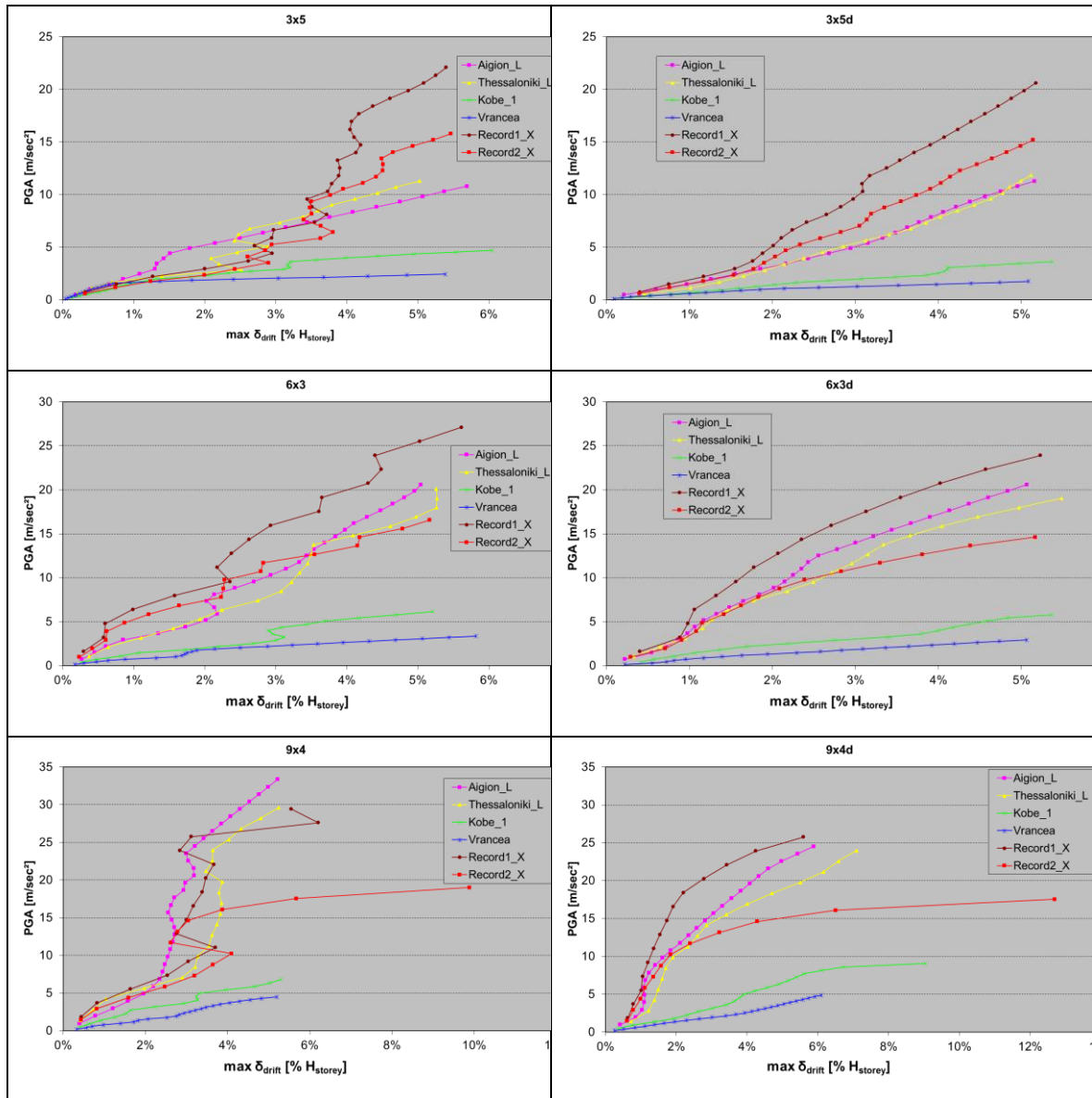


Fig. 1.21: Peak Ground Acceleration vs. maximum interstorey drift  $\delta_{drift}$  as a % of storey height

In Fig. 1.22 the maximum base shear for every dynamic analysis is plotted vs. the PGA. It is obvious that the seismic forces acting on the frames with INERD pin connections are significantly reduced, when compared to the frames with full-strength connections. This is caused due to the reduced stiffness of the INERD system which also leads to an increased eigen period and energy dissipation.

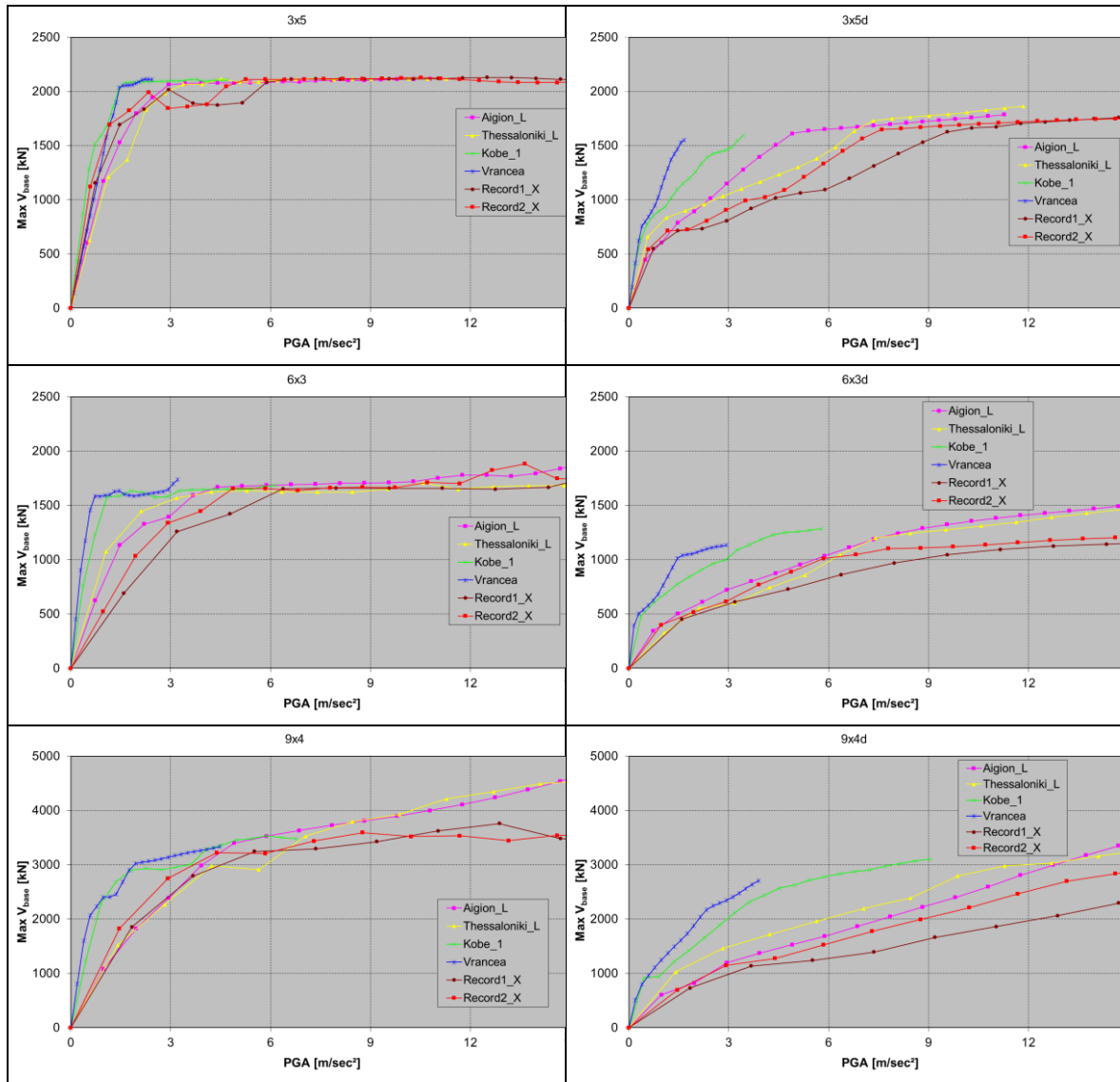


Fig. 1.22: Base shear  $V_{base}$  vs. Peak Ground Acceleration

The main conclusion of the dynamic analyses is that, for the «Life safety» performance level, the frames with INERD dissipative connections behave better than the classic frames with full-strength connections. This failure criterion, which is defined for an interstorey drift equal to 2.5%, practically corresponds to the design earthquake that is used in modern codes like EN1998, and is obviously more important. In particular, the displacements and internal forces that are recorded, are quite smaller in the case of frames with INERD connections. In addition, for the other performance levels, with an interstorey drift of 1.0% and 5.0% respectively, it is proved that the frames with INERD pin connections respond in a similar way as conventional CBF. This fact is also of significant importance, as it is verified that the introduction of a relatively flexible system at the ends of the braces, does not cause

any problems due to excessive deformations, either for serviceability earthquakes, or for extremely strong earthquakes.

#### 1.6.5 Calculation of the behaviour factor of frames with INERD pin connections

For the calculation of the behaviour factor, two different definitions of  $q$  are examined. The first definition is:

$$q_1 = \frac{PGA_{ult}}{PGA_y} \quad \text{Eq. (1.18)}$$

where  $PGA_{ult}$  is the PGA for which the failure criterion is satisfied, i.e. the interstorey drift of any storey is equal to 1.0, 2.5 or 5.0%, depending on the performance level.

$PGA_y$  is the PGA for which the first “yield” takes place in the structure, which could be buckling or tensile yield of a diagonal (for classic CBF) or yielding of an INERD connection in tension or compression.

For the second definition, the PGA for which the failure criterion is satisfied is initially calculated. Then, the behaviour factor is given by eq. (1.19):

$$q_2 = \frac{V_{base,ult,el}}{V_{base,ult,pl}} \quad \text{Eq. (1.19)}$$

where  $V_{base,ult,pl}$  is the base shear of the frame where all dissipative elements are allowed to behave in a nonlinear law, under the record with the PGA that caused failure (i.e. an interstorey drift at any storey equal to 1.0, 2.5 or 5.0%).

$V_{base,ult,el}$  is the base shear of the frame where all dissipative elements remain elastic, under the same record.

The basic advantage of the second definition is that it takes into account the reduced seismic forces due to the plastification of the structure, which results in a better estimate of the internal forces of the frame. In this way, the results of the nonlinear dynamic analyses can be better utilized, as they model the response of the structure and its capacity to dissipate energy with an increased accuracy. In addition, the second definition does not require the calculation of the PGA that causes yield, which can be debatable in case the bifurcation point is not easily defined, as is the case for frames with INERD connections.

The results of the dynamic analyses of the second definition of  $q$  are plotted in Fig. 1.23, as they proved to be more realistic and suitable for comparison between the two types of frames. Although the definition of the behaviour factor can be a subject for discussion, it is obvious from examining the ratio of  $q$  of the frames with INERD connections over  $q$  of the classic CBF, that it can be reliably taken larger

than 1.0, ranging between 1.25 and 2.5 for the frames that were examined. Practically, this means that a behaviour factor similar with the one assumed for the Moment Resisting Frames is appropriate for braced frames with INERD connections, e.g. by multiplying the value of  $q$  given for classic CBF by the minimum ratio of 1.25. Such an increase would lead to a behaviour factor of  $\sim 4$  for the Greek Seismic Code and 5 for EN1998-1. Nevertheless, until a more circumstantial justification of such a value is provided by additional analyses and tests, the conservative values of §1.5.2 are recommended for practical applications.

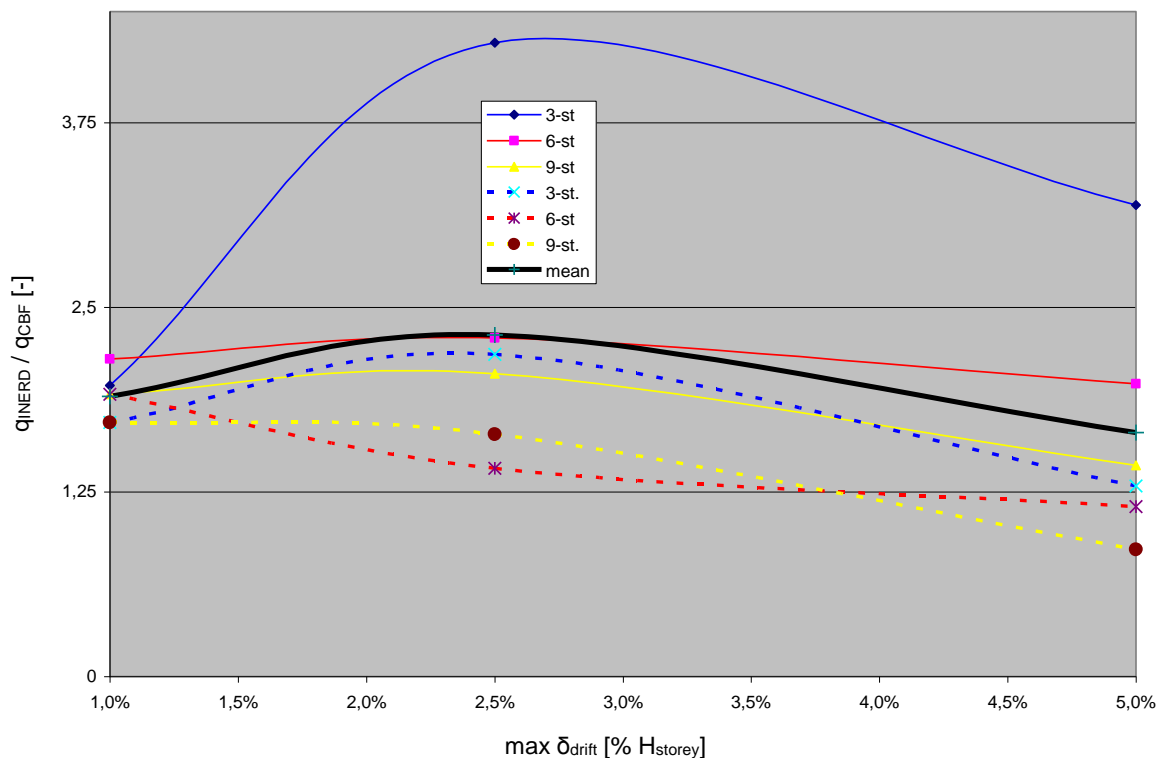


Fig. 1.23: Ratio of the behaviour factors  $q_2$  for frames with dissipative and full-strength connections

## 1.7 CONCLUSIONS

The innovative dissipative INERD pin connections were developed for steel frames with concentric braces. The main purpose of their use is to concentrate the damage of the structure in predefined, easy-to-repair plastification zones in case of a strong seismic event, while protecting all the connected elements from yielding and buckling.

The results of the experimental, analytical and numerical investigations which are briefly presented in this brochure and are presented in detail in the relevant literature [12, 13, 25, 26, 30], demonstrate the advantages of the systems containing INERD pin connections. These are outlined below:

- INERD pin connections exhibit high stiffness for lateral load of small intensity and high ductility for load of larger intensity.

- INERD pin connections protect the braces against buckling and yielding. Therefore, all the diagonals remain active, with practically stable properties, either they are loaded in tension or compression.
- The plastification of the structure is limited at the region of the connections, and specifically the pins. The position of the connections allows their immediate inspection and, if necessary, their replacement with low cost and in a short time. If this is the case, one more advantage of the INERD connections is that the weight of the material that will be replaced is quite small, resulting in reduced requirements of time and equipment.
- They exhibit excellent cyclic response, even for large deformations. The risk of brittle failure due to low-cycle fatigue is low, due to the lack of welds or notches near the plastification zones.
- The anti-seismic design of frames with INERD pin connections can be performed with a methodology similar to the one of the conventional frames. In addition, this type of frames exhibits high ductility, which can justify a larger value for the behaviour factor, similar to the one allowed for moment resisting and eccentrically braced frames. At the same time, the system has adequate stiffness for serviceability and extreme earthquakes, so that excessive deformations do not develop due to the introduction of the flexible connections.
- The use of the INERD pin connections can result in the reduction of the self-weight of the steel frame, which can eliminate the increased cost of the dissipative connections. This is mainly due to the reduced seismic forces that are derived as a result of the higher capacity for absorbing energy and the reduced requirements imposed from capacity design.

The proposed design rules provide the possibility to design frames containing INERD connections with common structural software. The methodology can be somewhat more complicated in comparison to the conventional CBF, but it is not prohibitive. On the other hand, there can be significant short-term benefits, due to the reduction of the seismic forces and the weight of the bearing frame, as well as long-term benefits, due to the reduced cost of repair in case of a strong seismic event.

## **1.8 FIELD OF APPLICATION**

The innovative INERD pin connections may be applied in short, medium or high-rise steel buildings as they demonstrate adequate stiffness and ductility. Their initial concept is for concentrically braced frames, but with a few modifications, additional structural systems may be deployed. In addition, the INERD braces could be applied in strengthening or restoration of existing structures, not necessarily steel ones.

All the advantages described in §7 should be taken into consideration, and if the deployment of the INERD system is found promising, the design rules briefly

presented in this brochure can be applied in order to effectively design the frame and its connections.

## 1.9 PREVIOUS PUBLICATIONS

In course of the INERD project, several publications were published in international journals and for international conferences which cover parts of the investigations of the research project.

Publications in international journals:

1. Vayas I. and Thanopoulos P.: Innovative dissipative (INERD) pin connections for seismic resistant braced frames, *International journal of steel structures*, vol. 5, no. 5, p. 453 – 463, 2005.
2. Vayas I. and Thanopoulos P.: Dissipative (INERD) Verbindungen für Stahltragwerke in Erdbebengebieten, *Stahlbau* 75, Heft 12, Ernst & Son, 2006.
3. Vayas I., Thanopoulos P. and Castiglioni C.: Stabilitätsverhalten von Stahlgeschossbauten mit dissipativen INERD-Verbindungen unter Erdbebenbeanspruchung, *Bauingenieur* 82, März 2007.

International conference presentations:

1. Vayas I., Calado L., Castiglioni C. A., Plumier A. and Thanopoulos P.: Innovative dissipative (INERD) connections for seismic resistant steel frames, *Proceedings of 3rd International Symposium on Steel Structures*, 10-11 March 2005, Seoul, Korea, 2005.
2. Vayas I., Thanopoulos P., Plumier A., Castiglioni C. A. and Calado L.: Behaviour of seismic resistant braced frames with innovative dissipative (INERD) connections, *Proceedings of the 4th European conference on steel and composite structures*, 8-10 June 2005, Maastricht, The Netherlands, Hoffmeister B. and Hechler O. eds., volume C, p. 5.2-25 – 5.2-32, Druck and Verlaghaus Mainz, Germany, 2005.
3. Vayas I. and Thanopoulos P.: Seismic resistant braced frames with dissipative (INERD) connections, *Proceedings of the 5th conference on Behaviour of steel structures in seismic areas (STESSA)*, Yokohama, Japan, 2006, Mazzolani and Wada eds., p. 801 – 806, Taylor & Francis Group, London.

## 1.10 BIBLIOGRAPHIC REFERENCES

In course of the INERD project, several bibliographic references were used. A selection of the most important is listed below:

1. ABAQUS User's Manual (2000), Versions 5.8 & 6.1, Hibbitt, Karlsson and Sorensen Inc., USA, 2000.
2. AISI: Seismic provisions for structural steel buildings, including supplement No. 1, American Institute of Steel Construction, Chicago, Illinois, USA, 2005.
3. Aribert J. M. and Grecea D.: The base shear force approach, *Moment resistant connections of steel frames in seismic areas*, Mazzolani F. M. ed., Section 8.3, E & FN Spon, London, England, 2000.
4. Ballio G., Mazzolani F. M., Plumier A. And Sedlacek G.: Background document on the q factors of dissipative earthquake resistant structures, *Background documents for Eurocode 8 Part 1 – Volume 2 – Design rules – Specific rules for steel structures*, pp. 128-133, Commission of the European Communities, 1988.
5. Ballio G. and Castiglioni C. A.: A unified approach for the design of steel structures under low and/or high cycle fatigue, *Journal of Constructional Steel Research*, Volume 34, pp. 75-101, Elsevier, 1995.



6. Bernuzzi C., Calado L. and Castiglioni C. A.: Ductility and load carrying capacity prediction of steel beam-to-column connections under cyclic reversal loading, *Journal of earthquake engineering*, vol. 1, no. 2, pp. 401-432, 1997.
7. Black R. G., Wenger W. A. and Popov E. P.: *Inelastic Buckling of Steel Struts Under Cyclic Load Reversal*. Report No. UCB/EERC-80/40. Berkeley: Earth. Eng. Research Center. Univ. of California, 1980.
8. Calado L. and Azevedo J.: A model for predicting the failure of structural steel elements, *Journal of Constructional Steel Research*, vol. 14, issue 1, pp. 41-64, 1989.
9. Calado L. and Castiglioni C.A.: Low cycle fatigue testing of semi-rigid beam-to-column connections, 3<sup>rd</sup> International workshop on connections in steel structures, Trento, pp. 371-380, 1995.
10. Calado L. and Castiglioni C.A.: Steel beam-to-column connections under low-cyclic fatigue experimental and numerical research, *Proceedings of XI world conference on earthquake engineering*, Acapulco, Mexico, 1996.
11. Calado L., Castiglioni C. A. and Bernuzzi C.: Seismic behaviour of welded beam-to-column joints: Experimental and numerical analysis, AISC, *Fourth International Workshop on Connections in Steel Structures*, pp. 244-256, October 22-25, Roanoke, VA, 2000.
12. Calado L., Ferreira J. and Feligioni S.: Characterization of dissipative connections for concentric bracing systems in steel frames in seismic areas, *Detailed Report*, IST Lisbon, 2004.
13. Castiglioni C. A., Brescianini J., Crespi A., Dell' Anna S. and Lazzarotto L.: *INERD – Dissipative connections for concentric bracing systems for steel frames in seismic areas – Final Report*, Politecnico di Milano, 2004.
14. Chopra A. K.: *Dynamics of structures – Theory and applications to earthquake engineering*, Prentice-Hall Inc., 1995.
15. European Committee for Standardisation (CEN): prEN 1990, *Eurocode - Basis of structural design*, 2001.
16. European Committee for Standardisation (CEN): prEN 1991, *Eurocode 1: Actions on structures - Part 1-1: General actions – Densities, self-weight, imposed loads for buildings*, 2001.
17. European Committee for Standardisation (CEN): prEN 1993, *Eurocode 3: Design of steel structures - Part 1-1: General rules and rules for buildings*, 2003.
18. European Committee for Standardisation (CEN): prEN 1993, *Eurocode 3: Design of steel structures - Part 1-8: Design of joints*, 2003.
19. European Committee for Standardisation (CEN): EN 1998, *Eurocode 8: Design of structures for earthquake resistance*, 2004.
20. European Convention for Constructional Steelwork (ECCS): *Recommended testing procedure for assessing the behaviour of structural steel elements under cyclic loads*, ECCS Publ. No 45, Rotterdam, The Netherlands, 1986.
21. Gioncu V. and F. M. Mazzolani: *Ductility of seismic resistant steel structures*, Spon Press, London, UK, 2002.
22. Mazzolani F. M. and Piluso V.: *Theory and design of seismic resistant steel frames*, E & FN Spon, London, UK, 1995.
23. Mazzolani F. M.: *Design of moment resisting frames*, *Seismic Resistant Steel Structures*, Mazzolani F. M. and Gioncu V. (eds), chapter 4, pp. 169-182, Springer-Verlag Wien New York, 2000.
24. OpenSees (Open System for Earthquake Engineering Simulation, edition 1.5, University of California, Berkeley, 2003.

25. Plumier A., Doneux C. and Stoychev L.: The INERD Project – Detailed report on experimental activity at University of Liege, Université de Liège, 2004.
26. Plumier A. (co-ordinator), Doneux C., Castiglioni C., Brescianini J., Crespi A., Dell' Anna S., Lazzarotto L., Calado L., Ferreira J., Feligioni S., Bursi O. S., Ferrario F., Somnavilla M., Vayas I., Thanopoulos P. and Demarco T.: Two Innovations for Earthquake Resistant Design – The INERD Project – Final Report, Research Programme of the Research Fund for Coal and Steel : Steel RTD, Technical Report No. 6, 2004.
27. Stahlbau Kalender 2004, 1A – Stahlbaunormen, A Kommentierte Stahlbauregelwerke, Dr.-Ing. Eggert. H., Ernst & Sohn, 2004.
28. Thanopoulos P.: Behaviour of seismic resistant steel frames with energy absorbing devices, PhD Thesis, NTUA, 2006.
29. Vayas I.: Design of braced frames, Seismic Resistant Steel Structures, Mazzolani F. M. and Gioncu V. (eds), chapter 5, pp. 241-288, Springer-Verlag Wien New York, 2000.
30. Vayas I. and Thanopoulos P.: INERD Project, Final Report, NTUA, 2004.
31. Zienkiewicz O. C., Chan A. H. C., Pastor M., Schrefler B. A. and Shiomi T.: Computational geomechanics with special reference to earthquake engineering, John Wiley & Sons, 1999.

## **2 INERD U CONNECTIONS**

### **2.1 INTRODUCTION**

In the frame of the European Research Program 7210-PR-316 “Two INnovations for Earthquake Resistant Design - The INERD Project”, two innovative dissipative connection system, namely a pin and a U-plate connection, were introduced. The current chapter presents the background of the U-plate INERD connection system with an example of application.

### **2.2 DESCRIPTION OF U-CONNECTION**

Seismic resistant steel structures are designed for stiffness, strength and ductility. Stiffness requirements are imposed in order to limit non-structural damage in case of minor to moderate earthquakes and limit instability effects, strength in order to ensure the capacity of the structure to resist safely the action effects and ductility in order to dissipate part of the seismic input energy through inelastic deformations and therefore reduce the action effects. Conventional frames, both unbraced and braced, have certain disadvantages in respect to the above design criteria. In addition, braced frames that are widely applied in Europe, face following problems after unusually strong earthquakes that result in some degree of damage: a) for concentric braced frames, the need for strengthening or replacement of damaged and buckled braces which have a certain length and are difficult to handle, b) for eccentric braced frames, the need for strengthening and repair of the links or the beams that are part of the main system that supports gravity loading. Such works require therefore considerable skill and are associated with high material and labour costs.

An alternative approach is to allow for energy dissipation in the connections rather than in the members. The introduction of flexible, partial strength connections is well known for moment resisting frames subjected to gravity loading. However, the application of semi-rigid connections in seismic resistant moment frames is associated with important problems. Indeed, moment resistant frames are generally flexible structural systems, so that lateral drift limitations at serviceability conditions are in many practical cases the prevailing design criteria. The introduction of semi-rigid connections enhances further the structural flexibility and would magnify the problems, which would not be solved by selection of heavier profiles for beams and columns.

For the above reasons, dissipative connections are better suitable for braced frames. Such frames are generally sufficiently stiff against lateral displacements, so that an introduction of flexible connections would not harm the overall behaviour. On the contrary, flexible connections may protect the braces from buckling and therefore

increase the overall ductility. Additionally, any repair works after strong seismic events would concentrate within the connections and would be easier to handle. In the frame of the INERD research project, dissipative (INERD) connections suitable for braced frames were developed. The advantages of braced frames with INERD-connections in comparison with conventional braced frames may be summarized as following:

- Better compliance with the seismic design criteria.
- Protection of compression braces against buckling.
- Activation of all braces, either in compression or in tension, even at large storey drifts.
- Limitation of inelastic action in small parts that may be easily replaced.
- Possibility for easy inexpensive repair after very strong earthquakes, if required.
- Reduction of overall structural costs for the same performance level.

The U-connections consist of one or two bent, U-shaped thick plates that connect the brace to the adjacent member (Fig. 2.1). Here again, energy dissipation takes place in the bent plate(s).

The advantage of these connections is that, by appropriate sizing, inelastic deformations are limited within exactly predetermined zones, the pins or the U-plates, whereas the adjacent parts remain elastic. Consequently, braces are protected from buckling and damage is restricted in the pins or the U-plates. These are small parts that may be easily replaced if they are largely deformed, after an unusually strong earthquake.

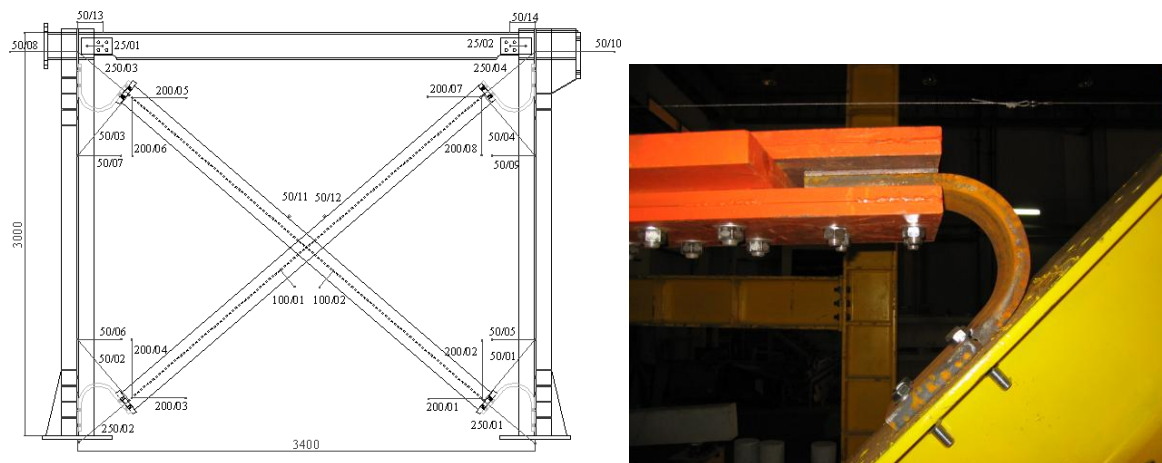


Fig. 2.1: INERD U-Connections

### 2.3 LIMIT STATE MODELS

The design of the U-connections is essentially controlled by its deformation capacity. The maximum displacement that could safely be imposed to the structure is equal to 120 mm, if resorting to the range of U-configurations validated in the frame of the project INERD. Some other configurations can of course be developed on demand

to target specific performances by varying the thickness and bending radius of the U-plate, taking into account the practical limitations related with the material properties and production technology. These non-standard geometries should however always be specifically validated by numerical models resorting to plate FE or by testing. It is therefore suggested to first evaluate the possibility to resort to pre-validated configurations.

## 2.4 EXPERIMENTAL INVESTIGATIONS ON U-CONNECTIONS

U-connections have been widely validated by experimental testing in the frame of the INERD project. Tests have been carried out at local level of the connections and at global level of a braced frame.

The parameters considered (Fig. 2.2) to optimize such a connection are mainly geometric ones:

- R : radius
- B : Length of plate
- e : Thickness
- Position : load way

The range of validated parameters is given in Table 2.1.

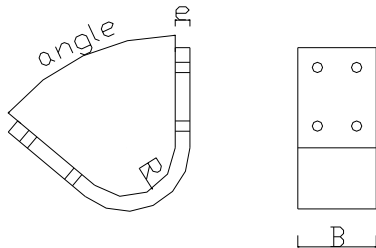


Fig. 2.2: Definition of parameters for U connections

**Table 2.1:: Range of possible dimension**

type	R	B	e	angle	position
2	100	160	25	45	
3	100	160	25	50	
4	100	160	30	50	
5	125	160	30	50	
6	125	160	25	30	
7	125	160	25	45	
8	125	160	25	50	
9	125	160	25	30	
10	125	160	25	39	
11	125	160	25	45	
12	125	160	30	39	

Even if all the above configurations have been validated, some suggestions are made regarding the ideal choice:

A radius of 100 mm allows better energy dissipation than the radius of 125 mm, for the same thickness (both 25 mm and 30 mm), and device configuration (U1 or U2). The best behavior of U-connections is obtained with a larger thickness (e.g. 30 mm) and a small radius (e.g. 100 mm). This is evident, because increasing the thickness and reducing the radius results in a larger bending stiffness of the device. So, as a general conclusion we can state that the best performance of the U-Device can be obtained by increasing the thickness and decreasing the radius.

## 2.5 SEISMIC DESIGN OF BUILDING FRAME

In this section an example of the seismic design of the building is presented. The equivalent lateral forces methods according to the EN1998-1-1 is used. For the U-Device connections of the bracings, dissipative devices, as at this stage no design model is available, the selection of the appropriate device is based on the test results of the INERD research project.

### 2.5.1 Description of the building and structural conception

The building used in this design example consists in a four story buildings. Fig. 2.3 presents the main geometric dimensions of the building. The building use category is office area.

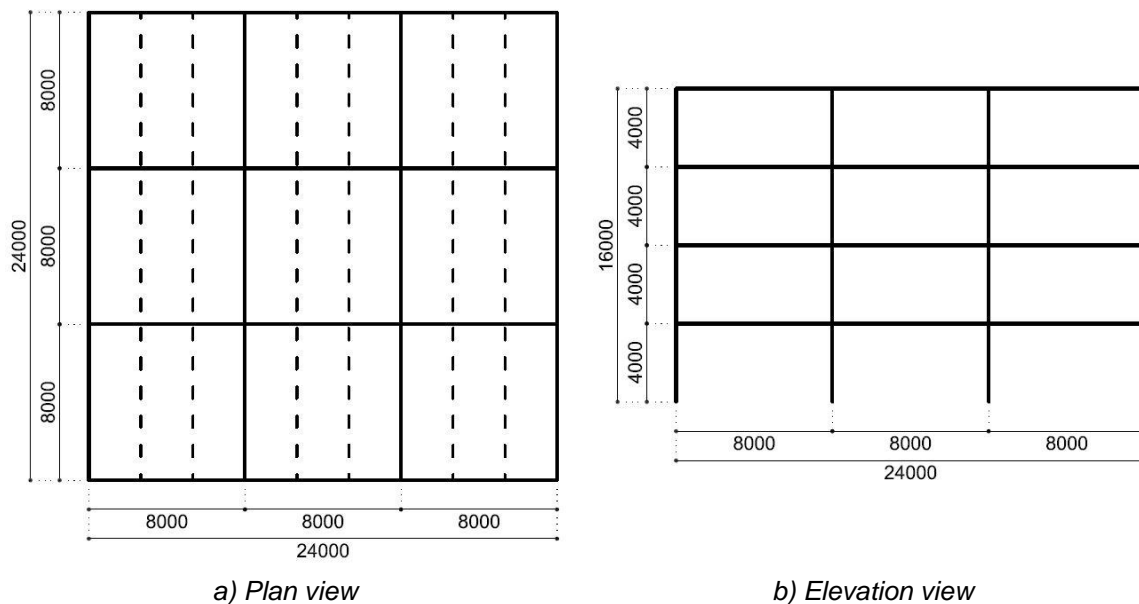
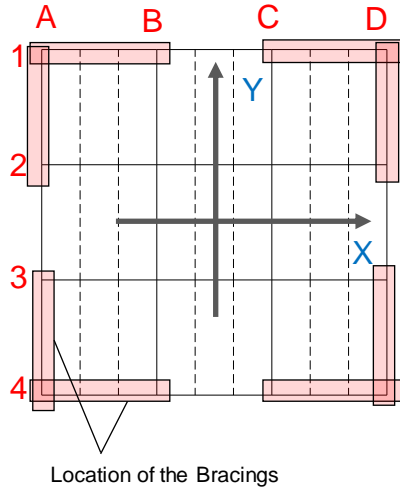


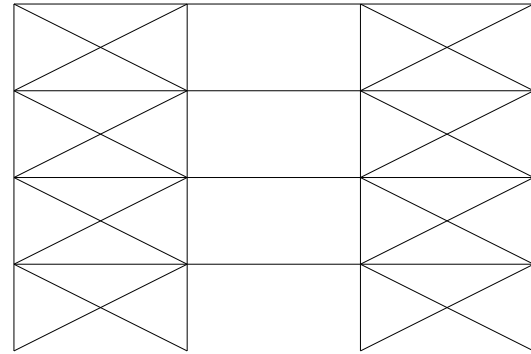
Fig. 2.3: Geometry of the building used in the design example

The building structure is a concentric braced frame structure implementing the U-connection as solution to connect braces to columns. The U-connection is the dissipative component of the structure. For each direction 4 braces are used and distributed as illustrated in Fig. 2.4. Initially, only 2 braces were considered however, due to the amplitude of the seismic forces and to the limitation of the U-connection

resistance, the option with 4 braces in each direction was taken. Here, only the final option is presented.



a) Plan view



b) Example frame with bracings (AL. 4)

Fig. 2.4: Building structural conception

In Table 2.2 are summarized the materials of the different building members. The composite slab is assumed to work in one direction (X-direction according to Fig. 2.4).

**Table 2.2: Materials of the structural members**

Member	Material
Columns	S355
Beam	
Bracings	
Slab	Composite Concrete C20/25 1mm steel sheet with 73mm height Total slab height 150mm
U-connection	According to INERD project

### 2.5.2 Loading and seismic action

The loading, base of the calculation of the seismic mass, is given in Table 2.3 and Table 2.4.

**Table 2.3: Permanent loads**

Dead loads		Superimposed loads		
Self-weight of steel members	78,5 kN/m <sup>3</sup> + 10% for connections, stiffeners	Service Ceiling Storeys	Intermediate Storey	0,7 kN/m <sup>2</sup>
			Top Storey	1 kN/m <sup>2</sup>
Self-weight of composite slab	2,75 kN/m <sup>2</sup>	Perimeter walls		4 kN/m

**Table 2.4: Live loads**

Offices	3 kN/m <sup>2</sup>
Movable partitions	0,8 kN/m <sup>2</sup>
Accessible roof	3 kN/m <sup>2</sup>

The seismic load is given in Table 2.5. For the behavior factor of the U-connection there is no value determine in the INERD project, the given value is assumed based on the experience and on the INERD project experimental results. These values have to be later verified. The vertical component of the seismic action was neglected.

**Table 2.5: Seismic action definition**

Importance factor, $\gamma_I$	1,0			
Peak ground acceleration, $a_{gR}$	0,24g			
Ground type B	S	$T_B$	$T_C$	$T_D$
Type 1 Spectrum	1,00	0,15s	0,50s	2,00s
Lower bound factor, $\beta$	0,2			
Behavior factor, $q$	3			

### 2.5.3 Pre-design based on gravity loads

Prior to the seismic design, the structural members' columns and beams were pre-design according to EN 1993-1.1. The results of the pre-design of these members are given in Table 2.6. The columns cross-sections were selected with margin to take the axial compression due to the seismic loads. In what regards the selection of the profiles for beams and columns it was decided the following: i) uniform columns, all columns with the same profile; ii) beams with different profiles according to the direction.

**Table 2.6: Columns and beams cross-sections**

Columns	HEB 260
Beams in X-direction	IPE 500
Beams in Y-direction	IPE 360



#### 2.5.4 Seismic calculation

The seismic forces on the building structure were determined according to the principles of the lateral force method prescribed by the EN 1998-1-1. The procedure may be divided in several steps. The results of these calculations are hereafter presented.

- Determination of the seismic mass

The seismic mass results from the gravity actions on the building and is quantified from the following combination of actions:

$$\sum G_{k,j} + \sum \psi_{E,i} Q_{k,i} \quad \text{Eq. (2.1)}$$

In Table 2.7 is given the total seismic mass per story determined according to equation (2.1) and to the loads presented in 2.5.2.

**Table 2.7: Seismic mass of the 4-stories building**

Story	Seismic Mass, m [ton]
1	323,67
2	323,67
3	323,67
4	301,44
Total	1272,45

- Determination of the base shear

According to the lateral force method and the seismic action (Table 2.5), the Base Shear was estimated. Equation (2.2) to (2.6) were used to determine: the fundamental period of the structure, the design pseudo acceleration and the base shear. In Table 2.8 are given the obtained results.

$$T_1 = C_t H^{2/3} \quad \text{Eq. (2.2)}$$

$$C_t = 0,05 \quad \text{Eq. (2.3)}$$

$$a_g = \gamma_I a_{gR} \quad \text{Eq. (2.4)}$$

$$T_B \leq T \leq T_C: S_d(T) = a_g S \frac{2,5}{q} \quad \text{Eq. (2.5)}$$

$$F_b = S_d(T_1) m \lambda \quad \text{Eq. (2.6)}$$

**Table 2.8: Results of the base shear calculation**

H [m]	C <sub>t</sub>	T <sub>1</sub> [s]	a <sub>g</sub> [m/s <sup>2</sup> ]	S <sub>d</sub> (T <sub>1</sub> ) [m/s <sup>2</sup> ]	λ	F <sub>b</sub> [kN]
16	0,05	0,4	2,35	1,96	0,85	2122,10

▪ Distribution of the seismic loads through the braced frames

The braced frames have the same stiffness therefore, a uniform distribution of the base shear was considered amongst these frames. As the structure is perfectly symmetric only the accidental eccentricity (0,05L) is taken into account for the global torsion of the structure and the consequent amplification of the horizontal forces. In Table 2.9 are given the forces per braced frame. Because the structure plan is a square and the brace frames are equally positioned in relation to the geometric center, the distributed forces are equal in both directions.

**Table 2.9: Distribution of the seismic forces per braced frames**

Frame	$F_b$ [kN]	X [m]	L [m]	$\delta$	$F_b'$ [kN]
1	1061,05	12	24	1,05	1114,1
4					
A					
D					

▪ Distribution of the seismic forces per story

The distribution of the masses per story is performed based on the mass of each story and the height of the story to the ground, as expressed in (2.7). In Table 2.10 are given the forces per story.

$$F_i = F_b' \frac{z_i m_i}{\sum z_j m_j} \quad \text{Eq. (2.7)}$$

**Table 2.10: Distribution of the seismic forces per story**

Storey	$z_i$ [m]	$m^* z_i$ [ton.m]	$F_i$ [kN]
1	4	1295	114,6
2	8	2589	229,1
3	12	3884	343,7
4	16	4823	426,7
	$\Sigma m^* z_i$	12591	

### 2.5.5 Selection of the U-connection

The selection of the U-connection for the bracing-to-column connections was performed using the test results of the INERD research project. According to the seismic forces on each story and on each braced frame, and considering that both compression and tension bracings are active, the forces in each connection was calculated. Remember that the forces on the bracings is cumulative with the decrease of the story level. In Table 2.11 are given forces on each connection using.

The selection of the U-connection was then performed according to the capacity of the connection tested in the INERD project. The latter is also included in the table. The connection ID is the name of the test specimen tested within the scope of the INERD research project (Table 2.1).

**Table 2.11: Selection of the U-connection for the bracings**

Storey	F <sub>Brac,con</sub> [kN]	Connection ID	F <sub>con,Test</sub> [kN]
4	119	Mola 3	144
3	215	Mola 10	260
2	279	Mola 12	390
1	311	Mola 12	390

#### 2.5.6 Design of building to seismic loading

The final design of the building members (columns and bracings) depending on the seismic loads, were design based on the principles of the capacity design. Thus, the design loads were not the loads resulting from the seismic load but the resistance of the U-connection. Then, because the resistance of the U-connection is the test value and not nominal design values, the over strength factor ( $\gamma_{ov}$ ) was assumed equal to 1. As mentioned above, the design of the steel members was performed according to the EN 1993-1-1. As the column profile was not changed from the design presented in 2.5.3, in Table 2.12 only the final bracings are given. The governing design verification of the bracings is the resistance to flexural buckling. In Table 2.12 this resistance is given.

**Table 2.12: Final design of bracings**

Storey	Profile	N <sub>b,Rd</sub> [kN]
4	HEA 120	186
3	HEA 140	298
2	HEA 160	447
1	HEA 160	447

Table 2.13 and Table 2.14 give details of the checks made on the limitation of P-Δ effects according to the EN 1998-1-1. The interstorey drift  $\theta$ , computed according to equation (2.8), for all stories is quite below the limit (0,1) and therefore the second-order effects may be neglected.

$$\theta = \frac{P_{tot} d_r}{V_{tot} h} \leq 0,10 \quad \text{Eq. (2.8)}$$

**Table 2.13: Sensibility to 2<sup>nd</sup> order effects for Frames in X-direction**

Lateral force method			$E_s + G + \Psi_{Ei}.Q$		$G + \Psi_{Ei}.Q$		
Storey	$d_i$ [m]	$d_r$ [m] ( $d_i - d_{i-1}$ )	$V_i$ [kN]	$V_{tot}$ [kN]	Ptot [kN]	$h_i$ [m]	$\theta$
1	4,86E-03	1,46E-02	142,5	1386,0	6241,4	4	0,016
2	9,66E-03	1,44E-02	285,0	1243,5	4653,7	4	0,014
3	1,49E-02	1,58E-02	427,5	958,5	3066,2	4	0,013
4	1,93E-02	1,31E-02	531,0	531,0	1478,6	4	0,009

**Table 2.14: Sensibility to 2<sup>nd</sup> order effects for Frames in Y-direction**

Lateral force method			$E_s + G + \Psi_{Ei}.Q$		$G + \Psi_{Ei}.Q$		
Storey	$d_i$ [m]	$d_r$ [m] ( $d_i - d_{i-1}$ )	$V_i$ [kN]	$V_{tot}$ [kN]	Ptot [kN]	$h_i$ [m]	$\theta$
1	4,51E-03	0,014	142,5	1386,0	6241,4	4	0,015
2	9,42E-03	0,015	285,0	1243,5	4653,8	4	0,014
3	1,46E-02	0,016	427,5	958,5	3066,2	4	0,013
4	1,89E-02	0,013	531,0	531,0	1478,6	4	0,009

## 2.6 FIELD OF APPLICATION

Due to its rather high deformability, the use of the INERD U-connection is mainly suitable for structures that proved to be not too sensitive to large displacement demand, thus mainly multi-storey buildings with a limited number of storeys (typically maximum 4 to 6 depending on the configuration of the U-connection).

## 2.7 BIBLIOGRAPHIC REFERENCES

1. ACI American Concrete Institute (1995): Building code requirements for structural concrete (ACI 318-95). Farmington Hills, MI.
2. AISC (1997), Seismic provision for structural steel buildings, Task Committee 113.
3. Aschheim M, Gulkan P., Sezen H. (2000): Chapter 11: Performance of Buildings, in Kocaeli, Turkey earthquake of August 17, 1999 Reconnaissance Report. Earthquake Spectra. Supplement A to Volume 16, 237–279.
4. Benats Valérie, "Développement du concept d'assemblages dissipatifs dans des structures parasismiques en treillis", Université de Liège, thesis, a.a. 2000-2001.
5. Chou C.C., Uang C.M. (2002): Cyclic Performance Of A Type Of Steel Beam To Steel-Encased Reinforced Concrete Column Moment Connection. Journal of Constructional Steel Research 58, 637-663.
6. ECCS (1986): Recommended Testing Procedure for Assessing the Behaviour of Structural Steel Elements under Cyclic Loads. ECCS Publication n° 45.
7. ECSC Project 7210-PR-316 (2001): Earthquake Resistant Design: the INERD Project.

8. Hibbitt, Karlsson & Sorensen Inc (2003): ABAQUS - User's Manual, Version 6.3. Vol.1-3, 2003.
9. Kanno R., Deierlein G.G. (2000): Design Model Of Joints For Rcs Frames. Composite Construction in Steel and Concrete IV – Proc. of Engrg. Found. Conference, Banff, May 28 – June 2, Banff, Alberta, 947-958.
10. Krawinkler H. (1978): Shear in Beam-Column Joints in Seismic Design of Steel Frames. Engineering Journal AISC Vol. 3.
11. Mander J.B., Priestley M.J. N., Park R. (1988): Theoretical Stress-Strain Model For Confined Concrete. Journal of Struct. Engrg., ASCE, vol. 114, No 8, 1804-1826.
12. Ministry of Public Works and Settlement (1975): Specification for structures to be built in disaster areas. Government of Republic of Turkey.
13. Penelis G.G., Kappos A.J. (1997): Earthquake-Resistant Concrete Structures. E & FN Spon, London.
14. prEN 1991-1-1:2001: Actions on structures, Part 1-1: general actions, densities, self-weight, imposed loads for buildings. Final Draft, July 2001.
15. prEN 1992-1:2001: Design of concrete. Part 1: general rules and rules for buildings. Draft n° 2, January 2001.
16. prEN 1993-1-1:2000: Design of steel structures. Part 1.1: general rules. Draft n° 2, August 2000.
17. prEN 1994-1-1:2001: Design of composite steel and concrete structures. Part 1-1: general rules and rules for buildings. Draft n° 3, March 2001.
18. prEN 1998-1:2001: Design of structures for earthquake resistance. Part 1: general rules, seismic actions and rules for buildings. Draft n°3, May 2001.
19. Scawthorn C.R. (2000): Turkey earthquake of August 17, 1999: Reconnaissance Report. Technical Report MCEER-00-0001. Buffalo, N.Y.: Multidisciplinary Center for Earthquake Engineering Research, State University of New York, NY. Editor. the Marmara.
20. Sezen H., Elwood K.J., Whittaker A.S., Mosalam K.M., Wallace J.W., Stanton J.F. (2000): Structural Engineering Reconnaissance of the August 17, 1999 Kocaeli (Izmit), Turkey Earthquake. PEER 2000/09. Technical Report. Berkeley, CA.: Pacific Earthquake Engineering Research Center, University of California, CA. <http://nisee.berkeley.edu/turkey>.
21. Turkish Standards Institute (1985). TS-500 Building Code Requirements for Reinforced Concrete. Ankara, Turkey.
22. Plumier A., Stoychev L., Doneux C., "Composite columns to mitigate soft storey in reinforced concrete structures submitted to earthquake", in the Proceedings of the Colloquium on Recent Advances and New Trends in Structural Design; Timisoara 7-8 May 2004. ISBN 973-638-119-6.
23. Ferrario F., Bursi O.S. and Colombo A., "Analysis and design of RC beam-to-column joints with encased steel profiles subjected to seismic actions", in the Proceedings of the 4th European Conference on Steel and Composite Structures - Eurosteel 2005, Maastricht, The Netherlands, June 8-10, 2005.
24. Doneux C., Plumier A., "Mitigation of seismic soft storey failures in reinforced concrete structures by composite steel-concrete columns", in the Proceedings of the 4th European Conference on Steel and Composite Structures - Eurosteel 2005, Maastricht, The Netherlands, June 8-10, 2005.
25. Vayas I., Thanopoulos P., "Behaviour of seismic resistant braced frames with innovative dissipative (INERD) connections", in the Proceedings of the 4th European Conference on Steel and Composite Structures - Eurosteel 2005, Maastricht, The Netherlands, June 8-10, 2005.

26. Plumier A., Doneux C., Stoychev T., Demarco T., "Mitigation of storey failures of RC Structures under Earthquake by Encased Steel Profiles ", in the Proceedings of the 4<sup>th</sup> International Conference on Advances in Steel Structures(ICASS'05).Shanghai 13-15 June, 2005.
27. Vayas I., Calado L., Castiglioni C., Plumier A., Thanopoulos P., "Innovative dissipative (INERD) connections for seismic resistant steel frames", in the Proceedings of the International Symposium on Steel Structures ISSS'05, Seoul, Korea, 2005.
28. Calado Luis and Castiglioni Carlo A., "Design Of Steel Dissipative Connections Under Cyclic Loadings", in the Proceedings of the 4<sup>th</sup> International Conference on Advances in Steel Structures(ICASS'05).Shanghai 13-15 June, 2005.
29. Castiglioni Carlo A. and Calado Luis, "Seismic Behaviour Of Steel Braced Frames With Dissipative Connections", in the Proceedings of the 4<sup>th</sup> International Conference on Advances in Steel Structures(ICASS'05).Shanghai 13-15 June, 2005.
30. Calado Luis and Castiglioni Carlo A., "Design Of Steel Dissipative Connections Under Cyclic Loadings", in the Proceedings of the 1<sup>st</sup> International Conference on Advances In Experimental Structural Engineering (AESE 2005). Nagoya July 19-21, Japan, 2005.
31. Castiglioni Carlo A. and Calado Luis, "Seismic Behaviour Of Steel Braced Frames With Dissipative Connections", in the Proceedings of the 1<sup>st</sup> International Conference on Advances In Experimental Structural Engineering (AESE 2005). Nagoya July 19-21, Japan, 2005.
32. Dell'anna Sergio, "Behaviour of dissipative connections for concentric bracings of steel frames in seismic areas", Politecnico di Milano, thesis, a.a. 2003-2004.
33. Feligioni Sandro, "Characterization of dissipative connections for concentric bracing systems of steel frames in seismic areas", Politecnico di Milano, thesis, a.a. 2003-2004.
34. Lazzarotto Luca, "Dissipative connections for concentric bracing systems in steel frames in seismic areas", Politecnico di Milano, thesis, a.a. 2003-2004.

### 3 FUSEIS BEAM LINKS

#### 3.1 INTRODUCTION

In the frame of the European Research Program RFSR-CT-2008-00032 “Dissipative Devices for Seismic Resistant Steel Frames” (Acronym: FUSEIS) two innovative dissipative systems, named FUSEIS 1 and FUSEIS 2 were introduced and relevant design guides developed [1][12]. Depending on the geometry of the fuse, the system FUSEIS 1 is further divided in two types: FUSEIS beam links and FUSEIS pin links. The current report deals with the FUSEIS beam link system, while for the FUSEIS pin link system an accompanying report exists.

#### 3.2 DESCRIPTION OF FUSEIS BEAM LINK SYSTEM

The FUSEIS beam link system is composed of two closely spaced strong columns rigidly interconnected by multiple beams. The beams run from column to column and can be of different cross section types, as for example RHS, SHS, CHS or I-shaped sections. The general layout is shown schematically in Figure 3.1. The FUSEIS beam link system resists lateral loads as a vertical Vierendeel beam, mainly by combined bending and shear of the beams and axial forces of the columns. The dissipative elements of the system are the beam sections between the columns. These elements are not generally subjected to vertical loads, as they are placed between floor levels.

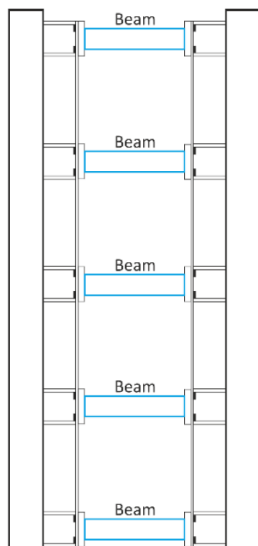


Figure 3.1: FUSEIS beam link system: general layout

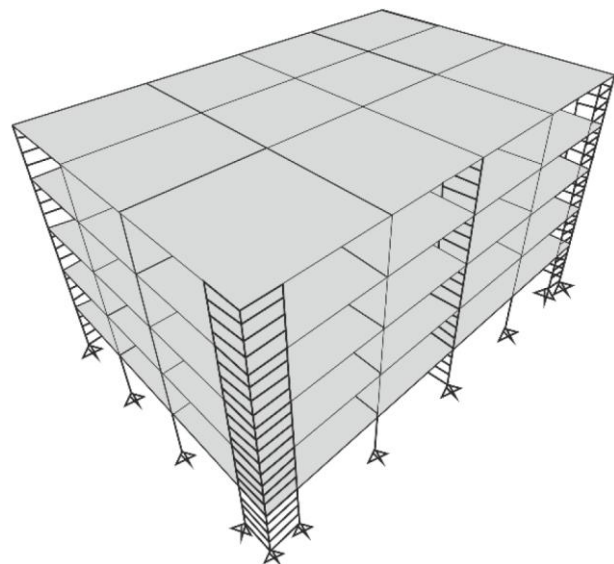


Figure 3.2: Exemplary assembly in steel frame structure

The seismic resistance of a building may be obtained by appropriate provision of a number of such systems in the relevant directions. See Figure 3.2 for an exemplary

assembly of several FUSEIS beam link systems in a steel frame structure. When beam-to-column connections of the building are formed as simple, this system provides alone the seismic resistance of the building. When the connections are rigid or semi-rigid, it works in combination with the overall moment resisting frame. In both cases the beam to system columns connections should be formed as simple, since the FUSEIS beam link system is not intended to consist a gravity load carrying part of the structure.

Aiming to minimise damage at the foundation locations pinned connections at the column bases are proposed. For multi-story buildings the column bases may be pinned or fixed, analytical investigations showed that the difference in the response was not significant. The beam link-to-column joints are formed as rigid to enable the Vierendeel action and are designed to have sufficient overstrength in order to achieve energy absorption only in the FUSEIS beam links. Bolted end-plate connections which enable an easy replacement of the beam links should be used. Beams may have closed sections (RHS) or open sections (I- or H- sections). Considering a typical floor height of 3.4 m, four or five beam links may be placed per storey. Their beam height depends on the required stiffness with the provision to leave the necessary vertical spacing between them. RHS sections are more beneficial to open sections due to their larger flexural and torsional rigidity and strength. Beam sections may vary between floors, following the increase of story shear from the top to the base of the building. Beams may also vary within the floor, either in respect to their cross-sections or to their lengths  $l_n$ , see Figure 3.3. Columns may be of open or closed section. Open sections are more beneficial, since they offer an easier connection to the beams. When closed sections are used, a T-section can be welded to it in order to offer the advantage of easier connection.

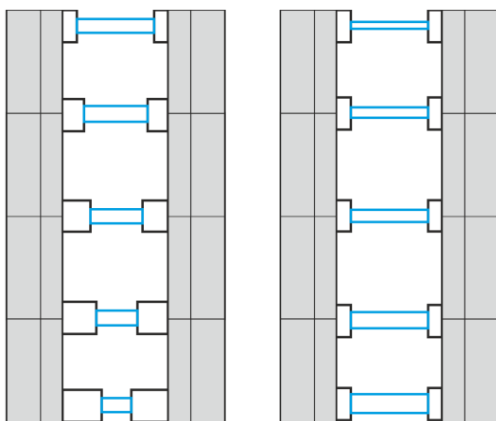


Figure 3.3: Adjustment of FUSEIS beam links system to story shear by variable beam lengths (left) or variable cross sections (right)

The most striking disadvantage of conventional frame typologies, such as MRF, CBF or EBF, is their inability to be repaired after a strong seismic event. Concerning



moment resisting frames, the beams and their connections have to be exchanged. As both of these elements belong to the gravity loading resistant system, their replacement is difficult. In eccentrically braced frames, the links, that are short parts of the beams, must be replaced. The damage in concentrically braced frames is expected in the braces, which are also difficult to exchange as they are long and heavy. These conventional structural systems can be substituted by the innovative FUSEIS beam links. Hereby the new system has the following advantages:

- Inelastic deformation only occurs in the dissipative beam link elements
- If plastically deformed, the beam links can be easily replaced as they are not part of gravity load carrying system and are moreover easy to handle
- To keep the architectural layout unaffected by the seismic resistant system, the FUSEIS beam link system may be positioned in small areas of the building
- At the same time, the beam links may be used as visible parts of the building to indicate its seismic resistant system
- For appropriately selected sections of the FUSEIS beam links, sequential plastification may be achieved

In order to ensure that dissipation of energy only takes place in the beam links, the beam link-to-column joints are formed rigidly and own a sufficient over-strength. Moreover, the beam links are attached through bolted endplates, enabling an easy replacement if the beam links should be deformed after a seismic event.

Intending to protect the beam-to-column connection against yielding and fracture, the FUSEIS beam links should be designed in such a manner that the plastic hinge forms away from the connection area. Therefore, reduced beam sections (RBS) are foreseen at the end of the beams, see Figure 3.4. Constant, tapered or radius cut shapes are possible to reduce the cross sectional area. In order to minimize stress concentrations, the radius cut is superior compared to other types of cuts. The typical length of plastic hinges in steel beams has the order of half the beam depth. Therefore, the reduced beam section, where the plastic hinge shall form, should be located at least that distance away from the connection. As an alternative to reducing the beam section, the connection region could be strengthened by means of additional plates.



Figure 3.4: Different section types for FUSEIS beam links with reduced beam sections (RBS): RHS or SHS, CHS and IPE- or HEA-section

### 3.3 LIMIT STATE MODELS

The FUSEIS beam link system works as a vertical Vierendeel beam. The theoretical static system and relations between internal forces is sketched in Figure 3.5. Considering hinges at the midpoints of beams and columns between the beam links, the internal moments and forces for horizontal loading in the elastic state may be derived from statics as following:

Columns

$$N_c = \frac{M_{ov}}{L} \quad \text{Eq. (3.1)}$$

$$V_c = \frac{V_{story}}{2} \quad \text{Eq. (3.2)}$$

$$M_c = V_c \cdot \frac{h}{2} = \frac{V_{story} \cdot h}{4} \quad \text{Eq. (3.3)}$$

Beams

$$M_b = 2 \cdot M_c = \frac{V_{story} \cdot h}{2} \quad \text{Eq. (3.4)}$$

$$V_b = 2 \cdot M_c = \frac{M_b}{L/2} = V_{story} \cdot \frac{h}{L} \quad \text{Eq. (3.5)}$$

Where

$M_{ov}$  = overturning moment of the frame

$V_{story}$  = story shear

$L$  = axial distance of columns

$H$  = vertical distance of FUSEIS beam links

The above Equations show that within a story the shears and moments of columns and beams remain constant, while the axial forces of columns moments increase linearly from the top to the base.

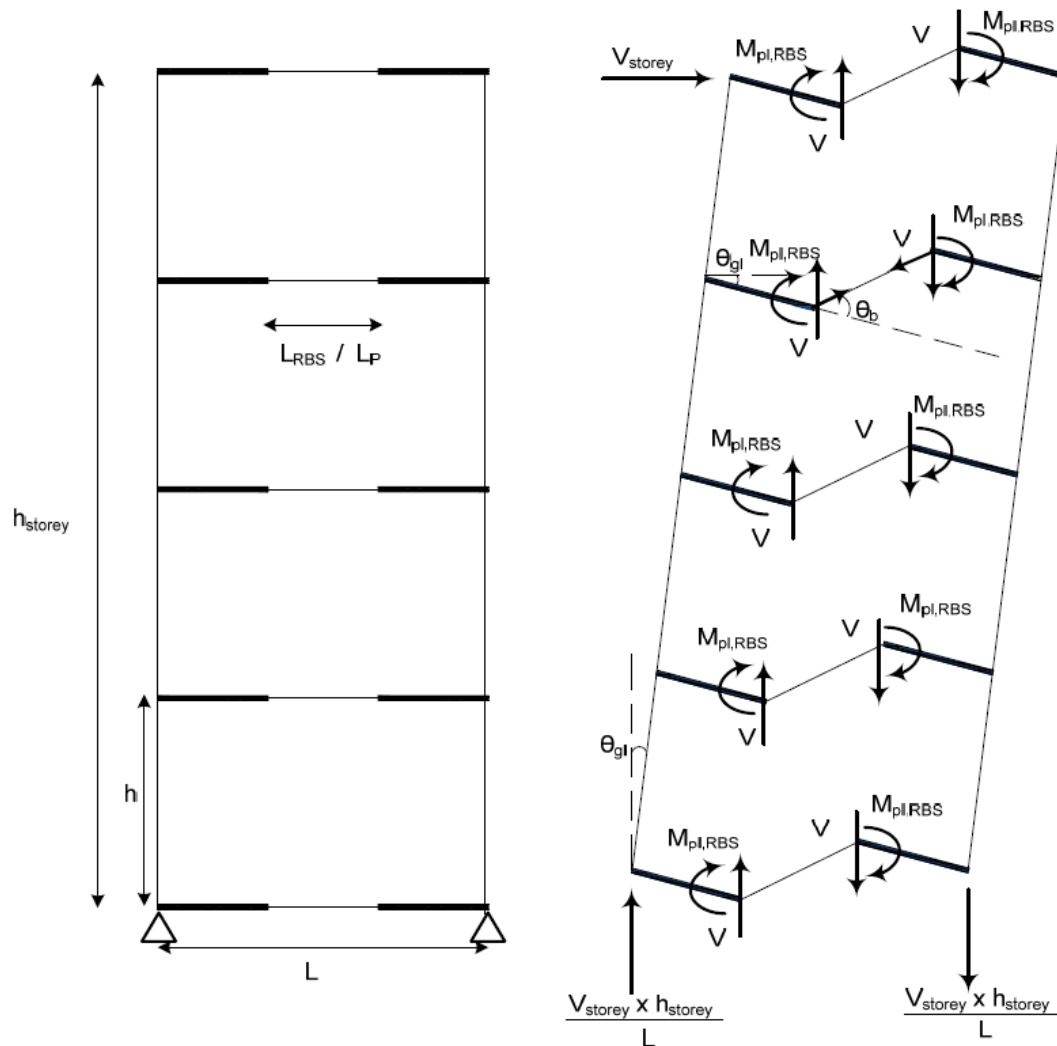


Figure 3.5: Theoretical internal forces and moments in beams and columns according to Vierendeel beam

### 3.4 EXPERIMENTAL INVESTIGATIONS ON FUSEIS BEAM LINKS

#### 3.4.1 Experimental investigations on individual beam links

##### 3.4.1.1 Experimental setup and tested beam links

Tests on the FUSEIS beam link system have been conducted during two European projects, namely the FUSEIS [12] and MATCH [26] project. Beam links have been investigated individually as described in this section. But also assembled and connected to strong columns, as reported in section 4.2. In total 40 tests have been conducted for individual beam links, 23 tests during the FUSEIS project and 17 during MATCH project. The test program covered variations of section types, material, length of beam links and loading conditions. Individual beam links have been placed between two girders of a four point hinged frame by bolted connections. A load actuator with a capacity of  $\pm 200$  mm was attached to the upper girder of the test frame, such that it could be moved horizontally, as shown in Figure 3.6. For

lateral stability a sliding panel has been mounted on the side, as can be seen in Figure 3.7.

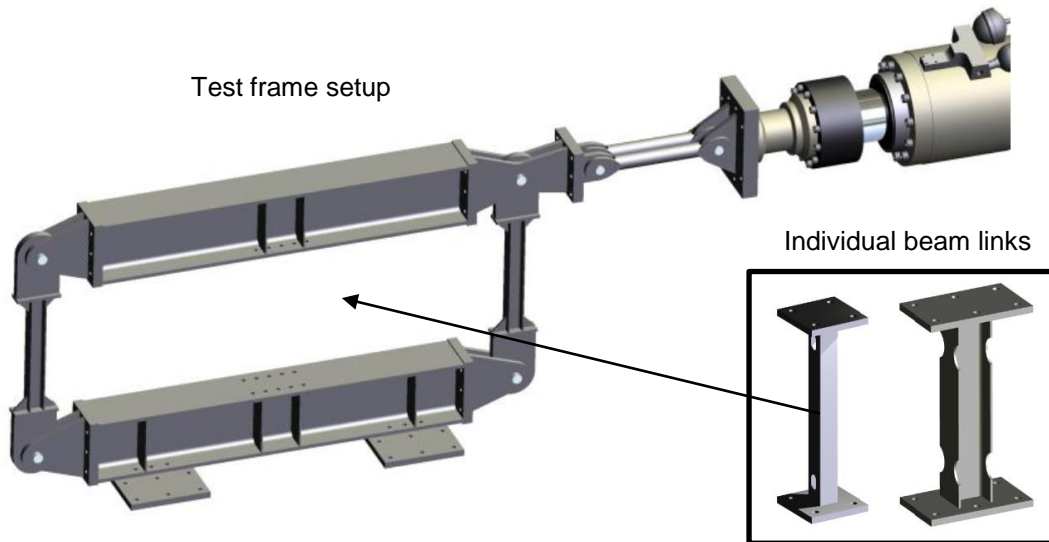


Figure 3.6: Illustration of test frame setup for testing of individual beam links

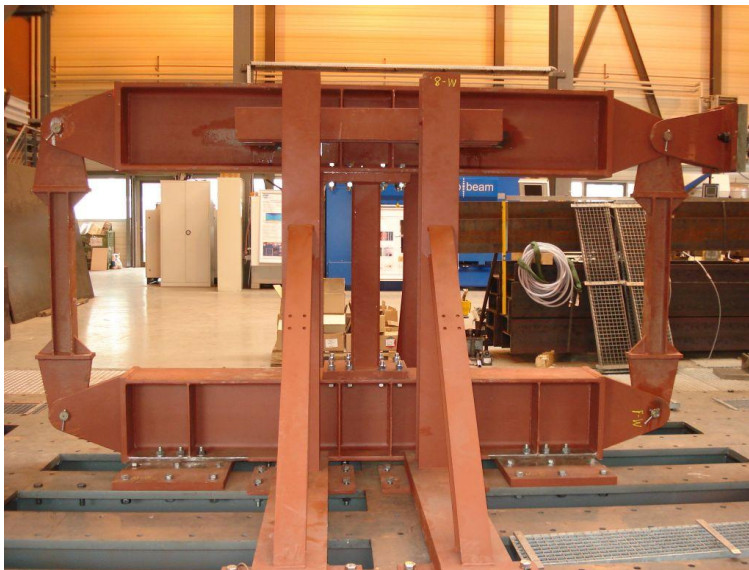


Figure 3.7: Picture of test frame setup with lateral support construction

#### 3.4.1.2 Results of monotonic tests

Long test specimens with a beam link length of 900 mm showed very ductile behavior with maximum displacements of more than 150 mm before collapsing. In comparison to these specimens the maximum displacement of shorter specimens with a length of 500 mm reached about 80 mm, whereas the hardening effect after exceeding the elastic range was much more significant in case of I-sections than CHS. This was most likely due to the high utilization degree of shear loading. Figure 3.8 shows an exemplary monotonic curve and a damage pattern for an IPE cross section FUSEIS beam link.

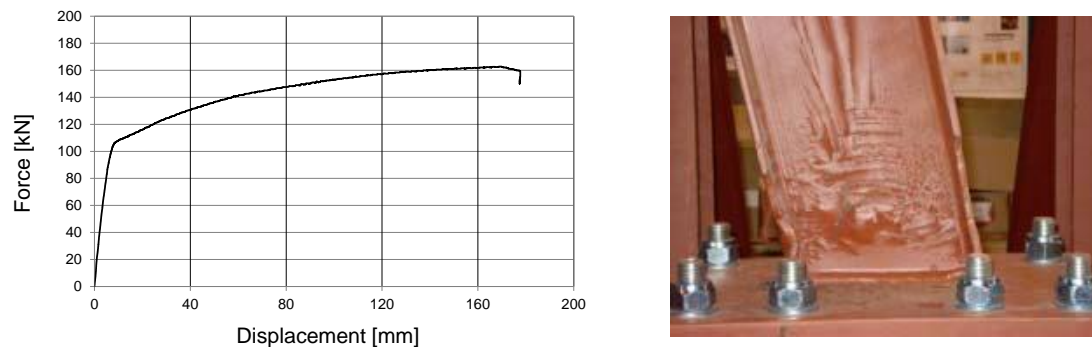


Figure 3.8: Exemplary hysteretic behavior and damage pattern for monotonic loading

#### 3.4.1.3 Results of cyclic tests

As reference for the testing procedure the ECCS – recommendation for assessing the behavior of structural steel elements under cyclic loads was used [14]. The maximum displacement value of 60 mm (4% interstory drift) was only reached with some of the FUSEIS beam links. Other beam links were not capable of this maximum displacement level. However, most of the beam links showed a very ductile behavior during cyclic loading. Although cracks and buckling effects occurred quite early during some of the tests – at displacements of approximately 20 to 30 mm – a high ductility was achieved. In most cases a distinctive ductile behavior with cracks in the base material and a slow crack propagation could be observed. The locations and the shapes of buckles were strongly dependent on the cross-section, the length of the specimen and the magnitude of loading. The points at which the first cracks occur are in general depending on these buckles. Only a few specimens failed in the area of the heat affected zone and a less ductile failure was noticed. The main remarks from the execution of the tests can be summarized as follows:

- The load-displacement curves between specimens of the same type had significant differences.
- Cracks appeared very early in some of the specimens. Anyway, in spite of cracks specimens had significant remaining capacity.
- The initial fillet welding of the SHS profiles was not sufficient. It is recommended to use full seam butt welds instead of fillet welds.

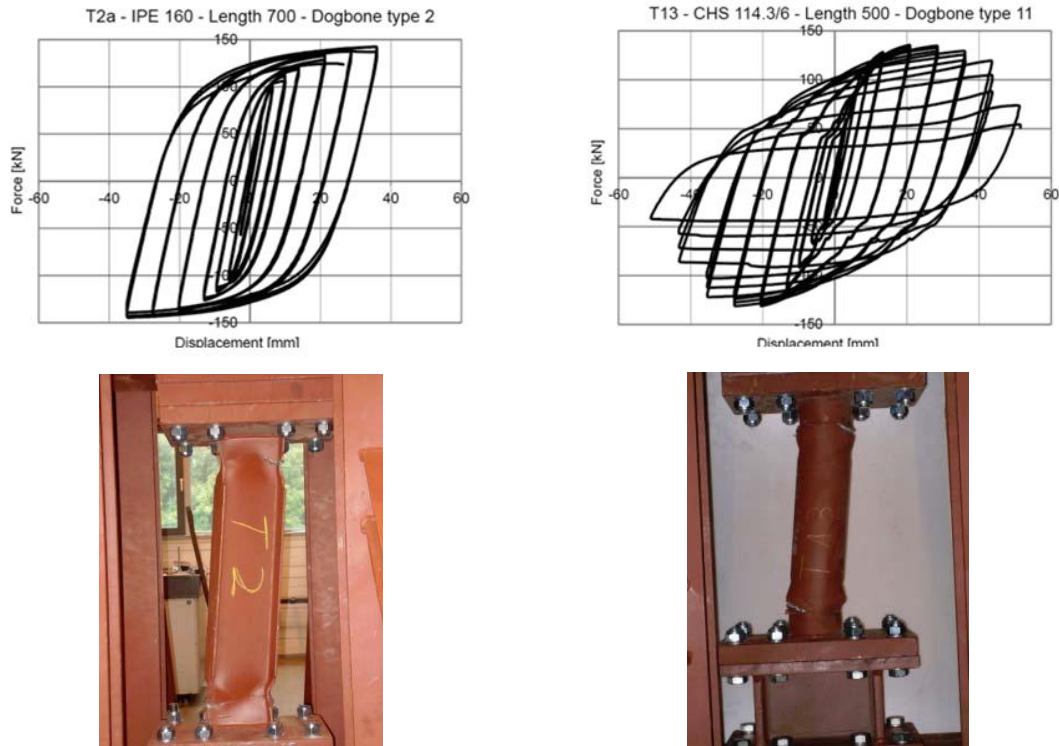


Figure 3.9: Exemplary hysteretic behavior and damage pattern for I-section (left) and CHS profile (right)

Figure 3.9 shows some exemplary hysteretic curves and damage pattern for an IPE and a CHS cross section FUSEIS beam link. In most cases cracks and buckling effects resulted in a degradation of the cyclic load displacement curves and consequently in reduced energy dissipation per cycle, which is shown in Figure 3.10. The cumulated energy dissipation is displayed in Figure 3.11. A comparison of the total dissipated energy of all FUSEIS beam links is given in Figure 3.12.

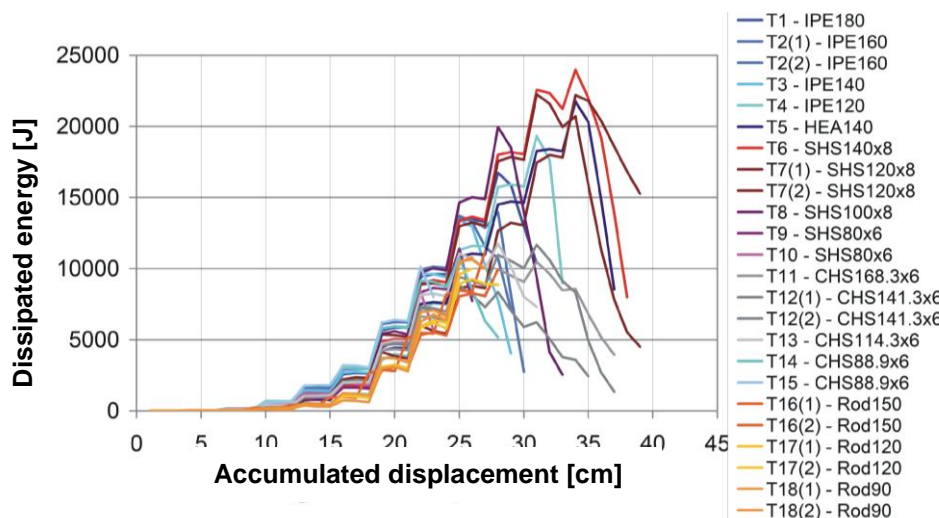


Figure 3.10: Results of cyclic testing of FUSEIS beam links: dissipated energy per cycle



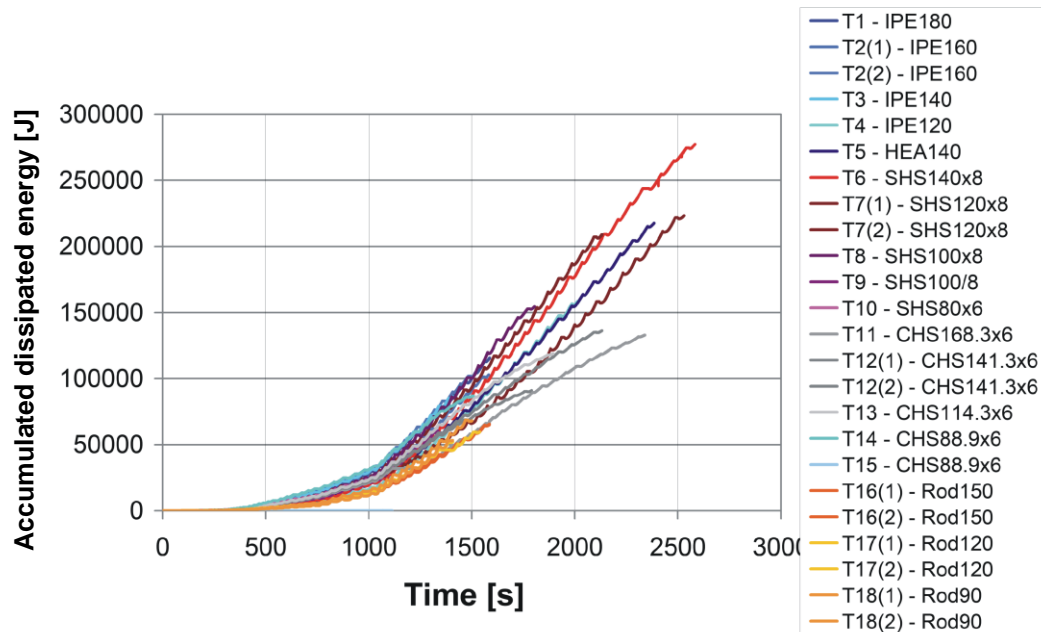


Figure 3.11: Results of cyclic testing of FUSEIS beam links: accumulated dissipated energy

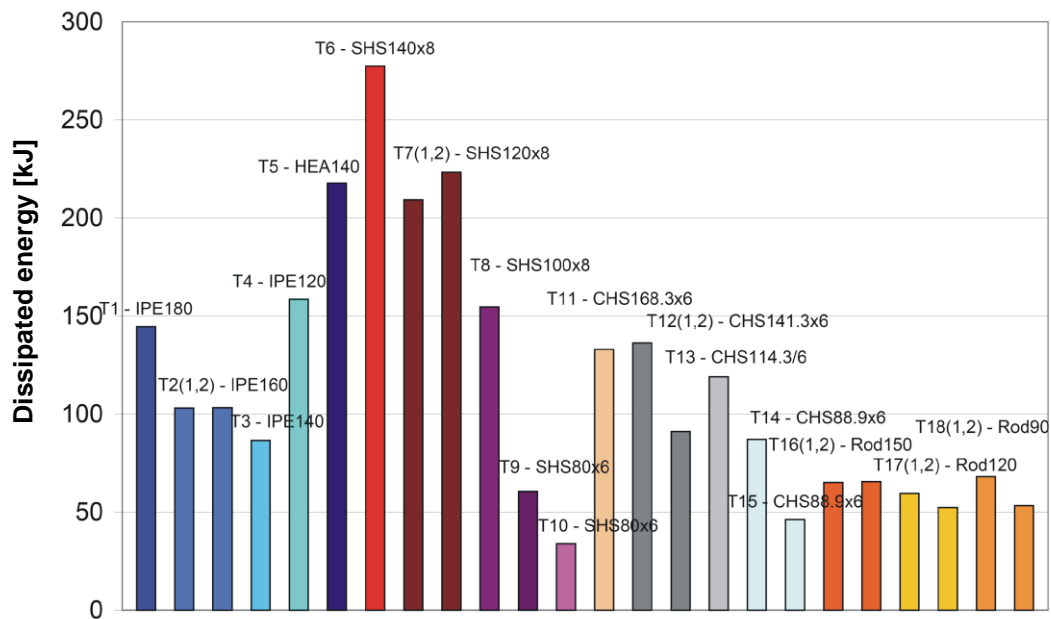


Figure 3.12: Results of cyclic testing of FUSEIS beam links: total dissipated energy

### 3.4.2 Experimental investigations on overall frames with FUSEIS beam links

#### 3.4.2.1 Experimental setup and tested frames

Two full scale tests on frames with FUSEIS beam links were conducted in the Laboratory of Steel Structures of NTUA [1]. The test frame was composed by two closely spaced strong columns rigidly connected by five beams, as illustrated in Figure 3.13. The dimensions of the frame correspond to a real building frame: its height is 3.4 m and the distance between the centrelines of the columns is 1.50 m.

The columns of the test frame were connected to the test rig by pin connections. Cyclic loading was applied through a hydraulic actuator positioned horizontally between the bottom of the columns and a base via two hinges.

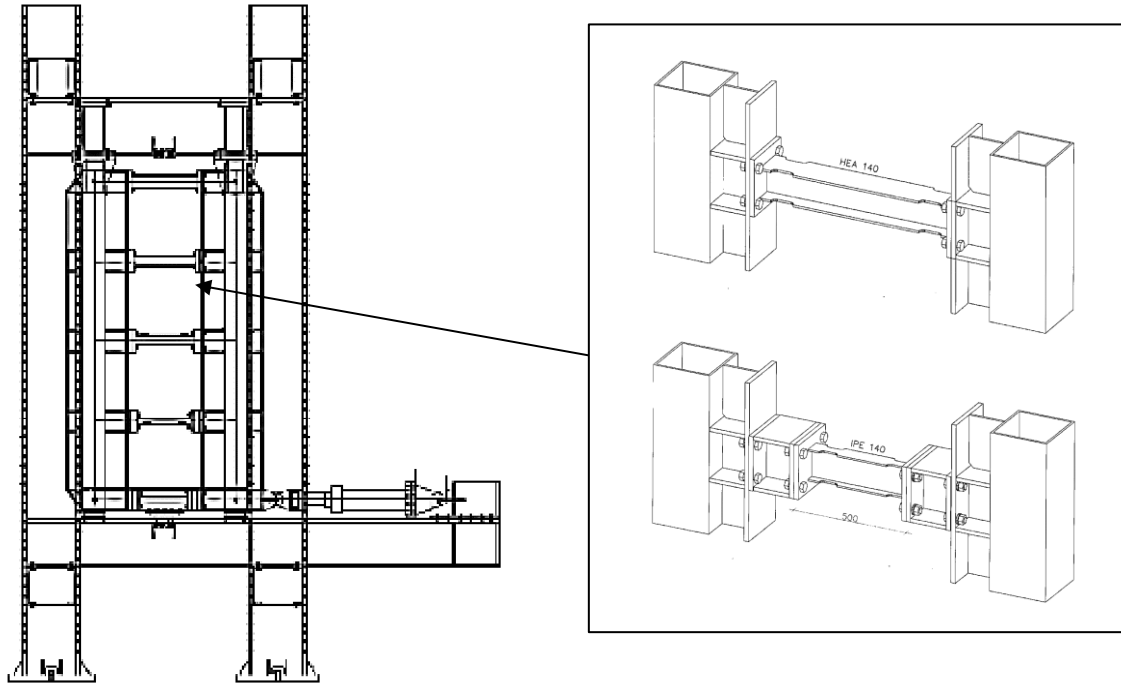


Figure 3.13: Side view on test frame with five individual beam links (left) and attachment details of individual beam links to strong columns (right)

#### 3.4.2.2 Test results

All test specimens showed good plastic deformation capacity. It is remarkable that the system's resistance kept increasing after the initial and during the sub sequential plastifications, mostly due to hardening, without losing its stability. Plastic deformations took place within the FUSEIS beam links only, while the columns remained elastic and undamaged until the completion of the last test. The time required for replacing one beam link was approximately 60 minutes.

The yielding of the beam specimens started at the dog-bone area. Ductile fractures were observed at the curve of the dogbones and finally the height of the beam shrank at the same position, as the deformation of the specimens got larger. After exhibition of maximum strength, the load degraded gradually with distortion of the dogbones. All frames reached an interstory drift between 2% and 4%. Generally, for the hollow sections it was observed that the load degraded more gradually compared to the IPE sections due to additional resistance provided by the webs. Specifically, the CHS sections behaved even better as the plastification was distributed along the section circumference. The hinge formation during the experiments was clearly visible on photos taken by a thermocamera, where red regions indicate higher temperature values at the dogbones. Figure 3.14 shows



photos of the deformed beam links. An exemplary hysteretic behavior of the total frames is shown in Figure 3.15.

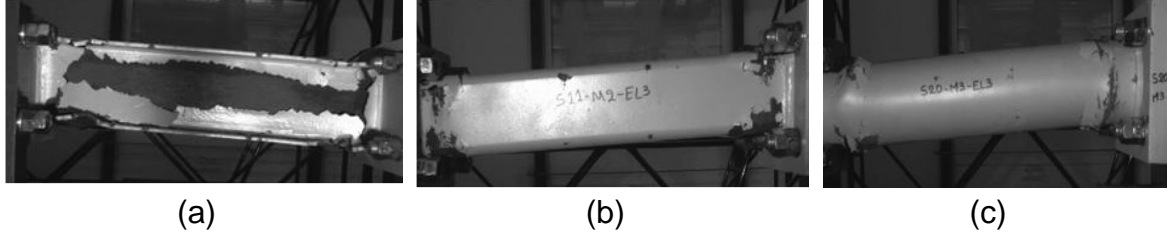


Figure 3.14: Photos of the deformed FUSEIS beam links: (a) IPE beams, (b) SHS beams, (c) CHS beams

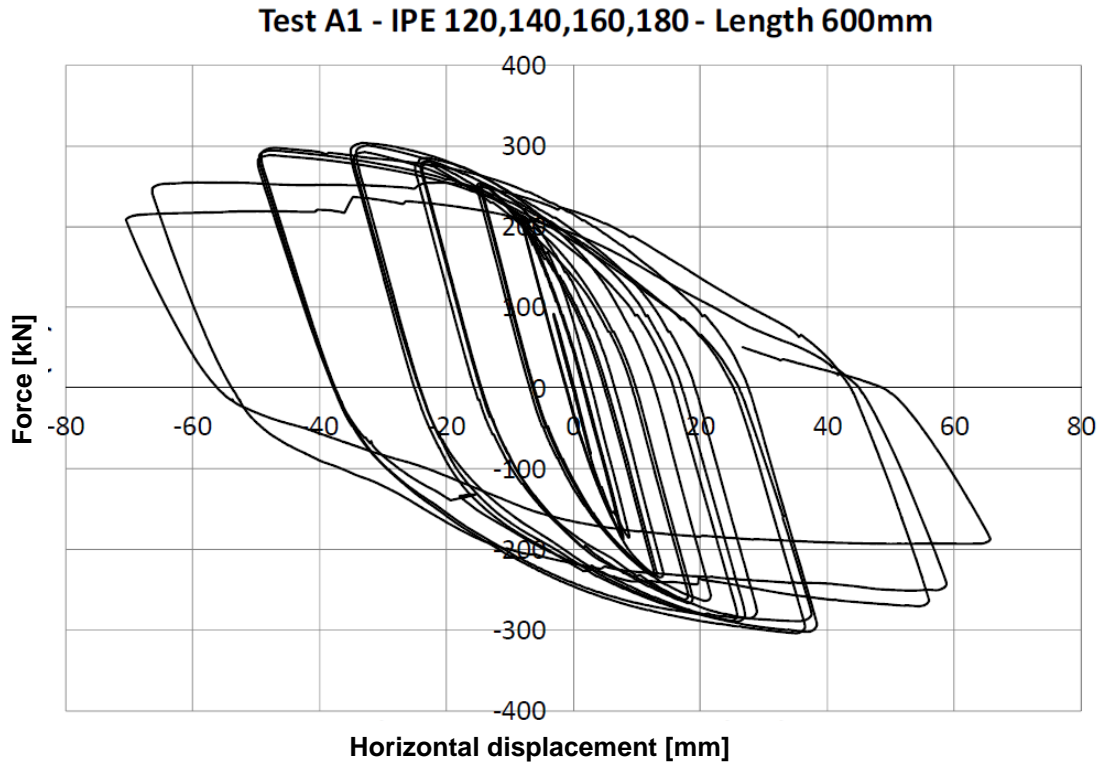


Figure 3.15: Exemplarily hysteresis of the frame equipped with IPE beams

#### 3.4.2.3 Comparison between experimental and theoretical shear forces

The experimental investigations showed that the system with beam specimens works as a vertical Vierendeel beam. It resists lateral loads mainly by bending moments of the beams and axial forces of the columns. Considering hinges at the midpoints of beams and columns, the internal moments and forces for horizontal loading in the elastic state may be derived from statics. Shear force due to the moment of resistance  $M_{pl,Rd}$  at beam ends is calculated as follows:

$$V_{storey} = \frac{2 \cdot \sum M_{pl,RBS,Rd}}{h_{storey}} \cdot \frac{L}{l_{RBS}} \quad \text{Eq. (3.6)}$$

where  $M_{pl,RBS,Rd} = W_{pl,RBS} \cdot f_y$  is the design moment resistance of the reduced beam section (RBS) of the FUSEIS beam link,  $l_{RBS}$  is the axial distance between RBS locations and  $L$  is the axial distance of FUSEIS columns. A comparison between experimental and theoretical values is given in Table 3.1. It shows that the Vierendeel beam theory is able to describe the real behavior quite well, with an underestimation of obtained shear forces of less than 25%.

**Table 3.1: Experimental vs theoretical shear forces**

Test label	$V_{exp}$	$V_{th}$	$V_{exp} / V_{th}$
A1	303.6	255.6	1.19
A2	349.9	298.0	1.17
A3	232.4	190.6	1.22
M1	367.0	345.8	1.06
M2	466.3	407.7	1.14
M3	349.4	305.0	1.15

#### 3.4.2.4 Energy dissipation – Failure criteria

In order to better understand the effect of the different types of cross sections on the energy dissipation of the system, it is important to compare the overall results. The hysteresis curves of all specimens are fairly wide, indicating good energy absorption of the system. The area enclosed by a hysteresis curve is a measure of the energy dissipated by the system during a load cycle.

For the elastic cycles up to yield, the absorbed energy was very small, so the amount of dissipated energy for each test was calculated taking into consideration the cycles after the frame yield force was reached. The yield force ( $V_{story}$ ) of the frame was computed analytically using the true steel stress ( $f_y$ ) as it is defined in the ECCS recommendations [14]. Diagrams in Figure 3.16 represent the average energy absorbed in every 3 cycles of equal amplitude, it is evident that the increase of the amplitude of the cycles (plastic cycles) leads to an increase in energy absorption. Figure 3.17 shows a comparison of the total amount of dissipated energy for all tests.

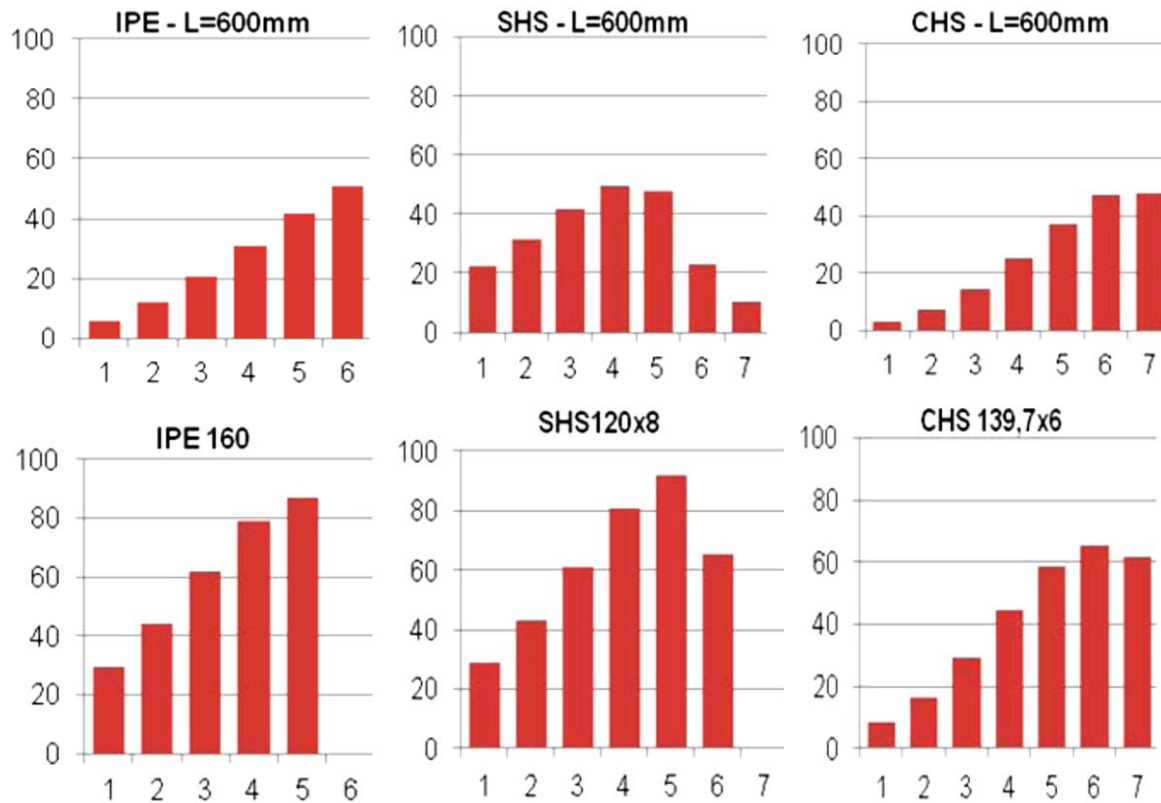


Figure 3.16: Dissipated energy in kJ per test

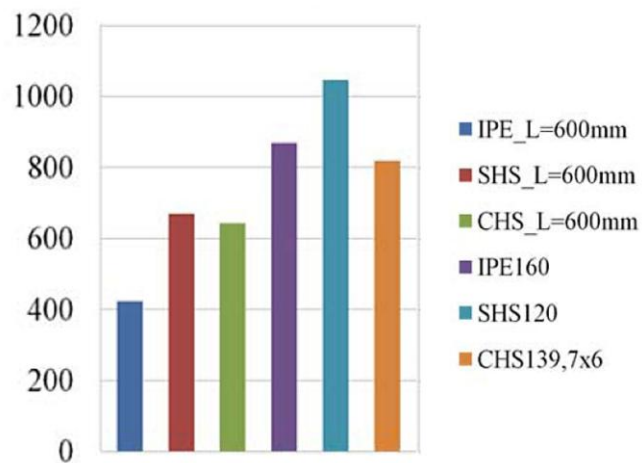


Figure 3.17: Total dissipated energy in kJ

In an attempt to evaluate the progression of accumulated damage during the tests, the criterion of the failure of steel components proposed by Calado and Castiglioni, 1996 [27], was applied. According to this criterion the dimensionless parameter  $\eta/\eta_0$  is limited to a constant value of 0.5, where  $\eta$  is the energy ratio at the end of each cycle and  $\eta_0$  is the energy ratio considering that the FUSEIS beam link has an elastic-perfectly plastic behavior. Below this limit failure occurs. This ratio was computed for all the cycles of the tests with FUSEIS beam links (Figure 3.18). It can

be observed that the limit value 0.5 was not exceeded. This result was predictable and is justified by the significant hardening effects. computed analytically using the true steel stress ( $f_y$ ) as it is defined in ECCS recommendations [14].

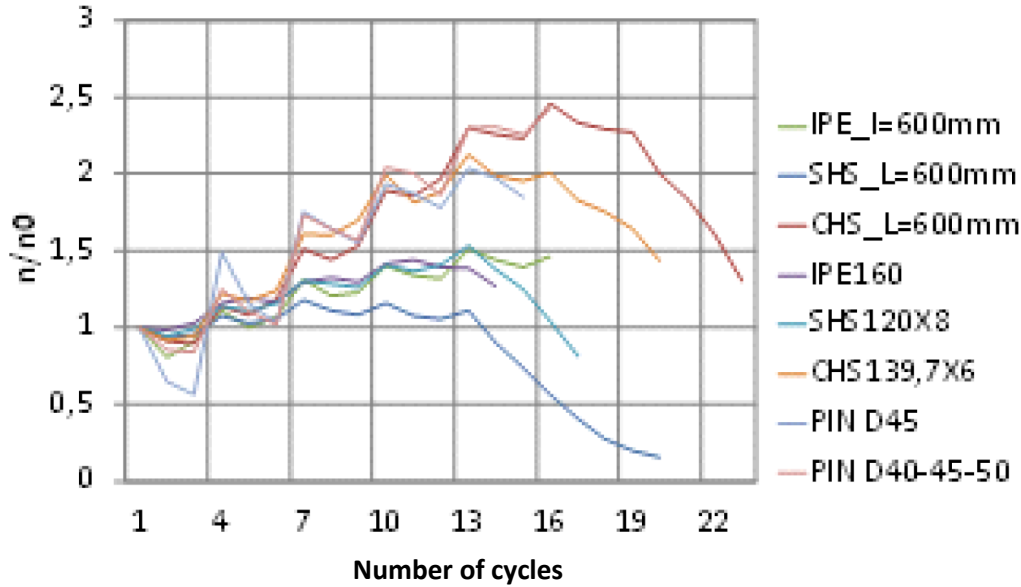


Figure 3.18: Failure Criteria

### 3.5 DESIGN RULES

Conclusions from analytical and numerical studies were summarized in a design guide [1]. The design guide gives recommendations on the selection and design of appropriate FUSEIS beam link systems. It is based mainly on provisions already contained in Eurocode 3 and Eurocode 8. However, some clauses of Eurocode 8 are appropriately rearranged to cover the use of the FUSEIS beam link system by the normal code provisions.

#### 3.5.1 Preliminary Design

As previously mentioned, the FUSEIS beam link system works as a vertical Vierendeel beam. At the ultimate limit state all beams reach, as the dissipative elements of the system, their moment capacity. If the total base shear of the building is  $V_B$ , and  $V_{story}$  is the story shear of the FUSEIS beam link system, the number of systems to be used for a preliminary design is equal to:

$$m = \frac{V_B}{V_{story}} \quad \text{Eq. (3.7)}$$

The column sections are chosen primarily from stiffness considerations in order to limit 2<sup>nd</sup> order effects. However, for  $m$  equal FUSEIS beam link systems the columns have to resist at least an axial force of  $N_{c,Ed}$ :

$$N_{c,Ed} = \frac{M_{ov}}{m \cdot L} \quad \text{Eq. (3.8)}$$

Where  $M_{ov}$  is the overturning moment of the frame and  $L$  is the axial distance of the FUSEIS beam link system columns.

The cross sections for beams and columns of the system as well as the required number of systems cannot be estimated from strength criteria alone. The deformations shall be also controlled in order to limit second order effects. The relevant code provisions require for buildings that the interstory drift sensitivity coefficient is limited to  $\theta \leq 0.1$ , if second order effects are ignored. In any case it shall be  $\theta < 0.3$ .

### 3.5.2 *Design for linear elastic analysis*

(1) For the conventional and seismic design of steel buildings with the FUSEIS beam link systems Eurocode 3 and Eurocode 8 apply. The following rules are additional to those given in these codes.

(2) The conventional method for determining the seismic effects for building frames is the modal response spectrum analysis, using a linear-elastic model of the structure and a design spectrum. The design spectrum shall be defined in accordance with Eurocode 8. The maximum  $q$ -factor to be used is 5.

(3) Frames with FUSEIS beam link systems shall be designed so that the beam links are able to dissipate energy by the formation of plastic bending mechanisms. The rules given hereafter are intended to ensure that yielding will take place in the beam links prior to any yielding or failure elsewhere. The beam links shall be designed to resist the forces of the most unfavourable seismic combination.

(4) In linear analyses the displacements induced by the design seismic action shall be calculated on the basis of the elastic deformations of the structural system through the expression:

$$d_s = q \cdot d_e \quad \text{Eq. (3.9)}$$

where

$d_s$  = displacement of a point of the structural system induced by the design seismic action

$q = q_\mu$  = the behavior factor that may be taken equal to the displacement ductility factor ( $\mu_d$ ) if  $T_1 \geq T_C$

$d_e$  = displacement of the same point of the structural system, as determined by a linear analysis based on the design response spectrum.

Usually the limitation of interstory drift defines the design of a structure with the FUSEIS beam link system, whereas the capacity ratios of the dissipative elements ( $\Omega$ ) are low. The calculation of the design interstory drift based on  $d_s$  is therefore conservative. A reduction factor ( $q_\Omega$ ) equal to the capacity ratio of the FUSEIS beam links may be employed as follows:

$$d_s = q_\mu \cdot q_\Omega \cdot d_e \quad \text{Eq. (3.10)}$$

For non-linear analysis, static or dynamic, the displacements induced by the seismic action are those obtained from the analysis.

(5) The non-dissipative elements, the FUSEIS beam link to columns connections and the system columns, should be designed taking into account the section overstrength  $\Omega$  and the material overstrength factor  $\gamma_{ov}$ .

(6) In the current state of the art, a spatial model representing the 3-D structure is used. The following modelling guidelines may be followed:

- a) The FUSEIS beam link elements shall be represented by appropriate beam-column FE-elements.
- b) Rigid zones shall be provided from column centers to column faces to exclude non-existent beam flexibilities.
- c) The net beam length shall be subdivided into 5 zones as shown in Figure 3.19. These zones shall represent the full sections (both end plus middle section) and the RBS sections. In this manner, the true system flexibility and strength will be accounted for.
- d) The remaining structural elements shall be represented as usually by appropriate finite elements.
- e) Beam-to-column joints will be represented as rigid, semi-rigid or hinged in accordance to the connection detailing.

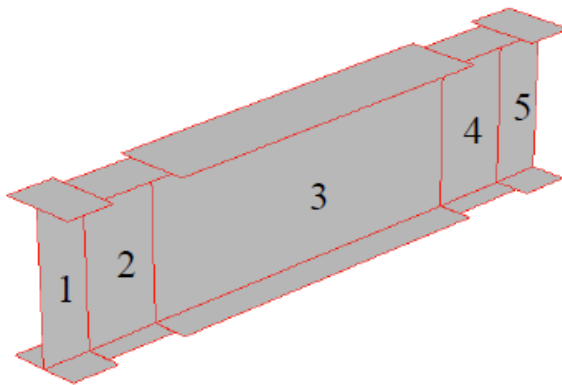


Figure 3.19: Numerical modelling of FUSEIS beam link

#### 3.5.2.1 Dissipative element verifications

(1) The dissipative elements of the system, i.e. beam links, shall be verified to resist the internal forces and moments as determined from the structural analysis.

(2) The moment capacity shall be verified as following:

$$\frac{M_{Ed}}{M_{pl,RBS,Rd}} \leq 1.0 \quad \text{Eq. (3.11)}$$

where:

$M_{Ed}$  = design bending moment

$M_{pl,RBS,Rd}$  = plastic, resistance design moment of RBS section

(3) The shear resistance shall be verified in accordance to:

$$\frac{V_{CD,Ed}}{V_{b,pl,Rd}} \leq 1.0 \quad \text{Eq. (3.12)}$$

Where:

$$V_{CD,Ed} = \frac{2 \cdot M_{pl,RBS,Rd}}{l_{RBS}} \quad \text{Eq. (3.13)}$$

$V_{CD,Ed}$  = capacity design shear force

$V_{b,pl,Rd}$  = design shear resistance of beam section

(4) It should be noted that the influence of shear should be accounted for in determining  $M_{pl,RBS,Rd}$ . This is the case when the ratio between acting shear and shear resistance is:

$$\frac{V_{CD,Ed}}{V_{b,pl,Rd}} > 0.5 \quad \text{Eq. (3.14)}$$

The combination of the above equations gives that the influence of shear should be accounted for if:

$$l_{RBS} < \frac{2 \cdot M_{pl,RBS,Rd}}{V_{b,Rd}} = \frac{4 \cdot W_{pl,RBS}}{A_v / \sqrt{3}} \quad \text{Eq. (3.15)}$$

Eq. (3.14) is seldom fulfilled due to the fact that  $A_v$  refers to the full section while  $W_{pl,RBS}$  to the reduced beam section. In order to avoid the interaction between shear and moments, the flanges should be reduced so that Eq. (3.15) is fulfilled.

(5) The beam end moment resistance shall be verified in accordance with:

$$\frac{M_{CD,Ed}}{M_{b,pl,Rd}} \leq 1.0 \quad \text{Eq. (3.16)}$$

Where:

$M_{CD,Ed} = \frac{l_b}{l_{RBS}} \cdot M_{pl,RBS,Rd}$  = capacity design bending moment

$M_{b,pl,Rd}$  = design bending moment of beam section

(6) Lateral torsional buckling verifications for the FUSEIS beam links are generally not necessary due to their small length.

### 3.5.2.2 Connection verifications

#### (1) Bending moment resistance

$$M_{CD,con,Ed} = \max\{M_1, M_2\} \quad \text{Eq. (3.17)}$$

Where

$$M_1 = 1.1 \cdot \gamma_{ov} \cdot \frac{l_b}{l_{RBS}} \cdot M_{pl,RBS,Rd} \quad \text{Eq. (3.18)}$$

$$M_2 = 1.1 \cdot \gamma_{ov} \cdot M_{u,b} \quad \text{Eq. (3.19)}$$

Where

$$M_{u,b} = W_{pl,b} \cdot f_u \quad \text{Eq. (3.20)}$$

$\gamma_{ov} = \frac{f_{y,act}}{f_y}$  if the actual yield strength of the beam is known or if not  $\gamma_{ov} = 1.25$

$l_b$  = net beam length

$l_{RBS}$  = axial distance of RBS sections

$f_{y,act}$  = actual yield strength of the beam

$f_u$  = ultimate strength of the beam

$W_{pl,b}$  = plastic moment of the beam section at beam end

#### (2) Shear force

$$V_{CD,con,Ed} = 1.1 \cdot \gamma_{ov} \cdot \frac{2 \cdot M_{pl,RBS,Rd}}{l_{RBS}} \quad \text{Eq. (3.21)}$$

(3) If RBS sections are not used and alternatively the connection region is strengthened by means of additional plates, the strengthened area and the connection shall have a capacity design moment equal to:



$$M_{con,CD} = \frac{l_b}{l_{net}} \cdot M_{u,b} \quad \text{Eq. (3.22)}$$

Where

$l_b$  = net beam length

$l_{net}$  = net un-strengthened beam length

$M_{u,b} = W_{pl,b} \cdot f_u$

The design shear of the connection may be calculated from:

$$V_{con,CD} = \frac{2 \cdot M_{con,CD}}{l_b} \quad \text{Eq. (3.23)}$$

(4) It should be added that both alternatives – weakening of beam links or strengthening of connections (see Figure 3.20) – have been experimentally proved to be effective in ensuring the plastic hinge formation away from the connection.

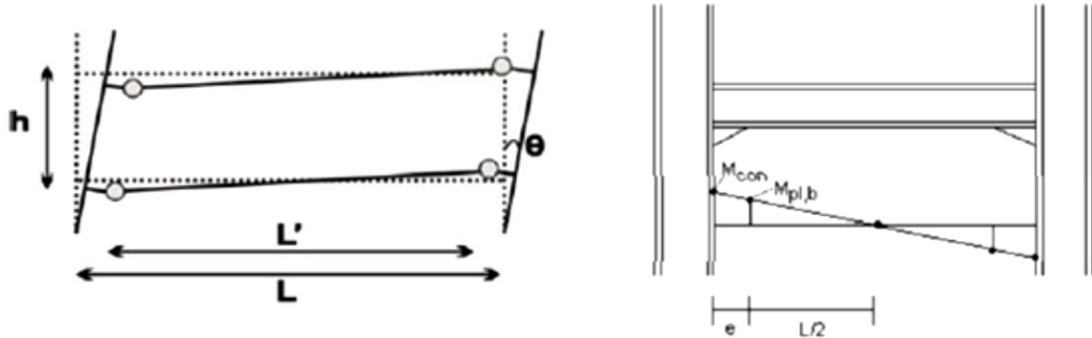


Figure 3.20: Plastic hinges with RBS sections and end strengthening of the beam

### 3.5.2.3 Non-dissipative element verifications

(1) The FUSEIS columns shall be verified to resist the capacity design action effects as following:

$$N_{CD,ED} = N_{Ed,G} + 1.1 \cdot \gamma_{ov} \cdot \Omega \cdot N_{Ed,E} \quad \text{Eq. (3.24)}$$

$$M_{CD,ED} = M_{Ed,G} + 1.1 \cdot \gamma_{ov} \cdot \Omega \cdot M_{Ed,E} \quad \text{Eq. (3.25)}$$

$$V_{CD,ED} = V_{Ed,G} + 1.1 \cdot \gamma_{ov} \cdot \Omega \cdot V_{Ed,E} \quad \text{Eq. (3.26)}$$

Where:

$N_{Ed,G}, V_{Ed,G}, M_{Ed,G}$  = axial forces, shear force and bending moment respectively in columns due to the non-seismic actions included in the combination of actions for the seismic design situation

$N_{Ed,E}, V_{Ed,E}, M_{Ed,E}$  = axial forces in columns due to the design seismic action

$$\Omega = \min \Omega_i = \min \left\{ \frac{M_{pl,RBS,Rd,i}}{M_{Ed,i}} \right\}$$

= minimum value of the relevant ratios for all FUSEIS beam links in the building.

### 3.5.3 Design for non-linear static analysis (Pushover)

(1) The structural model used for elastic analysis shall be extended to include the response of structural elements beyond the elastic state and estimate expected plastic mechanisms and the distribution of damage.

(2) Since the ductile elements are the FUSEIS beam links, potential plastic hinges shall be inserted at the ends of their reduced parts. The nonlinear properties for IPE, SHS, and CHS sections that derived from experimental and analytical investigations are given in Table 3.2.

(3) Additional potential plastic hinges may be inserted at the ends of the composite beams, the columns and the system columns to check if they also behave inelastic during the seismic event. The hinge properties shall be calculated according to the provisions of relevant codes (e.g. FEMA-356).

**Table 3.2: Non-linear hinge parameters for IPE, SHS and CHS sections**

HINGE PROPERTIES ( $\alpha_{pl}$ =shape factor)						
	IPE		SHS		CHS	
Point	M/SF	Rot./SF	M/SF	Rot./SF	M/SF	Rot./SF
E-	-0.6	-45	-0.4	-30	-0.2	-30
D-	-0.6	-40	-0.4	-25	-0.2	-25
C-	$-\alpha_{pl}$	-40	$-\alpha_{pl}$	-25	$-\alpha_{pl}$	-25
B-	1	0	-0.6	0	-1	0
A	0	0	0	0	0	0
B	1	0	0.6	0	1	0
C	$\alpha_{pl}$	40	$\alpha_{pl}$	25	$\alpha_{pl}$	25
D	0.6	40	0.4	25	0.2	25
E	0.6	45	0.4	30	0.2	30
ACCEPTANCE CRITERIA						
	IPE		SHS		CHS	
IO	15		5		6	
LS	25		12		10	
CP	35		18		16	

### 3.5.4 Design for non - linear dynamic analysis

(1) In order to obtain detailed time-dependent response of steel buildings when designed according to the provisions of the Eurocodes under real earthquake conditions, non - linear dynamic analyses shall be performed.

(2) For the dissipative elements of the structure the nonlinear hinge properties of Table 3.2 shall be assigned at their ends.

(3) For the non-dissipative elements the hinge properties shall be calculated according to the provisions of relevant codes (e.g. FEMA-356).

(4) Non-linear dynamic analyses provide information and thus the capability to restrict damage after a seismic event by evaluating and eliminating the residual drifts of the structure. If the FUSEIS beam link system is appropriately designed, it is able to work as a self-centering system, with practically zero residual drifts. When combined with moment resisting frame (MRF) action the deformations are concentrated in the FUSEIS beam links and the rest of the structure remains elastic, while the moment frame action helps the structure return to its initial state. On the contrary, when simple beam-to-column connections are used, the structure is not able to return at the end of the seismic event.

### **3.6 ANALYSES ON 2D BUILDING FRAMES**

The following section illustrates the successful application of a moment resisting frame combined with the FUSEIS beam link system for seismically designing typical 2D building frames. The seismic design parameters are briefly summarized. Emphasis is given on the seismic design process, assisted by FE analyses with performing a pushover analysis of the frame structures. To evaluate the sensitivity of the structures to higher seismic loads and the impact of using a behavior factor of  $q = 5$  in the design process for the structural design, a more detailed analysis was performed for different levels of seismic loading.

#### *3.6.1 Description of examined building frames*

##### *3.6.1.1 Geometry and assumptions*

A typical 2D building frame, part of a five-story composite building, is used for all the cases examined. The general layout of the frame is given in Figure 3.21. The composite building consists of similar frames with 8m axial distance which is the effective width for both the vertical loads, and the lateral mass during earthquake loading. The beams are composite ones and the thickness of the slab is 15 cm. The frame consists of two closely positioned vertical hollow strong columns, jointed together with horizontal beam links in a tight arrangement, similar to the test (five FUSEIS beam links per story). The center line distance of the columns is 2.0 m. The bays of the main frame are 6.0 m. The effective width of the composite beams was calculated based on Eurocode 2 and is equal to 1.5 m. Main assumptions of material and loads are given in Table 3.3.

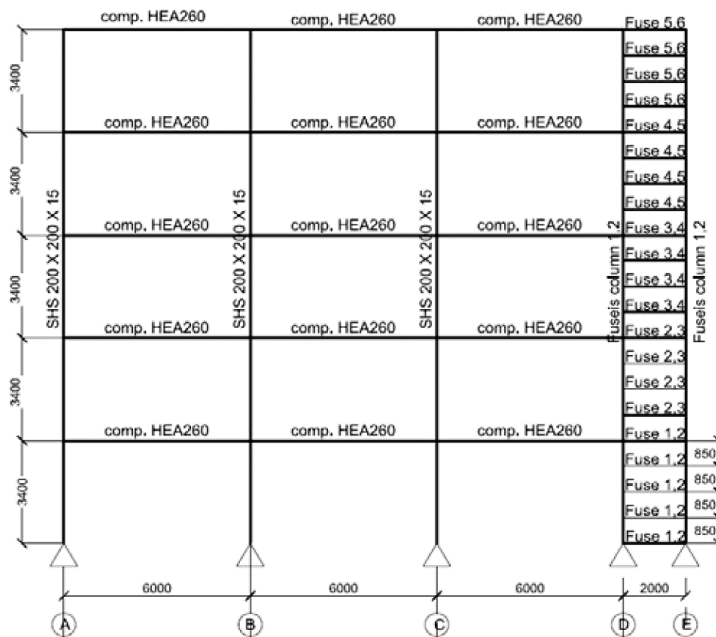


Figure 3.21: Layout of 2D building frame

Table 3.3: Assumptions for materials and loads

Materials	
Concrete	C25/30, $g = 25 \text{ kN/m}^3$ , $E = 31\,000 \text{ Mpa}$
Reinforcement	B500C
Structural steel	S235: Dissipative elements (FUSEIS beam links) S355: Non dissipative elements (beams and columns)
Vertical loads	
Dead loads apart from self-weight – G	$2.00 \text{ kN/m}^2$
Live loads – Q	$2.00 \text{ kN/m}^2$
Seismic loads	
Elastic response spectrum	Type 1
Peak ground acceleration	$A=0.16g - 0.24g - 0.36g$
Importance class II	$\gamma_I = 1.0$ (Ordinary buildings)
Ground type	B ( $T_B = 0.15 \text{ s}$ , $T_C = 0.50 \text{ s}$ )
Behavior factor q	5
Damping ratio	5%
Factors of operating loads for seismic comb.	$\varphi=1.00$ (roof), $\varphi=0.80$ (stories with correlated occupancies)
Seismic combination coefficient for the quasi-permanent value of variable actions	$\psi_2=0.30$

Firstly, the frame has been designed according to the provisions of Eurocode 3 for the ULS and SLS, taking into consideration limitations on 2<sup>nd</sup> order effects. Seismic design provisions according to Eurocode 8 have been further taken into account. Interstory drifts were limited to 0.0075 (buildings having ductile non-structural elements). The determination of the controlling structural members in terms of drifts within the structural system was accomplished through parametric studies on the

building frame. The seismic response of the building frame was assessed through a modal response spectrum analysis, using a linear-elastic model of the structure and a design spectrum. The analysis shows that the use of the first modes of vibration is enough to achieve the required 90% of effective mass. Cross section dimensions for the FUSEIS beam link system using different section types obtained from the design are listed in Table 3.4 for different design peak ground accelerations (PGA = 0.16, 0.24 and 0.36). For the first two - low and medium seismicity – identical cross sections have been chosen.

**Table 3.4: Cross section of FUSEIS beam links**

Story	PGA 0.16 & 0.24			PGA 0.36		
	IPE	SHS	CHS	IPE	SHS	CHS
1	220	180 x 8	193.7 x 8	240	200 x 8	219.9 x 8
2	240	200 x 8	219.9 x 8	270	220 x 8	244.5 x 8
3	270	220 x 8	244.5 x 8	300	240 x 8	273.0 x 8
4	300	240 x 8	273.0 x 8	330	260 x 8	323.9 x 8
5	330	260 x 8	323.9 x 8	360	280 x 8	355.6 x 8

The hysteretic behavior of the dissipative elements did not affect the overall stability of the structure. For plastic hinges in the beams it was verified that the full plastic moment of resistance and rotation capacity are not decreased by compression and shear forces. Therefore the FUSEIS beam links of the examined frames were designed to have adequate ductility and to resist the internal forces and moments as determined from the structural analysis.

#### 3.6.1.2 Simulation

The simulation concept for the FUSEIS beam links is as follows: elastic beam elements have been used for the main frame, rigid zones were provided from column centers to column faces, the net length of beam links was subdivided into 5 zones. The beam link-to-column joints are formed as rigid to enable the Vierendeel action and are designed to have sufficient overstrength in order to achieve energy absorption only in the beam links. Pin connections are introduced at the column bases to limit yielding at the foundation and thereby minimize damage to the columns. In order to introduce partial fixity conditions between the composite beams and the columns, rotational springs are assigned at the composite beams' ends. The spring constants were calculated analytically for each frame according to Eurocode 3, part 1.8, §6.3 and Eurocode 4, part 1 (Annex A), taking into account the longitudinal reinforcement of the concrete flange. The stiffness coefficients were much lower at the beams connected to columns A&D compared to the ones connected to the middle columns B&C (see Figure 3.21).

The loading is considered the same for all stories and the masses are lumped at the joints. Steel grade of the non-dissipative structural members is assumed to be S355 and for the dissipative elements (the FUSEIS beam links) is assumed to be S235 to eliminate the risk of possible overstrength of the dissipative elements.

### 3.6.2 Non - linear static analyses (Pushover)

#### 3.6.2.1 Evaluation of the non-linear behavior of the frames

The structural models used for elastic analysis were extended to include the response of structural elements beyond the elastic state via a non-linear static analysis (Pushover). The principal objective of this investigation was to estimate and verify the behavior factor  $q$ .

The base of the analysis was the target displacement applied at the roof of the frame equal to 0.68 m (interstory drift 4%). The analysis was carried out under conditions of constant gravity loads  $1.0 G + 0.3 Q$  and monotonically increasing lateral loads. Two vertical distributions of the lateral loads were applied: a “uniform” pattern and a “modal” pattern distribution in the direction under consideration, determined in elastic analysis. The results of the analysis according to the fundamental mode of vibration, 1st mode, are presented hereafter. The analysis was based on the assumption that the mode shape remains unchanged after the structure yields, P-Delta effects were also taken into account. In pushover analysis, the behavior of the structure is characterized by a capacity curve that represents the relationship between the base shear force and the displacement of the roof and the demand curve for the design earthquake based on ATC-40 [28]. The performance point is defined as the intersection of the demand curve with the capacity curve (Figure 3.22).

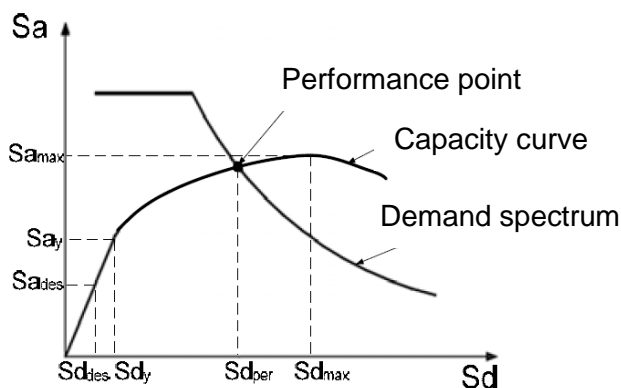


Figure 3.22: Definition of the performance point

In the implementation of pushover analysis, modelling of the plastic hinges is the most crucial step. The model requires the determination of the nonlinear properties of each component in the structure that are quantified by strength and deformation capacities. Non-linear hinge elements were assigned to the structural members. The

FUSEIS beam link hinges were inserted at the ends of the reduced parts and their properties were the proposed values that derived from the calibrated models of the tests (Table 3.2).

At the first non-linear analysis, potential plastic hinges were also inserted at the ends of the composite beams, the columns and the system columns to check if they also behave inelastic during the seismic event. For these elements due to the lack of experimental data the hinge properties were calculated according to FEMA-356. Specifically, for the composite beam the plastic moment considered for the definition of the plastic hinges, derived from the plastic modulus of the steel section disregarding the participation of the longitudinal reinforcement. This assumption had a minor effect on the results, however in a more detailed design the longitudinal reinforcement should be taken into account. On the beams, axial forces were assumed to be zero; on the columns, they were assumed to be constant and equal to the load due to the dead loads plus 30% of the live loads on the columns. Figure 3.23 shows the deformed frame with SHS beam links at the performance point. It is obvious that the plastic hinges formed throughout the height of the FUSEIS beam link system in the reduced parts of the beam links, but not in the rest of the structure. For this reason the results following contain hinges only in the FUSEIS beam links.

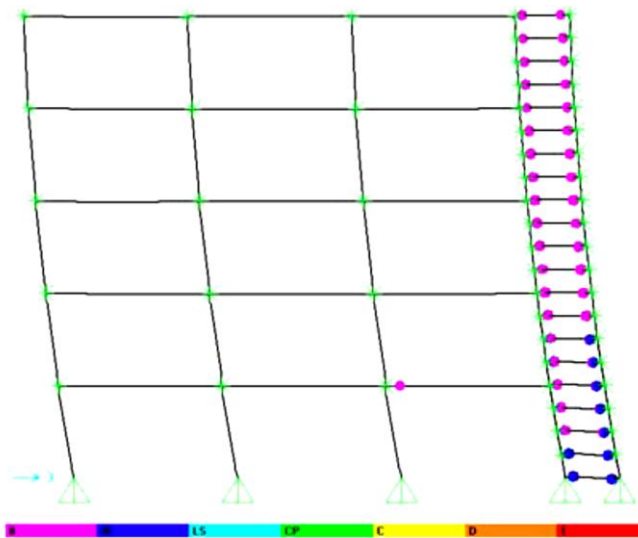


Figure 3.23: Deformed frame with SHS beam links at the performance point

The results of the pushover analysis including the distribution of plastic hinges in the examined building frame and the evaluation of the performance point are given in Figure 3.26. As expected the weak beam strong column concept is fulfilled for all frames studied and the sequence of plastic hinges starts with beams' ends from lower stories up to upper stories. The base shear ( $V$ ), the monitored displacement ( $D$ ), the spectral acceleration ( $S_a$ ) and the spectral displacement ( $S_d$ ), of 9 different building frames at the performance point are gathered in Table 3.5.

**Table 3.5: Response parameters for beam links with different cross section type**

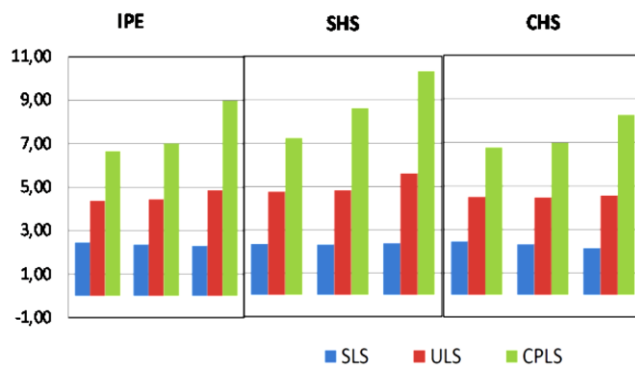
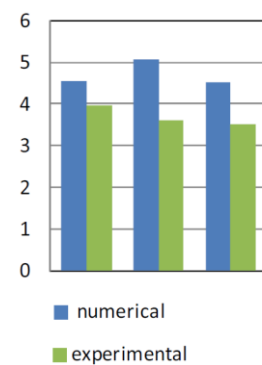
FUSEIS beam link type	0.16g				0.24g				0.36g			
	V	D	S <sub>a</sub>	S <sub>d</sub>	V	D	S <sub>a</sub>	S <sub>d</sub>	V	D	S <sub>a</sub>	S <sub>d</sub>
	(kN)	(cm)	(g)	(cm)	(kN)	(cm)	(g)	(cm)	(kN)	(cm)	(g)	(cm)
IPE	480	8.7	0.13	7.3	536	13.3	0.14	11.1	692	18.9	0.17	15.6
SHS	966	9.0	0.09	7.9	442	14.0	0.11	12.0	852	20.4	0.20	17.4
CHS	467	10.7	0.13	7.5	537	15.5	0.14	11.3	552	9.2	0.15	6.3

Except for the assessment of the structural performance of the building frames, pushover analysis also offers the possibility to estimate their ductility factor. The performance point was considered to be the key parameter for the determination of the ductility factor. So, the ductility factor required was defined as the ratio of the displacement at the performance point  $d_{per}$  to the design displacement  $d_{des}$ , as following:

$$\mu_{dem} = \frac{d_{per}}{d_{des}} \quad \text{Eq. (3.27)}$$

$$d_{des} = \frac{S_{a,des} \cdot d_y}{S_{a,y}} \quad \text{Eq. (3.28)}$$

where,  $S_{a,des}$  is the spectral acceleration that derives from the design spectra for the fundamental mode,  $S_{a,y}$  is the spectral acceleration and  $d_y$  is the displacement when the first hinges were formed. In order to check the seismic behavior and determine the  $\mu$  factor for different ground motion intensities (0.16g, 0.24g and 0.36g), three performance levels (Limit states) were considered: serviceability limit state (SLS  $\lambda = 0.5$ ), ultimate limit state (ULS  $\lambda = 1.0$ ) and collapse prevention limit state (CPLS  $\lambda = 1.5$ ). The calculated  $q$  factors are presented in the histodiagrams in Figure 3.24.

Figure 3.24: Histodiagrams of the calculated  $\mu$  factorsFigure 3.25: Comparison  $\mu$ -factors

It can be seen that behavior factor is ascending when the system passes from SLS to CPLS performance level, due to the fact that the amount of the dissipated energy



increases at higher performance levels. It should be noted that at the CPLS the hinges formed in the FUSEIS beam links were at the Life Safety performance level and the hinges formed at the rest of the structure (composite beams-columns) were below the Immediate Occupancy level, which means that the structure has light to moderate overall damages and repair works may be needed only for the FUSEIS beam links. In the diagram in Figure 3.25 the experimental values of the behavior factor are compared to the analytically determined. The experimental values are lower than the numerical ones.

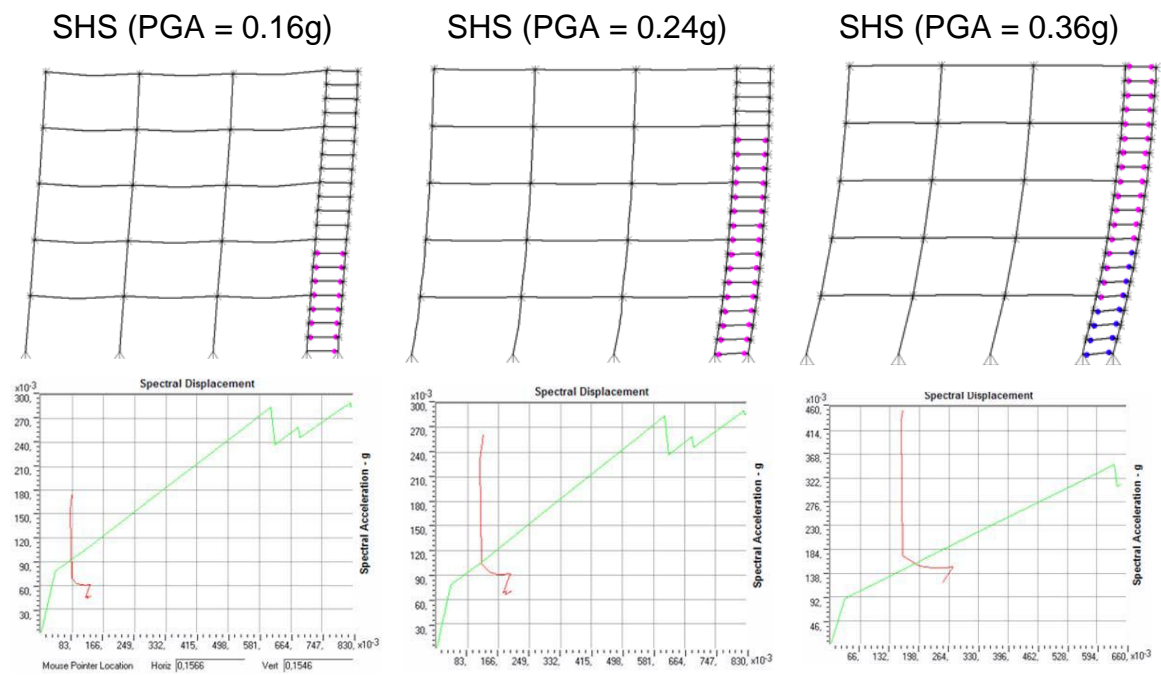


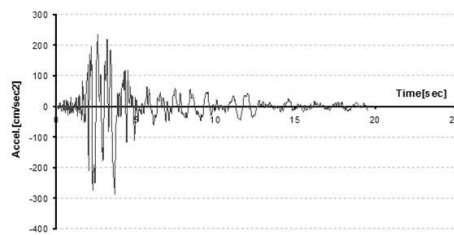
Figure 3.26: Pushover analysis results on frames with FUSEIS beam links with SHS section

### 3.6.3 Non-linear dynamic analyses (time-history)

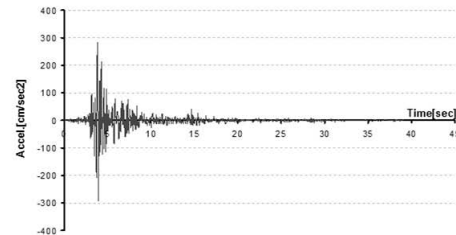
In order to define time-dependent response of steel buildings when designed according to the provisions of the European codes under real earthquake conditions, non - linear dynamic analyses on a representative 2D building frame were performed. These models reflect the response of the building frame over a wide range of events. Recent Greek earthquakes, that caused severe damage and loss of human lives, and the El Centro earthquake used widely as reference were selected. Additionally, artificial acceleration data were examined. The relevant information is given in Table 3.6 and Figure 3.27. The characteristics of these records were representative for the examined frame and thus the results were satisfactory in terms of deformation requirements. The records were scaled adequately to comply with the seismic zone 0.36g. Figure 3.28 combines the acceleration spectra of the selected records together with the design spectrum and the fundamental period of the frame.

**Table 3.6: Types and configurations of the seismic records**

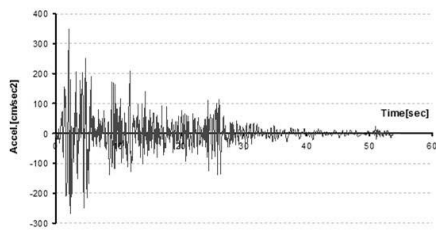
Type	Location	PGA[g]
Near field European (from Greece)	Kalamata (1985)	0.294
	Athens (1999)	0.298
Near field International	El. Centro	0.355
5 artificial accelerograms	-	0.300



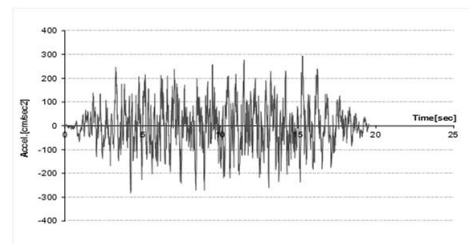
Kalamata 1985



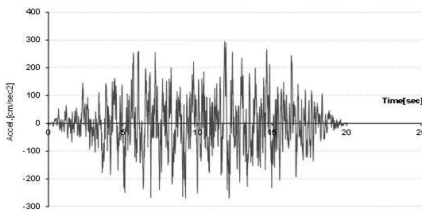
Athens 1999



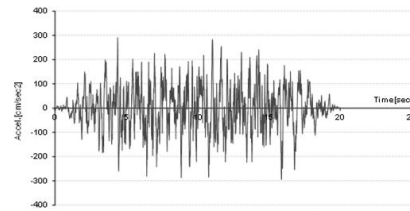
El Centro



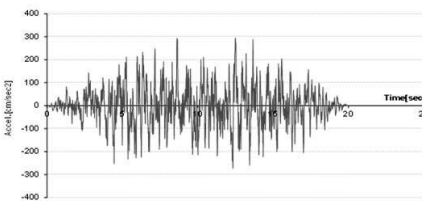
Artificial 1



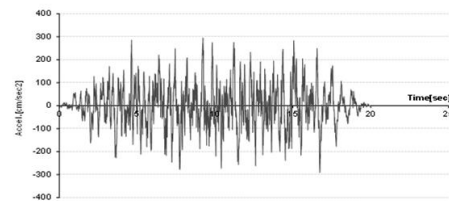
Artificial 2



Artificial 3



Artificial 4



Artificial 5

Figure 3.27: Time history representation of used records

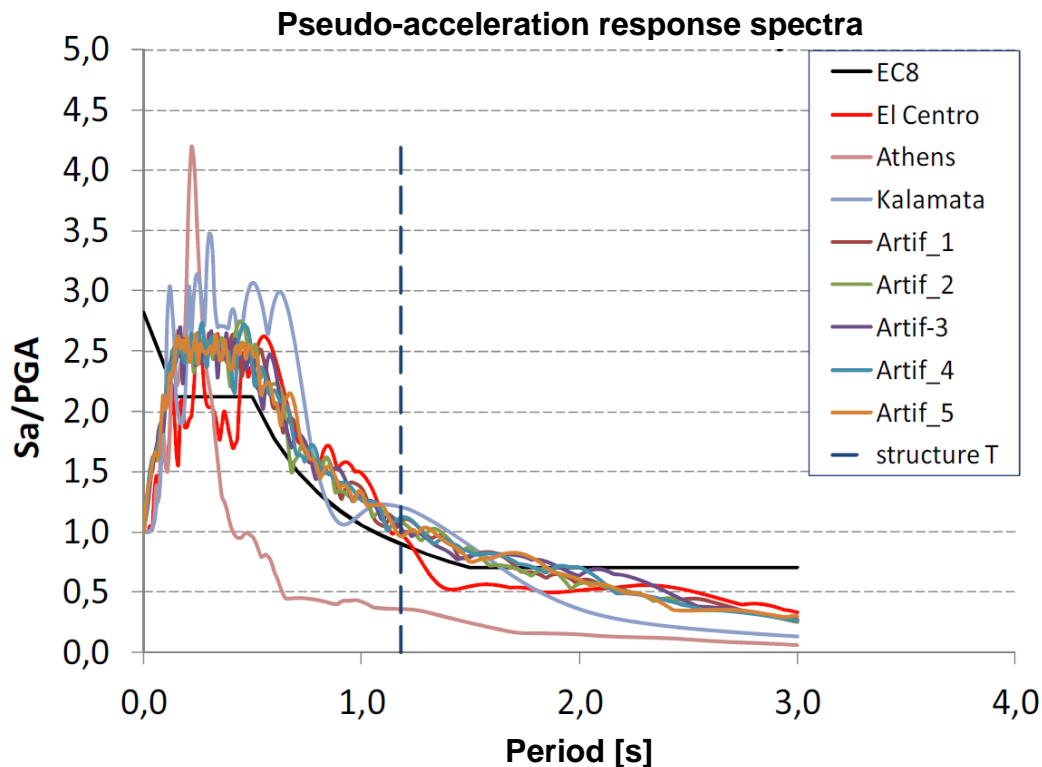


Figure 3.28: Acceleration spectra of the examined records and design code spectrum

Regarding the modeling assumptions, the loading condition at initial state ( $G+0.3Q$ ) and the nonlinear hinge properties assigned at the columns, the system columns and the FUSEIS beam links, were the same as for the pushover analyses. Specifically, for composite beam to column connection two cases were studied. In the first case the composite beams were partially fixed (MRF) with rotational springs and in the second they were hinged. The plastic hinges assigned at the ends of the composite beams were adjusted to fit the end releases. Indicatively, the analyses conducted for the building frame with the SHS FUSEIS beam links are presented hereafter. In all cases examined the behavior of the frame was similar verifying the pushover analysis. The sequence of plastic hinges started with beams' ends from lower stories up to upper stories contributing to the energy dissipation of the building frame. On the other hand, the composite beams and columns remained elastic with no yielding. Figure 3.29 indicates the location of plastic hinges within the FUSEIS beam link system.

The analysis provided the history of internal moments and forces and deformations of the building frame. Figure 3.30 illustrates representative results for the moments and the rotations at plastic hinges formed under the Athens earthquake loading. It may be seen that the number of moment reversals are higher than the corresponding ones for the rotations. This is due to the fact that inelastic behavior and accordingly plastic rotations develop mainly during the strong motion phase.

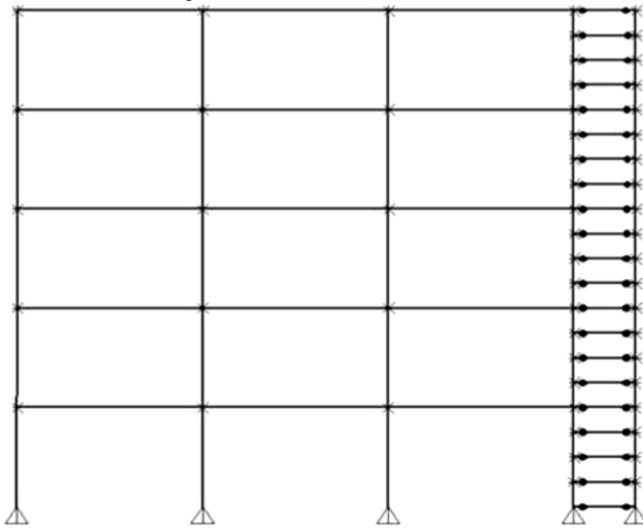


Figure 3.29: Plastic hinge locations after Nonlinear Dynamic Analysis

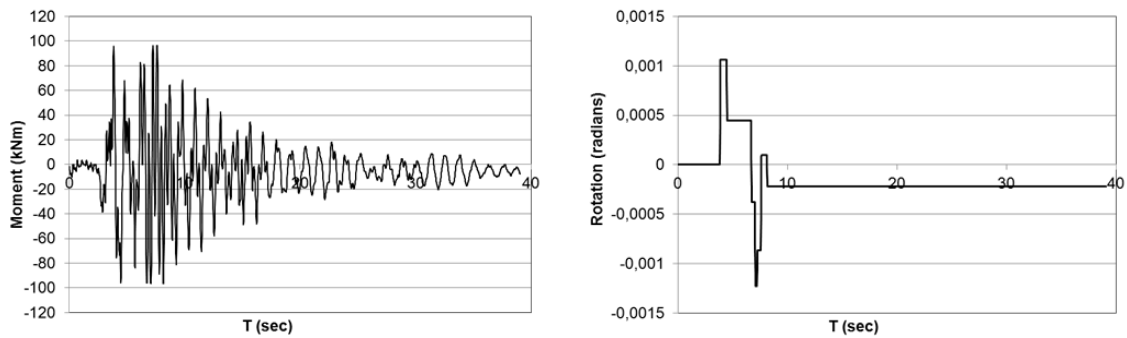


Figure 3.30: Bending moment and rotations history at plastic hinge (Athens)

Figure 3.31 shows the moment-rotation diagram of the most deformed FUSEIS beam links at the ground floor of the frame for the artificial earthquake 2 loading. A detail of the hysteresis loop is given in the left figure whereas the right figure illustrates its positioning on the hinge backbone curve. The loop is below the IO performance level, which means that minor local yielding takes place.

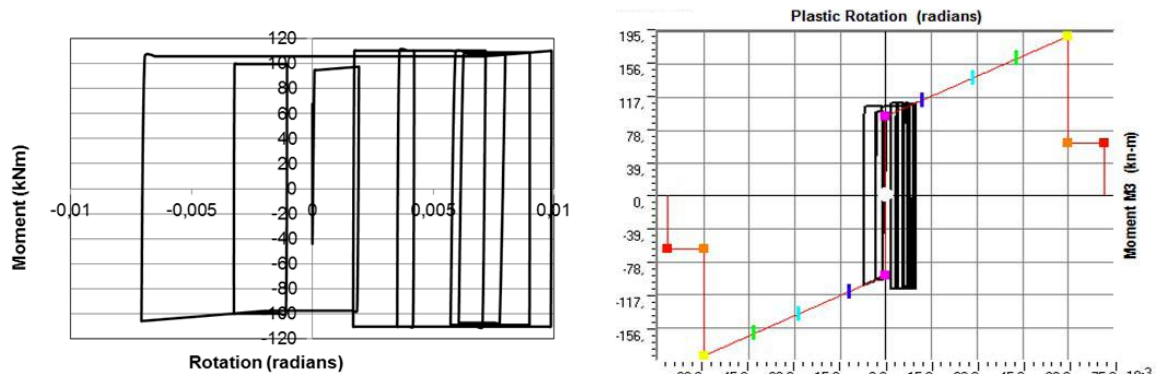
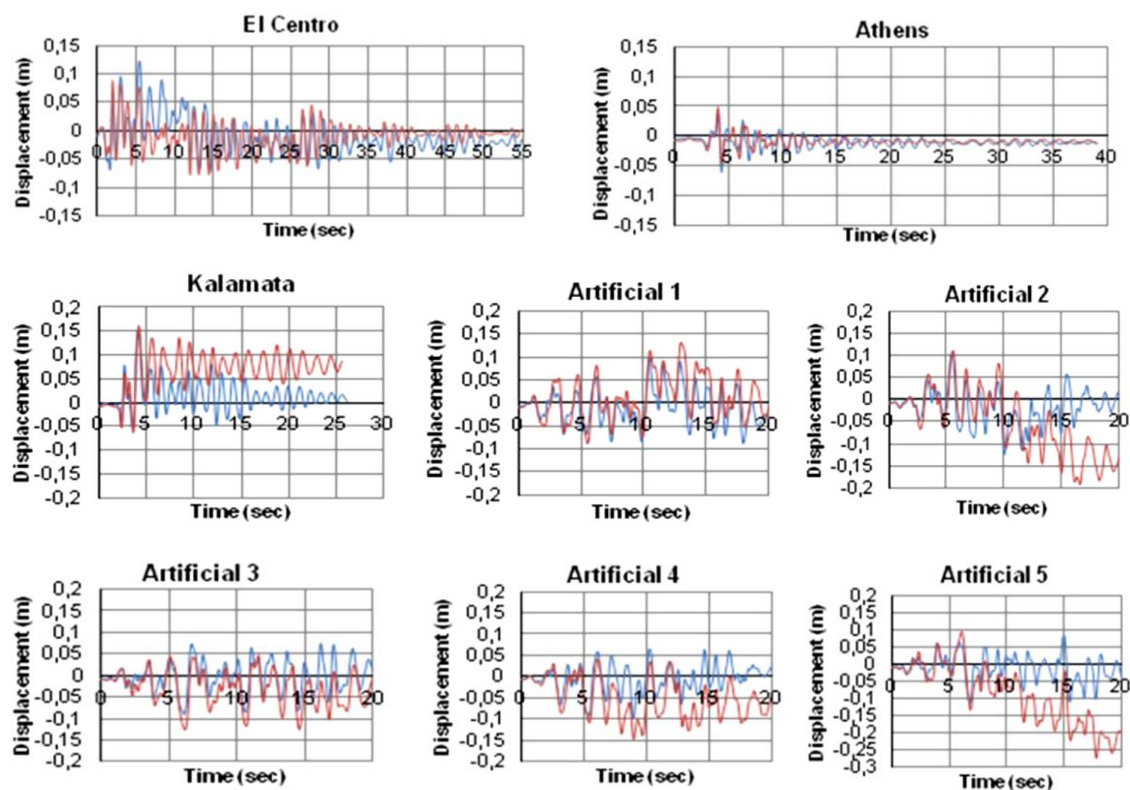


Figure 3.31: Moment rotation hysteresis loop – Artificial earthquake 2

The structural dynamic response of the frame under earthquake ground excitations was evaluated in terms of displacement history. Figure 3.32 displays roof

displacements versus time for all the examined ground motions for both cases studied, partially fixed and hinged composite beams. The diagrams show that the structure is vibrating with respect to the ground motion. It can be observed that when the structure combines the moment resisting frame (MRF) action (partial fixity) with the FUSEIS beam link system, the curve returns close to the neutral position at the end of the simulation. This happens because the deformations are concentrated in the FUSEIS beam link system and the rest of the structure remains elastic, while the moment frame action helps the structure to return to its initial state. On the contrary, when the composite beams are hinged, even though the plastic hinges are also formed in the FUSEIS beam links, the structure is not able to return and this explains the large displacements visible in the diagrams after the earthquake ends.



### FRAME and HINGES

Figure 3.32: Displacement responses for all the examined ground motions

The above mentioned observations demonstrate the self-centering behavior of the FUSEIS beam link system in the first case (partial fixity). This means that the system has controlled energy dissipation and is capable of eliminating the residual drift. After a seismic event, if no failure is observed, residual story drift may constitute a significant criterion for the evaluation of a building. The residual drifts, obtained by dividing the residual displacements at the top joint by the frame height, for all the seismic records and the comparison of the two cases examined are summarized in

Table 3.7. The residual drift values for the first case, are much lower compared to the limit value of 1% that corresponds to moment resisting steel frames at the Immediate Occupancy performance level (FEMA-356). Moreover, it may be seen that the demands are limited to a mean value of  $\sim 0.002\%$  and a maximal value of  $\sim 0.218\%$ , verifying that the FUSEIS beam link system is a self centering system. As a result, no significant structural damage occurs and repairs would not be required in any of the studied cases.

**Table 3.7: Residual drifts recorded after dynamic time history analysis**

Earthquake	Residual Drift frame (%)	Residual Drift hinges (%)	Ratio
El Centro	0.002	0.083	41.5
Athens	0.075	0.075	1.0
Kalamata	0.019	0.445	23.4
Artificial 1	0.181	0.054	0.3
Artificial 2	0.084	0.774	9.2
Artificial 3	0.079	0.045	0.6
Artificial 4	0.111	0.329	3.0
Artificial 5	0.218	1.184	5.4

The behavior of the MRF frame with FUSEIS beam links was also evaluated under the three performance levels (Limit states): SLS, ULS and CPLS for the El Centro, Kalamata, Artificial 2 & 4 earthquakes (Figure 3.33). The residual drifts for the CPLS limit state were higher than for the other limit states as expected, but in all cases lower than the limit value 1% maintaining the advantages of self centering systems. The building frame has a period  $T_1 = 1.178 > T_c = 0.5s$ , of the ground type B. According to Eurocode 8 the behavior factor ( $q$ ) may be taken equal to the displacement ductility factor ( $\mu$ ). Based on this definition, the displacement ductility factor for the system can be obtained from equation:

$$q = \mu = \frac{d_{max}}{d_{el}} \quad \text{Eq. (3.29)}$$

where  $d_{max}$  is the maximum plastic displacement (or ultimate displacement) that the system sustains during the examined earthquakes and  $d_{el}$  is the maximum displacement as determined by a linear analysis based on the design response spectrum. The ductility factors for various performance levels are given in the following Table 3.8.

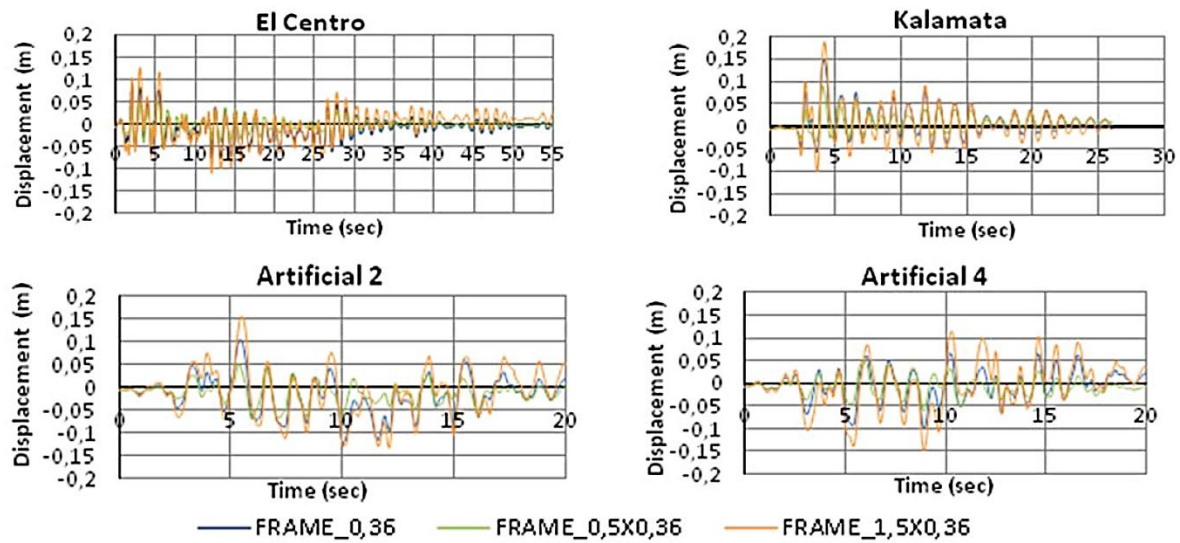


Figure 3.33: Displacement responses for SLS, ULS and CPLS limit states

**Table 3.8: Ductility factors for various performance levels**

Seismic record		SLS	ULS	CPLS
El Centro	$d_{max}$ [m]	0.049	0.087	0.126
	$\mu$ [-]	1.14	2.02	2.94
Athens	$d_{max}$ [m]	-	0.039	-
	$\mu$ [-]	-	0.91	-
Kalamata	$d_{max}$ [m]	0.092	0.150	0.188
	$\mu$ [-]	2.14	3.49	4.37
Art. 1	$d_{max}$ [m]	-	0.100	-
	$\mu$ [-]	-	2.33	-
Art. 2	$d_{max}$ [m]	0.051	0.104	0.152
	$\mu$ [-]	1.19	2.42	3.54
Art. 3	$d_{max}$ [m]	-	0.076	-
	$\mu$ [-]	-	1.77	-
Art. 4	$d_{max}$ [m]	0.051	0.065	0.115
	$\mu$ [-]	1.20	1.51	2.68
Art. 5	$d_{max}$ [m]	-	0.086	-
	$\mu$ [-]	-	2.00	-

In a comparison of the interstory drift maxima for the 5-story frame for the two cases (partially fixed and hinged composite beams) it was found that the drift values for the MRF are similar to and slightly lower than the values for the hinged frame. The maximum interstory drifts compared to the residual drifts of the 5 story frame for the examined earthquakes, are given in Figure 3.34 and Table 3.9. The difference is



that at the MRF system the maximum drift appears at the first story, as expected, whereas the maximum drift position in the case of the hinged frames is not clearly defined and cannot be predicted as it is affected by various parameters such as the ground motion. Moreover, these diagrams exhibit the self-centering behavior of the MRF since the residual drift values are close to zero.

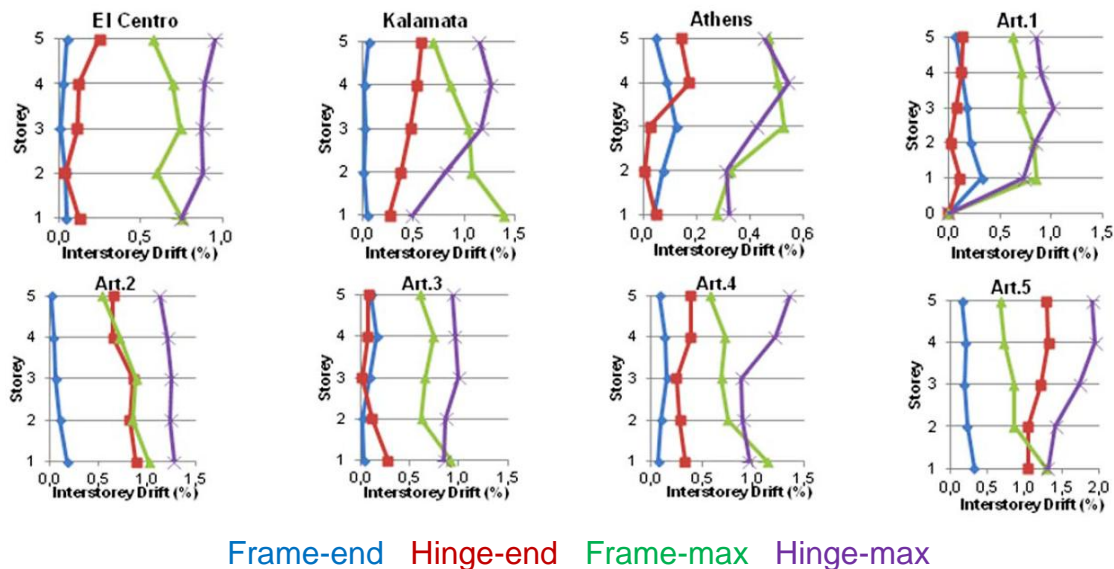


Figure 3.34: Maximum interstorey drifts for the examined earthquakes

**Table 3.9: Comparison of maximum interstorey drifts**

Earthquake record	Max Int. Drift - Frame (%)	Max Int. Drift - Hinges (%)	Ratio
El Centro	0.75	0.95	1.27
Athens	0.52	0.54	1.04
Kalamata	1.39	1.26	0.91
Artificial 1	0.85	1.02	1.20
Art.2	1.02	1.27	1.25
Art. 3	0.92	0.99	1.08
Art. 4	1.13	1.36	1.20
Art.5	1.29	1.95	1.50

### 3.6.4 Conclusions from numerical simulations

The above study illustrates the successful application of the moment resisting frame combined with the FUSEIS beam link system. The seismic design parameters are briefly summarized. Emphasis was given on the seismic design process, assisted by FE analysis - performing a pushover analysis of the framed structure. To evaluate the sensitivity of the structure to higher seismic loads and the impact of using behavior factor of  $q = 5$  in the design process for the structural design; a more detailed analysis was performed for different level of seismic loading.



From the analysis of typical 2D building frames the following observations are worth noting:

- The energy dissipating capacity of the FUSEIS beam link system as self-centering systems affects seismic performance in a positive way through yielding of replaceable parts.
- Focusing on global behavior, some of the important structural properties, such as materials, members, connections, global and local stability, and dynamic P-delta effects, were taken into consideration. The study has revealed some of the important global performance characteristics of the FUSEIS beam link systems
- The FUSEIS system works as an excellent lateral force resisting system in seismic regions, able to guarantee an efficient control both on drift and displacement deformations.

### 3.7 CONCLUSIONS

A number of experimental and numerical analyses were carried out for the development of the FUSEIS beam link system. Critical parameters for the design of this new seismic resistant system have been determined. The following general remarks/conclusions can be noted:

- The seismic resistance of a building may be obtained by appropriate provision of a number of FUSEIS beam links in the relevant directions.
- The beam links itself and frames equipped beam links have a very good behavior: strong, stiff and large capacity of energy absorption.
- Inelastic deformations are strictly limited to the dissipative elements preventing the spreading of damage into rest of the structural members (slab, beams, columns).
- The dissipative elements are easily replaceable if they are damaged after a strong seismic event, since they are small and are not part of the gravity loading resistant system. The assembling and disassembling after tests was easy from a practical point of view: the time required for replacing one FUSEIS beam link is approximately 60 minutes (from NTUA Full Scale Test experience).
- The method for determining the seismic effects for building frames is the modal response spectrum analysis in accordance with Eurocode 8, where the proposed q-factor for the FUSEIS beam link system is 5.
- Code relevant design rules for the seismic design of frames with dissipative FUSEIS have been formulated. They are presented in an accompanying "Design Guide".
- Practical recommendations on the selection of the appropriate beam links as a function of the most important parameters and member verifications have been

formulated. Structural details and constructional measures are defined. The recommendations are presented in the accompanying “Design Guide”.

More specifically, the following may be stated:

- The system resists lateral loads as a vertical Vierendeel beam.
- It may be designed as more flexible/rigid depending on the section types and their distribution between floor levels. The number of stories and supporting weight strongly affects the required sections and geometry.
- It provides an architecturally versatile solution for the lateral stability of building structures compared to the braced frames as they can be positioned in small areas of the building and do not interrupt the architectural plan. They can also constitute visible parts of the building indicating its seismic resistant system
- Sequential plastification may be allowed by appropriate selection of the sections of the dissipative elements.
- Aiming to minimise damage at the foundation locations pinned connections at the column bases are proposed. At multi-story buildings the column bases may be pinned or fixed, analytical investigations showed that the difference in the response is not significant.
- The FUSEIS beam link system is able to guarantee an efficient control both on drift and displacement deformations, exhibiting a self-centering behavior.

Conclusively, it may be noted that the present research, in line with the international trend in seismic engineering, introduces “intelligent” systems that are able to dissipate the seismic input energy and may be easily replaced and repaired, if required. The adoption of FUSEIS beam link systems enhances the well known advantages of steel under seismic conditions and provides better solutions in terms of economy and safety.

### 3.8 FIELD OF APPLICATION

The innovative FUSEIS beam link system may be applied to multi-story steel buildings and substitute the conventional systems used worldwide (such as concentric and eccentric braced frames, moment resisting frames etc.) by combining ductility and architectural transparency with stiffness. Hereby, the application of FUSEIS beam links can provide a more accurate and less expensive design of a building.

### 3.9 PUBLICATIONS

Publications in international journals

1. D. Dimakogianni, G. Dougka, I. Vayas, “Innovative seismic-resistant steel frames (FUSEIS 1-2) experimental analysis”, *Steel Construction Design and Research*, Volume 5, Issue 4, pp. 212-221, 2012.
2. D. Dimakogianni, G. Dougka, I. Vayas, “Seismic behavior of frames with innovative energy dissipation systems (FUSEIS1-2)”, *Engineering Structures*, Volume 90, pp. 83–95, 2015.

### 3.10 BIBLIOGRAPHIC REFERENCES

1. Vayas, I., Karydakis, Ph., Dimakogianni, D., Dougka, G., Castiglioni, C. A., Kanyilmaz, A. et al. Dissipative devices for seismic resistant steel frames - The FUSEIS Project, Design Guide. Research Programme of the Research Fund for Coal and Steel 2012.
2. I. Vayas, Ph. Karydakis, D. Dimakogianni, G. Dougka, Castiglioni, C. A., Kanyilmaz, A. et al. Dissipative devices for seismic-resistant steel frames (FUSEIS). Research Fund for Coal and Steel, European Commission; EU 25901 EN 2013.
3. Vayas I. and Thanopoulos P. Innovative Dissipative (INERD) - Pin Connections for Seismic Resistant Braced Frames. International Journal of Steel Structures 2005; 5(5):453-464.
4. Vayas I. and Thanopoulos P. Dissipative (INERD) - Verbindungen für Stahltragwerke in Erdbebengebieten. Stahlbau 2006; 75(12):993-1003.
5. Vayas I., Thanopoulos P. and Castiglioni C. Stabilitätsverhalten von Stahlgeschossbauten mit dissipativen INERD unter Erdbebenbeanspruchung. Bauingenieur 2007; 82(3):125-133.
6. Plumier, A., Doneux, C., Castiglioni, C., Brescianini, J., Crespi, A., Dell'Anna, S., Lazzarotto, L., Calado, L., Ferreira, J., Feligioni, S., Bursi, O., Ferrario, F., Somavilla, M., Vayas, I., Thanopoulos, P. and Demarco, T. (2004). "Two INnovations for Earthquake Resistant Design - The INERD Project, Final Report". Research Programme of the Research Fund for Coal and Steel.
7. Christopoulos, C., Filiatrault, A., Folz, B., and Uang, C-M. Post-Tensioned Energy Dissipating Connections for Moment-Resisting Steel Frames. ASCE Journal of Structural Engineering 2002; 128(9):1111-1120.
8. Saeki, E., Iwamatu, K., and Wada, A. Analytical study by finite element method and comparison with experiment results concerning buckling-restrained unbonded braces. Journal of Structural and Construction Engineering, Architectural Institute of Japan 1996 ; 484:111- 120.
9. Sabelli, R., Mahin, S., and Chang, C. Seismic demands on steel braced buildings with buckling-restrained braces. Engineering Structures 2003; 25(5):665-666.
10. Tsai, K. C., Chen, H.W. and Hong, C., and Su, Y. Design of steel triangular plate energy absorbers for seismic-resistant construction. Earthquake Spectra 1993; 9(3):505-528.
11. Dargush, G. and Soong, T. Behavior of metallic plate dampers in seismic passive energy dissipation systems. Earthquake Spectra 1995; 11(4):545-568.
12. Tena-Colunga, A. Mathematica modeling of the ADAS energy dissipation device. Engineering Structures 1997; 19(10):811-820.
13. EN1998-1-1, Eurocode 8: Design of structures for earthquake resistance – Part 1-1: General rules, seismic actions and rules for buildings. Brussels: Comitee Europeen de Normalisation (CEN); 2003.
14. ECCS document: Recommended testing procedure for assessing the behavior of structural steel elements under cyclic loads, Technical committee 1: structural safety and loadings, Technical working group 1.3: seismic design; 1986.
15. DIN 50125: Testing of metallic materials - Tensile test pieces; 2009.
16. EN1993-1-1, Eurocode 3: Design of steel structures - Part 1-1: General rules and rules for buildings. Brussels: Comitee Europeen de Normalisation (CEN); 2003.
17. FEMA – 356: Prestandard and Commentary for the seismic rehabilitation of Buildings. Washington; 2000.
18. EN1993-1-9, Eurocode 3: Design of steel structures – Part 1-9: General – Fatigue strength. CEN. 2005
19. EN1994-1-1: Eurocode 4: Design of composite steel and concrete structures. Part 1-1: General rules and rules for buildings. Brussels: Comité Européen de Normalisation (CEN); 2005.
20. EN 1993-1-8: Eurocode 3: Design of steel structures. Part 1-8: Design of joints. Brussels: Comité Européen de Normalisation (CEN); 2004.

21. FEMA – P695: Quantification of building seismic performance factors, Washington; 2009.
22. Seismomatch v.2.1.0, Seismosoft, [www.seismosoft.com](http://www.seismosoft.com).
23. Vamvatsikos D., Cornell C.A. The incremental dynamic analysis and its application to performance-based earthquake engineering. In: Proc.12th European Conference on Earthquake Engineering; 2002; 479; London.
24. Vamvatsikos D, Cornell CA. Incremental dynamic analysis. Earthquake Engineering and Structural Dynamics 2002; Vol. 31, Issue 3, pp. 491-514.
25. Vayas, I., Dougka, G., Dimakogianni, Umbau und Erweiterung des Kindergartens der Deutschen Schule Athen. Bauingenieur 2014; 6:253-260.
26. Material choice for seismic resistant structures (MATCH). RFSR-CT-2013-00024, 2nd Annual report, 2016
27. Calado, L. and Castiglioni, C. A. (1996). "Steel beam-to-column connections under low-cycle fatigue: Experimental and numerical research". In: Proceedings of XI WCEE.
28. ATC-40, Seismic Evaluation and Retrofit of Concrete Buildings – Volume 1, Applied Technology Council, California, USA, November 1996.

## 4 FUSEIS PIN LINKS

### 4.1 INTRODUCTION

In the frame of the European Research Program RFSR-CT-2008-00032 “Dissipative Devices for Seismic Resistant Steel Frames” (Acronym: FUSEIS) two innovative dissipative systems, named FUSEIS1 and FUSEIS2 were introduced and relevant design guides developed [11], [12]. Depending on the geometry of the fuse, the system FUSEIS1 is further divided in two types: FUSEIS beam links and FUSEIS pin links. Current report presents the results of the investigations on the seismic performance of FUSEIS pin links, introduces the design procedures for steel and composite buildings, in which the system is used as seismic resistant system, and proceeds to the design of several case studies.

### 4.2 DESCRIPTION OF FUSEIS PIN LINKS SYSTEM

The innovative seismic resistant system FUSEIS pin links, consists of a pair of strong columns jointed together by multiple links (Fig. 4.1). Each link includes two receptacle beams connected through a short steel pin as shown in Fig. 4.1. The system resists lateral loads as a vertical Vierendeel beam, where the main actions are bending and shear in the pins and axial forces and bending in the columns. Under strong seismic motion inelastic deformations are restricted to the pins, which will dissipate a large amount of input energy, leaving the rest of the structure elastic and undamaged. Repair works are easy, since they are restricted to the pins which are not generally subjected to vertical loads, as they are placed between floor levels. The pins may be circular or rectangular depending on whether the receptacle beams are of hollow section or of I- or H-section. With the aim of directing the plastic hinge formation away from the contact area between the face plate of the receptacles and the pins, the pins are weakened around their middle. In order to keep contact area away from the end of the plates, ensuring triaxial stress conditions, pin's diameter decrease starts away from the plate's face and the edges of the plate hole are smoothed. Additionally, their ends are fabricated with opposing threads to adjust their length during installation and facilitate their removal. The link may be easily installed, dispatched and replaced with the use of bolted end-plate connections between the receptacles and the columns. These connections are formed as rigid to realize the Vierendeel behavior. The receptacles, the columns and their connections are designed with overstrength to ensure the formation of plastic hinges in the pins. System columns may employ open or closed sections. Open sections are more beneficial for constructional purposes, since they offer easier connection to the beams. When closed sections are used, as appropriate at building corners with FUSEIS systems in both directions (Fig. 4.3), T-sections can be welded on to ease the connection.

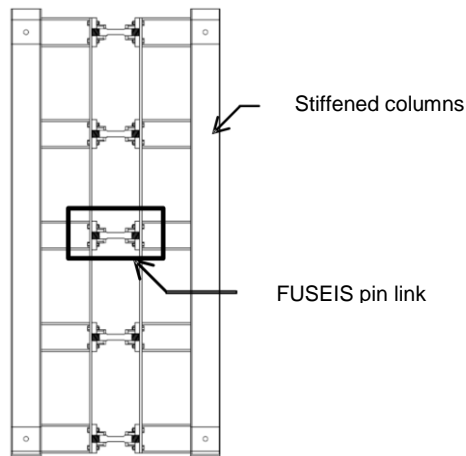


Fig. 4.1: FUSEIS pin link system

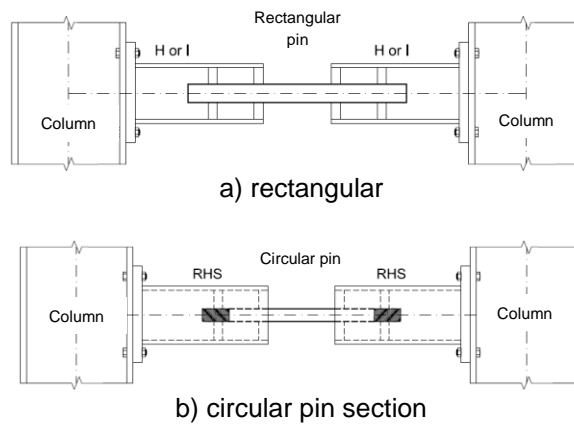


Fig. 4.2: FUSEIS pin link system with receptacles

The number of intermediate links per story, the selection of pin sections, the centerline distance and the sections of the columns are decisive parameters for the system's strength and stiffness. The number of receptacles and pins within a typical floor height of approximately 3,4 m may be four or five, depending on the height of the receptacles, the 'workspace' that is required to install the fuses and possible architectural restrictions. In addition, one fuse is introduced close to the column bases to absorb column base moments and allow a layout of column bases as hinged.

In order to avoid the application of receptacles that require some machining effort, pin links with slightly different end-detail were investigated and tested in the frame of the MATCH-project which was also financially supported by RFCS [28]. In this project threads of different directions (one left one right) are cut at the end of the pins which are directly bolted to end-plates that are connected to the column flanges (Fig. 4.3). In order to promote damage away from the connection area, the pin section is reduced in the middle part of the pin. Pins with such detail require less effort in fabrication and erection and lead to similar results.

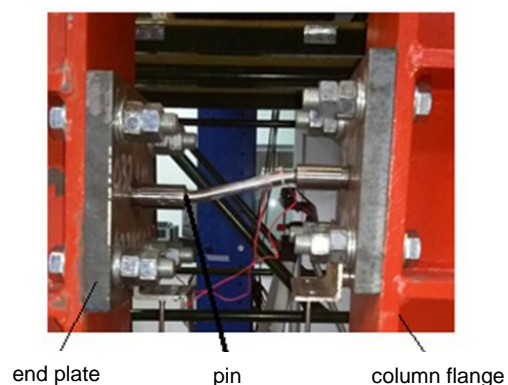


Fig. 4.3: FUSEIS pin links without receptacles

The system is versatile with regard to the selection of pin sections and offers the designer the possibility to control the plastification sequence of the pins. This can be achieved by changing either the sections or the length of the pins within the floor or between floors.

Aiming to avoid excessive overstrength, the steel material of the dissipative pins shall have controlled properties. In accordance with EN 1998-1-1 [13] its yield strength must have a maximum value of:

$$f_{y,max} \leq 1.1 \cdot \gamma_{ov} \times f_y \quad \text{Eq. (4.1)}$$

Where  $\gamma_{ov} = 1.25$  is the overstrength factor and  $f_y$  is the nominal value of the yield strength.

The nominal yield strength of the pins shall be low and preferably not exceed 235MPa. If the properties of the pin material are controlled and its maximal yield strength guaranteed below that described by eq. (4.1), the overstrength factor can be reduced and an even more economical design achieved.

The number of FUSEIS pin link systems required in a building is defined by the building topology (Fig. 4.4) and the earthquake intensity. The system may be generally combined with moment resisting frame (MRF) action, in which case lateral forces are shared between the MRF and the FUSEIS pin link system. Alternatively, if simple connections (shear tab connections) between floor beams and columns are used the FUSEIS pin link system resists alone the entire seismic action. In both cases the floor beams to the system columns are formed as simple to avoid their design by capacity design considerations in respect to the strong floor beams and introduce capacity design in respect to the weak pins only.

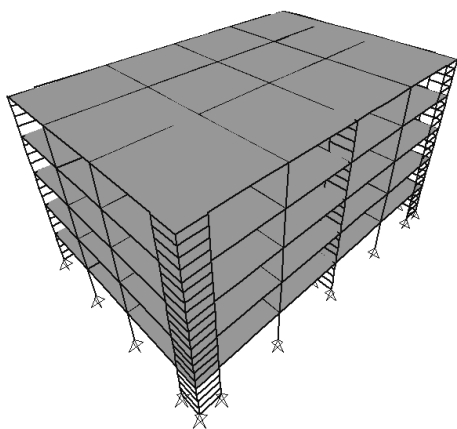


Fig. 4.4: Positioning of FUSEIS pin link systems in a building

### 4.3 LIMIT STATE MODELS

Experimental investigations showed that the system with beam specimens works as a vertical Vierendeel beam. It resists lateral loads, mainly by bending of the beams and axial forces of the columns (Fig. 4.5). Considering hinges at the midpoints of pins and columns, the internal moments and forces for horizontal loading in the elastic state may be derived from statics. Consequently, the shear force  $V_{pin}$  due to the moment of resistance  $M_{pl, pin}$  at pin ends is:

$$V_{pin} = \frac{2 \cdot M_{pl, pin}}{l_{pin}} \quad \text{Eq. (4.2)}$$

Where  $l_{pin}$  is the length of the weakened part of the pin,  $M_{pl, pin} = W_{pl, pin} \cdot f_y$ ,  $W_{pl, pin}$  is the design moment resistance of the weakened part of the pin and  $f_y$  is the yield stress of the pin.

The axial force of the columns  $N_{column}$  is equal to:

$$N_{column} = \frac{M_{ov}}{L} = \frac{V_{story} \cdot h_{story}}{L} = \sum V_{pin} \quad \text{Eq. (4.3)}$$

Where  $M_{ov}$  is the overturning moment of the frame,  $V_{story}$  is the story shear,  $h_{story}$  is the story height and  $L$  is the axial distance of system columns. Therefore, from Equations (4.2) and (4.3) the story shear that may be transferred is equal to (Eq. (4.4)).

$$V_{story} = \frac{\sum V_{pin}}{h_{story}} \cdot L = 2 \cdot \sum \frac{M_{pl, pin}}{l_{pin}} \cdot \frac{L}{h_{story}} \quad \text{Eq. (4.4)}$$

Considering rigid receptacles, the pin chord rotations  $\theta_{pl, pin}$  are determined from Equation(4.5):

$$\theta_{pl, pin} = \frac{L}{l_{pin}} \theta_{gl} \quad \text{Eq. (4.5)}$$

Where  $\theta_{gl}$  is the global interstory drift angle of the frame during seismic loading.



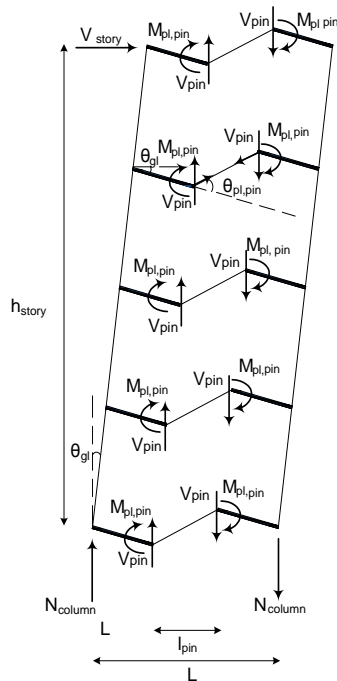


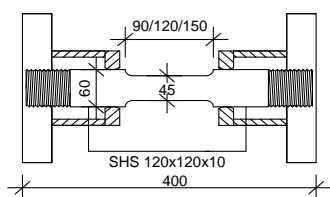
Fig. 4.5: Static System and theoretical internal forces (Vierendeel beam theory)

#### 4.4 EXPERIMENTAL INVESTIGATIONS ON FUSEIS PIN LINKS

##### 4.4.1 Experimental investigations on individual links

##### 4.4.1.1 Experimental setup and tested pin links

In total eight tests were conducted on pin links, two under monotonic and six under cyclic loading. The criterion for the selection of the pin specimen was their ability to dissipate energy through bending mechanisms. As a result, the design of the experimental setup depended on the plastic moment of resistance of the pins  $W_{pl,pin}$ , that was used for the calculation of the maximum applied load. The specimen tested consisted of a 400 mm circular pin weakened in the middle and two receptacle beams SHS120x10. The pin was divided to three parts. The diameter at the ends was  $\Phi 60$  and in the middle part the diameter was reduced to  $\Phi 45$  mm. The length of the weakened part was to ensure the development of a bending mechanism. Fig. 4.6 shows principal photos of the specimens.



a) Specimen dimensions



b) Specimen photos



c) Detail at the weakening

Fig. 4.6: Fabricated fuse specimens before testing

#### 4.4.1.2 Results of monotonic tests

The pin specimens showed a ductile behavior with a considerable load increase after leaving the elastic range. This effect was not mainly due to material hardening but due to a changing of the bearing mechanism. For small displacements, the load was transferred by pin bending and shear while for larger deformations the load was transferred also by axial forces in the pin, which increases the bearing capacity of the specimens significantly.

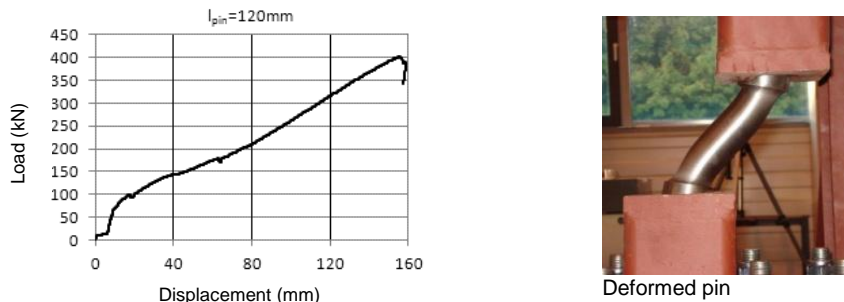


Fig. 4.7: Load - Displacement curves and deformed specimens under monotonic loading

#### 4.4.1.3 Results of the cyclic tests

As reference for the testing procedure the ECCS – recommendation [14] for assessing the behavior of structural steel elements under cyclic loads was used. The maximum displacement value reached during the tests was lower than the maximum applied displacement of 60 mm (4% interstory drift).

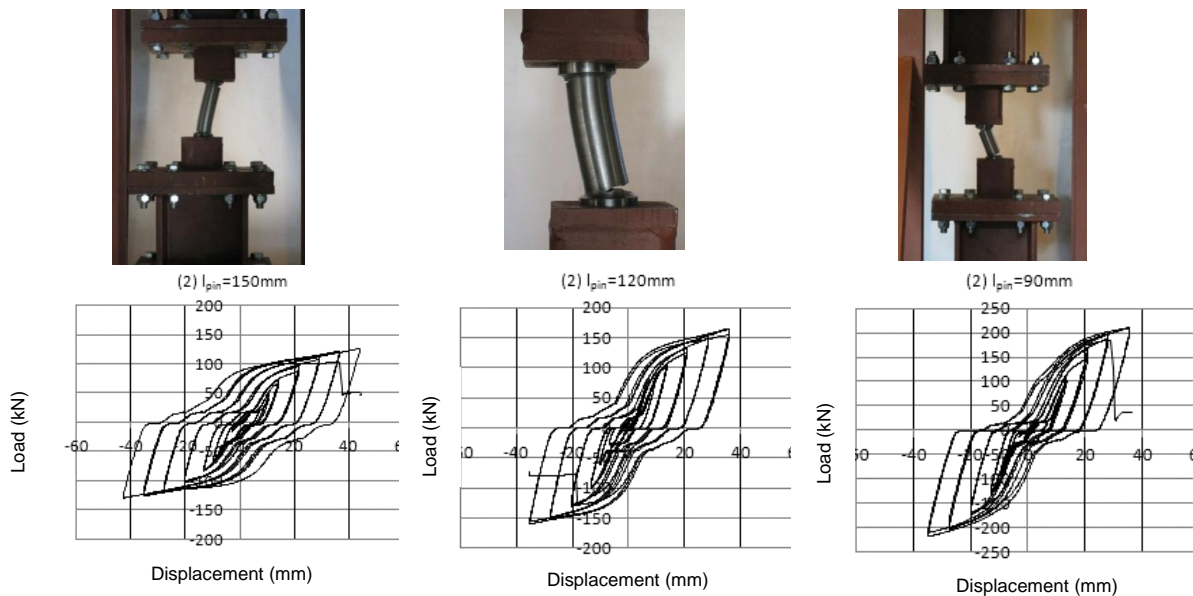


Fig. 4.8: Load - Displacement curves and deformed specimens under cyclic loading

Fig. 4.8, a and b, show the overstrength and the rotation capacity of the tests as dependent on the normalized pin length  $\rho$ . Both values and especially the

overstrength are many times higher for monotonic compared to cyclic loading. This indicates that when subjected to cyclic loading the pins failed due to low cycle fatigue and developed significantly less catenary action compared to those subjected to monotonic loading.

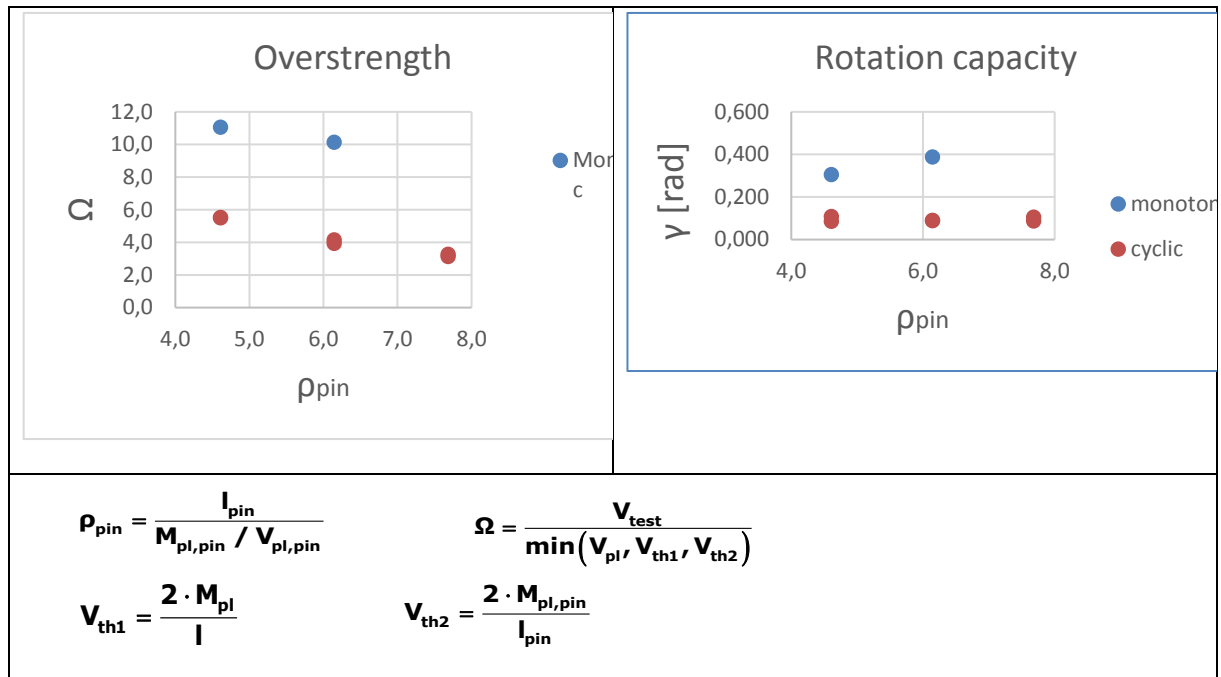


Fig. 4.9: Overstrength  $\Omega$  and rotation capacity  $\gamma$  of the pin specimens

#### 4.4.2 Experimental investigations on overall frames with FUSEIS pin links

##### 4.4.2.1 Experimental setup and tested frames

Two full scale tests on frames with FUSEIS pin links were conducted at the Institute of Steel Structures of NTUA. The experimental setup included a resistance space frame test rig, a computer-controlled hydraulic cylinder and the test frame. The test frame consisted of two strong columns rigidly connected to five fuses, as shown in Fig. 4.9. The dimensions of the structural elements corresponded to a real building frame and were defined according to the provisions of EN1993-1-1 [17] and EN1998-1-1 [13]. The height of the frame was 3.40 m and the centreline distance of the columns  $L=1.50$  m. The columns of the test frame were pin - jointed at the top and bottom connections and were stiffened by adding stiffening T-sections on their inner sides to remain elastic.

Similar to the tests on individual pin links, the fuse consisted of a 400 mm pin and two SHS beams as receptacles, see Fig. 4.10. The geometry of the weakened part of the pin was selected to ensure the development of bending mechanisms. Test M4 included pins with the same diameter ( $\Phi 45$ ) and three different lengths of the weakened part  $l_{pin}=90, 120, 150$  mm  $> 39$  mm and test M5 pins with different

diameters  $\Phi 40$ , 45, 50 and the same length of the weakened part  $l_{pin}=120$  mm > 43,4 mm. The steel grade of the pins was S235 and the steel grade of the remaining members of the test frame S355. To facilitate installation and removal of the fuse, the pins were fabricated with opposing threads so that they could be easily fastened to the receptacles.

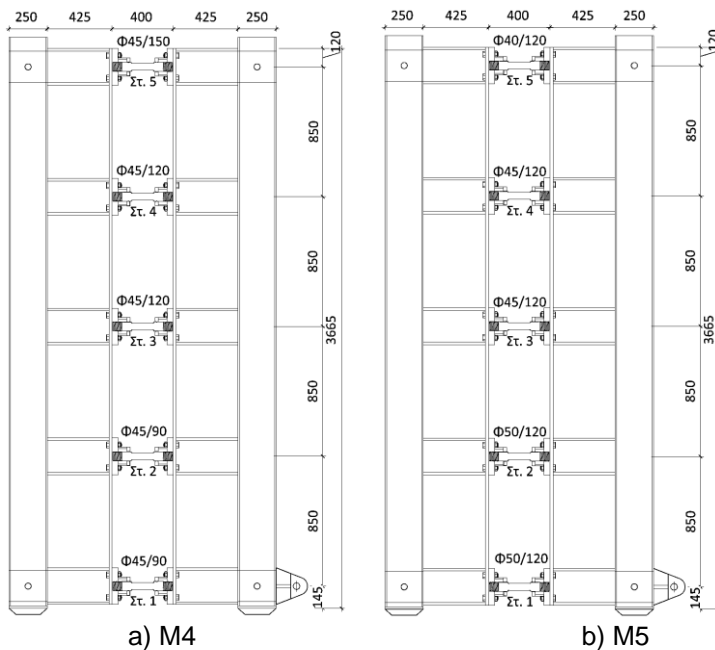
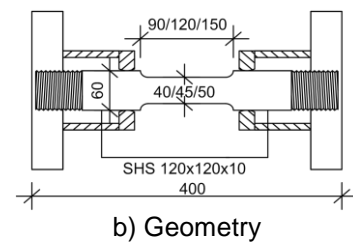


Fig. 4.10: Test frames



a) Pin link within the test frame



b) Geometry

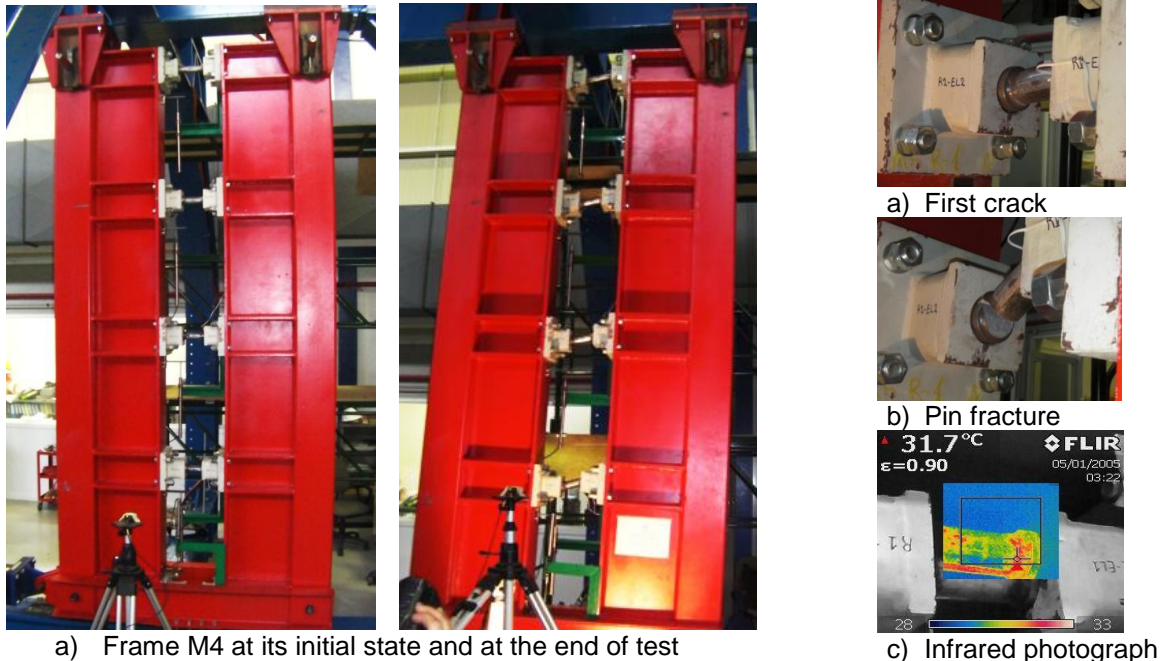
Fig. 4.11: Specimen

#### 4.4.2.2 Test results

Regarding the loading procedures of the experiments, the cyclic loading protocol was defined in terms of the ECCS – procedures. Starting with a displacement of 2,55 mm applied to the bases of system columns, the loading was increased up to 170 mm, which corresponds to an interstory drift of 5%. The cyclic loading protocol was followed by constant amplitude cycles of 5% until fracture.

The measured load increased at the beginning of the test and during several cycles. When the first crack formed at the ends of the weakened part of the pin (Fig. 4.10 b), the pins fractured (Fig. 4.10c), and as a result the load dropped. This means that there was a local stress concentration at the ends of the weakened pins as indicated by the photographs taken by an infrared camera (Fig. 4.10d). The above behavior of the pin is justified by the mechanisms developed. Specifically, the pin specimen first acted as a beam in flexure, then the resisting mechanism changed to a tension field action and plastic hinges were generated under large deformations. They developed extensive deformations and significant axial forces mostly due to their small length and the bolted connections at their ends that led to brittle fracture. In test M4, it was observed that the shorter pins  $l_{pin}=90$ mm fractured earlier at low interstory drift values, sustaining only a limited number of cycles (Fig. 4.12). They

developed significant chord rotations and their resistance dropped quickly due to low cycle fatigue. In test M5, where the pins had the same length and variable diameters, the pin that fractured first was  $\Phi 40/120$  at Level 5 (Fig. 4.13).



a) Frame M4 at its initial state and at the end of test

Fig. 4.12: Photos during test M4

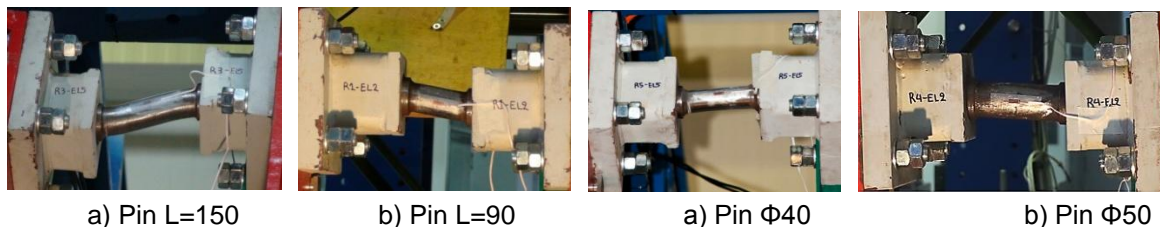


Fig. 4.13: Test M4 – photos of the deformed pins

Fig. 4.14: Test M5 – photos of the deformed pins

The hysteretic diagrams for each test are given in Fig. 4.14. It is remarkable that the system's resistance kept increasing after first yield and subsequent plastification of the pins due to development of catenary action in the pins and strain hardening. The system had wide hysteresis loops and exhibited large energy dissipation capacity. The first significant yield at the experimental curve appeared at an interstory drift equal to 0.66% and defines the SLS. After their plastification at the maximum load that appeared at an interstory drift equal to 1,38% and defines the ULS, the pins' deformation kept increasing until their fracture that corresponded to an interstory drift equal to 2.25% and defines the CPLS.

The hysteresis loops have a "pinching" due to the gap formed between the pin and the plate as a result of the extensive plastic deformation of the pin and the Poisson effect around the pin's circumference. This pinching of the hysteretic curve was accompanied by a substantial drop in the initial stiffness due to the release of the

tension field developed in the previous load excursion. Generally, it should be noted that the shorter pins failed at smaller drifts than those of the longer pins and the diagrams are not symmetrical possibly due to the tolerances of the bolted connections.

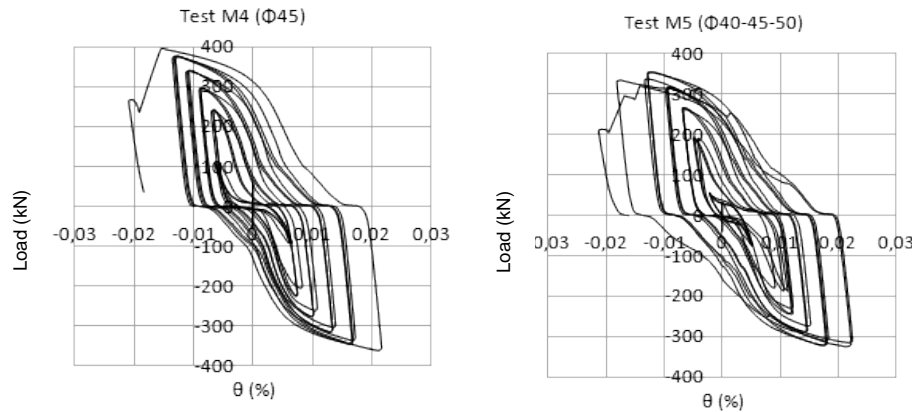


Fig. 4.15: Load – interstory drift diagrams

#### 4.4.2.3 Comparison between experimental and theoretical shear forces

The validity of the Vierendeel theory was examined using the experimental results. Initially, the theoretical story shear  $V_{th1}$  was calculated with the use of Equation (4.4) and the real yield stress of the steel defined through the tensile tests. This value was then compared to the maximum resistance the frames reached in the experiments  $V_{exp}$ . Table 4.1 shows that the experimental values were significantly higher than the theoretical and the ratio  $V_{exp}/V_{th1}$  was approximately 3.

These discrepancies are justified by the behavior of the pins during the experiments. At first cycles, the pin fuses behaved as beams in flexure, but after a few cycles the resisting mechanism changed and plastic hinges were generated under large deformations. This is the reason why when the equations of the Vierendeel beam were applied the story shear values were not similar to the measured. The pin chord rotations  $\theta_{pl,pin}$  may be calculated from Equation (4.5) considering that the rotation of the receptacles was minimal and that they remained rigid during the tests. The pin chord rotations  $\theta_{pin}$  are much higher than the global interstory drift  $\theta_{gl}$  due to the small pin length. The large rotations result in large axial deformations in the pins and, accordingly, a catenary action that has been proven to be beneficial to the overall response. Accordingly, at large rotations, bending of the pins transforms mainly into tension forces so that the pins develop their plastic axial resistance  $N_{pl}$ . In this case the story shear  $V_{th2}$  derives from Equations (4.6) and (4.7) taking into account the vertical component of the plastic axial force  $V_{pin}$ . The theoretical values are now close to the experimental and their ratio is close to 1 (Table 4.1).



$$V_{pin} = N_{pl,pin} \cdot (\theta_{pl,pin} - \theta_{gl}) = N_{pl,pin} \cdot \theta_{gl} \cdot \left( \frac{L}{l_{pin}} - 1 \right) \quad \text{Eq. (4.6)}$$

$$V_{th2} = \frac{\sum V_{pin}}{h_{story}} \cdot L = \sum N_{pl,pin} \cdot \theta_{gl} \cdot \left( \frac{L}{l_{pin}} - 1 \right) \cdot \frac{L}{h_{story}} \quad \text{Eq. (4.7)}$$

The above illustrate that 3rd order theory gives a better estimation for the shear capacity of the system than the Vierendeel beam theory but it is a rather complicated method and is not used widely by the designers. Through the calibration of tests and the analysis on 2D frames it was proven that the Vierendeel beam consideration can be applied instead.

**Table 4.1: Experimental vs theoretical shear forces**

Test	$V_{exp}$	$V_{th1}$	$V_{exp}/V_{th1}$	$V_{th2}$	$V_{exp}/V_{th2}$
M4	393.3	129.9	3.03	329.2	1.19
M5	354.1	129.4	2.74	314.4	1.13

#### 4.4.2.4 Low cycle fatigue

Preliminary analyses and experiments on pin fuses showed that pins can sustain a limited number of cycles. The number of cycles to be sustained is dictated by low-cycle fatigue considerations. The S-N lines for pin tests carried out in both the frames (NTUA) and the pin links (RWTH) have been determined. The S-N lines reformulated in deformations may be written as:

$$\log N = -m \log \Delta \phi \quad \text{Eq. (4.8)}$$

Where  $\Delta \phi$  is the fatigue pin rotation,  $N$  is the number of rotation range cycles and  $m$  is the slope constant of the fatigue strength curves. The damage index may be calculated with the Palmgren–Miner accumulation law. After a certain number of various amplitudes cycles failure occurs when:

$$D = \frac{n_1}{N_{f1}} + \frac{n_2}{N_{f2}} + \dots + \frac{n_i}{N_{fi}} \geq 1 \quad \text{Eq. (4.9)}$$

Where  $n_i$  is the number of cycles carried out at the same stress range  $S_i$ ,  $N_{fi}$  is the number of cycles at which failure occurs in case of constant amplitude and  $i$  is the total number of constant amplitude cycles.

Due to the lack of experimental results from constant amplitude cyclic tests, a hypothesis was made considering the slope of the lines equal to 3 and 2 as proposed

in EN1993-1-9 [19]. The comparison with the test results indicated that  $m = -3$  is a better approximation for the slope.

Fig. 4.15 shows the S-N lines that derived from both the tests on individual pin links and the tests on frames with fuses. The relevant validated relations are given in Equations (4.10) for individual pin links and (4.11) for multiple pin links. It may be observed that the individual pin links led to a more conservative approach, whereas the frames with fuses gave more realistic results due to the combined action of multiple beams. Therefore, the equation of the tests with frames is considered to be representative for the determination of the damage index of pin fuses.

$$\log N = -1.41 - 3 \cdot \log \Delta \phi \quad \text{Eq. (4.10)}$$

$$\log N = -0.90 - 3 \cdot \log \Delta \phi \quad \text{Eq. (4.11)}$$

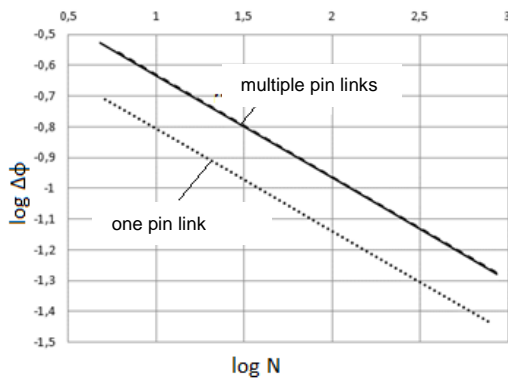


Fig. 4.16: Low cycle fatigue diagrams  $\log \Delta \phi$  -  $\log N$  diagrams

## 4.5 DESIGN RULES

The conclusions from the analytical and numerical studies were summarized in a design guide for the practical application. The design methodology, described in the design guide, is based on the provisions of EN 1993-1-1 [17] and EN 1998-1-1 [13]. Some clauses of EN 1998-1-1 were appropriately rearranged to cover the use of the pin links by the normal Code provisions. It also includes structural details and constructional measures.

### 4.5.1 Preliminary Design

As previously mentioned (Chapter 4.2), the FUSEIS1 system works as a vertical Vierendeel beam. Considering that the «FUSEIS pin link» resists alone the lateral loads of the structure, a rough estimation of the required number of FUSEIS systems for a building in each direction and the type of their cross sections can be made from the theoretical limit state model of the system (Section 3) according to the following equation (4.12). This calculation is based on the assumption that at the ultimate limit



state all pins reach, as the dissipative elements of the system, their moment capacity.

$$m = \frac{V_B}{V_{story}} \quad \text{Eq. (4.12)}$$

Where  $V_B$  is the total base shear of the building and  $V_{story}$  is the story shear of FUSEIS pin link system based on the vertical Vierendeel beam theory (Equation (4.4)). The column sections are chosen primarily from stiffness consideration in order to limit 2nd order effects. However, for  $m$  equal FUSEIS systems the columns have to resist at least an axial force equal to:

$$N_{column} = \frac{M_{ov}}{m \cdot L} \quad \text{Eq. (4.13)}$$

Where  $M_{ov}$  is the overturning moment of the frame. The above methodology gives the main directions for the design of the system; however the cross sections for beams and columns as well as the required number of systems cannot be estimated from strength criteria alone. The stiffness of the system should also be controlled through the limitation of the deformations in order to limit 2<sup>nd</sup> order effects according to the provisions of EN1998-1-1 [13].

#### 4.5.2 Design for linear elastic analysis

The design rules are intended to ensure that yielding, will take place in the pins prior to any yielding or failure elsewhere. Therefore, the design of buildings with FUSEIS pin link is based on the assumption that the pins are able to dissipate energy by the formation of plastic bending mechanisms. The following design methodology may be applied:

##### 1) Simulation

In the current state of the art, a building with FUSEIS pin links may be simulated with a linear-elastic model by appropriate beam elements. The beam elements representing the FUSEIS pin links are divided in three parts with different cross sections: the receptacle beams at the ends and the weakened pin in the middle. To enable the Vierendeel action the joints between receptacle beams and system columns are simulated as rigid. Rigid zones shall be provided from column centers to column faces to consider their clear length in the analysis and thus exclude non-existent beam flexibilities. In this manner, the true system flexibility and strength are accounted for.

The joints between floor beams and system columns are formed as simple to avoid their design by capacity design considerations in respect to the strong floor beams

and introduce capacity design in respect to the weak pins only. Floor beam-to-column joints of the main frame may be represented as rigid, semi-rigid or hinged in accordance to the connection detailing. In the first and second case lateral forces are shared between the MRF and the FUSEIS pin link system while in the third the system resists alone the entire seismic action. The bases of all the columns of the building are pinned.

Analyses on building frames with the system showed that when rigid connections are used, the beams of the main frame have to be capacity designed to resist lateral loads and so the use of a second system like FUSEIS leads to a heavier, more expensive structure and may be omitted. On the contrary, hinged connections are optional but more unfavorable for the FUSEIS system, which has to be extremely stiff and heavy with oversized cross sections that are difficult to install and repair. The most effective solution is the use of semi-rigid connections that offer the advantages of both the above solutions and additionally they are easier to realize in practice and restrict the damage in the pins leading to a more economic design. In this type of connections the rotation capacity of the plastic hinge  $\theta_p$  shall exceed 40mrad to ensure that this area will not yield prior to the pins. This value has derived from the non - linear analyses on frames with “FUSEIS pin links” and is a bit higher than the corresponding value indicated in EN1998-1-1 [13] for beam to column joints in MRF.

## 2) Analysis

Static linear analysis is performed under dead and live loading and the members of the main frame are dimensioned according to the provisions of EN1993-1-1 [17] at ULS and SLS. The conventional method for the calculation of internal forces under seismic loading is Multi-Modal Response Spectrum Analysis, where the number of modes of vibration considered in each direction is such that the sum of the effective mass is at least equal to 90% of the total mass. The design spectrum shall be defined with a maximum behavior factor equal to 3, which was confirmed through non-linear static analyses (Pushover).

## 3) Limitation of interstory drift

Limitation of interstory drift ensures the protection of non-structural elements under seismic loading and consists a basic criterion for the design of «FUSEIS pin link». It provides an estimation of the damage for different performance levels and defines the distribution of stiffness within the structure and eventually the size and type of the cross sections applied on the system.

In linear analysis the displacements induced by the design seismic action  $d_s$  shall be calculated on the basis of the elastic deformations  $d_e$  of the structural system through the expression:

$$d_s = q \cdot d_e \quad \text{Eq. (4.14)}$$

In case the capacity ratios of the dissipative elements ( $\Omega$ ) are low, the calculation of the design interstory drift based on  $d_s$  is conservative and a therefore reduction factor ( $q_\Omega$ ) equal to the capacity ratio of the pins may be employed as follows:

$$d_s = q \cdot q_\Omega \cdot d_e \quad \text{Eq. (4.15)}$$

The design interstory drift  $d_r$  is defined as the difference of the average lateral displacements at the top and bottom of the story under consideration. Depending on the type of the non – structural elements (brittle materials, ductile or not connected) and the importance class of the building, the design interstory drift  $d_r$  is compared to the corresponding values of the Code. The optimal design is achieved when the maximum interstory drifts of the structure are close to the limit values. Since the horizontal displacements are multiplied by the behavior factor the limitation of interstory drift does not depend on it.

#### 4) 2<sup>nd</sup> order effects

The possible influence of 2<sup>nd</sup> order effects shall be controlled by the limitation of the interstory drift sensitivity coefficient  $\theta$  below the limit values of the Code. Coefficient  $\theta$  is calculated from Equation (4.16) for each floor at x and y directions of the building.

$$\theta = \frac{P_{tot} \cdot d_r}{V_{tot} \cdot h_{story}} \quad \text{Eq. (4.16)}$$

Where  $P_{tot}$  is the total gravity load at and above the story considered in the seismic design situation and  $V_{tot}$  is the seismic story shear.

Alternatively, the interstory drift sensitivity coefficient  $\theta$  may be calculated more accurately by a linear buckling analysis through the factor  $\alpha_{cr}$ , the factor by which the design loading would have to be increased to cause elastic instability in a global mode. The analysis is carried out under conditions of the constant gravity loads of the seismic combination ( $1,0 \cdot G + 0,3 \cdot \varphi \cdot Q$ ) and produces the buckling modes. The modes that move the building at x and y directions are chosen and the correspondent  $\alpha_{cr}$  values are calculated as follows:

$$\alpha_{cr} = \frac{1}{\theta} = \frac{F_{cr}}{F_{Ed}} \quad \text{Eq. (4.17)}$$

Where  $F_{cr}$  is the elastic critical buckling load for global instability mode based on initial elastic stiffnesses and  $F_{Ed}$  is the design loading for the seismic combination.

To take into consideration the inelastic displacements of the building,  $\alpha_{cr}$  shall be divided by the  $q$  factor. The values of  $\theta$  in this case are given by Equation (4.18).

$$\theta = \frac{q}{\alpha_{cr}} \quad \text{Eq. (4.18)}$$

The relevant Code provisions require for buildings that the interstory drift sensitivity coefficient is limited to  $\theta \leq 0.1$ , if second order effects are ignored. If  $0.1 < \theta < 0.2$ , second-order effects may approximately be taken into account by multiplying the relevant seismic action effects by a factor equal to  $1/(1 - \theta)$ . If  $0.2 < \theta < 0.3$  a more accurate second order analysis applies. In any case it shall be  $\theta < 0.3$ .

#### 5) Dissipative elements verifications

The pins shall be verified to resist the internal forces and moments of the most unfavorable seismic combination and fulfill the following conditions:

##### a) Axial Forces

It should be verified that the full plastic moment of resistance and shear forces are not decreased by compression forces through inequality (4.19):

$$\frac{N_{Ed}}{N_{pl,pin,Rd}} \leq 0.15 \quad \text{Eq. (4.19)}$$

##### b) Shear resistance

The shear resistance shall be verified with capacity design criteria, considering that plastic hinges are developed at both ends of the weakened part of the pin simultaneously.

$$\frac{V_{CD,Ed}}{V_{pl,pin,Rd}} \leq 1 \quad \text{Eq. (4.20)}$$

Where  $V_{CD,Ed} = \frac{2 \cdot M_{pl,pin,Rd}}{l_{pin}}$  is the capacity design shear force due to application of

moments of resistance  $M_{pl,pin,Rd}$  in opposite direction and  $V_{pl,pin,Rd}$  is the design shear resistance of the weakened section of the pin.

##### c) Moment capacity

It was found in the tests that the full moment resistance develops in the weakened pins despite the presence of high shear. Therefore, this is the critical check for the pins considering that their length is such that a bending mechanism develops. The moment capacity shall be verified as following:

$$\frac{M_{Ed}}{M_{pl, pin, Rd}} \leq \frac{1}{\Omega} \leq 1.0 \quad \text{Eq. (4.21)}$$

Where  $M_{Ed}$  is the design bending moment,  $M_{pl, pin, Rd}$  is the design moment plastic resistance of weakened pin section and  $\Omega$  is the overstrength of the weakened pin section.

In order to ensure that  $M_{pl, pin, Rd}$  will not be reduced due to the influence of shear, the length and the thickness of the weakened pin should be such that the ratio between acting shear and shear resistance in Equation (4.20) is less or equal to 0.5. In this case the length of the weakened part of the pin shall be well above the length calculated from Equation (4.22).

$$l_{pin} \geq \frac{4 \cdot M_{pl, pin, Rd}}{V_{pl, pin, Rd}} = \frac{4 \cdot W_{pl, pin}}{A_v / \sqrt{3}} \quad \text{Eq. (4.22)}$$

#### d) Global dissipative behavior

To achieve a global dissipative behavior of the structure, it should be checked that the maximum ratios  $\Omega$  over the entire structure do not differ from the minimum value  $\Omega$  by more than 25%.

$$\frac{\max \Omega}{\min \Omega} \leq 1.25 \quad \text{Eq. (4.23)}$$

#### e) Pin rotations

Since the length of the weakened part of the pin  $l_{pin}$  is much smaller than the columns centerline distance  $L$ , considerable pin rotations develop during seismic excitation. However, tests have shown that such rotations can be accommodated by the pins. In order to ensure that pin rotations are below those reached in the tests the additional check in Equation (4.24) shall be verified. The limit value of  $\theta_{pl, pin}$  shall be calculated considering that the global interstory drift  $\theta_{gl}$  is equal to 1.38%, the value at which the frames with FUSEIS pin links reached the maximum horizontal load during the tests and is defined as the limit at ULS (Section 4.2.2). Considering rigid receptacles as in the tests, the pin chord rotations are determined from:

$$\theta_{pin} \leq \theta_{pl, pin} = \frac{L}{l_{pin}} \theta_{gl} \quad \text{Eq. (4.24)}$$

#### 6) Non-dissipative element verifications

The non-dissipative elements, the system columns, the receptacle beams and their connections, shall be capacity designed for increased values of internal forces compared to the ones derived from the analyses with the most unfavourable seismic combination, to ensure that the failure of the pins occurs first.

d) The FUSEIS columns and the receptacle beams shall be verified to resist the capacity design action effects as following:

$$N_{CD,Ed} = N_{Ed,G} + 1.1 \cdot \alpha \cdot \gamma_{ov} \cdot \Omega \cdot N_{Ed,E} \quad \text{Eq. (4.25)}$$

$$M_{CD,Ed} = M_{Ed,G} + 1.1 \cdot \alpha \cdot \gamma_{ov} \cdot \Omega \cdot M_{Ed,E} \quad \text{Eq. (4.26)}$$

$$V_{CD,Ed} = V_{Ed,G} + 1.1 \cdot \alpha \cdot \gamma_{ov} \cdot \Omega \cdot V_{Ed,E} \quad \text{Eq. (4.27)}$$

Where  $N_{Ed,G}$  ( $M_{Ed,G}$ ,  $V_{Ed,G}$ ) are the axial forces (shear forces and bending moments accordingly) due to the non-seismic actions included in the combination of actions for the seismic design situation,  $N_{Ed,E}$  ( $M_{Ed,E}$ ,  $V_{Ed,E}$ ) are the axial forces (shear forces and bending moments accordingly) due to the design seismic action,

$\Omega = \min \Omega_i = \min \left\{ \frac{M_{pl,pin,Rd,i}}{M_{Ed,i}} \right\}$  is the minimum overstrength factor for all pins in the

building, see expression (5.10),  $\gamma_{ov} = 1.25$  is the material overstrength factor, see expression (2.1),  $\alpha = 1.5$  is an additional overstrength factor derived from the nonlinear analysis to ensure that the weakened pins will yield prior to the rest of the structural members. The total magnification factor of seismic loads cannot exceed the value of the behavior factor used in the analysis. The selection of pin's dimensions shall be such that the value of  $\Omega$  is close to 1 and the real yield stress of the steel approximately equal to its nominal value in order to achieve an economic design.

e) The moment resistance of the full pin section shall be verified at its contact area with the face plate of the receptacles, in accordance with:

$$\frac{M_{CD,Ed}}{M_{pl,Rd}} \leq 1.0 \quad \text{Eq. (4.28)}$$

Where  $M_{CD,Ed} = \frac{l}{l_{pin}} M_{pl,pin,Rd}$  is the capacity design bending moment ( $l$  is the length

between the face plates of the receptacles) and  $M_{pl,Rd}$  is the design bending moment of full pin section.

- f) Categories B and C of bolted joints with high strength bolts of category 8.8 or 10.9 should be employed between system columns and receptacles. These connections must have sufficient overstrength to ensure that their yielding will take place after the plastification of the pins. The capacity design bending moment of the connection is:

$$M_{CD,con,Ed} = 1.1 \cdot \gamma_{ov} \frac{L_{net}}{l_{pin}} M_{pl,pin,Rd} \quad \text{Eq. (4.29)}$$

Where  $L_{net}$  is the total length of the link between the flanges of the columns. The capacity design shear force of the connection is calculated as follows:

$$V_{CD,con,Ed} = 1.1 \cdot \gamma_{ov} \frac{2 \cdot M_{pl,pin,Rd}}{l_{pin}} \quad \text{Eq. (4.30)}$$

#### 4.5.3 Design for non - linear analysis (Pushover)

- 1) The structural model used for elastic analysis shall be extended to include the response of structural elements beyond the elastic state and estimate expected plastic mechanisms and the distribution of damage.
- 2) Since the ductile elements are the FUSEIS pins, potential plastic hinges shall be inserted at the ends of their weakened parts. These hinges are of bending type M3 and their properties were determined from calibration of experimental results.
- 3) Fig. 4.17 summarizes the proposed non-linear properties. It should be noted that the limit values that define the yield (B) and failure (C) points are lower than the corresponding measured during the tests where the system exhibited significant overstrength due to strain hardening and catenary action. However, for the design of buildings with the system a more conservative approach is adopted so that yielding of the pins starts when their bending plastic resistance is exhausted (Vierendeel beam theory). Fig. 4.17 also includes the limit values for the three Performance Levels: Immediate Occupancy (IO), Life Safety (LS) and Collapse Prevention (CP).
- 4) The hinge properties of the non-dissipative elements shall be calculated according to the provisions of relevant codes (e.g. FEMA-356 [18]). Plastic hinge properties for the receptacles shall be of bending type (M3 hinge), while in columns the interaction between bending moments and axial forces (P-M3 hinges) shall be accounted for.

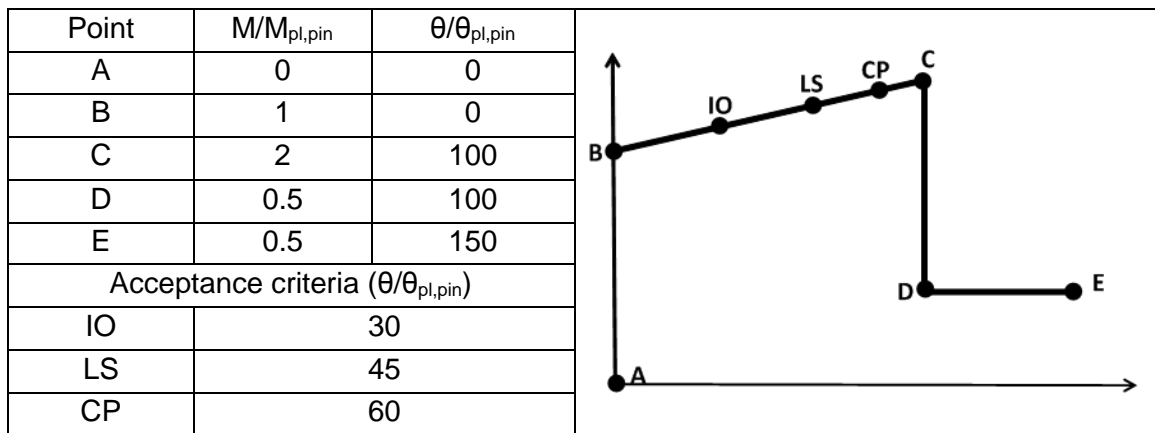
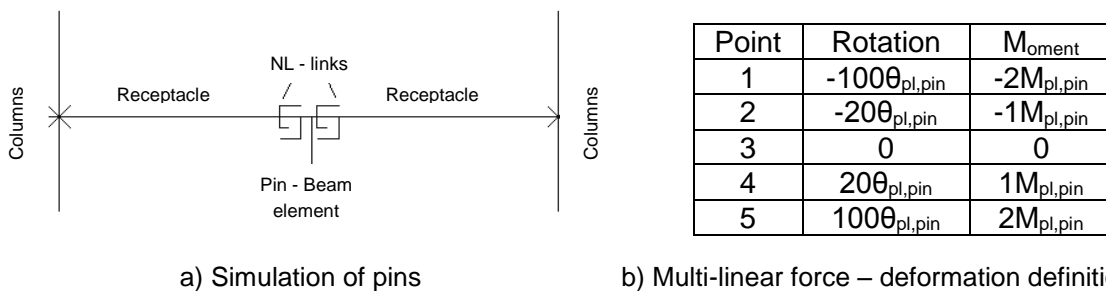


Fig. 4.17: Proposed non - linear hinge parameters for the pins

#### 4.5.4 Design for non - linear dynamic analysis

1) It shall be performed in order to define time-dependent response of steel buildings when designed according to the provisions of the EN1998-1-1 under real earthquake conditions. The analysis provides the capability to restrict damage after a seismic event by evaluating and eliminating the residual drifts of the structure. If the FUSEIS pin link system is appropriately designed it can work as a self-centering system, with practically zero residual drifts.

2) In order to obtain the non-linear response of the pin, it is modelled as follows: two multi-linear plastic link elements with a length approximately equal to 25% of its length are assigned at the ends and the remaining middle part is simulated as a beam with the initial cross section (Fig. 4.18a). The behavior of the non-linear link is defined only for the rotational degree of freedom with respect to the major axis of inertia while the remaining degrees of freedom are modelled as linear. The nonlinear properties applied include a moment rotation input with positive and negative moment capacities equal to the plastic moment capacity and initial stiffness of the pin under positive and negative moments (Fig. 4.18b). The hysteresis type should be the one provided by the Multi-linear plastic kinematic model (Fig. 4.18 c).

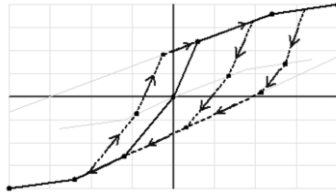


a) Simulation of pins

b) Multi-linear force – deformation definition

Fig. 4.18: Proposed non - linear links simulation for non-linear dynamic analysis





c) Multi-linear plastic kinematic model

Fig. 4.18: Proposed non - linear links simulation for non-linear dynamic analysis (continuation)

3) The plastic rotations are considerable due to the small pin length. Non-linear Time history analyses shall be used to determine the damage index for variable amplitude cycles by the Palmgren – Miner law of damage accumulation (Equation (4.9)). The number of cycles to be sustained by the system is dictated by low-cycle fatigue considerations, which deal with the deformation and strain histories rather than the stress histories (high - cycle fatigue). The drift ranges ( $\Delta\phi$ ) per cycle can be applied at the experimental fatigue curve (defined in Chapter 4.4.2.4, Equation (4.11)) to calculate the number of the correspondent cycles  $N$ . The calculation is based on the assumption that the receptacle beams remain rigid. This results in higher values of pin drifts than the actual and consequently the introduction of a safety factor for the determination of the pin's damage index is not required.

## 4.6 ANALYSES ON 2D BUILDING FRAMES

Equations, element properties, design recommendations, critical checks and proposed behavior factor, included in the Design Guide, were verified through numerical analyses on real 2D building frames with FUSEIS pin links with the use of the software SAP2000 [20]. Initially the frames were designed through elastic analysis at ULS and SLS. Nonlinear static and dynamic analyses followed to investigate their behavior beyond the elastic range and confirm the behavior factor  $q=3$ .

### 4.6.1 Description of examined building frames

#### 4.6.1.1 Geometry and assumptions

The case study presented hereafter was based on the extraction of a plane frame from a five-story composite building, Fig. 4.19. The frame consisted of a semi-rigid PF frame (partially fixed moment frame) with three 6m bays and one FUSEIS pin link system applied at its end to provide seismic resistance. The columns had rectangular hollow sections (RHS) and the floor beams composed of steel beams with wide flange I-sections (HEA-Type) that acted compositely with the concrete slabs (C25/30, B500C), except at beam ends where the concrete slab was not connected to the steel beam.

The system consisted of a pair of hollow strong columns at a center-to-center distance of 2.0 m and five links per story with circular pins with a net length of 200

mm. A link was provided at the foundation level and the receptacle beams had rectangular and square hollow sections (RHS, SHS) and were connected rigidly to the system columns. The resulting cross sections for beams HEA260 and columns SHS200x15 of the main semi-rigid frame are indicated in Fig. 4.19. Table 4.2 summarizes the diameters of the fuses pins in the weakened portion, the cross sections of the system's columns and the receptacles. The dissipative pins had lower steel grade (S235) than the rest of the structural members (S355). The pin production was not considered to be fully controlled, so that the properties of the pin material had to comply with Equation (4.1) with  $\gamma_{ov} = 1.25$ . This overstrength factor was also considered in the capacity design.

**Table 4.2: Cross sections of pins, columns and receptacles**

Story	Pins $\Phi$ (mm)	System columns	Receptacle beams
1	95	RHS 400x300x35	RHS 260x220x25
2	90	RHS 400x300x35	RHS 260x220x25
3	85	RHS 400x300x20	SHS 240x20
4	80	RHS 400x300x20	SHS 240x20
5	70	RHS 400x300x20	SHS 240x20

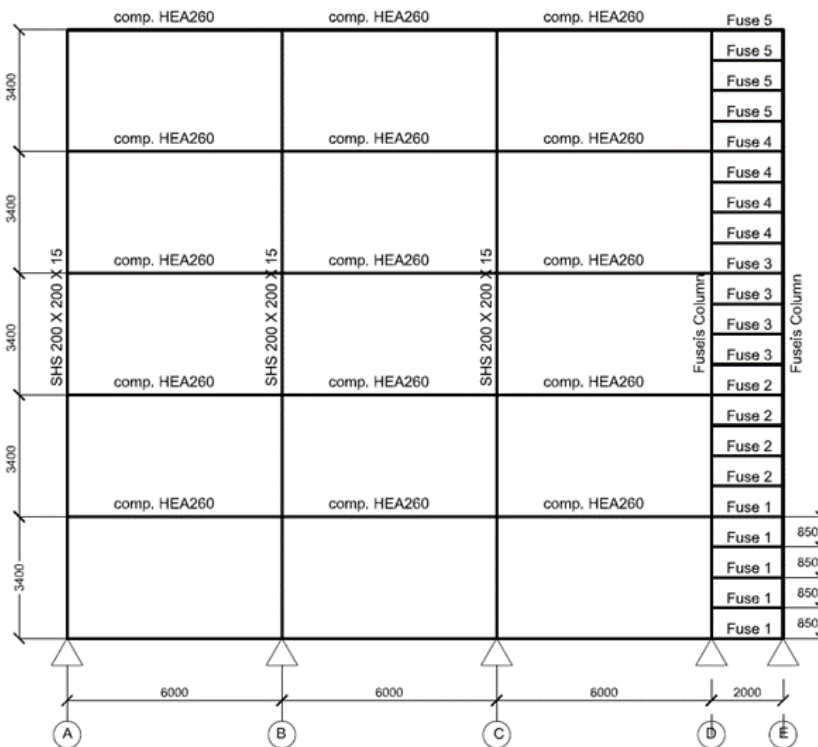


Fig. 4.19: 2D building frame

Table 4.3 includes the assumptions for gravity and seismic loads. The dead and live loads considered were equal to 2.00kN/m<sup>2</sup>. Considering that equal plane frames

were placed at a distance of 8 m in the building, the corresponding line loads on the beams were 16.00kN/m.

**Table 4.3: Assumptions for loads**

Vertical loads	
Dead loads apart from self-weight – G	2.00kN/m <sup>2</sup>
Live loads – Q	2.00kN/m <sup>2</sup>
Seismic loads	
Elastic response spectra	Type 1
Peak ground acceleration	A=0.36g
Importance class II	$\gamma_I = 1.0$ (Ordinary buildings)
Ground type	B ( $T_B = 0.15$ s, $T_C = 0.50$ s)
Proposed behavior factor q	3
Damping ratio	5%
Factors of operating loads for seismic comb.	$\phi = 1.00$ (roof), $\phi = 0.80$ (stories with correlated occupancies)
Seismic combination coefficient for the quasi-permanent value of variable actions	$\psi_2 = 0.30$

#### 4.6.1.2 Simulation

The structural model was a linear-elastic model with beam elements and was formed according to the rules given in Section 4.5.2 (1) as follows:

- 1) Since the joints between main frame floor beams and columns were semi – rigid, rotational springs were assigned at beams' ends to introduce these partial fixity conditions with properties determined in accordance with EN1994-1-1 [21] and EN1993-1-8 [22]. The structure was designated as FUSEIS+PF to indicate the fact that the seismic resistant system is a combination of the FUSEIS system and a partially fixed moment frame.
- 2) The main frame floor beams were subdivided into three segments; steel sections were assigned at the ends (0,15L) where negative moments develop and the concrete slab does not bear loads due to cracked analysis (EN1994-1-1 [21]) and composite beam sections consisting of the steel beams and the associated 15 cm concrete slab over its effective width in the middle part. Rigid end length offsets were included at the beams to consider their clear length and their actual stiffness in the analysis.
- 3) The beam elements representing the FUSEIS pin links were divided in three parts with different cross sections: the receptacle beams at the ends and the weakened pin in the middle. The joints between receptacle beams and system columns were considered as rigid.
- 4) The joints between floor beams and system columns were considered as simple. Columns bases were designed and formed as pinned to prevent a moment transfer to the foundation.

#### 4.6.2 Response spectrum analysis

Multi-modal response spectrum analysis was performed and the results are summarized in Table 4.4. The first and the second modes, which were translational, activated more than 90% of the mass.

**Table 4.4: Participating mass ratio and periods**

Mode No	Eigen Period (s)	Participating mass ratio (%)	Total (%)
1	0.990	74.80	93.60
2	0.295	18.80	

According to EN1998-1-1 when  $T_B \leq T \leq T_D$  the lower bound for the horizontal design spectrum has to be checked with Equation (4.31):

$$S_d(T) = \frac{V_{tot}}{P_{tot}} \geq \beta \cdot a_g \quad \text{Eq. (4.31)}$$

Where  $V_{tot}$  is the total base shear from the response spectrum analysis,  $P_{tot}$  is the total axial force from the effective mass of the frame for the seismic combination and  $\beta=0.2$  is the lower bound factor for the horizontal design spectrum. The check was verified and there was no need for an increase of the base shear (Table 4.5).

**Table 4.5: Check of the lower bound for the horizontal design spectrum**

$V_{tot}$ (kN)	$P_{tot}$ (kN)	$V_{tot}/P_{tot}$	$\beta \cdot a_g$
716	4666	0.153	0.072

#### 4.6.3 Seismic design

It is noted that for the seismic design following conditions were to be fulfilled in accordance with the design rules described in Section 5.2 and EN 1998-1-1 [13] rules.

##### 4.6.3.1 Limitation of interstory drift

Considering that the building has ductile non-structural elements the following Equation (4.32) is checked.

$$d_r \cdot v \leq 0.0075 \cdot h = 0.0075 \cdot 3400 = 25.5 \text{ mm} \quad \text{Eq. (4.32)}$$

Where  $v = 0.5$  is a reduction factor on the design displacements due to the importance class of the building (ordinary buildings) and  $h$  is the story height. Table 4.6 includes the results of the analysis; the check is verified for all stories with values much lower than the limit value 25.5mm. The selection of the columns' and the receptacle beams' sections was defined by this check.

**Table 4.6: Limitation of interstory drift**

Story	1	2	3	4	5
$d_{e,top}$ (mm)	8.20	19.10	32.80	47.50	61.00
$d_{e,bottom}$ (mm)	0.00	8.20	19.10	32.80	47.50
$d_r = (d_{e,top} - d_{e,bottom}) \cdot q$ (mm)	24.6	32.70	41.10	44.10	40.50
$d_r \cdot v$	12.3	16.35	20.55	22.05	20.25

#### 4.6.3.2 2<sup>nd</sup> order effects

A linear buckling analysis for the seismic combination  $1.0 \cdot G + 0.3 \cdot \varphi \cdot Q$  was carried out in order to control 2<sup>nd</sup> order effects. From this analysis the critical buckling modes and the corresponding buckling factors derived. The buckling mode that moved the frame with  $PGA=0.36g$  is given in Fig. 4.20.

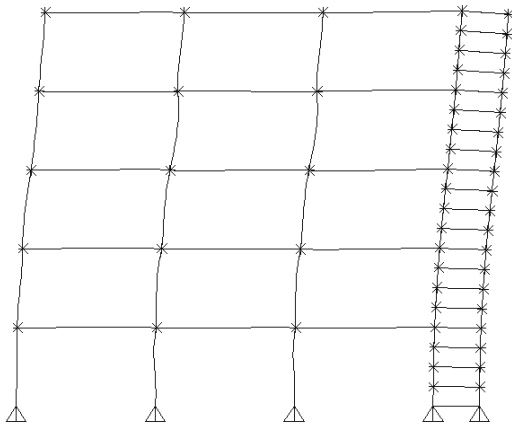


Fig. 4.20: 1st buckling mode (SAP2000 [20])

The values of  $\theta$  were calculated from the critical buckling factors and it was checked whether 2<sup>nd</sup> order effects should be taken into account (Table 4.7). Since  $\theta < 0.1$ , 2<sup>nd</sup> order effects were neglected.

**Table 4.7: 2<sup>nd</sup> order effects**

Critical buckling factors	$\alpha_{cr}$	$\theta$	Seismic load multiplier $\beta$
47.30	15.77	0.063	1.00

#### 4.6.3.3 Dissipative elements – pins

The FUSEIS pins were designed to resist the forces of the most unfavorable seismic combination  $1.0 \cdot G + 0.3 \cdot \varphi \cdot Q + Ex$ . The minimum required length to ensure the development of a bending mechanism at the pins is calculated from Equation (4.22) and ranges between 114mm - 154mm. Therefore, the length of the weakened part of the pin was taken equal to 200mm which is much higher than the required. Table 4.8 to Table 4.10 summarize the results of all the pin verifications. Table 4.10 also includes the pin overstrength values  $\Omega$  used to check the global dissipative behavior of the system which is ensured when the  $\Omega$  values of all the pins in all stories differ no more than 25% of its minimum value.

**Table 4.8: Check of axial forces**

Story	$N_{Ed}$ (kN)	$N_{pl,pin,Rd}$ (kN)	$\frac{N_{Ed}}{N_{pl,pin,Rd}} \leq 0.15$
1	59.40	1655.11	0.04
2	76.00	1485.44	0.05
3	74.40	1324.93	0.06
4	75.00	1173.59	0.06
5	123.00	898.41	0.14

**Table 4.9: Check of shear forces**

Story	$V_{Ed}$ (kN)	$V_{pl,pin,Rd}$ (kN)	$\frac{V_{Ed}}{V_{pl,pin,Rd}} \leq 0.50$
1	332.53	862.91	0.39
2	282.71	774.17	0.37
3	238.29	690.60	0.35
4	198.60	611.90	0.32
5	133.03	468.36	0.28

**Table 4.10: Check of bending moments**

Story	$M_{Ed}$ (kN.m)	$M_{pl,pin,Rd}$ (kN.m)	$\frac{M_{Ed}}{M_{pl,pin,Rd}} \leq 1.00$	$\Omega = \frac{M_{pl,pin,Rd}}{M_{Ed}}$	$\frac{\max \Omega}{\min \Omega} \leq 1.25$
1	28.70	33.25	0.86	1.16	1.09
2	26.30	28.27	0.93	1.07	
3	20.40	23.83	0.86	1.17	
4	17.20	19.86	0.87	1.15	
5	11.40	13.30	0.86	1.17	

It was also checked that the pin chord rotations were below those reached in the tests. It was verified that:

$$\theta_{pin} \leq \theta_{pl,pin} = \frac{2000}{200} \cdot 1.38\% = 13.8\% (138 \text{ mrad}) \quad \text{Eq. (4.33)}$$

The values of  $\theta_{pin}$  are given in Table 4.11, it may be observed that they are lower than the limit value.

**Table 4.11: Pin rotations  $\theta_{pin}$  (%)**

Story	$\theta_{pin}$ (%)
1	1.19
2	1.30
3	1.21
4	0.96
5	0.72

#### 4.6.3.4 System columns, receptacle beams and full pin section

The system columns and the receptacle beams are designed following capacity design criteria in accordance with Equations (4.25) - (4.27) taking into account the minimum overstrength factor  $\Omega$  for all the pins, the material overstrength factor, an additional overstrength factor  $\alpha=1.5$  derived from the nonlinear analysis and the seismic load multiplier  $\beta$  derived from the limitation of the 2nd order effects. The utilisation factors of the system columns and the receptacle beams were calculated according to the provisions of EN1993-1-1 [17] and were lower than 1 (Table 4.12).

**Table 4.12: Utilisation factors of the system columns and the receptacle beams**

Columns FUSEIS pin link		Receptacle beams	
RHS 400x300x20	0.776	RHS 240x240x20	0.758
RHS 400X300x35	0.903	RHS 260x220x25	0.854

The bending resistance of the full pin section at the contact of the pin with the face plates of the receptacles  $M_{pl,Rd}$  derives from the bending resistance of the weakened pin section from Equation (4.28). As shown in Table 4.13 the calculated values are lower than the corresponding bending resistances in all stories.

**Table 4.13: Check of the full pin section**

Story	$M_{Ed}$ (kNm)	$M_{pl,Rd}$ (kNm)	$\frac{M_{CD,Ed}}{M_{pl,Rd}} \leq 1.00$
1	49.88	52.13	0.96
2	42.41	52.13	0.81
3	35.74	52.13	0.69
4	29.79	52.13	0.57
5	19.96	52.13	0.38

#### 4.6.4 Non - linear static analyses (Pushover)

##### 4.6.4.1 Evaluation of the non-linear behavior of the frames

Nonlinear static (pushover) analysis was performed to verify the collapse mechanism and check the behavior factor used in the linear analysis. The results presented hereafter are in accordance with the fundamental mode of vibration including P-Delta effects. Nonlinear plastic hinges of bending type M3 were assigned at the ends of the weakened parts of the pins, their properties being determined from calibration of experimental results and analytical investigations (Design Rules, Fig. 4.17). For the frames under consideration the limit rotations ranged from 55 to 109 mrad for the small pins  $\phi 70$  and 40 to 80 mrad for the large pins d95, depending on the performance level (IO, LS, CP). These values were well below 225 mrad that were reached in the experiments.

Nonlinear plastic hinges were also introduced at the ends of the rest of the structural members. The hinge properties of the rotational springs that simulated the semi rigid joint were of bending type (M3 hinge) and were calculated for positive and negative

moments. The rotation capacity of the plastic hinge region  $\theta_p$  was equal to 40 mrad (Section 5.2 (1)). As referred in the design rules, plastic hinge properties for the receptacles were also of bending type (M3 hinge), while in columns the interaction between bending moments and axial forces (P-M3 hinges) were accounted for. These properties were calculated according to FEMA 356 [18].

The plastic hinge distribution at first yield, at the performance point and at the maximum experimental interstory drift is given in Fig. 4.21. It is observed that the columns remained elastic and that plastic hinges formed at the pins and the ends of the beams of the semi - rigid frame. The deformation capacity of the pins was exhausted at stories 2-3, where the first plastic hinges appeared. It is worth noting that at the maximum experimental interstory drift of the tests the plastic hinges of the pins are at the LS performance level and the plastic hinges of the beams of the semi – rigid frame at the IO performance level.

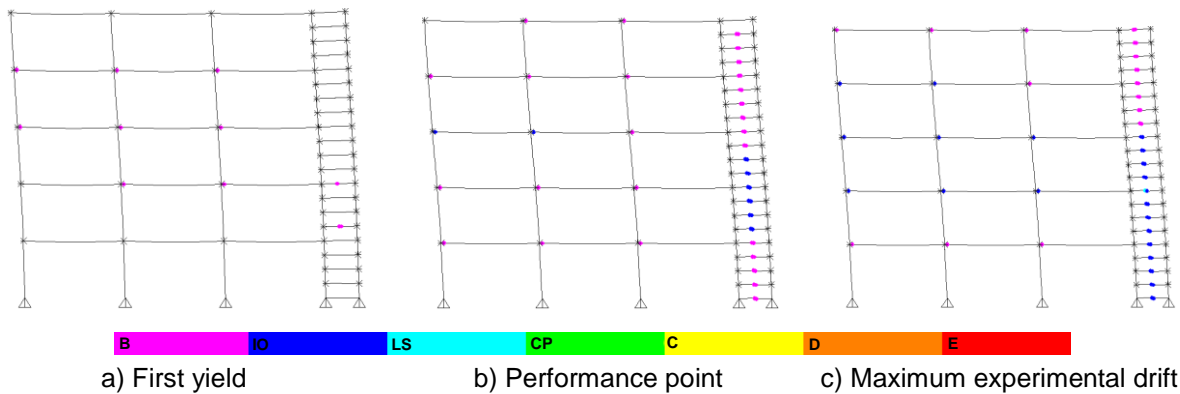


Fig. 4.21: Deformed frame and plastic hinge formation

In order to check the structural performance at smaller and higher seismic excitations, three design levels, Serviceability (SLS), Ultimate (ULS), Collapse (CPLS), were introduced. This was done by application of a scaling factor to the PGA of the design earthquake as following: SLS scaling factor 0,5, ULS scaling factor 1.0, CPLS scaling factor 1.5. For these design levels the performance points were determined and the interstory drifts recorded. Table 4.14 shows the maximum values of interstory drifts, the experimentally recorded drifts (Section 4.2.2) and the values proposed by FEMA-356 [18] for Steel Braced Frames. It may be noted that the analytical drift values are lower than the experimental which are similar to those proposed by FEMA-356 for Steel Braced Frames.

**Table 4.14: Comparison between experimental, analytical and FEMA interstory drifts (%)**

Limit states	Experimental	Analytical	FEMA-356 Braced Frames
SLS	0.66	0.66	0.50
ULS	1.38	1.19	1.50
CPLS	2.25	1.82	2.00



The performance of buildings with FUSEIS pin links was also evaluated for different types of floor beam-to-column joints. Two additional cases, with fully restrained and simple joints, were examined. In the former case the rotational springs were removed and hinge properties of bending type (M3 hinge) introduced. The structure was designated as FUSEIS+FR to indicate the fact that the seismic resistant system is a combination of the FUSEIS system and a fully restrained moment frame. In the latter case hinges were introduced at beam ends with nonlinear properties of shear type (V2 hinge). The structure was designated as FUSEIS which was the only seismic resisting system. As already mentioned the initial structure with the semi – rigid floor beam-to-column joints was designated as FUSEIS+PF.

The capacity curves of the three above mentioned connection types (FUSEIS+FR, FUSEIS+PF, FUSEIS), are given in Fig. 4.22. The shape of the capacity curves, indicates that the plastification of individual pins did not change the slope of the curve. On the contrary when many pins became simultaneously plastic the slope of the curve changed and the structure became softer. It is observed that the MRF action (FUSEIS+FR or FUSEIS+PF) increased the capacity of the frame and led to lower drifts compared to the hinged frame (FUSEIS). These results confirm Section 5.2 (2) where the PF frame is proposed as the most effective system to be combined with FUSEIS pin link since it exploits the advantages of both the MRF and the FUSEIS system and is easier to realize in practice compared to FUSEIS+FR.

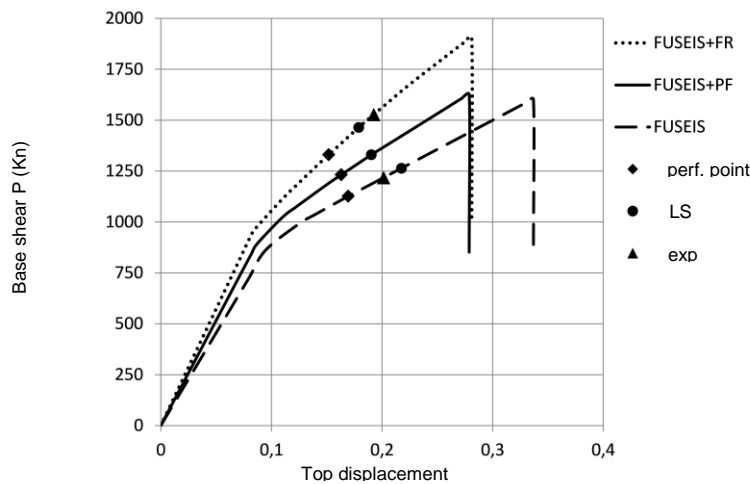


Fig. 4.22: Comparison of the capacity curves of frames FUSEIS+FR, FUSEIS+PF και FUSEIS

#### 4.6.4.2 Evaluation of the behavior factor $q$

For the evaluation of the behavior factor ( $q$  factor) of the structure the procedure described below was followed. The behavior factor was defined from Equation (4.34) as the product between the ductility ( $q_\mu$ ) and the overstrength ( $\Omega$ ).

$$q = q_\mu \cdot \Omega$$

Eq. (4.34)

In Fig. 4.23a typical capacity curve and the parameters used for the evaluation of the behavior factor are given. The ductility  $q_\mu$  is determined as the ratio between the actual displacement when the pin rotations reach the experimental drift at ULS or the LS performance level  $\delta_{LS,exp}$ , whichever is more unfavorable, to the yield displacement of an equivalent bilinear system  $\delta_{el}$ , Equation (4.35).

$$q_\mu = \frac{\delta_{LS,Exp}}{\delta_{el}} \quad \text{Eq. (4.35)}$$

Overstrength is defined as the ratio between the yield force ( $V_{LS,Exp}$ ) of the bilinear system to the design force ( $V_d$ ) which is calculated according to the first mode of vibration, Equation (4.37).

$$\Omega = \frac{V_{LS,Exp}}{V_d} \quad \text{Eq. (4.36)}$$

$$V_d = n \cdot M \cdot S_d(T_1) \quad \text{Eq. (4.37)}$$

Where  $n$  is the participating mass ratio of the fundamental mode,  $M$  is the total mass and  $S_d(T_1)$  is the spectral acceleration of the design spectrum at the fundamental period of vibration  $T_1$ .

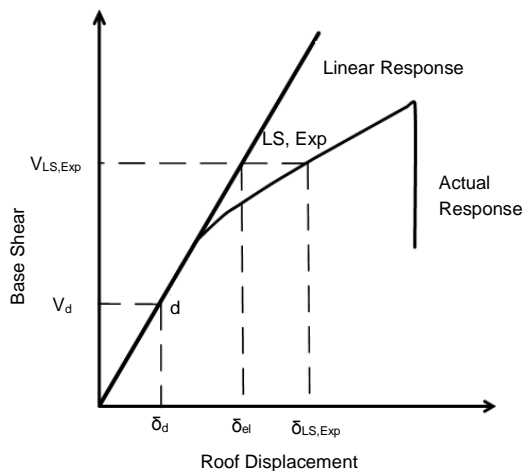


Fig. 4.23: Evaluation of the behavior factor from the capacity curve

The calculated ductility, overstrength and behavior factors, of the FUSEIS+PF frame are given in Table 4.15. The calculated  $q$ -factor is above 3, the value considered in design.

**Table 4.15: Calculated behavior factors  $q$**

$q_\mu$	$\Omega$	$q$
1.48	2.08	3.07

#### 4.6.5 Non-linear dynamic analyses (time-history)

Using characteristic seismic records from real strong motions, non-linear dynamic analyses on the examined building frame were performed to assess whether the elastic design with behavior factors meets the seismic performance objectives. Similar to the non-linear static analysis, simple floor beam-to-column joints were examined (FUSEIS) in addition to the semi-rigid ones (FUSEIS+PF). The initial loading conditions were the same as in non-linear static analysis considering the gravity loads of seismic combination. The models used in the previous analyses were appropriately modified to include the hysteretic behavior of the pins. Nonlinear links with multi-linear kinematic plasticity properties, according to Section 5.4, were assigned at the pins and are given in Table 4.16.

**Table 4.16: Nonlinear link properties**

Pin $\Phi 70$			Pin $\Phi 80$			Pin $\Phi 85$		
Point	$\theta(\text{rad})$	M(kNm)	Point	$\theta(\text{rad})$	M(kNm)	Point	$\theta(\text{rad})$	M(kNm)
1	-0.181	-26.61	1	-0.159	-39.72	1	-0.150	-47.66
2	-0.036	-13.30	2	-0.032	-19.86	2	-0.030	-23.83
3	0	0	3	0	0	3	0	0
4	0.036	13.30	4	0.032	19.86	4	0.030	23.83
5	0.181	26.61	5	0.159	39.72	5	0.150	47.66

Pin $\Phi 90$			Pin $\Phi 90$		
Point	$\theta(\text{rad})$	M(kNm)	Point	$\theta(\text{rad})$	M(kNm)
1	-0.141	-56.54	1	-0.141	-56.54
2	-0.028	-28.27	2	-0.028	-28.27
3	0	0	3	0	0
4	0.028	28.27	4	0.028	28.27
5	0.141	56.54	5	0.141	56.54

##### 4.6.5.1 Ground motion records

Non-linear dynamic (response history) analyses were performed according to the procedures described in FEMA - P695 [23]. The examined frame was subjected to a suite of ground motion records obtained from the Far-Field record set since it is considered appropriate for collapse evaluation of buildings. This set includes twenty-two component pairs of the strongest horizontal ground motions from the PEER NGA database and refers to sites located greater than or equal to 10 km from fault rupture.

Scaling of ground motion was achieved through the software SeismoMatch [24] which is able to adjust ground-motion records so that their spectral acceleration response matches a target response spectrum. The matching of the records was based on the EN 1998-1-1 [13] rules for Recorded accelerograms. According to Vamvatsikos and Cornell [25], for mid-rise buildings, ten to twenty records are

usually enough to provide sufficient accuracy in the estimation of seismic demands. The scaling process was performed for all pairs of Far – Field records, and finally twelve of them were selected based on the criterion of EN 1998-1-1 [13], which indicates that in the range of periods between  $0.2T_1$  and  $2T_1$  ( $T_1$  fundamental period) no value of the mean spectrum should be less than 90% of the corresponding value of the elastic response spectrum. The characteristics of these records were representative for the examined frame which is validated from the deformation results given in Sections 4.6.5.2 and 4.6.5.3

**Table 4.17: Types and configurations of the PEER-NGA seismic records (FEMA - P695 [23])**

No	Year	Horizontal Records	Station	max PGA (g)
1	1999	Chi-Chi, Taiwan	TCU045	0.51
2	1999	Duzce, Turkey	Bolu	0.82
3	1976	Friuli, Italy	Tolmezzo	0.35
4	1999	Hector Mine	Hector	0.34
5	1979	Imperial Valley	Delta	0.35
6	1995	Kobe, Japan	Nishi-Akashi	0.50
7	1999	Kocaeli, Turkey	Duzce	0.36
8	1992	Landers	Coolwater	0.42
9	1989	Loma Prieta	Gilroy Array	0.37
10	1990	Manjil, Iran	Abbar	0.51
11	1994	Northridge	Canyon Country-WLC	0.48
12	1987	Superstition Hills	El Centro Imp. Co.	0.26

Fig. 4.24 displays the response spectra of the normalized far field records and the matched spectra along with the target spectrum respectively. Fig. 4.24b also illustrates the mean spectral response, calculated from all time histories which in the range of periods between  $0.2T_1$  and  $2T_1$ , deviates less than 6.7% from the corresponding values of the target spectrum. The matched records were stronger than the initial as they derived from matching them to the peak values of the target response spectrum. Even though this approach is unfavorable and leads to conservative results it was considered to be suitable to evaluate the performance and verify the design methodology of the innovative FUSEIS pin link system.

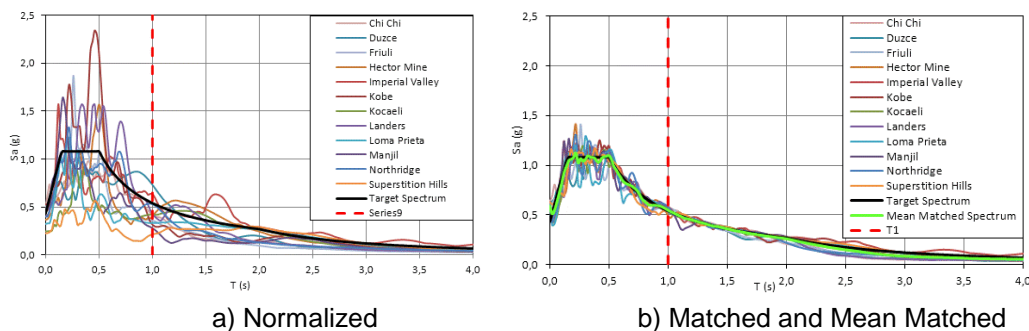


**Fig. 4.24: Pseudo – accelerations response**

#### 4.6.5.2 Residual roof drifts

The dynamic response of the system under real seismic excitations was initially evaluated through the roof displacement time histories of the examined frame for the selected seismic records. Fig. 4.25 shows the displacement time histories for the two types of beam-to-column joints, FUSEIS and FUSEIS+PF recorded for Kobe and Duzce earthquakes indicatively.

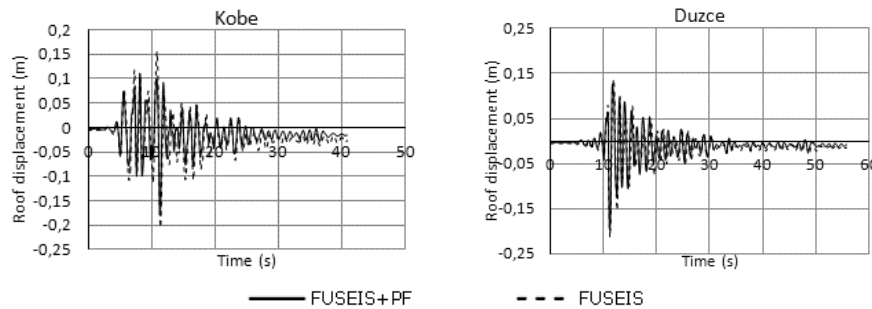


Fig. 4.25: Roof displacements time histories

The residual roof displacements were then divided by the frame height (17m) to calculate the residual global drifts, which are considered an essential criterion not only for the design of new buildings but also for the assessment of existing after a seismic event. The values of the residual global drifts are summarized in Table 4.18. Their values are close to zero with a maximal value of 0.157%, at FUSEIS frame, lower compared to the limit value of 0.5% of FEMA 356 [18] for Braced Steel Frames at IO.

**Table 4.18: Residual global drifts (%)**

Seismic record	FUSEIS + PF	FUSEIS
Chi-Chi, Taiwan	0.043	0.026
Duzce, Turkey	0.045	0.084
Friuli, Italy	0.043	0.053
Hector Mine	0.062	0.040
Imperial Valley	0.027	0.073
Kobe, Japan	0.090	0.156
Kocaeli, Turkey	0.021	0.117
Landers	0.052	0.069
Loma Prieta	0.034	0.013
Manjil, Iran	0.023	0.048
Northridge	0.064	0.003
Superstition Hills	0.010	0.011
Average	0.043	0.058
Standard deviation ( $\pm$ )	0.022	0.046

These results indicate that the FUSEIS pin link system is capable of self-recentering the structure after a major earthquake. The floor beams and the columns remained elastic and did not participate in the lateral resistance of the building. On the contrary, inelastic deformations concentrated only in the FUSEIS pins, while the strong system columns and the receptacle beams returned the structure at its initial

position. Therefore, it may be stated that the FUSEIS pin link system, with appropriate design, may be considered to possess self-centering properties, leaving the structure with minimal residual drifts and allowing for immediate occupancy after earthquake.

#### 4.6.5.3 Interstory drifts

The performance of FUSEIS pin link was also examined through the interstory drift. In Fig. 4.26, the residual and the maximum interstory drift curves are given indicatively for Kobe and Duzce records.

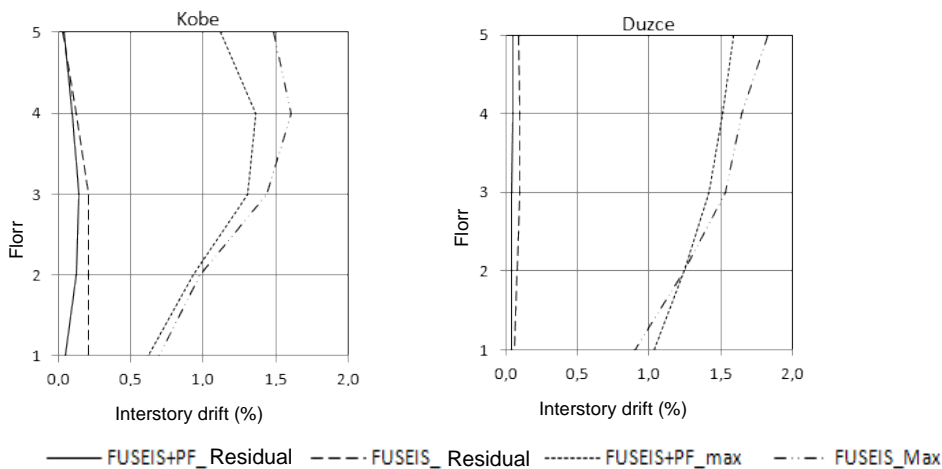


Fig. 4.26: Roof displacements time histories

The curves are similar for both cases considered, FUSEIS+PF and FUSEIS. It may be noted that the residual interstory drift values are close to zero, similar to the residual roof drifts, and that the interstory drifts for the FUSEIS+PF are lower compared to those when the FUSEIS system works alone. Table 4.19 shows the maximum interstory drifts which are between the experimental limit value at ULS (1.38%) and CPLS (2.25%).

**Table 4.19: Comparison of maximum interstory drifts (%)**

Seismic record	FUSEIS+PF	FUSEIS	Ratio
Chi-Chi, Taiwan	1.63	1.91	1.18
Duzce, Turkey	1.59	1.83	1.15
Friuli, Italy	1.47	1.79	1.22
Hector Mine	1.41	1.52	1.08
Imperial Valley	1.34	1.56	1.17
Kobe, Japan	1.37	1.61	1.18
Kocaeli, Turkey	1.47	1.61	1.10
Landers	1.53	1.79	1.16
Loma Prieta	1.48	1.58	1.07
Manjil, Iran	1.02	1.17	1.15
Northridge	1.56	1.80	1.15
Superstition Hills	1.34	1.60	1.20

#### 4.6.5.4 Low cycle fatigue

Cyclic tests in Section 4.2.2 indicated that the pins develop large plastic rotations due to their small length and thus it is possible to fail earlier under low-cycle fatigue during a seismic event. Non-linear time history analyses allowed the determination of the damage index of the pins as described in Section 4.5.4 (3). Table 4.20 summarizes the damage index calculated for the frame FUSEIS+PF for all the examined records and, as it is shown the Miner's criterion is fulfilled in all cases.

**Table 4.20: Damage Index**

Seismic record	Damage index ( $D \leq 1$ )
Chi-Chi, Taiwan	0.09
Duzce, Turkey	0.16
Friuli, Italy	0.11
Hector Mine	0.45
Imperial Valley	0.88
Kobe, Japan	0.15
Kocaeli, Turkey	0.13
Landers	0.26
Loma Prieta	0.34
Manjil, Iran	0.19
Northridge	0.27
Superstition Hills	0.15

#### 4.6.5.5 Incremental Dynamic Analysis (IDA)

The inelastic response of the system was further evaluated through the Incremental Dynamic Analysis (IDA) method according to the procedures given by Vamvatsikos and Cornell [26] and FEMA 695 [23]. In order to generate the IDA curves the ground motions of Section 6.5.1 were scaled initially to five intensities 0.50/0.75/1.00/1.25/1.50 and then to increasing intensities until numerical non-convergence was encountered. Each IDA curve was defined by the most representative ground motion Intensity Measure (IM) and Damage Measure (DM), which correspond to the 1st mode spectral acceleration  $S_a(T1.5\%)$  and the maximum interstory drift  $\theta_{max}$ , respectively.

Fig. 4.27 includes the IDA curves for all the examined records. It is observed that all curves start with an elastic part with constant slope until yielding which occurs at  $S_a(T1.5\%) \approx 0.4g$  and  $\theta_{max} \approx 1.0\%$ , followed by a part with slightly larger slope due to hardening, and end with a "flatline" at the highest numerically converging run when global dynamic instability happened and any increase in the IM would result in practically infinite DM response. Additionally, it should be noted that the IDA curves are conservative in terms of IM and have small dispersion, which is justified by the matching method applied by software SeismoMatch [24], as described in Section 4.6.5.1.

In order to be able to evaluate the performance of the system the three limit states Immediate Occupancy (IO), Life Safety (LS), Collapse Prevention (CP) were defined on the IDA curves based on the maximum experimental drifts (SLS, ULS, CPLS). The corresponding IM and DM values are given in Table 4.21.

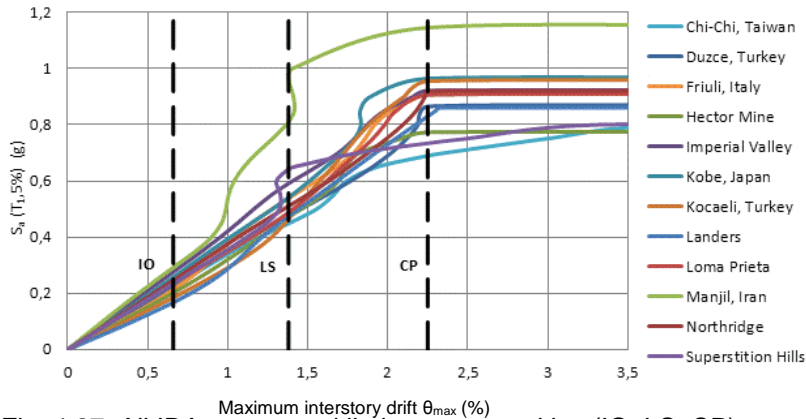


Fig. 4.27: All IDA curves and limit state capacities (IO, LS, CP)

**Table 4.21: The IM and DM values of capacity for all records and each limit-state (IO, LS, CP)**

Seismic record	$S_a(T_1, 5\%)$ (g)			$\theta_{max}$ (%)		
	IO	LS	CP	IO	LS	CP
Chi-Chi, Taiwan	0.22	0.45	0.69	0.66	1.38	2.25
Duzce, Turkey	0.23	0.48	0.87			
Friuli, Italy	0.21	0.54	0.91			
Hector Mine	0.20	0.47	0.77			
Imperial Valley	0.28	0.59	0.92			
Kobe, Japan	0.26	0.54	0.96			
Kocaeli, Turkey	0.18	0.46	0.96			
Landers	0.17	0.48	0.83			
Loma Prieta	0.24	0.49	0.91			
Manjil, Iran	0.29	0.81	1.15			
Northridge	0.25	0.51	0.92			
Superstition Hills	0.24	0.64	0.73			

The IDA curves were summarized into their 16%, 50% and 84% percentiles. Fig. 4.28 shows only the median curve (50%) since the other two deviate slightly from it due to the small dispersion of the IDA curves. This figure also includes the points at IO, LS and CP, defined by the interstory drifts calculated from experimental results  $\theta_{max}$  and the mean values (50%) of  $S_a(T_1, 5\%)$  obtained from Table 4.21 after arranging them in ascending order ( $S_a(T_1, 5\%) = 0.23g, 0.49g, 0.91g$ ). It is observed that these three points are very close to the median curve verifying the definition of these limit states.



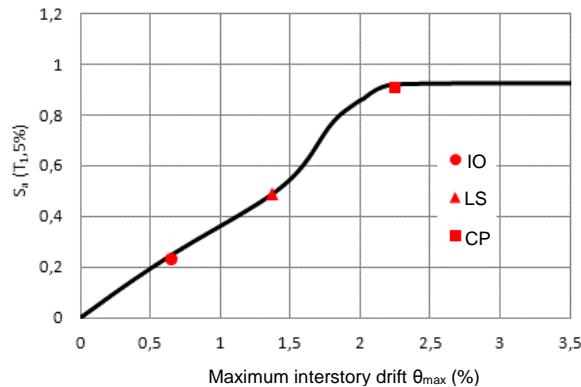


Fig. 4.28: 50% fractile IDA (median curve)

#### 4.6.6 Comparison of the results between methods of analysis

In an attempt to check the proposed design methodology, except for the analytical results of elastic multi modal, non-linear static (Pushover) and non-linear dynamic time history analyses (IDA) given in previous sections, it was considered necessary to compare them. Interstory drift was selected as the most representative parameter for this comparison since it provides an evaluation of the damage level of the structures for different limit states and it was proven to be crucial for the design of FUSEIS pin link system. Fig. 4.29 summarizes the interstory drifts calculated by the different analysis methods.

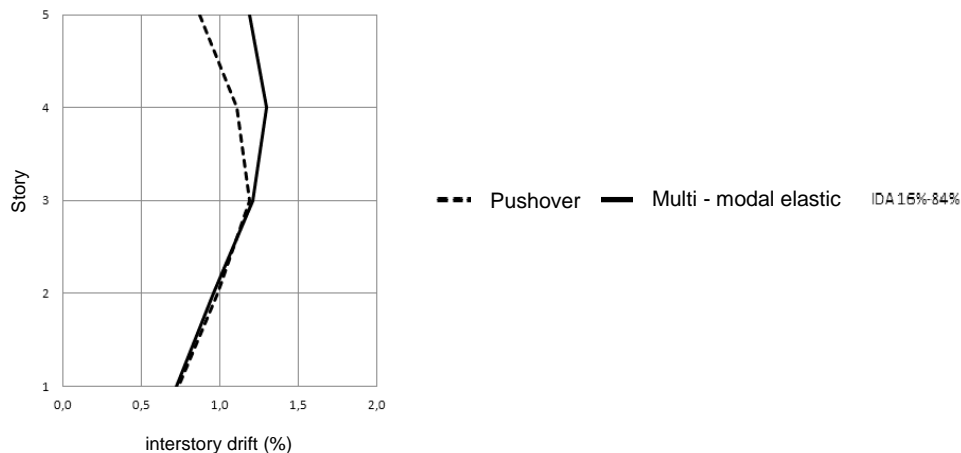


Fig. 4.29: Interstory drifts from linear, pushover (SPO) and IDA analyses

The results of the time history analyses were represented by an area limited between the values that correspond to the 16% and 84% fractiles of IDA. The elastic curve is within the range of the IDA curves while the pushover curve (SPO) is slightly smaller at the two upper stories as it did not account for the influence of higher vibration modes. No soft story mechanism appeared and the interstory drifts did not exceed in neither analysis type the experimental limit value of 1.38% at ULS which indicates the adequacy of the proposed design rules that do not consider test measurement errors or large test data dispersion.

## 4.7 CONCLUSIONS

The above study introduces the innovative lateral force resisting system FUSES pin link and reveals some of the important global performance characteristics of the system, the following observations are worth noting:

- a) The system exhibits a very good behavior under seismic loading: strong, stiff, large capacity of energy absorption. The seismic resistance of a building may be obtained by appropriate provision of a number of systems in the relevant directions.
- b) It may be designed as more flexible/rigid depending on the section types and their distribution between floor levels. The number of stories and supporting weight strongly affects the required sections and geometry.
- c) It consists an architecturally versatile solution for the lateral stability of building structures compared to the braced frames as they can be positioned in small areas of the building and do not interrupt the architectural plan. They can also constitute visible parts of the building indicating its seismic resistant system.
- d) Inelastic deformations are strictly limited to the dissipative pins preventing the spreading of damage into the rest of the structural members. The pins are easily fabricated, installed and removed, if they are damaged after a strong seismic event, since they are small with a simple detail and are not part of the gravity loading resistant system.
- e) Code relevant design rules for the seismic design of frames with FUSEIS pin link, including practical recommendations on the selection of the appropriate fuses and member verifications, have been formulated in a Design Guide. Structural details and constructional measures were also defined.
- f) The damage index of a building with pin fuses may be determined through the fatigue curve proposed in the Design Guide.
- g) The system is able to guarantee an efficient control both on drift and displacement deformations, exhibiting a self-centering behavior allowing for immediate occupancy after earthquake.

Conclusively, it may be noted that the present research, in line with the international trend in seismic engineering, introduces “intelligent” systems that are able to dissipate the seismic input energy and may be easily replaced and repaired, if required. The adoption of FUSEIS pin link systems enhances the well-known advantages of steel under seismic conditions and provides better solutions in terms of economy and safety.

## 4.8 FIELD OF APPLICATION

The innovative fuses may be applied to multi-story steel buildings and substitute the conventional systems used worldwide (such as concentric and eccentric braced frames, moment resisting frames etc.) by combining ductility and architectural transparency with stiffness.

## 4.9 PUBLICATIONS

### Publications in international journals

1. D. Dimakogianni, G. Dougka, I. Vayas, "Innovative seismic-resistant steel frames (FUSEIS 1-2) experimental analysis", *Steel Construction Design and Research*, Volume 5, Issue 4, pp. 212-221, 2012.
2. D. Dimakogianni, G. Dougka, I. Vayas, "Seismic behavior of frames with innovative energy dissipation systems (FUSEIS1-2)", *Engineering Structures*, Volume 90, pp. 83–95, 2015.

## 4.10 BIBLIOGRAPHIC REFERENCES

1. Vayas I. and Thanopoulos P. Innovative Dissipative (INERD) - Pin Connections for Seismic Resistant Braced Frames. *International Journal of Steel Structures* 2005; 5(5):453-464.
2. Vayas I. and Thanopoulos P. Dissipative (INERD) - Verbindungen für Stahltragwerke in Erdbebengebieten. *Stahlbau* 2006; 75(12):993-1003.
3. Vayas I., Thanopoulos P. and Castiglioni C. Stabilitätsverhalten von Stahlgeschossbauten mit dissipativen INERD unter Erdbebenbeanspruchung. *Bauingenieur* 2007; 82(3):125-133.
4. Plumier, A., Doneux, C., Castiglioni, C., Brescianini, J., Crespi, A., Dell'Anna, S., Lazzarotto, L., Calado, L., Ferreira, J., Feligioni, S., Bursi, O., Ferrario, F., Sommariva, M., Vayas, I., Thanopoulos, P. and Demarco, T. (2004). "Two INnovations for Earthquake Resistant Design - The INERD Project, Final Report". Research Programme of the Research Fund for Coal and Steel.
5. Christopoulos, C., Filiatrault, A., Folz, B., and Uang, C-M. Post-Tensioned Energy Dissipating Connections for Moment-Resisting Steel Frames. *ASCE Journal of Structural Engineering* 2002; 128(9):1111-1120.
6. Saeki, E., Iwamatu, K., and Wada, A. Analytical study by finite element method and comparison with experiment results concerning buckling-restrained unbonded braces. *Journal of Structural and Construction Engineering*, Architectural Institute of Japan 1996 ; 484:111- 120.
7. Sabelli, R., Mahin, S., and Chang, C. Seismic demands on steel braced buildings with buckling-restrained braces. *Engineering Structures* 2003; 25(5):665-666.
8. Tsai, K. C., Chen, H.W. and Hong, C., and Su, Y. Design of steel triangular plate energy absorbers for seismic-resistant construction. *Earthquake Spectra* 1993; 9(3):505-528.
9. Dargush, G. and Soong, T. Behavior of metallic plate dampers in seismic passive energy dissipation systems. *Earthquake Spectra* 1995; 11(4):545-568.
10. Tena-Colunga, A. Mathematica modeling of the ADAS energy dissipation device. *Engineering Structures* 1997; 19(10):811-820.
11. Vayas, I., Karydakis, Ph., Dimakogianni, D., Dougka, G., Castiglioni, C. A., Kanyilmaz, A. et al. Dissipative devices for seismic resistant steel frames - The FUSEIS Project, Design Guide. Research Programme of the Research Fund for Coal and Steel 2012.
12. I. Vayas, Ph. Karydakis, D. Dimakogianni, G. Dougka, Castiglioni, C. A., Kanyilmaz, A. et al. Dissipative devices for seismic-resistant steel frames (FUSEIS). Research Fund for Coal and Steel, European Commission; EU 25901 EN 2013.
13. EN1998-1-1, Eurocode 8: Design of structures for earthquake resistance – Part 1-1: General rules, seismic actions and rules for buildings. Brussels: Comitee Europeen de Normalisation (CEN); 2003.
14. ECCS document: Recommended testing procedure for assessing the behavior of structural steel elements under cyclic loads, Technical committee 1: structural safety and loadings, Technical working group 1.3: seismic design; 1986.
15. DIN 50125: Testing of metallic materials - Tensile test pieces; 2009.
16. Abaqus 6.10 online documentation, Simulia, 2010

17. EN1993-1-1, Eurocode 3: Design of steel structures - Part 1-1: General rules and rules for buildings. Brussels: Comité Européen de Normalisation (CEN); 2003.
18. FEMA – 356: Prestandard and Commentary for the seismic rehabilitation of Buildings. Washington; 2000.
19. EN1993-1-9, Eurocode 3: Design of steel structures – Part 1-9: General – Fatigue strength. CEN. 2005
20. SAP2000, CSI, Computers and Structures Inc., [www.csiberkeley.com](http://www.csiberkeley.com).
21. EN1994-1-1: Eurocode 4: Design of composite steel and concrete structures. Part 1-1: General rules and rules for buildings. Brussels: Comité Européen de Normalisation (CEN); 2005.
22. EN 1993-1-8: Eurocode 3: Design of steel structures. Part 1-8: Design of joints. Brussels: Comité Européen de Normalisation (CEN); 2004.
23. FEMA – P695: Quantification of building seismic performance factors, Washington; 2009.
24. Seismomatch v.2.1.0, Seismosoft, [www.seismosoft.com](http://www.seismosoft.com).
25. Vamvatsikos D., Cornell C.A. The incremental dynamic analysis and its application to performance-based earthquake engineering. In: Proc.12th European Conference on Earthquake Engineering; 2002; 479; London.
26. Vamvatsikos D, Cornell CA. Incremental dynamic analysis. Earthquake Engineering and Structural Dynamics 2002; Vol. 31, Issue 3, pp. 491-514.
27. Vayas, I., Dougka, G., Dimakogianni, Umbau und Erweiterung des Kindergartens der Deutschen Schule Athen. Bauingenieur 2014; 6:253-260.
28. Material choice for seismic resistant structures (MATCH). RFSR-CT-2013-00024, 2nd Annual report, 2016

## **5 FUSEIS BOLTED BEAM SPLICES**

### **5.1 INTRODUCTION**

In the frame of the European Research Program RFSR-CT-2008-00032 “Dissipative Beam splices for Seismic Resistant Steel Frames” (Acronym: FUSEIS) two innovative dissipative systems, named FUSEIS1 and FUSEIS2 were introduced and relevant design guides developed. The first type (FUSEIS1) is used as a dissipative “shear wall”, whereas the second type (FUSEIS2) resembles “replaceable plastic hinges” for moment resisting frames. Depending on the type of connection, FUSEIS2 is further divided in two systems: FUSEIS bolted or welded beam splices. Current report presents the results of the investigations on the seismic performance of FUSEIS bolted beam splices, introduces the design procedures for steel and composite buildings, in which the system is used as seismic resistant system, and proceeds to the design of case studies.

### **5.2 DESCRIPTION OF THE FUSEIS BOLTED BEAM SPLICES**

The FUSEIS bolted beam splices are a kind of seismic fuses for steel and composite steel-concrete moment resisting frames that provide good seismic performance and easiness of the repair work. They consist in a cross-sectional weakening located at the beam ends at a certain distance from the beam-to-column connections, avoiding in this way potential brittle failures at the welds. It acts as dissipative seismic fuses, force the plastic hinge to develop at the fuse through concentration of inelastic behaviour, preventing the spreading of damage into the beams and columns concentrating all the damage efficiently and are easily replaceable, so that repair work after an earthquake is limited to replacing the fuses by new ones, thus ensuring low-cost and very quick repair work. Having a simple detail and calculation procedure make them easy to manufacture.

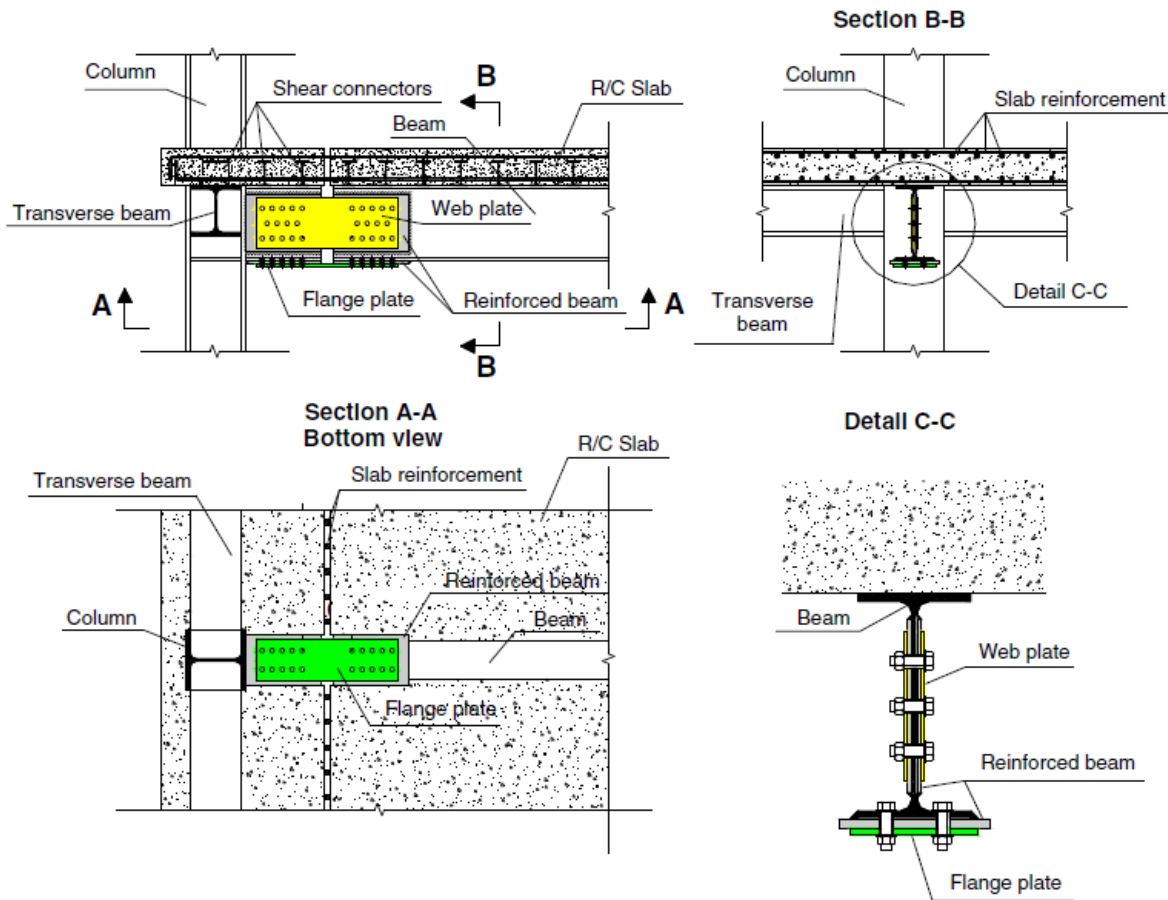


Fig. 5.1: FUSEIS main section elements

FUSEIS bolted beam splice achieves seismic resistance performance by introducing a discontinuity on the composite beams of a moment resisting frame and assembling the two parts of the beam through steel plates bolted to the web and flange of the beam. The connections between the steel plates and the beams are obtained by means of high strength friction grip (HSFG) bolts. These bolts are tightened according to the provisions given in EN 14399-2:2005 [1]. The part of the beam near the connection is reinforced with additional steel plates welded to both web and flange of the beam. In order to obtain an adequate over-strength and hence concentrates all the damage to the fuse, the part of the column near to the connection is also reinforced. There are no strict design indications for these reinforcement plates, but the tested specimens were fitted with reinforcement plates with cross sectional areas roughly equivalent to those of the corresponding parts of the steel profile (web or flange). The duplication of the web and flange areas prevents the deformation that might otherwise develop at the holes, simplifying the repair procedures and limiting slippage at the corresponding bolts. Fig. 5.1 shows the configuration of the fuse on a typical beam-to-column connection.

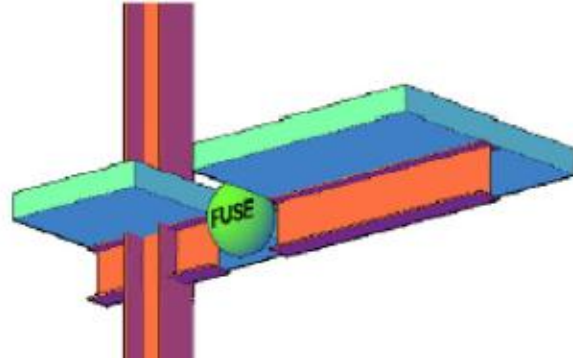


Fig. 5.2: Fuse in a moment resisting frame

To avoid cracking of the concrete in the fuse section due to flexural deformation, a gap is left in the concrete slab in the section of the fuse. The steel reinforcement is not interrupted in the gap section. The scope of this gap is to allow concentrated rotational deformation to occur in the gap section, avoiding both crushing of the concrete as well as damage to the floor finishes (like tiles, or other). For this reason, the gap is conceived to exist anywhere there is a need to accommodate concentrated rotational deformation according to the global deformed shape of the building under seismic action, provided that diaphragm action is ensured.

Additional steel reinforcement is positioned in the area of the gap in order to guarantee elastic behavior of the steel beam as well as that center of rotation remains between the two steel layers. This additional top and bottom steel reinforcement also ensures the diaphragm action to take place in real structures. Length of the additional reinforcement bars is such that adhesive bond with concrete is fully developed. Thanks to this arrangement, the steel plates in the fuse devices can be easily deformed and buckled, causing energy dissipation without damaging the whole structure. At the same time the reinforced concrete slab does not get a significant damage even under large inter-story drifts.

### 5.3 EXPERIMENTAL INVESTIGATIONS

#### 5.3.1 *Experimental investigations on individual dissipative beam splices*

Experimental tests were conducted on three different sub-assemblies of a beam-to-column of connection to the structural engineering laboratory of the Instituto Superior Tecnico of the University of Lisbon.

##### 5.3.1.1 *Test setup and specimen geometry*

The basic test assembly consisted of a typical beam-to-column sub-assembly, comprising a composite beam with an IPE300 profile supporting a 150 mm thick and 1450 mm wide reinforced concrete slab, with a HEB240 profile column.

The gap width in the reinforced concrete part of the fuse could be different from that of the steel parts of the fuse. The recommended values for the gap width in the reinforced concrete (slab) and in the steel parts are, respectively, 20% of the height

of the slab and 10% of the total height of the composite cross-section. Non-linear behaviour is expected to concentrate in the fuse plates only, which can be easily replaced by unbolting of the damaged plates and bolting the new ones.

The difference between the test specimens is the free buckling length  $L_0$  measured between the innermost bolt rows of the fuses. Within this length both flange and web plates are unrestrained and therefore, are free to buckle. The following three different values of  $L_0$  were chosen for each sub-assembly: 140, 170 and 200 mm. These fuses differed in terms of the geometric parameters of the flange plates, while the web plates designed to withstand shear forces should have the same dimensions in all tests. Therefore, the only cross-section dimensions that changed between tests, were the thickness ( $t_f$ ) and width ( $b_f$ ) of the flange plate. Each test was performed until complete failure of the fuse flange plate, after which the fuse plates were replaced by new ones and another test had been carried out. The testing order was as follows: first plates D, A, B, and C, followed by a repetition of this set of plates, performed in the same order. Table 5.1 illustrates the dimensions of the flange plates of the fuse specimens. The monotonic tests were conducted after the conclusion of the cyclic tests.

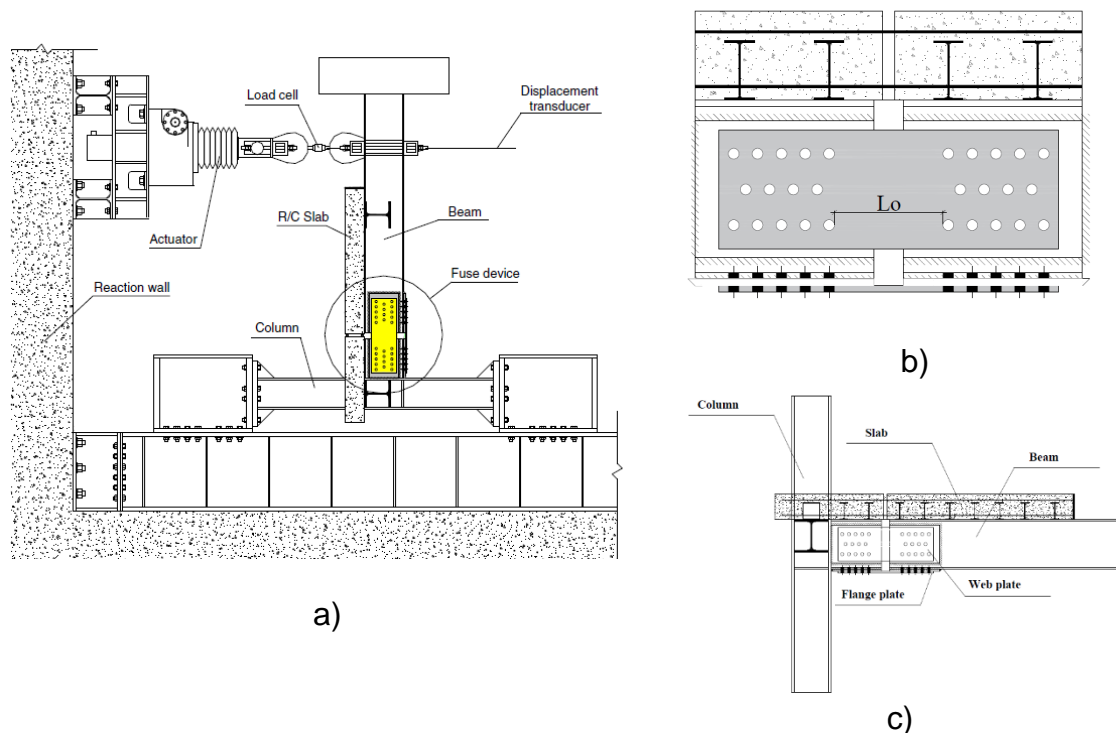


Fig. 5.3: Experimental test set-up a) experimental test overview b) free buckling length c) positioning of the bolted beam splice



**Table 5.1: Dimensions of the flange plates of the fuse specimens (in mm)**

Flange Plate	A	B	C	D
$t_f$	10	10	12	8
$b_f$	120	170	150	140

### 5.3.1.2 Results of monotonic tests

The monotonic behaviour can be compared with the cyclic behaviour in Fig. 5.4. Both diagrams are very similar in terms of the initial stiffness and yield moments. The monotonic diagram seems to adjust well to the cyclic diagram, for the same rotation range, closely resembling the cyclic envelope curve. The differences in terms of the deformation capacity shown by the monotonic tests, can be attributed to damage accumulation due to low cycle fatigue effects. This aspect is more marked in the case of the hogging tests, because the hogging monotonic test was conducted after the sagging one, stiffness at the end of each cycle, which imposed high ductility demands to the specimen, resulting in increased deterioration of the concrete slab.

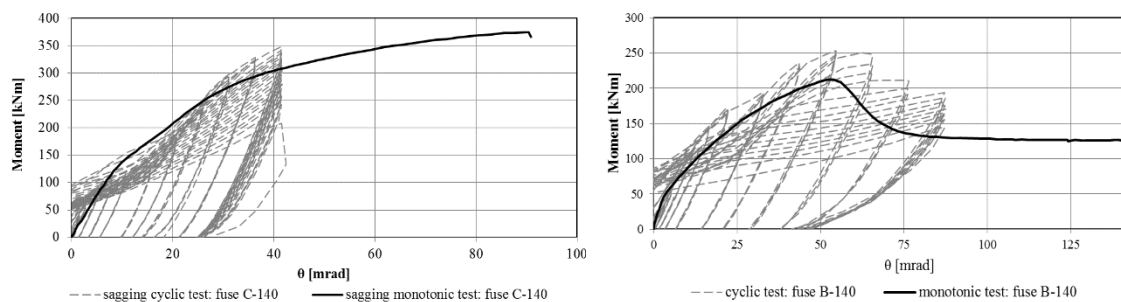


Fig. 5.4: Comparison between monotonic and cyclic tests conducted on fuse C-140 and B-140 in both, sagging and hogging respectively

### 5.3.1.3 Results of cyclic tests

The analysis of the results is based on Moment-Rotation diagrams of the fuse ( $M-\theta$ ). As shown in Fig. 5.5 the hysteretic behaviour of the fuses is stable, characterized by a marked pinching phenomenon, due to the slippage of the bolts and the buckling of the fuse plates.

Asymmetry of the diagram in terms of moments, is due to the strength loss caused by buckling of the fuse plates when subject to hogging bending moment. Nevertheless, deformation capacity is achieved because all specimens are able to perform  $\pm 41$  mrad rotations, which is higher than the minimum value recommended by EC8 (35 mrad for DCH structures).

Comparing the moment-rotation diagrams between two tests of the same fuse specimen shows slightly deterioration in terms of strength and energy dissipation. This could be one of the consequences of the damage accumulation on the parts of the test that are not replaced between tests, such as that due to cracking on the concrete slab.

Fuses with same buckling length but having different area Fig. 5.6 shows an higher moment capacity, consequently widely spread hysteresis cycle for the Fuse C compare to Fuse D that have an area  $1800 \text{ mm}^2$  and  $1120 \text{ mm}^2$ , respectively.

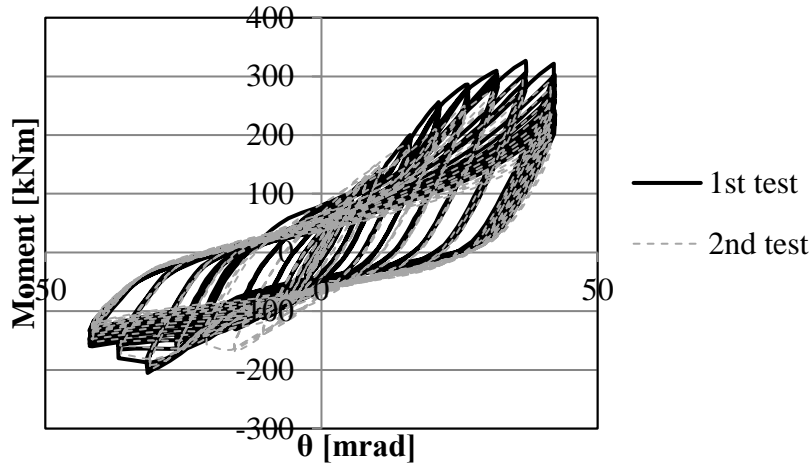


Fig. 5.5: Moment -rotation ( $M - \theta$ ) diagram of fuse C

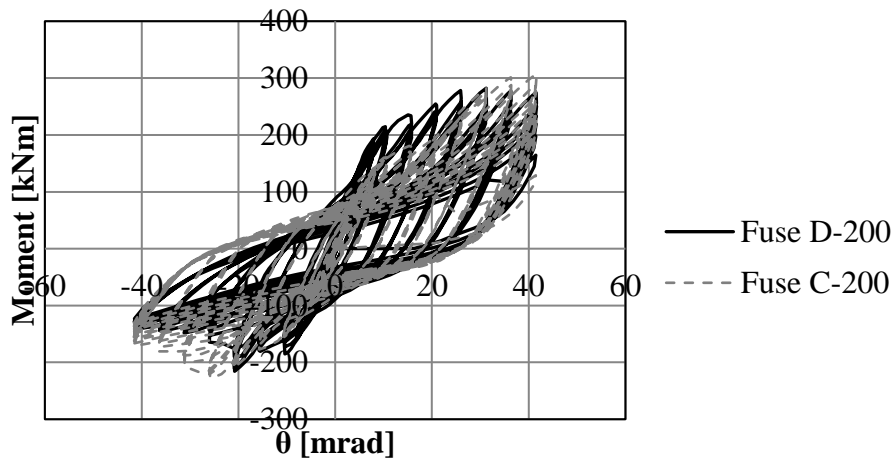


Fig. 5.6: Comparison in terms of moment -rotation ( $M-\theta$ ) of fuse C and fuse D

### 5.3.2 Experimental investigations on overall frames with dissipative beam splices

#### 5.3.2.1 Test setup and specimen geometry

The frame specimens consist of four HEB240 steel columns, two IPE300 steel beams, and a 150-mm thick reinforced concrete slab (see Fig. 5.7). The slab is supported by IPE160 secondary-transverse beams placed every 1.4 m, in addition to a pair of transverse beams that are placed at each beam-column connection. Full shear connection is provided between the slab and the steel beam by means of IPE100 sections welded on top of the beam flange, acting as shear studs. The design of the composite slab is made according to Eurocode 4. High strength friction grip (HSFG) bolts are used in order to connect the steel plates to the beams in the fuse parts. The bolts are tightened according to the provisions given in BS EN 14399-2:2005. Longitudinal reinforcements (designed according to the provision of

EC 8, Annex J) consist of B450C  $\varnothing 20/100$  bars on the upper level, and  $\varnothing 16/200 + \varnothing 12/200$  bars on the lower level. The transverse reinforcements consist of  $\varnothing 12/72$  bars near the fuse section and  $\varnothing 10/72$  bars in the rest of the slab.

It is evident that the seismic response of a frame with FUSEIS bolted beam splice depends mainly on the stiffness and strength of the flange plate. Therefore, in order to achieve a controlled yielding of the plate and improve the behaviour of the frame under cyclic loading, design should try to achieve a sequential yielding of the fuses. During the full-scale tests, the web plate and the free buckling length of the flange plate were left constant while changing only the thickness ( $t_f$ ) and width ( $b_f$ ) of the flange plate.

The frame, hence, is subjected to four cyclic (quasi static according to ECCS) loadings which are displacement-controlled (pushover tests) with velocity of 21 mm/min are implemented. The tests are considered satisfactory when a drift causing at least a 35 mrad rotation in the bolted beam splices will be obtained without significant inelastic deformation on the structural elements as well as on the reinforced concrete slab.



Fig. 5.7: Overall frame test layout

#### 5.3.2.2 Test results

Eight cyclic tests are implemented on the steel-composite frame with four different fuses. Each test is performed until complete failure of the fuse flange plate occurs, whichever fails first. The fuse elements had to be designed weaker than the adjacent members in order to force the positioning of the plastic hinge, to remain within the fuse and to avoid that damage spreads to the non-dissipative zones. In order to do so, the just previously described testing parameter  $\alpha$  was introduced, which relates the resistance capacity of the fuse with the plastic resistance of the cross-section of the composite beam.

Measurements of relative rotations and displacements in the vicinity of beam-to-column connection showed that the columns and beams remained elastic with no

evidence of plastic deformation or local buckling. The beam-to-column connections, which have larger moment capacity than the fuse parts, remained almost perfectly rigid. At the end of each test, the damage plates were dispatched instantly then a new plate was installed (the time required to replace one bolted beam splice was approximately 30 min).

The deformations in the steel reinforcement did not go beyond the elastic range, as expected. Maximum relative displacement between the slab and the beam was 0.5 mm, which means the composite action between the reinforced concrete slab and the steel beam had satisfactorily achieved. Since the rotation center (plastic neutral axis) is quite above (between the two layers of the steel reinforcement of the slab), all the deformation is concentrated in the plates of the bolted beam splices. Both rotations and moments are computed at the mid-section of the fuse. The maximum rotation observed in the bolted beam splices is 40 mrad and after all the tests implemented, there was not any significant damage in the concrete slab (see Fig. 5.9). Considering the fact that Eurocode 8 provisions require the connections to have a rotation capacity of the plastic hinge zone of at least 35 mrad (achieved with a strength degradation less than 20%) for the structures of high ductility class (DCH), and 25 mrad for the structures of medium ductility class (DCM), it can be concluded that the bolted beam splices performed well reaching plastic rotations larger than 35 mrad without significant reduction in strength and stiffness. The displaced shape of the frame can be observed in Fig. 5.8.

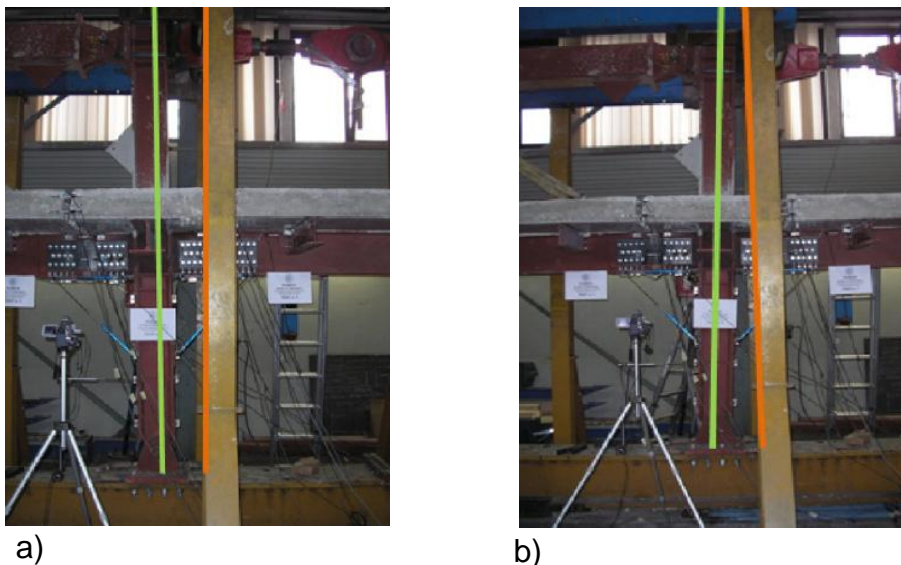


Fig. 5.8: Frame displacement under loading in the a) -X and b) +X direction

The overall behaviour of the bolted beam splices is summarized by means of moment rotation diagrams. The hysteretic behaviour of the fuses is stable and characterized by a pinching phenomenon, due to the slippage of the bolts and to the buckling of the fuse plates when they are under hogging rotations. The fuse

elements deform beyond their yield limit and contribute to the energy dissipation in the frame.

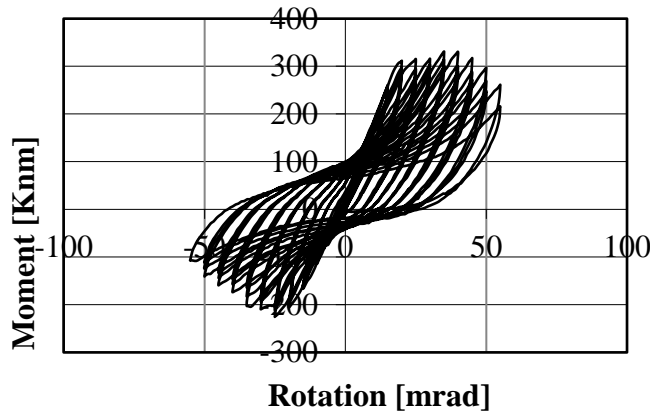


Fig. 5.9: An example of moment rotation ( $M-\theta$ ) diagram (Plate D).

The loss of resistance in hogging bending that can be seen on the negative side of the moment rotation diagrams is caused by the buckling of the lower plate connected to the flange. The max. Plastic capacity achieved by the fuse elements was up to 335 kNm during sagging and up to 260 kNm during hogging of the element. The area under the hysteresis loops represents the energy dissipated in the fuse system during horizontal cyclic loading. Maximum displacement achieved without any significant damage to the structure and the composite slab was 55 mm at the top joint of the frame which means an inter-storey drift of 1.9%.

#### 5.3.2.3 Comparison between experimental and analytical models

The bolted beam splice behaviour is studied by means of two different numerical approaches. In order to have a better understanding of the connection response and to allow for the development of a simple engineering model, first a refined finite element modelling technique is used (by adopting the software package ABAQUS) in which the computational effort is very expensive, when it is necessary to demonstrate that the whole plasticization occurs in the fuses only (see Fig. 5.10). Then, a simple engineering model is developed with the commercial software SAP2000. In order to do so, multilinear plastic pivot hysteresis has been defined to model the moment-rotation capacity of the fuse.

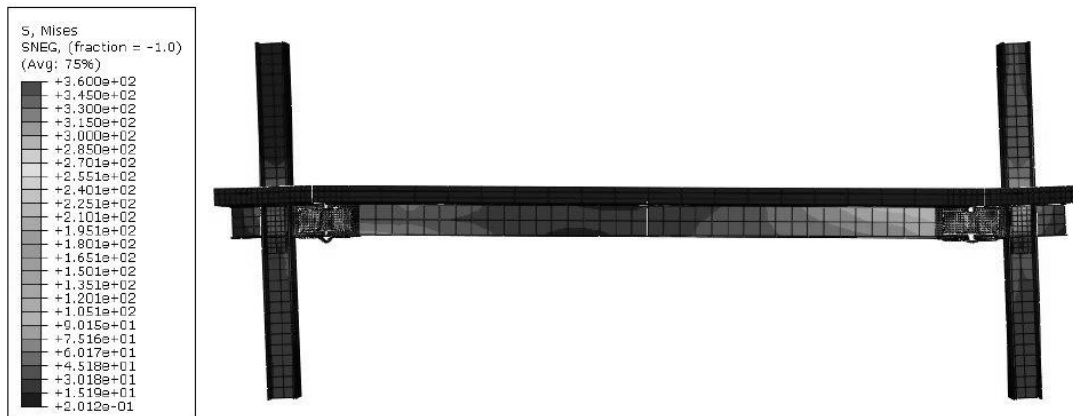


Fig. 5.10: Von Misses stress of the deformed shape

In this case, the fuse cross section behaviour obtained from the analytical model based on the stress-strain relationship of the materials are given as a moment rotation diagram input along with the pivot model parameters that are calibrated with the component tests. Then the results of the analyses are compared with the experimental results of the frame in terms of global force displacement behaviour. The model consists of a simple beam and link with the same geometry used in the experimental test set-up. Fig. 5.11 shows the comparison between the experimental and analytical investigations based on moment-rotation diagram for plate D as an example.

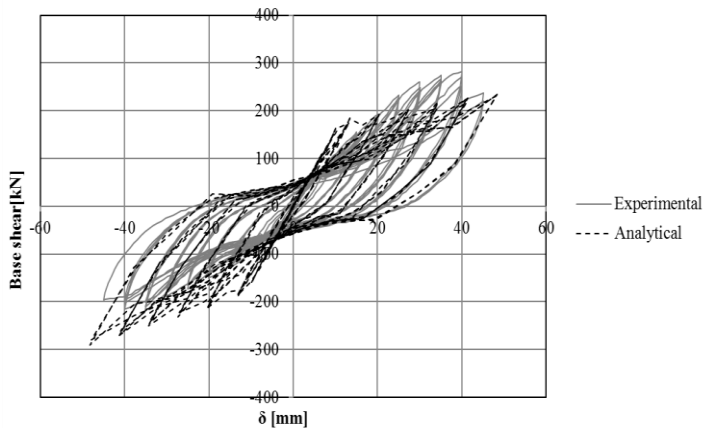


Fig. 5.11: An example of moment-rotation diagram (Plate D)

#### 5.3.2.4 Low cycle fatigue

The trend of the resistance ratio with cycling seems to be very similar in all specimens for both directions, presenting a relatively small hardening, with maximum values close to unity for all specimens. The maximum strength is achieved earlier in every case in the test at hogging than at sagging, since the strength in hogging is always lower due to buckling phenomena. In fact, most of the fuses present strength degradation at sagging only after the 30th cycle, whereas the degradation at hogging starts between the 20th and the 30th cycles. The strength loss occurs due to the instability of the fuse plates, which precipitates to the early

strength degradation at hogging, due to low cycle fatigue effects which comprise the opening and closing of cracks on the steel parts.

The total amount of dissipated energy  $W$  was computed for each test and its variation with respect to the value of the capacity ratio is shown in Fig. 5.12. Since the cyclic buckling along with the low cycle fatigue effects seem to have a fundamental influence on the energy dissipation capacity of the specimens, hogging capacity ratio  $\alpha$ - was chosen.

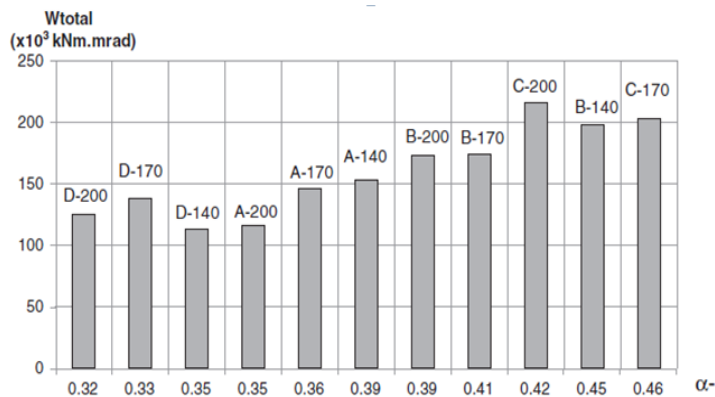


Fig. 5.12: Amount of dissipated energy vs.  $\alpha$ -

However, low cycle fatigue effects associated to buckling at maximum amplitude are more severe for the fuse with lower hogging resistance, which is the one with lower  $\alpha$ - (fuse D-200). Therefore, fuse C-200 withstood more cycles (42 cycles) and, consequently, dissipated more energy than fuse D-200, which withstood only 36 cycles. The number of cycles withstood by each specimen is presented in Table 5.2.

**Table 5.2 Number of cycles to failure**

Specimen	Nr.of cycles	Specimen	Nr.of cycles
A-140	35	D-170	36
B-140	38	A-200	36
D-140	31	B-200	43
A-170	38	C-200	42
B-170	40	D-200	36
C-170	40		

The evolution of the energy dissipation along the cycles may also provide an idea of the progression of accumulated damage during the tests. To study this aspect, the dimensionless parameter  $\eta/\eta_0$  was computed, where  $\eta$  is an energy ratio at the end of each cycle and  $\eta_0$  is the same energy ratio at the end of the first plastic cycle. According to ECCS, the energy ratio  $\eta_0$  at the end of a cycle  $i$  is given by Eq. 5.1



$$\eta_i = \frac{W_i}{\Delta M_y (\Delta \theta_i - \Delta \theta_y)} \quad \text{Eq. (5.1)}$$

Where  $W_i$  is the energy dissipated in cycle  $i$ ,  $\Delta M_y$  is the range of the yield moments,  $\Delta \theta_i$  is the range of the imposed rotations at cycle  $i$  and  $\Delta \theta_y$  is the range of the yield rotations. In practice, this parameter is the ratio between the energy dissipated by the fuse and the energy that would be dissipated by the equivalent fuse with an elastic-perfectly plastic behaviour (EP).

#### 5.4 ANALYTICAL MODELS

Experimental investigations showed that the bending resistance of the bolted beam splices can be evaluated by defining the value of the capacity ratio  $\alpha$  of the fuse. In general, the results showed that fuses with higher values of capacity ratios ( $\alpha$ ) provide higher performance levels in terms of stiffness, resistance, ductility and dissipated energy. Nevertheless, fuses with values of  $\alpha$  close to unity and, therefore, whose strength is like that of the composite beam, induce more damage in the unreplaceable parts and thus fail to concentrate plasticity within the fuse section. Hence the optimal values of this parameter in order to obtain the best performance of the bolted beam splice in terms of capacity and energy dissipation,  $\alpha$  values should be assumed as:

$$\begin{aligned} 0,60 \leq \alpha^+ &\leq 0,75 \\ 0,30 \leq \alpha^- &\leq 0,50 \end{aligned} \quad \text{Eq. (5.2)}$$

$\alpha$  can be evaluated by the following equation

$$\alpha = \frac{M_{Rd,fuse}}{M_{pl,Rd,beam}} \quad \text{Eq. (5.3)}$$

Where

$M_{pl,Rd,beam}$  is the resistant values of the pre-designed composite beams

$M_{Rd,fuse}$  is the resistant moment of the bolted beam splice

The maximum moment resistance of the composite beams  $M_{pl,Rd,beam}$  is the value of maximum bending in hogging and sagging.

Note that, in order to reduce the crushing of the slab and hence concentrate all the damages in the bolted beam splices, the plastic neutral axis as shown in Fig. 5.13 must be located between the two layers of rebars in the slab.

Since the fuse plates may buckle at hogging rotations, the bending behaviour of the fuses is asymmetric in most of the cases. During earthquake both case can occur and the global behaviour is governed by the lower resistance. Therefore, there is a need for computing both sagging and hogging resistant moments of the fuse,  $M_{Rd,fuse}^+$  and  $M_{Rd,fuse}^-$ , respectively.



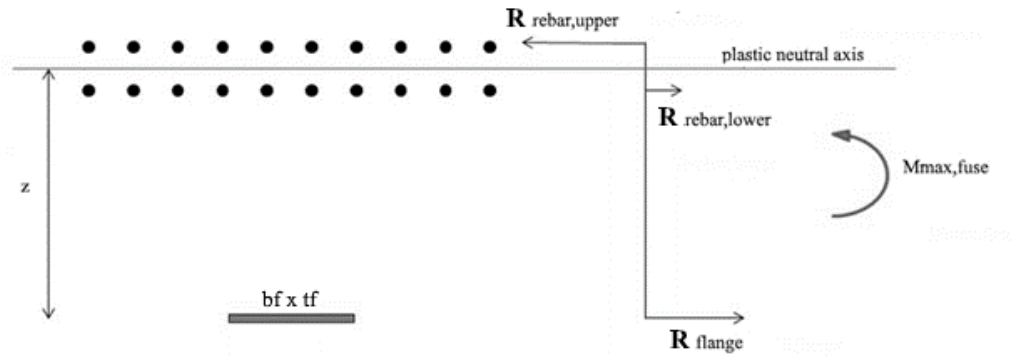


Fig. 5.13: Fiber layout

The buckling behaviour of the fuse plates may be controlled by the geometric slenderness which is function of the free buckling length  $L_0$  and thickness of the flange plate  $t_f$  by the Eq. 5.4.

$$\lambda = \frac{L_0}{t_f} \quad \text{Eq. (5.4)}$$

Where  $L_0$  based on the buckling mechanism of the FUSEIS (see Fig. 5.14) can be calculated by the Eq. 5.5.

$$L_0 = \frac{2\sqrt{2} M_p}{A f_y \sqrt{\varepsilon}} \quad \text{Eq. (5.5)}$$

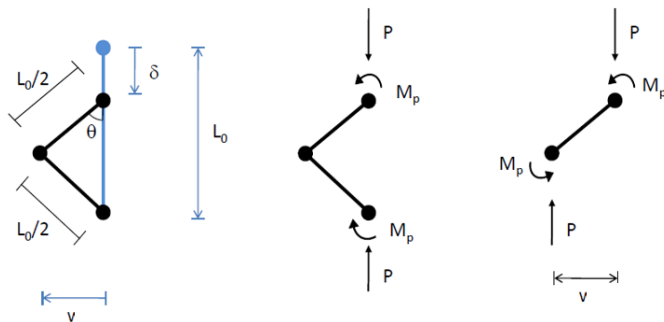


Fig. 5.14: Buckling mechanism of the FUSEIS bolted beam slice based on experimental results



Fig. 5.15: Failure mechanism during experimental tests

The axial load acting on flange plate can be calculated as:

$$P = \frac{M_p}{v} \quad \text{Eq. (5.6)}$$

Where  $M_p$  is plastic moment of the rectangular cross-section of the plate which can be calculated by equation.

$$M_p = \frac{b_f * t_f^2}{4} * f_y \quad \text{Eq. (5.7)}$$

For small displacements:

$$v = \sqrt{\frac{\delta * L_0}{2}} \quad \text{Eq. (5.8)}$$

$$\delta = L_0 * (1 - \cos \theta) \quad \text{Eq. (5.9)}$$

## 5.5 DESIGN RULES

Based on the experimental and analytical research carried out during the FUSEIS project Design Rules were developed giving all necessary information for conceptual design. The design of a building with FUSEIS bolted beam splices should be in compliance with the requirements of the relevant EN, in particular with EN1993-1-8 [2].

Since the damage and energy dissipation may only occur due to inelastic behaviour of the replaceable parts i.e. FUSEIS beam splices, irreplaceable parts i.e. beams and columns must be elastically designed to ensure that they remain undamaged when the bolted beam splice achieves its resistant capacity. On the other hand, beams must be locally reinforced at the “interface” with the fuse, to reduce any sort of damage which might develop at the holes. The local reinforcement of the beam may consist of an additional steel plate welded to both sides of the web and lower

flange for the same length of the fuses cover plates. The bending resistance of the bolted beam splices can be evaluated by defining the value of the capacity ratio  $\alpha$  of the fuse.

#### 5.5.1 Design for linear elastic analysis

In the building design process, the cross-sections of the relevant structural elements should be first pre-designed for the same building but without fuses, considering the relevant limit states. The bolted beam splices then should be included at the all beam ends that belong to the MRF system.

##### 5.5.1.1 Bending Resistance of the Fuse

Since the fuse plates may buckle at hogging rotations, the bending behaviour of the fuses is asymmetric in most of the cases. During earthquake both case can occur and the global behaviour is governed by the lower resistance. Therefore, there is a need for computing both sagging and hogging resistant moments of the fuse,  $M_{Rd,fuse}^+$  and  $M_{Rd,fuse}^-$ , respectively. The buckling behaviour of the fuse plates may be controlled by the geometric slenderness, given in Eq. 4.2. By assuming a plastic distribution of forces for bending-shear interactions, the contribution of the web plates of the fuse to the bending resistance should be neglected. The bending resistance of the bolted beam splice should be obtained through an elastic-plastic analysis considering an adequate value for  $\alpha$ .

##### 5.5.1.2 Design of Flange plate

The dimensions of the flange plate of the bolted beam splices control the resistant bending moment of the cross-section of the fuse and is therefore dependent on the value of the capacity ratio of the device. If the plastic neutral axis is coincident with the centre of gravity of the longitudinal reinforcement the area of the flange plate may be estimated in pre-design by the expression:

$$A_{f,fuse} = \frac{M_{Rd,fuse}^+}{f_{yd} z} \quad \text{Eq. (5.10)}$$

Where  $M_{Rd,fuse}^+$  is the sagging resistant moment of the bolted beam splice,  $f_{yd}$  is design yield strength of the structural steel according to EN1993-1-1 and  $z$  is the distance between the flange plate and the center of gravity of the rebar layers (see Fig. 5.13). The hogging resistance of the fuse  $M_{Rd,fuse}^-$  should be obtained through an elastic-plastic analysis on the cross section with a modified constitutive relationship for the flange plate  $\sigma_{mod,b}(\varepsilon)$ , given by:

$$\sigma_{mod,b}(\varepsilon) = \min\{\sigma(\varepsilon); \sigma_b(\varepsilon)\} \quad \text{Eq. (5.11)}$$

Where  $\sigma_t(\varepsilon)$  is the stress-strain relationship obtained through experimental tensile tests or according to the Annex C.6 of EN1993-1-5 and  $\sigma_b(\varepsilon)$  is the buckling stress-strain relationship given by:

$$\sigma_b(\varepsilon) = \frac{f_{yd}}{\lambda_f \sqrt{2\varepsilon}} \quad \text{Eq. (5.12)}$$

Where  $\lambda_f$  is the geometric slenderness of the flange plate.

### 5.5.2 Design for nonlinear analysis

#### 5.5.2.1 Moment-rotation diagram definition

Hysteretic behaviour of bolted beam splice should be defined as Moment–Rotation diagram used as an input data to define the nonlinear behaviour. Contribution of the web plates should be neglected. Hence, the general hysteretic behaviour of the bolted beam splice can be defined as in Fig. 5.16.

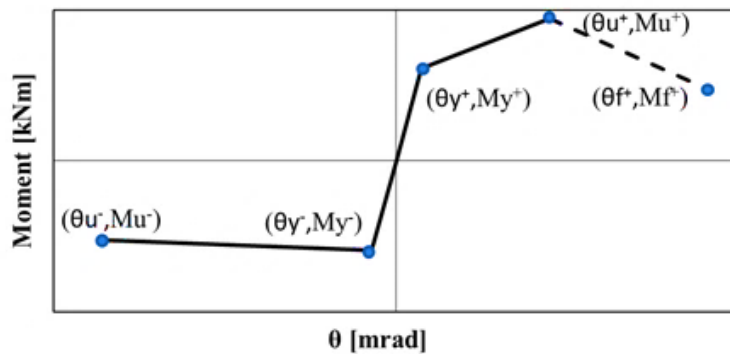


Fig. 5.16: Moment-rotation diagram of the typical bolted beam splice

#### 5.5.2.1.1 Sagging moment

In order to define sagging moment of the bolted beam splice the following assumption should be taken into account:

- Cross section remains plane
- The fuse is in its elastic behaviour

Fig. 5.17 indicates the schematic view of the sagging moment of the flange plate of the bolted beam splice.

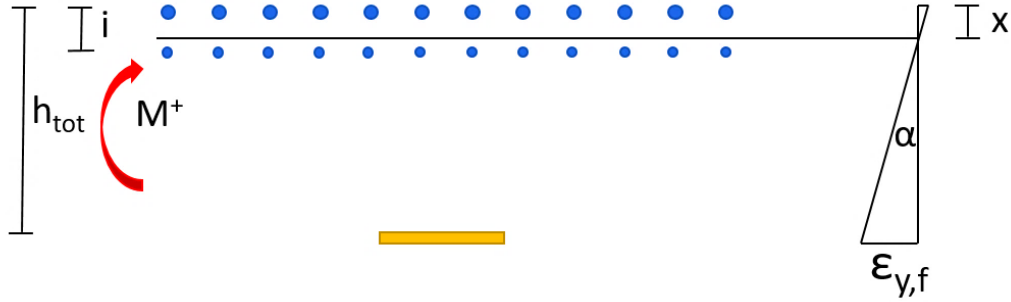


Fig. 5.17: Schematic view of the sagging moment of the flange plate of the bolted beam splice

$$M_y^+ = f_{y,fuse} A_f (h_{tot} - x) + f_{y,fuse} A_s \frac{x^2}{h_{tot} - x} + f_{y,fuse} A's \frac{(x - i)^2}{h_{tot} - x} \quad \text{Eq. (5.13)}$$

$$\theta y^+ = \arctan \left( \frac{\epsilon y_f L_0 + \Delta}{h_{tot} - x} \right) \quad \text{Eq. (5.14)}$$

$$x = \frac{h_{tot} A_f + i A's}{A_f + A_s + A's} \quad \text{Eq. (5.15)}$$

Where

- $L_0$  Is the free buckling length
- $\Delta$  Is the clearance between hole and bolt
- $i$  Is the distance between two layers of reinforcement
- $t_f$  Is the thickness of flange plate
- $b_f$  Is the width of flange plate
- $h_{tot}$  Is the distance between the upper rebar-centre of the flange plate
- $gap$  Is the gap of concrete slab
- $A_s$  Is the area of upper rebar
- $A's$  Is the area of lower rebar
- $A_f$  Is the area of flange plate

$$N = 0 = f_y A_f - A_s \sigma_s + A's \sigma's \quad \text{Eq. (5.16)}$$

$$M = M_y = f_y A_f (h_{tot} - x) - A_s \sigma_s x + A's \sigma's (i - x) \quad \text{Eq. (5.17)}$$

$$\alpha = \epsilon_{y,f} / (h_{tot} - x) \quad \text{Eq. (5.18)}$$

$$\sigma_s = \epsilon_s E_s = \alpha x E_s \quad \text{Eq. (5.19)}$$

$$\sigma's = \epsilon's E's = \alpha (i - x) E_s \quad \text{Eq. (5.20)}$$

$$\epsilon_s, \epsilon's < \epsilon_y \quad \text{Eq. (5.21)}$$

Ultimate moment-rotation of the flange plate can be calculated by the following formula.

$$M_u^+ = f_{u,fuse} A_f h_{tot} \quad \text{Eq. (5.22)}$$

$$\theta_u^+ = 6\theta_y \quad \text{Eq. (5.23)}$$

The ultimate rotation ( $\theta_u^+$ ) is determined from calibration of experimental results and analytic investigations.

Failure point can be obtained when the maximum tensile stress of the flange plate achieved.

$$M_f^+ = 0.8 M_u^+ \quad \text{Eq. (5.24)}$$

$$\theta_f^+ = 2 \theta_u \quad \text{Eq. (5.25)}$$

This rotation value has been theoretically assumed, therefore it should be validated by experimental results.

#### 5.5.2.1.2 Hogging moment

Hogging moment of the flange plate which is subjected to compression load inducing buckling (see Fig. 5.14) can be achieved as an intersection of elastic stability and plastic mechanism. Fig. 5.18 indicates plastic mechanism and elastic stability overview. Where plastic mechanism can be calculated by Eq. 5.29 and Eq. 5.30 respectively.

$$N = N_{pl} * M_{pl} / (M_{pl} + N_{pl} * v) \quad \text{Eq. (5.26)}$$

$$v = \frac{1}{\left(1 - N/N_{cr}\right)} * v_0 \quad \text{Eq. (5.27)}$$

Where

$$v_0 = L_0 / 1000 \quad \text{Eq. (5.28)}$$

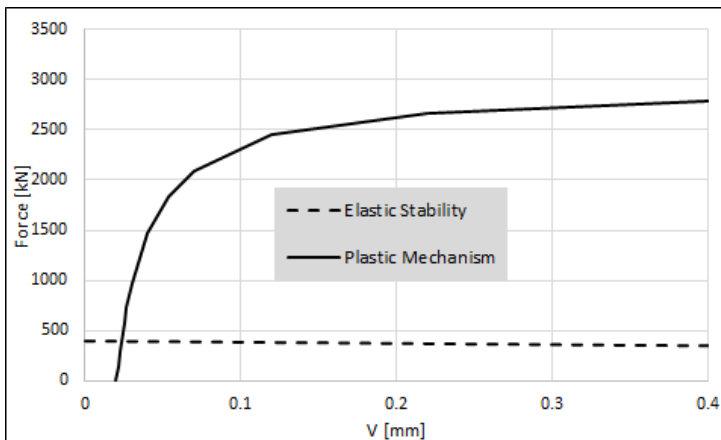


Fig. 5.18: Plastic mechanism and elastic stability overview

Finally, hogging moment-rotation can be calculated by the following equations:

$$M_y^- = N_{buckling} (h_{tot} - \frac{i}{2}) \quad \text{Eq. (5.29)}$$

$$\theta_y^- = M_y^- * \frac{1}{K_y^+} \quad \text{Eq. (5.30)}$$

Where

$$K_y^+ = \frac{M_y^+}{\theta_y^+} \quad \text{Eq. (5.31)}$$

Ultimate point can be obtained as follow:

$$\theta_u^- = 12 \theta_y^- \quad \text{Eq. (5.32)}$$

The ultimate rotation ( $\theta_u^-$ ) is determined from calibration of experimental results and analytic investigations.

By the intersection of the two curves (Fig. 5.18) it can be obtained  $v_{buckling}$  which multiplied by a factor equal to 12 gives the transversal displacement of the flange plate associated to failure ( $v_{lim}$ ). Substituting this value in Eq. 5.32 the compression force  $N_{lim}$  at failure of plate is provided. Finally, ultimate hogging moment results:

$$M_u^- = M_y^- (N_{lim}/N_{buckling}) \quad \text{Eq. (5.33)}$$

#### 5.5.2.2 Longitudinal Reinforcement

The longitudinal reinforcement should be computed to remain elastic when the maximum resistant moment is developed by the fuse. In order to avoid yielding of the rebar, their area has to be computed so that the plastic neutral axis lies between the upper and lower rebar layers of the slab. It is recommended to provide the upper rebar layer with the double of the area of the lower layer. One should notice that only the rebar that are located within the effective width of the concrete flange of the composite beams at the sections adjacent to the fuse should be accounted for the bending resistance. The effective widths should be computed according to EN1993-1-8 (7.6.3) and EN1994-1-1 (5.4.1.2). The position of the plastic neutral axis should be obtained by an elastic-plastic analysis of the cross section with the material properties obtained experimentally or as defined in annex C.6 of EN1993-1-5. The non-yield condition should be verified by imposing the plastic curvature  $\chi_p$  to the cross-section of the bolted beam splice at sagging, assuming that the ultimate strain of the structural steel  $\varepsilon_u$  is developed at the flange plate. The plastic curvature is given by  $\theta_p = L_0 \chi_p$ , where  $\theta_p$  is the plastic rotation. The verification consists in performing an elastic-plastic analysis and checking that the strains on both rebar layers  $\varepsilon_s$  are lower than the yield strain of the material  $\varepsilon_{sy}$  according to EN1993-1-1.

Finally, the total upper and lower area of the rebar can be determined from the following equation.

$$A_{upper\ rebar} = 5 A_{flange\ plate} \frac{f_{yd}}{f_{sd}} \quad \text{Eq. (5.34)}$$

$$A_{lower\ rebar} = \frac{A_{upper\ rebar}}{2} \quad \text{Eq. (5.35)}$$

### 5.5.2.3 Design of the bolted beam splices for Shear

The web plates should be considered alone for the shear resistance of the fuse. The resistance of the web plates should be computed according to EN1993-1-1 (6.2.6), considering a shear area  $A_v$  equal to the area of the cross-section of the web plates. Special attention should be given to the verification of shear buckling, as specified in EN1993-1-5 (5). Shear deformability may be neglected for common spans in buildings. Hence, the minimum area of the web plate of the fuse can be determined by the following equation:

$$A_w = \frac{V_{Ed} \sqrt{3}}{f_{yd}} \quad \text{Eq. (5.36)}$$

Where  $V_{Ed}$  is the total shear force

$$V_{Ed} = V_{Ed,M} + V_{Ed,G} \quad \text{Eq. (5.37)}$$

$V_{Ed,M}$  is the shear force due to moment resistance of the fuse

$$V_{Ed,M} = \frac{M_{fuse,Rd}^+ - M_{fuse,Rd}^-}{d} \quad \text{Eq. (5.38)}$$

$V_{Ed,G}$  is the shear force due to gravity loads,  $d$  is the distance between the fuses. Verification of shear buckling can be examined by the following equation:

$$\frac{h_w}{t_w} < \frac{72}{\eta} \sqrt{\frac{235}{f_{yd}}} \quad \text{Eq. (5.39)}$$

Where  $\eta$  is a parameter that may be assumed to be equal to 1.2 steel grades up to and including S460. For higher steel grades  $\eta = 1.00$  is recommended

### 5.5.2.4 Design of the Bolted Connection

The bolts that connect the fuse plates to the beam should be designed to remain elastic when the fuse reaches its maximum moment. Despite being replaceable parts, irrecoverable deformations on the bolts could compromise the unbolting



process when trying to replace the fuse plate and so, these should remain elastic and be treated as non-dissipative elements. The following expression should be satisfied for non-dissipative bolted connections:

$$F_{v,Rd} > \frac{F_{Sd}}{n} \quad \text{Eq. (5.40)}$$

Where  $F_{v,Rd}$  is the shear resistance per shear plane, according to EN1993-1-8 [2] (see Table 5.3) computed with the yield strength of the bolts  $f_{yd}$ ,  $F_{Sd}$  is the design force of the non-dissipative connections,  $n$  is the number of bolts used to transmit the shear forces. The bolts should be pre-loaded and designed to behave as type B shear connections according to of EN1993-1-8 [2] (3.4 and 3.9). In case of high-strength structural bolting for preloading the connection must satisfy rules included in EN 14399 [1].

**Table 5.3: Yield and Ultimate strength of the bolts**

Bolts class	4.6	4.8	5.6	5.8	6.8	8.8	10.9
$f_{yb} [\text{N/mm}^2]$	240	320	300	400	480	640	900
$f_{ub} [\text{N/mm}^2]$	400	400	500	500	600	800	1000

The bolts should be checked under shear action according to EN1993-1-8 [2].

$$F_{v,Rd} = n \frac{k f_{tb} A_{res}}{\gamma_{M2}} \geq F_{v,Sd} \quad \text{Eq. (5.41)}$$

Where  $n$  is the number of face connected,  $\gamma_{M2}$  assume to be equal to 1.25 and  $A_{res}$  is the gross area reduced for the presence of the hole in the section perpendicular to the acting force.  $k$  is 0.5 for bolts classes of 4.8, 5.8, 6.8 and 10.9 and 0.6 for bolts classes of 4.6, 5.6, and 8.8.

#### 5.5.2.5 Additional Detailing Remarks

The detailing rules which are not mentioned in this guide should be considered in the provisions of the relevant EN. In particular, special attention should be given to the provisions of EN1998-1 [3] regarding the detailing of the concrete slab of the composite beam. The transverse reinforcement of the beam flange of the composite beam should be computed according to the provisions of EN1994-1-1 [4] and EN1998-1 [3]. In particular, they should be designed taking into account the shear resistance of the shear connectors and the axial forces on the concrete flange and on the steel profile, according to the design procedures of EN1994-1-1[4] (6.6.6).

### 5.5.3 Design for non - linear static analysis

The structural model used for elastic analysis shall be extended to include the response of structural elements beyond the elastic state and estimate expected plastic mechanisms and the distribution of damage.

Lumped plasticity modelling approach may be employed for the non-linear models of the frames. Nonlinear material property should be concentrated at the ends/mid-span of the frame elements by using particular features provided by the software for this scope (i.e. link and hinge property). Beam and column elements shall be modelled as frame elements and non-linearity can be concentrated in the plastic hinges at their ends/mid-span. To characterize the non-linear behaviour of the plastic hinge, the generalized force–deformation properties suggested in FEMA 356 [5] can be implemented. The plastic hinge property of the columns considers the interaction between axial force and bending moment. The multi-linear plastic pivot model can be used as a hysteresis rule for the fuses. The values of the parameters used for the hysteretic model should be defined after designing the fuse dimension and properties. Fig. 5.19 shows the simulation model and positioning of different elements type.

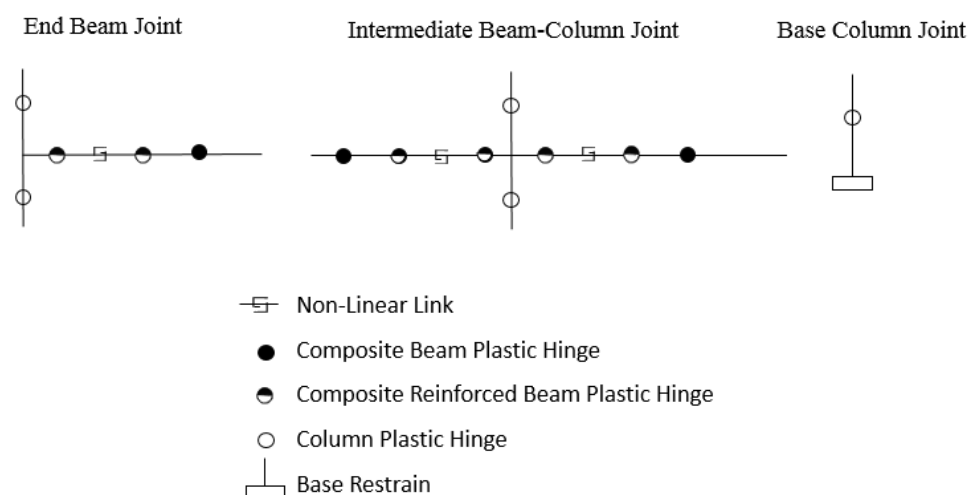


Fig. 5.19: Summary of lumped plasticity modelling-approach

At least two vertical distributions of the lateral loads should be applied:

- “Uniform” Load pattern, based on lateral forces that are proportional to mass regardless of elevation (uniform response acceleration);
- “First Mode” Load pattern, proportional to lateral forces consistent with the lateral force distribution in the direction under consideration determined in elastic analysis.

### 5.5.4 Design procedure summary

To design a building equipped with FUSEIS bolted beam splices, different steps should be carried out.

First of all, conventional building without dissipative elements should be pre-designed and verified according to EC2, EC4 and EC8. At the end of this step, the cross sections of the steel columns and the composite steel-concrete beams are selected. Using a response spectrum reduced to the elastic one by behaviour factor assumed (in first iteration) according to EC8, seismic response spectrum analysis (RSA) on the building is performed and the bending moment  $M_{Ed}$  at the ends of the beams are identified. These values are taken as reference for the performance required to the dissipative beam splices in terms of moment resistance ( $M_{Ed} \approx M_{y, fuse}$ ). In fact, in the building subjected to the design seismic actions (ULS), the exploitation of the post-elastic resources of the dissipative and reparable joints is to be guaranteed. It is worth noting that the distribution of the bending moment associated to seismic actions is not uniform along the different floors, resulting that the beams of lower stories are more stressed than the ones of the upper levels. This observation leads to assume several reference resistance thresholds for the beam splices in multi-storey buildings. Therefore, the final layout of the structure should be characterized by increasing the beam splice dimensions for lower beam levels in order to activate a global collapse mechanism and avoid the onset of brittle soft-storey mechanisms.

By Eq. 5.1 it is possible to calculate the area of the flange plates related to each moment resistance required. Fixing the width of the flange plate equal or comparable with the flange width of the designed steel beam, the thickness of the FUSEIS flange plate can be obtained. Consequently, the free buckling length of the beam splices can be calculated according to Eq. 4.4. The value of free buckling length obtained for the fuses of the lowest storey should be adopted for all different beam splices along the whole height of the structure. The total longitudinal rebar quantity  $A_{sl, total}$  of the concrete slabs is achieved by Eq. 5.25.

After defining the geometrical properties of the joints, the non-linear moment-rotation diagram of each beam splice configuration can be derived.

At this point, response spectrum analysis is to be performed using, in correspondence of the beam splices, linear elastic springs with stiffness defined according to the initial branch of the moment-rotation diagram.

All verifications (damage limitations, second order effects, column stability checks, etc.) are carried out according to EC8. If they are not successful, previous steps are repeated in iterative way starting from a new definition of performance level required to the dissipative beam splice in terms of moment resistance and/or elastic stiffness. Once all checks are successful, non-linear static analysis is to be run in order to evaluate the non-linear behaviour of the dissipative elements, verify the onset of a diffuse plasticization of the beam splices in the whole building and validate the behaviour factor initially assumed.

## 5.6 ANALYSES AND DESIGN OF 2D FRAMES

In order to investigate the behaviour of composite steel-concrete frames using dissipative bolted beam splices (FUSEIS) and examine the contribution of these fuse to the energy dissipation, three buildings with different height will be examined in this session. All buildings have composite steel concrete slab and secondary beams which transfer the loads to the main frames, where the innovative bolted beam splices are employed.

### 5.6.1 Case studies

Three archetype configurations which are vertically regular and square-plan, have been selected. They are considered as general office (class-B) buildings and they are designed according to EN1993-1 [6] /EN1998-1 [3] and to the specific design guideline of the dissipative system. The case studies comprise three configurations as follows:

- 2 storeys, low-rise buildings
- 4 storeys, mid-rise buildings
- 8 storeys, high -rise buildings

#### 5.6.1.1 Geometry and general assumptions

A common plan view has been selected for all buildings. The number of bays in both direction is 3 with a span length of 8 m. The height of each story is 4m. They consist of a steel-concrete composite moment resisting frame in the Y direction and concentrically braced steel frame in the middle span of the X direction. bolted beam splices are included in the structure at the end of the all beams in Y direction, (FUESIS), while the INERD<sup>TM</sup> device are equipped at the end of all steel bracing elements in X direction. The concentric bracing system is located to accommodate the columns around their weak axis bending and the FUSEIS 2-1 are located in the direction along which the column are placed with strong axes bending. Fig. 5.20 and Fig. 5.21 represent the archetype structure and elevation view of examined 2/4/8 storey building.

#### 5.6.1.2 Materials

##### 5.6.1.2.1 Non-dissipative zones

The materials used in the three buildings are given below:

- Structural steel: S355
- Concrete: C25/30
- Steel sheeting: Fe320
- Reinforcing steel: B500C

##### 5.6.1.2.2 Dissipative zones

During the earthquake, it is expected that the dissipative zones yield before other zones i.e., non-dissipative zones, hence, according to EC 1998-1, the yield strength  $f_{y,max}$  of the dissipative zones must be satisfied by the Eq. 5.42.

$$f_{y,max} \leq 1,1\gamma_{ov} f_y \quad \text{Eq. (5.42)}$$

where

$\gamma_{ov}$  is the overstrength factor, the recommended value is 1.25

$f_y$  is the nominal yield strength of the steel

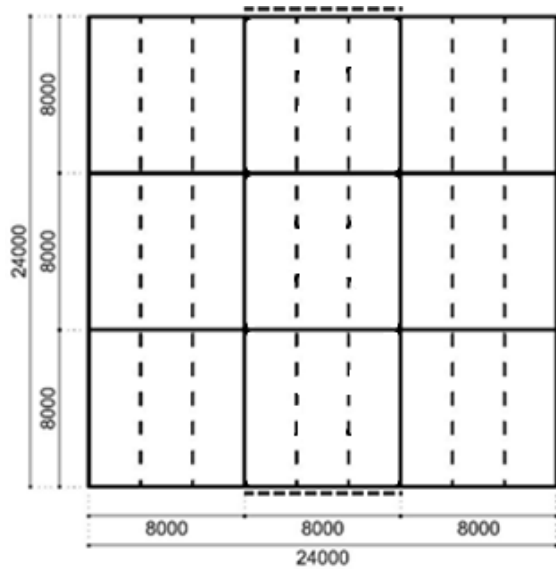


Fig. 5.20: Plan of the 2/4/8-story archetype structures

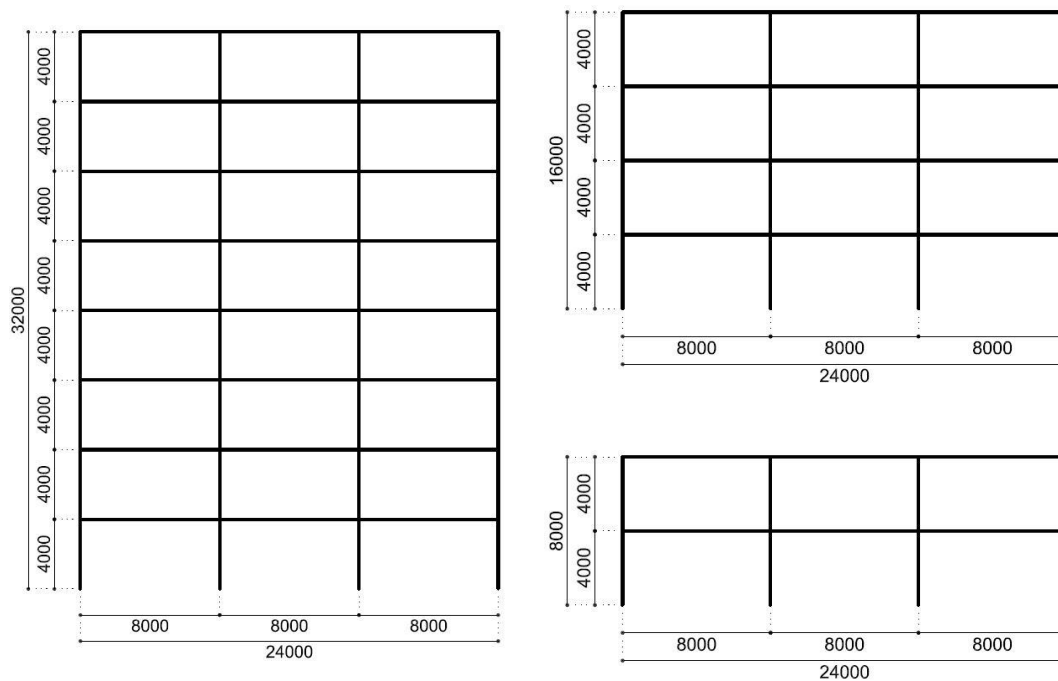


Fig. 5.21: Elevation View of the 2/4/8-Story Archetype Structures

### 5.6.1.3 Loads and load combinations

A summary of the applied loads is given in the following:

- Dead Loads:

2.75 kN/m<sup>2</sup> composite slab + steel sheeting

- Superimposed Loads:

Services, ceiling, raised floor:  $0.70 \text{ kN/m}^2$  for intermediate floors

$1.00 \text{ kN/m}^2$  for top floor

Perimeter walls  $4.00 \text{ kN/m}$

- Live Loads:

Offices (Class B):  $3.00 \text{ kN/m}^2$

Movable partitions  $0.80 \text{ kN/m}^2$

Total live load:  $3.80 \text{ kN/m}^2$

Snow load to be ignored

- Seismic Load:

Importance factor:  $\gamma_I = 1.0$

Peak ground acceleration:  $\alpha_{gR} = 0.20 \cdot g$

Ground Type C – Type 1 spectrum:

$S = 1.15$        $T_B = 0.20 \text{ sec}$        $T_C = 0.60 \text{ sec}$        $T_D = 2.00 \text{ sec}$

Lower bound factor:  $\beta = 0.2$

Vertical ground acceleration to be ignored.

Behaviour factor  $q = 4$

#### 5.6.1.4 Simulation

A building with FUSEIS 2-1 may be simulated with a linear-elastic model by appropriate beam elements. The simulation has done based on The design rules which are intended to ensure that yielding, will take place in the fuse prior to any yielding or failure elsewhere. Therefore, the design of buildings with FUSEIS 2-1 is based on the assumption that the fuses are able to dissipate energy by the formation of plastic bending mechanisms.

The modelling of the buildings were performed by means of the finite element program SAP2000. All beams and columns were simulated as beam elements, while no-section shell elements were used for the distribution of the load's area.

#### 5.6.2 Design of buildings with FUSEIS bolted beam splices

The analysis and design of the buildings, were performed by means of the finite element program SAP2000. The composite slabs were designed by the program SymDeck Designer, which takes into account construction phases both for the ultimate and serviceability limit states. Columns are designed as steel members, with their section varying depending on the floor and the building. The assigned sections are given in detail in Table 5.4, Table 5.5 and Table 5.6.

For all floors and buildings, IPE450 has been chosen for primary composite beams. Secondary beams are composite and simply supported with steel profile HEA200. Construction phases were critical for the design of these beams, so temporary supports need to be placed in order to reduce both bending deformation and section size. Slabs are composite for all floors. They have been designed and checked according to the requirements of Eurocode 4 for all possible situations and no temporary supports are needed during construction phases. Fig. 5.22 shows the

composite slab section. The thickness of the steel sheet is 0.80mm and the longitudinal reinforcement is  $\varnothing 8/100$ . The steel beam is assumed to be connected to the concrete slab with the full shear transfer.

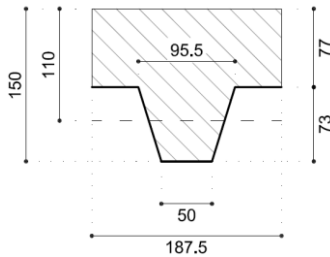


Fig. 5.22: Composite slab section

In order to verify both static and seismic loading combinations for the building without dissipative beam splices, the steel columns profiles adopted are reported in the following tables.

**Table 5.4: Columns section for the 2 storey building**

Floor	Centre	Perimeter
1-2	HEM360	HEB360

**Table 5.5: Columns section for the 4 storey building**

Floor	Centre	Perimeter
1-2	HEM450	HEB450
3-4	HEM360	HEB360

**Table 5.6: Columns section for the 8 storey building**

Floor	Centre	Perimeter
1-2	HEM550	HEB550
3-4	HEM500	HEB500
5-6	HEM450	HEB450
7-8	HEM360	HEB360

As explained in section 5.4, the design procedure to identify the properties of the dissipative beam splices is iterative. Within the design process, two main parameters of the joints govern the verification results: the bending moment resistance and the initial elastic stiffness of the FUSEIS beam splices.

Once it is clear the moment resistance and the stiffness level required to verify the structure, the geometrical properties of beam splices have been finalized.

An example is reported for the definition of beam splice No.1 adopted for the first four storeys of the 8-storey building. Based on Eq. 5.4, the area of flange plate is calculated referring to the hogging moment resistance required (230 kNm).

The level arm  $z$  is calculated from the centre of rotation in the middle of the rebar and the flange plate

$$z = h_a + h_p + \frac{h_c}{2} = 450\text{mm} + 73\text{mm} + \frac{77}{2}\text{mm} = 561.5\text{mm}$$

$$A_{f,fuse} = \frac{M_{Rd,fuse}^-}{f_{yd} z} = \frac{230 \times 10^6 \text{ Nmm}}{\frac{235}{1.15} \frac{\text{N}}{\text{mm}^2} \times 561.5 \text{ mm}} = 2004 \text{ mm}^2$$

Fixing the width of the flange plate equal to 170 mm, slightly lower than the flange width of the steel beam IPE450 (190 mm); the thickness of the plate is obtained.

$$t_{f,fuse} = \frac{2004 \text{ mm}^2}{170 \text{ mm}} = 11.79 \text{ mm}$$

Therefore, a thickness of 12 mm is selected.

**Table 5.7: Dimension of the flange plates and their distribution in height for 8 storey building**

Storey	Beam Splice No.	Dimension (mm)
1-4	1	170x12
5-6	2	170x10
7-8	3	170x8

**Table 5.8: Dimension of the flange plates and their distribution in height for 4 storey building**

Storey	Beam Splice No.	Dimension (mm)
1-2	2	170x10
3-4	3	170x8

**Table 5.9: Dimension of the flange plates and their distribution in height for 2 storey building**

Storey	Beam Splice No.	Dimension (mm)
1-2	3	170x8



The free buckling length is calculated based on Eq. 4.4 for the beam splice No.1 associated to the lower storey.

$$L_0 = \frac{2\sqrt{2} M_p}{A f_y \sqrt{\varepsilon}} = \frac{2\sqrt{2} \times \left(\frac{1}{4}\right) \times 170 \text{ mm} \times 12 \text{ mm}^2 \times 235 \text{ N/mm}^2}{12 \text{ mm} \times 170 \text{ mm} \times 235 \text{ N/mm}^2 \times \sqrt{0.002}} = 189.73 \text{ mm}$$

Therefore, a free buckling length equal to 200 mm is applied for all beam splice joints.

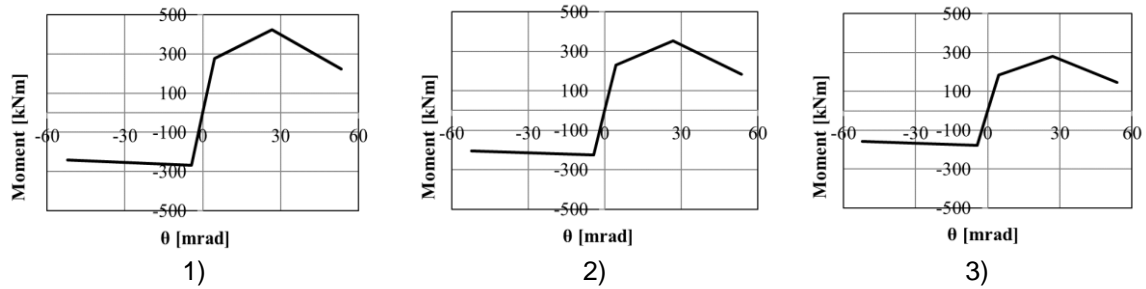


Fig. 5.23: Beam splices hysteresis rule in terms of moment-rotation 1) 170x12mm 2) 170x10mm 3) 170x8mm

Once identified all geometric parameters, using the formula presented in section 5.3.1, the nonlinear moment-rotation behaviour of the designed beam splices is entirely defined.

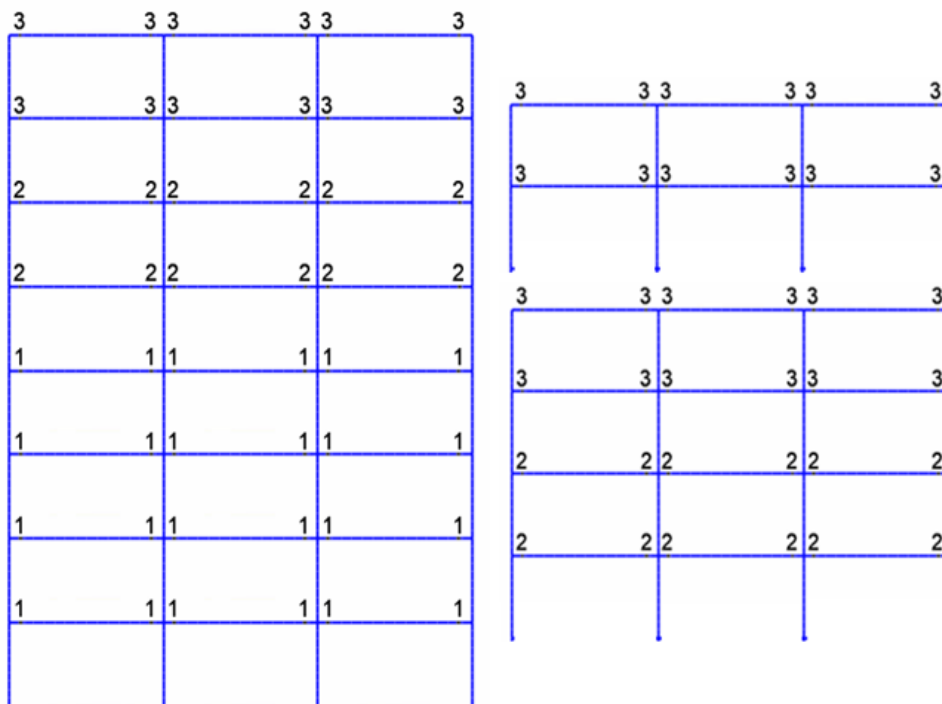


Fig. 5.24: Distribution of assigned bolted beam splices

The main properties are summarized in the following figures.

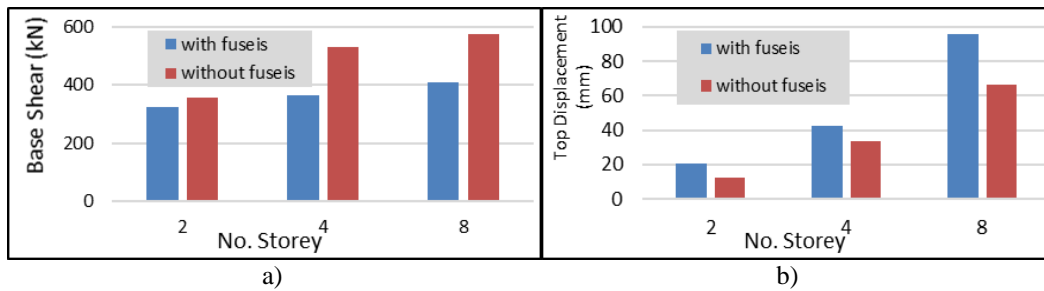


Fig. 5.25: Resistance capacity ratio (a) and elastic stiffness for beam splices 1, 2 and 3 (b)

The web plates of the bolted beam splice are designed to resist shear forces only. According to the capacity design principles, the maximum shear forces that could possibly be developed on the beam ends depend on the resistant capacities of the beams. The minimum required area of the design web plate of the bolted beam splice for shear force according to section 5.5.2.3 result as follows:

Web Plate dimensions = 170 x 6 mm

The design should assure that the rebar remain elastic. In order to optimize the solution, an iterative procedure should be conducted, aiming at obtaining a lower amount of rebar quantity. The following values were estimated. One should notice that only the rebar positioned within the effective width of the slab will account for the bending resistance.

Table 5.10: Area of longitudinal rebar in the beam splices

Beam Splice No.	A, upper rebar (mm <sup>2</sup> )	A, lower rebar (mm <sup>2</sup> )
1	4800	2400
2	4000	2000
3	3200	1600

#### 5.6.2.1 Limitation of interstorey drift

Limitation of inter-storey drift ensures the protection of non-structural elements under seismic loading. It provides an estimation of the damage for different performance levels and defines the distribution of stiffness within the structure and eventually the size and type of the cross sections applied on the system.

Fig. 5.26 shows the inter-storey drift which are limited to the specified criteria in EC8.

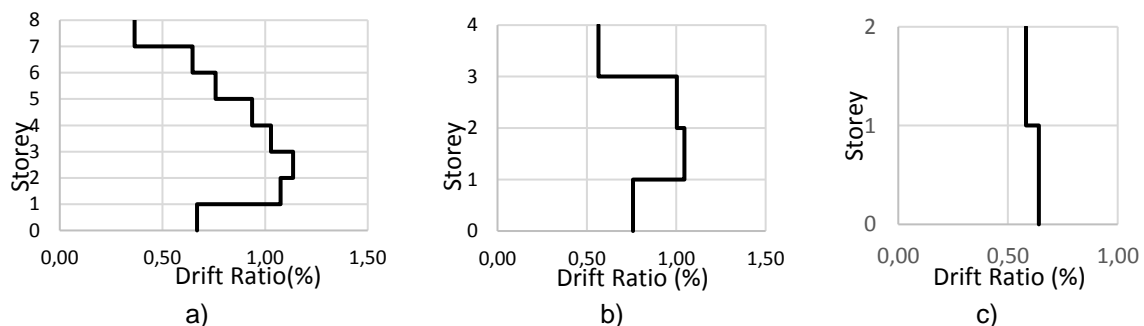


Fig. 5.26: Maximum Interstorey Drift Ratio for Conventional Frames and Buildings Having Beam Splices

### 5.6.2.2 *P-delta effects*

According to EC8 the second order effect can be evaluated by the following equation:

$$\theta = \frac{P_{tot} \cdot d_r}{V_{tot} \cdot h} \quad \text{Eq. (5.43)}$$

Where

$\theta$  is the interstorey drift sensitivity coefficient

$P_{tot}$  is the total gravity load at and above the storey considered in the seismic design situation

$d_r$  is the design interstorey drift, evaluated as the difference of the average lateral displacements  $d_s$  at the top and bottom of the storey under consideration

$V_{tot}$  is the total seismic storey shear

$h$  is the interstorey height

Note that the value of the coefficient  $\theta$  shall not exceed 0,3. Table 5.11, Table 5.12 and Table 5.13 show the calculated drift sensitivity for all examined buildings.

**Table 5.11: Drift sensitivity for 8 storey building**

Floor	Disp (m)	Drift,real (m)	dr/h	Vtot (kN)	Ptot (kN)	$\theta$	Check
1	0.0075	0.030	0.008	346	7205	0.16	< 0.3
2	0.0142	0.057	0.014	336	6294	0.27	< 0.3
3	0.0158	0.063	0.016	316	5383	0.27	< 0.3
4	0.0150	0.060	0.015	287	4473	0.23	< 0.3
5	0.0139	0.056	0.014	248	3564	0.20	< 0.3
6	0.0121	0.048	0.012	199	2653	0.16	< 0.3
7	0.0103	0.041	0.010	139	1742	0.13	< 0.3
8	0.0070	0.028	0.007	71	834	0.08	< 0.3

**Table 5.12: Drift sensitivity for 4 storey building**

Floor	Disp (m)	Drift,real (m)	dr/h	Vtot (kN)	Ptot (kN)	$\theta$	Check
1	0.008298	0.033	0.008	230	3531	0.13	< 0.3
2	0.014198	0.057	0.014	206	2631	0.18	< 0.3
3	0.014495	0.058	0.014	158	1731	0.16	< 0.3
4	0.010212	0.041	0.010	87	829	0.10	< 0.3

**Table 5.13: Drift sensitivity for 2 storey building**

Floor	disp (m)	drift,real (m)	dr/h	Vtot (kN)	Ptot (kN)	$\theta$	Check
1	0.009082	0.036	0.009	152	1722	0.10	< 0.3
2	0.011675	0.047	0.012	117	824	0.08	< 0.3

### 5.6.3 Non - linear static analyses

Pushover analysis is a non-linear static analysis carried out under conditions of constant gravity loads that monotonically increasing horizontal loads which is used to verify or revise the overstrength ratio values ( $\alpha_u/\alpha_1$ ) and to estimate the expected plastic mechanisms and the damage distribution.

Push-over (Nonlinear static analysis) should be performed first in order to provide statistical data on the structure's overstrength " $\Omega$ " as well as ductility time dependent factor " $\mu$ ". This data might be then revised by the further nonlinear analysis.

#### 5.6.3.1 Evaluation of the non-linear behaviour of the frames

Numerical results highlight that the number of plastic hinges and their distribution in height are similar for the different conventional structures. As expected for conventional frames, all the formation of plastic hinges occurred at the beam ends and at the base of the ground columns, based on the design rules of EC8. While plastic deformation concentrates mainly in the beam splices, the main elements remain in the elastic region, which means they are protected from any sort of damages. It has to be noted that the formation of plastic mechanism occurs more or less simultaneously in all floors for frames having beam splices (see Fig. 5.29) ensuring that no soft storey mechanism occur at the structures. Fig. 5.27 shows the pushover curve of the examined buildings having bolted beam splices.

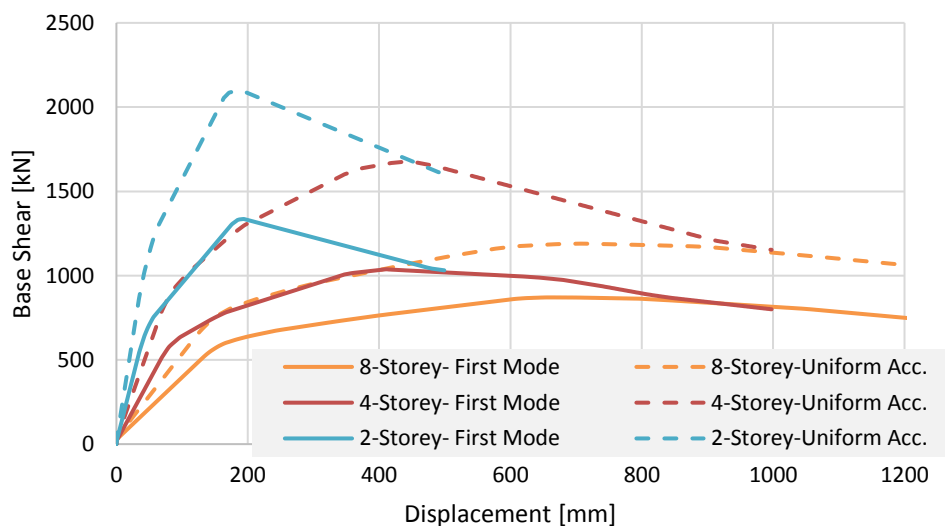


Fig. 5.27: Push-over curve for 2,4 and 8 storey-building

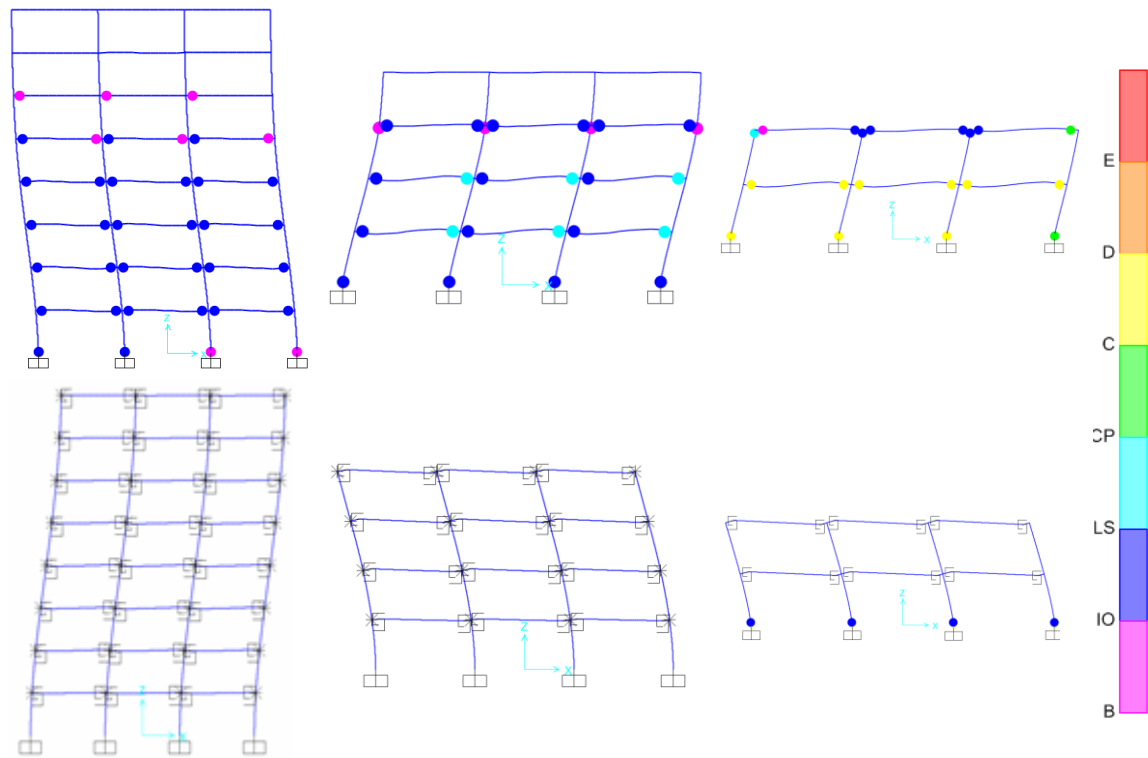


Fig. 5.28: non linear pushover analysis-the formation of plastic hinges at the displacement equal to 60cm ( $\delta = 60\text{cm}$ ), (top) conventional structures (bottom) building with bolted beam splices

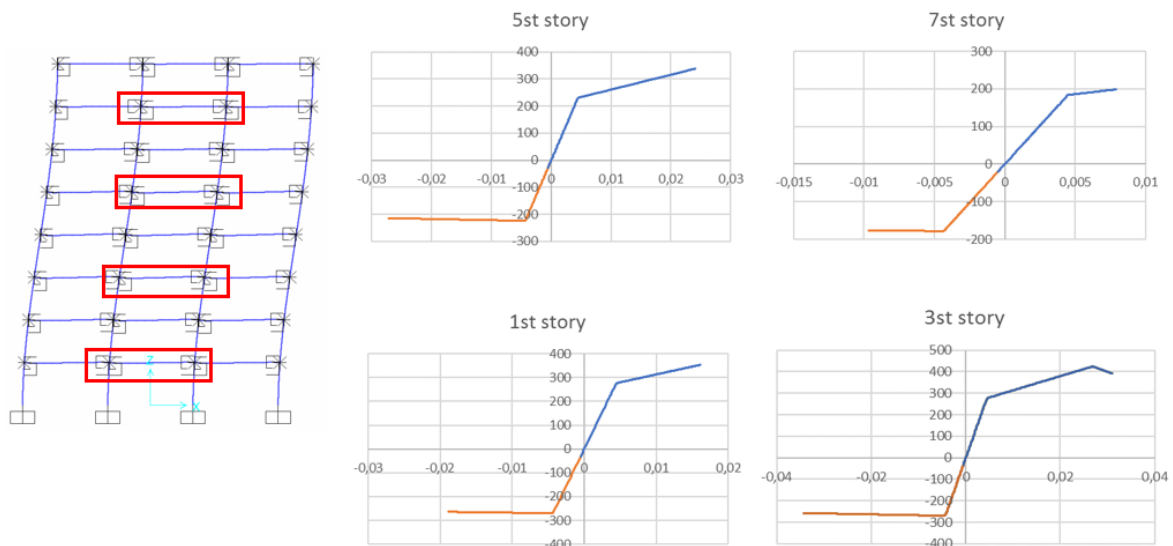


Fig. 5.29: Global plastic mechanism at  $\delta = 60\text{cm}$

### 5.6.3.2 Evaluation of the behaviour factor $q$

A preliminary value of the  $q$ -factor may be established from the analysis, using the classic overstrength ( $\Omega$ ) and ductility behavior factor ( $q$ ) decoupling:  $q_{\text{stat}} = q \cdot \Omega$ . If the estimated  $q_{\text{stat}}$  factor is found to be more than 20% different from the one originally assumed for design for any of the archetypes, redesign may be required.

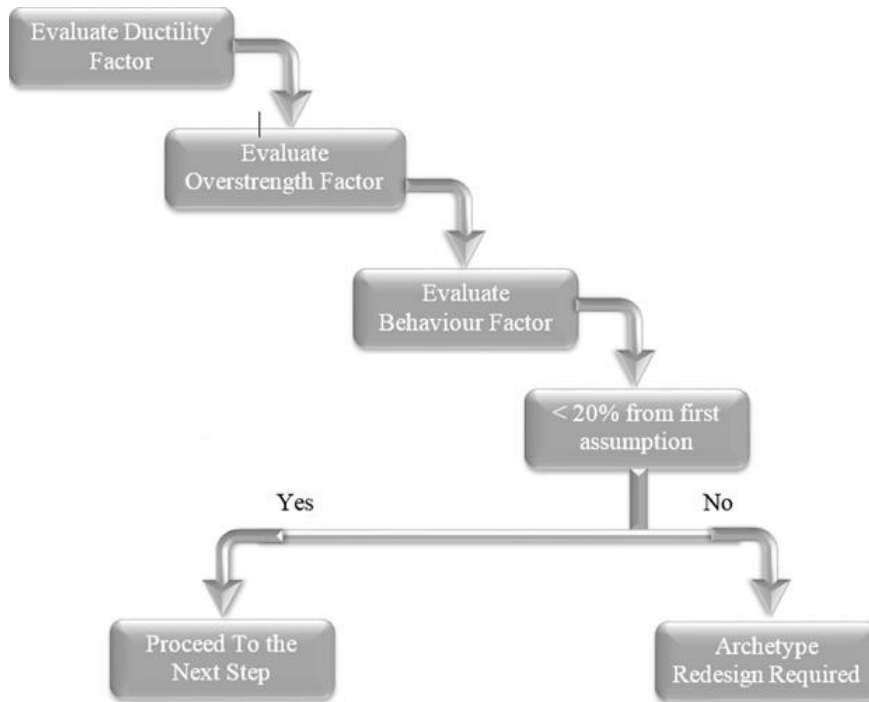


Fig 5.30 Trial behaviour factor evaluation procedure

Behaviour factor is a force reduction factor in which the linear spectra modify to equivalent nonlinear spectra. This behaviour factor, also called reduction factor by some researchers, play an important role in the evaluation of the design forces of the structure. The value of q-factor is directly related to the ductility, redundancy, viscous damping, and the overstrength of the members. These parameters have a great influence on the energy dissipation capacity of the structure.

Behaviour factor can be calculated as the product of the ductility and the overstrength factor by the following equation:

$$q = q_{\Omega} \cdot q_{\mu} \cdot q_{\xi} \quad \text{Eq. (5.44)}$$

Where

$q_{\Omega}$  is an overstrength dependent factor also called strength reduction factor

$q_{\mu}$  is a ductility dependent factor also expressed as a function of displacement ductility

$q_{\xi}$  is the allowable stress factor also called damping reduction factor which theoretically can be defined as a unit factor (by assuming the same damping ratio uses for both elastic and inelastic analysis).

Among several methods available in literature and codes to calculate these factors, one of these options is presented and explained in order to quantify the behaviour factor of the case studies.

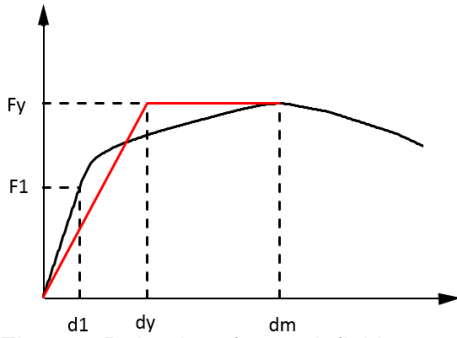


Fig 5.31 Behaviour factor definition

Referring to Fig 5.31, a proper approximation of quantification of the force-reduction factor may be calculated as:

$$q_{\Omega} = \frac{F_y}{F_1} \quad \text{Eq. (5.45)}$$

Where:

$F_y$  is the strength corresponding to the idealized bilinear yield strength which can be assumed as the maximum base shear.

$$F_y = F_m \quad \text{Eq. (5.46)}$$

$F_m$  is the maximum actual strength of the structure

$F_1$  is the strength corresponding to the first significant yield which can be found as where any member of the structure reaches to its plastic zone first.

The ductility reduction factor  $q_{\mu}$  according to Newmark and Hall [7] can be expressed as the system ductility  $\mu$  related to the natural period of vibration  $T$ , proposed by the following equations:

$$\begin{aligned} q_{\mu} &= 1.0 && \text{(for } T < 0.03\text{s)} \\ q_{\mu} &= \sqrt{2\mu - 1} && \text{(for } 0.03\text{s} < T < 0.5\text{s)} \\ q_{\mu} &= \mu && \text{(for } T > 0.5\text{s)} \end{aligned} \quad \text{Eq. (5.47)}$$

System ductility  $\mu$  can be calculated by the following equation:

$$\mu = \frac{d_m}{d_y} \quad \text{Eq. (5.48)}$$

where

$d_m$  is the maximum displacement corresponding to the maximum actual base shear

$d_y$  is the displacement corresponding to the idealized bilinear yield strength

$$d_y = 2(d_m - \frac{E_m}{F_y}) \quad \text{Eq. (5.49)}$$

$E_m$  is the area under the curve up to  $d_m$

**Table 5.14: Behaviour factor calculation for 2,4 and 8 storey buildings**

	8-Storey	4-Storey	2-Storey	
$d_m$ (mm)	660.55	412.35	193.16	
$d_y$ (mm)	329.06	222.68	131.88	
$F_m$ (kN)	870.73	1037.53	1335.92	
$F_y$ (kN)	870.73	1037.53	1335.92	
$F_1$ (kN)	525.59	515.636	549.55	
$d_1$ (mm)	135.15	69.43	35.06	Average
$\mu$	2.01	1.85	1.46	1.77
$\Omega$	1.66	2.01	2.43	2.03
$q$	3.33	3.73	3.56	3.53
			Dispersion	4.3%

Table 5.14 represents the trial behaviour factor calculation for three examined buildings having bolted beam splices. The average calculated behaviour factor is 3.53 with the dispersion of 4.3%. However, it is worth to point that the evaluation of the behaviour factor summarized in Table 5.14 is based only with one method presented in this chapter. Within the INNOSEIS research project, a more consistent evaluation procedure of q-factor is being developed in order to take into account several methods presented in literature and modern seismic codes to quantify a reliable procedure to calculate the final value of the behaviour factor.

## 5.7 FIELD OF APPLICATION

The innovative dissipative fuses may be applied to multi-story composite steel-concrete buildings. An optimized configuration consists of a steel-concrete composite moment resisting frame in the one direction (usually along the column strong axis) and concentric bracings in the other direction (usually along the column weak axis). In this direction, generally the structure is pendular, characterized by simple joints at beam to column connections. FUSEIS bolted beam splices are included in the structure at the end of the all beams in MRF direction.

## 5.8 CONCLUSIONS

The developed bolted fuses proved to be very easy to replace and showed good performance indicators in terms of ductility, stiffness, energy dissipation and resistance. The FUSEIS bolted beam splices successfully protected the majority of the irreplaceable parts, which generally remained in the elastic domain as intended,



which was achieved by concentrating the inelastic behaviour in the fuse plates. These fuses also proved to be easy to manufacture, to assemble and to replace.

The dissipative elements are easily replaceable if they are damaged after a strong seismic event. The assembling and disassembling after test is easy from a practical point of view: the time required for replacing one FUSEIS bolted beam splice is 45 minutes (from POLIMI Full Scale Test experience).

Code relevant design rules for the seismic design of frames with dissipative FUSEIS have been formulated. Practical recommendations on the selection of the appropriate fuses as a function of the most important parameters and member verifications have been formulated. Structural details and constructional measures are defined.

## 5.9 PUBLICATIONS

- [1] L. Calado, J.M. Proença, M. Espinha, C.A. Castiglioni & I. Vayas – Hysteretic behavior of dissipative devices for seismic resistant steel frames (FUSEIS 2). Stessa 2012, January 9-11, 2012, Santiago, Chile.
- [2] C.A. Castiglioni, A. Kanyilmaz, A. Drei, L. Calado, M. Espinha, R.M. Gonçalves, T. Rauert & I. Vayas – Seismic resistant composite steel frames with dissipative devices. Stessa 2012, January 9-11, 2012, Santiago, Chile
- [3] I. Vayas, C.A. Castiglioni, A. Kanyilmaz, A. Drei, L. Calado, T. Rauert, R.M. Gonçalves – Dissipative devices for seismic resistant steel frames. Eurosteel 2011, August 31- September 2, 2011, Budapest, Hungary.
- [4] A. Kanyilmaz, C.A. Castiglioni, A. Drei, I. Vayas, L. Calado, T. Rauert – Nonlinear dynamic response of dissipative devices for seismic resistant steel frames: experimental behaviour and numerical simulation. Compdyn 2011, 26-28 May, Corfu, Greece.

## 5.10 REFERENCES

- [1] E. Commission, BS EN 14399-2 High-strength structural bolting assemblies for preloading Part 2: Suitability for preloading. British Standards, 2005.
- [2] E. Commission, BS EN 1993-1-8: 2005 Design of steel structures — Design of joints. 2005.
- [3] E. Commission, BS EN 1998-1: 2004 Design of structures for earthquake resistance-part 1: general rules, seismic actions and rules for buildings. British Standards, 2004.
- [4] D. ENV, “BS EN 1994-1-1:2004; Eurocode 4: Design of composite steel and concrete structures- Part 1-1: General rules and rules for buildings,” Eur. Stand., 2004.
- [5] FEMA 356, PRESTANDARD AND COMMENTARY FOR THE SEISMIC REHABILITATION OF BUILDINGS. Washington, D.C.: FEMA, 2000.
- [6] C. de Normalización, “EN 1993-1-1: Eurocode 3: Design of Steel Structures. Part 1-1: General Rules and Rules for Buildings,” 2005.
- [7] N. Newmark and W. Hall, “Earthquake spectra and design,” Earth Syst. Dyn., 1982



## 6 FUSEIS WELDED BEAM SPLICES

### 6.1 INTRODUCTION

The seismic resistance of steel buildings is obtained by combining a variety of traditional structural systems such as moment resisting frames, shear walls, concentric and eccentric braced frames. Under severe earthquakes, these systems may suffer significant damage and exhibit large residual drifts, leading to loss of occupancy and high repair costs of the structures.

In recent years, several dissipative connections, systems and devices have been proposed which combine strength, stiffness, and ductility. They are able to restrict plastic deformations in replaceable fuses that not only prevent collapse but also limit structural damage. In addition, some of them are also capable of eliminating residual drifts by exhibiting self-centering properties. In this respect, they allow the structure to be immediately occupied after the earthquake, provided that the damaged fuses are replaced.

Current brochure presents the results of the investigations on the seismic performance of the welded FUSEIS beam splices, introduces the design procedures for steel and composite buildings, in which the splices are used in the seismic resistant systems, and proceeds to an example of design.

The welded FUSEIS beam splices use replaceable web and flange plate fuses to provide energy dissipation. The system consists in the interruption at both ends of the MRFs' composite beams which are then connected through the slab's rebar and the fuse plates. While the plates are designed to mobilize their maximum strength, the rebar are maintained in the elastic regime.

The results of experimental and analytical investigations on individual fuses under monotonic and cyclic loading performed at IST are presented. The tests provided data for the nonlinear parameters of the fuses which are used in 2D nonlinear static and dynamic analysis of representative 3D building frames with welded FUSEIS.

The use of welded FUSEIS beam splices is an economical solution and can be applied in multi-storey steel buildings offering the following advantages:

- (a) inelastic deformations are concentrated in the dissipative fuses;
- (b) they can be easily fabricated, installed and removed, limiting cost and time required to make the building operational after the earthquake.

### 6.2 DESCRIPTION OF THE WELDED FUSEIS BEAM SPLICES

The innovative seismic system of welded FUSEIS beam splices comprises in the interruption at both ends of the MRFs' composite beams which are then connected through the concrete slab's rebar and the web and flange plate fuses (Fig. 6.1). This lateral load resisting system is very similar to the conventional MRFs. However, under strong seismic motion, inelastic deformations are restricted to the web and

flange plate fuses, which will dissipate a large amount of input energy, leaving the rest of the structure elastic and undamaged. Since the damages are restricted to the fuses, the repair works are relatively simple and less expensive comparing to a conventional seismic resistant building.

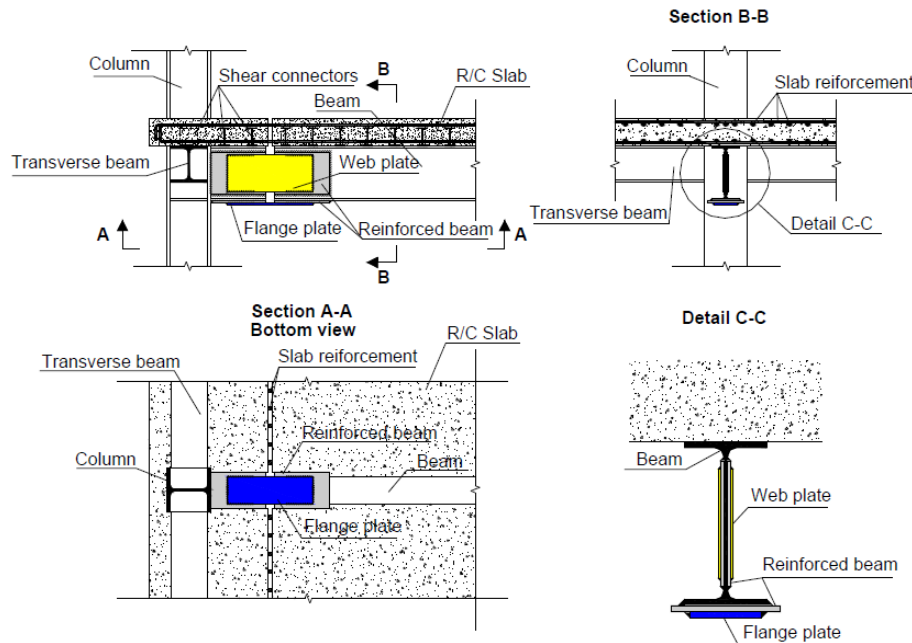


Fig. 6.1: Schematic representation of the welded FUSEIS beam splices

The gap in the slab just over the fuse is intended to avoid major damage to the concrete, by allowing the fuse to develop larger rotations, without concrete-to-concrete contact. The gap width in the reinforced concrete part of the fuse can be different from that of the steel parts of the fuse. The recommended values for the gap width in the reinforced concrete (slab) and in the steel parts are, respectively, 10% of the height of the slab and 10% of the total height of the composite cross-section.

The longitudinal rebar are continuous over the gap, thus ensuring the transmission of stresses. Considering that the rebar are irreplaceable, their yielding is prevented by forcing the plastic neutral axis to lie in between the upper and lower layers. To achieve the mentioned objective, it is recommended that the total area of the upper rebar is more than twice that of the flange plate.

The reinforced beam zone is an area reinforced with additional welded plates, both at the web and the flange of the beam, with the objective to avoid any sort of damage (e.g. spreading of plasticity) at the connection and in the adjacent irreplaceable steel parts of the beam. There are no strict design indications for these reinforcement plates as long as the aforementioned conditions are verified.

The system is versatile with regard to the selection of web and flange plate fuses and offers the designer the possibility to control the plasticization sequence of the welded FUSEIS beam splices. This can be achieved by changing either the sections or the length of the flange plate fuses.

Aiming to avoid excessive overstrength, the steel material of the dissipative fuses shall have controlled properties. In accordance with EN 1998-1-1, their yield strength must have a maximum value of:

$$f_{y,max} \leq 1.1 \cdot \gamma_{ov} \cdot f_y \quad \text{Eq. (6.1)}$$

where  $\gamma_{ov} = 1.25$  is the overstrength factor and  $f_y$  is the nominal value of the yield strength.

The nominal yield strength of the flange fuses shall be low and preferably not exceed 235 MPa. If the properties of the fuses' material are controlled and their maximum yield strength guaranteed below that described by Eq. (6.1), the overstrength factor can be reduced and an even more economical design can be achieved.

### 6.3 EXPERIMENTAL INVESTIGATIONS ON THE WELDED FUSEIS BEAM SPLICES

#### 6.3.1 *Experimental setup, tested devices and loading history*

The experimental test set-up is shown schematically in Fig. 6.2. Apart from the top displacement and force controlling transducers depicted in Fig. 6.2, the tested specimens are instrumented with a series of 21 more displacement transducers, shown in Fig. 6.3, to monitor the rigid body motion at the supports, the rotations and transversal displacements at different positions along the beam length and the beam-to-slab slip.

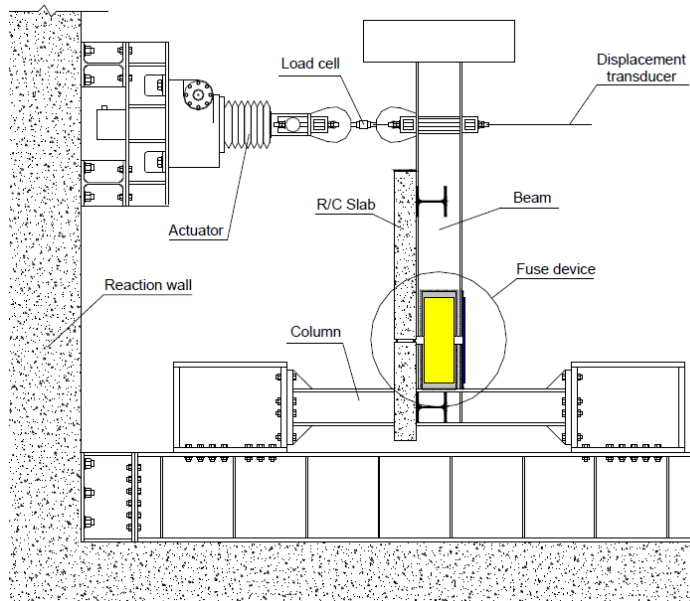


Fig. 6.2: Experimental test set-up

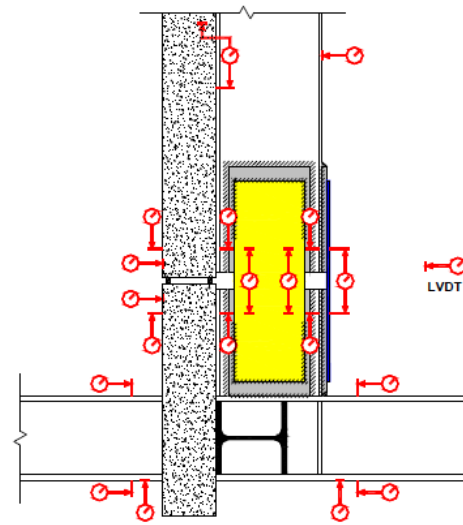


Fig. 6.3: Location of the remaining LVDTs (close-up)

The basic test assembly consists of a typical beam-to-column sub-assembly, comprising a composite beam with an IPE300 profile supporting a 150 mm thick and 1450 mm wide reinforced concrete slab, with a HEB240 profile column. The longitudinal reinforcement of the slab is composed in  $\Phi 20//100$ , top layer, and  $\Phi 16//100 + \Phi 12//200$ , bottom layer (dimensions in mm). Although not mandatory for the fuse concept under study, the tested specimens are manufactured with flexible (also termed ductile) connectors designed for full connection capacity.

To assess the performance of the fuse device, a total of ten cyclic and two monotonic experimental tests are conducted on the single sub-assembly of beam-to-column connection fitted with fuses with different geometric parameters. Each test is conducted until complete failure of the fuse flange plate, after which the fuse plates are replaced by new ones and another test is performed. The web plates are designed to withstand shear forces and have the same dimensions in all tests ( $200 \times 4 \text{ mm}^2$ ). The only dimensions that changes between tests are the thickness ( $t_f$ ) and width ( $b_f$ ) of the flange plates, since the free buckling length of the steel plates is 170 mm for all specimens. The buckling susceptibility is described by the geometric slenderness  $\lambda_G$ , computed as the ratio between free length ( $L_0$ ) and thickness of the flange plates.  $L_0$  is set constant so that the tensile strain imposed in the flange plates for the intended fuse rotation amplitudes can adequately be placed in the plastic range, yet far from that of tensile fracture for monotonic tests. The dimensions presented in Table 6.1 are chosen to provide the fuses with different values of the controlling design parameter, the capacity ratio  $\alpha$ , defined by Eq. (6.2).

$$\alpha = \frac{M_{max,fuse}}{M_{pl,beam}} \quad \text{Eq. (6.2)}$$

where  $M_{max,fuse}$  is the maximum moment developed by the fuse device and  $M_{pl,beam}$  is the plastic resisting moment of the non-reinforced segment of the composite cross-section of the beam (away from the fuse, without the web and flange reinforcing plates).

**Table 6.1: Dimensions of the flange plate of the welded FUSEIS beam splices (in mm) and corresponding geometric slenderness**

Plate	A	B	C	D	E	F
$t_f$	10	10	12	8	12	8
$b_f$	80	130	110	100	150	140
$\lambda_G$	17.0	17.0	14.2	21.3	14.2	21.3

The corresponding values of the capacity ratio are presented in Table 6.2 for both sagging ( $\alpha^+$ ) and hogging ( $\alpha^-$ ) moments.

**Table 6.2: Capacity ratios of the welded FUSEIS beam splices**

Plate	A	B	C	D	E	F
$\alpha^+$	0.45	0.57	0.57	0.47	0.71	0.54
$\alpha^-$	0.27	0.38	0.39	0.25	0.48	0.30

Testing is conducted in three main phases – first, cyclic, for plates D, A, B and C, in that order, with repetitions – and afterwards, cyclic, for a new set of plates – F and E, in that order – and in the end, monotonic, sagging and hogging, for plate C. The testing sequence is devised to reduce the effects of accumulated damage induced by previous tests, i.e., in the order of increasing strength (capacity ratio) and, in cases of equivalent strength, decreasing geometric slenderness.

The cyclic displacements are imposed on the specimen by the actuator at the top of the beam, at a vertical distance of approximately 1.5 m from the centre of the fuse device. The loading history was based on a protocol similar to the one proposed in the ECCS Recommendations (1986), translated in terms of the approximate device rotation (Krawlinker, 2009). The loading history protocol is described in **Table 6.3** in terms of the step index  $n$ . If failure is not reached after completing the eleven steps of the proposed loading history, cycles with 40 mrad device rotation amplitude (60 mm) are performed until complete failure of the flange plate.

**Table 6.3: Loading history protocol**

Step (n)	Imposed top displacement (mm)	Approximate device rotation $\theta$ (mrad)	No. of cycles
1	2.25	1.5	3
$2 \leq n \leq 6$	$3.75(n-1)$	$2.5(n-1)$	3
$6 \leq n \leq 11$	$7.50(n-3)$	$5.0(n-3)$	3
$n > 11$	60	40	3

### 6.3.2 Material characterization tests

#### 6.3.2.1 Steel tensile tests

The characterization of the steel resistance is achieved through standard tensile tests based on the European recommendations of EN10002-1. Testing on specimens with different thickness in structural steel and diameter in rebar steel are performed in the Instron universal testing machine. The average values of the yield and ultimate parameters obtained from these tests are presented in Table 6.4 and Table 6.5 for the structural and rebar steel, respectively.

**Table 6.4: Average yield and ultimate parameters of the S275 structural steel**

Thickness (mm)	$f_{ym}$ (MPa)	$f_{um}$ (MPa)	$\varepsilon_{um}$ (%)
4	271.7	402.2	26.3
8	262.8	417.2	26.7
10	274.6	430.3	24.2
12	276.8	429.5	24.9

**Table 6.5: Average yield and ultimate parameters of the A500 reinforcement steel**

$\phi$ (mm)	$f_{sm}$ (MPa)	$f_{um}$ (MPa)	$\varepsilon_{um}$ (%)
10	535.1	644.3	13.7
12	549.0	674.6	13.0
16	577.9	694.2	13.2
20	550.5	675.3	14.8

Considering the obtained values, the structural steel satisfies the minimum requirements to be considered as S275 grade and the rebar steel as A500 grade.

#### 6.3.2.2 Concrete compression tests

The average compressive strength of the concrete  $f_{cm}$  is assessed through a uniaxial compression test conducted on six 150 mm sided cube specimens at the age of the cyclic tests. The obtained failure modes are adequate. The results can be visualized in Table 6.6. From these results, and according to the prescriptions in 3.1.2 of EN1992-1-1, the characteristic value of the concrete compressive cylinder strength  $f_{ck}$  may be obtained approximately by the expression:  $f_{ck} = f_{cm} - 8$  (MPa).



Based on this expression, it is concluded that the concrete is closer to the C30/37 strength class.

**Table 6.6: Concrete compression test results**

Specimen no.	F (kN)	$f_c$ (MPa)
1	910.7	40.5
2	940.1	41.8
3	856.1	38.0
4	951.0	42.3
5	869.7	38.7
6	878.3	39.0

### 6.3.3 Assessment of the experimental results

#### 6.3.3.1 Overall hysteric behaviour

The analysis of the results is mainly based on the moment-rotation on the fuse ( $M - \theta$ ) diagrams of the specimens. As an example,  $M - \theta$  diagrams for both tests on fuse D are shown in Fig. 6.4 (rotation  $\theta$  is approximately computed dividing the top displacement by the distance to the centre of the fuse).

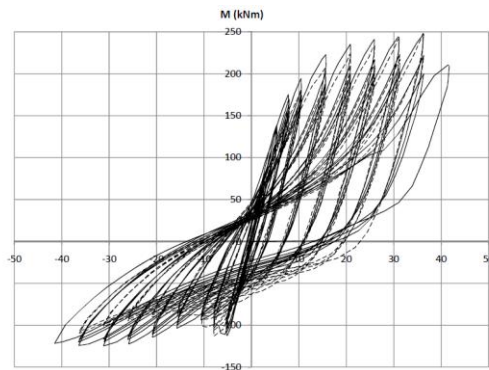


Fig. 6.4:  $M - \theta$  diagram of plate D

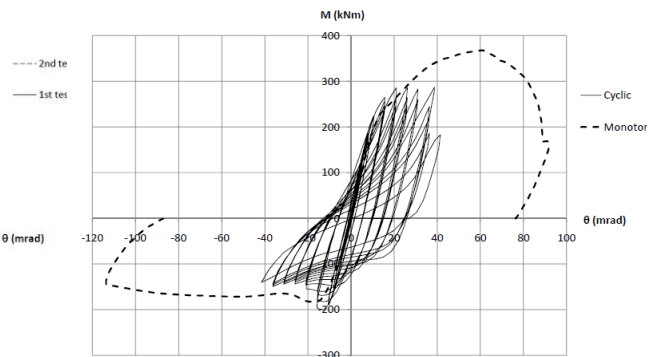


Fig. 6.5: Comparison between monotonic and cyclic tests conducted on fuse C

The diagrams show that the hysteretic behaviour of the fuses is stable, characterized by a marked pinching phenomenon, due to the buckling of the fuse plates when under hogging rotations, explaining also the asymmetry of the diagram in terms of moments. The deformation capability of the fuses is demonstrated by the fact that all specimens have been able to perform  $\pm 35$  mrad rotations, which is the minimum value recommended by EN1998-1-1.

Comparison of the  $M - \theta$  diagrams between the first and second tests of the same fuse specimen shows that there is a slight deterioration in terms of strength and energy dissipation. This deterioration is a consequence of the accumulated damage to the parts of the test assembly that are not replaced between tests. The failure

modes of all specimens are similar, comprising the development of cracks at the mid-section of the flange plate under tension.

In addition, measurements show that both the column and the composite beam remained in the elastic range, moving similarly to rigid bodies with little elastic deformations. The specimens have shown a significant composite behaviour, where the slippage at the slab-beam interface proved to be relatively small, with values below 0.20 mm for all specimens.

The monotonic behaviour can be compared with the cyclic behaviour through the superimposition of the corresponding  $M - \theta$  diagrams, as shown in Fig. 6.5 for fuse with plate C. The diagrams are very similar in terms of the initial stiffness and yield moments. The monotonic diagram seems to adjust well to the cyclic diagram for the same rotation range, closely resembling the cyclic envelope curve. The combination of kinematic strain hardening (which increases monotonic strength) with low cycle fatigue (which decreases cyclic strength) justifies the strength differences observed in the sagging direction. Strength in the hogging direction is controlled by the buckling phenomenon which occurs irrespective of the fact that the tests are monotonic or cyclic. The deformation capacity of the cyclic tests is considerably reduced due to damage accumulation effects (e.g. low cycle fatigue of the flange plate).

#### 6.3.3.2 *Stiffness*

Results obtained from the first cyclic test of each fuse plate shows that the  $\xi$  parameter, defined in the ECCS Recommendations (1986) as being the ratio between the unloading stiffness at the end of each cycle and the initial elastic stiffness of the specimen, progressively decreases with cycling, translating into a continuous loss of stiffness. This loss is found to be more expressive for hogging rotations owned by cyclic buckling of the fuse plates. Moreover, specimens with lower values of  $\alpha$  have a higher stiffness decrease rate as well, in particular at sagging rotations.

#### 6.3.3.3 *Strength*

In order to simplify the test comparisons, the dimensionless resistance ratio  $\varepsilon$  at the end of each cycle is presented. This ratio is defined in ECCS Recommendations (1986) as the bending moment at the end of each cycle divided by the yield moment of the specimen in the corresponding direction.

The trend of the resistance ratio with cycling seems to be very similar for all specimens in sagging rotation, presenting a considerable hardening, which in some cases reaches a value of 1.5 times the yield moment. This phenomenon is mainly due to the hardening of the flange plate in tension.

However, for hogging rotation, the aforementioned strain hardening effects are balanced by those attributable to buckling, also in the flange plates. As a result, the

resistance ratio is generally lower than unity. The sagging and hogging resistance of the fuses are expected to be directly controlled by the values of the capacity ratios  $\alpha^+$  and  $\alpha^-$ , respectively. This dependence can be shown in Fig. 6.6 and Fig. 6.7.

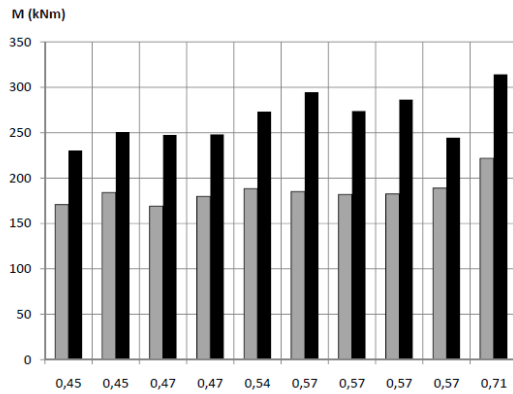


Fig. 6.6: Sagging resistance vs.  $\alpha^+$

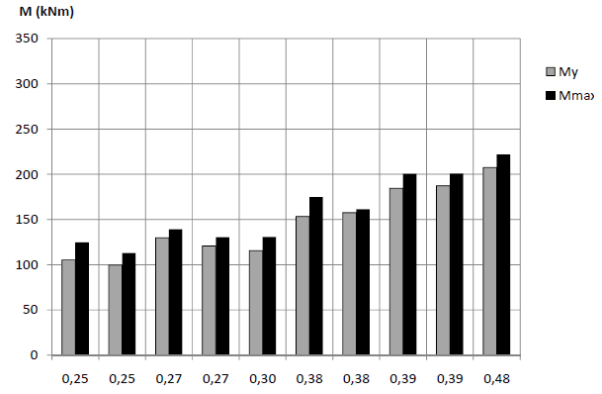


Fig. 6.7: Hogging resistance vs.  $\alpha^-$

The sagging resistance chart indicates that both yield ( $M_y$ ) and maximum moments ( $M_{max}$ ), determined according to ECCS Recommendations (1986), increase with  $\alpha^+$ , showing a reasonable correlation. Nevertheless, there are some exceptions, in which the same value of  $\alpha^+$  corresponds to different values of resistance. This apparently contradictory behaviour is observed in the specimens tested last, in which the damage accumulation effects from previous tests led to resistance losses that are disregarded in the computation of  $\alpha$ .

As for the hogging moments, Fig. 6.7 shows that strength exhibits a more consistent increase with the capacity ratio. This shows that the hogging resistance of the fuse is more sensitive to a geometry variation of the flange plate and, consequently, of  $\alpha^-$ .

#### 6.3.3.4 Energy dissipation capacity

Energy dissipation capacity plays one of the most important roles in describing the seismic performance of the fuses. The total amount of dissipated energy  $W_{total}$  is shown to be dependent of  $\alpha$ , stressing the fact that the severity of the yielding and buckling of the fuse parts have a fundamental influence on the energy dissipation performance of the fuse.

The evolution of the deterioration between tests may also be interpreted through energy considerations. For this, the total amount of dissipated energy in different fuse plates is compared at the end of the first and second tests of each fuse. With the exception of plate D, the first tests of the other fuses were able to reach higher levels of energy dissipation. This indicates that the deterioration of the irreplaceable parts, particularly the cracking on the upper surface of the concrete slab influences the energy dissipation capacity.

The evolution of the energy dissipation along the cycles may also provide an idea of the progression of accumulated damage during the tests. In order to study this aspect, the dimensionless parameter  $\eta/\eta_0$  is computed, where  $\eta$  is an energy ratio at the end of each cycle and  $\eta_0$  is the same energy ratio at the end of the first plastic cycle. According to ECCS Recommendations (1986), the energy ratio  $\eta_i$  at the end of a cycle  $i$  is given by Eq. (6.3):

$$\eta_i = \frac{W_i}{\Delta M_y (\Delta \theta_i - \Delta \theta_y)} \quad \text{Eq. (6.3)}$$

where  $W_i$  is the energy dissipated in cycle  $i$ ,  $\Delta M_y$  is the range of the yield moments,  $\Delta \theta_i$  is the range of the imposed rotations at cycle  $i$  and  $\Delta \theta_y$  is the range of the yield rotations. The corresponding diagram is presented in Fig. 6.8 for the first test of each specimen.

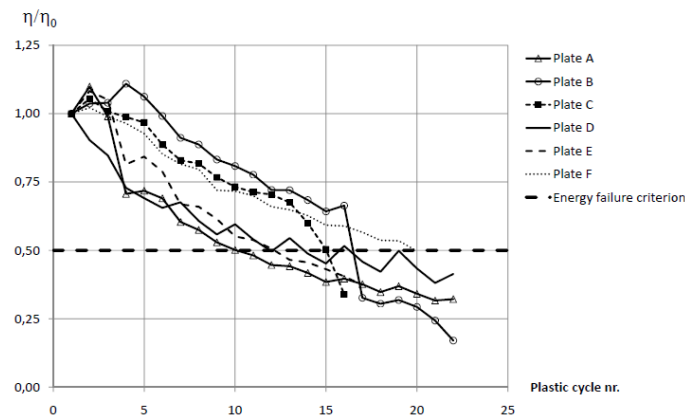


Fig. 6.8: Comparison between first and second tests in terms of energy dissipation

One possible energy failure criterion can be setting the  $\eta/\eta_0$  parameter to a constant value (possibly dependent on the geometric and material properties of the specimen) below which failure occurs. This criterion is used by Castiglioni and Pucinotti (2009) and Agatino (1995) to model the failure of steel components. As initially proposed by Calado and Castiglioni (1996), a simplified approach is to set the parameter to a constant value of 0.5. This limit appears in the diagram as the dashed line curve, which seems to fit adequately the experimental results, especially for fuse plates with a higher value of  $\alpha$ . The same diagram also shows that the curves of fuse plates A and D cross this limit earlier in the test, with reference to their first plastic cycle. The corresponding plates tend to buckle more easily, showing a more pronounced pinching effect.

In general, the results indicate that fuses with higher values of  $\alpha$  provide higher performance levels in terms of stiffness, resistance, dissipated energy and rate of deterioration. Nevertheless, fuses with values of  $\alpha$  close to unity, and whose strength

is similar to that of the composite beam, induce more damage outside the fuse, failing to concentrate plasticity within the fuse section. This behaviour contradicts one of the underlying concepts of the fuses. Therefore, the value of  $\alpha$  should be limited by an upper bound to prevent the spread of plasticity in the irreplaceable parts.

## 6.4 NUMERICAL MODELLING OF THE WELDED FUSEIS BEAM SPLICES

### 6.4.1 *Modelling assumptions*

A set of numerical finite element models are developed in Abaqus with the objective of reproducing the experimental results. These models assume that both the beam and the column are sufficiently stiff to be considered as rigid and that the composite beam present full shear connection. Since the behaviour of the fuse is mainly dependent on the yielding and buckling of the steel plates and no major cracking is observed on the first tests, concrete is modelled with an elastic behaviour, reducing considerably the computational costs (Espinha, 2011). The adopted uniaxial stress-strain relationship for steel is based on the results provided by experimental tensile tests carried with samples extracted from the steel profiles. The properties of the steel are modelled with linear hardening and the Von Mises yield criterion, bearing in mind the provisions of the EN 1993-1-1 and EN 1993-1-5.

### 6.4.2 *Result assessment*

Fig. 6.9(a) and (b) illustrate the plastic deformations developed on the fuse under sagging and hogging moments, respectively.

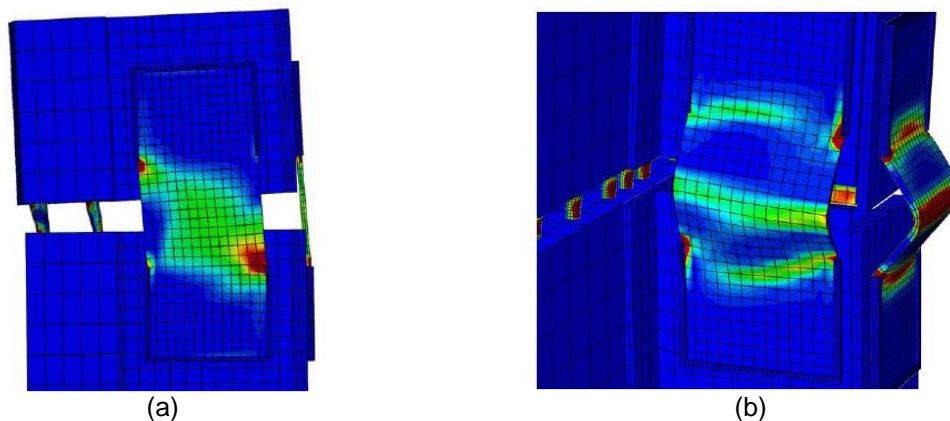


Fig. 6.9: Development of plastic strains on the fuse under (a) sagging and (b) hogging moments

The figures show the plastic deformation of the fuse in terms of the equivalent plastic strain contour plot. These plots illustrate the ability of the fuse to concentrate plasticity within its plates. The numerical simulations consisted of displacement controlled increasing loading (monotonic) history, allowing for the comparison with the experimental cyclic envelopes.

In general, the models predict the experimental behaviour with relative accuracy, especially under the elastic range. Regarding the maximum moment, a more expressive hardening is observed in the numerical model, since the finite element model is loaded monotonically from non-deformed and undamaged condition and, thus, failing to reproduce the strength deterioration from previous cycles that is observed in the experimental tests. As far as the stiffness is concerned, the finite element model is stiffer than the one tested experimentally. This stiffness superiority is more expressive for plates C, E and F, which are among the last to be tested experimentally, suggesting that the difference maybe a consequence of the elastic stiffness loss shown by those specimens, due to the damage accumulation on the irreplaceable parts, cracking of the concrete and low cycle fatigue effects.

Another aspect evidenced in the numerical results is that the sections do not remain plane despite the fact that the plastic neutral axis lied close to the centre of gravity of the rebar layers. Bernoulli's hypothesis is not entirely valid in this sense, which complicates the development of analytical design models.

## **6.5 DESIGN GUIDELINES**

The conclusions from the analytical and numerical studies are now summarized in the design guide presented herein for practical application. The design guide gives recommendations on the selection of the appropriate fuses as a function of the most important parameters, like frame configuration, seismic zone, spectrum, and more generally the strength and deformation demand. The design methodology, described in the design guide, is based on the provisions of EN1993-1-1, EN1994-1-1 and EN1998-1-1. Some clauses of EN1998-1-1 are appropriately rearranged to cover the use of the devices by the normal code provisions. It also includes structural details and constructional measures.

### **6.5.1 Preliminary design**

#### **6.5.1.1 Proposed procedure**

It is more complex to design elements to withstand seismic actions. Their effects in terms of internal forces are hard to predict because the severity of the action depends on the mechanical characteristics of the elements. The design of the beam splices is, therefore, a rather iterative procedure. In this respect, the present section aims to give the designer some recommendations on the pre-design of the beam splices' dimensions.

Firstly, since the fuses are mainly used to resist lateral loads (their positioning should be near the null moment zones for fundamental load combination), the cross-section of the composite beam should be determined based on the ultimate limit state fundamental load combination, assuming a frame without fuses.

Secondly, a seismic design of the conventional structure (without the welded FUSEIS beam splices) should be performed with an appropriate  $q$ -factor. The resulting internal moments at the location where the beam splices will be placed should then be considered as design moments for the splices. With these values, one may also compute the pre-design values of  $\alpha^+$  to check whether they are acceptable or not. The design of the beam splices should be done such that their plastic hinge formation sequence approximately accompanies the structure's deformation caused by the seismic action.

Thirdly, with the design moment of the beam splices and considering the plastic neutral axis located near the centre of gravity of the upper and lower layer rebar, the cross section of the flange plate fuse can be computed.

Fourthly, the gap distance and the free length  $L_0$  are determined to allow the development of the desired rotation without inducing too severe buckling on the fuse plates or on the rebar, assuring that the connection is ductile.

Fifthly, provided that the plastic neutral axis remains approximately on the considered location, the upper and lower rebar layer as well as the ultimate hogging and sagging moment of the beam splices is calculated simultaneously through the resistance model detailed in 5.1.2. The computed rebar area should be considered as the lower bound value. One may use higher quantities of rebar to achieve a more conservative design ensuring their permanence in the elastic regime, as long as the deformation in the flange plate is higher than its yielding strain. The real  $\alpha^+$  and  $\alpha^-$  values may then be computed. It is not recommended that these two values have high discrepancies due to the negative influence on the behaviour of the structure, since the moment-rotation diagram should be as symmetric as possible.

Sixthly, with the maximum fuse moments, several aspects can be determined: (a) the maximum shear force can be computed based on equilibrium considerations and assuming a constant shear force along the beam during seismic situations. The shear force allows the design of the web plates, so that they withstand the totality of the shear. (b) The length and the necessary area for the web and flange reinforcement plates placed on the reinforced beam zones can be calculated to ensure, on one hand, their resistance to the imposed actions and, on the other hand, that the non-reinforced parts of the beam remain elastic.

Finally, the yielding moment and its corresponding rotation (consequently, stiffness of the fuse) may be computed with the method described in 6.5.1.3. The hysteric constitutive relation of the fuse is ultimately obtained and used in both linear and non-linear analyses of the final structure to check if it verifies the safety conditions.

### 6.5.1.2 Resistance model

The maximum sagging moment may be computed based on the scheme illustrated in Fig. 6.10. Herein, two assumptions are made: (a) the web plates are not considered and (b) the model assumes Bernoulli's plain section hypothesis.

However, findings from the numerical model show that the deformation along the height of the fuse cross section is nowhere near linear which lowers and even changes the sign on the normal stress diagram reducing the mobilized resisting moment.

On the other hand, the consideration of a non-linear distribution of strains goes against the philosophy of practical design because it complicates considerably the computation of the resistance of the fuses.

To this end and considering that the reduction of the mobilized resisting moment can somewhat compensate the exclusion of the web plates' resistance, the proposed model can be considered as a good approximation for the fuse maximum and minimum moment calculation. It should be noted that Fig. 6.10 is valid for sagging moments. For hogging moments, the direction of the forces and moment should be inverted.

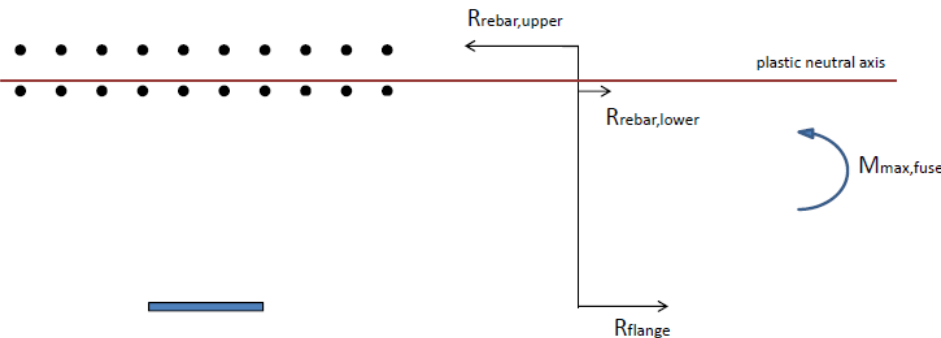


Fig. 6.10: Model to compute the maximum sagging moment of the fuse

For sagging moments:

Firstly, with the location of the plastic neutral axis fixed, the ultimate curvature of the splice is calculated by imposing the ultimate strain of the steel on the flange plate. The maximum axial force exhibited by the flange plate is  $R_{flange} = f_{u,flange} \cdot A$ , where  $A$  is the cross-sectional area of the element and  $f_{u,flange}$  is the ultimate tensile stress of the flange plate's steel.

Secondly, the strain in the upper and lower rebar layer can be determined through the linear strain diagram. Given that the rebar should remain in the elastic regime, the rebar stresses may be obtained by multiplying their strains by the elastic modulus  $E$ .

Thirdly, the upper and lower rebar layer area is now chosen to satisfy the equilibrium condition expressed in Eq. (6.4). The assumption made for the location of the plastic neutral axis is also validated implicitly by satisfying Eq. (6.4). As a starting point,



twice the area of the flange plate shall be applied for the upper rebar layer area. Then, the lower rebar layer area shall be calculated to achieve the equilibrium.

$$\sum_i R_i = 0 \quad \text{Eq. (6.4)}$$

where  $R_i$  is the force exhibited by each element  $i$ .

Fourthly, knowing the forces of each component the ultimate fuse moment is calculated with Eq. (6.5).

$$M_{max,fuse} = \sum_i R_i \cdot z_i \quad \text{Eq. (6.5)}$$

where  $z_i$  is the lever arm of each element  $i$ .

Finally, the ultimate sagging rotation may be obtained by multiplying the ultimate curvature of the splice with the free length of the fuse plates.

For hogging moments:

Additional attention must be paid on the estimation of the flange's maximum compression stress due to the effects of buckling. The derivation of this value can be done based on the model proposed by Gomes and Appleton (1992) which is presented in Fig. 6.11. The resulting expression is given in Eq. (6.6).

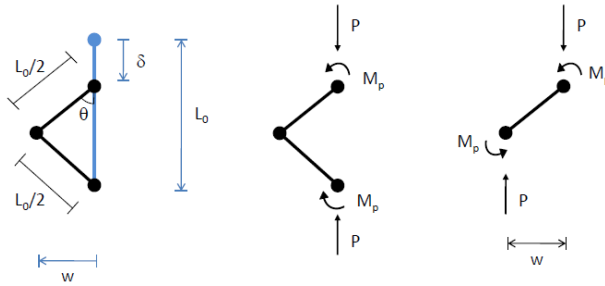


Fig. 6.11: Plastic mechanism

$$\sigma = \frac{2\sqrt{2}M_p}{AL_0} \frac{1}{\sqrt{\varepsilon}} \quad \text{Eq. (6.6)}$$

where  $A$  is the area of the cross-section of the fuse plate,  $\sigma$  is the maximum compression stress,  $L_0$  is the free buckling length,  $M_p$  is the plastic moment of the flange plate and  $\varepsilon$  is the strain. The stress-strain relationship of the flange's steel under compression is then obtained and illustrated in Fig. 6.12.

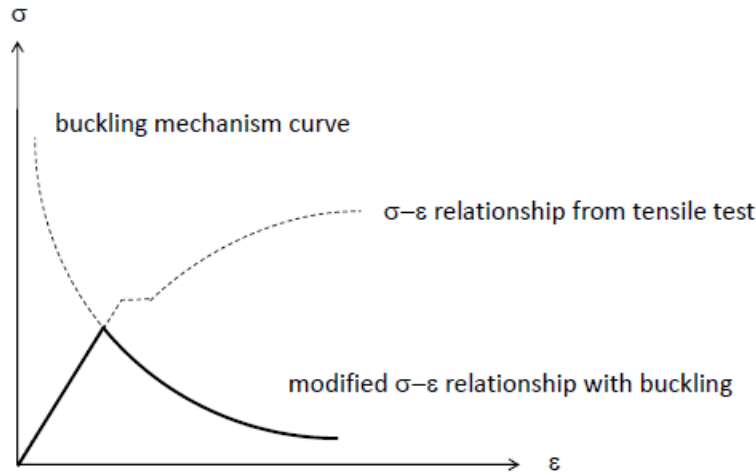


Fig. 6.12: Definition of the modified  $\sigma - \varepsilon$  curve with buckling

To simplify the estimation of the negative branch of the splice's hysteric curve, the present document considers a maximum compression stress of the flange plate equal to the yielding stress of the steel. This implies that the maximum compression stress is the minimum between two values: the stress computed by the buckling mechanism curve or the yielding stress of the steel.

The mobilized compression force is then determined by multiplying the resulting compression stress by the area of the flange plate. Finally, the hogging moment is approximated by the product of the force and the distance between the centres of gravity of the plate and the rebar.

Shear force:

As for the web plates, which should resist solely to shear, their shear resistance should account for the effects of shear buckling, according to 5.2 of EN1993-1-5:

$$V_{b,Rd} = \frac{\chi_w h_w t_w f_{y,w}}{\sqrt{3}} \quad \text{Eq. (6.7)}$$

where  $h_w$  is the height of the cross section of the web plate,  $t_w$  is the thickness of the cross-section of the web plate,  $f_{y,w}$  is the yield stress of the web steel,  $\chi_w$  is the shear buckling reduction factor.

The value of  $\chi_w$  is equal to 1.0 as long as the following condition is valid:

$$\frac{h_w}{t_w} < \frac{72}{\eta} \sqrt{\frac{235}{f_{y,w}}} \quad \text{Eq. (6.8)}$$

where  $\eta$  is a parameter that should be taken as 1.2, as recommended by the code. It should be noted that the equation is valid only for unstiffened plates.

#### 6.5.1.3 *Stiffness model*

The methodology to compute the stiffness of the welded beam splices also bases on the resistance model scheme. The yielding moment, curvature and the first approximation of the yield rotation can be obtained once the centre of rigidity is known, assuming the yielding strain of steel for the flange plate.

The yield rotation is then readjusted with a coefficient to take into account the reduction of stiffness owned by shear deformations. The resulting value of the coefficient, calibrated based on the laboratory findings presented in chapter 3, is 6.26.

This value was calibrated from an interval of plate dimensions that varies from 10x80 mm<sup>2</sup> to 12x150 mm<sup>2</sup>. It should be advised that extra caution must be paid when one is designing beam splices with dimensions beyond the specified interval. Nevertheless, a sensibility analysis was also carried out to check how the variability of the calibrated value affects the global behaviour of the structure. The observed effects of this variance on the global behaviour of the structure were very small and, therefore, can be disregarded.

#### 6.5.2 *Design for linear elastic analysis*

The design rules are intended to ensure that yielding takes place in the fuses prior to any yielding or failure elsewhere. In this sense, the design of buildings with welded FUSEIS is based on the assumption that the fuses are able to dissipate energy by the formation of plastic bending mechanisms.

##### 6.5.2.1 *Simulation and preliminary value of the behaviour factor*

A building with welded FUSEIS may be simulated with a linear-elastic model by introducing appropriate rotational springs at both ends of the MRFs' beams. The stiffness of the springs should be equal to the ones estimated in 5.1.3. The resulting internal forces of the analysis are then divided by the behaviour factor  $q$ . Since only the fuses are expected to have inelastic behaviour, the  $q$  factor depends mainly on the ductility reserves of the fuses and on the structural type and regularity. Some preliminary indications on the behaviour factor is given herein but further investigations with non-linear analysis should be conducted to appropriately estimate its value. In the general case, when the beam-to-column connections provide sufficient stability without inducing severe second order effects, the value of  $q$  can be taken as 4.0 and 5.0 for ductility class medium and high, respectively. In cases where the overall stiffness of the structure is very low to accommodate the imposed displacements, the structure should be considered as an inverted pendulum with a behaviour factor of 2.0.

##### 6.5.2.2 *Analysis and safety check*

Static linear analysis is performed under dead and live loading and the members of the main frame are designed according to the provisions of EN1993-1-1 at ULS and

SLS. The conventional method for the calculation of internal forces under seismic loading is to perform a Multi-Modal Response Spectrum Analysis, where the number of modes of vibration considered in each direction is such that the sum of the effective mass is at least equal to 90% of the total mass.

#### 6.5.2.2.1 2<sup>nd</sup> order effects

The possible influence of 2<sup>nd</sup> order effects shall be controlled by the limitation of the interstorey drift sensitivity coefficient  $\theta$  below the limit values given by the code. Coefficient  $\theta$  is calculated from Eq. (6.9) for each floor for both x and y directions of the building.

$$\theta = \frac{P_{tot} \cdot d_r}{V_{tot} \cdot h_{story}} \quad \text{Eq. (6.9)}$$

where  $P_{tot}$  is the total gravity load on and above the storey considered in the seismic design situation,  $V_{tot}$  is the seismic storey shear,  $d_r$  is the interstorey displacement and  $h_{story}$  is the height of the corresponding storey.

The relevant code provisions require for buildings to limit their interstorey drift sensitivity coefficient to  $\theta \leq 0.1$ , if second order effects are ignored. If  $0.1 < \theta < 0.2$ , second-order effects may approximately be taken into account by multiplying the relevant seismic action effects by a factor equal to  $1/(1 - \theta)$ . If  $0.2 < \theta < 0.3$  a more accurate second order analysis applies. In any case, the value shall be less than 0.3.

#### 6.5.2.2.2 Limitation of interstorey drift

In linear elastic analyses, the real displacements induced by the seismic action  $d_s$  shall be calculated on the basis of the elastic deformations  $d_e$  of the structural system through the expression:

$$d_s = q \cdot d_e \quad \text{Eq. (6.10)}$$

The interstorey drift  $d_r$  is defined as the difference of the average lateral displacements at the top and bottom of the storey under consideration. Depending on the type of the non-structural elements (brittle materials, ductile or not connected) and the importance class of the building, the interstorey drift  $d_r$  is compared to the corresponding values of the code.

#### 6.5.2.2.3 Dissipative elements verifications

The welded FUSEIS shall be verified to resist the internal forces and moments of the most unfavourable seismic combination and fulfil the following conditions: axial forces, shear resistance and moment capacity.

Firstly, it should be verified that the full plastic moment of resistance and shear forces are not decreased by compression forces through Eq. (6.11):

$$\frac{N_{Ed}}{N_{pl,fuse,Rd}} \leq 0.15 \quad \text{Eq. (6.11)}$$

where  $N_{Ed}$  is the design axial force and  $N_{pl,fuse,Rd}$  is the design axial resistance of the welded FUSEIS.

The shear resistance shall be verified with capacity design criteria, considering that plastic hinges are developed at both ends of MRFs' beams simultaneously. Note that the shear resistance of the welded FUSEIS is assumed to be solely conferred by the web plates.

$$\frac{V_{CD,Ed}}{V_{pl,fuse,Rd}} \leq 1.0 \quad \text{Eq. (6.12)}$$

where  $V_{CD,Ed} = 2M_{max,fuse}/L_{fuses,ij}$  is the capacity design shear force,  $M_{max,fuse}$  is the maximum developed by the fuses,  $L_{fuses,ij}$  is the distance between the fuses of the same beam and  $V_{pl,fuse,Rd}$  is the resistance conferred by the web plates.

The moment capacity shall be verified as following:

$$\frac{M_{Ed}}{M_{max,fuse}} \leq \frac{1}{\Omega} \leq 1.0 \quad \text{Eq. (6.13)}$$

where  $M_{Ed}$  is the design moment,  $M_{max,fuse}$  is the maximum moment of the fuse and  $\Omega$  is the overstrength factor.

#### 6.5.2.2.4 Global dissipative behaviour

To achieve a global dissipative behaviour of the structure, it should be checked that the maximum ratios  $\Omega$  over the entire structure do not differ from the minimum value  $\Omega$  by more than 25%.

$$\frac{\max \Omega}{\min \Omega} \leq 1.25 \quad \text{Eq. (6.14)}$$

#### 6.5.2.2.5 Fuse rotations

To guarantee that the rotation of the fuses does not exceed the maximum value obtained from experimental results, it has been decided to limit the rotation of the fuses to 3%. Given that their rotation maybe directly evaluated by the intersotry drift, it results on the imposition of an interstorey drift of 3%.

#### 6.5.2.2.6 Non-dissipative elements verifications

The non-dissipative elements (columns, current and reinforced composite beams) shall be capacity designed for increased values of internal forces compared to the ones derived from the analyses with the most unfavourable seismic combination, to ensure that the failure of the welded FUSEIS occurs first.

All the elements shall consider the following capacity design actions:

$$N_{CD,Ed} = N_{Ed,G} + 1.1 \cdot \gamma_{ov} \cdot \Omega \cdot N_{Ed,E} \quad \text{Eq. (6.15)}$$

$$M_{CD,Ed} = M_{Ed,G} + 1.1 \cdot \gamma_{ov} \cdot \Omega \cdot M_{Ed,E} \quad \text{Eq. (6.16)}$$

$$V_{CD,Ed} = V_{Ed,G} + 1.1 \cdot \gamma_{ov} \cdot \Omega \cdot V_{Ed,E} \quad \text{Eq. (6.17)}$$

where  $N_{Ed,G}$ ,  $M_{Ed,G}$  and  $V_{Ed,G}$  are respectively the axial forces, shear forces and bending moments due to the non-seismic actions included in the combination of actions for the seismic design situation.  $N_{Ed,E}$ ,  $M_{Ed,E}$  and  $V_{Ed,E}$  are respectively the axial forces, shear forces and bending moments due to the design seismic action.  $\Omega = \min \Omega_i = \min \{M_{max,fuse,i} / M_{Ed,i}\}$  is the minimum overstrength factor for all welded FUSEIS in the building, see Eq. (6.14).  $\gamma_{ov} = 1.25$  is the material overstrength factor, see Eq. (6.1).

#### 6.5.3 Design for non-linear analysis (Pushover)

The structural model used for elastic analysis shall be extended to include the response of structural elements beyond the elastic state and estimate expected plastic mechanisms and the distribution of damages.

The hinge properties of the non-dissipative elements shall be calculated according to the provisions of relevant codes (e.g. FEMA-356). Plastic hinge properties for the current beams shall be of bending type (M3 hinge), while in columns the interaction between bending moments and axial forces (P-M3 hinges) shall be accounted for.

### 6.6 ANALYSES ON A 3D BUILDING

In this chapter, equations, element properties, design recommendations, critical checks and proposed behaviour factor, included in the design guide, are verified through numerical analyses on 3D building frames with welded FUSEIS beam splices using the software *SAP2000*.

#### 6.6.1 Description of examined building frames

##### 6.6.1.1 Geometry

The case study presented hereafter is based on an 8-storey composite building, its side views are illustrated in Fig. 6.13(a) and (b) and its plan view in Fig. 6.14. The structure is simulated using a 3D model but with Y plane degrees of freedom.

It consists of a rigid fully fixed moment frame with three 8 m spans in both X and Y directions. The height of each floor is constant and equal to 4 m and rigid connections are considered for the foundation. Fig. 6.15 presents the dimensions of the assigned composite slab which modelling of its composite action with the structural beams is explained in 6.6.1.4. The elements and materials used are:

In the Y direction – moment resisting frame

- IPE450 composite beams (S275 steel grade and C25/30, A500 NR concrete)
- HEA200 composite beams (S355 steel grade and C25/30, A500 NR concrete) – resist vertical loads only
- Columns with S355 steel grade (strong moment of inertia)

In the X direction (not studied) – bracings

- IPE500 beams (S355 steel grade)
- Columns with S355 steel grade (weak moment of inertia)
- 2UPN120 and 140 /15/ bracings with S355 steel grade

The welded fuses are placed 0.75 m from the beam-column joints whereas the reinforced beams span up to 1.5 m from the same joints. The dissipative devices have lower steel grade (S235) than the rest of the structural member. Table 6.7 summarize the implemented fuses' dimensions.

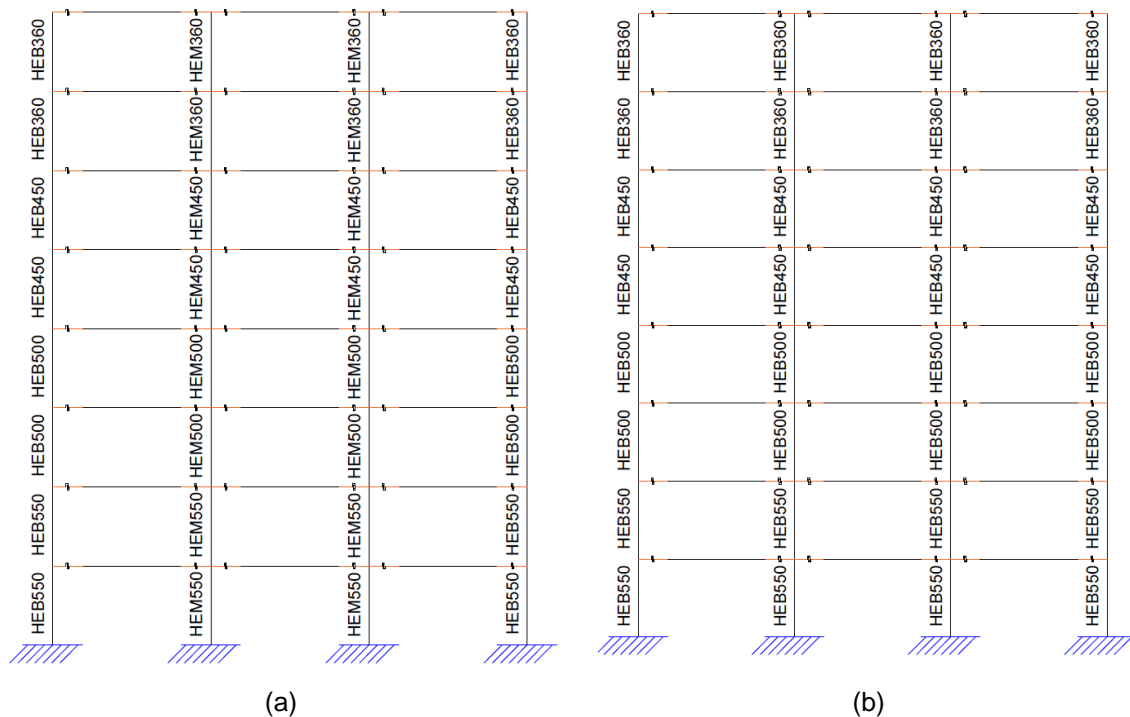


Fig. 6.13: Side view of the modelled building: (a) internal frames and (b) external frames. The reinforced beam zones are highlighted in orange in which the marks that represent the welded FUSEIS can be observed.

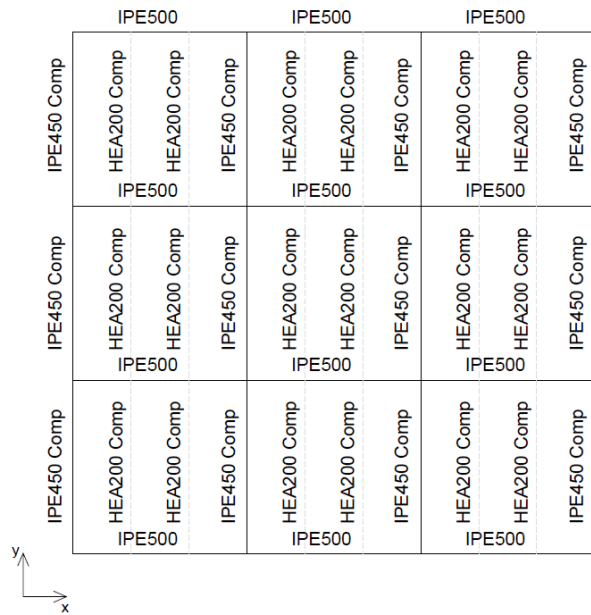


Fig. 6.14: Plan view of the modelled building (the reinforced beam zones and the welded FUSEIS are not represented)

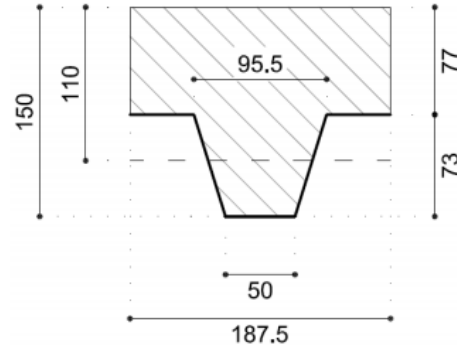


Fig. 6.15: Schematic representation of the composite slab

**Table 6.7: Fuse plates and rebar dimensions**

Floor	FUSE flange plate dimensions		Upper rebar	Lower rebar	FUSE web plate dimensions	
-	$b_f$ (mm)	$t_f$ (mm)	(mm)	(mm)	$h_w$ (mm)	$t_w$ (mm)
1 to 4	170	12	12 $\Phi$ 16	8 $\Phi$ 10	170	8
5 to 6	170	10	12 $\Phi$ 16	8 $\Phi$ 12	170	8
7 to 8	170	8	12 $\Phi$ 16	12 $\Phi$ 12	170	8

#### 6.6.1.2 Loads

The loads are quantified according to EN1991-1-1, EN1993-1-1 and EN1994-1-1 which include the dead load of the structure, superimposed loads, live loads, movable partitions and perimeter walls.



**Table 6.8: Quantification of the applied gravity loads**

Load Class	Type of load	Value
Dead Load	Composite slab with profile sheeting	2.75 kN/m
Superimposed loads	Services, ceiling and raised floors	0.70/1.00 kN/m <sup>2</sup> <sup>1</sup>
	Perimeter walls	4.00 kN/m
Live loads	Office (Class B)	3.00 kN/m <sup>2</sup> <sup>2</sup>
	Movable partitions	0.80 kN/m <sup>2</sup>

Regarding the seismic actions, these can be quantified through EN1998-1-1 with the associated parameters given in **Table 6.9**.

**Table 6.9: Quantification of the seismic action**

Importance factor (Classe II)	$\gamma_I=1.00$
Soil acceleration	$a_{gr}=0.30g$
Soil type	C
$S_{max}$	1.15
$T_B$	0.20 sec
$T_C$	0.60 sec
$T_D$	2.00 sec

#### 6.6.1.3 Load Combinations

Following the guidance of EN1990-1-1, the safety check of a building for Ultimate Limit States should be done for both persistent fundamental and seismic combination which are given by equations 6.10 and 6.12b of EN1990-1-1, respectively. In addition, the total mass of the structure to quantify the seismic actions should be determined with equation 3.17 of EN1998-1-1. **Table 6.10** gives all the coefficients used for the load combinations.

**Table 6.10: Coefficients used for the load combinations**

Coefficient	Value
$\gamma_G$	1.35
$\gamma_Q$	1.50
$\Psi_2$ Office (Class B)	0.30
$\Psi_2$ Roof	0.00
$\varphi$ Correlated floors	0.80
$\varphi$ Roof	1.00

<sup>1</sup> 0.70 kN/m<sup>2</sup> for intermediate floors and 1.00 kN/m<sup>2</sup> for the roof

<sup>2</sup> The roof is considered as accessible and, according to the paragraph 6.3.4.1(2) of *EN1991-1-1*, this has the same live load value as the service floors.

#### 6.6.1.4 Simulation

The structure is modelled with frame type elements where the distributed mass of each floor is concentrated in its centre of gravity. This approach simplifies the model calculations and is considered as an acceptable approximation due to several factors: (a) the structure presents a very regular geometry (doubly symmetric in plane and no variations along its height), (b) the mass of each floor is well distributed which disregards the necessity to verify vertical seismic modes and (c) the rigidity in plane of the composite slab is high enough to consider a diaphragmatic behaviour for each floor.

The program *SAP2000* offers a wide variety of commercial steel profiles to be used in the frame elements. However, to model the composite behaviour between the slab and the IPE500 or HEA200 beams, it was necessary to define their cross section in the *cross-section designer* available in the program. Two types of cross section are defined herein to represent beams located on the hogging/sagging moment zones. On the sagging moment zones, where the concrete can be considered as non-cracked, only the concrete above the profile steel sheeting is considered with an effective width determined by paragraph 5.4.1.2(5) of EN1994-1-1. On the other hand, on the hogging moment zones, cracking can be verified on the concrete and thus, rebar are considered instead. With the introduction of the welded FUSEIS, the beams in the hogging moment zones are reinforced with extra web and flange steel plates. A schematic representation of the modelled hogging and sagging moment zone cross-sections are presented in Fig. 6.16(a) and (b).

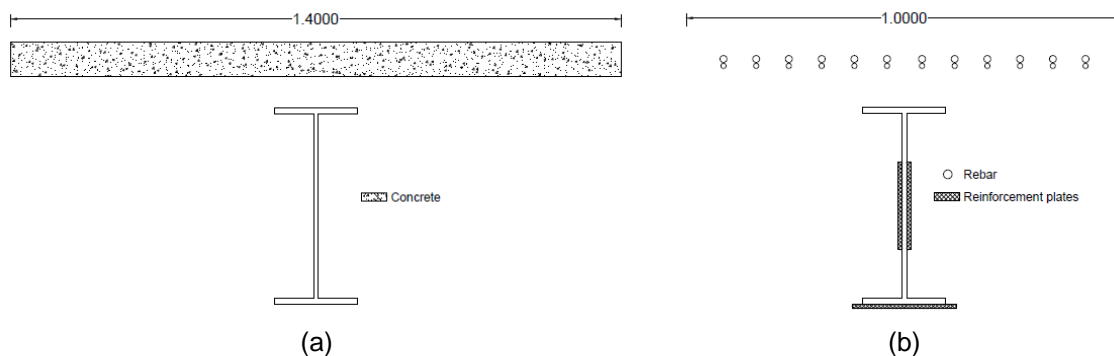


Fig. 6.16: Schematic cross-section representation of the (a) sagging and (b) hogging moment zones of the MRFs' beams

For the linear elastic analysis, the welded fuses are simulated by support links where there is the option to assign the rotational stiffness. The rotational stiffness is determined by applying the methodology described in 5.1.3 with the components illustrated in Fig. 6.17.



Fig. 6.17: Schematic cross-section representation of the welded FUSEIS to calculate their resistance and stiffness

### 6.6.2 Linear Elastic Analysis

#### 6.6.2.1 Response spectrum analysis

Multi-modal response spectrum analysis is performed and the results are summarized in Table 6.11. The first three modes, which are translational in the Y direction, activated more than 90% of the mass.

**Table 6.11: Participating mass ratios and periods**

Mode	Period (s)	Mass Ratio	Accumulated MR
1	1.942	0.775	0.775
2	0.629	0.108	0.883
3	0.344	0.046	0.929

According to EN1998-1-1 for a period higher than  $T_D$ , the lower bound for the horizontal design spectrum has to be checked with Eq. (6.18):

$$S_d(T) \begin{cases} = a_g \cdot S \cdot \frac{2.5}{q} \cdot \left[ \frac{T_C T_D}{T^2} \right] \\ \geq \beta \cdot a_g \end{cases} \quad \text{Eq. (6.18)}$$

where  $S_d(T)$  is the design spectrum acceleration,  $q$  is the behaviour factor set equal to 4 and the rest of the parameters are explained in Table 6.9. Since the resulting design spectrum acceleration value is below the lower bound defined by the  $\beta$  coefficient due to the high period of the structure, this is taken as the lower bound value, meaning that the subsequent IFMs shall be governed by the same value as well. The total base shear  $V_{tot}$ , vertical load  $P_{tot}$ , their ratio and the lower bound factor are given in Table 6.12.

**Table 6.12: Check of the lower bound for the horizontal design spectrum**

V (kN)	P (kN)	V/P	Lower Bound
1463.36	25256.26	0.058	0.060

### 6.6.2.2 Seismic design

#### 6.6.2.2.1 Limitation of Interstorey drift

Considering that the building has ductile non-structural elements, the limitation of interstorey drift shall be checked with the following equation:

$$d_r \cdot \nu \leq 0.0075 \cdot h = 0.0075 \cdot 4 = 0.03 \text{ m} \quad \text{Eq. (6.19)}$$

where  $\nu = 0.5$  is a reduction factor on the design displacements due to the importance class of the building (in this case ordinary buildings) and  $h$  is the storey height. **Table 6.13** gives the results of the analysis in which the check is verified for all stories. The maximum drift verified by the analysis, which can be recovered by removing the  $\nu$  coefficient of the 3<sup>rd</sup> floor  $d_r \cdot \nu$  value and dividing the result by the height of the floor, is 1.45% and thus below the maximum fuse rotation established.

**Table 6.13: Limitation of interstorey drift**

Floor	$d_r \cdot \nu$	$0.0075 \cdot h$	Verification
0	0.0000	0.03	TRUE
1	0.0138	0.03	TRUE
2	0.0260	0.03	TRUE
3	0.0289	0.03	TRUE
4	0.0271	0.03	TRUE
5	0.0245	0.03	TRUE
6	0.0204	0.03	TRUE
7	0.0167	0.03	TRUE
8	0.0100	0.03	TRUE

#### 6.6.2.2.2 2<sup>nd</sup> order effects

The limitation of 2<sup>nd</sup> order effects is assumed as the basis of the design herein for the columns and beams. The verification is made through Eq. (6.9). Although the sensibility coefficient is higher than 0.2 on the 3<sup>rd</sup> floor, the value does not exceed the maximum one imposed by the code (0.3). However, further studies with non-linear pushover analysis must be conducted.

**Table 6.14: 2<sup>nd</sup> order verification**

Floor	$\Theta_y$	$\Theta_y < 0.1$	$\Theta_x < 0.2$
1	0.115	FALSE	TRUE
2	0.199	FALSE	TRUE
3	0.208	FALSE	FALSE
4	0.181	FALSE	TRUE
5	0.144	FALSE	TRUE
6	0.101	FALSE	TRUE
7	0.066	TRUE	TRUE
8	0.030	TRUE	TRUE

#### 6.6.2.2.3 Verification of the welded FUSEIS

The welded FUSEIS are designed based on the acting moments of the conventional structure's composite beam but also bearing in mind the values of  $\alpha^+$  and  $\alpha^-$ . Table 6.15 gives the verification of the fuses on each floor and their respective overstrength value  $\Omega = M_{max}/M_{ed}$ ,

Table 6.16 presents the values of  $\alpha^+$  and  $\alpha^-$  for each fuse type and Table 6.17 shows the shear forces verification.

**Table 6.15: Check of the bending moments**

Floor	Med design	Mrd hogging	Mrd sagging	Usage hogging	Usage sagging	$\Omega$ hogging	$\Omega$ sagging
1	173.65	272.7 7	423.38	0.64	0.41	1.57	2.44
2	217.32	272.7 7	423.38	0.80	0.51	1.26	1.95
3	219.41	272.7 7	423.38	0.80	0.52	1.24	1.93
4	207.02	272.7 7	423.38	0.76	0.49	1.32	2.05
5	182.59	226.9 1	365.06	0.80	0.50	1.24	2.00
6	161.81	226.9 2	365.06	0.71	0.44	1.40	2.26
7	117.99	162.7 3	292.83	0.73	0.40	1.38	2.48
8	72.99	162.7 3	292.83	0.45	0.25	2.23	4.01

**Table 6.16: Values of  $\alpha^+$  and  $\alpha^-$** 

Floor	$\alpha^-$ (beam $M_{pl} = 511 \text{ kNm}$ )	$\alpha^+$ (beam $M_{pl} = 841 \text{ Nm}$ )
170 x 12	0.5338	0.5034
170 x 10	0.4441	0.4341
170 x 8	0.3185	0.3482

**Table 6.17: Check of the shear forces**

Floor	Ved capacity	Ved gravity	Ved design	Vrd	Usage
1	107.10	42.30	149.40	184.52	0.81
2	107.10	42.30	149.40	184.52	0.81
3	107.10	42.30	149.40	184.52	0.81
4	107.10	42.30	149.40	184.52	0.81
5	91.07	42.30	133.37	184.52	0.72
6	91.07	42.30	133.37	184.52	0.72
7	70.09	42.30	112.39	184.52	0.61
8	70.09	42.30	112.39	184.52	0.61

**6.6.2.2.4 Global dissipative behaviour**

Excluding the last floor, the ratio  $\max \Omega / \min \Omega$  yields a value of 1.26 for the hogging moments. Although a little bit over the speculated value, it is still possible to conclude that the structure presents a fairly good dissipative behaviour.

**6.6.2.2.5 Verification of the non-dissipative elements**

The reinforced beams and their span were designed to resist the full development of plastic hinges of the fuses and, therefore, they verify the safety check for the imposed seismic action. Since the columns are based on the conventional structure, they shall be safety checked (Table 6.18). The imposed column actions are estimated through Eq. (6.15) to Eq. (6.17). No bending-shear interaction are considered because the ratio of applied shear force to plastic shear resistance of the columns are lower than 0.5.

**Table 6.18: Resistance verification of the non-dissipative elements**

Column	Ped (kN)	Vz,ed (kN)	Vy,ed (kN)	Mx,ed (kNm)	My,ed (kNm)	Mny,rd (kNm)	Mnx,rd (kNm)	Usage
HEM360	315.60	144.81	27.45	54.92	344.82	1771.10	689.41	0.12
HEM450	687.35	195.19	29.38	58.97	439.36	2247.51	688.35	0.12
HEM500	1059.66	238.04	29.44	59.27	490.85	2518.37	685.86	0.12
HEM550	1431.29	267.31	16.15	44.35	1089.44	2816.22	687.64	0.21

### 6.6.3 Non-linear static analysis (Pushover)

#### 6.6.3.1 Evaluation of the non-linear behaviour of the structure

Nonlinear static (pushover) analysis is performed to verify the collapse mechanism and check the behaviour factor used in the linear analysis. The results presented hereafter are in accordance with the fundamental mode of vibration and uniform acceleration force distribution, both including P-delta effects.

The assignment of plastic hinges for the non-dissipative devices were already explained in 5.3. As for the welded FUSEIS, non-linear plastic hinges of bending type M3 are assigned, their properties being determined from calibration of experimental results and analytic investigations (also explained in the present document). A moment-rotation diagram is presented for one of the welded FUSEIS beam splice in Fig. 6.18. It should be noted that Pivot type hysteric curve were chosen for the plastic hinges.

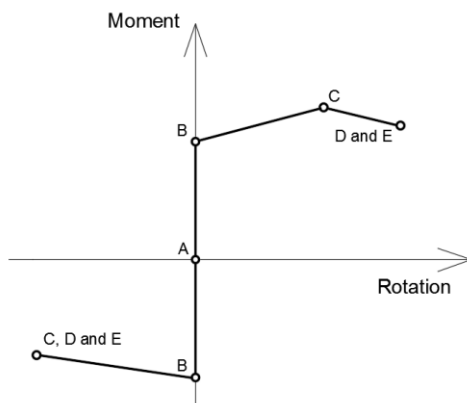


Fig. 6.18: Schematic representation of a welded FUSEIS hinge moment-rotation diagram

**Table 6.19: 170 x 10 flange plate fuse hinge properties. SF – scale factor**

Point	Moment SF	Rotation SF
E	-0.750	-10.453
D	-0.750	-10.453
C	-0.750	-10.453
B	-1.000	-1.000
A	0.000	0.000
B	1.000	1.000
C	1.595	10.453
D	1.276	13.501
E	1.276	13.501
<b>Yield Moment for SF</b>		<b>228.93 kN - hogging and sagging</b>
<b>Yield Rotation for SF</b>		<b>0.0037 rad - hogging and sagging</b>

These hinges present a maximum rotation of 38 to 40 mrad, which is above the minimum rotation speculated in the code. The safety criteria to assess the performance point were set according to Table 6.20 which are approximately 10, 60 and 80 percent of the beam splice's ultimate rotation.

**Table 6.20: Values for safety criteria**

Safety level	Immediate Occupancy (IO)	Life Safety (LS)	Collapse Prevention (CP)
Hinge rotation SF	-1 / 1	-6 / 6	-8 / 8

A pushover curve using link properties is performed as well to further assess the pushover curve obtained with the plastic hinge method. The link properties equivalent to the ones presented for the hinge approach are given in Fig. 6.19 and Table 6.21. It should be noted that the positive descendant branch is crucial to

reproduce the reduction in forces after the collapse of the fuses while the negative one can somewhat mimic the reduction in forces due to buckling effects.

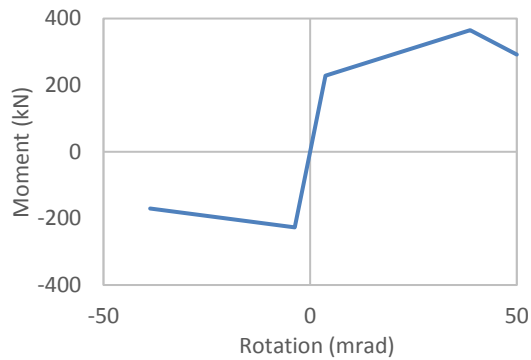


Fig. 6.19: Schematic representation of a welded FUSEIS link moment-rotation diagram

Table 6.21: 170 x 10 flange plate fuse link properties.

Point	Rotation (rad)	Moment (kNm)
1	-0.0387	-170.187
2	-0.0037	-226.916
3	0.0000	0.0000
4	0.0037	228.9388
5	0.0387	365.0577
6	0.0500	292.0461

**Stiffness for  
linear  
analysis cases**

61816 kNm/rad

The resulting pushover curves based on the link approach are presented in Fig. 6.20.

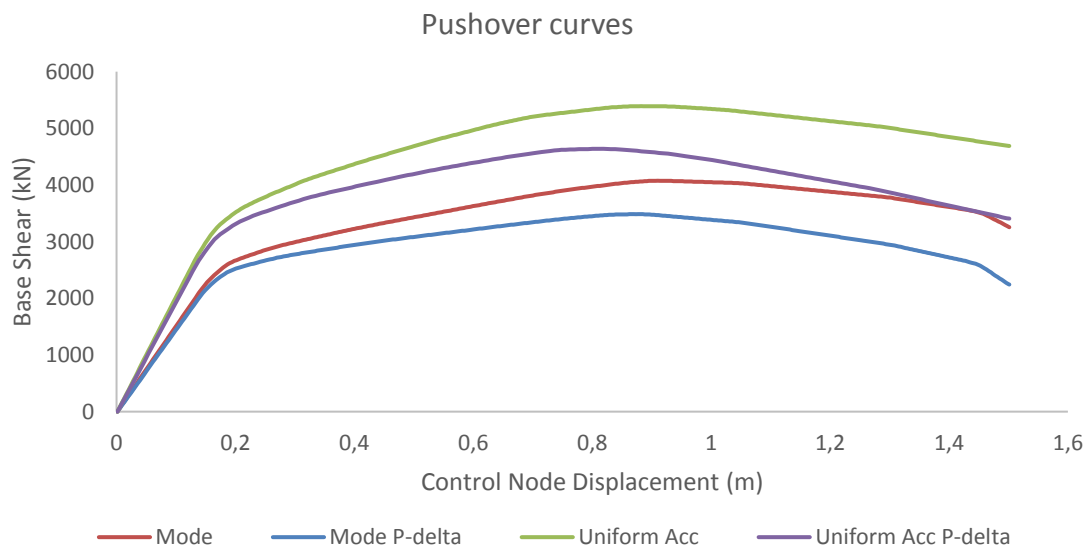


Fig. 6.20: Pushover curves from the link approach

The curve considering 1<sup>st</sup> mode force distribution with P-delta effects is further studied herein. The associated performance point and plastic hinge formation sequence are illustrated. These findings will then be compared to the results obtained from the linear elastic analysis.

The performance point is calculated with the N2 method speculated in Eurocode 8. The resulting displacement, its period and mobilized behaviour factor (estimated with method one as proposed by POLIMI3) are represented in Table 6.22 whereas the non-idealized and the idealized (1<sup>st</sup> iteration and at performance point) pushover



curves of the equivalent single degree of freedom structure are illustrated in Fig. 6.21.

**Table 6.22: Performance point characteristics**

Performance point displacement (m)	Corresponding period $T^*$ (s)	Mobilized behaviour factor $q$ at performance point
0.345	2.048	2.155

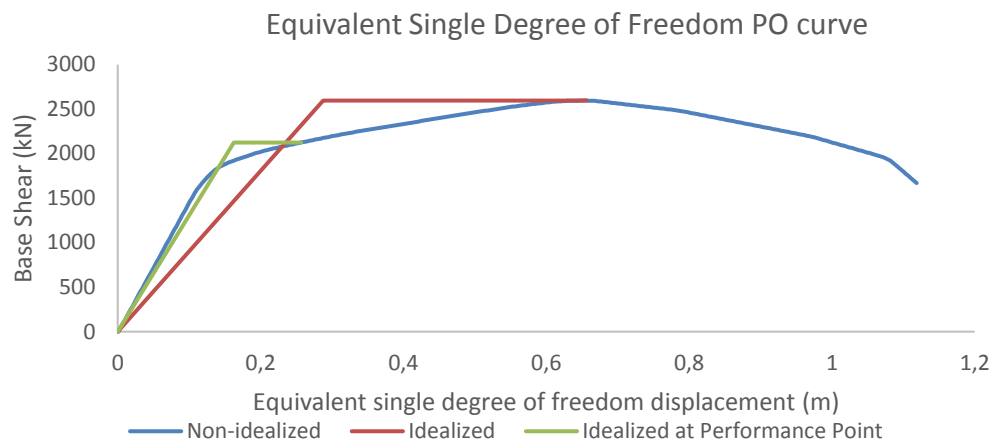


Fig. 6.21: Equivalent single degree of freedom PO curves

Fig. 6.22 shows that the pushover curves obtained from both analysis (link and hinge) are in almost perfect match. Hence, the plastic hinge formation sequence, in particular the one at the performance point, maybe directly obtained based on the plastic hinge pushover curve.

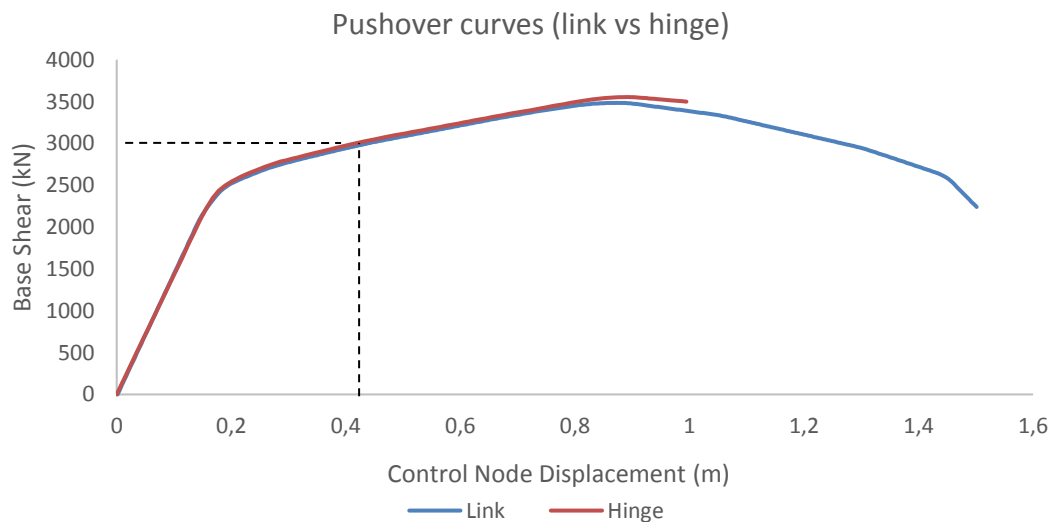


Fig. 6.22: Comparison between pushover curves obtained by the two approaches

The plastic hinge distribution at first yield, at performance point and at the first hinge collapse for the pushover is given in Fig. 6.23(a) to (c). First yield occurred at a welded FUSEIS placed on the interior frame due to the mobilization of higher moments. It is possible to observe that the beam splices effectively protected the non-structural elements from yielding during the entire force application procedure.

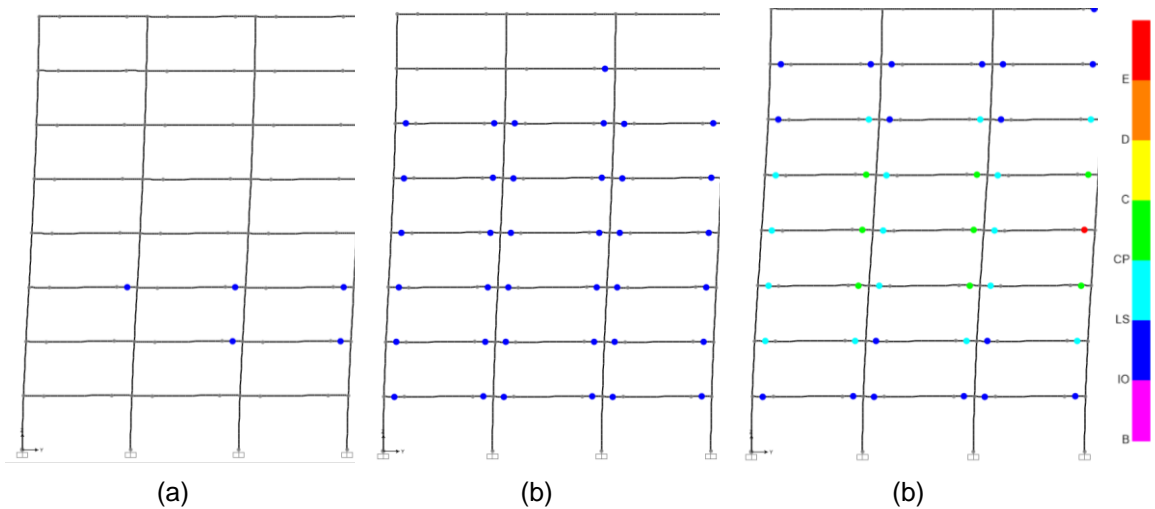


Fig. 6.23: Plastic hinge development sequence (a) first hinge, (b) at performance point and (c) first hinge collapse

Fig. 6.24 shows that the performance point is located in the region between immediate occupancy and life safety which somewhat indicates the possibility to reutilize the building by performing the necessary repairs only (substituting the beam splices in this case) after the earthquake.

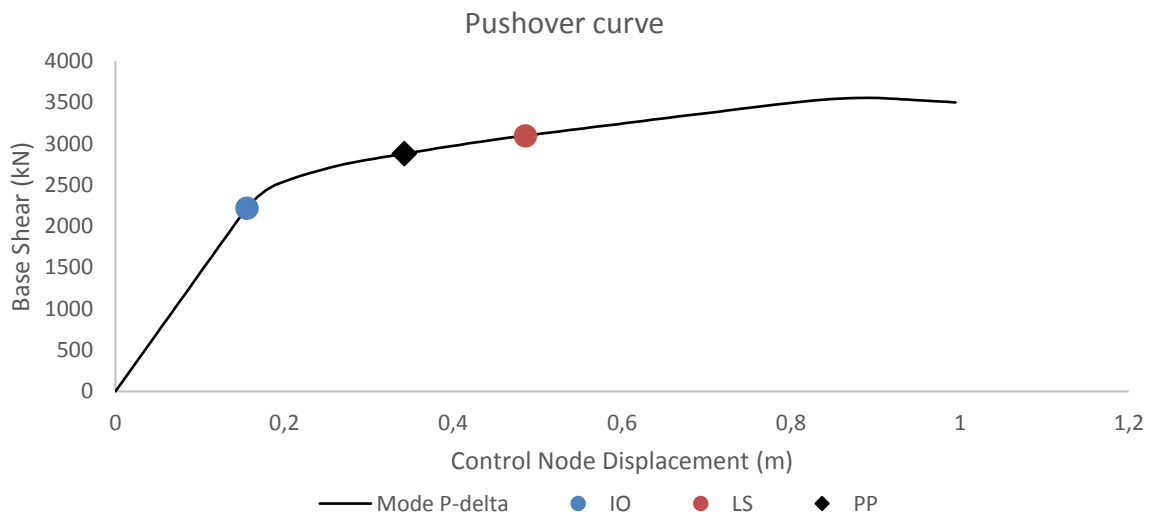


Fig. 6.24: Assessment of performance point

### 6.6.3.2 Interstorey drift at performance point

The interstorey drift at performance point for each floor is presented in **Table 6.23**. The values show that the maximum drift is 2.15% which is below the maximum established in 6.5.2.2.5.

**Table 6.23: Interstorey drift at performance point**

Floor	d (m)	dr (m)	h (m)	drift (%)
1	0.025	0.025	4.000	0.625
2	0.084	0.059	4.000	1.470
3	0.164	0.080	4.000	1.993
4	0.249	0.086	4.000	2.148
5	0.329	0.080	4.000	2.000
6	0.392	0.063	4.000	1.575
7	0.432	0.040	4.000	0.998
8	0.450	0.018	4.000	0.440

### 6.6.3.3 Evaluation of the behaviour factor

The approach, proposed by POLIMI<sup>4</sup>, to evaluate the behaviour factor bases on the information of the structure's pushover curve. It considers over twenty different methodologies to define the two variables necessary to calculate the behaviour factor: the overstrength ( $\Omega$ ) and ductility factor ( $\mu$ ) (see Eq. (6.20)).

$$q = \mu \cdot \Omega \quad \text{Eq. (6.20)}$$

Herein, five of the twenty plus methods are chosen to check whether the applied behaviour factor in the linear elastic analysis is acceptable. These five methods were considered the ones that best suited the proposed structure. **Table 6.24** gives the behaviour factor estimated by each of the five methods.

**Table 6.24: Evaluation of behaviour factor**

Method	q
1	3.81
4	4.63
5	4.40
6	3.43
7	3.26
Average	3.91

<sup>4</sup> Methods presented in Attachment A

The values vary between 3.26 to 4.63, with an average value of 3.91. The applied behaviour factor is acceptable because its value locates inside the calculated interval. However, it should be noted that the provided interval is only a rough estimation of the behaviour factor since only the five best suited methods were used. A more precise study should be done considering all the methods. Nevertheless, one can always perform a conservative design by using a lower behaviour factor.

## **6.7 CONCLUDING REMARKS**

The above study introduces the innovative lateral force resisting MRFs with welded FUSEIS beam splices and illustrates their successful application on steel and composite buildings in seismic regions. A number of experimental and numerical analyses were carried out to evaluate its performance and determine the critical parameters for their design. Emphasis was given on the seismic design process, assisted by nonlinear static finite element analysis of a representative framed structure. Focusing on global behaviours, some of the important structural properties such as materials, members, connections, global and local stability and dynamic P-delta effects were taken into consideration. The study has revealed some of the important global performance characteristics of the system, the following observations are worth noting:

- a) The system exhibits a very good behaviour under seismic loading: relatively strong and stiff with large capacity of energy absorption.
- b) Because the main aim is to have the fuses working in the plastic regime they are more useful in low rise buildings. For high rise buildings with high flexibility, the governing parameter in its design is the coefficient of sensibility or the interstorey drift value which may lead to an overdesigned solution in terms of resistance. If that is the case and to ensure that the  $\alpha$  parameter does not go below a certain limit, the beam splices might be too resistant and, thus, their yielding will be prevented.
- c) Inelastic deformations are strictly limited to the dissipative fuses preventing the spreading of damage into the rest of the structural members. The fuses are easily fabricated, installed and removed, since they are small and with a simple detail. By appropriate selection of their sections, sequential and controlled plastification of the fuse are possible.
- d) Code relevant design rules for the seismic design of frames with welded FUSEIS, including practical recommendations on the selection of the appropriate fuses and member verifications, have been formulated in a Design Guide. Structural details and constructional measures were also defined.

Conclusively, it may be noted that the present research, in line with the international trend in seismic engineering, introduces “intelligent” systems that are able to dissipate the seismic input energy and may be easily replaced and repaired, if required. The adoption of welded FUSEIS MRFs systems enhances the well-known

advantages of steel under seismic conditions and provides better solutions in terms of economy and safety.

The innovative fuses may be applied to multi-storey steel buildings and substitute the conventional systems used worldwide (such as concentric and eccentric braced frames, etc.) by combining ductility and architectural transparency with stiffness. The application of the system provides a more accurate and less expensive design of a building. The steel quality of the dissipative fuses can be controlled and thus their resistance can be calibrated avoiding excessive overstrength. Additionally, their easy replacement after the earthquake prevents the total replacement of main structural members.

## 6.8 REFERENCES

- [1] Agatino, M.R. (1995), "Criteri di collasso e modelli di danneggiamento per dettagli strutturale in acciaio soggetti a carichi ciclici", MSc Thesis, Politecnico di Milano. (in Italian)
- [2] BS EN 10002-1:2001: Tensile testing of metallic materials. Method of test at ambient temperature
- [3] Calado, L. and Castiglioni, C.A. (1996), "Steel beam-to-column connections under low-cycle fatigue: Experimental and numerical research", Proceedings of 11th WCEE, Acapulco, Mexico, August.
- [4] Calado L, Proença JM, Espinha M, Castiglioni CA, Vayas I. "Hysteretic behaviour of dissipative devices for seismic resistant steel frames (FUSEIS 2)". Proceedings of the 7<sup>th</sup> International Conference on Behaviour of Steel Structures in Seismic Areas – STESSA2012; 2012.
- [5] Calado L, Proença JM, Espinha M and Castiglioni CA. "Hysteretic behavior of dissipative welded fuses for earthquake resistant composite steel and concrete frames." *Steel and Composite Structures* 14, no. 6 (2013): 547-569.
- [6] Castiglioni, C.A. and Pucinotti, R. (2009), "Failure criteria and cumulative damage models for steel components under cyclic loading", J. Constr. Steel Res., 65(4), 751-765.
- [7] ECCS document: Recommended testing procedure for assessing the behavior of structural steel elements under cyclic loads, Technical committee 1: structural safety and loadings, Technical working group 1.3: seismic design; 1986.
- [8] EN1990, Eurocode 0: Basis of structural design. Brussels: Comitee Europeen de Normalisation (CEN); 2002.
- [9] EN1991-1-1, Eurocode 1: Actions on structures - Part 1-1: General actions - Densities, self-weight, imposed loads for buildings. Brussels: Comitee Europeen de Normalisation (CEN); 2002.
- [10] EN1993-1-1, Eurocode 3: Design of steel structures - Part 1-1: General rules and rules for buildings. Brussels: Comitee Europeen de Normalisation (CEN); 2003.
- [11] EN1993-1-5, Eurocode 3: Design of steel structures - Part 1-5: Plated structural elements. Brussels: Comitee Europeen de Normalisation (CEN); 2004.
- [12] EN1993-1-8: Eurocode 3: Design of steel structures. Part 1-8: Design of joints. Brussels: Comité Européen de Normalisation (CEN); 2004.
- [13] EN1994-1-1: Eurocode 4: Design of composite steel and concrete structures. Part 1-1: General rules and rules for buildings. Brussels: Comité Européen de Normalisation (CEN); 2005.
- [14] EN1998-1-1, Eurocode 8: Design of structures for earthquake resistance – Part 1-1: General rules, seismic actions and rules for buildings. Brussels: Comitee Europeen de Normalisation (CEN); 2003.

- [15] Espinha, M. (2011), "Hysteretic behaviour of dissipative welded devices for earthquake resistant steel frames", MSc Thesis, Instituto Superior Técnico, Technical University of Lisbon.
- [16] Gomes, A. and Appleton, J. (1997), "Nonlinear cyclic stress-strain relationship of reinforcing bars including buckling", *Eng. Struct.*, 19(10), 822-826.
- [17] Krawinkler, H. (2009), "Loading histories for cyclic tests in support of performance assessment of structural components", *Proceedings of the 3rd International Conference on Advances in Experimental Structural Engineering*, San Francisco, US, October.

## 6.9 ATTACHMENT A

### Behaviour factor estimation proposed by POLIMI

#### Method 1

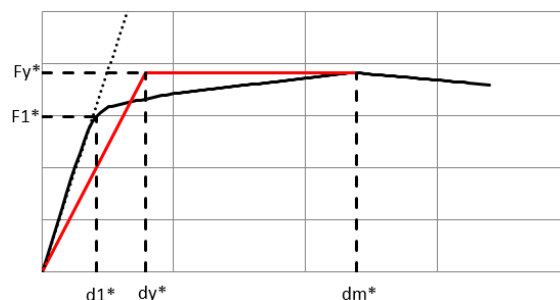


Fig. A.1: q-factor estimation proposed by POLIMI - Method 1

#### Method 4 and 5

Method 4:  $\Omega = \frac{F_y^*}{F_1^*}$

Method 5:  $\Omega = \frac{0.95F_y^*}{F_1^*}$

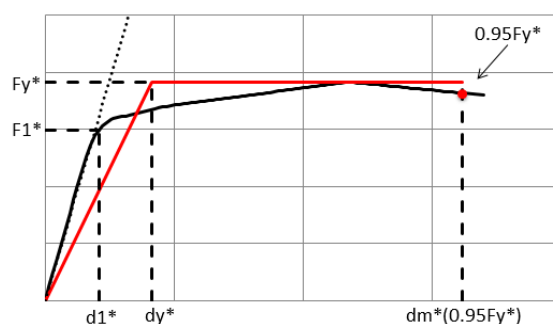


Fig. A.2: q-factor estimation proposed by POLIMI - Method 4 and 5

#### Method 6 and 7

Method 6:  $\Omega = \frac{F_y^*}{F_1^*}$

Method 7:  $\Omega = \frac{0.95F_y^*}{F_1^*}$

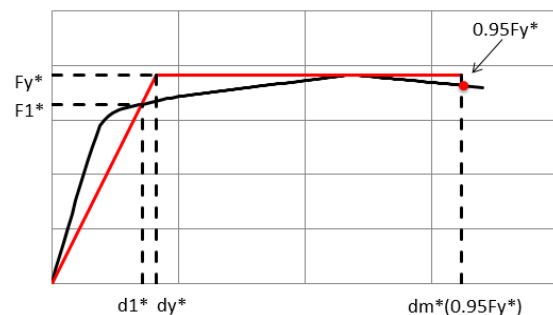


Fig. A.3: q-factor estimation proposed by POLIMI - Method 6 and 7





## 7 REPLACEABLE BOLTED LINK

### 7.1 INTRODUCTION

Conventional seismic design philosophy is based on dissipative response, which implicitly accepts damage of the structure under the design earthquake and leads to significant economic losses. Repair of the structure is often impeded by the permanent (residual) drifts of the structure. In order to reduce the repair costs and downtime of a structure hit by an earthquake, and consequently obtain a more rational design approach in the context of sustainability, the concepts of removable dissipative members and re-centring capability of the structure were employed. These concepts are implemented in a dual structure, obtained by combining steel eccentrically braced frames (EBFs) with removable bolted links with moment resisting frames (MRFs). The bolted links are intended to provide the energy dissipation capacity and to be easily replaceable, while the more flexible MRFs would provide the necessary re-centring capability to the structure. Re-centring dual eccentrically braced frames (D-EBF) with replaceable bolted links were previously studied and developed by Politehnica University Timisoara (UPT) in the frame of several research projects.

### 7.2 DESCRIPTION OF REPLACEABLE BOLTED LINKS SYSTEM

#### 7.2.1 *Principles of re-centring dual systems*

Most of the structures designed to modern codes would experience inelastic deformations even under moderate seismic action, with permanent (residual) displacements after an earthquake. Repair is difficult in such cases. Solutions providing self-centring of the structure exist, but are technically demanding (post-tensioned strands, shape memory alloy devices, etc.). An alternative solution is the one that provides re-centring capability (as opposed to self-centring), through removable dissipative members and dual (rigid-flexible) structural configuration.

Structural systems that aim at reducing structural damage by isolating plastic deformations in removable or "repairable" fuses, and have the ability to return to the initial un-deformed shape after an earthquake have received much attention.

As proposed by Stratan and Dubina [1-2], in order to provide the re-centring capability of a structure with eccentrically braced frames with removable dissipative members, it was suggested to use dual structural configurations, obtained by combination of EBFs and moment resisting frames (MRFs). If the more flexible MRFs are kept elastic (a possible way to favor this is to realize some members from high-strength steel), they would provide the restoring force necessary to re-centre the structure upon removal of damaged removable links.

An idealized dual system consisting of two inelastic springs connected in parallel is shown in Fig. 7.1a. In order to provide the re-centring capability, the flexible

subsystem should be kept in the elastic range up to the displacements at which the rigid subsystem attains its ultimate plastic deformation capacity. However, a conventional dual system that satisfies this condition will not return to the initial position following deformations into the inelastic range, even if permanent displacements  $\delta_{pD}$  in the dual system are smaller than the ones that would be obtained in a rigid system alone  $\delta_{pr}$  (Fig. 7.1b). Permanent deformations can be eliminated if the rigid subsystem is realized to be removable. Upon unloading of the dual system, there is a permanent displacement  $\delta_{pD}$ , and corresponding residual forces in the flexible ( $F_{pf}$ ) and rigid ( $F_{pr}$ ) subsystems. Once removable dissipative members are dismantled, stiffness and strength of the system is provided by the flexible subsystem alone ( $F_{pr}=0$ ). If the flexible subsystem is still in the elastic range, it will return the system to the initial position, implying zero permanent deformations (Fig. 7.1c).

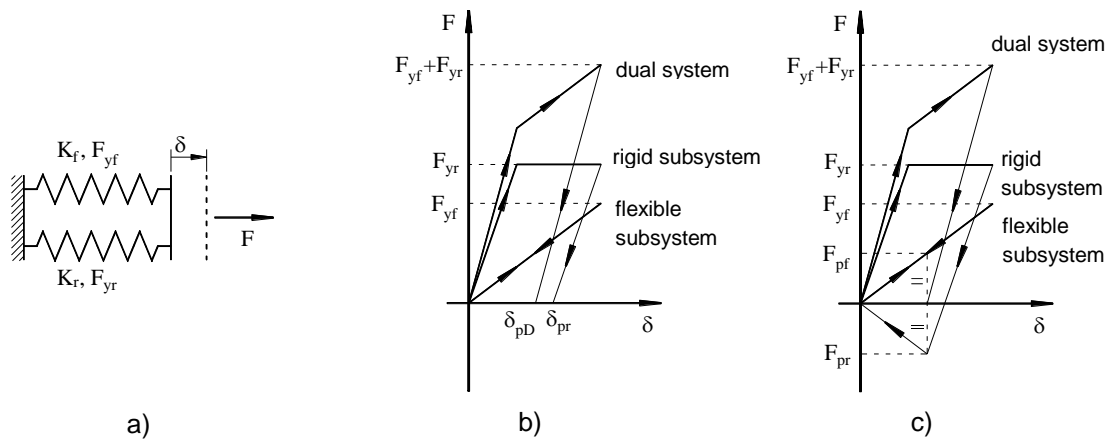


Fig. 7.1: Simplified model of a generalized dual system (a), and permanent deformations in a conventional dual system (b) and in a dual system with removable dissipative members (c)

### 7.2.2 Description of D-EBF systems

Application of the concept of removable dissipative members to EBFs, where links act as dissipative zones, is presented in Fig. 7.2. The link to beam connection is realized by a flush end-plate and high-strength friction grip bolts. The main advantage over other dissipative devices is that removable links can be designed using methods readily available to structural engineers and can be fabricated and erected using procedures standard to the profession.

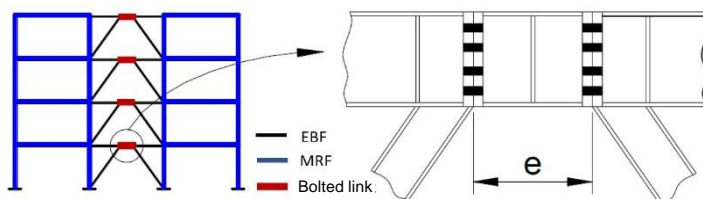


Fig. 7.2: Replaceable link concept

The re-centring of the system is attained by designing the structure as a dual frame, combining EBFs and MRFs. The elastic response of the flexible subsystem (MRFs) provides the restoring forces, once the links damaged during an earthquake are removed. For this principle to be efficient the flexible subsystem should remain in the elastic range.

The solution was validated experimentally using component and system tests. An experimental program was carried out at UPT, CEMSIG Research Centre, to determine cyclic performance of isolated bolted links [1-2] and another at the European Laboratory for Structural Assessment (ELSA) of the Joint Research Centre (JRC) in Ispra, Italy, to validate the feasibility of the proposed solution through a pseudo-dynamic testing campaign of a full-scale model of a dual EBF structure [3].

### 7.3 EXPERIMENTAL INVESTIGATIONS ON REPLACEABLE BOLTED LINKS SYSTEM

#### 7.3.1 *Experimental investigations on individual links*

##### 7.3.1.1 *Experimental setup and tested bolted links*

An experimental program was carried out at UPT, CEMSIG Research Centre, to determine cyclic performance of bolted links [1-2], for which the experimental set-up of only isolated link is presented in Fig. 7.3.

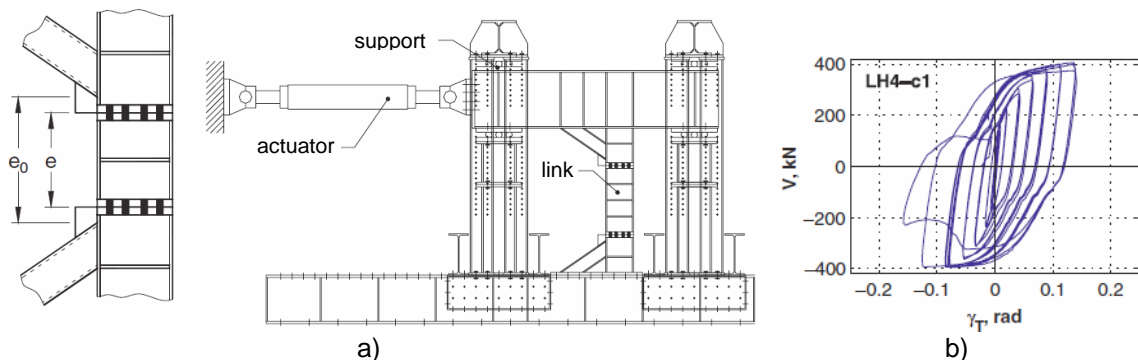


Fig. 7.3: a) Experimental set-up and b) force–total deformation relationship  $V$ – $\gamma_T$  for specimen LH4-c1 [1].

The removable link was fabricated from IPE240 profile of S235 grade steel, while the rest of the structure – from S355 grade steel. Four link lengths were considered:  $e_0=400$  (denoted with 4), 500 (denoted with 5), 600 (denoted with 6) and 700 (denoted with 7) mm, with “rare” (L) and “close” (H) spacing of stiffeners, and all links were classified as short ones according to AISC [4] and EN1998-1-1 [5]. During this experimental program, small height section links were investigated, the same as the ones from the DUAREM Project (240 mm section height). The complete ECCS 1985 [6] loading procedure was then applied, consisting of one monotonic (m) and two

cyclic (c1 and c2) tests for each specimen. Meanwhile, for future investigations on links, AISC [4] has a dedicated loading protocol that is recommended.

The strategy adopted for the design of the flush-end plate connections was to provide sufficient over-strength of the connection over the link shear resistance. A reduction in total initial stiffness of the bolted link in comparison with the classical solution, as a result of both the semi-rigid end-plate and slip in the connection, was observed. Therefore, it was concluded that either explicit modelling of the semi-rigid connection behavior or consideration of equivalent link stiffness is necessary for global analysis of frames with bolted links.

### 7.3.1.2 Behavior of specimens

Table 7.1 shows that cyclic loading reduced by 40% to 70% rotation capacity, with the maximum reduction for short links. Rotation capacity increases slightly for shorter links, with the exception of LL4 and LH4 specimens.

**Table 7.1: Ultimate deformation  $\gamma_{Tu}$ , in radians**

Specimen	LL7	LL6	LL5	LL4	LH7	LH6	LH5	LH4
m	0.155	0.273	0.360	0.395	0.235	0.278	0.345	0.420
c1	0.097	0.129	0.106	0.101	0.114	0.143	0.170	0.126
c1	0.092	0.133	0.156	0.112	0.109	0.136	0.182	0.125

The behavior of long specimens was much influenced by the response of the bolted connection (see Fig. 7.4a), characterized by a gradual reduction in strength due to bolt thread stripping and a pinching cyclic response. The latter effect reduced the energy dissipated in the group of cycles of constant amplitude. Full bolt preloading reduced partially this effect. Response of short specimens was controlled by the shear of the link web (see Fig. 7.4b), characterized by important hardening and energy dissipation capacity, but a more rapid degradation in strength after web tearing. Stiffener spacing had maximum importance for short links. Their effect was to limit plastic local buckling of the web, increasing the maximum force and deformation capacity, and providing a more stable cyclic response. However, after the attainment of ultimate deformation, failure of LH4 specimens was more rapid in comparison with LL4 specimens.

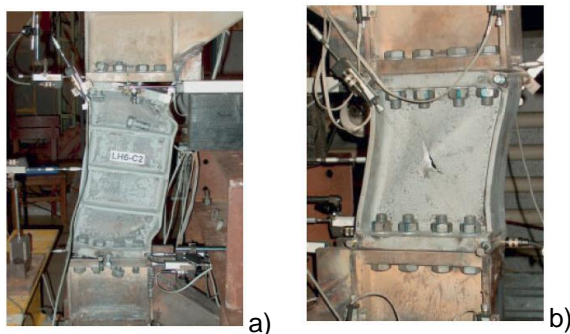


Fig. 7.4 Failure by connection degradation at the LH6-c2 specimen (a) and plastic web buckling at the LL4-c1 specimen (b) [1].

Therefore, choosing the link's length is of high importance, since in case of longer lengths ( $e < 1.6M_{p,link}/V_{p,link}$ , where  $M_{p,link}$  is the moment resistance of the link and  $V_{p,link}$  is the shear resistance of the link) is difficult to dimension an elastic flush end-plate connection that might get damaged and make the replacement procedure more problematic, as opposed to using very short links ( $e < 0.8M_{p,link}/V_{p,link}$ ), as was the case of both JRC and UPT tests.

From available tests, bolted links specimens with rare stiffeners showed a stable deformation capacity of at least 0.09 rad, while the ones with close stiffeners showed a stable de-formation capacity of at least 0.11 rad. In case of LH5 specimens, with a length  $e = 0.8M_{p,link}/V_{p,link}$ , the ultimate deformation capacity reached a value of at least 0.17 rad.

### 7.3.2 Experimental investigations on dual frames with replaceable bolted links

#### 7.3.2.1 Experimental program, setup and specimen

The validation of the proposed solution was realized through a pseudo-dynamic testing campaign of a full-scale model of a dual EBF structure at the European Laboratory for Structural Assessment (ELSA) of the Joint Research Centre (JRC) in Ispra, Italy within FP7 SERIES DUAREM Project ("Full-scale experimental validation of dual eccentrically braced frame with removable links").

The test specimen is presented in Fig. 7.5. There are 2 central EBFs and 4 MRFs on test direction that represent the lateral load resisting system.



Fig. 7.5 The test specimen: a) 3D view; b) plan layout [3].

Steel structural components were designed in S355 grade steel, with two exceptions. Grade S460 steel was used for columns and links were designed from S235 steel grade.

The testing sequence on the mock-up in the reaction wall facility of ELSA consisted in pseudo-dynamic (PsD) tests, together with some monotonic and link replacement tests [3].

One ground motion record was chosen (from seven selected by matching the elastic response spectrum used in design) to be used in the pseudo-dynamic tests in order

to evaluate the structural performance of the test structure, applied with several input levels (see Table 7.2, where  $a_{gr}$  is the reference peak ground acceleration and  $a_g$  represents the peak ground acceleration for a specific earthquake level):

**Table 7.2: Limit states and corresponding scaling factors for seismic input.**

Limit state	Performed PsD tests	Return period, years	Probability of exceedance	$a_g/a_{gr}$	$a_g/g$	Additional monotonic tests
Full Operation	FO1, FO2, FO3	-	-	0.062	0.020	
Damage Limitation	DL	95	10% / 10 years	0.59	0.191	
Significant Damage	SD	475	10% / 50 years	1.00	0.324	PO1
Near Collapse	NC	2475	2% / 50 years	1.72	0.557	PO2, PO3

The testing program was completed with two link replacement tests:

- First link replacement (LR1) – after DL test, where links were removed from the structure by unscrewing the bolts;
- Second link replacement (LR2) – after PO1 test, where links were removed by means of flame cutting with a torch;

### 7.3.2.2 Test results

FO tests were performed in order to assess the elastic response of the structure with each new set of links, before the main DL, SD and NC PsD tests, the selected seismic record being scaled to have the PGA of 0.02g. During these tests, the structure manifested an elastic response.

DL test was performed, in order to simulate a moderate earthquake, causing moderate structural damage, the selected seismic record being scaled to have the PGA of 0.191g. SD test was performed in order to simulate a stronger earthquake, causing larger structural damage, the selected seismic record being scaled to have the PGA of 0.324g. During these tests, no yielding was observed in the elements outside links and small to moderate maximum plastic deformations occurred in links. Minor to moderate cracks were observed in the concrete slab (see Fig. 7.6). The structure exhibited low residual top displacement. Also low residual inter-story drifts were observed.

PO1 test (a monotonic pushover test until an additional displacement of 55 mm) starting from the end of the SD test position was necessary. This was done to obtain larger residual displacements that were necessary in order to validate the feasibility of the link removal process and re-centring of the structure. During this test, no yielding was observed in the elements outside links. Higher maximum plastic deformations occurred in links (see Fig. 7.6). More visible cracks were observed in



the concrete slab (see Fig. 7.6). After this test, the structure exhibited significant larger residual top displacement. Larger residual inter-story drifts amounting were observed.

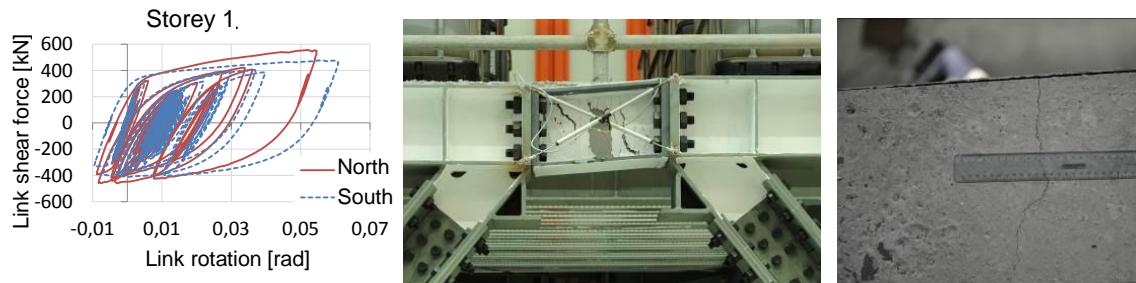


Fig. 7.6 PO1 test results [3]

Because after the DL test the structure exhibited low residual top displacement and low residual drifts were observed, the decision was to remove the first set of damaged links, by removing the bolts, on a level by level basis, starting from the lower level to the upper one. The low value of the residual top displacement from the end of the DL test decreased after the elimination of the damaged links. A new set of unused links was then mounted into the structure.

Because after the PO1 test the structure exhibited significant larger residual top displacement and larger residual drifts were observed, the decision was to remove the second set of damaged links, by flame cutting both the web and flanges of the links, from the top story downwards. The value of the residual top displacement from the end of the PO1 test was decreased after the elimination of the damaged links. A new set of unused links was then mounted into the structure.

NC test was proposed in order to simulate a much stronger earthquake and to obtain extensive damage throughout the structure, the re-centring capability being lost due to yielding in other members apart from the links, the selected seismic record being applied with a scaling factor of 0.557. This test was prematurely stopped because the available actuator capacity (1000 kN per frame at every floor) was not enough to carry it out with the imposed null torsion at every floor.

Another cyclic pushover test (PO2) with maximum displacement amplitudes of 150 mm was further proposed after the actuators' release of force from the NC test and afterwards a final cyclic pushover test (PO3) with maximum displacement amplitude of 400 mm. The last three tests brought extensive plastic behavior throughout the entire structure (see Fig. 7.7).

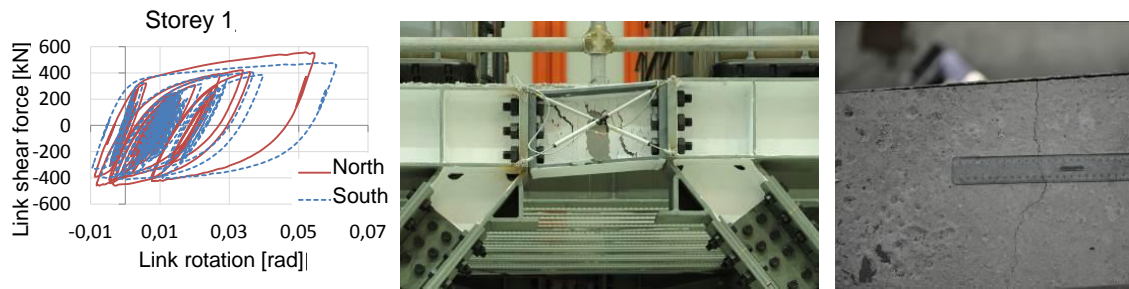


Fig. 7.7 State of the specimen after the last test [3]

The maximum link demand after PO1 test is of 0.075 rad (see Table 7.3), smaller than the acceptable criterion for this limit state adopted by FEMA356 [7], which is of 0.11 rad.

**Table 7.3: Deformation demands for links, in radians**

Test	DL	SD	PO1
Maximum link rotation [rad]	0.032	0.061	0.075
Residual link rotation [rad]	0.014	0.022	0.066

After the DL test, the structure exhibited a low residual top displacement of 5 mm (0.05%), the maximum top displacement being 32 mm. Also, a low residual inter-story drift amounting to a maximum of 3 mm (less than 0.1%) was observed. At the end of the LR1 procedure, a very small residual drift ( $H/5250$  for both frames) that is lower than the erection tolerance ( $H/300$ ) was observed, the structure being almost re-centred.

After the completion of PO1 test, the structure exhibited a significantly larger residual top displacement of 45 mm (0.43%), the maximum top displacement being 68 mm. Larger residual inter-story drift amounting to a maximum of 18 mm (0.5%) was observed. At the end of the LR2 procedure, a small residual drift ( $H/5250$  for the south frame and  $H/1750$  for the north frame) that was lower than erection tolerance was observed.

## 7.4 DESIGN RULES

### 7.4.1 Design procedure

Structural design of dual structures, obtained by combining steel eccentrically braced frames with removable bolted links and moment resisting frames, can be performed using general code-based approach (see Chapter 7.4.1.1), but some additional criteria (see Chapters 7.4.1.2 to 7.4.1.6) need to be considered.

A flowchart that briefly illustrates the design of D-EBFs is shown in Fig. 7.8.



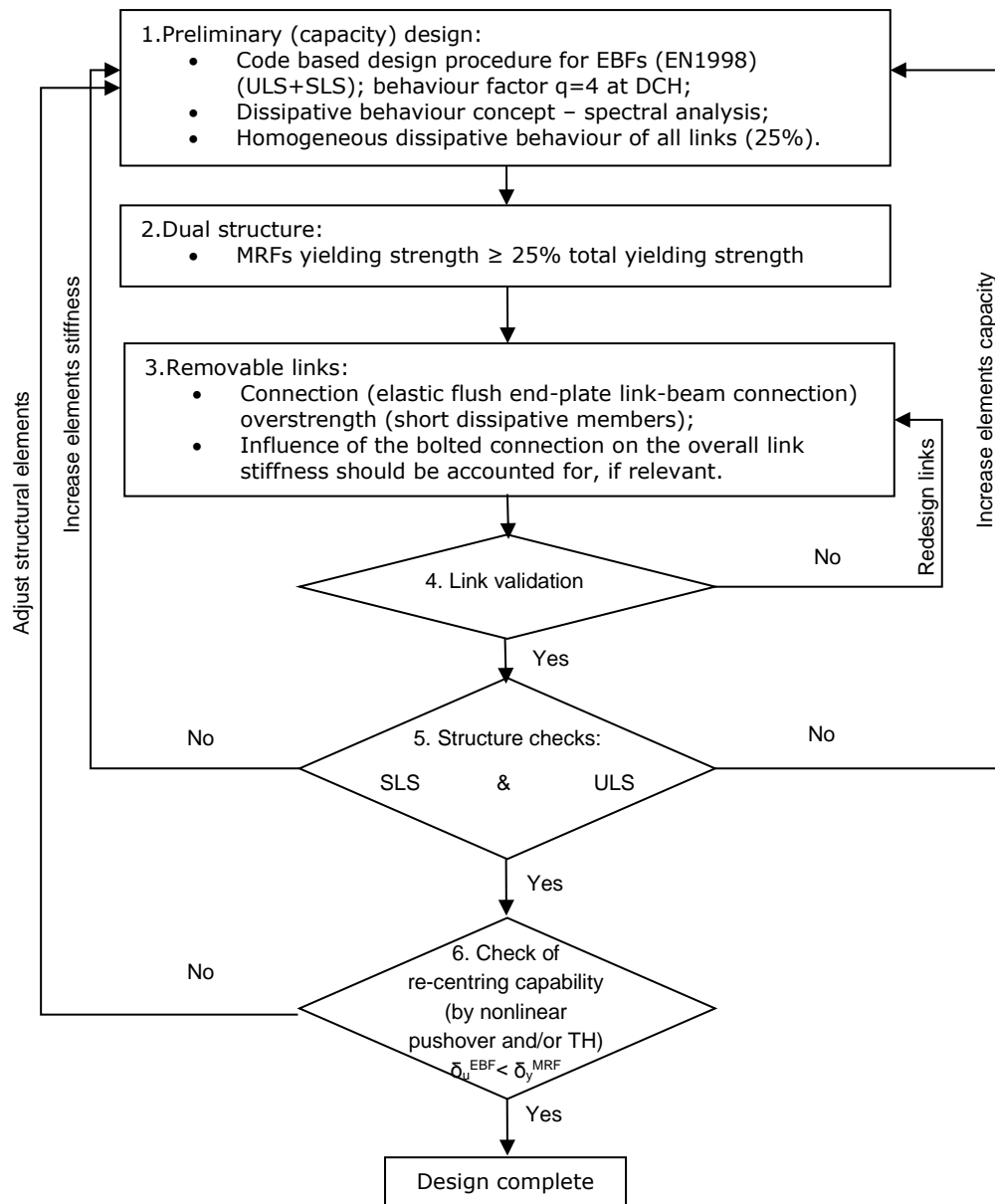


Fig. 7.8 Design flowchart for EBFs with removable links and re-centring capacity [3]

#### 7.4.1.1 General design rules

Gravitational loads and seismic action should be accounted for. Masses should be computed from 1.0·Dead+0.3·Live load combination. The capacity of structural elements should be determined using EN1993-1 [8] at Ultimate Limit State and deflections should be checked at Serviceability Limit State, using persistent situation load combinations.

A capacity design can be performed, according to EN1998-1 [5], to design moment resisting frames (where beams act as dissipative elements dissipating energy through bending) and eccentrically braced frames (where short links act as dissipative elements dissipating energy through shear). The dissipative behavior

concept is recommended. A global dissipative behavior of the structure should be achieved, checking that the individual values of the ratios  $\Omega_i$  for each short link not to exceed the minimum value  $\Omega$  by more than 25% [5].

Internal forces under seismic loading are determined using response spectrum analysis, where the number of modes of vibration considered in each direction is such that the sum of the effective mass is at least equal to 90% of the total mass. The capacity of structural elements should be checked at ULS and drifts should be checked at SLS, using seismic situation load combinations.

Global and local imperfections should be accounted for and the importance of second order effects should be checked.

#### 7.4.1.2 Dual configuration

The weaker, more flexible, subsystem (MRF) should provide a minimum strength of the structure. Therefore, the duality of the structure should be checked by verifying that the MRFs should be able to resist at least 25% of the total seismic force [9-11]:

$$F_y^{MRF} \geq 0.25 (F_y^{MRF} + F_y^{EBF}) \quad \text{Eq. (7.1)}$$

$$F_y^{EBF} = \frac{L}{H} V_{p,link} \quad \text{Eq. (7.2)}$$

$$F_y^{MRF} = \frac{4M_{pl,b}}{H} \quad \text{Eq. (7.3)}$$

where:  $F_y^{MRF}$  is the yield strength of MRF,  $F_y^{EBF}$  is the yield strength of EBF,  $L$  is the frame span,  $H$  is the frame story height,  $V_{p,link}$  is the shear strength of the link and  $M_{pl,b}$  is the beam plastic moment.

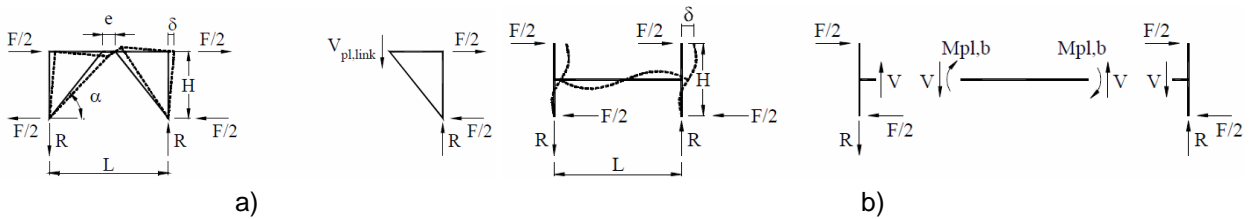


Fig. 7.9: Basic one-story a) EBF and b) MRF components [11].

#### 7.4.1.3 Replaceable links

The links should be designed as removable and replaceable (bolted). This can be done by using a flush end-plate link-beam connection that should be kept elastic. This means that the connection should have a design shear force  $V_{j,Ed}$  and bending moment  $M_{j,Ed}$  corresponding to a fully yielded and strain hardened link, computed as follows:

$$V_{j,Ed} = \gamma_{sh} \gamma_{ov} V_{p,link} \quad \text{Eq. (7.4)}$$

$$M_{j,Ed} = \frac{V_{j,Ed} e}{2} \quad \text{Eq. (7.5)}$$

where  $\gamma_{ov}$  is 1.25 and  $\gamma_{sh}$  is adopted as 1.8 for DCH (according to DUAREM project results) and 1.5 for DCM.

In order to achieve the connection over-strength, very short dissipative members were adopted (with length  $e$  as small as  $0.8M_{p,link}/V_{p,link}$ , where  $M_{p,link}$  is the moment resistance of the link and  $V_{p,link}$  is the shear resistance of the link).

It is considered that the bolted connection has no influence on the overall link stiffness because of preloading of bolts.

#### 7.4.1.4 Re-centring capability

The issue of permanent (residual) deformations of the structure after a damaging earthquake, which can lead to difficulties in replacing removable links, can be solved by realizing a structure as a dual one, by combining EBFs with MRFs. If the more flexible MRFs are kept elastic (a possible way to favor this is to realize some members from high-strength steel) and the plastic deformations are constrained to removable dissipative members only, the MRFs would provide the restoring force necessary to re-centre the structure upon removal of damaged removable links.

In order to verify the re-centering capability of eccentrically braced frames with removable links structures, the ultimate displacement of the EBFs ( $\delta_u^{EBF}$ ) at ultimate limit state (ULS) (corresponding to the plastic deformation capacity of the link) should be smaller than the yield displacement of the MRFs ( $\delta_y^{MRF}$ ), meaning the yielding in MRFs is prevented up to the attainment of ultimate deformation capacity in the EBFs with removable links. This can be done analytically, using formulas below [11]:

$$\delta_u^{EBF} = \delta_y^{EBF} + \delta_{pl}^{EBF} = \frac{F_y^{EBF}}{K^{EBF}} + \frac{e}{L} H \quad \gamma_{pl,\mu} < \delta_y^{MRF} = \frac{F_y^{MRF}}{K^{MRF}} \quad \text{Eq. (7.6)}$$

$$K^{EBF} = \frac{K_{link}^{EBF} K_{br}^{EBF}}{K_{link}^{EBF} + K_{br}^{EBF}} \quad \text{Eq. (7.7)}$$

$$K_{link}^{EBF} = \frac{L}{H^2} (L - e) \frac{G A_s}{e} \quad \text{Eq. (7.8)}$$

$$K_{br}^{EBF} = 2 \frac{E A}{I_{br}} \cos^2 \alpha \quad \text{Eq. (7.9)}$$

$$K^{MRF} = \frac{4}{H^2 \left( \frac{L}{6 E I_b} + \frac{H}{12 E I_c} \right)} \quad \text{Eq. (7.10)}$$

where  $\delta_y^{EBF}$  is the yield displacement of the EBF,  $\delta_{pl}^{EBF}$  is the plastic displacement of the EBF,  $K^{EBF}$  is the EBF stiffness,  $e$ ,  $L$  and  $H$  are illustrated in Fig. 7.9,  $\gamma_{pl,u}$  is the plastic deformation capacity of the link,  $K^{MRF}$  is the MRFs stiffness,  $K_{link}^{EBF}$  is the link's stiffness,  $K_{br}^{EBF}$  is the braces stiffness,  $G$  is the shear modulus,  $A_s$  is the link shear area,  $E$  is the Young's modulus,  $A$  is brace cross-section area,  $l_{br}$  is the brace length  $\alpha$  is the brace angle.

This analytical procedure should be used as a pre-design of re-centring capability and is recommended for low-rise structures, where lateral deformation of the structure is dominated by a shear-type response. It could also be used as pre-design for mid-rise and high-rise buildings (where a global bending behavior may arise in elevation), but re-centring of is strongly recommended to be checked through pushover and/or time-history analyses.

Because using formulas is an approximate and simplified approach, nonlinear static and/or dynamic analyses are recommended for all structures in order to check the re-centering capability. Modelling for this type of analyses is presented in Chapters 7.4.2 and 7.4.3.

#### 7.4.1.5 Appropriate behavior factor

The necessity of having very short links (as short as  $e=0.8M_{p,link}/V_{p,link}$ ) because of using a non-dissipative flush end-plate bolted connection (see Chapter 7.4.1.3) leads to larger deformation demands in links under the design seismic motion. As a result, EBF frames with very short links fail to fulfil the performance requirements at ULS when designed for a behavior factor  $q=6$  at DCH. In order to reduce these requirements and obtain acceptable performance is necessary to limit the behavior factor  $q$  at 4 at DCH. In case of DCM a behavior factor of 2.5 is recommended.

#### 7.4.1.6 Link validation

All the additional design requirements presented above lead to the necessity of short removable links prequalification (validation) [12]. Since there's only a limited number of experimental tests on short bolted links involving this type of connection (flush-end plate) and link section (I section with 240 mm height), when using other types of sections and connections it is recommended to confirm the links performance through experimental validation and/or numerical testing.

### 7.4.2 Modelling for static non-linear (pushover) analysis

In order to perform pushover analysis, nonlinear behavior has to be defined, both for materials used, as well as for structural members.

Expected (based on  $\gamma_{ov}$ ) material properties should be used for dissipative elements and nominal material properties for non-dissipative elements.

Nonlinear plastic hinges of bending type M3 should be assigned at the ends of the MRFs beams and of bending with axial force type P-M3 at the ends of columns and EBFs beams. For braces, nonlinear plastic hinges of axial type P may be used, being assigned at the middle of bars. These properties may be computed according to ASCE41-13 [13].

Calibration of numerical model of D-EBFs with replaceable links, based on experimental results from DUAREM program, was performed, obtaining a good match in terms of global and storey behaviour (see Fig. 7.10).

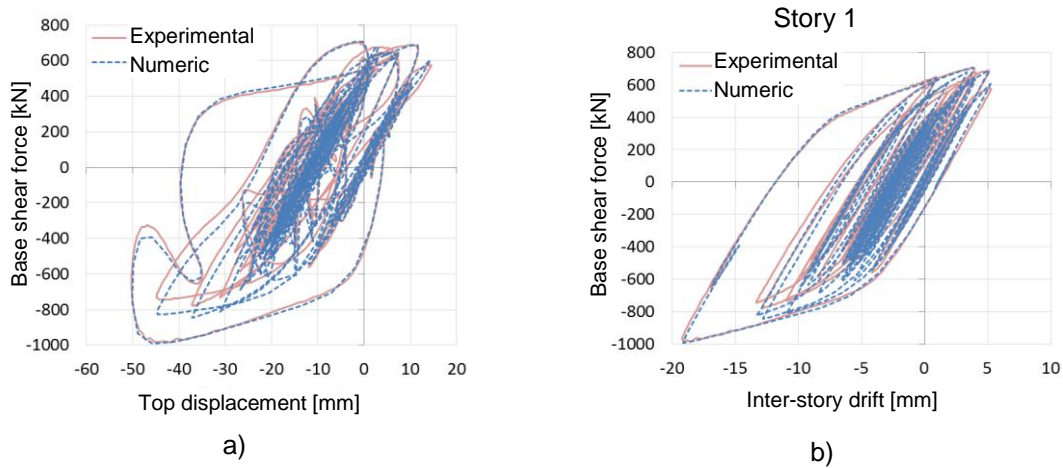


Fig. 7.10: Global a) and storey b) behavior.

In order to account for the short links nonlinear behaviour in shear ( $V_2$ ), multi-linear plastic link elements should be defined, with shear nonlinear behaviour, described by the following backbone curve (Fig. 7.11):

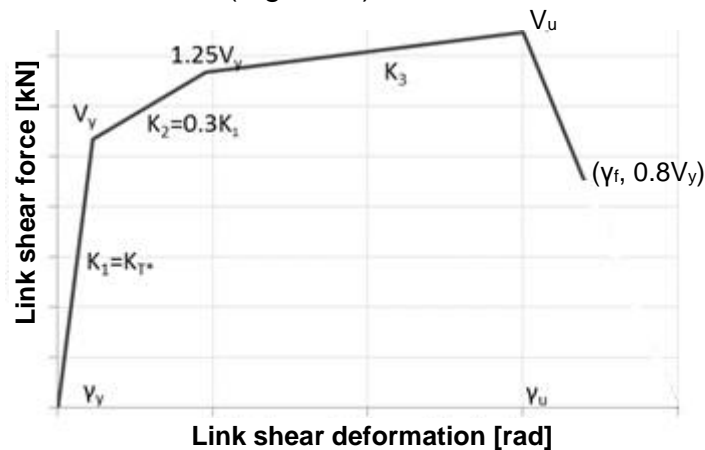


Fig. 7.11: Shear links nonlinear behavior.

where:  $K_1$  is the initial (elastic) stiffness of the link (accounting for shear and bending stiffness),  $V_y$  is the shear resistance of links ( $V_{p,link}$ ),  $V_u$  is considered  $1.8V_y$  in case of DCH and  $1.5V_y$  in case of DCM,  $\gamma_u$  is the ultimate shear rotation considered 0.15

rad for DCH and 0.1 rad for DCH and  $\gamma_f$  was considered 0.17 rad for DCH and 0.11 rad.

Link elements with the above properties are to be assigned between end-joints of every bolted link and the short links bars are to be pinned at the ends.

Pushover analysis should be performed in displacement control, until reaching a monitored displacement at the top of the structures. Firstly, gravitational loads (from load combination  $1.0 \cdot \text{Dead} + 0.3 \cdot \text{Live}$ ) should be applied in force control and secondly, lateral forces under a modal distribution will act on the analyzed frames in displacement control.

#### 7.4.3 Modelling for dynamic non-linear (time-history) analysis

As well as in case of pushover analysis, nonlinear behavior has to be defined, both for materials used, as well as for structural members when performing dynamic nonlinear (time-history) analyses.

Multi-linear plastic link elements, defined for pushover analysis to account for the nonlinear behavior in shear of the short links, should be appropriately modified to include the hysteretic behavior. A “smooth” hysteresis loop, as described by Sivaselvan and Reinhorn [14-15] was successfully used when calibrating experimental results from DUAREM project, using time-history analysis (see Fig. 7.12). It has been formulated with rules for stiffness and strength degradation, and pinching. Twenty-two parameters need to be defined in order to fully characterize this response curve. There are two groups of parameters: common parameters, related to the backbone curve, and then specific parameters for the hysteretic rules. The set of parameters for hysteretic rules used in case of the above mentioned calibration are presented below.

**Table 7.4: Example of parameters for hysteretic behaviour of “smooth” loop**

Specific parameter	Value
Stiffness degrading parameter	20
Ductility-based strength decay parameter	0.001
Hysteretic energy-based strength decay parameter	0.001
Smoothness parameter for elastic-yield transition	0.5
Parameter for shape of unloading	0.2
Slip length parameter	0
Slip sharpness parameter	100
Parameter for mean moment level of slip	0
Exponent of gap closing spring	10
Gap closing curvature parameter	1000
Gap closing stiffness coefficient	1

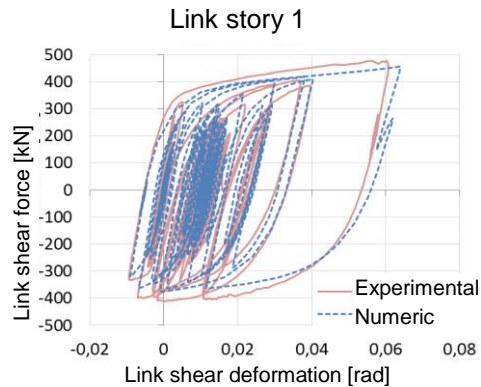


Fig. 7.12: Shear link numerical calibration.

## 7.5 ANALYSIS OF 2D BUILDING FRAMES

Application of the design procedure described in chapter 7.4 on a case-study structure is shown in the following. Initially the frames were designed through elastic analysis at ULS and SLS. Nonlinear static analyses followed to investigate their behaviour beyond the elastic range.

### 7.5.1 Description of examined building frames

#### 7.5.1.1 Geometry and assumptions

The case study presented hereafter consists of designing and analyzing 2 four-story and 2 eight-story buildings. The common plan view for the buildings is presented in Fig. 7.13a. The number of bays in both directions is 3, with a span length of 8m. The height of each story is 4m. The main lateral load resisting system is composed of four MRFs and two EBFs on transversal direction and two MRFs and two EBFs on longitudinal direction. The marginal frames on transversal direction consist of dual steel frames, combining two moment resisting frames (MRFs) (which provide the necessary re-centering capability to the structure, assuring the restoring forces after an earthquake) with one central eccentrically braced frame (EBF) with replaceable bolted links (which are intended to provide the energy dissipation capacity and to be easily replaceable) (Fig. 7.13b-c). These are the plane frames that will be further designed and analyzed. All the other frames are gravitational loads resisting systems (with pinned HE200A composite steel-concrete beams). The main beams, columns and braces are made of European I-sections (IPE, HEA, HEB and HEM type), while the removable links are made of welded I-sections. The material used for structural elements is S355 steel.

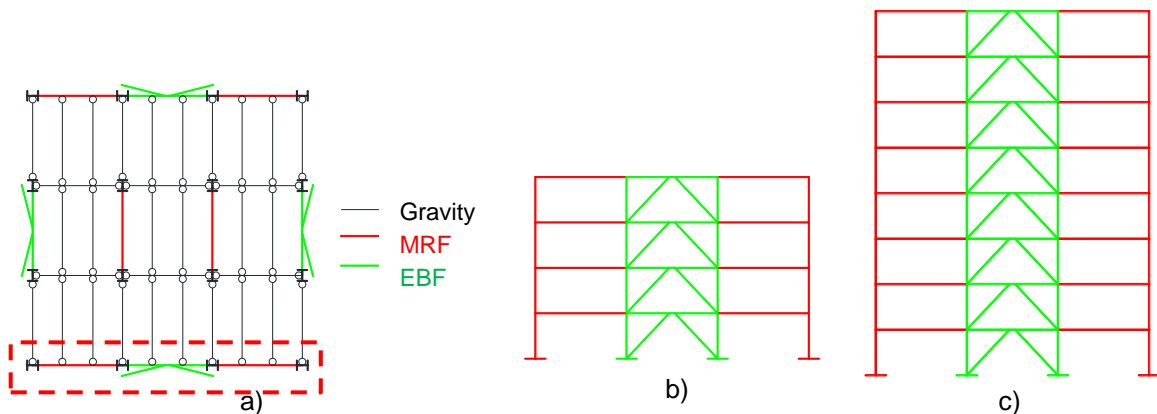


Fig. 7.13: Structures description: a) plane configuration, b) 4-story frame elevation and c) 8-story frame elevation.

Table 7.5 includes the assumptions for gravity and seismic loads. The gravity loads were applied as uniform distributed loads on the secondary beams and reduced to concentrated loads on the main frames. The dead load takes into account the composite slab and steel sheeting, resulting  $2.75 \text{ kN/m}^2$ . There were considered superimposed loads from services, ceilings and raised floors of  $0.7 \text{ kN/m}^2$  at intermediate floors and  $1.0 \text{ kN/m}^2$  at last floor. A  $4.0 \text{ kN/m}^2$  permanent load was taken into account for perimeter walls. The live load takes into account the destination of the buildings (offices - class B) and movable partition walls, resulting  $3.8 \text{ kN/m}^2$ . All gravitational loads assigned to the analysed frames correspond to half the bay (4m). Two different design cases are taken into account: moderate (considering DCM) and high (considering DCH) seismicity cases. Type 1-C spectrum was selected for design considering two peak ground accelerations:  $0.3g$  for high seismicity case and  $0.15g$  for moderate seismicity case (Fig. 7.14).

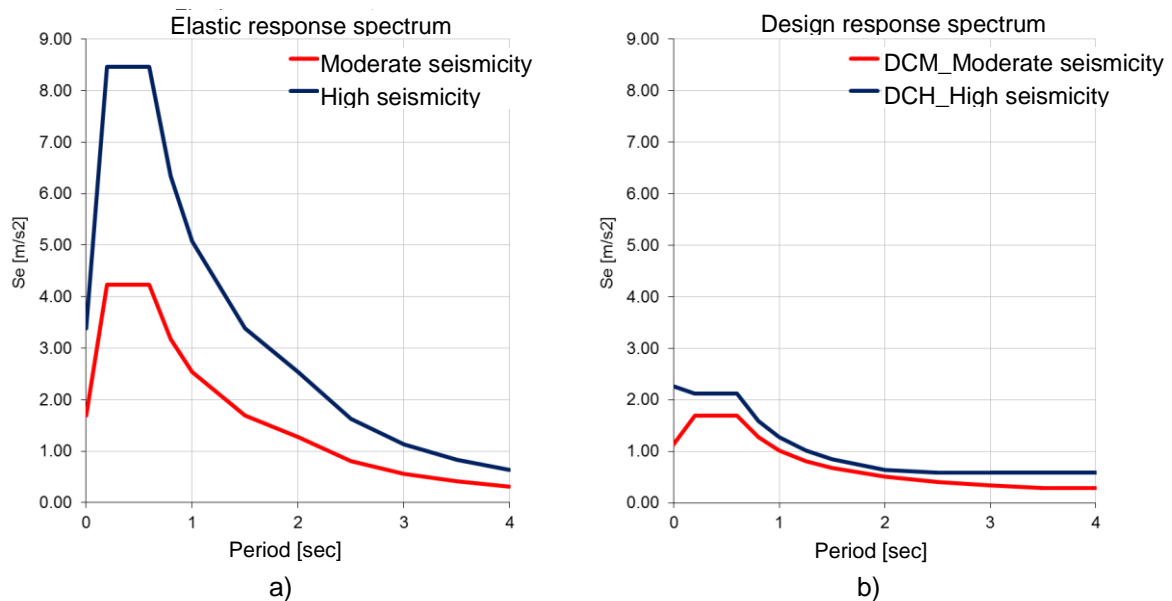


Fig. 7.14: Response spectra for two seismicity cases: a) elastic and b) design.



A behaviour factor  $q=4$  was adopted for DCH (see Chapter 7.4.1.5). In case of DCM a behaviour factor of 2.5 has been considered.

**Table 7.5: Loading details**

Vertical loads	
Dead loads (composite slab + steel sheeting)	2.75 kN/m <sup>2</sup>
Superimposed loads (Services, ceiling, raised floor)	0.7 kN/m <sup>2</sup> - intermediate floors 1.0 kN/m <sup>2</sup> – last floor
Perimeter walls	4.0 kN/m <sup>2</sup>
Live loads – (office class B + movable partition)	3.00+0.800=3.8 kN/m <sup>2</sup>
• DCH design:	
Elastic response spectra	Type 1
Peak ground acceleration	$a_{gR}=0.3g$
Importance class II	$\gamma_I = 1.0$ (Ordinary buildings)
Ground type	C ( $T_B = 0.2$ s, $T_C = 0.60$ s)
Proposed behavior factor $q$ (DCH)	4
Damping ratio	5%
Seismic combination coefficient for the quasi-permanent value of variable actions	$\psi_2=0.30$
• DCM design:	
Elastic response spectra	Type 1
Peak ground acceleration	$a_{gR} = 0.15g$
Importance class II	$\gamma_I = 1.0$ (Ordinary buildings)
Ground type	C ( $T_B = 0.2$ s, $T_C = 0.60$ s)
Proposed behavior factor $q$ (DCM)	2.5
Damping ratio	5%
Seismic combination coefficient for the quasi-permanent value of variable actions	$\psi_2=0.30$

#### 7.5.1.2 Modelling for linear elastic analysis

The modelling, analysis and design of the buildings, was performed with the finite element program SAP2000 [16]. The structural model was a linear-elastic 2D model. Rigid diaphragms were assigned at each level to account for the effect of reinforced concrete slabs.

The structural masses (in tons) considered from half of the total bay of the structure (12m) were assigned in the frames' structural nodes, since only the marginal frames resist to lateral loads (Fig. 7.15).

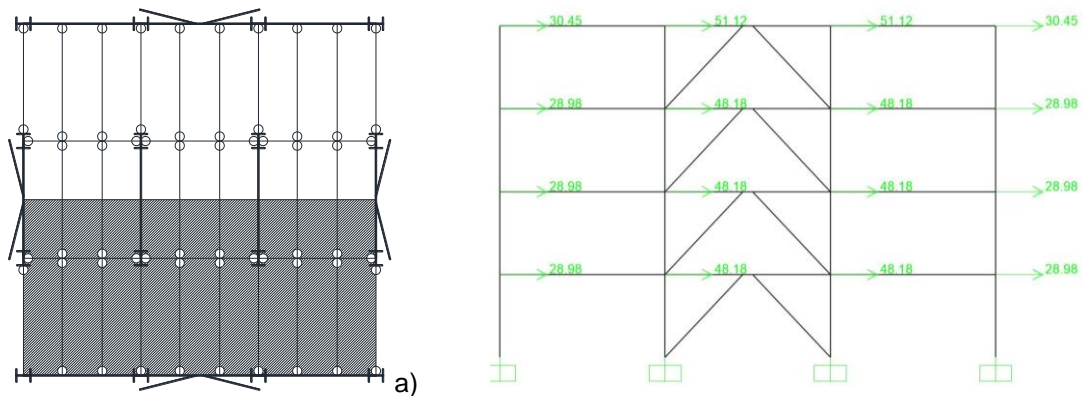


Fig. 7.15: Structural masses: a) considered from half the structure b) assigned in structural nodes of 2D model.

## 7.5.2 Persistent design situation

### 7.5.2.1 Ultimate Limit State

MRFs were designed from fundamental Ultimate Limit State (ULS) load combination  $1.35 \cdot G + 1.5 \cdot Q$ , where  $G$  are permanent loads (dead load) and  $Q$  are variable loads (live load). IPE330 sections were obtained for beams, HE160B sections for columns of 4-story buildings and HE200B sections for columns of 8-story buildings.

### 7.5.2.2 Serviceability Limit State

Beams deflections were checked from fundamental load combination  $1.0 \cdot G + 1.0 \cdot Q$ . They had to be increased to IPE360 to have deflections less than  $L/350$  (22.86mm).

### 7.5.3 Response spectrum analysis

Multi-modal response spectrum analysis was performed and the results are summarized in Table 7.6. The first two modes, for 4-story buildings and the first three modes, for 8-story buildings, activated more than 90% of the mass.

The design base shear force of the analysed frames is shown in Table 7.6. It can be observed that the 8-storey structure has a similar design base shear force with the 4-storey structure. Even if the 8-storey structure has roughly twice the mass of the 4-storey one, larger fundamental period of vibration of the former one leads to smaller design spectral acceleration.

**Table 7.6: Response spectrum analysis results**

Frame	$a_g$	Design base shear force, $V_b$ [kN]	Mode No	Period (s)	Participating mass ratio (%)	Total (%)
4-st.	0.30g	2935.45	1	0.517	78.89	95.09
			2	0.193	16.2	
	0.15g	1754.12	1	0.576	79.32	94.89
			2	0.213	15.57	
8-st.	0.30g	3082.59	1	1.126	71.58	94.85
			2	0.385	17.76	
			3	0.221	5.51	
	0.15g	2064.79	1	1.246	72.56	94.91
			2	0.437	17.25	
			3	0.253	5.1	

#### 7.5.4 Global imperfections and second order effects

Global imperfections were considered in the structural analysis, according to EN1993-1-1, through equivalent lateral forces  $H_i$ , from combination  $1.35 \cdot \text{Dead} + 1.5 \cdot \text{Live}$ . These forces were computed based on total gravitational loads and initial global imperfection  $\phi$ , level by level, and considered in every load combination further on. Small lateral equivalent forces were obtained, of 8.7 kN for current levels and 8.9 kN for roof level.

Second order effects were not accounted for in design because the inter-storey drift sensitivity coefficient  $\theta$  was computed according to EN1998-1-1 and found to be smaller than 0.1.

#### 7.5.5 Seismic design

##### 7.5.5.1 Ultimate Limit State - Dissipative elements

Shear links are the dissipative elements of the system. They are designed from welded ( $h \times b \times t_f \times t_w$ ) class 1 I-sections.

In order to achieve the connection over-strength, very short dissipative members were adopted (see Chapter 7.4.1.3). Therefore, links have lengths of 0.5 m in case of 4-story buildings and 0.9 m in case of 8-story buildings.

Links sections were obtained from the following governing seismic load combination:  $1.0 \cdot G + 0.3 \cdot Q + 1.0 \cdot A_{Ed}$  (where  $A_{Ed}$  is seismic action) and are presented in the following tables:

**Table 7.7: 4-story frame dissipative elements**

Frame	$a_g$	Story	Link section	$\Omega_i$	Min $\Omega_i$	$\Omega$
4-story	0.3g	1	350x190x18x9	2.28	2.13	2.67
		2	350x190x18x9	2.42		
		3	290x190x16x8	2.23		
		4	230x140x16x6	2.16		
	0.15g	1	350x130x18x6	1.59	1.59	2.00
		2	350x130x18x6	1.70		
		3	290x140x16x6	1.77		
		4	230x120x16x5	1.92		

**Table 7.8: 8-story frame dissipative elements**

Frame	$a_g$	Story	Link section	$\Omega_i$	Min $\Omega_i$	$\Omega$
8-story	0.3g	1	490x260x20x8	2.44	1.96	2.45
		2	490x260x20x8	2.41		
		3	440x230x20x7	2.09		
		4	440x230x20x7	2.31		
		5	390x200x20x6	1.96		
		6	390x200x20x6	2.29		
		7	330x210x16x5	2.25		
		8	250x190x14x4	1.97		
	0.15g	1	440x230x20x7	2.34	1.93	2.41
		2	440x230x20x7	2.27		
		3	390x220x18x6	1.93		
		4	390x220x18x6	2.19		
		5	350x220x18x6	2.24		
		6	330x210x16x5	2.08		
		7	290x210x16x5	2.23		
		8	210x190x14x4	2.15		

For each building, a homogeneous dissipative behavior was ensured between links (25%). The structural over-strength was computed as [5]:

$$\Omega = \gamma_{ov} \Omega_i \quad \text{Eq. (7.11)}$$

$$\Omega_i = \gamma_{sh} \frac{V_{p,linkj}}{V_{Ed,j}} \quad \text{Eq. (7.12)}$$

where:  $\gamma_{ov}$  is 1.25 and  $\gamma_{sh}$  was adopted 1.8 for DCH (according to DUAREM project [1] results) and 1.5 for DCM.

### 7.5.5.2 Ultimate Limit State – Non-dissipative elements

EBFs columns, braces and beams are the non-dissipative elements of the system and were designed from the seismic load combination that provides over-strength ( $\Omega$ ) to these elements with respect to dissipative ones:  $1.0 \cdot G + 0.3 \cdot Q + \Omega \cdot A_{Ed}$ . The sections are presented below:

**Table 7.9: 4-story frame non-dissipative elements**

Frame	$a_g$	Story	Braces	Beams	Columns
4-story	0.3g	1	HE280B	HE360A	HE320B
		2	HE280B	HE360A	HE320B
		3	HE240B	HE300A	HE300B
		4	HE200B	HE240A	HE300B
	0.15g	1	HE240B	HE360A	HE260B
		2	HE220B	HE360A	HE260B
		3	HE220B	HE300A	HE240B
		4	HE180B	HE240A	HE240B

**Table 7.10: 8-story frame non-dissipative elements**

Frame	$a_g$	Story	Braces	Beams	Columns
8-story	0.3g	1	HE320B	HE500A	HE340M
		2	HE320B	HE500A	HE340M
		3	HE300B	HE450A	HE300M
		4	HE280B	HE450A	HE300M
		5	HE280B	HE400A	HE300B
		6	HE260B	HE400A	HE300B
		7	HE240B	HE340A	HE280B
		8	HE200B	HE260A	HE280B
	0.15g	1	HE260B	HE450A	HE300M
		2	HE260B	HE450A	HE300M
		3	HE260B	HE400A	HE280M
		4	HE240B	HE400A	HE280M
		5	HE220B	HE360A	HE280B
		6	HE220B	HE340A	HE280B
		7	HE200B	HE300A	HE260B
		8	HE180B	HE220A	HE260B

### 7.5.5.3 Serviceability Limit State (Limitation of inter-story drift)

Considering that the buildings have ductile non-structural elements the following Eq. (7.13) is checked.

$$d_r \quad v \leq 0.0075 \quad h = 0.0075 \quad 4000 = 30mm \quad \text{Eq. (7.13)}$$

Where  $d_r$  is the design inter-storey drift,  $v=0.5$  is a reduction factor on the design displacements due to the importance class of the building (ordinary buildings) and  $h$  is the story height. Table 7.11 includes the results of the analysis; the check is verified for all stories with values much lower than the limit value 30mm.

**Table 7.11: Limitation of inter-story drift**

Frame	$a_g$	Drift [mm]
4-st.	0.3g	11.26
	0.15g	14.62
8-st.	0.3g	15.3
	0.15g	7.83

#### 7.5.5.4 Dual configurations

The duality of the structures were checked by verifying that the MRFs should be able to resist at least 25% of the total seismic force (see Chapter 7.4.1.2).

In order to have dual frames, the MRFs beams were increased as follows:

**Table 7.12: 4-story frame MRFs beams**

Frame	Story	Sections
4-story	1	IPE400
	2	IPE400
	3	IPE360
	4	IPE360

**Table 7.13: 8-story frame MRFs beams**

Frame	$a_g$	Story	Sections
8-story	0.3g	1	IPE450
		2	IPE450
		3	IPE400
		4	IPE400
		5	IPE360
		6	IPE360
		7	IPE360
		8	IPE360
	0.15g	1	IPE400
		2	IPE400
		3	IPE360
		4	IPE360
		5	IPE360
		6	IPE360
		7	IPE360
		8	IPE360

#### 7.5.5.5 Weak beam-strong column

Columns from all buildings were increased in order to satisfy the “weak beam-strong column” condition:

$$\sum M_{Rc} \geq 1.3 \sum M_{Rb} \quad \text{Eq. (7.14)}$$

where:  $\sum M_{Rc}$  is the sum of upper and lower columns moment resistance and  $\sum M_{Rb}$  is the moment resistance of the MRF beam.

The final sections of MRFs column from elastic design are the following:

**Table 7.14: 4-story frame MRFs columns**

Frame	Story	Sections
4-story	1	HE240B
	2	HE240B
	3	HE220B
	4	HE220B

**Table 7.15: 8-story frame MRFs columns**

Frame	a <sub>g</sub>	Story	Sections
8-story	0.3g	1	HE260B
		2	HE260B
		3	HE240B
		4	HE240B
		5	HE220B
		6	HE220B
		7	HE220B
		8	HE220B
	0.15g	1	HE240B
		2	HE240B
		3	HE220B
		4	HE220B
		5	HE220B
		6	HE220B
		7	HE220B
		8	HE220B

Frame sections after elastic design are the following:

**Table 7.16: 4-story frame sections**

$a_g$	Story	Links	Braces	Beams	Columns	MRFs beams	MRFs columns
0.3g	1	350x190x18x9	HE280B	HE360A	HE320B	IPE400	HE240B
	2	350x190x18x9	HE280B	HE360A	HE320B	IPE400	HE240B
	3	290x190x16x8	HE240B	HE300A	HE300B	IPE360	HE220B
	4	230x140x16x6	HE200B	HE240A	HE300B	IPE360	HE220B
0.15g	1	350x130x18x6	HE240B	HE360A	HE260B	IPE400	HE240B
	2	350x130x18x6	HE220B	HE360A	HE260B	IPE400	HE240B
	3	290x140x16x6	HE220B	HE300A	HE240B	IPE360	HE220B
	4	230x120x16x5	HE180B	HE240A	HE240B	IPE360	HE220B

**Table 7.17: 8-story frame sections**

$a_g$	Story	Links	Braces	Beams	Columns	MRFs beams	MRFs columns
0.3g	1	490x260x20x8	HE320B	HE500A	HE340M	IPE450	HE260B
	2	490x260x20x8	HE320B	HE500A	HE340M	IPE450	HE260B
	3	440x230x20x7	HE300B	HE450A	HE300M	IPE400	HE240B
	4	440x230x20x7	HE280B	HE450A	HE300M	IPE400	HE240B
	5	390x200x20x6	HE280B	HE400A	HE300B	IPE360	HE220B
	6	390x200x20x6	HE260B	HE400A	HE300B	IPE360	HE220B
	7	330x210x16x5	HE240B	HE340A	HE280B	IPE360	HE220B
	8	250x190x14x4	HE200B	HE260A	HE280B	IPE360	HE220B
0.15g	1	440x230x20x7	HE260B	HE450A	HE300M	IPE400	HE240B
	2	440x230x20x7	HE260B	HE450A	HE300M	IPE400	HE240B
	3	390x220x18x6	HE260B	HE400A	HE280M	IPE360	HE220B
	4	390x220x18x6	HE240B	HE400A	HE280M	IPE360	HE220B
	5	350x220x18x6	HE220B	HE360A	HE280B	IPE360	HE220B
	6	330x210x16x5	HE220B	HE340A	HE280B	IPE360	HE220B
	7	290x210x16x5	HE200B	HE300A	HE260B	IPE360	HE220B
	8	210x190x14x4	HE180B	HE220A	HE260B	IPE360	HE220B

### 7.5.6 Non - linear static analysis (Pushover)

Because the height of case-study frames is relatively low, the buildings being regular in plan and elevation and higher modes of vibration do not affect the structural response, assessment of seismic performance was adopted using static nonlinear (pushover) analysis.

#### 7.5.6.1 Frame modeling for static non-linear analysis

Nonlinear static analyses were performed to check the re-centring capability, using SAP2000.



Pushover (PO) analyses were performed on both 4-story and 8-story frames, considering a modal lateral forces distributions. P-Delta effects were also included in PO analyses.

A leaning column was modelled in order to account for the gravitational loads acting on interior gravity frames (Fig. 7.16).

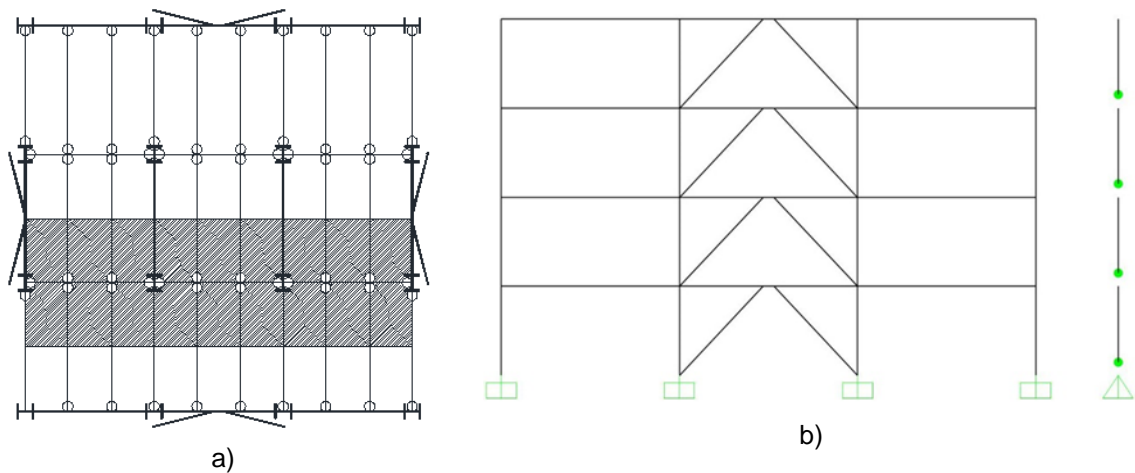


Fig. 7.16: Leaning column approach: a) gravitational loads on interior frame and b) leaning column modelling.

Expected material properties were used for dissipative elements, based on  $\gamma_{ov}=1.25$  and nominal material properties for non-dissipative elements.

Nonlinear plastic hinges of bending type M3 were assigned at the ends of the MRFs beams and of bending with axial force type P-M3 at the ends of columns and EBFs beams. For braces, nonlinear plastic hinges of axial type P were used, being assigned at the middle of bars. These properties were calculated according to ASCE41-13 [13].

In order to account for the short links nonlinear behaviour in shear (V2), MultiLinear Plastic Link elements were defined, with nonlinear behaviour on 2-direction, presented below:

**Table 7.18: Links nonlinear properties for 4-story frame**

Frame	$a_g$	Story	$K_l$ [kN/m]	$V_y$ [kN]
4-story	0.3g	1	433680	612
		2	433680	612
		3	310683	449
		4	174867	263
	0.15g	1	289798	408
		2	289798	408
		3	232550	337
		4	146315	219

**Table 7.19: Links nonlinear properties for 8-story frame**

Frame	$a_g$	Story	$K_l$ [kN/m]	$V_y$ [kN]
8-story	0.3g	1	255735	771
		2	255735	771
		3	191066	603
		4	191066	603
		5	151086	455
		6	151086	455
		7	115904	322
		8	65865	193
	0.15g	1	179466	603
		2	179466	603
		3	140361	457
		4	140361	457
		5	146401	408
		6	114501	322
		7	97069	281
		8	50887	161

2-Joint Link elements with the above properties were used between end-joints of every link and, in parallel, short links bars were modelled to account only for the axial stiffness (pinned at the ends).

#### 7.5.6.2 Pushover analysis results

After running the PO analyses on elastic designed frames, in case of 4-story and 8-story buildings, at DCH, yielding was observed in MRFs before the attainment of ultimate deformation capacity in the EBFs with removable links. Therefore, some sections were replaced as follows: for the 4-story frame, EBF columns were increased and for the 8-story frame, MRFs were made from S690 steel.

The new obtained frames were re-checked for all the conditions from elastic design (fundamental combinations, seismic combinations, duality, weak beam - strong column) and the final sections for 4 and 8-story frames at DCH are the following:

**Table 7.20: Final frame sections at DCH**

Frame	Story	Links	Braces	Beams	Columns	MRFs beams	MRFs columns
4-story	1	350x190x18x9	HE280B	HE360A	HE280M	IPE400	HE240B
	2	350x190x18x9	HE280B	HE360A	HE280M	IPE400	HE240B
	3	290x190x16x8	HE240B	HE300A	HE280B	IPE360	HE220B
	4	230x140x16x6	HE200B	HE240A	HE280B	IPE360	HE220B
8-story	1	490x260x20x8	HE320B	HE500A	HE300M	IPE360	HE220B
	2	490x260x20x8	HE320B	HE500A	HE300M	IPE360	HE220B
	3	440x230x20x7	HE300B	HE450A	HE260M	IPE360	HE220B
	4	440x230x20x7	HE280B	HE450A	HE260M	IPE360	HE220B
	5	390x200x20x6	HE280B	HE400A	HE260B	IPE360	HE220B
	6	390x200x20x6	HE260B	HE400A	HE260B	IPE360	HE220B
	7	330x210x16x5	HE240B	HE340A	HE240B	IPE360	HE220B
	8	250x190x14x4	HE200B	HE260A	HE240B	IPE360	HE220B

Further on, it is observed that no yielding appears before reaching 0.15 rad in links at DCH and 0.1 rad at DCM (Fig. 7.17).

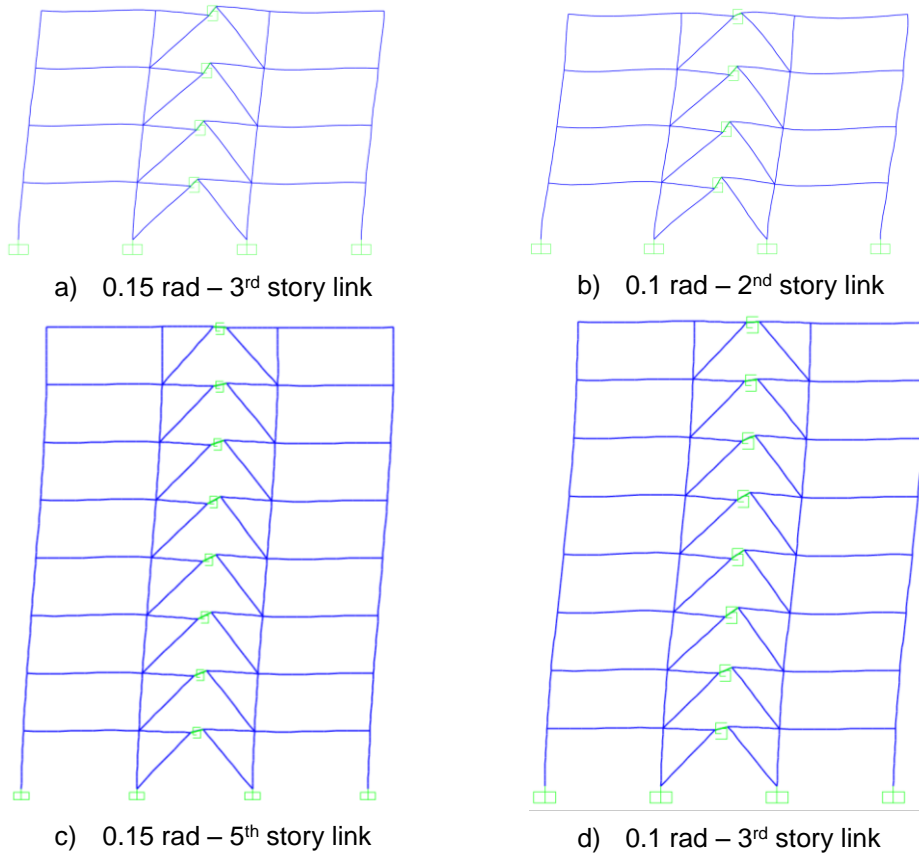


Fig. 7.17: Deformed frames under PO with modal distribution: a) 4-story at DCH, b) 4-story at DCM, c) 8-story at DCH and d) 8-story at DCM.

It was observed that no yielding in any other structural elements appears before reaching 0.15 rad in links at DCH and 0.1 rad at DCM. For DCH frames, when peak link rotation reaches 0.15 rad, full plastic mechanism is attained with plastic rotations in other links ranging between 0.102 rad and 0.128 rad for 4-story frame and between 0.066 rad and 0.149 rad for 8-story frame. For DCM frames, when peak link rotation reaches 0.1 rad, other links show de-formations ranging between 0.061 rad and 0.094 rad for 4-story frame and between 0.024 rad and 0.095 rad for 8-story frame.

Pushover curves for all frames are presented in Fig. 7.18.

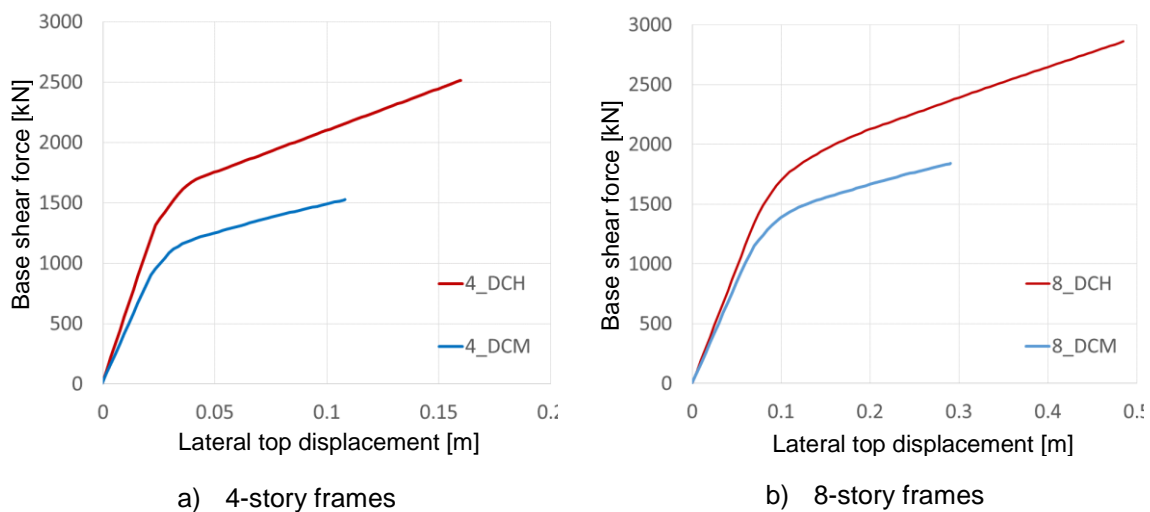


Fig. 7.18: Pushover curves.

The frames designed assuming DCH, have a larger capacity and ductility than the ones designed assuming DCM. The 8-story frames are more ductile than the 4-story frames and were designed to resist similar seismic forces (within the same ductility class) (see Chapter 7.5.3).

The curves are represented until the maximum capacity (when the links reach their ultimate shear deformation), because convergence was not attained for larger displacements.

The objective of having no yielding in the MRFs before the attainment of the SD deformation in the removable links (0.14 rad) of the EBFs is accomplished, representing the basic design requirement for dual frames with removable dissipative members. MRFs provide the re-centring of the specimen until the links ultimate deformation (0.15 rad).

#### 7.5.6.3 Seismic performance assessment

Seismic performance of the studied frames was assessed using the N2 method [17], with the bilinear idealization of the equivalent single degree of freedom system to match the initial stiffness of the system (P100 [10] approach).

Structural performance was evaluated for the limit states shown in Table 7.2 (DL,

SD and NC) and illustrated in Fig. 7.19. Target displacements ( $D_t$ ) were computed for each limit state and corresponding link rotations are presented below.

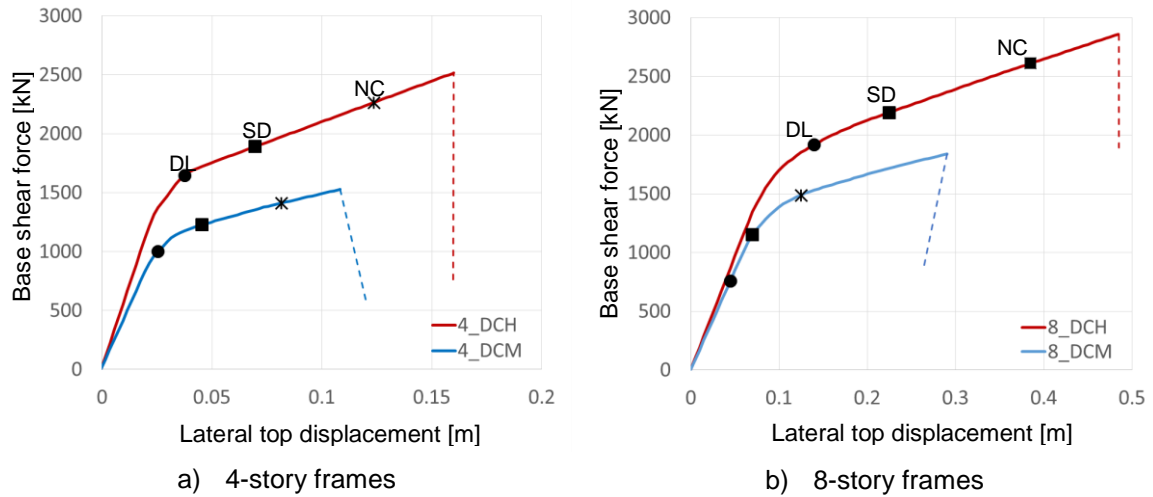


Fig. 7.19: Seismic performance assessment.

**Table 7.21: Performance assessment of the 4-storey frame.**

Ductility class	Limit State	Dt [mm]	Link rotation at Dt [rad]	Accepted rotation [rad]	Corresponding top displacement [mm]
DCH	DL	36.8	0.016	0.005	23.5
	SD	69.7	0.053	0.14	151.5
	NC	127.4	0.115	0.16	-
DCM	DL	26.5	0.009	0.003	19.5
	SD	46.3	0.037	0.09	99.5
	NC	81.3	0.074	0.11	-

**Table 7.22: Performance assessment of the 8-storey frame.**

Ductility class	Limit State	Dt [mm]	Link rotation at Dt [rad]	Accepted rotation [rad]	Corresponding top displacement [mm]
DCH	DL	107.3	0.031	0.005	59.9
	SD	182.2	0.062	0.14	404.9
	NC	313.3	0.109	0.16	-
DCM	DL	41.9	0.003	0.003	44.9
	SD	71.2	0.009	0.09	259.9
	NC	122.4	0.036	0.11	-

The performance objectives are accomplished for SD and NC limit states. Although the performance objectives are not satisfied for DL using the N2 approach, the objective of having no yielding in the MRFs before the attainment of the SD deformation in the removable links (0.14 rad) of the EBFs is accomplished, representing the basic design requirement for dual frames with removable dissipative members. MRFs provide the re-centring of the specimen until the links ultimate deformation (0.15 rad).

#### 7.5.6.4 Links removal and frames re-centring

In what concerns the link removal and re-centring of frames, static nonlinear staged construction analysis from SAP2000 was used on 4-storey frame, at DCH. The steps of the analysis are the following: firstly the frame is loaded with gravitational forces and afterwards with lateral forces (until reaching ultimate deformation in links), then it is unloaded, secondly the links are removed storey by storey, starting from the first level to the top [18]. After the elimination of the last link, the structure comes back to its initial position (see Fig. 7.20).

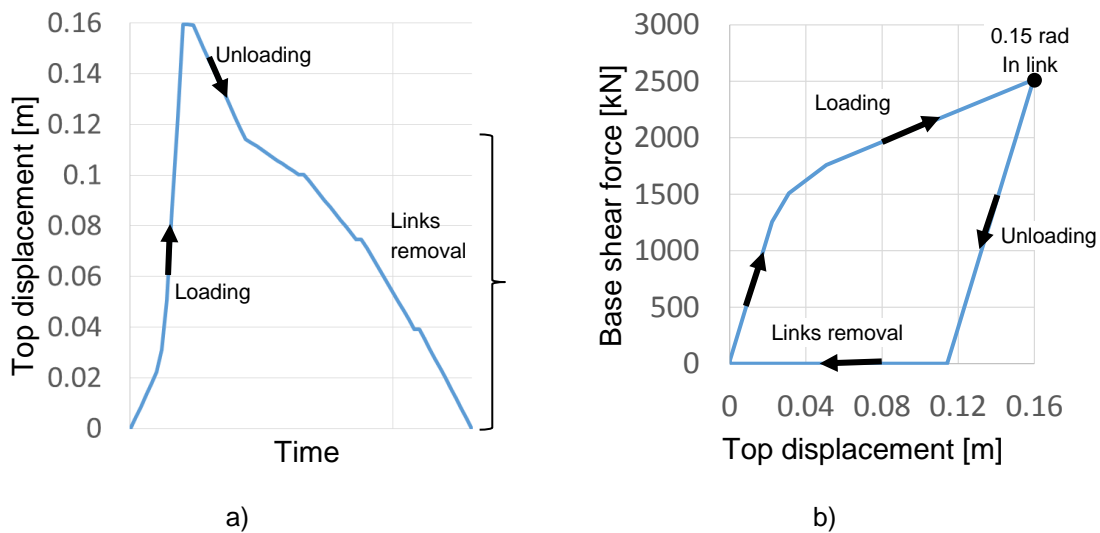


Fig. 7.20: Frame re-centring after link removal: a) top displacement in time and b) base shear force vs. top displacement.

The technically easiest way to release the forces in links is by flame cutting the web and flanges of the link [19] if large permanent drifts occur or by unbolting otherwise, on a storey by story basis [20], as proved by the adopted procedure for the test structure in the DUAREM project.

The procedure is similar for the other 3 case study frames.

## 7.6 CONCLUSIONS

Re-centring dual eccentrically braced frames with replaceable links represent an efficient solution for reducing the repair costs due to structural damage experienced during a strong earthquake. A design procedure is proposed, which uses a few additional checks in addition to conventional ones.

The dual eccentrically braced structure showed an excellent performance at the SLS and ULS earthquakes within experimental program. Small permanent deformations were recorded for both seismic intensity levels, which are within the erection tolerance limits defined in EN 1090. This behaviour occurs mostly due to the large post-elastic stiffness of the system, provided by the MRFs. Small permanent deformations effectively mean that the structure is self-centring to a certain degree.

A design procedure is presented and provides recommendations for re-centring dual EBFs with replaceable links. Additionally to existing current code specifications for designing this system, specific design provisions are recommended in order to ensure the re-centring capability and duality of the case study frames.

Short removable links validation is necessary. Since there's only a limited number of experimental tests on short bolted links involving this type of connection (flush-end plate) and link section (I section with 240 mm height), when using other types of sections and connections it is recommended to confirm the links performance through experimental validation and/or numerical testing based on parametric studies.

Nonlinear static and/or dynamic analyses are recommended in order to check the re-centring capability of the system. Seismic performance of the studied frames was assessed using the N2 method. Performance objectives are accomplished for SD and NC limit states. Although the performance objectives are not satisfied for DL using the N2 approach, the objective of having no yielding in the MRFs before the attainment of the SD deformation in the removable links (0.14 rad) of the EBFs is accomplished, representing the basic design requirement for dual frames with removable dissipative members.

## 7.7 FIELD OF APPLICATION

Dual re-centring EBFs with replaceable bolted links may be applied to multi-storey steel buildings in order to reduce the repair costs and downtime of a structure in the aftermath of a strong earthquake, the elastic response of the flexible subsystem (MRFs) providing the restoring forces, once the links damaged during an earthquake are removed.

## 7.8 PUBLICATIONS

1. A. Ioan, A. Stratan, D. Dubina, M. Poljanšek, F. J. Molina, F. Taucer, P. Pegon, G. Sabău, „Experimental validation of re-centering capability of eccentrically braced frames with removable links”, *Engineering Structures*, Volume 113, pp. 335-346, 2016;
2. A. Ioan, A. Stratan, D. Dubina, “Re-centering dual eccentrically braced frames with removable links” - *Proceedings of the Romanian Academy - series A: Mathematics, Physics, Technical Sciences, Information Science*, volume 17, number 2/2016, pp. 169-177;
3. Gabriel-Alexandru Sabau, Martin Poljansek Fabio Taucer, Pierre Pegon, Francisco-Javier Molina, Daniel Tirelli, Bernard Viaccoz, Aurel Stratan, Adriana Ioan-Chesoan, Dan Dubina, Final Report FP7 SERIES DUAREM Project – “Full-scale experimental validation of dual eccentrically braced frame with removable links” (2014) (<http://publications.jrc.ec.europa.eu/repository/handle/JRC93136> ).
4. Dubina D, Stratan A, Dinu F. Dual high-strength steel eccentrically braced frames with removable links. *Earthquake Engineering and Structural Dynamics Journal*, Volume 37, pp. 1703–1720, 2008;

## 7.9 BIBLIOGRAPHIC REFERENCES

1. Stratan A, Dubina D. Bolted links for eccentrically braced steel frames. In: Bijlaard FSK, Gresnigt AM, van der Vegte GJ (Eds.), Proc. of the fifth AISC/ECCS international workshop "connections in steel structures V. behavior, strength & design", June 3–5, Delft University of Technology, The Netherlands; 2004. p. 223–32;
2. Dubina D, Stratan A, Dinu F. Dual high-strength steel eccentrically braced frames with removable links. *Earthquake Engineering and Structural Dynamics Journal*, Volume 37, pp. 1703–1720, 2008;
3. Ioan A., Stratan A., Dubina D., Poljansek M., Molina F. J., Taucer F., Pegon P., Sabau G., Experimental validation of re-centring eccentrically braced frames with removable links, *Engineering Structures* 113 (2016) 335–346;
4. AISC. *Seismic Provisions for Structural Steel Buildings*. American Institute of Steel Construction, Chicago, IL, 2002;
5. EN1998-1-1, Eurocode 8: Design of structures for earthquake resistance - Part 1, General rules, seismic actions and rules for buildings, CEN, European Committee for Standardization, 2004;
6. ECCS (1985). "Recommended Testing Procedures for Assessing the Behavior of Structural Elements under Cyclic Loads", European Convention for Constructional Steelwork, Technical Committee 1, TWG 1.3 – Seismic Design, No.45;
7. Federal Emergency Management Agency and American Society of Civil Eng., Pre-standard and commentary for the seismic rehabilitation of buildings, FEMA 356, Washington DC, USA, 2000;
8. EN1993-1-1, Eurocode 3: Design of steel structures - Part 1-1: General rules and rules for buildings. Brussels: Comité Européen de Normalisation (CEN); 2003;
9. NEHRP (2003). NEHRP Recommended provisions for new buildings and other structures (FEMA 450). Part 1: Provisions and Part 2: Commentary. Building Seismic Safety Council, National Institute of Building Sciences, Washington, D.C.;
10. P100-1/2013 (2013). Seismic design code – Part 1: Rules for buildings;
11. Stratan A., Dinu F., Dubina D., "Replacement of bolted links in dual eccentrically braced frames", 14th European Conference on Earthquake Engineering, August 30 – September 3, 2010, Ohrid, Republic of Macedonia;
12. Dubina D., Stratan A., Ioan-Chesoan A., Design of steel frames with replaceable bolted links eccentric bracing systems, 1st EU-Sino Workshop on Earthquake-resistance of Steel Structures Shanghai, China, October 27, 2016;
13. Seismic Evaluation and Retrofit of Existing Buildings – ASCE/SEI 41-13, 2013;
14. Sivaselvan M., Reinhorn A.M. [1999] "Hysteretic models for cyclic behavior of deteriorating inelastic structures," Report MCEER-99-0018, MCEER/SUNY/Buffalo;
15. Sivaselvan M., Reinhorn A.M. [2001] "Hysteretic models for deteriorating inelastic structures," *Journal of Engineering Mechanics*, ASCE, Vol. 126, No. 6, pp. 633-640, with discussion by Wang and Foliente and closure in Vol. 127, No. 11;
16. SAP2000, CSI, Computers and Structures Inc., [www.csiberkeley.com](http://www.csiberkeley.com);
17. Fajfar P., A nonlinear analysis method for performance-based seismic design, *Earthquake Spectra*, 16(3):573-592, 2000;
18. A. Ioan, A. Stratan, D. Dubina, M. D'Aniello and R. Landolfo, "Seismic performance and re-centring capability of dual eccentrically braced frames with replaceable links", 8th International Conference on Behavior of Steel Structures in Seismic Areas Shanghai, China, July 1-3, 2015;
19. Stratan, A., Ioan, A., Dubina, D. 2012. Re-centring capability of dual eccentrically braced frames with removable bolted links. STESSA 2012 (Behaviour of Steel Structures in Seismic Areas) Conference, 9-11 January 2012, Santiago, Chile, pp. 723-728;



20. Ioan, A., Stratan, A., Dubina, D. 2012. Evaluation of restoring capacity of dual steel EBFs with removable links. The 8th International PhD & DLA Symposium, 29-30 October, 2012, Pecs, Hungary.



## 8 REPLACEABLE SHEAR PANEL

### 8.1 INTRODUCTION

In the frame of the European Research Program RFSR-CT-2008-00032 "Dissipative Devices for Seismic Resistant Steel Frames" an innovative dissipative systems, called replaceable shear panels was introduced and relevant design guides developed. Current report presents the results of the investigations on the seismic performance of the system, introduces the design procedures for steel structures, in which the system is used as removable seismic resistant system, and proceeds to the design of several case studies.

### 8.2 DESCRIPTION OF REPLACEABLE SHEAR PANELS

#### 8.2.1 *Principles of re-centring dual frame systems*

Most of the structures designed to modern codes would experience inelastic deformations even under moderate seismic action, with permanent (residual) displacements after an earthquake. Repair is difficult in such cases. Solutions providing self-centring of the structure exist, but are technically demanding (post-tensioned strands, shape memory alloy devices, etc.). An alternative solution is the one that provides re-centring capability (as opposed to self-centring), through removable dissipative members and dual (rigid-flexible) structural configuration.

Structural systems that aim at reducing structural damage by isolating plastic deformations in removable or "repairable" fuses, and have the ability to return to the initial un-deformed shape after an earthquake, have received much attention.

As proposed by Stratan and Dubina [1], in order to provide the re-centring capability of a structure with removable dissipative members, it was suggested to use dual structural configurations, obtained by combination of a moment resisting frames (MRFs) with replaceable shear panels. If the more flexible MRFs are kept elastic, they would provide the restoring force necessary to re-center the structure upon removal of damaged removable panels. A possible way to favor this is to realize the shear panels for low-yield-strength steel.

An idealized dual system consisting of two inelastic springs connected in parallel is shown in Fig. 8.1a. In order to provide the re-centring capability, the flexible subsystem should be kept in the elastic range up to the displacements at which the rigid subsystem attains its ultimate plastic deformation capacity. However, a conventional dual system that satisfies this condition will not return to the initial position following deformations into the inelastic range, even if permanent displacements  $\delta_{pD}$  in the dual system are smaller than the ones that would be obtained in a rigid system alone  $\delta_{pr}$  (Fig. 8.1b). Permanent deformations can be eliminated if the rigid (dissipative) subsystem is realized to be removable. Upon unloading of the dual system, there is a permanent displacement  $\delta_{pD}$ , and

corresponding residual forces in the flexible ( $F_{pf}$ ) and rigid ( $F_{pr}$ ) subsystems. Once removable dissipative members are dismantled, stiffness and strength of the system is provided by the flexible subsystem alone ( $F_{pr}=0$ ). If the flexible subsystem is still in the elastic range, it will return the system to the initial position, implying zero permanent deformations (Fig. 8.1c).

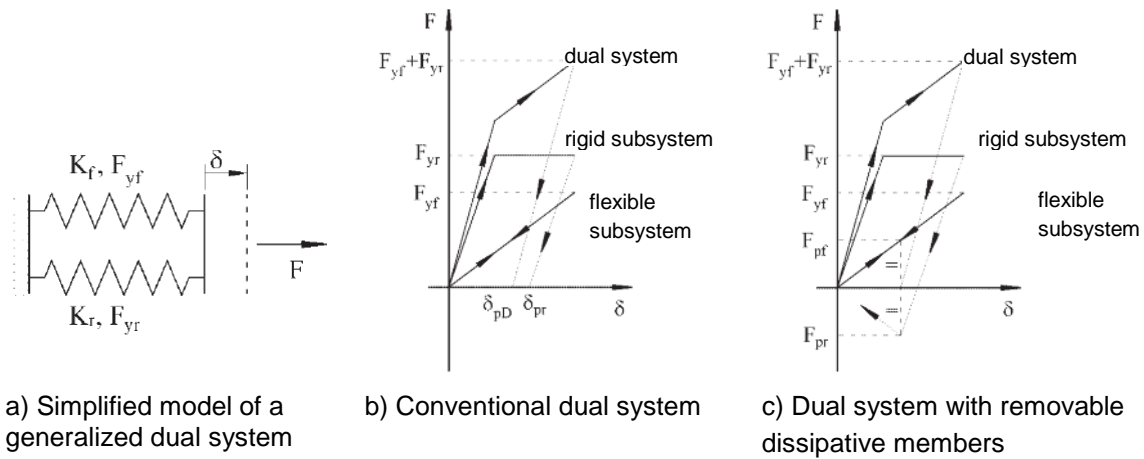


Fig. 8.1: Permanent deformations

### 8.2.2 Description of the system

Structures with replaceable shear panels are efficient lateral load resisting systems and can act as an alternative to traditional systems. Depending on their slenderness, shear panels may yield under applied shear before they buckle or may buckle while almost elastic.

The main advantages of slender shear panels consist of economy in steel weight due to thinner walls, fast construction time and easier retrofit [2]. Furthermore, with appropriate design and detailing, the systems may be classified as ductile systems. Code designed structures with replaceable shear panels are also capable of meeting drift limitations when subjected to ground motions that approximate the design shaking [3]. However, there are some concerns regarding the seismic response of the systems because they buckle during the early stages of lateral loading and therefore the response of the system is characterized by a pinched cyclic behavior. The pinching effect decreases the area of the hysteresis loops and, as a result, decreases the energy absorption. In order to reduce pinching and increase energy absorption, the panels may be combined with frames that have rigid moment connections between boundary elements. The resulting frame action provides some stiffness around zero story drift [4].

A dual system include either singular frame with shear panels (Fig. 8.2a) or a coupled systems with parallel moment frames (Fig. 8.2b). For large bays, singular shear panel inside the moment frame results in a large length to height ratio ( $L/h$ ) that can make the shear panel to be excessively flexible. A coupled system is a

specific dual system, whereby a coupling beam connects two shear panel bays.

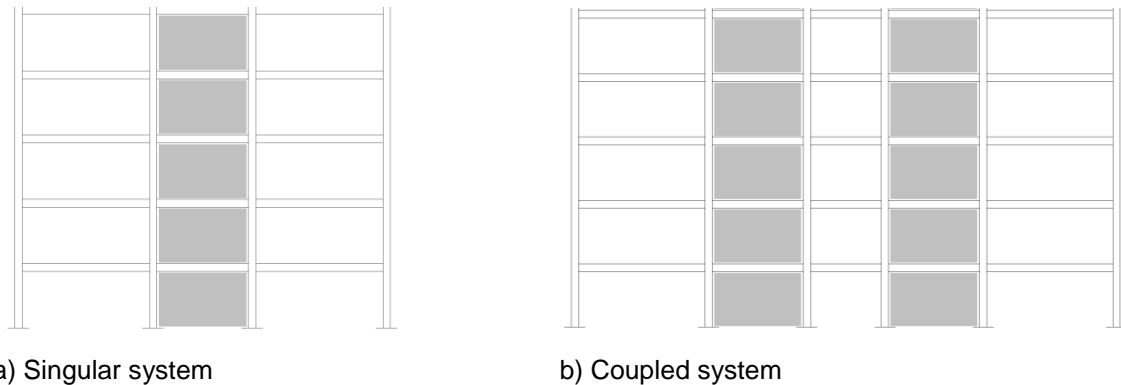


Fig. 8.2: Dual systems with shear panels

The innovative system is a particular system, which consists of inserting 2 shear panels inside moment frames, aiming at providing additional lateral stiffness (Fig. 8.3). The shear panels are bordered by additional vertical elements (stanchions) having simple connections at their ends to the beams. The beam outside the panels act as a short, intermediate or long link, depending on the width of the panel and bay.

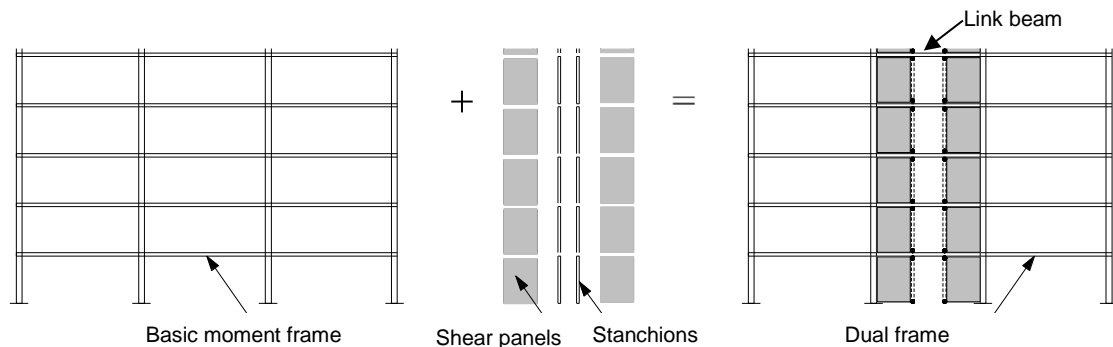


Fig. 8.3: Dual frames with replaceable shear panels

During severe earthquakes, the panels buckle in shear and yield by developing a diagonal tension field, together with plastic deformations in the ends of the beam. Such systems may be applied for new constructions and also for upgrading the lateral resistance of existing constructions. These systems have good seismic response, high dissipation capacity, and small residual drifts. Their use may also improve the overturning stiffness and reduce the axial force demand on panel's vertical boundary elements (VBEs).

An important aspect of this system is related with the reduction of residual displacements after an earthquake so as to reduce to cost of intervention. Residual or permanent displacements are considered harmful because they suggest structural damage. Repairing damaged structural elements can be technically tasking if not impossible; nevertheless, the process is expensive. If the damage is localized in easily replaceable members, repairing is easier and costs less. In

addition, the re-centring of the structure allows for easy replacement of damaged or “sacrificial” members. The particular behavior of system makes them appropriate for such applications [5], [6].

This solution was partially validated by experimental tests. An experimental program was developed within the Steel Structures Laboratory at the Politehnica University Timisoara ([7], [8]) in order to validate the technical solution and obtain benchmarks for calibration of numerical models for steel structures with shear panels.

### 8.3 EXPERIMENTAL INVESTIGATIONS ON SHEAR PANELS

#### 8.3.1 Experimental models and testing set-up

Four specimens were designed and constructed. The specimens were isolated from the second and third story of a six-story reference structure (Fig. 8.4a).

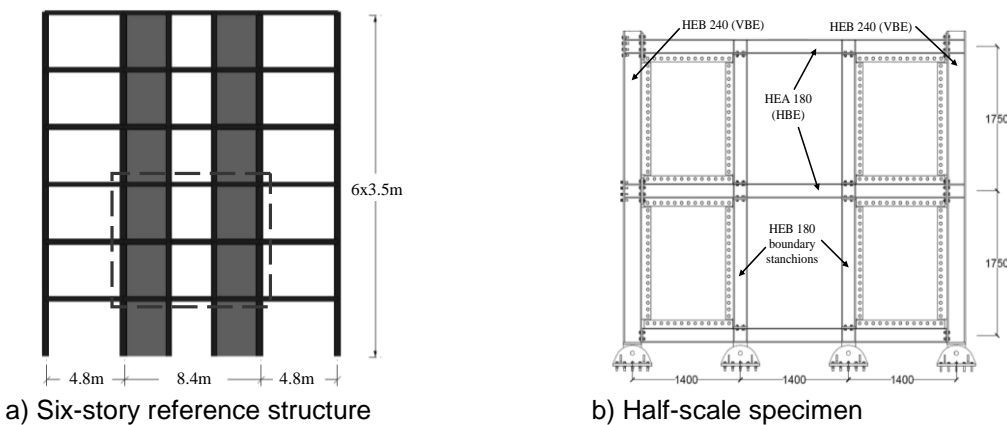


Fig. 8.4: Construction of half-scale specimen

Due to laboratory limitations, the specimens half scaled. This scaling resulted in frame specimens that were 3500-mm-tall and 4200-mm-wide between member centerlines (Fig. 8.4b). The thickness of shear panels was considered 2 mm. The aspect ratio of the shear panel,  $L/h$ , was 0.8, whereas the slenderness factor  $L/t_w$  was 595. It can be noted that the constructional system is composed of a moment resisting frame, two shear panels that are attached to the beams, and two additional stanchions that are placed as vertical boundary members. Each specimen was installed in the reaction frame as shown in Fig. 8.5.

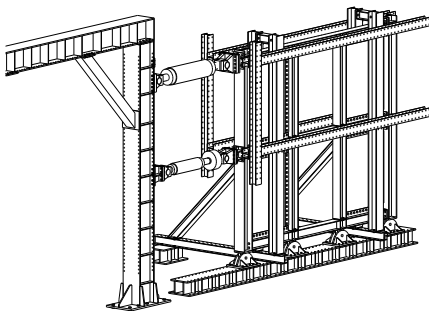


Fig. 8.5: Test set-up

The reaction frame was braced to reduce the in plane deformations. At first and second story levels, guide beams were installed to allow in plane displacement of the specimens. A lateral bracing system was used to prevent out of plane deformations of the guide beams.

Two types of bolted end plate HBE–VBE connections were employed for investigating the influence of connection type on the overall behavior of the frame. The first type is a flush end plate bolted connection (Fig. 8.6a), whereas the second is an extended end plate bolted connection (Fig. 8.6b). Fig. 8.6c shows the connection between the stanchions and the beam.

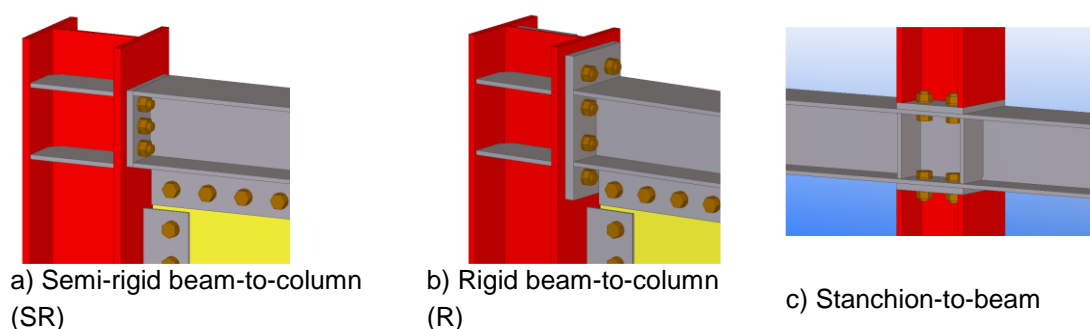


Fig. 8.6: Type of connections used in experimental frames

According EN1993-1-8 [9] classification, this connection can be classified as a nominally pinned connection. The flush end plate beam-to-column connection is semi-rigid and partial strength ( $M_{j,Rd} = 0.53M_{b,Rd}$ ) (further denoted as semi-rigid SR), and the extended end plate connection is rigid and partial strength, but with a capacity almost equal to that of the connected beam ( $M_{j,Rd} = 0.96M_{b,Rd}$ ), (further denoted as rigid R) (Fig. 8.7).

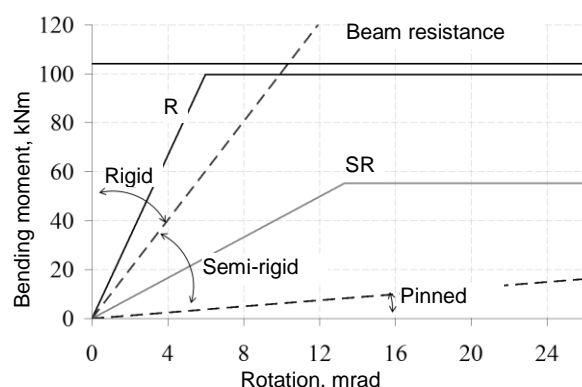
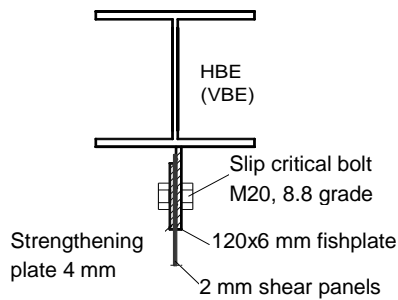


Fig. 8.7: Classification of connections for frame specimens [9]

Panels were bolted to boundary members at all edges using 6-mm-thick, 120-mm-wide fishplates and M20 8.8 grade slip critical bolts (Fig. 8.8). Bolted connections were considered more appropriate than welded ones owing to the difficulties in execution and quality control of welding onsite. Moreover, with bolted connections, removing damaged panels is easier. Welding the panels together can be a solution,

but the authors did not consider this as practical as compared to the bolted connection owing to the abovementioned conditions. To increase the bearing capacity of the panels, and, consequently, to reduce the number of bolts, additional plates were welded to the side of the panels in order to avoid bearing failure. Thus, the 2 mm panels had 4 mm additional plates, welded with metal active gas welding. Welding current intensity was adapted to prevent the thin panel's material from burning.



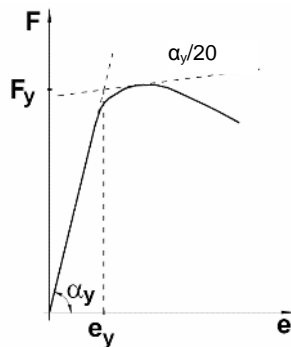
a) Cross section

b) Front view

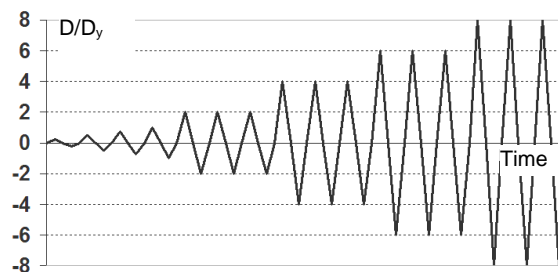
Fig. 8.8: Connection between shear panels and boundary elements

### 8.3.2 Loading protocol

Quasi-static cyclic testing was performed in accordance with ECCS Recommendations [10]. A monotonic test was first carried out for obtaining the force vs. displacement curve (Fig. 8.9a). Using this curve, the yielding displacement  $D_y$ , was obtained by intersecting a tangent having 20% of the initial stiffness slope to the maximum force with the initial stiffness line, see [8]. The yielding displacement is then used for establishing cyclic loading, which involves generating four successive cycles for the  $\pm 0.25D_y$ ,  $\pm 0.5D_y$ ,  $\pm 0.75D_y$ , and  $\pm 1.0D_y$  amplitude ranges, followed further to failure by series of three cycles each of amplitude  $\pm 2n \times D_y$ , where  $n = 1, 2, 3, \dots$  (Fig. 8.9.b).



a) Yielding displacement determination



b) Cyclic loading protocol

Fig. 8.9: Loading protocol

The lateral load was applied under displacement control, with triangular distribution. It is important to note that  $D_y$  has no standardized or even harmonized definition for



these systems. The ECCS procedure [10] for the evaluation of  $D_y$  was initially developed for testing beam-to-column joints, and therefore, because the different behavior of shear panels,  $D_y$  may be quantified using other methods. In fact, because both shear buckling and bearing work of bolted connections are included in the frame response, one can refer to “pseudo-yield displacement”.

### 8.3.3 Results of monotonic testing

The first specimen (R-M-T2), used R beam-to-column connections and 2-mm shear panels. Fig. 8.10 shows a plot of the lateral force against top displacement. The out-of-plane deformations were recorded on the left 1<sup>st</sup> story panel using optical measurement system. Fig. 8.11 presents the initial state of the experimental test. An 8.1 mm initial out-of-plane deformations was recorded. These initial deformations occurred during fabrication as well as after test setup installation.

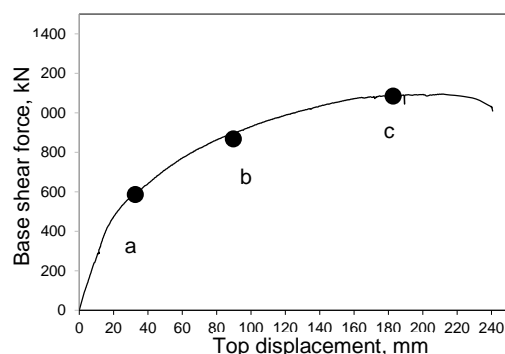


Fig. 8.10: Capacity curve of experimental frame with R connection

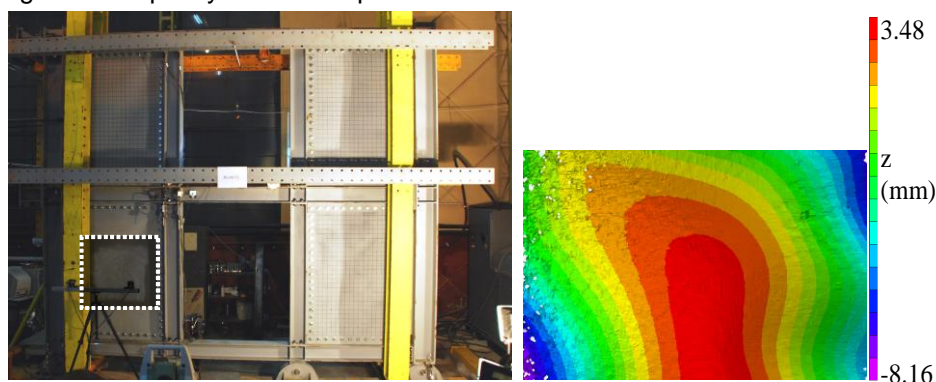


Fig. 8.11: Initial stage

The specimen exhibited an elastic behavior up to 0.6% of inter-story drift. The panels yielded first, and this was indicated by a change in stiffness (Fig. 8.10 point a). At this point, the base shear force reached 482 kN and the corresponding top displacement was 20.7 mm. The out of plane deformation was 23.6 mm (Fig. 8.12).

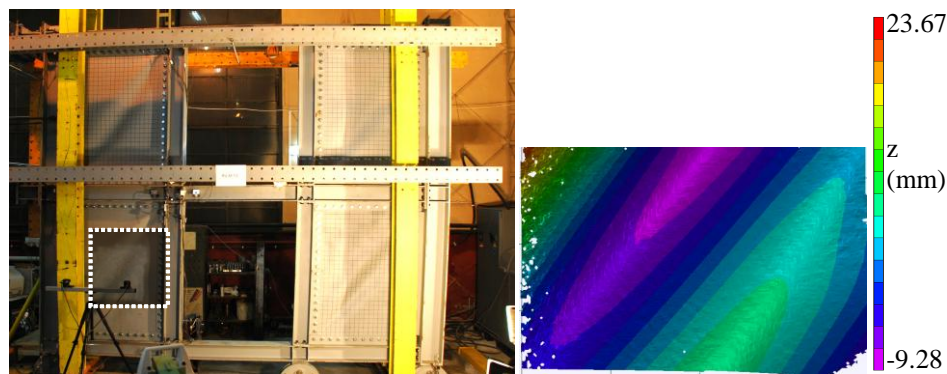
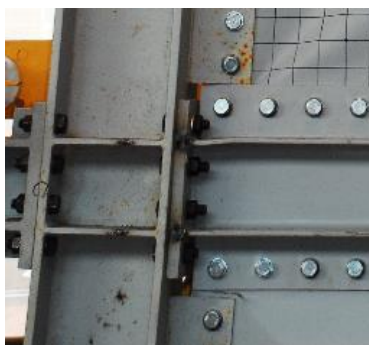


Fig. 8.12: Yielding stage

Up to 2% inter-story drift, there were no plastic deformations in the boundary elements and beam-to-column connections. For drifts larger than 2%, plastic deformations developed in the flange under compression at the beam end. The development of plastic deformations at beam end for 2% inter-story drift is in good agreement with the change in the slope of the force–displacement curve shown in Fig. 8.10 point b. At 2% drift, some cracks were also initiated at the panel corners, then, these cracks propagated along the fillet welds that connected the panels to the additional fishplates (Fig. 8.13.b).



a) Beam damage



b) Corner cracks

Fig. 8.13: 2% inter-story drift

There were no indications of any deterioration in the load carrying capacity owing to these local fractures. It was found that the cracks occurred mainly owing to insufficient clearance between the two adjacent fishplates, which collided when the beam rotated relative to the column. The peak capacity was reached at 6% drift (or a top displacement of 210 mm) at a corresponding base shear force of 1094 kN (Fig. 8.10.a). At peak capacity the out-of-plane deformations were 36.1 mm and the corner cracks started to propagate towards the middle of the panel. The test was stopped at 240 mm, not owing to the specimen collapse but owing to the limitation of the actuator stroke.

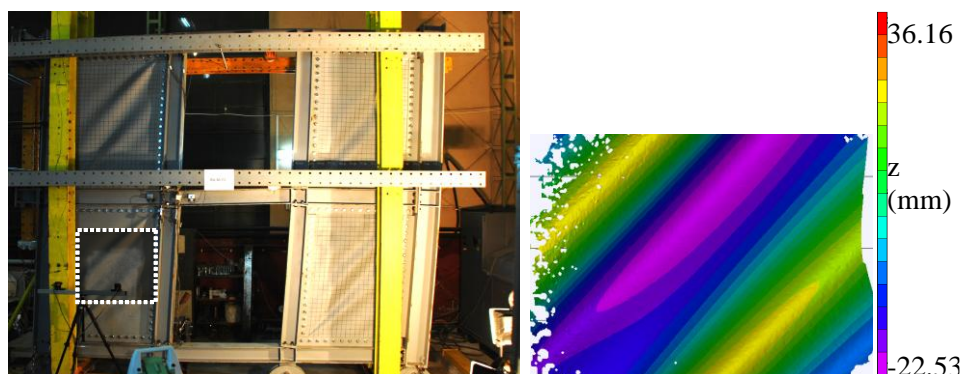
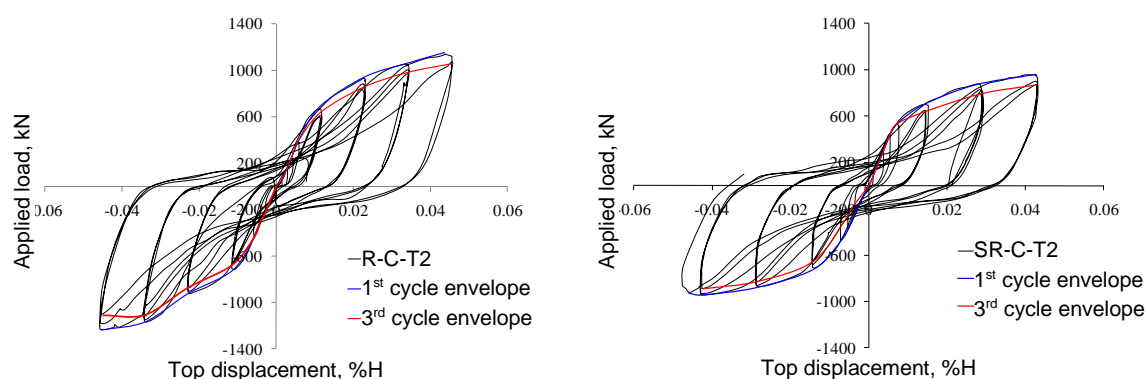


Fig. 8.14: Peak stage

### 8.3.4 Results of cyclic testing

All specimens (R-C-T2 and SR-C-T2) exhibited stable force-displacement behavior, with some pinching of hysteresis loops that are in line with the characteristics commonly observed in other tests. Plots of lateral load vs. top displacement of the specimens tested under cyclic loading are shown in Fig. 8.15.



a) R beam to column connection specimen

b) SR beam to column connection specimen

Fig. 8.15: Experimental frames hysteretic behavior

Fig. 8.16 presents the deformations that were recorded during cyclic test. The initial out-of-plane deformations affected the initial stiffness and yield strengths of the panels, but had a negligible effect on their ultimate capacity. The specimens, yielded at 0.65% and 0.7% drift, respectively. This indicates that until the yielding, the stiffness of the beam-to-column joint has little effect on the behavior. Some local cracks were initiated at the panel corners at approximately 2% drift, which then propagated along the fillet weld of the panels to the additional fishplate. At the same drift level, local plastic deformations were observed at the beam flange under compression for rigid connections. For the semi-rigid specimens plastic deformations were initiated in the connections because of the beam end plate in bending at approximately 2.5% drift. All specimens exhibited stable behavior up to cycles of 4% story drift, at which point the strength deteriorated. The ultimate displacement of the specimens is approximately 4.5% story drift, not owing to the specimen collapse but owing to the limitation of the actuator stroke. The contribution

of the frame to overall response increases with lateral displacement. Thus, the difference between SR-C-T2 and R-C-T2 in terms of yield resistance and yield displacement was small, as mentioned before, but ultimate capacity decreased by 20% when connections with low rigidity were used. As for the peak drift level, there was a small difference between the rigid and semi-rigid specimens.

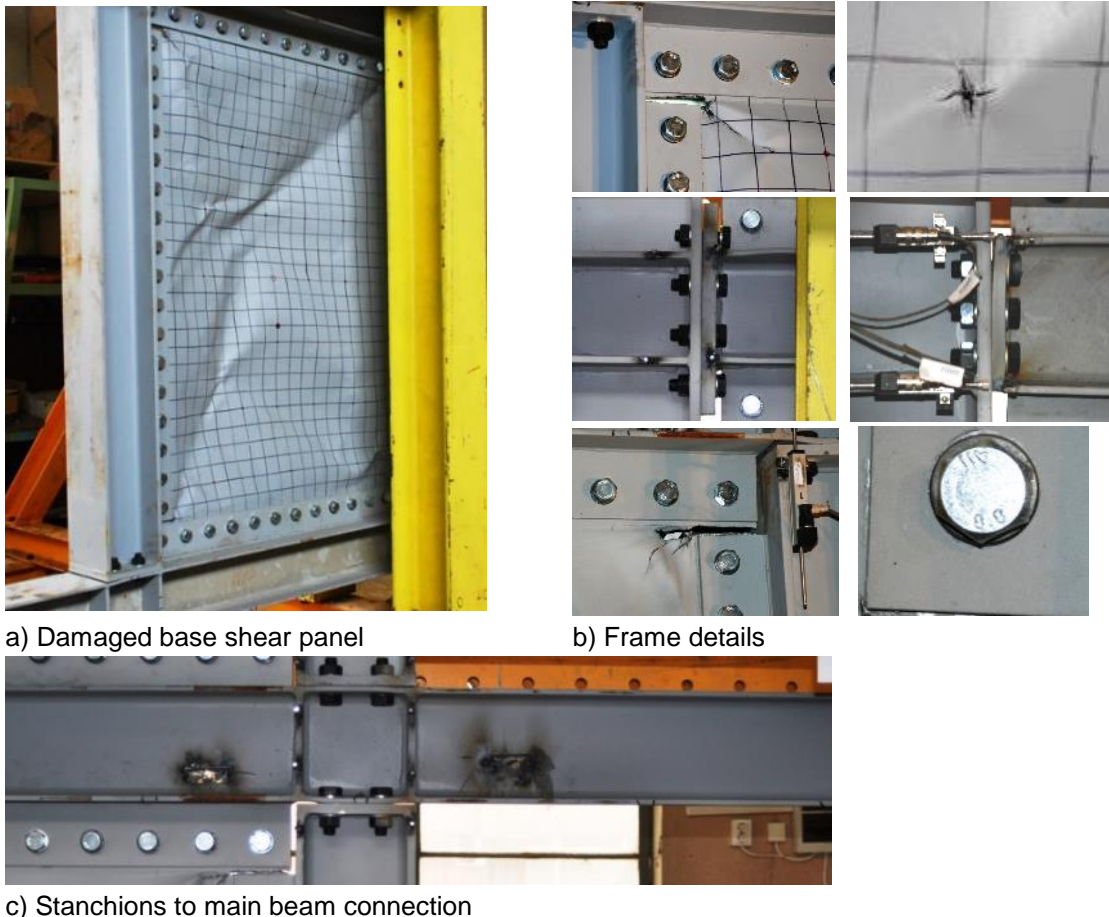


Fig. 8.16: Experimental tests

One goal of the experimental program was to evaluate the behavior factor  $q$ , for details see [7]. The average  $q$  factor obtained from experimental results amounts 6.2.

#### 8.3.5 Concluding remarks

Behavior of frames with shear panels, link beams and different beam-to-column connection rigidities has been investigated. The results showed that the shear panel system is an efficient system for resisting seismic loads, due to their stable cyclic behavior and good ductility. Semi-rigid connections reduce the ultimate capacity and dissipated energy when compared to the rigid connections, but their simpler detailing makes them more compatible with the corner details of the panels. To note also that the built-up dual frame with bolted steel panels and pinned boundary stanchions proved to be an effective lateral load resisting system.

## 8.4 DESIGN RULES

### 8.4.1 Design procedure

Structural design of dual structures, obtained by combining moment resisting frames and replaceable steel shear panels, can be performed using general code-based approach, but some additional criteria need to be considered (8.4.1.1 to 8.4.1.7). A flowchart that briefly illustrates the design of re-centring system with shear panels is shown in Fig. 8.18.

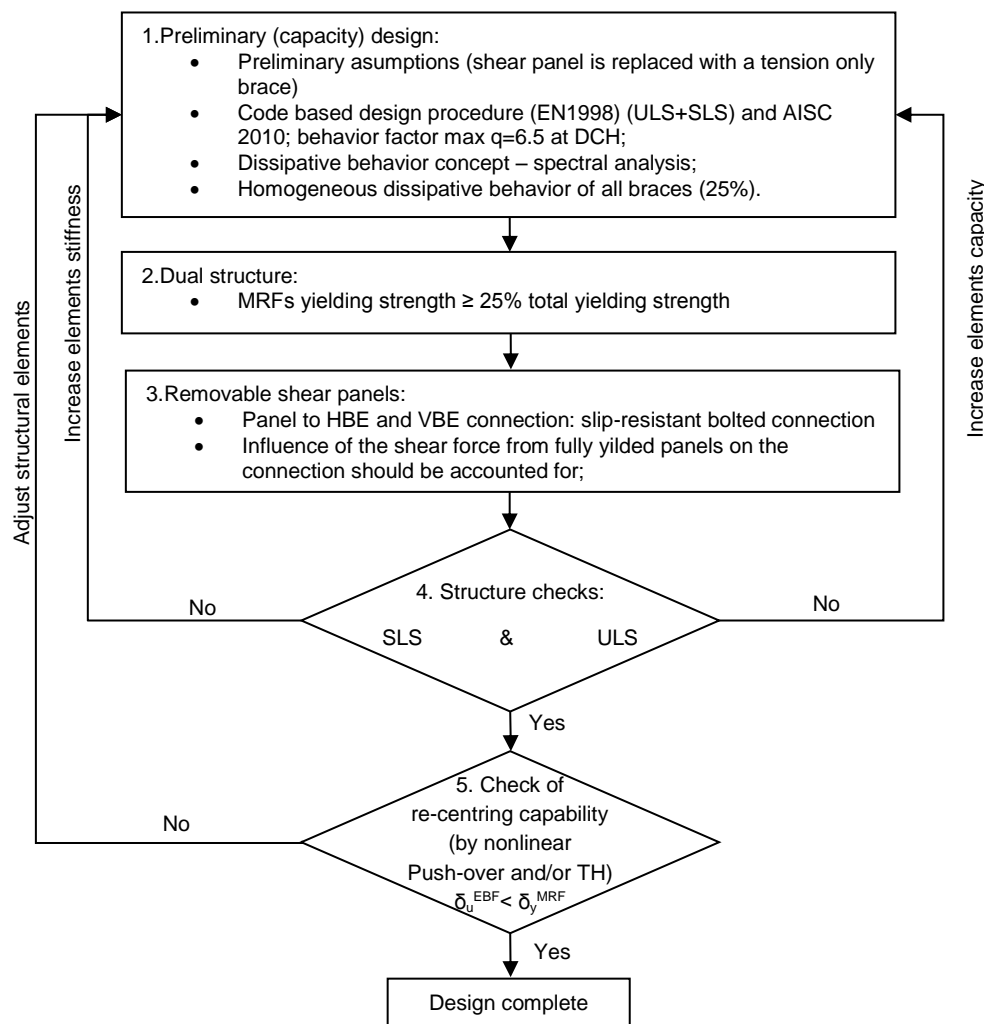


Fig. 8.17: Design flowchart for re-centring system with shear panels

#### 8.4.1.1 General design rules

For preliminary design, a number of analytical approaches are possible to achieve capacity design and determine the size of the panel's horizontal and vertical boundary elements (HBE and VBE) including the shear panel thickness. One of these methods is the approximation by a vertical truss with tension diagonals only (further denoted as equivalent braced frame) (Fig. 8.18), in line with AISC 2010 [13].



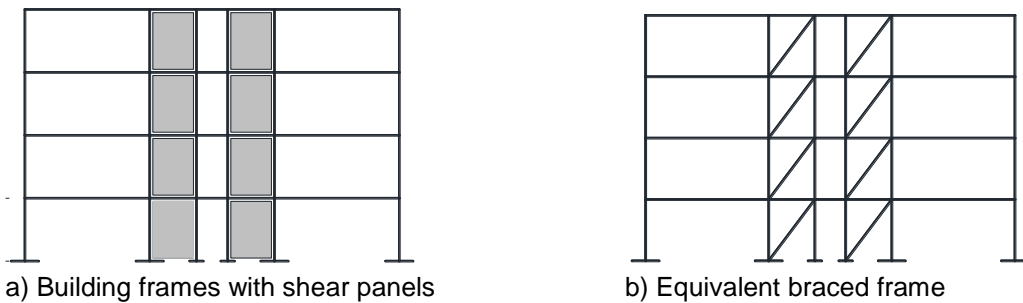


Fig. 8.18: Approximation of the frame shear panels by a vertical truss

According to AISC 2010 Provisions [13] for design of this system the applicability is limited to panels having aspect ratios of  $0.8 < L/h < 2.5$ . This limit is based on past experimental research done in U.S till the 2005 edition of AISC [14]. Since then, the design is in compliance with these Provisions and lower aspect ratios have been observed to perform satisfactorily. For example, specimens having  $L/h$  of 0.6 (Lee and Tsai, 2008 [15]) exhibited ductile hysteretic behavior comparable to that of walls with larger aspect ratios.

No theoretical upper bound exists on  $L/h$ , but as the aspect ratio increases, progressively larger HBEs will be required, driven by the capacity design principles embodied in the design requirements. This will create practical limit beyond which the shear panel design will become uneconomical and impractical, and no arbitrary limit (such as 2.5) needs to be specified provided the engineer ensures that all strips yield at the target drift response (Bruneau and Bhagwagar, 2002 [16]).

Because the shear panels don't account for gravitational loads, the capacity of MRFs structural elements should be determined using EN1993-1 [11] at Ultimate Limit State and deflections should be checked at Serviceability Limit State, using persistent situation load combinations.

A capacity design can be performed, according to EN1998-1 [13], to design moment resisting frames (where beams act as dissipative elements dissipating energy through bending) and equivalent braced frame (where braces act as dissipative elements dissipating energy through tension). The dissipative behavior concept is recommended.

A global dissipative behavior of the structure should be achieved, checking that the individual values of the ratios  $\Omega_i$  for each short link not to exceed the minimum value  $\Omega$  by more than 25% [13].

Internal forces under seismic loading are determined using response spectrum analysis, where the number of modes of vibration considered in each direction is such that the sum of the effective mass is at least equal to 90% of the total mass.

The capacity of structural elements should be checked at ULS and drifts should be checked at SLS, using seismic situation load combinations.

Global and local imperfections should be accounted for and the importance of second order effects should be checked.

It is recommended a maximum reduction factor value of 6.5, based of experimental and numeric analysis done at PUT Timisoara, Romania [8].

#### 8.4.1.2 Vertical and horizontal shear panel boundary elements (VBE and HBE)

According to AISC 2010 [13] the horizontal and vertical boundary element are designed to resist the maximum forces developed under the tension field action of the fully yielded panels. Axial forces, shear forces, and bending moments develop in the boundary elements because of the overall overturning, shear, and tension field action in the panels. HBEs and VBEs should remain essentially elastic under forces generated by fully yielded panels, but flexural hinges are allowed at the ends of HBEs.

##### - HBE

In order to account for the unbalanced load given by the panels located below and above the HBE, HBE shall have moments of inertia about an axis taken perpendicular to the plane of the web,  $I_b$ , not less than:

$$I_b \geq 0.0031 \cdot \frac{\Delta t_w \cdot L^4}{L} h \quad \text{Eq. (8.1)}$$

Where  $L$  is the width of the panel,  $h$  is the height of the panel and  $\Delta t_w$  is the difference between two consecutive stories panel;

For long spans, transverse loading due to shear panel's tension may be difficult to resist at the top and bottom HBE (where only one panel connects so there is no counter-balancing distributed load). The loading at the bottom HBE is typically more sever, as the panel is often thicker there (particularly for taller buildings). Where piers or piles can be used in the foundation system, one or two of these may be located between columns to reduce the required flexural strength on the bottom HBE.

##### - VBEs

In order to prevent excessive deformations leading to premature buckling under the pulling action of the panels, the minimum moment of inertia of the VBE,  $I_c$ , shall be verified using the following equation. If different sections are used for boundary elements (columns and pin-ended stanchions), then the average values of moment of inertia may be used in calculation.

$$I_c \geq \frac{0.00307 t_w h^4}{L} \quad \text{Eq. (8.2)}$$

#### 8.4.1.3 HBE-to-VBE connection

Analyses on building frames with the system showed that the use of simple connections between boundary beams and columns reduces the re-centring force; thus, rigid moment connections may prove more beneficial. When shear panels are placed inside a moment frame, the corners of the panels act as gusset plates above and below the moment connection and impose considerably less rotation demand on rigid connections. This particular behavior suggests that connections with lower stiffness (i.e., semi-rigid connections) can be used instead of rigid ones. Moreover, semi-rigid connections reduce costs and enhance constructability

The required shear strength of an HBE-to-VBE connection shall be based on the load combinations given in EN 1998 [13] that include the amplified seismic load. In determining the amplified seismic load, the effect of horizontal forces including overstrength, shall be taken as the shear calculated according to EN1998 [13] together with the shear resulting from the yield strength, in tension of the webs yielding at an angle  $\alpha$  (see Ch. 8.4.1.4).

For partial strength connections, the same requirement applies but the maximum end moment that the connection is capable of resisting is taken into account. When partial strength connections are used, the capacity of the connection should be larger than 50% of the connected beam. Simple connections may be used, also.

#### 8.4.1.4 Shear panels

After beams, columns and stanchions are sized, the equivalent braces are converted into shear panels having the thickness,  $t_w$ , calculated with the Eq. 8.3, according to AISC2010 [13]:

$$t_w = \frac{2 \cdot A_{brace} \cdot \Omega_s \cdot \sin \theta}{L \cdot \sin 2\alpha} \quad \text{Eq. (8.3)}$$

Where  $A_{brace}$  is the area of the equivalent tension brace,  $\Omega_s$  is the system overstrength factor,  $\theta$  is the angle between the vertical and the longitudinal axis of the equivalent diagonal brace (Fig. 8.19) and  $\alpha$  is the angle of inclination of the tension field measured from the vertical, may be taken as  $40^\circ$ , or may be calculated with Eq. 8.4 [13].

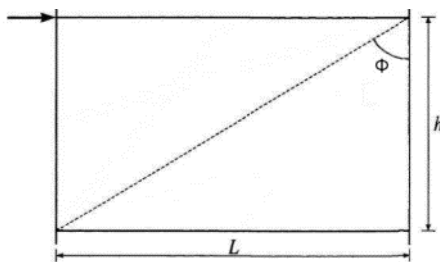


Fig. 8.19: Angle of inclination of the equivalent brace



$$\tan^4 \alpha = \frac{1 + \frac{t_w \cdot L}{2 \cdot A_c}}{1 + t_w \cdot h \cdot \left( \frac{1}{A_b} + \frac{h^3}{360 \cdot I_c \cdot L} \right)} \quad \text{Eq. (8.4)}$$

Where,  $I_c$  is the column moment of inertia,  $A_b$  and  $A_c$  are the areas of beams and columns, respectively.

The plastic shear strength of a panel is obtained with Eq.8.5 based on the assumption that each panel may be modelled by a series of inclined pin-ended strips, see chapter. 4.4:

$$V_n = 0.42 \cdot F_y \cdot t_w \cdot L_{cf} \cdot \sin 2\alpha \quad \text{Eq. (8.5)}$$

Where  $L_{cf}$  is the clear distance of the panel between HBEs and  $F_y$  is the yielding strength of the panel.

#### 8.4.1.5 Shear panel to boundary elements connection

The required strength of panel connection to the surrounding HBE and VBE shall equal the expected yield strength, in tension, of the web. Two typical details of connections of steel shear panel to boundary beams and columns are shown in Fig. 8.20. The welded connection (Fig. 8.20a) should be designed such that the connection panels (fin plates) and welds develop the shear strength of the panel. If re-centring capacity is of interest, field-bolted connections are recommended (Fig. 8.20b). The bolts should be slip-resistant and able to develop the shear strength of the panels. Even if bolts are slip-resistant, it is expected that during the cyclic loading of the panels, the bolts slip before the tension field yields. Therefore, the design shear resistance and the design bearing resistance should be also verified [9]

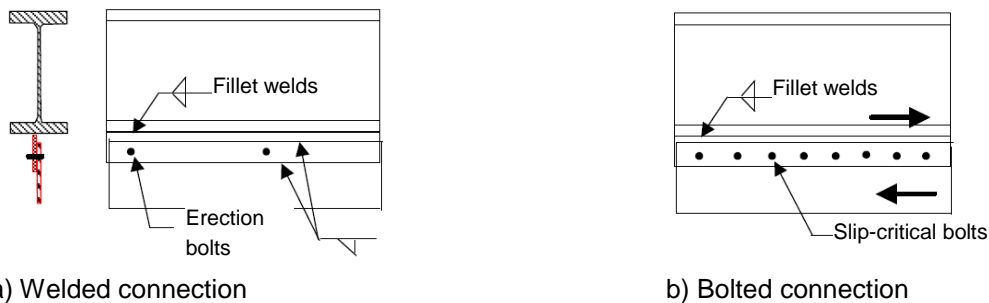


Fig. 8.20: Shear panel to boundary elements connection

#### 8.4.1.6 Dual configuration

The duality of the structure should be checked by verifying that the MRFs is able to resist at least 25% of the total seismic force (Eq.8.6).

$$F_y^{MRF} > 0.25 \cdot (F_y^{MRF} + F_y^{SP}) \quad \text{Eq. (8.6)}$$

Where,  $F_y^{MRF}$  is the yield strength of MRF,  $F_y^{SP}$  is the yield strength of shear panels.

#### 8.4.1.7 Re-centring capability

The re-centering capability of frames with shear panels should be verified using nonlinear static and/or dynamic analyses. The modellings for this type of analyses are presented in chapters 7.4.2 and 8.4.3.

#### 8.4.2 Modelling for static non-linear (pushover) analysis

In order to perform pushover analysis, nonlinear behavior has to be defined, both for materials used, as well as for structural members.

Expected material properties (based on  $\gamma_{ov}$ ) should be used for MRF beams and nominal material properties for non-dissipative elements (columns). It is recommended that the shear panels have lower yield resistance than the rest of the elements.

To facilitate the analysis and design of structural elements for building applications, including the gravity beams and columns, a simplified methodology for modelling the shear panels may be used. The shear panels are replaced by minimum of 10 inclined pin-ended strip members at angle  $\alpha$  with respect to vertical, capable of transmitting tension forces only, and oriented in the same direction as the principal tensile stresses in the panel (strip model) [18]. Fig. 8.21 shows the strip model representation of a typical shear panel.

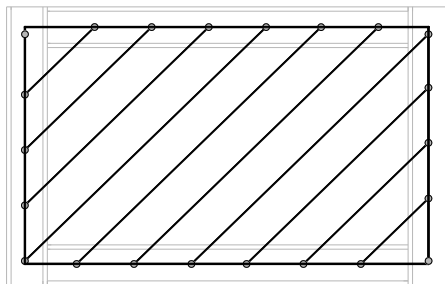


Fig. 8.21: Strip model for static nonlinear analysis

The strips may be modelled as double pinned beam elements having a trilinear plastic axial P type hinge (Fig. 8.22 and Table 8.1) at the middle. Non-linear acceptance criteria are given in Table 8.2 (based on ASCE 41-13 provisions [19] and results of the research program at PUT, Timisoara, Romania [8]).

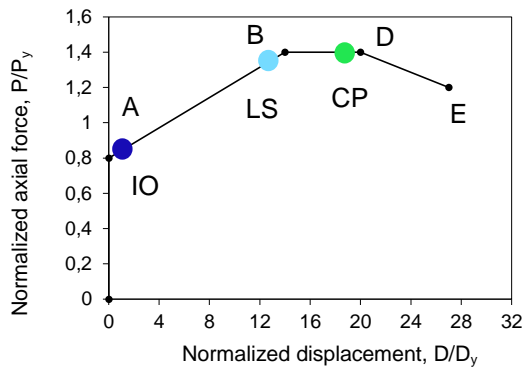


Fig. 8.22: Proposed strip tension only plastic hinge

**Table 8.1: Proposed strip tension only plastic hinge values**

Hinge	A		B		C		D		E	
	$\frac{P}{P_y}$	$\frac{\Delta}{\Delta_y}$	$\frac{P}{P_y}$	$\frac{\Delta}{\Delta_y}$	$\frac{P}{P_y}$	$\frac{\Delta}{\Delta_y}$	$\frac{P}{P_y}$	$\frac{\Delta}{\Delta_y}$	$\frac{P}{P_y}$	$\frac{\Delta}{\Delta_y}$
Tension	0	0	0.8	0	1.4	14	1.4	20	1.2	27

**Table 8.2: Proposed acceptance criteria**

Criteria	IO	LS	CP
$\Delta / \Delta_y$	0.5	13	19

The area of the strips may be calculated as following [13]:

$$A_s = (L \cdot \sin \alpha + h \cdot \cos \alpha) / n \quad \text{Eq. (8.7)}$$

Where,  $n$  is the number of strips per panel.

Nonlinear plastic hinges of bending type M3 may be assigned at the ends of the MRFs beams and of bending with axial force type P-M3 at the ends of columns and stanchions. Additionally, V2 type plastic hinges may also placed at the ends of the beam between the shear panels. These properties should be computed according to ASCE41-13 [19]. In order to verify the plastic mechanisms and re-centring capability, the target displacement corresponding to ultimate limit state (design) needs to be determined using N2 method [20]. The non-linear modelling procedure was validated in [8] and is presented in Fig. 8.23.

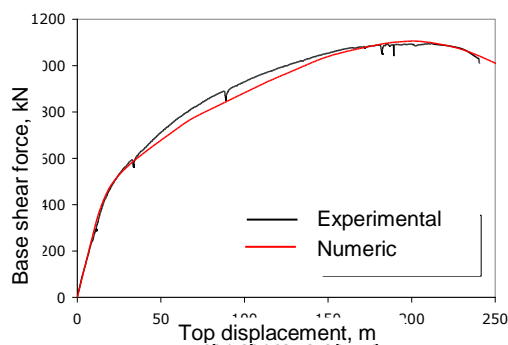
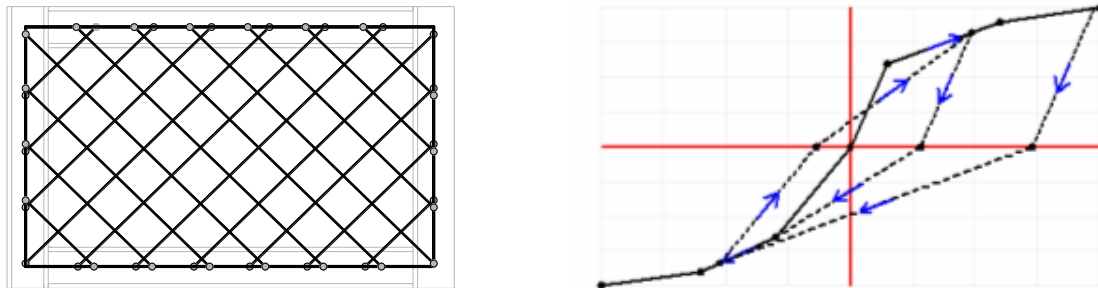


Fig. 8.23: Strip model for static non - linear analysis

Pushover analysis should be performed in displacement control, until reaching a monitored displacement at the top of the structures. Firstly, gravitational loads (from load combination  $1.0 \cdot \text{Dead} + 0.3 \cdot \text{Live}$ ) should be applied in force control and secondly, lateral forces under a modal distribution will act on the analyzed frames in displacement control.

#### 8.4.3 Modelling for dynamic non - linear analysis

In order to perform a dynamic non-linear analysis the frame is modelled in the same manner as for static non-linear analysis but in this case the same tension only strip are oriented in both directions Fig. 8.24a. The strip plastic hinges have a Takeda type hysteretic behavior presented in Fig. 8.24b



a) Dual strip model

b) Takeda type hysteretic behavior

Fig. 8.24: Strip model for dynamic non - linear analysis

The non - linear dynamic analysis [21] shall be performed in order to define time-dependent response of steel buildings when designed according to the provisions of the EN1998-1-1 [13] under real earthquake conditions.

### 8.5 ANALYSIS ON 2D BUILDING FRAMES

Application of the design procedure described in chapter 8.4 on a case-study structure is shown in the following. Initially the frames were designed through elastic analysis at ULS and SLS. Nonlinear static analyses followed to investigate their behavior beyond the elastic range.

#### 8.5.1 Description of examined building frames

##### 8.5.1.1 Geometry and assumptions

The case study presented hereafter was based on the extraction of an exterior plane frame from a four and eight story composite building, Fig. 8.25. The frame consisted of rigid moment frames (MRF) with three 8 m bays with two shear panel spans of 3 m located in the interior bay. The story height of all buildings was considered 4 m. Panel aspect ratio  $L/h$  was equal 0.75.

The beams, columns and stanchions are made of European wide flange I-sections (IPE, HEB and HEM type).

The shear panels had lower steel grade (S235) than the rest of the structural members (S355). The beams production was not considered to be fully controlled, so that the properties of the beam material had to comply with EN1993-1-1 [11] recommendations with  $\gamma_{ov} = 1.25$ .

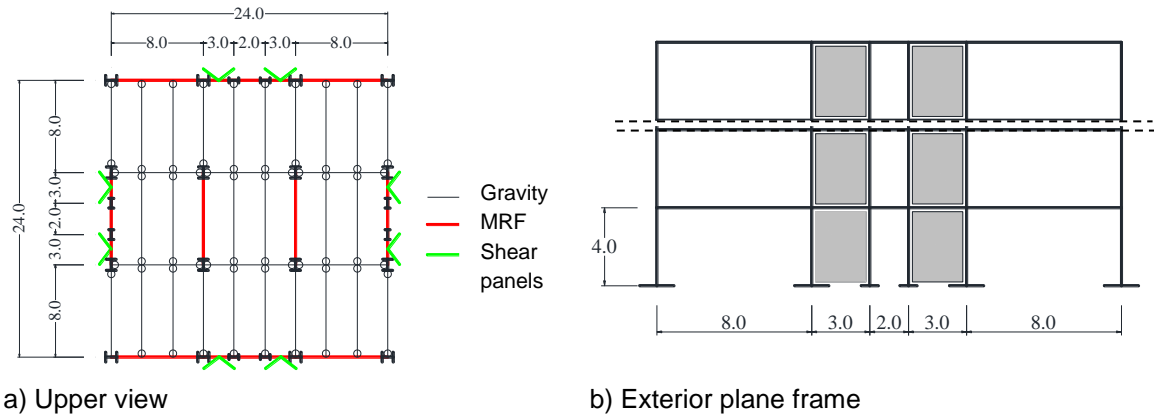
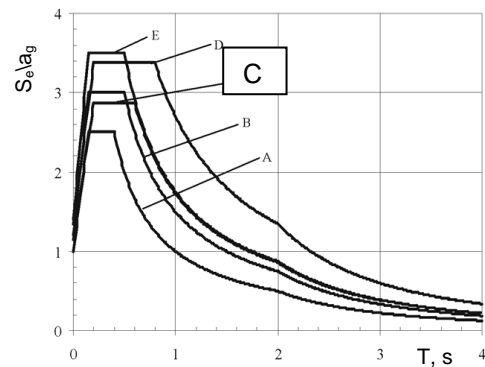


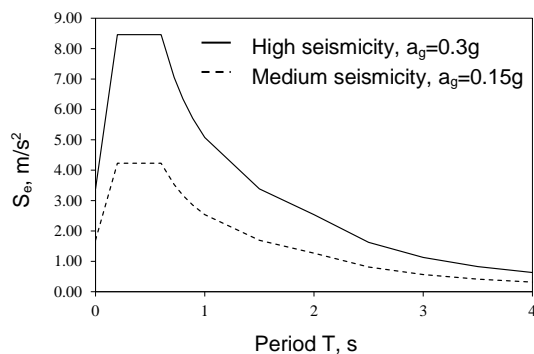
Fig. 8.25: Geometry of the buildings

Table 8.3 includes the gravity and seismic loads taken into account. The gravity loads were applied as uniform distributed loads on the secondary beams and reduced to concentrated loads on the main frames. The dead load takes into account the composite slab and steel sheeting, resulting  $2.75 \text{ kN/m}^2$ . There were considered some superimposed loads from services, ceilings and raised floors of  $0.7$  for intermediate floors and  $1$  for last floor, respectively. A  $4.0 \text{ kN/m}^2$  was taken into account for perimeter walls. The live load takes into account the destination of the buildings (offices - class B) and movable partition walls, resulting  $3.8 \text{ kN/m}^2$ .

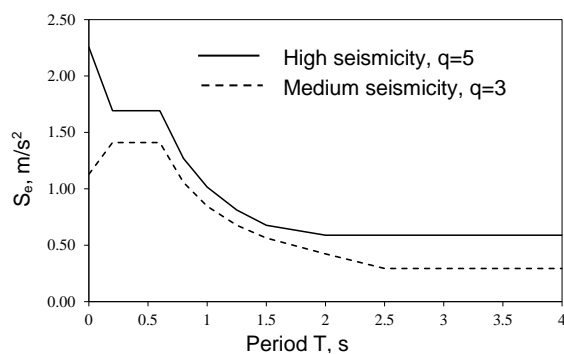
Two different design cases were considered: moderate seismicity with medium class ductile building frames (DCM) and high seismicity with high class ductile building frames (DCH). Type 1-C spectrum (Fig. 8.26a) was selected for design [6] considering two peak ground accelerations  $0.3$  for high seismicity case and  $0.15$  for moderate seismicity case, respectively (Fig. 8.26b and c). Because no recommendation for reduction factor,  $q$ , is given in EN1998 [13], a value of  $5$  was taken into consideration for high ductility class structure, based on previous research [8], [7]. In case of moderate seismicity where medium ductility class structure is needed, a reduction factor of  $3$  was selected.



a) Type 1 elastic response spectra [13]



b) Elastic spectra



c) Design spectra

Fig. 8.26: Response spectra for high and moderate seismicity

**Table 8.3: Loading details**

Vertical loads	
Dead loads (composite slab + steel sheeting)	2.75 kN/m <sup>2</sup>
Superimposed loads (Services, ceiling, raised floor)	0.7 kN/m <sup>2</sup> - intermediate floors 1.0 kN/m <sup>2</sup> – last floor
Perimeter walls	4.0 kN/m <sup>2</sup>
Live loads – (office cl.B +movable partition)	3.00+0.800=3.8 kN/m <sup>2</sup>
• DCH	
Elastic response spectra	Type 1
Peak ground acceleration	A=0.3g
Importance class II	$\gamma_I = 1.0$ (Ordinary buildings)
Ground type	C ( $T_B = 0.2$ s, $T_C = 0.60$ s)
Proposed behavior factor q (DCH)	5
Damping ratio	5%
Seismic combination coefficient for the quasi-permanent value of variable actions	$\psi_2=0.30$
• DCM	
Elastic response spectra	Type 1
Peak ground acceleration	A=0.15g
Importance class II	$\gamma_I = 1.0$ (Ordinary buildings)
Ground type	C ( $T_B = 0.2$ s, $T_C = 0.60$ s)
Proposed behavior factor q (DCM)	3
Damping ratio	5%
Seismic combination coefficient for the quasi-permanent value of variable actions	$\psi_2=0.30$

The frame with shear panels is replaced with a vertical truss with tension diagonals only (Fig. 8.27). Then the equivalent structure is designed according to considered codes [11], [13] and [13].

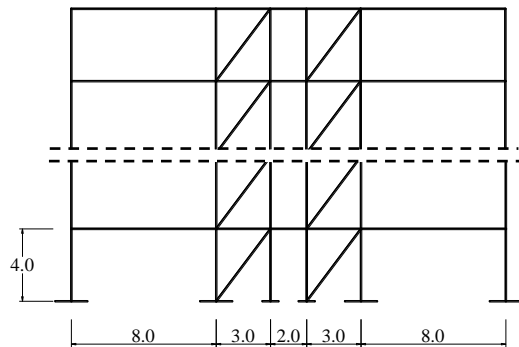
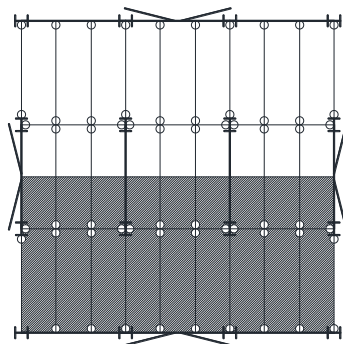


Fig. 8.27: Equivalent frame

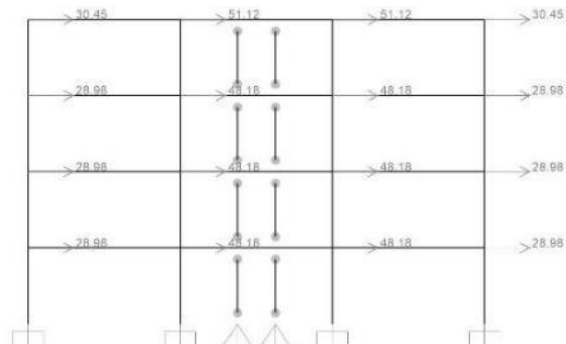
#### 8.5.1.2 Modelling for linear elastic analysis

The modelling, analysis and design of the buildings, was performed with the finite element software SAP2000 [22]. The structural model is a linear-elastic 2D model with beam elements. Rigid diaphragms were assigned at each level to account for the effect of reinforced concrete slabs.

The structural masses (in tons) considered from half of the total bay of the structure (12m) were assigned in the frame's structural nodes, since only the exterior frames represent the lateral load resisting system, see Fig. 8.28.



a) Considered from half the structure  
Fig. 8.28: Structural masses



b) Assigned in structural nodes of 2D model.

#### 8.5.2 Persistent design situation

As the shear panels are not designed to account for gravitational loads, the moment resisting frame was designed at ultimate and serviceability limit state under persistent design situation.

##### 8.5.2.1 Ultimate Limit State

MRFs were designed from fundamental design load combination. IPE360 sections were obtained for beams, HE260B (ext.) and HEB300 (int.) sections for columns of 4 and 8 story buildings.

### 8.5.2.2 Serviceability Limit State

Beams deflections were checked from fundamental load combination and founded are less than the limit taken into account,  $L/350$ .

### 8.5.3 Response spectrum analysis

Multi-modal response spectrum analysis was performed and the results are summarized in Table 8.4, presenting the modes that activated more than 90% of the mass.

**Table 8.4: Participating mass ratio**

Frame	Design seismicity case	Mode No	Eigen Period (s)	Participating mass ratio (%)	Total (%)
4-st.	High	1	<u>0.929</u>	81.1	94.3
		2	0.321	13.2	
	Moderate	1	<u>1.001</u>	80.6	94.1
		2	0.345	13.5	
8-st.	High	1	<u>1.701</u>	74.4	94.0
		2	0.539	14.8	
		3	0.208	4.8	
	Moderate	1	<u>1.865</u>	76.1	90.7
		2	0.584	14.6	

### 8.5.4 Global imperfections and 2<sup>nd</sup> order effects

Global imperfections were considered in the structural analysis, according to EN1993-1-1, through equivalent lateral forces  $H_i$ , from combination  $1.35 \cdot G + 1.5 \cdot Q$ . These forces were computed based on total gravitational loads and initial global imperfection  $\phi$ , level by level, and considered in every load combination further on. Second order effects were not accounted for in design because the inter-story drift sensitivity coefficient  $\theta$ , computed according to EN1998-1-1 [13], found to be smaller than 0.1.

### 8.5.5 Seismic design

#### 8.5.5.1 Ultimate Limit State - Dissipative elements design

The equivalent braces were designed to resist the forces of the most unfavorable seismic combination. Table 8.5 presents the minimum and maximum overstrength values  $\Omega$ . In order to satisfy a homogeneous dissipative behavior of the diagonals, the 25% limit between the maximum overstrength  $\Omega_{\max}$  and the minimum value  $\Omega_{\min}$ , was ensured.



**Table 8.5: Homogeneity of equivalent braces**

Frame	Design seismicity case	$\Omega_{\min}$	$\Omega_{\max}$	Homogeneity
4-st.	High	1.27	1.69	25%
	Moderate	1.32	1.75	25%
8-st.	High	1.56	2.00	21%
	Moderate	1.54	1.90	19%

#### 8.5.5.2 Ultimate Limit State – Non-dissipative element design

The non-dissipative elements, MRF columns and VBEs were checked with the most unfavorable seismic combination, to ensure that the failure of the shear panels occurs first. The VBEs minimum moments of inertia, about an axis taken perpendicular to the plane of the web, were checked and found to be greater than the minimum values.

#### 8.5.6 Limitation of inter-story drift

Considering that the building has ductile non-structural elements the inter-story drift is limited to 0.0075. The inter-story drifts were computed with Sap2000 [22] and are presented in Table 8.6.

**Table 8.6: Maximum inter-story drift**

Frame	Design seismicity case	Inter-story drift, mm/mm
4-st.	High	0.0047
	Moderate	0.0049
8-st.	High	0.0060
	Moderate	0.0064

#### 8.5.6.1 Dual configurations

The duality of the structures was checked by verifying that the MRFs are able to resist at least 25% of the total seismic force. Adjustments of the structural elements were needed in order to satisfy the minimum criteria for a dual system (Table 8.7 and Table 8.8).

**Table 8.7: 4-story frame**

Frame	Design seismicity case	Story	Beams		Columns		Stanchions
			Ext.	Int.	Ext.	Int.	
4-st.	High	1	IPE450	IPE360	HEB260	HEB320	HEB320
		2	IPE450	IPE360	HEB260	HEB320	HEB320
		3	IPE450	IPE360	HEB260	HEB320	HEB300
		4	IPE450	IPE360	HEB260	HEB320	HEB280
	Moderate	1	IPE450	IPE360	HEB260	HEB300	HEB300
		2	IPE450	IPE360	HEB260	HEB300	HEB300
		3	IPE400	IPE360	HEB260	HEB300	HEB300
		4	IPE400	IPE360	HEB260	HEB300	HEB280

**Table 8.8: 8-story**

Frame	Design seismicity case	Story	Beams		Columns		Stanchions
			Ext.	Int.	Ext.	Int.	
8-st.	High	1	IPE450	IPE400	HEB260	HEB400	HEB400
		2	IPE450	IPE400	HEB260	HEB400	HEB400
		3	IPE450	IPE400	HEB260	HEB400	HEB400
		4	IPE450	IPE400	HEB260	HEB400	HEB400
		5	IPE450	IPE400	HEB260	HEB400	HEB400
		6	IPE450	IPE400	HEB260	HEB400	HEB400
		7	IPE450	IPE400	HEB260	HEB400	HEB400
		8	IPE450	IPE400	HEB260	HEB400	HEB300
	Moderate	1	IPE400	IPE360	HEB260	HEB400	HEB400
		2	IPE400	IPE360	HEB260	HEB400	HEB400
		3	IPE400	IPE360	HEB260	HEB400	HEB400
		4	IPE400	IPE360	HEB260	HEB400	HEB400
		5	IPE400	IPE360	HEB260	HEB400	HEB400
		6	IPE400	IPE360	HEB260	HEB400	HEB400
		7	IPE400	IPE360	HEB260	HEB400	HEB400
		8	IPE400	IPE360	HEB260	HEB400	HEB300

#### 8.5.6.2 Weak beam-strong column

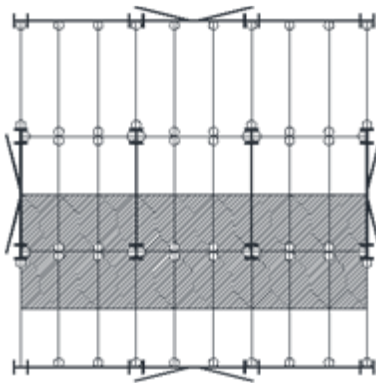
The “weak beam-strong column” condition was checked and found to comply with recommendation given in EN 1993-1 [11].

#### 8.5.7 Non - linear static analyses (Pushover)

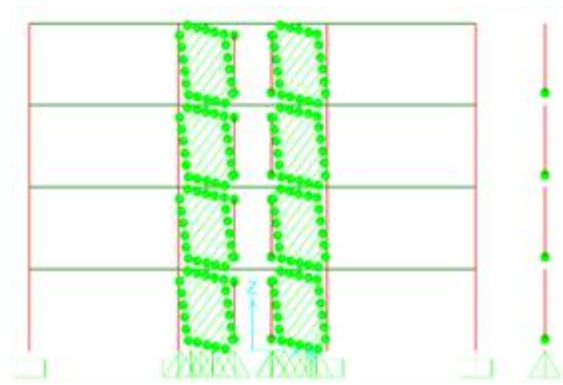
Because the height of case-study frames is relatively low, and the buildings are regular in plan and elevation the higher modes of vibration do not affect the structural response. Thus, the assessment of seismic performance was done using static nonlinear (pushover) analysis only.

##### 8.5.7.1 Frame modelling for static non-linear analysis

Nonlinear static (pushover) analysis was performed to verify the collapse mechanism and re-centring capability. P–Delta effects were also included. A leaning column was modelled (Fig. 8.29) in order to account for the gravitational loads from the remaining half of structure (8 m) that were not considered in the analyzed.



a) 3D structure



b) Numerical model

Fig. 8.29: Capacity curves for all building frames

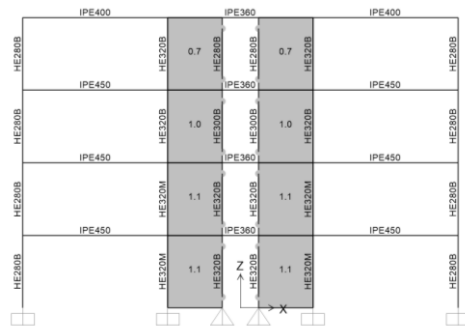
In the Table 8.9 are given parameters needed to model the strips (strip areas  $A_s$ , angle of inclination of strips  $\alpha$  and strip diameter,  $D$ ).

**Table 8.9: Strip non-linear modelling parameters**

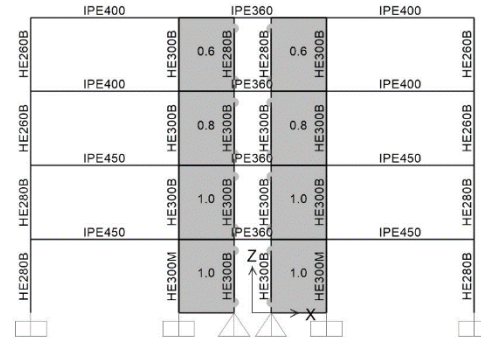
Frame	Design seismicity case	$\alpha$ [°]	Stories	$A_s$ [mm <sup>2</sup> ]	$D$ [mm]
4-st	High	40	1,2	535.6	26.1
			3	486.9	24.9
			4	340.8	20.8
	Moderate	40	1,2	486.9	24.9
			3	389.5	22.3
			4	292.2	19.3
8-st.	High	40	1,2,3	973.9	35.2
			4,5,6	730.4	30.5
			7	584.3	27.3
			8	486.9	24.9
	Moderate	40	1,2,3	730.4	30.5
			4,5,6	584.3	27.3
			7	486.9	24.9
			8	340.8	20.8

#### 8.5.7.2 Pushover analysis results

Further adjustments of the structural columns were needed in order to have re-centring capacity at ultimate limit state (design). Fig. 8.30 and Fig. 8.31 presents the final configuration of the building frames. Further, only the results of the final configuration of the building frames is presented.

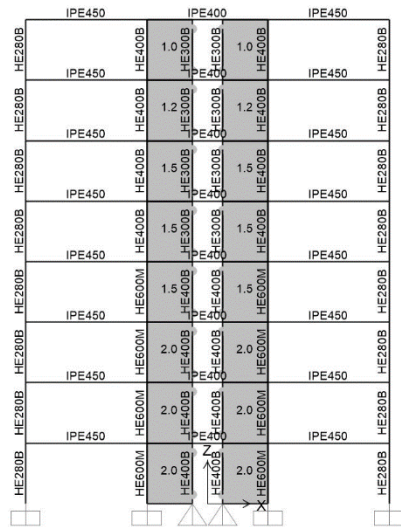


a) high seismicity case

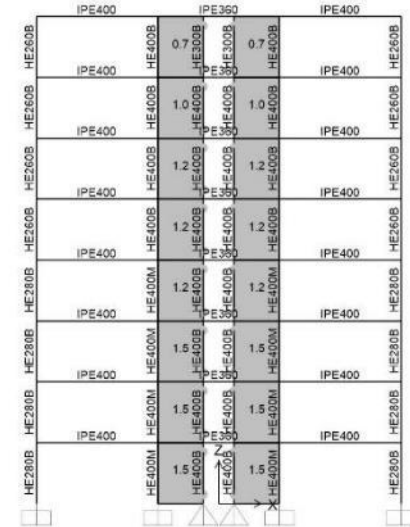


b) moderate seismicity case

Fig. 8.30: 4 story building frames



a) high seismicity case



b) moderate seismicity case

Fig. 8.31: 8 story building frames

The target displacements corresponding to ultimate limit state (ULS) were calculated using N2 method [20]. Table 8.10 presents target displacements (top displacement) and maximum inter-story drift ratios corresponding to ultimate limit state (blue dot in Fig. 8.32) and the maximum displacement of re-centering capacity,  $d_{re-centering}$  (red dot in Fig. 8.32) with corresponding inter-story drift ratios, for all 4 building frames. After this point ( $d_{re-centering}$ ), plastic deformations occur in MRF beams or columns depending on frame.

**Table 8.10: ULS target displacement, maximum re-centering displacement and corresponding inter-story drift ratios.**

Frame	Seismicity design case	ULS		$d_{re-centering}$	
		Top displacement, m	Inter-story drift ratio, %	Max. displacement, m	Inter-story drift ratio, %
4-st.	high	0.209	1.6	0.217	1.7
	moderate	0.117	0.9	0.216	1.8
8-st.	high	0.310	1.3	0.334	1.4
	moderate	0.156	0.6	0.339	1.5

Fig. 8.32 presents the capacity curves for all 4 build frames in terms of base shear force and top displacement, taking into account an in-verted triangle lateral force pattern. The frames designed assuming DCH, have a larger capacity and ductility than the ones designed assuming DCM. The 8-story frames are more ductile than the 4-story frames and were designed to resist similar seismic forces (within the same ductility class).

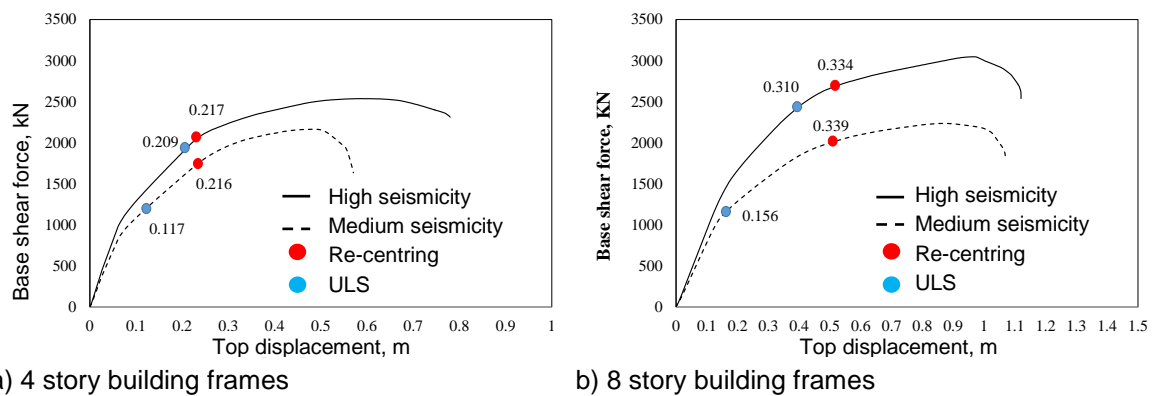
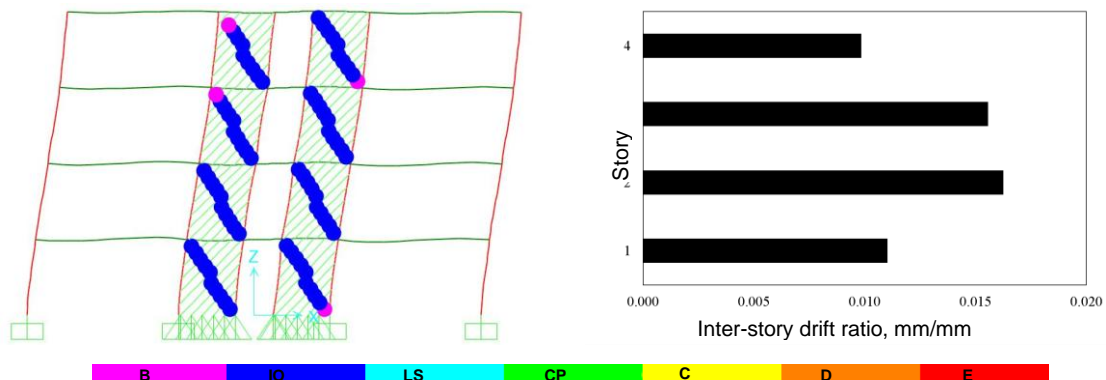
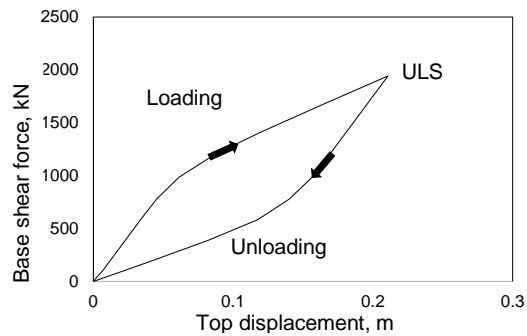


Fig. 8.32: Capacity curves

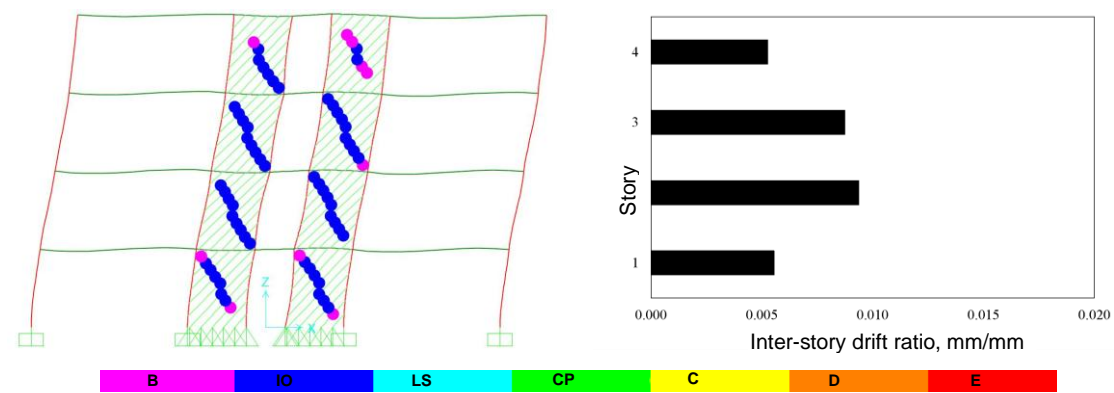
In order to evaluate the re-centering capacity of the frames, the plastic mechanisms are presented at target displacement corresponding to ULS (Fig. 8.33 to Fig. 8.36). Also, a re-centering analysis was performed, loading the frames till the target displacement corresponding to ULS and then unloading to 0 force. It can be seen that the plastic hinges are developed only in the shear panels with no damage in the MRF. Thus, the MRF has the necessary restoring force to re-center the building frames and then replace the damaged shear panels. This was also confirmed by the re-centering analysis done, which has showed that after unloading, no residual drift is present.





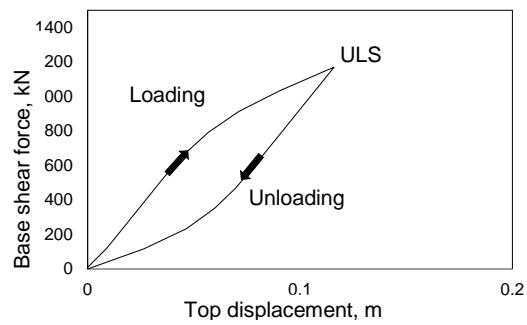
c) Re-centering capacity

Fig. 8.33: 4 story building frame at high seismicity design case



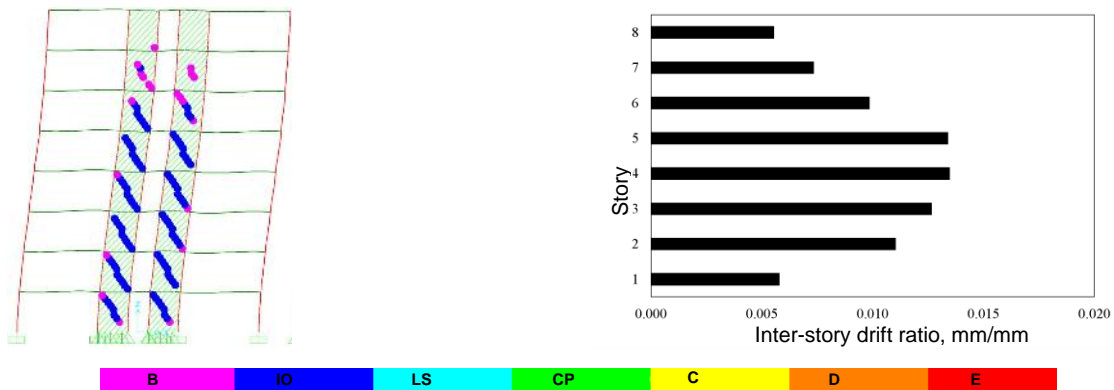
a) Plastic mechanism

b) Inter-story drift ratios on story



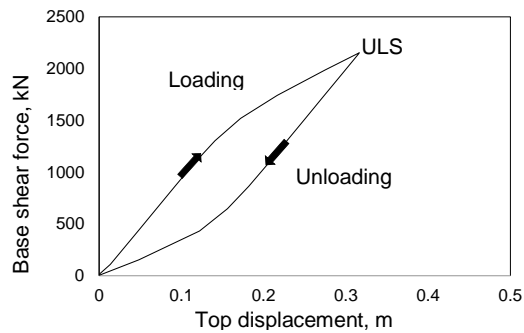
c) Re-centring capacity

Fig. 8.34: 4 story building frame at moderate design case



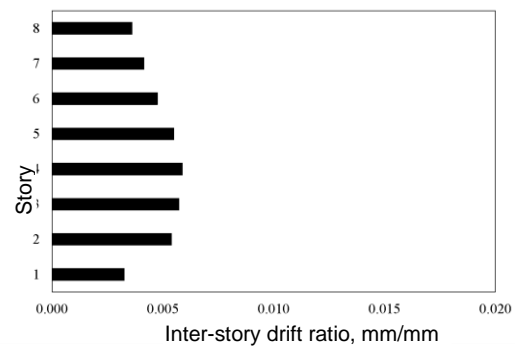
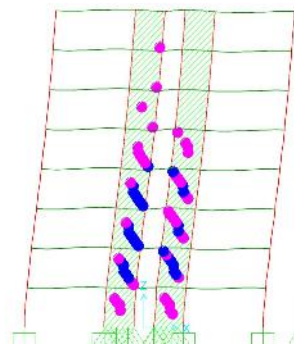
a) Plastic mechanism

b) Inter-story drift ratios on story



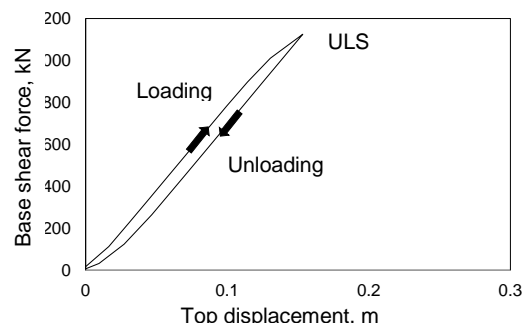
c) Re-centring capacity

Fig. 8.35: 8 story building frame at high seismicity design case



a) Plastic mechanism

b) Inter-story drift ratios on story



c) Re-centring capacity

Fig. 8.36: 8 story building frame at moderate seismicity design case

## 8.6 CONCLUSIONS

The above study introduces the innovative lateral force resisting dual frame with shear panel system and reveals some of the important global performance characteristics of the system, the following observations are worth noting:

- Efficient structural system which increase strength and stiffness having higher ductility and stable cyclic behavior (e.g. high dissipation capacity).
- With a proper design, the inelastic deformations can be concentrated in the dissipative shear panels only.

- c) Since the MR frames are designed to remain elastic during earthquakes, they would provide the necessary restoring force to re-center the structure upon removal of damaged shear panels ("fuse" elements).
- d) The shear panels can be easily removed, even when they are damaged after a severe seismic event, since they are very thin and are not part of the gravity loading resistant system.
- e) The system enables for an efficient control, both on drift and displacement deformations, exhibiting a self-centering behavior allowing for immediate occupancy after earthquake.
- f) The demand of having no yielding in the MRFs before the attainment of ULS, is the basic design requirement for dual frames with removable dissipative members.
- g) Code relevant design rules for the seismic design of frames with replaceable shear steel panels, have been formulated in a Design Guide. Structural details were also defined.
- h) The re-centering capability of frames with shear panels should be verified and validated using advanced finite element models. Replacing the shear panel with the simplified strip model for non-linear modelling allows the use of conventional analysis software.

## **8.7 FIELD OF APPLICATION**

The innovative dual frame with shear panel may be applied to existing and new multi-story steel and concrete building frames and can be used as an efficient, both technically and costly, lateral load resisting system (like removable links, buckling restrained braces, etc.).

## **8.8 PUBLICATIONS**

1. Dubina D., Dinu F. Experimental evaluation of dual frame structures with thin-walled steel panels. *Thin-Walled Structures* 2013; 78:57-69.
2. Neagu C., Dinu F., Dubina D. Global ductility of dual steel frames with replaceable dissipative shear walls. *Mathematical Modelling in Civil Engineering* 2015; 11(3): 23-30.

## **8.9 BIBLIOGRAPHIC REFERENCES**

1. Dubina D., Stratan A. and Dinu F. Re-centering capacity of dual-steel frames. *Steel Construction: Design and Research* 2011; 2(4):73-81.
2. Seilie I., Hooper J. *Steel Plate Shear Walls: Practical Design and Construction*. Modern Steel Construction 2005.
3. Berman J.W. Seismic behavior of code designed steel plate shear walls. *Engineering Structures* 2011; 33(1): 230–244.
4. Caccese V., Elgaaly M., Chen R. Experimental Study of Thin Steel-Plate Shear Walls Under Cyclic Load. *Journal of Structural Engineering* 1993; 119(2): 573–587.
5. Berman J.W., Clayton P.M., Lowes L.N., Bruneau M., Fahnestock L.A., Tsai K.C. Development of a recentering steel plate shear wall and addressing critical steel plate shear wall research



- needs: Proc. of the 9th U.S. National and 10th Canadian Conference on Earth-quake Engineering; 2010; Toronto; 1087; Ontario.
6. Alinia M.M., Dastfan M. Cyclic behaviour, deformability and rigidity of stiffened steel shear panels. *Journal of Constructional Steel Research* 2007; 63: 554–563.
  7. Dubina D., Dinu F. Experimental evaluation of dual frame structures with thin-walled steel panels. *Thin-Walled Structures* 2013; 78:57-69.
  8. Neagu C. Multi-story building frames stiffened with dissipative shear wall: PHD Thesis; Ed. Politehnica; University Politehnica Timisoara; Romania, 2011.
  9. EN 1993-1-8: Eurocode 3: Design of steel structures. Part 1-8: Design of joints. Brussels: Comité Européen de Normalisation (CEN); 2004.
  10. ECCS document: Recommended testing procedure for assessing the behavior of structural steel elements under cyclic loads, Technical committee 1: structural safety and loadings, Technical working group 1.3: seismic design; 1986.
  11. EN1993-1-1. Eurocode 3: Design of steel structures - Part 1-1: General rules and rules for buildings. Brussels: Comitee Europeen de Normalisation (CEN); 2003.
  12. EN1998-1-1, Eurocode 8: Design of structures for earthquake resistance – Part 1-1: General rules, seismic actions and rules for buildings. Brussels: Comitee Europeen de Normalisation (CEN); 2003.
  13. AISC 341-10. Seismic provisions for structural steel buildings; American Institute for Steel Construction: 2010.
  14. AISC 341-05. Seismic provisions for structural steel buildings; American Institute for Steel Construction: 2005.
  15. Lee C.S., Tsa K.C. Experimental Response of Four 2-Story Narrow Steel Plate Shear Walls: Proceeding of the 2008 Structures Congress; Vancouver.
  16. Bruneau M., Bhagwagar T. Seismic Retrofit of Flexible Steel Frames using Thin Infill Panels. *Engineering Journal* 2002; 24(4):443–453.
  17. Berman J. W., and Bruneau M. Plastic Analysis and Design of Steel Plate Shear Walls. *Journal of Structural Engineering* 2003; 129(11):448-1456.
  18. Driver R. G., Kulak G.L., Kennedy D.J.L and Elwi A.E. Cyclic Test of a Four-Story Steel Plate Shear Wall. *ASCE Journal of Structural Engineering* 1998; 124(2):112-120.
  19. ASCE 41-13. Publication Anticipated Seismic Evaluation and Upgrade of Existing Buildings: American Society of Civil Engineers; Reston, Virginia. Public Comment Edition available through the American Society of Civil Engineers.
  20. Fajfar P. A nonlinear analysis method for performance-based seismic design. *Earthquake Spectra* 2000; 16(3): 573-92.
  21. Vamvatsikos D., Cornell C. A. Incremental dynamic analysis. *Earthquake Engineering and Structural Dynamics* 2002; 31(3):491-514.
  22. SAP2000. CSI: Computers and Structures Inc., [www.csiberkeley.com](http://www.csiberkeley.com).



## **9 CONCENTRICALLY BRACED FRAME WITH MODIFIED BRACES (CBF-MB)**

### **9.1 INTRODUCTION**

Centrically braced frames (CBFs) are traditional structural system in steel construction. They are used for resisting lateral forces due to wind, earthquakes and others. This system has proved its efficiency for lateral loads by providing sufficient stiffness and strength due to its complete truss action. That is the main reason for its popularity. Nowadays CBFs are widely implemented in single storey industrial frames, multistorey buildings and industrial engineering facilities. Their application in new constructions is expanded to seismic retrofit of steel, composite and concrete structures as well.

The contemporary seismic design requires that the lateral force resisting system should have adequate strength and stiffness, but also ductility and energy dissipation capacity. Requirements should be tuned according to the seismicity of the site and the objectives of the structural performance level to be achieved. It has been evident from past earthquakes that some bracing members in CBFs perform severe concentration of plastic deformation in their mid-length section. The result of such structural response would be inadequate ductility and energy dissipation capacity illustrated by premature brace fracture and frame failure. Such non-satisfactory seismic behaviour demands improvement of the design practice.

Looking for proper seismic behaviour, last generation of codes often postulates requirements that in many cases are controversial and difficult to be achieved by conventional design approach. In search of practical and affordable solution for CBFs design, during the period 2011-2012 in the Universitet po Arhitektura Stroitelstvo i Geodezija (UACEG) in Sofia a National Research Project was conducted. It was focused on the improvement of seismic behaviour of braced frames. During the project concentrically braced frames with modification of the braces (acronym CBF-MB) were designed, tested and elaborated. The proposed modification is based on introduction of different cross sections within the length of a brace, enabling the practicing engineer with low-tech approach to achieve needed stiffness and strength, improved ductility, adequate energy dissipation and self-centering capability of the system.

### **9.2 DESCRIPTION OF THE CBF-MB SYSTEM**

The system CBF-MB was developed based on traditional X-CBFs with two types of innovations. A classical single storey frame of the proposed system consists of columns, diagonal braces, beam and splitting beam (Fig. 9.1). Columns and beams are non-dissipative elements. Columns may be designed with hot rolled HEA or HEB sections and their major axis could be either in or out of the frame plane. In order to

facilitate frame joints and connections design, it is preferable to orientate the column with its web coinciding with the frame plane. Beams are located at the floor levels and they could be of IPE or HEA cross sections. Diagonals are the main dissipative elements while splitting beam in some occasions may partially participate.

The first type of innovation requires introduction in the frame of a horizontal intermediate member called splitting beam. It aims at separating the diagonals thus making them identical and non-interacting (Fig. 9.1). Except for the avoidance of complicated detailing of the joint between crossing diagonals, the splitting beam stiffness is of essential importance. Splitting beam in cooperation with the columns has a crucial impact on the brace buckling sequence and on the type of global plastic mechanism. That issue will be further discussed and clarified in Section 3 of this brochure.

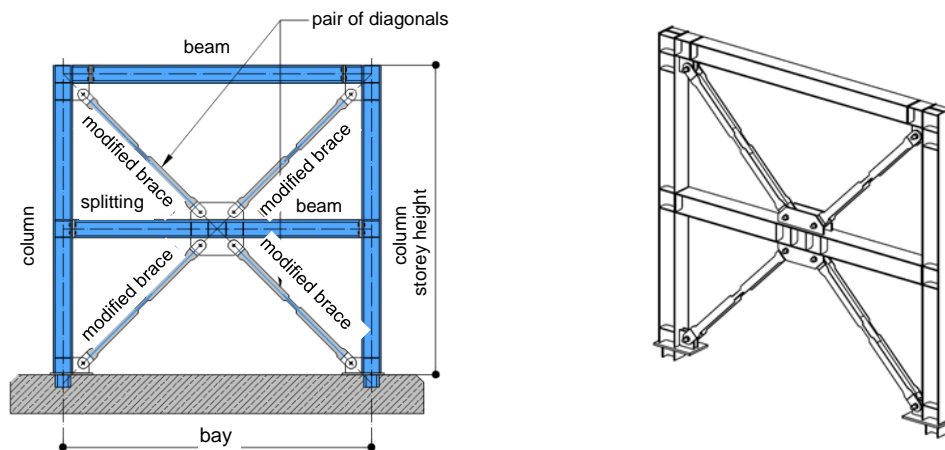


Fig. 9.1: CBF-MB system

The second type of innovation refers to the introduction of a variable "H"-shaped welded built-up cross-section for the diagonals. Further in the explanation diagonals will be named modified braces (MB). Flanges and web of the MB vary along the member length so that zones with different cross-sections are defined as illustrated in Fig. 9.2. The end zones of the diagonals are strengthened by increasing the width and thickness of the flanges and are named strong sections (SS). That also enables easy connection design and provides fully elastic response of the end zones. In the middle part of the diagonal a modified cross-section (MS) is introduced. It is characterized by reduced bending stiffness and increased cross-sectional area, thus MS is weakened for bending and strengthened for axial forces (Fig. 9.2). Reduced cross section (RS), which is characterized with lower axial load capacity than MS, is located between the end zone and middle section. Between MS, RS and SS transition sections (TS) are designed. It is authors' intention that the mode of brace buckling in compression is pre-defined and that fully concentration of plastic strains due to bending is achieved in the middle MS. In load reversal, tensile force appears and the element is straightened. Plastic strains are directed to the reduced cross-

section (RS) rather than to the MS (Fig. 9.3). Thus the diagonal is designed in a manner that yielding in tension and flexural plastic strains due to buckling occur in different zones along the brace length. That differentiation of the zones with inelastic strains leads to improved low cycle fatigue endurance and avoidance of premature failure of the diagonals. Finally, it reflects in overall improvement of the system hysteretic behaviour. The introduction of "H"-shaped and welded built-up cross-section enables the designer to vary the flange and web thicknesses, heights and width and consequently to tune the MB design as per the particular need of the structure.

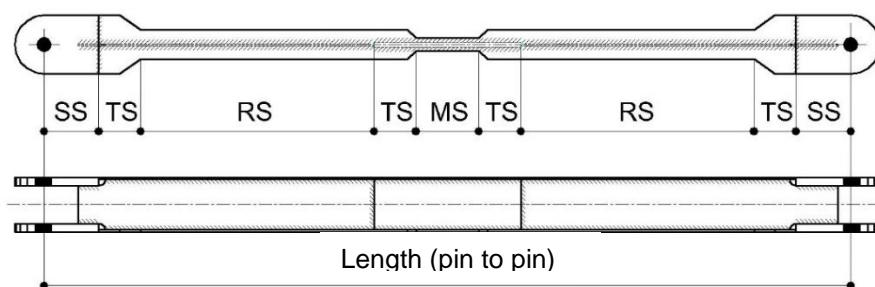


Fig. 9.2: Overview of modified brace member

In such a way the controversial code requirements for brace slenderness limitations and homogeneous dissipative behaviour of the diagonals in all storeys is much easier to be achieved.

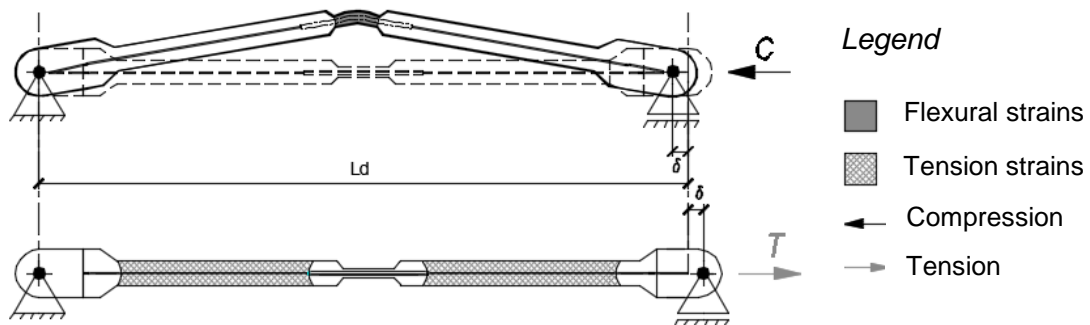


Fig. 9.3: Principle of inelastic behaviour of MB

Excessive overstrength in steel material for dissipative elements leads to uneconomical design of the non-dissipative elements. In that perspective built-up welded cross-section might be composed of steel sheets from steel S235 which is not the case for hot rolled sections.

It is recommended that connections between MB and frame elements are designed by fitted bolts providing simple and unrestrained mechanism of rotation during brace buckling. For practical implementation of this approach, gusset plates may be field-welded to the columns and beams, resulting in compensation of any fabrication and erection tolerances.

The number of CBF-MB systems required in a building structure depends on the building topology and the earthquake intensity. The system may be integrated within

the steel skeleton for vertical load (Fig. 9.4, a and b) or might be inserted in the structure (Fig. 9.4, c) acting independently. The proposed CBF-MB system may be generally combined with moment resisting frame (MRF) action if beam-to-column connections out of the braced bay are formed as rigid or semi-rigid. In this case a dual system is constituted and the lateral forces are shared between the MRF and the CBF-MB system. Alternatively, if simple connections (shear tab connections) between floor beams and columns are used the CBF-MB system resists the entire seismic action. In authors' opinion, the 'pure' CBF action shall be preferred as more predictable, it better demonstrates the advantages of CBF-MB and is easy for design. Therefore, implementation of CBF-MB in dual systems will not be discussed in this brochure.

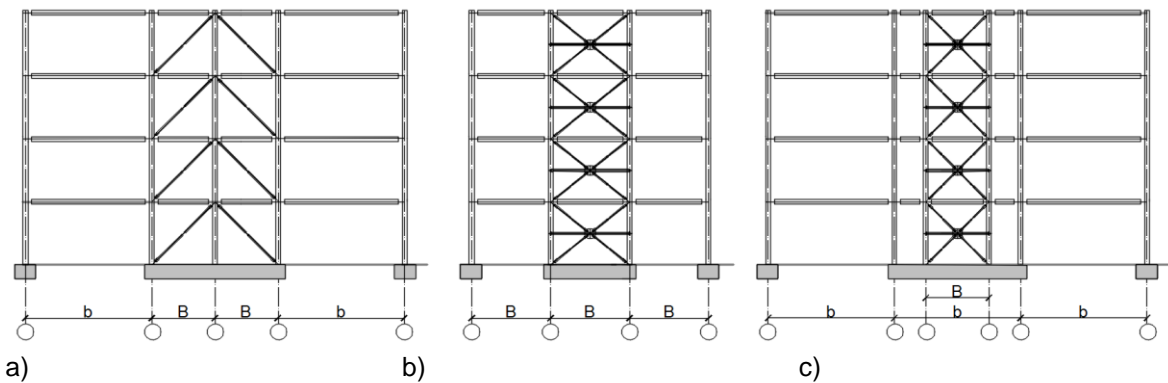


Fig. 9.4: Frame configurations with implemented CBF-MB

As mentioned in the text above, splitting beam stiffness has to be adjusted to the buckling resistance of the brace. In addition, it is recommended that splitting beam should be rigidly or semi-rigidly connected to the columns. This results in increase of the beam stiffness and moreover, in cooperation with columns, it establishes a source of frame stiffness that improves the inelastic CBF-MB behaviour and provides self-centering capacity of the system. The experience gained from the research of CBF-MB clearly indicates that splitting beams should be kept fully elastic with possible development of some flexural plastic hinges after Ultimate Limit State performance level.

### 9.3 ANALYTICAL MODELS

Traditional European approach for calculating CBFs with crossed diagonals by elastic analysis is to rely on the truss analogy with tension diagonal only (Fig. 9.5). It relies on the assumption that once the compressed diagonal has buckled, it gives negligible contribution to lateral stiffness and strength of the frame. The internal forces may be derived from the static equilibrium as function of lateral story shear (Fig. 9.5) and Eq. (9.1). Column forces may be obtained by Eq. (9.2) and the relation between story lateral displacement and diagonal elongation is given by Eq. (9.3). In the case of CBF-MB, all inelastic elongations are realised in the RS while shortening

of the compressed diagonal is realised through buckling with bending of the MS (Fig. 9.3).

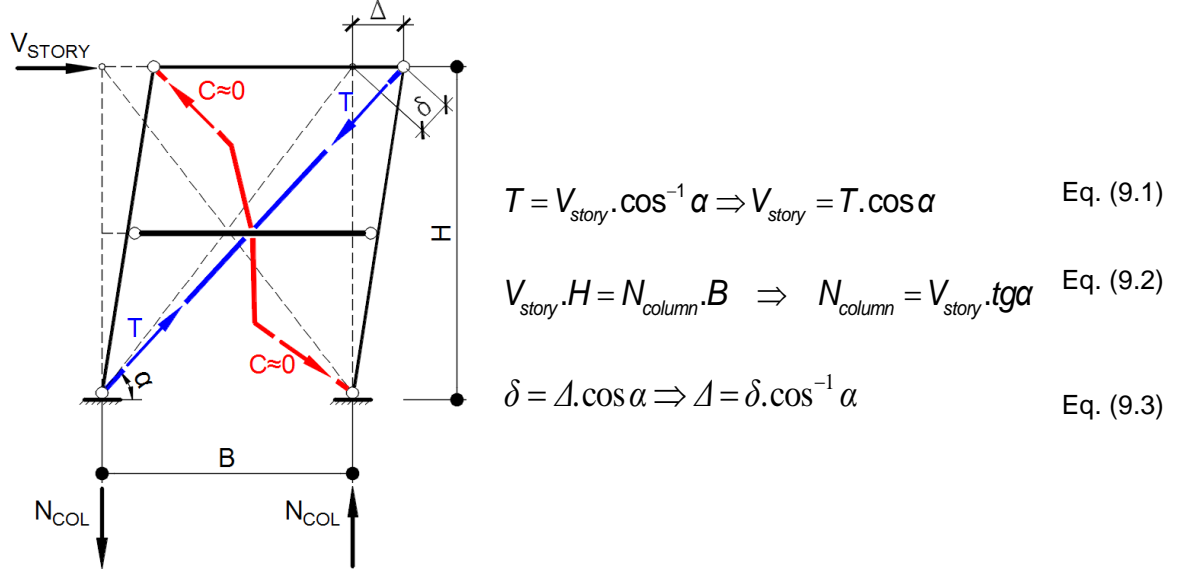


Fig. 9.5: Static system and internal forces based on truss theory

In order to define analytical relation between story lateral displacement,  $\Delta$ , and buckling transverse displacement,  $f$ , of the mid-section as a relation between the storey global ductility and the critical member (MB) local ductility, some assumptions are made:

- The deformed shape of the compressed diagonal is represented by a polygonal line (Fig. 9.6, a and b). This assumption has been justified by the performed tests.
- Total diagonal shortening  $\delta$  is equally shared between the upper-left and lower-right diagonals or  $\delta = 2\delta_d$  (Fig. 9.6, a & b). This assumption is justifiable in case of proper design of the splitting beam stiffness [2]. Based on the above mentioned the following Eq. (9.4) is derived:

$$f = \sqrt{I_d \cdot \delta_d} \quad \text{Eq. (9.4)}$$

Further using Eq. (9.3) with the assumption that  $\delta = 2\delta_d$ , it is easy to derive relation between the storey global ductility represented by  $\Delta$  and member local ductility in terms of  $f$ . Such relation is given by Eq. (9.5).

$$f = 0.707 \cdot \sqrt{I_d \cdot \Delta} \cdot \sqrt{\cos \alpha} \quad \text{Eq. (9.5)}$$

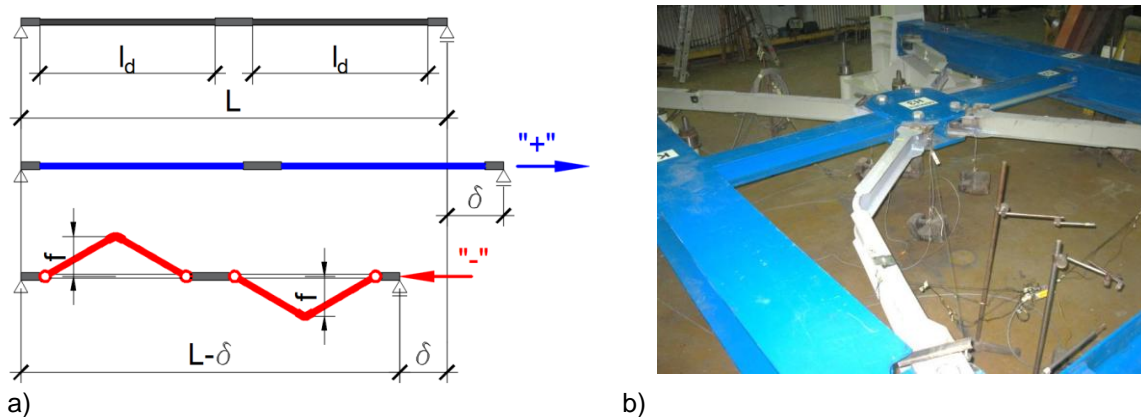


Fig. 9.6: Static system and internal forces based on truss theory

## 9.4 EXPERIMENTAL INVESTIGATIONS

The experimental programme was performed in the Laboratory of Steel and Timber Structures in UACEG. It was part of a national research project focused on improvement of seismic

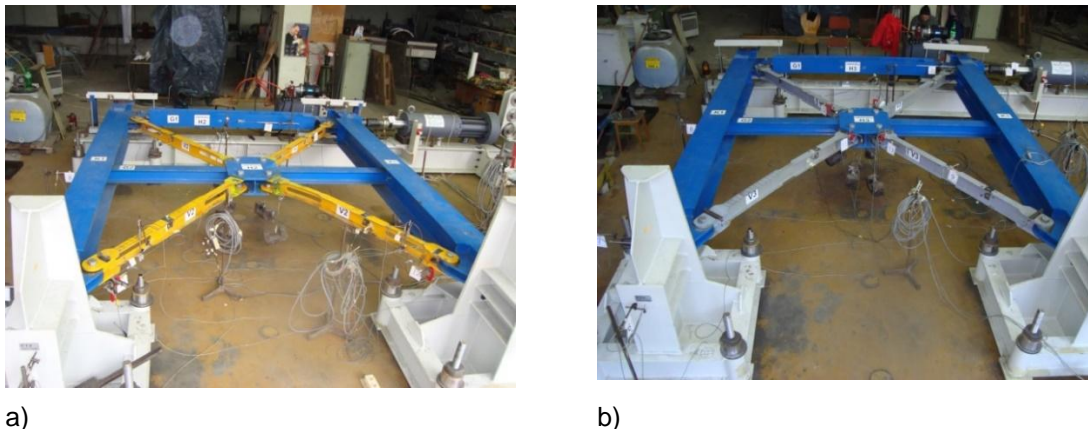


Fig. 9.7: Concentrically braced frames with: a) reduced brace sections; b) modified braces

performance of concentrically braced frames [2]. Two types of frames were subject of investigation: CBF-MB (concentrically braced frames with modified braces) and CBF-RBS (concentrically braced frames with reduced brace sections), as shown in Fig. 9.7. Within this brochure only CBF-MB will be elaborated and presented.

### 9.4.1 Experimental investigations on frame with modified bracings

#### 9.4.1.1 Specimen scale and fabrication

The test specimens with dimensions 4000 mm height and 3000 mm spacing between columns have been considered appropriate, thus corresponding approximately to full-scale storey frame from multi-storey building skeleton (as illustrated in Fig. 9.4 c) or 1:2 geometry scale of industrial building structure. Fabrication and trial erection of the specimens were outsourced to a professional fabricator, while the design and the QA was accomplished by the research team.



#### 9.4.1.2 Specimen geometry and test setup

The specimen contour frame (columns and beams) was designed following the principles of capacity design according to [1] so that they were supposed to remain elastic during the experiment. Columns were designed with HEA320 of S275JR and the beam was HEA240 of S275JR [3]. Columns were oriented with their minor axes in the frame plane while the beam was traditionally oriented with its major axis. Semi-rigid connections between beam and columns were realized by two welded tab shear plates. Connection between the column and the laboratory test rig frame was also designed as semi-rigid since it is closer to the real practice. The splitting beam was realized by HEA140 of S275JR. Diagonals, which are the dissipative elements, were designed as built-up “H-shape” welded members. Due to their dimensions the modified braces were fabricated by manual technology of assembling and welding. According to the concept, the web of the brace is interrupted in the middle portion and thicker web plate is inserted there. The last operation is also manual, so we might expect presence of geometrical imperfections that do not fully comply with the standard tolerances [4] and effects of the post-welding residual stresses. The above comment is important for those who want to establish FE model with initial brace imperfections. Some useful guidelines may be found in [19]. Pin connection between the braces and the frame was provided by fitted bolts M36 grade 10.9. The clearance between the bolt and the hole was 0.3 mm.

The experimental set-up is shown in Fig. 9.8. It is composed of supporting stand, loading system (hydraulic actuator), stabilizing system and the experimental model (test specimen). The experiment is carried out in a horizontal plane. The load is applied quasi-statically by controlled displacement at the top of the frame. The loading protocol is symmetrical displacement history with stepwise incremented amplitudes, consistent with the recommendations of the ECCS [5]. To obtain information about the strains and displacements of the diagonals, strain gauges (SGs) and inductive displacement transducers (ITs) were installed.

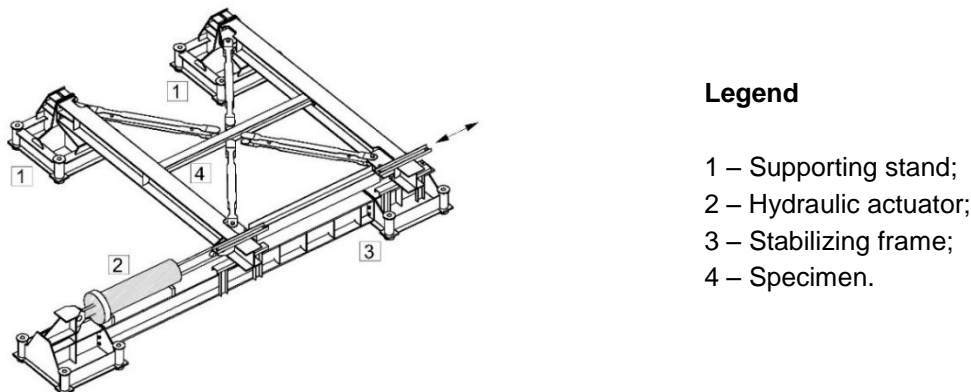


Fig. 9.8: Test set-up

#### 9.4.1.3 Material tensile tests

Standard tensile tests were performed for all materials used for the dissipative members (diagonals) of the system. Two standard flat specimens from 4 mm and four from 5 mm sheet were taken. The tests were conducted according to ISO 6892-1 [6] with strain rate 3 mm/minute. The material test specimens demonstrated ductile behaviour, typical for low carbon steel, but the actual yield strength of the 5 mm thickness steel sheet differed significantly from the declared value in the material certificate.

#### 9.4.1.4 Results of cyclic tests

Cyclic tests with full deformation reversals consistent with the recommendations of the ECCS [5] were performed. All critical elements (braces) were successively loaded in tension and compression. The obtained hysteresis loops are characterized with the typical for CBF pinching effect. Almost constant strength degradation was observed in the second and the third cycle with constant amplitude. The degradation appeared to be about 15% of the initial strength. The same drop of the back-bone curves is proposed in the nonlinear link models, elaborated in Sections 5 and 6 of the brochure.

It was planned that cycling loading should continue until fracture in the diagonal due to low cycle fatigue or exhaustion of the ductility of the braces. However, the above mentioned limit state has not been reached and the test has finished until exhaustion of the working arm of the piston. The whole history of frame hysteresis loops and single cycle loop are illustrated in Fig. 9.9. Unfortunately, due to technical problem in the recording devices, the cycles in positive directions after 70 mm roof displacement have not been reported correctly. That is the main reason for the presence of straight lines in the first quadrant of Fig. 9.9. It is important to be emphasized that during the test no local buckling either in the RS or in MS was observed – Fig. 9.10. Maximum transverse displacement of the brace mid-section was also point of interest. Due to its relatively large magnitude, the latter was measured manually.

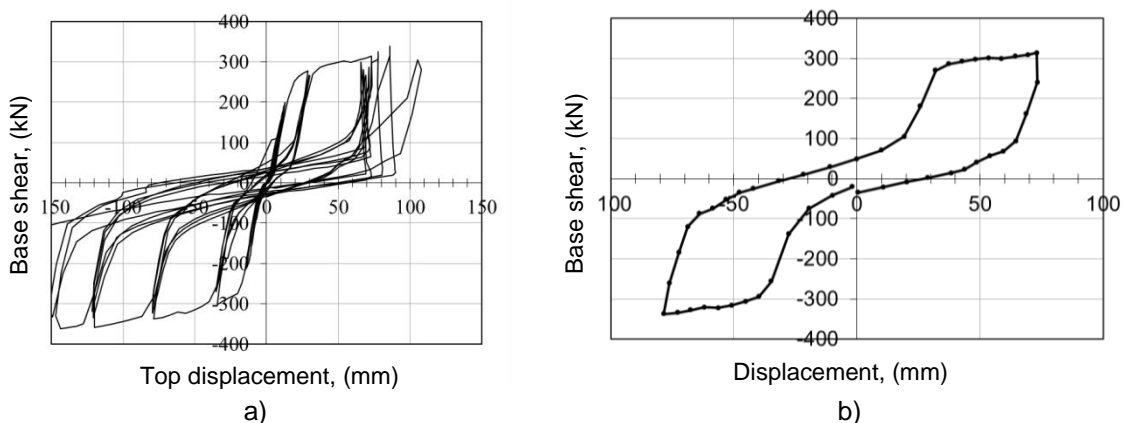


Fig. 9.9: Frame hysteresis loops, a) whole cyclic history; b) cycle 15 only



a)



b)

Fig. 9.10: Last group of cycles, a) buckling shape of pair of braces; b) Bent MS in brace buckling

The experiments have demonstrated that the stiffness of the splitting beam is important and directly affects the type of plastic mechanism of the CBF. Depending on the splitting beam stiffness and strength, two types of mechanisms were identified: either both diagonals in a pair buckle or only one diagonal buckles – Fig. 9.11.



a)



b)

Fig. 9.11: Splitting beam influence, a) unfavourable plastic mechanism; b) bending of splitting beam

The latter mechanism should be avoided, since it leads to concentration of plastic strains and premature exhausting of brace ductility or reduction of brace cyclic life.

#### 9.4.1.5 Results of monotonic tests

Classical monotonic tests were not included in the experimental programme, but the capacity curves were obtained from the result of every first cycle from the group of three. The results are plotted in Fig. 9.12. Bi-linear approximation was also added.

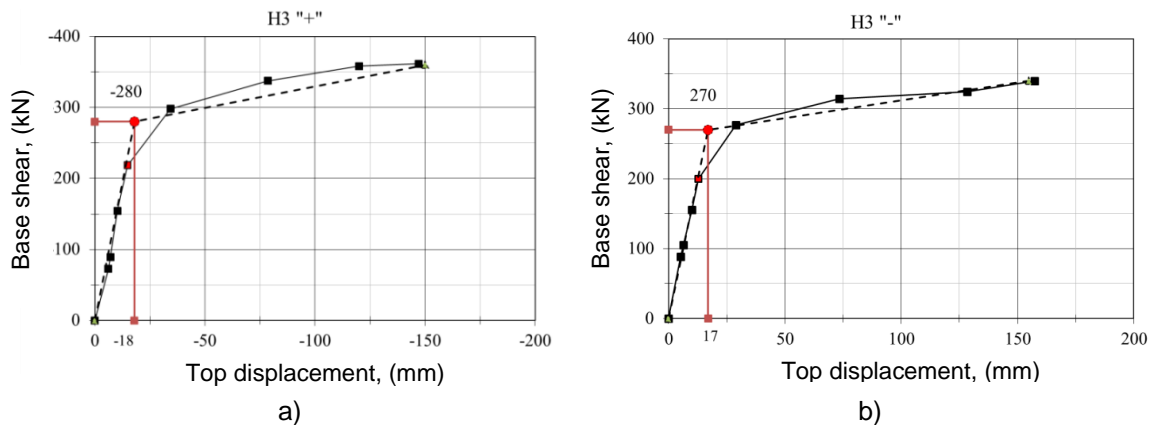


Fig. 9.12: Capacity curve, a) positive direction; b) negative direction

#### 9.4.1.6 Test of contour frame

The participation of the contour frame into the strength, stiffness and dissipation capacity of the CBF is a matter of interest. It was investigated by performing a single cycle test of the bare contour frame (without braces). Two full cycles with different amplitudes were applied. The test set-up and results are illustrated in Fig. 9.13.

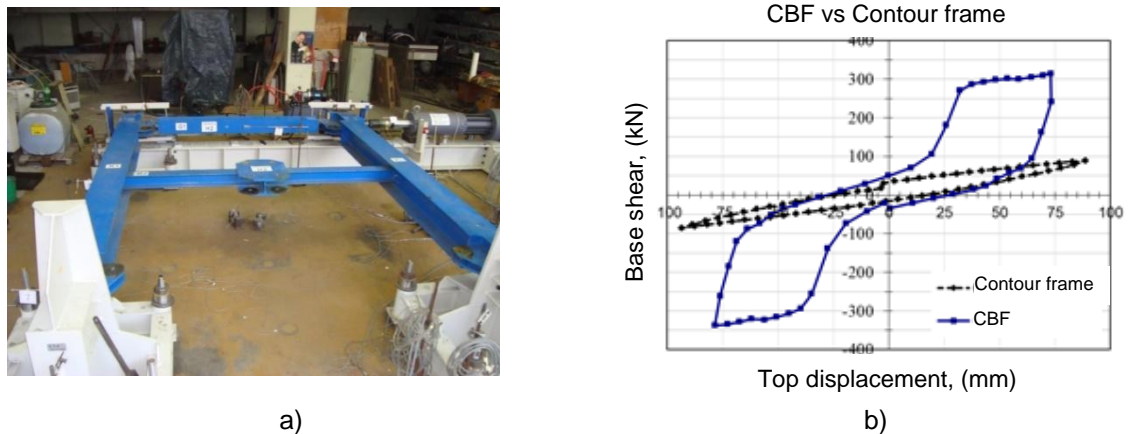


Fig. 9.13: Contour frame, a) test set-up; b) overlap of hysteresis loops

Expectedly the contour frame has much lower stiffness compared to the case when it is braced. In spite of that, its stiffness has very positive impact to reduction of the hysteresis pinching effect and improves the dissipation capacity of the system. It is worth noting that in order to achieve some self-centring ability of the system, the contour frame shall be kept almost elastic and fixing the splitting beam to the columns seems advantageous. That issue will be demonstrated in Section 9.6 and some additional comments may be read there.

#### 9.4.2 Numerical simulations

Series of numerical simulations with Seismostruct [7] and ANSYS [8] software have been carried out aiming a better understanding of the cyclic behaviour of the specimen. The comparison between experimental hysteresis loop and numerically obtained one demonstrates a good agreement (Fig. 9.14).

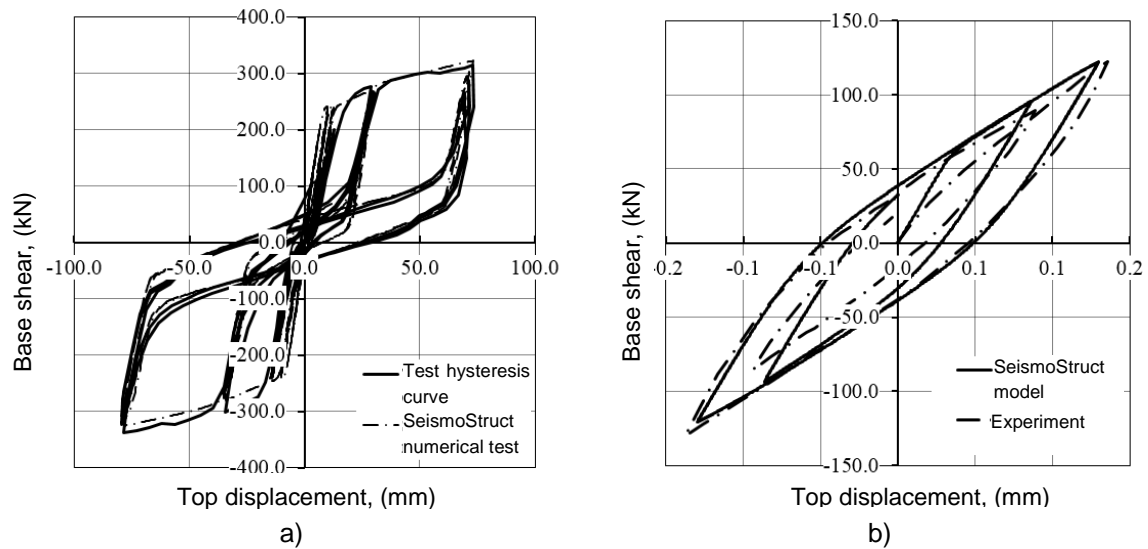


Fig. 9.14: Comparison of numerical and test results, a) frame cycling response; b) contour frame response

The numerical model was used to extract single brace cyclic response relationships that form the basis for calibration of backbone curves used for nonlinear analysis performed in Section 6. ANSYS model was used for sophisticated analysis of a single brace behaviour. Calibrated material model of Chaboche [9] and FE type SHELL181 with mesh size 10 mm were used. FEM model proved that the plastic strains caused by brace buckling are directed toward the MS while strain excursions caused by tension are realized within RS. The Strong Section (SS) exhibits elastic behaviour proving the initial concept. ANSYS model (Fig. 9.15) was also used for obtaining strain range history in the critical sections and to perform the low cycle fatigue checks.

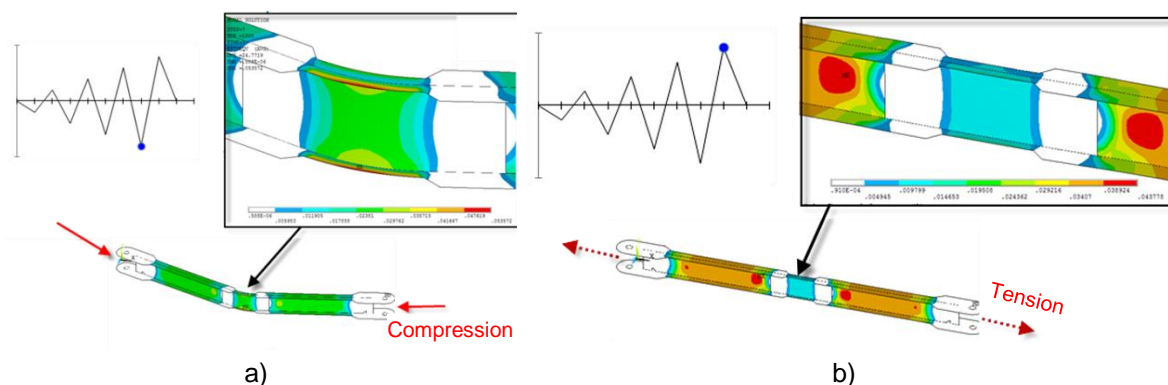


Fig. 9.15: FEA by ANSYS, a) plastic strains in compression; b) plastic strains in tension

#### 9.4.3 Comparison between experimental and analytical models

Validity of the analytical truss model was examined by comparison between theoretical and experimental results for the story base shear. Theoretical storey base shear and the top storey displacement were calculated using Eq. (9.1) and Eq. (9.3), respectively, with the actual material properties. The experimental curves and

bi-linear approximations are illustrated in Fig. 9.12. Table 9.1 shows the comparison between experimental and theoretical shear forces. Calculation of  $\Delta y$  is based on the assumption that the whole length of the diagonal is elongated elastically to strains  $\varepsilon_y=0,002$ . The test results for specimen H3 were used for comparison, where abbreviations H3" + " and H3" - " indicate positive and negative direction of loading. It shall be mentioned that the theoretical model fully complies with the recommendations of [1] for crossed diagonal CBFs. It shall be expected that theoretical results for the frame resistance is lower than the monotonic test results due to the exclusion of the compressed pair of diagonals and the contour frame in the theoretical model. This tendency is proved by the comparison of base shear forces reported in Table 9.1. It is worth noting that the theoretical model marks very well the yielding point in bilinear capacity curve, indicated by red dot on Fig. 9.12. Due to its simplicity and compliance with [1], the truss model with tension diagonal only is considered as most appropriate for preliminary design of CBF-MB.

**Table 9.1: Experimental vs theoretical shear force**

Specimen	$V_{y,exp}$ – bilinear apr.	$V_{y,th}$	$V_{y,exp}/$ $V_{y,th}$	$\Delta y_{exp}$ – bilinear apr.	$\Delta y_{th}$	$\Delta y_{exp}/$ $\Delta y_{th}$
-	kN	kN	-	mm	mm	-
H3" + "	-280.0	-199.65	1.402	-18.0	-16.66	1.08
H3" - "	+270.0	+199.65	1.352	+17.0	16.66	1.02

Another aspect of interest is the relation between global (storey drift) and local ductility (plastic strains) of the system. The methodology for obtaining final plastic elongation in the area of reduced brace sections is reported in [30]. The average strain elongation in the pairs of diagonal members was estimated at 3.315% and 3.195% respectively.

The last point of interest is the comparison of results for the maximum transverse displacement  $f$  of the brace mid-section. The displacement  $f$  was measured during the test and hereafter is compared with the theoretical results derived from Eq. (9.4). It is worth reminding that Eq. (9.4) is valid when the splitting beam is properly stiff to force both compressed diagonals to buckle almost simultaneously. Since it was not the case in the test, some adjustments of the brace shortening within the pair has been done. Comparison of theoretical and test results is shown in Table 9.2.

**Table 9.2: Experimental vs theoretical transverse mid-section displacement**

Cycle No	$f_{exp}$	top displ.	$\delta_d$	$f_{th}$	$f_{th} / f_{exp}$
-	mm	mm	mm	mm	-
12	72.94	34.36	10.31	140.69	1.93
15	145.89	78.49	23.55	212.63	1.46
18	248.01	120.01	36.00	262.92	1.06
21	271.52	147.12	44.14	291.11	1.07

It is evident from the last column that with increase of the top displacement, agreement of the results improves. This is attributed to the fact that the hypothesis for deriving Eq. (9.4) relies on the pre-assumed polygonal deformed shape of the buckled brace. As the story drift increases, the deformed shape of the compressed pair of diagonals goes closer to the one shown on Fig. 9.6.

#### 9.4.4 Limit states from the cyclic test

Cyclic test was performed in accordance with the initial loading protocol and ended with reaching the limit of the actuator working stroke. It is worth saying that the specimen has achieved neither fracture, nor global collapse. On the other hand, the test was conducted without taking into account axial forces in the frame columns, therefore  $P-\Delta$  effects were not included into the test. For the recognition of limit states the recommendations of FEMA-356 [10] were followed. Relation between the definitions of FEMA-356 and the current design manual are given in Table 9.3. Additionally, some conservative assumptions were implemented because of the lack of physical evidence for the influence of  $P-\Delta$  effects on the experimental frame behaviour.

**Table 9.3: Limit states**

Structural performance levels according to FEMA 356	FEMA 356 story drift ratio	Limit states adopted in this brochure	Experimental estimation
Immediate occupancy (IO)	0.50%	SLS	0.625%
Life Safety (LS)	1.50%	ULS	1.89%
Collapse prevention (CP)	2.00%	CPLS	3.00%

First significant yielding of the braces during the experiment appeared in cycle 12, at interstorey drift of 25 mm which is equal to drift rotation of 0.625%. At that stage the SLS was defined. During SLS the compressed diagonals have buckled and the internal tension force produced first yielding. ULS was recognized at cycle 15 when additional tension yielding of the braces was observed and some minor weld failure in semi-rigid frame connections was noted. ULS was registered at interstorey drift of 75.8 mm which is equal to drift rotation of 1.89%. CPLS was considered at cycle 18, at interstorey drift of 121 mm which is equal to drift rotation of 3.00%. During CPLS no local buckling or section fracture was observed in the braces. Welds in the frame semi-rigid connections failed. It should be noted that the above values of interstorey drift at the three basic performance levels are similar to the values proposed by FEMA-356 [10] for buildings with CBFs (0.5%, 1.5%, 2.0%) with major difference in CPLS.

#### 9.4.5 Low cycle fatigue

Constant amplitude cyclic test of single brace was not performed during the experimental programme. In order to find some relations between MB endurance of cyclic elongation and shortening, a set of FEA by ANSYS models was conducted.



The amplitude of axial brace shortening and elongation,  $\delta_d$  was varied and the strain history was obtained. Data for cyclic endurance of similar materials was found in technical literature [11], [12], [13] – Fig. 9.16. On the basis of numerical results for maximum strain range and number of reversals from numerical analysis and technical literature data the authors propose the formula in Eq. (9.6). It presents the relation between axial deformation amplitude,  $\delta_d$  corresponding to the number of cycles to failure,  $N$ . The proposed formula was shifted to the safe side with mean ratio of 0.533 and standard deviation of 0.339.

$$\delta_d(N) = 110 - 52\log(N) \quad \text{Eq. (9.6)}$$

The results from CBF-MB cyclic test as per loading protocol of ECCS [5] and the measured data for maximum brace transverse displacement were used for check of the reliability of Eq. (9.6). The Damage Index (DI) for the most loaded brace from specimen H3 was determined by Eq. (9.6) and the Palmgren–Miner’s rule [14], [15], [16]. Value of  $DI=0.752$  was calculated. Then the MSs from specimen H3 were detected for surface and close adjacent subsurface discontinuities by Magnetic Particle Inspection (MPI) and ultrasonic test.

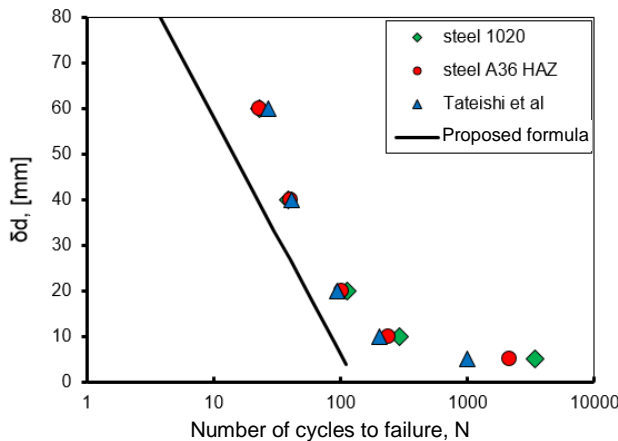


Fig. 9.16: Relation between axial brace displacement and number of cycles to failure

Two of the most loaded diagonals were subjected to MPI and no surface cracks in flanges or web of the elements were detected. Considering that the thickness of the MS flanges is only 5 mm, it might be concluded that there are no cracks in the flange area of maximum curvature and that Eq. (9.6) is sufficiently conservative and might be used for CBF-MB low cycle fatigue design.

## 9.5 DESIGN RULES

In this section brief design guidelines are summarised for the CBF-MBs. Recommendations are given on the preliminary design of appropriate modified



braces and the design of the splitting beams. Since the CBF-MBs belong to structural configurations covered by the Eurocode the proposed design procedure is in compliance with the provisions of [17] and [1].

#### 9.5.1 Preliminary design

As previously mentioned (Section 3), the CBF-MB system may be assumed to be working as vertical truss with tension-only diagonal. A rough estimation of the required number of bracing systems for a building in each direction ( $m$ ) can be made by Eq. (9.7).

$$m = V_{\text{building}} / V_{\text{storey}} \quad \text{Eq. (9.7)}$$

where  $V_{\text{building}}$  is the total base shear of the building and  $V_{\text{storey}}$  is the story shear of one CBF-MB system, based on the vertical truss model – Eq. (9.1). The first storey column cross section should be chosen as the member to resist the axial force equal to:

$$N_{\text{column}} = M_{\text{ov}} / m.B \quad \text{Eq. (9.8)}$$

Where  $M_{\text{ov}}$  is the overturning moment of the building and  $B$  is the axis-to-axis distance between CBF-MB columns. The first choice of the bracing reduced section at  $i$ -th story, may be derived from Eq. (9.9), where  $V_{\text{storey},i}$  is storey base shear for  $i$ -th floor and  $\alpha_i$  is defined in Fig. 9.5.

$$A_{\text{RS},i} = V_{\text{storey},i} / f_y \cdot \cos \alpha_i \quad \text{Eq. (9.9)}$$

The above methodology gives only the main general directions for the design of the system.

#### 9.5.2 Design of modified braces and splitting beam

Modified braces are the critical members of the system. They shall meet both the criteria of Chapter 6 of [1], and the specific recommendations prescribed in this Manual. As illustrated in Fig. 9.2, several zones with different cross-sections should be defined within the modified brace. For their proper design the following procedure is suggested.

##### 9.5.2.1 Length of MS, RS and TS

First step estimation of the length of modified brace  $l_d$  is  $(0.375-0.40)l$ , where  $l$  is axis-to-axis diagonal geometric length. Recommendations for the length of modified section are summarised by Eq. (9.10), where  $l_{\text{MS}}$  is the length of the MS. It should be neither too short since severe flexural strains are expected to arise there, nor too

long since this may provoke double curvature buckling shape. Eq. (9.11) gives direction for the choice of the reduced section length  $l_{RS}$ .

$$l_{MS} = (0.067 \div 0.085)l_d \quad \text{Eq. (9.10)}$$

$$l_{RS} \approx (0.3)l_d \quad \text{Eq. (9.11)}$$

#### 9.5.2.2 Area ratio

The area of RS should be estimated by Eq. (9.9). In order to ensure that reduced section will yield in tension rather than the modified section, the following Eq. (9.12) should be met.

$$K_A = A_{MS}/A_{RS} \geq 1.4 \quad \text{Eq. (9.12)}$$

Where  $A_{MS}$  is the modified section area and  $A_{RS}$  is the reduced section area. The strong section (SS) dimensions and area should be chosen to provide fully elastic response in the net section for pin connection and to fulfil the bearing checks of bolts.

#### 9.5.2.3 Section modulus ratio

In order to ensure that modified section has lower bending capacity than the reduced section even in stage of large plastic strains and strain hardening, the following Eq. (9.13) should be fulfilled:

$$K_M = W_{pl,RS}/W_{pl,MS} \geq 2.0 \quad \text{Eq. (9.13)}$$

Where,  $W_{pl,RS}$  and  $W_{pl,MS}$  are the reduced and the modified section plastic moduli, respectively.

#### 9.5.2.4 Effective length of modified brace element

Since there is modified section inserted in the mid-length, then the real buckling length  $l_{cr} = \mu \cdot l_d$  will be longer than  $l_d$ . A formula for the effective length is proposed by Eq. (9.14), where  $K_L = l_{RS}/l_{MS}$ ,  $K_I = l_{MS}/l_{RS}$ .

$$\mu = l_{cr} / l_d = 0.88 K_L^{(0.033)} \cdot K_I^{(0.1 \ln(K_L) - 0.36)} \quad \text{Eq. (9.14)}$$

Eq. (9.14) may give deviations of up to 10% , depending on the geometry. Nevertheless the user may perform a quick elastic buckling analysis of a single modified brace, based on frame FE model to obtain the particular modifying parameter  $\mu$  for his design case.

#### 9.5.2.5 Limitation of slenderness

According to [1] braces of CBFs with X-configuration must have non-dimensional slenderness in the range of  $1.3 \leq \bar{\lambda} \leq 2.0$ . The effective slenderness is defined by Eq. (9.15).

$$\lambda_{eff} = \frac{\mu \cdot l_d}{i_{RS}}, \quad \text{Eq. (9.15)}$$

where  $\mu$  is the effective length multiplier defined by Eq. (9.14) and  $i_{RS}$  is the minor radius of gyration of the reduced section.

#### 9.5.2.6 Preliminary selection of the splitting beam

Previous tests and numerical studies have demonstrated possible formation of two types of storey plastic mechanisms named favourable and unfavourable (Fig. 9.17). The favourable mechanism is when both compressed diagonals in a pair buckle and plastic elongations are within the pair of tensioned diagonals. The unfavourable one is when only one from the pair of compressed diagonals buckles and additional plastic hinges appear in the splitting beam or even in the columns (Fig. 9.17 b), c)). Unfavourable mechanisms could be avoided by a proper design of the splitting beam, assuring sufficient strength and bending stiffness.

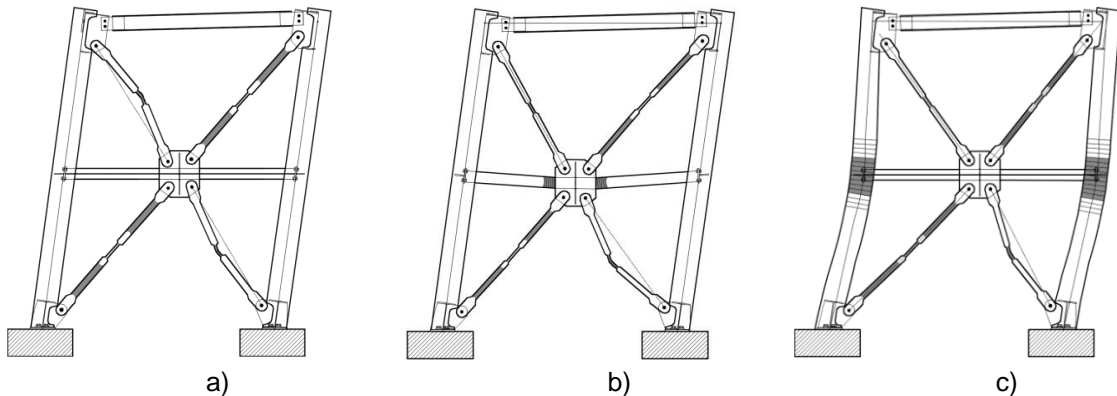


Fig. 9.17: Plastic mechanisms: a) Favourable; b) Weak splitting beam; c) Weak columns

The CBF-MB is proposed to be designed with splitting beam fixed to the columns thus forming a H-shape frame. Splitting beam and columns should remain elastic until reaching ULS. In that way some major benefits are obtained:

- By elastic H-frame the self-centering capability of the CBF-MB after major earthquake excitations is enhanced;
- H-frame provides positive tangent stiffness in the range of zero lateral displacements of the CBF-MB when inelastic deformations in braces develop.

The limit state when the H-shaped frame provides sufficient elastic stiffness and thus forces the unbuckled diagonal to eventually buckle is illustrated in Fig. 9.18. Conservatively assuming that the tensioned diagonals are equally stressed and that

the post-buckling resistance of the early buckled brace is negligible, satisfying the equations of joint equilibrium reveals the formation of unbalanced horizontal and vertical forces. They may be determined through Eq. (9.16) and Eq. (9.17), where  $N_{b,Rd}$  (Eq. (9.18)) is the buckling resistance of the brace according to [17] and  $\chi$  is reduction factor for first buckling mode calculated with  $\lambda_{eff}$ .

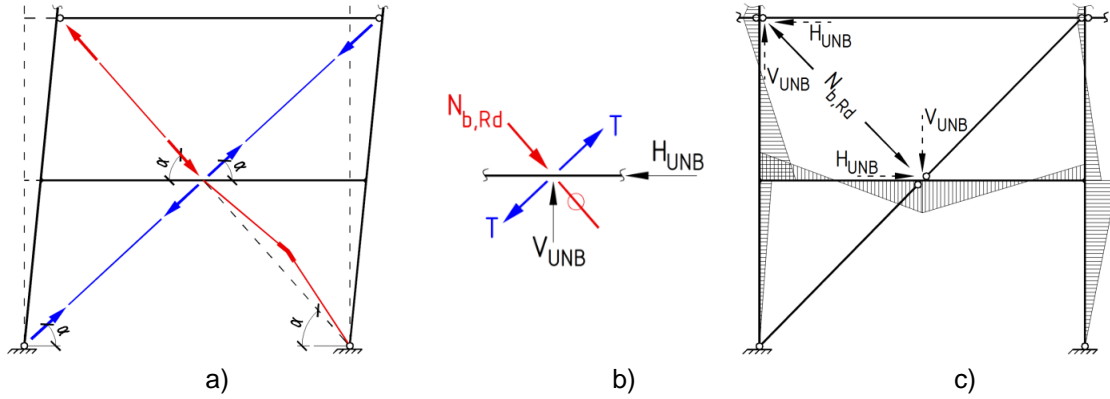


Fig. 9.18: a) Stage “just before buckling”; b) Unbalanced forces; c) Internal moments ( $M_{UNB}$ ) resulting from the unbalanced forces (load case UNB)

$$V_{UNB} = N_{b,Rd} \cdot \sin \alpha \quad \text{Eq. (9.16)}$$

$$H_{UNB} = N_{b,Rd} \cdot \cos \alpha \quad \text{Eq. (9.17)}$$

$$N_{b,Rd} = \chi \cdot A_{RS} \cdot f_y / \gamma_{M1} \quad \text{Eq. (9.18)}$$

In the considered state “just before buckling” a case with additional bending moments and axial forces (load case UNB) within the storey H-frame occurs – Fig. 9.18 c). That state has to be accounted for into design. It may be simulated in the model for elastic analysis by introducing unbalanced forces separately for every floor or integrally in all stories simultaneously.

It is also important to emphasize that the splitting beam shall be designed so as to avoid lateral-torsional buckling effects, e.g. by satisfying Eq. (9.19).

$$\bar{\lambda}_{LT} \leq 0.40 \quad \text{Eq. (9.19)}$$

Following the requirements of 4.4.2.3 (4) [1], the sections of splitting beam and columns shall be chosen to satisfy Eq. (9.20). It proves that in all states of structural performance, plastic hinge may appear in the splitting beam, not in column.

$$2.M_{Rc} \geq 1.3M_{Rb} \quad \text{Eq. (9.20)}$$

where  $M_{Rc}$  and  $M_{Rb}$  are the design bending resistances of the column and the splitting beam. Splitting beams must be designed with caution following the proposed principles as they control the damage limitation and must be kept elastic and stiff enough in order to prevent formation of unfavourable storey mechanism and brace buckling modes out of the frame plane.

#### 9.5.2.7 Design of the non-dissipative elements

The non-dissipative CBF's elements are the columns, the floor beams and the splitting beams. Columns and splitting beams are rigidly connected while columns and floor beams may be simply connected or partially or fully restrained. All joints shall be modelled adequately and the existence of bending moments and shear forces in columns and beams, defined by Eq. (9.21) to Eq. (9.29), shall be accounted for in the design. The internal forces including second order effects  $M_E$ ,  $V_E$  and  $N_E$  in the seismic load case obtained through elastic analysis (Fig. 9.19), shall be multiplied by capacity multiplier  $1.1\gamma_{OV}\Omega_{min}\rho$ . The first three parameters are strictly according to [1] and the parameter  $\rho=1.15$  is proposed by the authors to account for the available overstrength of the system and the possible higher actual buckling resistance of the brace. The unbalanced forces, formed in the considered "just before buckling" state defined in point 5.2.6. and illustrated in Fig. 9.18 should be included in the design situation. The additional internal forces induced by them are designated hereafter by the subscript "UNB".

Columns shall be designed for the internal forces through Eq. (9.21) to Eq. (9.23). They must also fulfil Eq. (9.20).

$$N_{col,Ed} = N_{Ed,G} + 1.1\gamma_{OV}\Omega_{min}\rho.(N_E + N_{UNB}) \quad \text{Eq. (9.21)}$$

$$M_{col,Ed} = M_{Ed,G} + 1.1\gamma_{OV}\Omega_{min}\rho.(M_E + M_{UNB}) \quad \text{Eq. (9.22)}$$

$$V_{col,Ed} = V_{Ed,G} + 1.1\gamma_{OV}\Omega_{min}\rho.(V_E + V_{UNB}) \quad \text{Eq. (9.23)}$$

The design forces for the splitting beams shall be obtained by Eq. (9.24) to Eq. (9.26). The conditions Eq. (9.20) and Eq. (9.19) shall be satisfied as well.

$$N_{sb,Ed} = N_{Ed,G} + 1.1\gamma_{OV}\Omega_{min}\rho.(N_E + N_{UNB}) \quad \text{Eq. (9.24)}$$

$$M_{sb,Ed} = M_{Ed,G} + 1.1\gamma_{OV}\Omega_{min}\rho.(M_E + M_{UNB}) \quad \text{Eq. (9.25)}$$

$$V_{sb,Ed} = V_{Ed,G} + 1.1\gamma_{OV}\Omega_{min}\rho.(V_E + V_{UNB}) \quad \text{Eq. (9.26)}$$

The design forces for the floor beams shall be obtained by Eq. (9.27) to Eq. (9.29).

$$N_{b,Ed} = N_{Ed,G} + 1.1\gamma_{OV} \cdot \Omega_{min} \cdot \rho \cdot (N_E + N_{UNB}) \quad \text{Eq. (9.27)}$$

$$M_{b,Ed} = M_{Ed,G} + 1.1\gamma_{OV} \cdot \Omega_{min} \cdot \rho \cdot (M_E + M_{UNB}) \quad \text{Eq. (9.28)}$$

$$V_{b,Ed} = V_{Ed,G} + 1.1\gamma_{OV} \cdot \Omega_{min} \cdot \rho \cdot (V_E + V_{UNB}) \quad \text{Eq. (9.29)}$$

### 9.5.3 Design for linear elastic analysis

CBF-MB is a structural system belonging to the family of braced frames. In that sense the requirements for elastic design of CBF-MB shall comply with EN 1998-1 [1]. In this section only some specificities will be emphasized.

#### 9.5.3.1 Simulation

The CBF-MB may be reliably analysed by a linear-elastic model with appropriate beam FEs. The elements simulating the modified braces are defined through constant H-shape section with characteristics of RS and joined to the frame by simple pin connections. Columns are modelled as continuous through the stories. Joints between columns and floor beam and column bases may be modelled as nominally pinned.

Related to the geometry of the system, two different types of structural models are proposed, named centreline-to-centreline (CL-to-CL) model and joint offset truss model. It is recommended that only offsets of braces and floor beam joints shall be considered. Illustration is presented in Fig. 9.19.

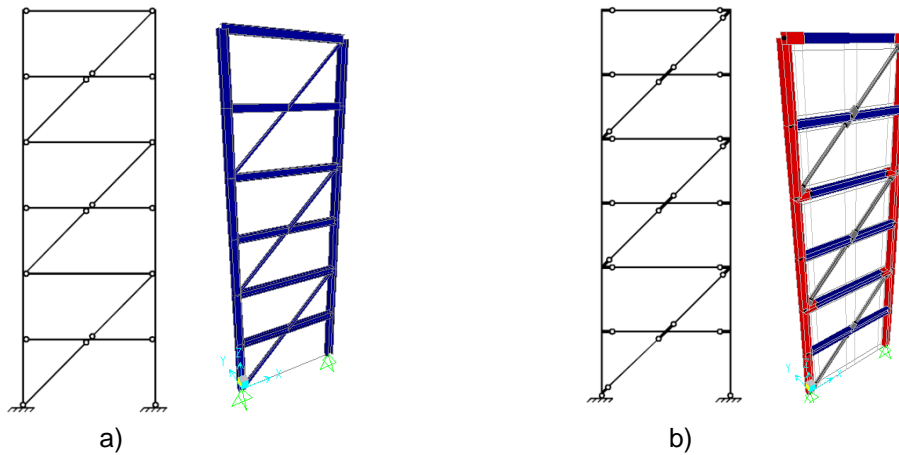


Fig. 9.19: Models for elastic analysis. a) CL-to-CL model; b) Joint offset model

#### 9.5.3.2 Structural analysis and behaviour factor

The structure should be designed as having dissipative structural behaviour and belonging to structural ductility class DCH. It is recommended to use Multi-Modal Response Spectrum Analysis, with proposed behaviour factor  $q = 5.0$ .

#### 9.5.3.3 Limitation of interstorey drift and 2nd order effects

Limitation of interstorey drift should fulfil 4.4.3.2. and second-order effect should be checked and included respectively as per 4.4.2.2. [1].

#### 9.5.3.4 Diagonal members

The non-dimensional brace effective slenderness calculated by Eq. (9.15) should meet Eq. (9.30).

$$1.3 \leq \bar{\lambda}_{eff} \leq 2.0 \quad \text{Eq. (9.30)}$$

According to 6.7.3 of EN 1998-1[1] the design of the diagonals shall be based on the yield resistance  $N_{pl,Rd}$  of the gross cross-section, which for MB is

$$N_{pl,Rd} = A_{RS} \cdot f_y / \gamma_{M0} \quad \text{Eq. (9.31)}$$

The connections of the diagonals to floor beams and splitting beams should satisfy the design rules of 6.5.5. of [1].

#### 9.5.3.5 Global dissipative behaviour

In order to achieve a global homogeneous dissipative behaviour of the structure, the maximum overstrength ratio  $\Omega_{max}$  over the entire structure shall not differ from the minimum value  $\Omega_{min}$  by more than 25% as stated in Eq. (9.32).

$$\Omega_{MAX} / \Omega_{MIN} \leq 1.25 \quad \text{Eq. (9.32)}$$

Authors recommend that the top two storeys of the building are interpreted per clause 6.7.3 (4) of [1] as Eq. (9.30) in most cases appears too conservative.

#### 9.5.4 Design for static non-linear analysis

The joint offset structural model proposed in section 5 should be upgraded for static non-linear analysis with concentrated plasticity and the range of element behaviour shall be extended to post-yield and post-buckling behaviour by introducing different types of hinges. The lateral force distribution adopted in the brochure is proportional to the first natural mode of vibration. The  $P-\Delta$  effects may be accounted for by modelling of 'leaning column'. According to 5.3.2 (3) of EN-1993-1-1 [17], the initial sway imperfection of the frame is accounted for by initial inclination of the column  $\Phi = \Phi_0 \cdot \alpha_h \cdot \alpha_m$ . At each joint of the leaning column a vertical force corresponding to the attributed floor mass is assigned. Fig. 9.20 illustrates the structural model for static non-linear analysis.

The model demonstrated here is based on SAP2000 [18]. Two types of hinges are proposed in the model. Brace inelastic response is simulated by P-hinge inserted in its mid-point. For beam and column sections with potential flexural plastic strains, P-M hinges are used (Fig. 9.20, b). The backbone curve of brace P-hinge is illustrated in Fig. 9.21. It is constituted by the geometrical and slenderness characteristics of

the brace member and nominal strength of the material – Table 9.4. The post-yield and post-buckling characteristic points are adopted as per FEMA-356 [10]. The backbone curve is compared with cyclic curve obtained by distributed plasticity model of single brace in Seismostruct [7] and calibrated with test results.

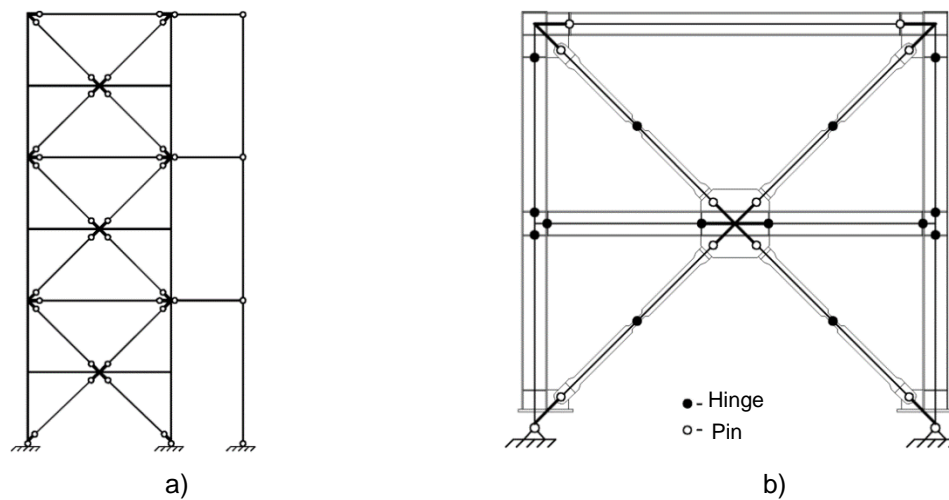


Fig. 9.20: Frame model for static non-linear analysis. a) Overview; b) Hinge locations

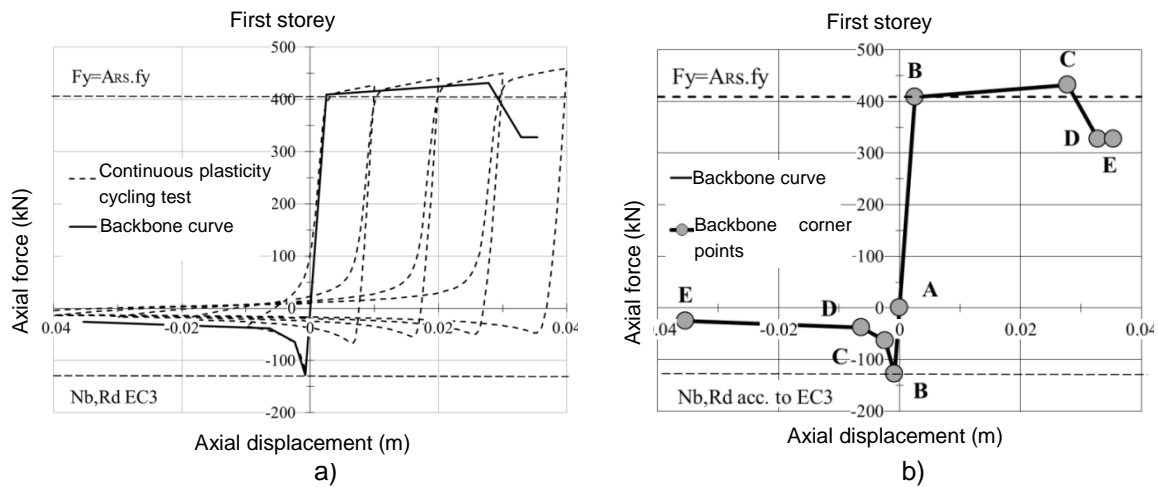


Fig. 9.21: Backbone curve: a) comparison with test calibrated model; b) backbone curve for analysis

**Table 9.4: Backbone curve characteristic points.**

Point	Tension		Point	Compression	
	Force	Displacement		Force	Displacement
A	0	0	A	0	0
B	$F_y = A_{RS} \cdot f_y$	$\Delta y$	B	$N_{b,Rd}$	$\Delta c$
C	$F_{SH}$	$11\Delta y$	C	$0.5N_{b,Rd}$	$3\Delta c$
D	$0.8F_y$	$13\Delta y$	D	$0.3N_{b,Rd}$	$8\Delta c$
E	$0.8F_y$	$14\Delta y$	E	$0.2N_{b,Rd}$	$14\Delta y$



The following Eq. (9.33) to Eq. (9.37) shall be used for definition of the characteristic points.  $N_{b,Rd}$  is the buckling resistance of the brace as per [17] and  $\chi$  is the buckling reduction factor.

$$\Delta_y = f_y \cdot L / E \quad \text{Eq. (9.33)}$$

$$F_y = A_{RS} \cdot f_y \quad \text{Eq. (9.34)}$$

$$F_{SH} = F_y + (F_y / \Delta_y \cdot 0.005) \cdot (11 \Delta_y) \quad \text{Eq. (9.35)}$$

$$N_{b,Rd} = \chi A_{RS} \cdot f_y \quad \text{Eq. (9.36)}$$

$$\Delta_C = N_{b,Rd} \cdot \Delta_y / F_y \quad \text{Eq. (9.37)}$$

Plastic hinges for splitting beams and columns are P-M3 hinge type. The interaction curve ‘axial force – bending moment’ may be defined using [17] or [10]. The post-yield characteristic points are according to [10].

#### 9.5.5 Design for non-linear dynamic analysis

In order to investigate the time-dependant response of the whole system and the critical members, non-linear dynamic analysis (NDA) should be performed. It provides information for residual global and interstorey drifts and enables the designer to evaluate the damage index of the brace members caused by certain seismic record. The structural model used for static non-linear analysis shall be modified by substituting brace members and the *P*-hinges by Multi-linear Plastic Link with Pivot hysteresis type – Fig. 9.22.

The *P*– $\Delta$  effects shall be accounted for as explained in the previous section. The non-linear link element used in the model in SAP2000 is constituted by several parameters calibrated with the experimental results. The pivot points for directing the pivot hysteresis are located by the parameters  $\alpha_1$ ,  $\alpha_2$ ,  $\beta_1$  and  $\beta_2$ , presented in Table 9.5 ([18], [20]). For proper definition of hysteresis behaviour, the multi-linear plastic link requires definition of backbone curve (section 5.4.). The test data and the numerical results indicate that there is a cyclic strength reduction of about 15%, which is taken into account (Fig. 9.22 b).

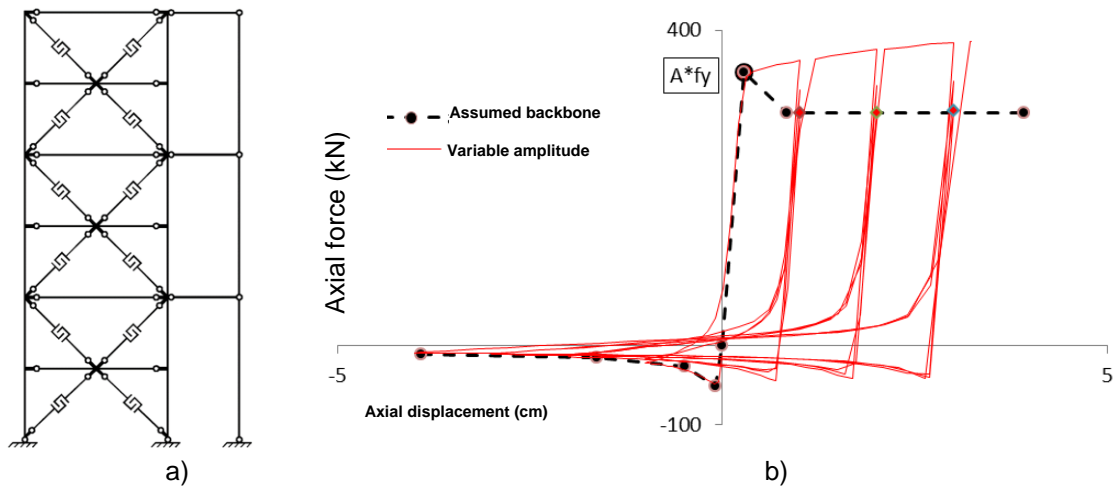


Fig. 9.22: Model for NDA: a) Model overview; b) Backbone curve

**Table 9.5: Pivot points description**

Pivot point parameter	$\alpha_1$	$\alpha_2$	$\beta_1$	$\beta_2$	$\eta$
Value	100	0.1	0.02	0.4	0.0

## 9.6 ANALYSES AND DESIGN OF 2D FRAMES

Equations, element properties, design recommendations, critical checks and proposed behaviour factor, included in the brochure, were verified by numerical analyses of real 2D building frames with CBF-MB using SAP2000. Initially the frames were designed through elastic analysis for ULS and SLS. Nonlinear static and dynamic analyses followed to investigate their behaviour beyond the elastic range and confirm the proposed behaviour factor value  $q=5$ .

### 9.6.1 Case studies

#### 9.6.1.1 Geometry and general assumptions

The case study presented hereafter is based on a plane CBF-MB frame extracted from a three-storey building, Fig. 9.23. The frame consists of three 8m bays with nominally pinned beam-to-column joints and pinned column bases. The CBF-MB systems are located as shown in the figure. Hot rolled HEA profiles for columns and IPE profiles for floor beams are used. Composite action with the concrete slab is not considered. Each CBF-MB is integrated in the middle of the bay. In this way columns of the braced frame are loaded primarily with axial forces resulting from the seismic action and the rest of the frame columns carry the gravity loads. Similar structural approach may be seen in Fuseis-2 system proposed by Vayas et al. [21], [22], [23].

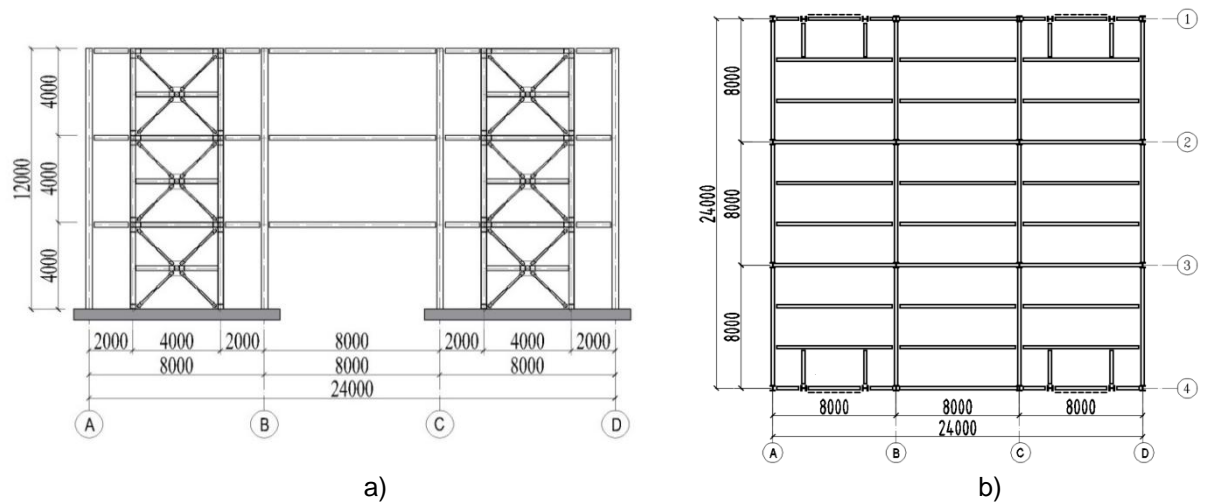


Fig. 9.23: 2D building frame and building plan

A preliminary design is conducted for vertical loads. Table 9.6 summarizes the cross-sections of the main frames and the cross-sections of proposed system for seismic resistance. These sections will be subsequently refined through response spectrum analysis (RSA).

#### 9.6.1.2 Materials

For the design of dissipative elements (modified braces) steel grade S235 is adopted and for column design the steel grade is S355. Floor beams and splitting beams are designed by steel grade S275. Floor slabs are designed by Hi-Bond metal decking used for formwork only, concrete C25/30 and reinforcing steel B500B.

Table 9.6: Cross sections of CBF and building frame

	CBF - MB				Building frame		
Storey	Braces <sup>5</sup>	Columns	Beams	Splitting beams	External columns	Internal columns	Beams
1	F95.6W120.5-M180.45-T16	HEA 260	HEA 240	HEA 260	HEB 500	HEB 500	IPE 360 IPE 500
2	F85.5W120.5-M180.35-T14	HEA 260	HEA 240	HEA 240	HEB 500	HEB 500	IPE 360 IPE 500
3	F75.4W90.4-M180.35-T12	HEA 260	HEA 240	HEA 240	HEB 500	HEB 500	IPE 360 IPE 500

#### 9.6.1.3 Loads and load combinations

Table 9.7 summarizes the assumptions for gravity loads and seismic action parameters. Top floor loads are adopted as for occupied roof terrace.

<sup>5</sup> The MB cross sections will be described by abbreviations that should be read as follows: F (flange) 95.6 width 95 mm, thickness 6 mm; W (web) 120.5 width 120 mm, thickness 5 mm; – M (modified section) 180.45 length 180 mm, flange width 45 mm – T16 (web thickness of MS) 16 mm.

**Table 9.7: Loads and actions**

Vertical loads	
Structure self-weight ( $G_{k1}$ )	3.00 kN/m <sup>2</sup>
Other permanent loads (ceiling, raised floor), ( $G_{k2}$ )	
– Intermediate floors	0.75 kN/m <sup>2</sup>
– Roof floor (terrace)	1.35 kN/m <sup>2</sup>
Perimeter walls, storey height 4 meters ( $G_{k3}$ )	2.40 kN/m
Imposed loads (category B + movable partitions):	
– Intermediate floors ( $Q_{k,1}$ )	3.00 kN/m <sup>2</sup>
– Roof floor (terrace) ( $Q_{k,2}$ )	2.00 kN/m <sup>2</sup>
Seismic action	
Design response spectrum for elastic analysis	Type 1
Reference peak ground acceleration	$a_{g,R} = 0.32g$
Importance class II (Ordinary building)	$\gamma_I = 1.0$
Ground type	B ( $T_B = 0.15$ s, $T_C = 0.50$ s)
Proposed behaviour factor $q$	5.0
Damping ratio	5%
Factors for storey occupancy in seismic design situation	$\phi = 0.80$ (correlated occupancies including roof terrace)
Seismic combination coefficient for the quasi-permanent value of variable actions	$\psi_2 = 0.60$ , $\psi_E = 0.48$

Floor masses per braced frame are summarized in Table 9.8. It is assumed that total seismic mass is distributed equally between both CBF-MB in axes 1 and 4. Torsional effects from eccentricities of story masses are not taken in consideration in this example.

**Table 9.8: Seismic masses per braced frame**

Floor 1 mass = 82.05 t	Floor 2 mass = 82.05 t	Floor 3 mass = 82.35 t
------------------------	------------------------	------------------------

#### 9.6.1.4 Simulations

The structural linear elastic model was formed according to the rules given in Section 9.5.3.1. All joints between floor beams and CBF-MB columns are nominally pinned as well as the joints between building columns and floor beams in direction of axes 1, 2, 3 and 4. The last implies that all lateral loads will be resisted by CBF-MB systems only. Column (offset) to braces joints are nominally pinned. The joints between splitting beams and columns are assumed to be rigid and full strength so they are modelled as continuous. This can be achieved by welded connection or bolted haunch connection. The advantages of this design approach were discussed in section 9.5.2.6. Column bases were designed and detailed as pinned. The elastic analysis requires a tension-only diagonal model [1], while non-linear static and dynamic analyses models include both couples of braces.

### 9.6.2 Design for static combinations

Distinctive feature of the structural configuration demonstrated in that case study is the fact that the proposed seismic resistant system (CBF-MB) is arranged so as to be free of gravity loads, excluding its self-weight. Since the latter is negligible, gravity load design is not presented. It is evident that the seismic design situation is prevailing for the CBF-MB system and therefore wind combination will not be considered.

### 9.6.3 Design for seismic combinations

Multi-modal RSA was performed. The results from the analysis are summarized in Table 9.9. The first and the second modes activated more than 90% of the total mass.

**Table 9.9: Participating mass ratio and periods**

Mode No	Eigen Period (s)	Participating mass ratio (%)	Total activated mass (%)
1	0.881	83.8	97.2
2	0.309	13.4	

According to [1] when  $T_C \leq T \leq T_D$  the spectrum acceleration has to be greater or equal to the lower bound. Since the first mode dominates the response, the check may be done by Eq. (9.38):

$$S_d(T) = \frac{V_{tot}}{P_{tot}} \geq \beta a_g, \quad \text{Eq. (9.38)}$$

where  $V_{tot}$  is the total base shear from the response spectrum analysis,  $P_{tot}$  is the total vertical load, corresponding to the effective mass of the frame in seismic design situation and  $\beta = 0.2$  is the lower bound factor for the horizontal design spectrum. The check proves that there is no need to increase the base shear (Table 9.10).

**Table 9.10: Check of the lower bound for the horizontal design spectrum**

$V_{tot}$ (kN)	$P_{tot}$ (kN)	$V_{tot} / P_{tot}$	$\beta a_g$
234.2	2417.7	0.097	0.064

### 9.6.4 Detailed design

#### 9.6.4.1 Limitation of interstorey drift

Assuming that the building has ductile non-structural elements the verification is:

$$d_r \cdot v \leq 0.0075h = (0.0075) \cdot 4000 = 30.0 \text{ mm}, \quad \text{Eq. (9.39)}$$

where  $v=0.5$  is reduction factor [1],  $h$  is the story height and  $d_r$  is the design interstorey drift. Table 9.11 includes the results from the analysis for each of the stories.

**Table 9.11: Limitation of interstorey drift**

Storey	1	2	3
$d_{e,top}$ (mm)	8.2	18.0	27.6
$d_{e,bottom}$ (mm)	0.0	8.2	18.2
$d_r = (d_{e,top} - d_{e,bottom})$ q (mm)	41.0	49.0	47.0
$d_r$ v	20.5	24.5	23.5

#### 9.6.4.2 P-delta effects

The sensitivity to second order (P–D) effects is estimated by the inter-storey drift sensitivity coefficient  $\theta$  given by Eq. (9.40), where  $P_{tot}$  and  $V_{tot}$  are the total gravity load at and above the storey considered in the seismic design situation and storey seismic shear, respectively, at the storey under consideration. The calculated values of  $\theta$  are listed in Table 9.12.

$$\theta = \frac{P_{tot} d_r}{V_{tot} h} \quad \text{Eq. (9.40)}$$

**Table 9.12: 2<sup>nd</sup> order effects**

Storey	1	2	3
$d_r = (d_{e,top} - d_{e,bottom})$ q (mm)	41.0	49.0	47.0
$P_{tot} / V_{tot}$	2417.7 / 234.2	1612.8 / 193.1	807.9 / 129.6
$\theta$	0.11	0.10	0.07

The maximum value of the sensitivity coefficient is  $0.1 < \theta = 0.11 < 0.2$  and second order effects may be approximately accounted for by multiplying the effects from seismic load case by the multiplier  $k_\theta = 1/(1-\theta) = 1.12$ .

#### 9.6.4.3 Design of dissipative members

The necessary cross section of the modified braces is defined by check of available plastic resistance of the reduced cross section (RS):  $N_{pl,Rd} \geq N_{Ed}$ . The design load effects are obtained from the seismic load combination  $1.0.G_{k,j} + 0.48.Q_{k,i} + E$ . Table 9.13 summarizes the verified cross sections for the braces of each floor. It also includes check for global homogeneous dissipative behaviour of the system achieved when the braces overstrength values  $\Omega$  differ by no more than 25% of its minimum value.

**Table 9.13: Verification of braces and check for homogeneous dissipative behaviour**

Storey	Brace cross section	Cross section area (mm <sup>2</sup> )	$N_{Ed}$ (kN)	$N_{pl,RS,Rd}$ (kN)	$\Omega = \frac{N_{pl,RS,Rd}}{N_{Ed}}$	$\frac{\max \Omega}{\min \Omega} < 1.25$
1	F95.6W120.5-M180.45-T16	1740	348.2	389.4	1.12	1.063
2	F85.5W120.5-M180.35-T14	1450	279.9	324.5	1.16	
3	F75.4W90.4-M180.35-T12	960	180.0	214.9	1.19	

Table 9.14 summarizes the effective slenderness  $\lambda_{z,eff}$  values of modified braces obtained by Eq. (9.15) and compared to the values obtained by buckling analysis of a single brace FE model in SAP2000 [18].

**Table 9.14: Effective slenderness of modified braces**

Storey	Brace cross-sections	$\lambda_{z,eff}$ Eq. (5-7)	$\lambda_{z,eff}$ buckling	deviation [%]	$1.3 \leq \bar{\lambda}_{z,eff} \leq 2.0$
1	F95.6W120.5-M180.45-T16	136.9	128.79	6.31	1.46
2	F85.5W120.5-M180.35-T14	170.2	164.54	3.45	1.81
3	F75.4W 90.4-M180.35-T12	175.2	169.38	3.46	1.87

#### 9.6.4.4 Capacity design of non-dissipative members

The non-dissipative CBF members (columns, floor beams and splitting beam) are designed following the capacity design criteria according to Section 5.2.7 and Eq. (9.21) – Eq. (9.29). The overall amplification factor for internal forces in Seismic and UNB load case is  $1.1\gamma_{ov} \Omega_{min} \rho$ , where  $\rho = 1.15$ . The total capacity amplifier is 1.771. It is worth reminding that all the internal forces have already been amplified also by  $k_\theta = 1.12$ . The utilization factors of columns, floor beams and splitting beam were calculated according to the provisions of [17]. Table 9.15, Table 9.16 and Table 9.17 present the non-dissipative member verification.

**Table 9.15: CBF columns verification**

Storey	Column cross-section / Material	$N_{col,Ed}$	$M_{col,Ed}$	Utilization factor
1	HEA 260 / S355	-1141.1	131.6	0.991
2	HEA 260 / S355	-642.8	75.9	0.566
3	HEA 260 / S355	-264.3	63.2	0.331

For the design of splitting beam the criterion of Eq. (9.19) was governing. It is worth noting that cross-sections should be checked based on elastic section modulus.

**Table 9.16: Splitting beam verification**

Storey	Splitting beam cross-section / Material	$N_{sb,Ed}$	$M_{sb,Ed}$	Utilization factor	$\bar{\lambda}_{LT}$
1	HEA 260 / S275	123.8	-148.7	0.734	0.394
2	HEA 240 / S275	107.7	-86.7	0.544	0.362
3	HEA 240 / S275	54.9	-83.5	0.499	0.365

**Table 9.17: Floor beam verification**

Storey	Floor beam cross-section / Material	$N_{b,Ed}$	$M_{b,Ed}$	Utilization factor
1	HEA 240 / S275	-504.0	-18.7	0.356
2	HEA 240 / S275	-360.5	-18.7	0.285
3	HEA 240 / S275	-156.6	-17.0	0.178

It is recommended that the member size is not adjusted per the internal force demand and rather be kept nearby constant in all storeys since splitting beams together with columns provide elastic stiffness of the frame, which is essential for self-centering capability of the system after diagonals has yielded.

### 9.6.5 Non-linear static analyses

#### 9.6.5.1 Evaluation of the non-linear behaviour of the frames

The non-linear static analysis (pushover) is performed to estimate the sequence and locations of the plastic hinges and the achieved collapse mechanism. The influence of different type of semi-rigid floor beam to column joints is investigated as well. Through pushover analysis is also verified the proposed behaviour factor. A FE joint offset-truss model is created in SAP2000 [18] as described in point 5.3. Inverted triangular type distribution of horizontal incremental forces is used and  $P-\Delta$  effects are accounted for by modelling a leaning column. According to the design rules presented in 5.3, plastic hinges of type P are assigned in the braces and plastic hinges of type P-M3 are assigned in columns and splitting beams. Their locations in the analytical model are illustrated in Fig. 9.20.

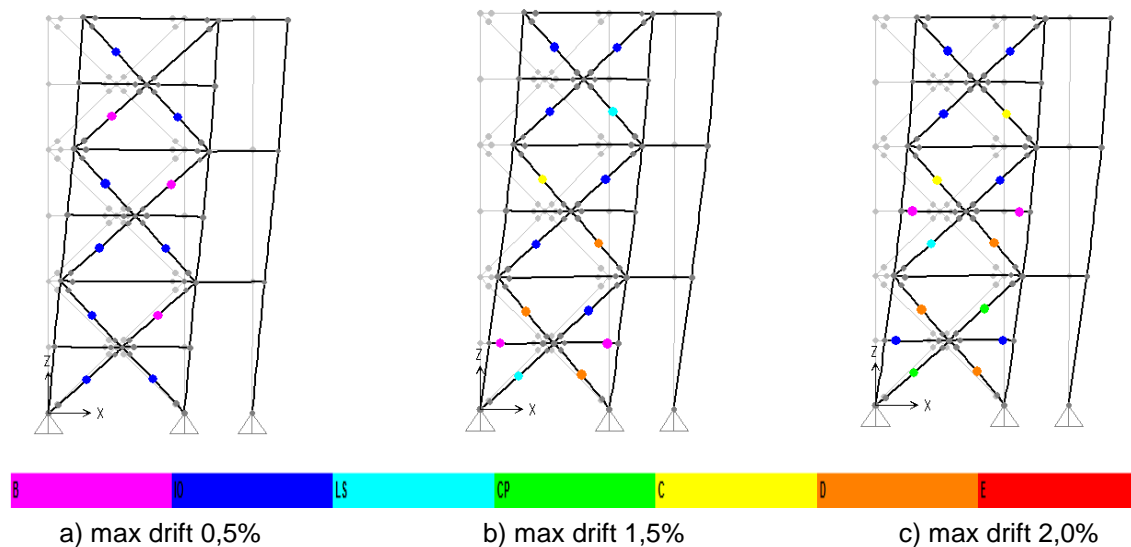


Fig. 9.24: Deformed shape and plastic hinge formation at structural performance levels to FEMA 356.

The properties of the adopted concentrated plasticity model for columns and splitting beams are defined following the prescriptions of [10] and the assumed M–N interaction rule is according to [17]. The resulting plastic hinge distribution and the CBF-MB deformed shape are presented in Fig. 9.24. Plastic deformations develop within the modified braces and at large interstorey drifts (1.5% beyond ULS) yielding occurs also in the splitting beams at first and second storey.

In order to assess the structural performance at various seismic excitations it was assumed introducing three design levels related to SLS, ULS and CP limit states.



The resultant capacity curve with indicated limit states and the corresponding plastic mechanisms are illustrated in Fig. 9.25. The plastic hinge distribution at ULS is characterized with considerable and regular yielding of tension braces and buckling in compressed ones within the building height, the frame contour remains elastic. CP limit state is characterized by yielding of the splitting beam and concentration of inelastic brace elongations in the first storey. The deformation capacities of braces are not exhausted and all columns remain elastic. The anticipated plastic mechanism with distributed plasticity along the entire height of the frame is obtained. The prescriptions of two design approaches based on EN 1998-1 target displacement [1], [24] and FEMA 356 storey drift ratio limits were compared and reported in Table 9.18 for each of the three limit states. The results are generally similar with more recognizable difference for ULS, that may be seen yet in the hinge distributions shown on Fig. 9.24 b) and Fig. 9.25 b).

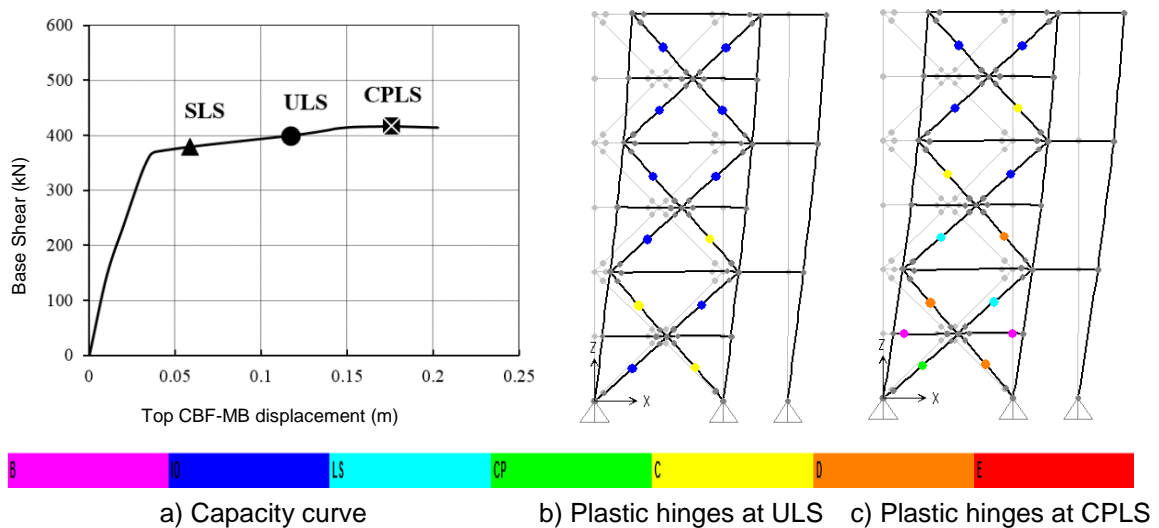


Fig. 9.25: SNA according to EN 1998-1

**Table 9.18: Comparison between EN 1998-1 and FEMA 356**

Limit states	Roof displacement, [m]	
	EN 1998-1, N2 method	FEMA 356 story drift ratio
SLS	0.0578	0.0513
ULS	0.116	0.150
CP	0.174	0.181

#### 9.6.5.2 Evaluation of the behaviour factor $q$

The behaviour factor was defined from Eq. (9.41) as the product of the ductility  $q_\mu$  and the overstrength  $\Omega$  [25].

$$q = q_\mu \Omega \quad \text{Eq. (9.41)}$$

Typical capacity curve and the parameters used for the evaluation of the behaviour factor are illustrated in Fig. 9.26.

The ductility  $q_\mu$  is determined as the ratio between the target displacement for ULS and the yield displacement  $\delta_{el}$  in the equivalent bilinear system:

$$q_\mu = \delta_{ULS} / \delta_{el} \quad \text{Eq. (9.42)}$$

Overstrength (Eq. (9.43)) is defined as the ratio between the yield force  $V_y$  of the bilinear relation “base shear–roof displacement” to the design force  $V_d$  which is calculated by the system spectral acceleration and first mode modal mass as defined by Eq. (9.44).

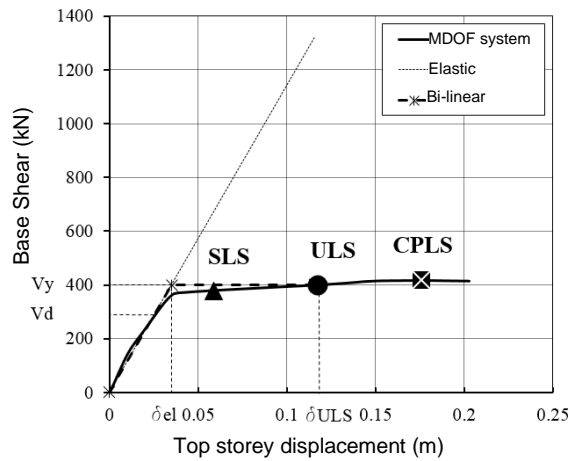


**Table 9.19: Calculated behaviour factors  $q$**

$q_\mu$	3.30
$\Omega$	1.67
$q$	5.51

Fig. 9.26: Evaluation of behaviour factor from capacity curve

$$\Omega = V_y / V_d \quad \text{Eq. (9.43)}$$

$$V_d = n M S_d(T_1), \quad \text{Eq. (9.44)}$$

$n$  being the participating mass ratio of the fundamental mode,  $M$  is the total mass and  $S_d(T_1)$  is the design spectrum acceleration at the fundamental period of vibration  $T_1$ . The calculated ductility, overstrength and behaviour factors of the proposed MB-CBF are given in Table 9.19. The calculated  $q$ -factor exceeds the value of 5.0, which was proposed for this system.

#### 9.6.6 Non-linear dynamic analyses

In order to assess if the elastic design of the CBF-MB with the proposed behaviour factor meets the seismic performance objectives, ten NDAs with real strong motions were performed. The FE joint offset truss model in SAP2000 used for SNA was slightly modified. The hysteretic nonlinear behaviour of modified braces is simulated in the model by pivot multilinear plastic link. The properties of pivot links used are presented briefly in Table 9.22 and Table 9.23. The initial loading conditions are the same as in the SNA considering the gravity loads of seismic combination.

**Table 9.20: Multi linear force-deformation definition**

Floor 1		Floor 2		Floor 3	
Deformation	Force	Deformation	Force	Deformation	Force
[m]	[kN]	[m]	[kN]	[m]	[kN]
-0.0354	-26	-0.0354	-15.4	-0.0354	-9.48
-0.00633	-38	-0.0045	-22.56	-0.00425	-14.22
-0.00237	-64	-0.0017	-37.60	-0.00159	-23.70
-0.00079	-128	-0.0006	-75.20	-0.00053	-47.40
0.0000	0	0.0000	0	0.0000	0
0.00253	409	0.0025	340.70	0.00253	225.6
0.00758	348	0.0076	289.60	0.00758	191.76
0.0354	348	0.0354	289.60	0.0354	191.76

**Table 9.21: Pivot points description**

Pivot point parameter	$\alpha_1$	$\alpha_2$	$\beta_1$	$\beta_2$	$\eta$
Value	100	0.1	0.02	0.4	0

#### 9.6.6.1 Ground motion records

Non-linear dynamic analyses (time history with direct integration) were performed. The examined braced frame was subjected to a family of ground motion records obtained from Far-Field-Record set with PGA not much larger than 0.32g. This set was considered appropriate for collapse evaluation of the investigated frame. The set includes ten real records of the strongest horizontal ground motions from the PEER NGA database and refers to sites located greater than or equal to 10 km from fault rupture, all having magnitude more or equal to 6.5. The last 3 signals were normalized as per the recommendations of [28] while the first 7 signals were as recorded. Adjusting of the selected strong ground motion records was achieved through the software SeismoMatch [29] which is able to process ground-motion records so that their spectral acceleration response matches target response spectrum (TRS). Matching of the records was based on [1] rules for recorded accelerograms. The adjusting process was performed for all ten signals. Records No 2, 3 and 5 were initially scaled with scale factors 1.3, 1.5 and 1.5 respectively, and the rest of the records were processed without scaling. The criterion of [1], stating that in the range of periods between  $0.2T_1$  and  $2T_1$  no value of the mean spectrum should be less than 90% of the corresponding value of the elastic response spectrum, was fulfilled – Fig. 9.28. List of selected strong ground motion records and their basic characteristics is shown in Table 9.24.

**Table 9.22: List of selected strong ground motion records**

Earthquake				Recording Station	Recorded Motions		Matched Motions	
ID No	M	Year	Name	Name	PGA max (g)	PGV max (cm/s)	PGA max (g)	PGV max (cm/s)
1	7.1	1999	Hector Mine, USA	Hector (90)	0.34	42	0.52	32
2	6.9	1995	Kobe, Japan	Kakogawa (CUE90)	0.34	23	0.33	31
3	7.5	1999	Kocaeli, Turkey	Duzce (270)	0.35	11	0.67	31
4	6.9	1989	Loma Prieta, USA	090 CDMG	0.39	45	0.34	45
5	6.5	1987	Superst. Hills, USA	Poe Road (temp)	0.35	10	0.52	40
6	7.6	1999	Chi-Chi, Taiwan	TCU 045	0.36	22	0.52	49
7	6.5	1976	Friuli, Italy	Tolmezzo (000)	0.35	22	0.52	69
8	7.3	1992	Landers, USA	Coolwater	0.33	30	0.34	32
9	7.4	1990	Manjil, Iran	Abbar	0.51	54	0.44	40
10	6.6	1971	San Fernando, USA	LA-Hollywood Stor	0.21	19	0.49	38

As TRS the Eurocode type 1 Response Spectrum (RS), based on PGA 0.32g and Soil Type B was used. Fig. 9.27 illustrates the RSs of the recorded accelerograms and the TRS. The Mean Matched RS of the matched accelerograms, the TRS and the 90% TRS are shown in Fig. 9.28. The mean spectral response, calculated from all of the 10 records in the range of periods between 0.18 s and 2.0 s, deviates less than 2% from the corresponding values of the TRS. The maximum misfit is 5.1%. The carried out processing of the records fully complies with EN 1998-1 prescriptions and it is considered suitable for evaluating the performance and verifying the design methodology of the CBF-MB system.

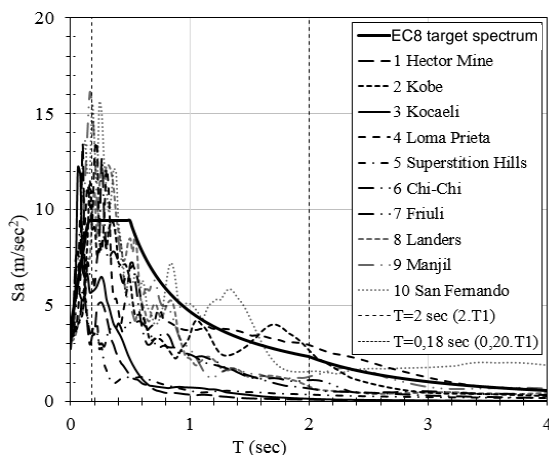


Fig. 9.27: Response spectra of the recorded accelerograms and Target RS

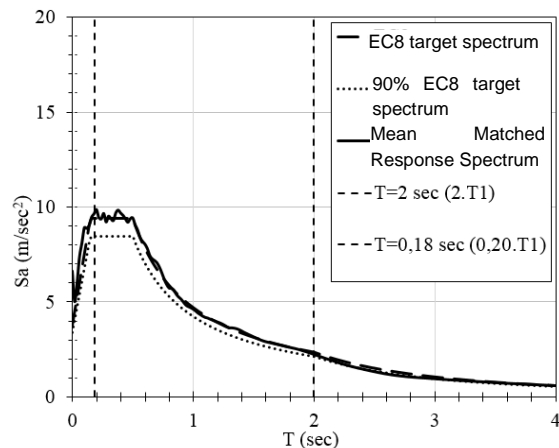


Fig. 9.28: Target Response Spectrum, 90% Target RS and Mean Matched RS

### 9.6.6.2 Residual global drifts

Initial assessment of dynamic response of the CBF-MB under seismic excitations is made through the roof displacement time histories for each of the ten matched signals. Fig. 9.29 illustrates the roof displacement time histories for Kobe and Loma Prieta earthquake records. Table 9.25 summarizes the residual global drift ratios for each of the seismic records calculated by dividing the residual roof displacements by the MB-CBF height (12 m). It should be noticed that the residual global drift ratio does not exceed 0.16% which is three times lower than the limit value of 0.5% of FEMA-356 [10] for braced steel frames at IO. This is indicative for the very good self-centering ability of the examined structure and is essential for assessment of the performance state after a major seismic event. This effect is attributed to the horizontal stiffness of the CBF-MB with splitting beams fixed to the columns.

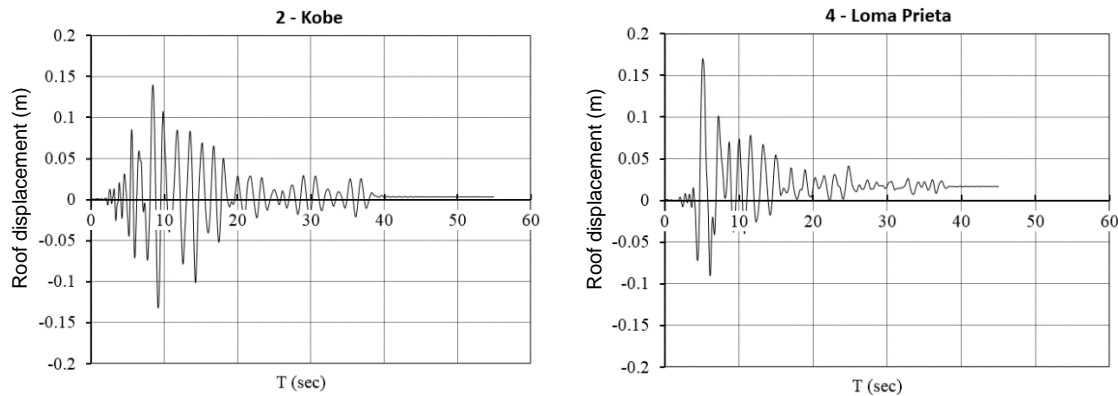


Fig. 9.29: Roof displacement time histories

**Table 9.23: Residual global drift ratios (%)**

Seismic record	MB-CBF	Seismic record	MB-CBF
1.Hector Mine	0.08%	6.Chi-Chi	0.00%
2.Kobe	0.02%	7.Friuli	0.05%
3.Kocaeli	0.02%	8. Landers	0.02%
4.Loma Prieta	0.14%	9. Manjil	0.02%
5.Superstition Hills	0.09%	10. San Fernando	0.16%
Average	0.06%	Standard deviation	0.056%

### 9.6.6.3 Interstorey drifts

The performance of CBF-MB was also examined through the interstorey drifts. In Fig. 9.30, the residual and the maximum interstorey drift ratios are given indicatively for Kobe and Loma Prieta records.

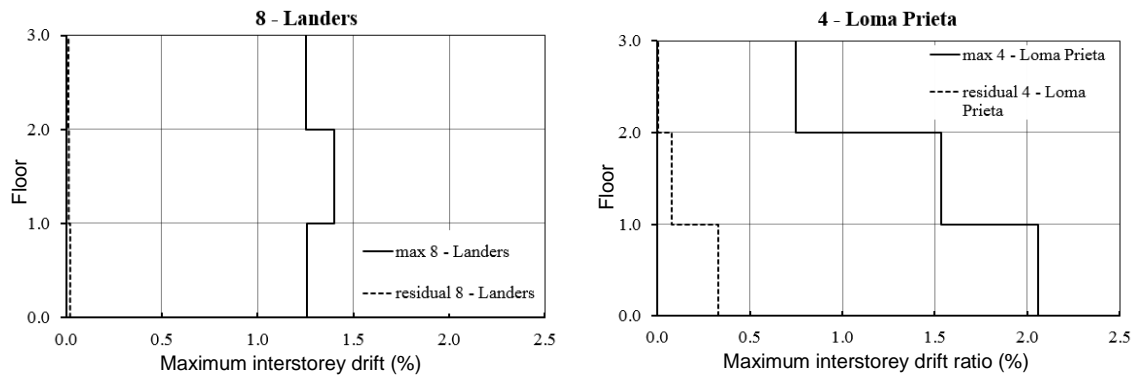


Fig. 9.30: Maximum and residual interstorey drifts for Kobe and Loma Prieta earthquakes

It is seen that the residual interstorey drift values are close to zero, similar to the residual roof drifts. Critical stories with maximum interstorey drifts are 1<sup>st</sup> or 3<sup>rd</sup> depending on the characteristics of the seismic records. The maximum interstorey drifts for each of the ten seismic records are summarized in Table 9.26.

**Table 9.24: Maximum interstorey drift ratios (%)**

Seismic record	MB-CBF	Seismic record	MB-CBF
1.Hector Mine	1.78%	6.Chi-Chi	1.26%
2.Kobe	1.47%	7.Friuli	1.90%
3.Kocaeli	1.68%	8. Landers	1.40%
4.Loma Prieta	2.06%	9. Manjil	1.02%
5.Superstition Hills	1.76%	10. San Fernando	2.23%
Average	1.66%	Standard deviation	0.371%

The maximum values of interstorey drifts appear between the two FEMA-356 limiting values at ULS (1.5%) and at CPLS (2.0%) with the exception of the values for seismic records Loma Prieta (2.06%) and San Fernando (2.23%). Due to the experimentally obtained higher limits for the CBF-MB system (1.89% for ULS and 3.00% for CPLS (section 4.4)) it is concluded that these values are not indicative for collapse.

#### 9.6.6.4 Low cycle fatigue

In order to make low cycle fatigue life assessment of the system, Eq. (9.6) is used. It gives a conservative relation between the axial deformation amplitude  $\delta_d$  corresponding to the number of cycles to failure  $N$ . The time history of brace axial elongations and shortenings are taken from the SAP 2000 joint offset nonlinear model output for the pivot multilinear plastic link. Number of cycles was counted by rainflow method, ignoring all cycles with amplitudes less than 5mm. The former was adopted since the proposed formula is very conservative for amplitudes less than 5mm – (Fig. 9.16). Based on Eq. (9.6) and the Miner's rule, damage index was calculated and reported in Table 9.25. In all cases the damage index appears well

below unity, demonstrating very good low cycle fatigue behaviour of the proposed system.

**Table 9.25: Damage index**

Seismic record	Damage index ( $D < 1,0$ )	Seismic record	Damage index ( $D < 1,0$ )
1. Hector Mine	0.070	6. Chi-Chi	0.144
2. Kobe	0.257	7. Friuli	0.076
3. Kocaeli	0.063	8. Landers	0.140
4. Loma Prieta	0.178	9. Manjil	0.155
5. Superstition Hills	0.048	10. San Fernando	0.127

#### 9.6.6.5 Incremental Dynamic Analysis (IDA)

Other method for evaluating the non-linear response of the CBF-MB system is the Incremental Dynamic Analysis (IDA). The analysis procedure is presented by Vamvatsikos and Cornell [26], [27] and FEMA-P695 [28]. The procedure is based on the relation between the most representative ground motion Intensity Measure (IM) and the Damage Measure (DM). For the examined system the IM is represented by the matched signal spectral acceleration corresponding to the structural first natural mode of vibration considering 5% viscous damping  $S_a(T_1, 5\%)$  and the DM is defined through the maximum interstorey drift  $\theta_{max}$ . In order to generate the IDA curves the ground motions of Section 6.6.1 were scaled by factors 0.50; 0.75; 1.00; 1.25; 1.50 and higher until numerical non-convergence was reached.

IDA curves for all of the ten examined records are illustrated in Fig. 9.31. The resultant curves are characterized by an elastic part with constant slope until yielding which occurs at  $S_a(T_1, 5\%) \approx 0.25g$  and  $\theta_{max} \approx 0.6\%$ , followed by a zone with varying slope attributed to development of inelastic deformations, and flat end portion at the highest numerically converging run when global dynamic instability occurred and any increase in the IM would result in practically infinite DM response.

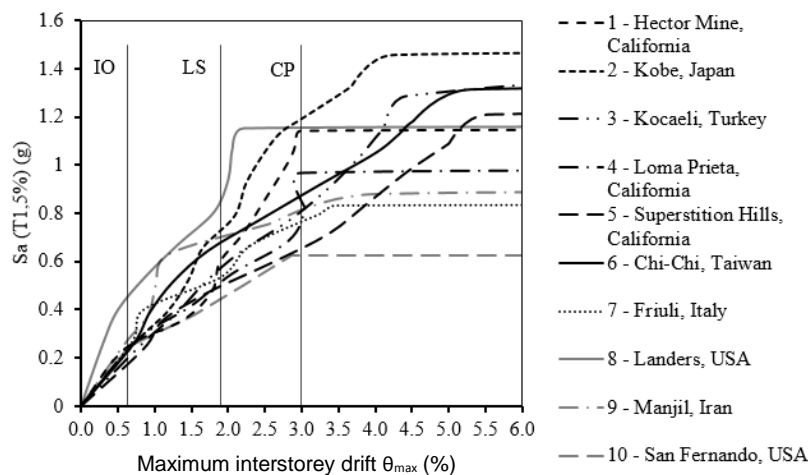


Fig. 9.31: IDA curves for each of the seismic record used and experimentally obtained limit state capacities (IO, LS, CP)

To evaluate the performance of the system, the three limit states Immediate Occupancy (IO), Life Safety (LS) and Collapse Prevention (CP) were defined for the IDA curves. These are based on the maximum experimental drifts (SLS, ULS, CPLS). The corresponding IM and DM values for each of the seismic records are given in Table 9.26.

**Table 9.26: IM and DM values for all of the ten records and each limit state (IO, LS, CP)**

Seismic record	$S_a(T_1, 5\%)$ (g)			$\theta_{max}$ (%)		
	IO	LS	CP	IO	LS	CP
1. Hector Mine, California	0.242	0.597	1.141	0.625	1.89	3.00
2. Kobe, Japan	0.223	0.729	1.193			
3. Kocaeli, Turkey	0.195	0.566	0.812			
4. Loma Prieta, California	0.224	0.509	0.797			
5. Superstition Hills, California	0.174	0.495	0.657			
6. Chi-Chi, Taiwan	0.226	0.674	0.874			
7. Friuli, Italy	0.240	0.535	0.765			
8. Landers, USA	0.444	0.860	1.152			
9. Manjil, Iran	0.269	0.695	0.794			
10. San Fernando, USA	0.237	0.442	0.627			
16 % percentile	0.207	0.501	0.705	0.625	1.89	3.00
50% percentile	0.232	0.582	0.804			
84% percentile	0.257	0.714	1.147			
Arithmetic Mean	0.248	0.610	0.881			

IDA curves are summarized into their 16%, 50% and 84% percentiles. Fig. 9.32 illustrates the representative median curve (50%). The figure also includes the points at IO, LS and CP, defined by the experimentally obtained interstorey drifts  $\theta_{max}$  and the arithmetic mean values of  $S_a(T_1, 5\%)$  obtained from Table 9.26 after arranging them in ascending order ( $S_a(T_1, 5\%) = 0.25g, 0.61g, 0.88g$ ). It is observed that these three points are very close to the median curve verifying the definition of these limit states.

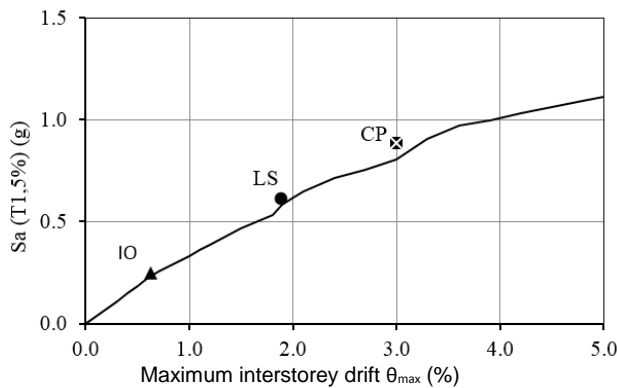


**Fig. 9.32: Median curve (50% percentile) and limit states points (IO, LS, CP)**



### 9.6.7 Comparison of the methods of analysis

In order to verify the proposed rules for design of CBF-MB, a comparison between the results from the performed types of analysis is made. The interstorey drift presents an estimation of the damage level of the structure for the three limit states defined (SLS, ULS and CPLS). Fig. 9.33 illustrates the maximum interstorey drift resultant from the elastic multi-modal analysis (RSA), static non-linear analysis (SNA) and incremental dynamic analysis (IDA). The values obtained by IDA are represented by the area enclosed by the 16% and 84% percentile curves.

It can be noticed that both the SNA and RSA curves are situated within the range defined by IDA curves predominantly in the mid-region which may be considered indicative for the agreement of the results derived by the three types of analysis. Larger deviation between SNA (Pushover) and the other two methods is observed in the third floor. It may be attributed to the influence of higher modes of vibration. Only the first mode load pattern of the incremental load was used in SNA. No value of interstorey drift exceeds the experimentally obtained limit value of 1.89% at ULS. In conclusion, it may be stated that the proposed design rules have proved to be adequate.

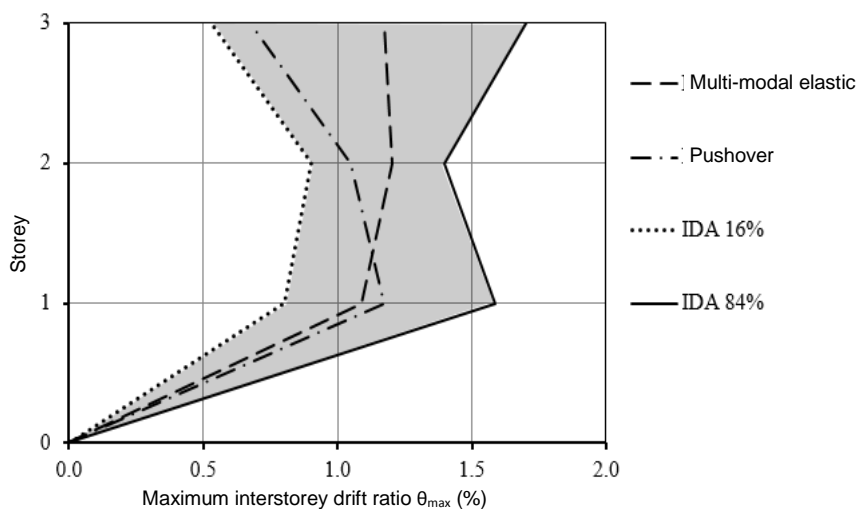


Fig. 9.33: Comparison between interstorey drift ratios obtained by RSA, SNA (Pushover) and IDA for ULS

## 9.7 CONCLUSIONS

The presented study introduces concentrically braced frame lateral force resisting system with innovative modification of braces named CBF-MB. The current brochure illustrates its successful application in steel structures in seismic regions. The study has manifested some of the specific characteristics of the system related to its improved seismic behaviour. The main conclusions are summarized below:

- The proposed system is similar to traditional concentrically braced frames with crossed diagonals. It manages to keep their advantages and to overcome their weaknesses without undue complication of the design, fabrication and erection;
- The modified braces designed by H-shaped welded built-up cross-section enable the designer to vary the cross-sectional properties and consequently to tune the MB design for the particular needs of the structure. In such way, the homogeneous yielding of tensioned diagonals in all storeys is much easier to be achieved.
- The modified braces show improved low cycle fatigue endurance and premature fracture of the diagonals is avoided, leading to overall improvement of the system hysteretic behaviour.
- Inelastic deformations are strictly limited to the modified braces and splitting beams so they prevent spreading of damage to the rest of the structural members. If braces and splitting beams are damaged after a strong seismic event, they can be removed and replaced since they are not part of the gravity load resistant system.
- The system is able to guarantee an efficient control both on drifts and residual displacements. It exhibits a self-centering features allowing immediate occupancy after earthquake.

## 9.8 FIELD OF APPLICATION

The CBF-MB systems are representative of the braced frames family. Their topology does not differ much from the topology of classical cross diagonal braced frame. In that sense, they may be successfully implemented in office and commercial buildings and in industrial constructions for pipe rack frames or engineering facilities.

## 9.9 PREVIOUS PUBLICATIONS

1. Georgiev Tzv., "Study on seismic behaviour of "X" CBFs with reduced diagonal sections", PhD Thesis (in Bulgarian), UACEG, Sofia 2013.
2. Tzvetan Georgiev, „Improvement of X-CBF hysteresis behaviour by introduction of MCS", 8th Hellenic National Conference on Steel Structures, Tripoli, Greece, 2-4 October 2014, page 75.

## 9.10 BIBLIOGRAPHIC REFERENCES

1. Eurocode 8: Design of structures for earthquake resistance - Part 1: General rules, seismic actions and rules for buildings; EN 1998-1:2004.
2. Georgiev Tzv., "Study on seismic behaviour of "X" CBFs with reduced diagonal sections", PhD Thesis (in Bulgarian), UACEG, Sofia 2013.
3. Hot rolled products of structural steels – Part 2: Technical delivery conditions for non-alloy structural steels; EN 10025-2:2001
4. Execution of steel structures and aluminium structures – Part 2: Technical requirements for steel structures; EN 1090-2:2008
5. ECCS, "Study of Design of Steel Buildings in Earthquake Zones", Technical Committee 1 – Structural Safety and Loadings; Technical Working Group 1.3 – Seismic Design. 1986.

6. Metallic materials – Tensile testing – Part 1: Method of test at room temperature; ISO 6892-1:2009
7. Seismosoft [2014] "SeismoStruct v7.0 – A computer program for static and dynamic nonlinear analysis of framed structures," available from <http://www.seismosoft.com>.
8. ANSYS Release 14.0 Documentation, Theory reference for ANSYS and ANSYS workbench 14.
9. J. Chaboche, "A review of some plasticity and viscoplasticity constitutive theories," International Journal of Plasticity, vol. 24, no. 10, pp. 1642-1693, 2008.
10. FEMA – 356: Prestandard and Commentary for the seismic rehabilitation of Buildings. Washington; 2000.
11. K. Tateishi, T. Hanji and K. Minami, "A prediction model for extremely low cycle fatigue strength of structural steel" ,International Journal of Fatigue, no. 29, pp. 887-896, 2007.
12. W. C. Chen and F. V. Lawrence, "A model for joining fatigue crack initiation and propagation analyses," University of Illinois, 1979.
13. J. Burk and F. V. Lawrence, "The effect of residual stresses on weld fatigue life," University of Illinois, 1978.
14. Dimo Zhelev, Ductile Behavior of Beam-to-Column Joint with End Plate Connection, PhD Thesis (in Bulgarian), UACEG Sofia, 2016.
15. Giulio Ballo, Carlo Castiglioni, "A Unified Approach for the Design of Steel Structures under Low and/or High Cycle Fatigue", Journal of Constructional Steel Research, Volume 34, Issue 1, pp. 75–101, 1995.
16. Luis Calado, João Azevedo, "A model for predicting the failure of structural steel elements", Journal of Constructional Steel Research, Volume 14, Issue 1, pp. 41–64, 1989.
17. EN1993-1-1, Eurocode 3: Design of steel structures - Part 1-1: General rules and rules for buildings. Brussels: Comitee Europeen de Normalisation (CEN); 2003.
18. SAP2000, CSI, Computers and Structures Inc., [www.csiberkeley.com](http://www.csiberkeley.com).
19. M. D'Aniello, G. La Manna Ambrosino, F. Portioli and R. Landolfo, "Modelling aspects of the seismic response of steel concentric braced frames", Steel and Composite Structures, Vol. 15, No. 5, pp. 539-566, 2013.
20. R. K. Dowell, F. Seible and E. L. Wilson, "Pivot Hysteresis Model for Reinforced Concrete Members," ACI Structural Journal, pp. 607-617, 1998.
21. Georgia Dougka, Danai Dimakogiannia and Ioannis Vayas, "Seismic behavior of frames with innovative energy dissipation systems (FUSEIS 1-1)", Earthquakes and Structures, Vol. 6, No. 5 (2014) pp. 561-580.
22. Georgia Dougka, Danai Dimakogianni, Ioannis Vayas, "Innovative energy dissipation systems (FUSEIS 1-1) — Experimental analysis", Journal of Constructional Steel Research Vol. 96, May 2014, pp 69–80.
23. Vayas, I., Dougka, G., Dimakogianni, Umbau und Erweiterung des Kindergartens der Deutschen Schule Athen. Bauingenieur 2014; 6:253-260.
24. Fajfar P., Gaspersic P., "The N2 Method for the Seismic Damage Analysis of RC Buildings", Earthquake Engineering and Structural Dynamics, Vol. 25, 31-46, 1996.
25. Dubina D., "Experimental Evaluation of q Factors", Proc. of 7Th Greek National Conference of Steel Structures, volume I, Invited papers, Volus, 2011.
26. Vamvatsikos D., Cornell C.A. The incremental dynamic analysis and its application to performance-based earthquake engineering. In: Proc.12th European Conference on Earthquake Engineering; 2002; 479; London.
27. Vamvatsikos D, Cornell CA. Incremental dynamic analysis. Earthquake Engineering and Structural Dynamics 2002; Vol. 31, Issue 3, pp. 491-514.
28. FEMA – P695: Quantification of building seismic performance factors, Washington; 2009.
29. Seismomatch v.2.1.0, Seismosoft, [www.seismosoft.com](http://www.seismosoft.com).

30. Georgiev Tzv., „Improvement of X-CBF hysteresis behaviour by introduction of MCS”, 8th Hellenic National Conference on Steel Structures, Tripoli, Greece, 2-4, page 75, 2014.

## 10 STEEL SELF - CENTRING DEVICE

### 10.1 INTRODUCTION

Current design techniques for buildings in seismic areas adopt the *capacity design* approach, determining specific “dissipative” elements in which plastic hinges are expected to develop to dissipate the energy stored in the building during the earthquake. The foreseen global ductile collapse mechanism of the structure is then achieved through the oversizing of protected members through the adoption of overstrength factors related to both materials ( $\gamma_{ov}$ ) and design actions ( $\Omega$ ).

According to the capacity design approach, buildings can show significant *residual displacements* after seismic event, with the following partial (or total) loss of the operational capacity of the building and of the safety of occupants. These consequences often imply a relevant economical effort necessary to restore the original configuration that the approach has not deeply taken in consideration.

For this reason, during the last decades new seismic-resistant systems able to attain a high level of safety towards seismic action minimizing the eventual repairing costs have been developed. In fact, modern approaches foreseen the adoption of specific *passive dissipation elements* devoted to limit the entry of energy during the seismic event or, otherwise, to allow its dissipation introducing specific devices. In this context, *passive protection systems*, including both *isolation* and *damping* devices, strongly developed during the last decades due to their high performance and the connected economic advantages.

#### 10.1.1 Passive protection systems

Compared with *active* and *semi-active systems*, the passive devices are designed to behave without an external source of energy or electronic devices. Their components cannot be modified in relation to the variation of the response to seismic action.

Passive protection systems are characterized by high efficacy towards seismic events and do not require specific controls once applied to the building, despite the necessity to eventually replace the damaged or wasted structural components. The application of passive protection systems leads to the modification of significant parameters of the structure, such as stiffness, displacement and dissipative capacity, increasing the performance level of the whole building.

The structural performance of passive protection system is generally optimized for high-intensity seismic events, while their potential decreases for low-intensity earthquakes: to solve this problem, when applied to buildings, passive protection systems are usually couples with active or semi-active control devices.

Referring to the energy balance equation proposed by Uang and Bertero<sup>6</sup> (Uang C.M., Bertero V.V. (1990)) the passive protection systems can be used both to decrease the demand, introducing *isolation devices*, or to increase the capacity of the building with *dissipative systems* that modify the dissipated hysteretic energy related to plastic deformation.

#### 10.1.1.1 Self-Centering Energy Dissipative devices (SSCD)

In particular, in the field of passive protection systems, re-centering devices have been the object of ever increasing research study (Priestley et al 1999; Christopoulos et al 2002 a,b ; Christopoulos and Filiatrault 2006; Christopoulos et al 2008a; Maetal 2011; Braconi et al 2012). This type of dissipative device is characterized by the presence of a re-centering force that mitigates, and may even eliminate, the residual deformations in buildings after earthquakes.

Although the earliest examples of self-centering structures date back to ancient times (e.g., in Greek temples, where the weight acted as the re-centering force), and similar principles were adopted in the 80's in the seismic design of a railway bridge (Cormack 1988), it is only in recent years that re-centering systems have been object of systematic development and application in civil structures. In particular, modern self-centering structures rely on suitable re-centering devices such as smart materials (DeRoches and Smith 2004) or post-tensioned elements (Filiatrault et al 2000).

Applications of post-tensioned re-centering systems to steel and precast structures have already been successfully implemented (Priestley et al 1999) coupling pre-tensioned elements with suitable dissipative elements. This allows to obtain the so-called “flag-shaped” structural response that is characterized by a low quantity of global dissipated energy towards the capability to recover (o reduce) the residual displacements at the end of each hysteretic cycles (i.e. seismic action) (Fig. 10.1 a)).

The ideal F/d relationship of a self-centering dissipative device is represented in Fig. 10.1 b). Besides the ultimate and yielding force and displacements, the curve is characterized by two coefficient called  $\alpha$  and  $\beta$ , respectively defined as the post-elastic stiffness coefficient and the energy dissipation coefficient. The coefficient  $\beta$  strongly influences the behaviour and the shape of the hysteretic cycle: the lower limit  $\beta=0$  leads to the bilinear-elastic system without dissipative capacity, while the upper limit  $\beta=1$  represents the limit for re-centering capacity.

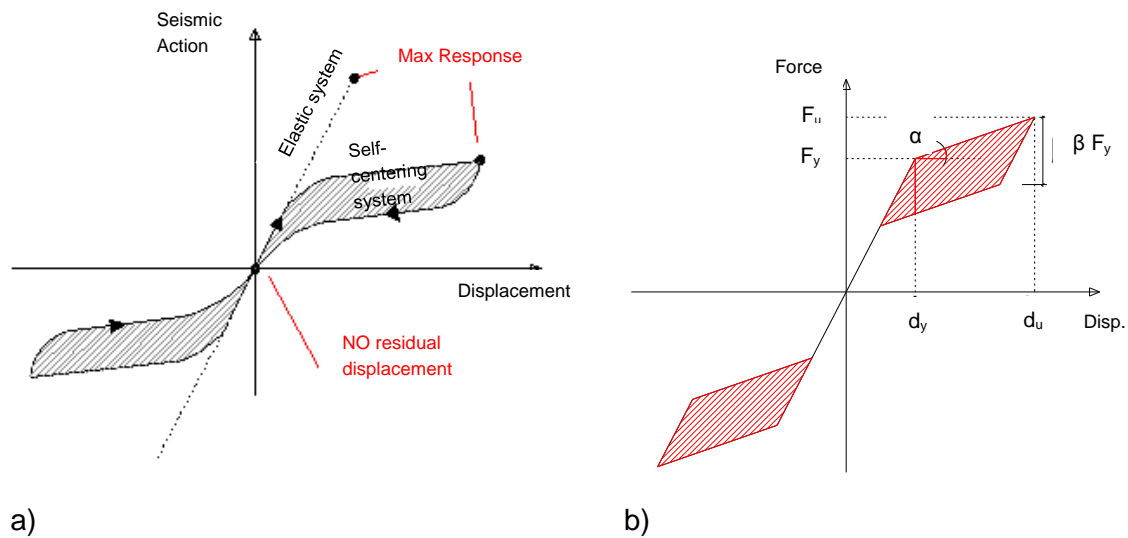


Fig. 10.1: The ideal Force/Displacement relationship for: a) a self-centering device; b) a hysteretic self-centering system.

Based on this principle, the general idea for a Self-Centering Energy Dissipative (SCED) device was proposed by Christopoulos et al (2008a). The system is made up of two bracing members, a number of post-tensioned elements, an energy dissipation system and two abutting elements (Fig 10.2), arranged and linked so that the relative movement of the bracing members dissipates energy, and the post-tensioned elements apply a force that tends to restore them to their original relative positions.

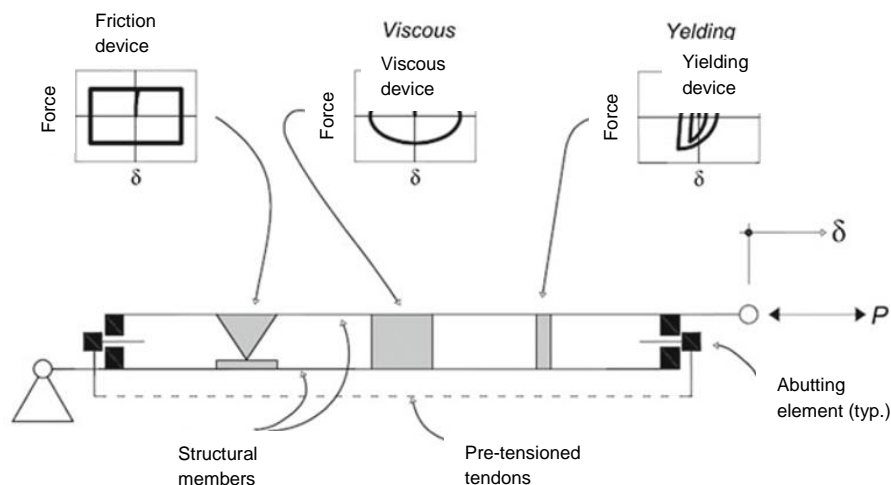


Fig. 10.2: SCED system concept (Christopoulos et al 2008a)

As shown in Fig 10.2, such an energy dissipation system can be fashioned using friction, viscous and yielding dissipative devices or a suitable combination thereof. The mechanical behavior of an SCED device, including its re-centering capacity or

the force level at which the relative movement of the bracing members begins, depends on the geometrical and mechanical characteristics of the single elements. In the following documentation, design and experimental validation of a Steel Self Centering Device (SSCD) is described. The SSCD was developed within the framework of the PRECASTEEL (PREfabriCated STEEL structures for low-rise buildings in seismic areas, Alderighi et al 2010) and STEELRETRO projects (STEELsolutions for seismic RETROfit and upgrade of existing constructions, Bonessio et al 2010; Caprili et al 2012), carried out with a grant from the European Commission Research Programme of the Research Fund for Coal and Steel. The device is based on the same basic idea as that formulated by Christopoulos et al (2008a) combining a hysteretic dissipative system with a steel pretension system for re-centering. The proposed system is made completely of steel and can be easily fashioned by any steelworks. The dissipative system is made up of steel fuses that are easy to replace after use. These characteristics make the proposed SSCD very well suited to protecting new buildings, as well as existing ones. A patent for the proposed SSCD is currently pending.

## 10.2 THE STEEL SELF-CENTERING DEVICE (SSCD)

The SSCD system (Braconi et al.) is made up of three groups of elements, each one with specific functions: *Skeleton*, the *Dissipative Elements* and the *Pretension Elements*. The Skeleton transmits and distributes any external forces between the Dissipative Elements and the Pretension Elements. Fig. 10.3 shows the main Skeleton elements (i.e. External Carter, Internal Sliding Frame and Endplates), the Dissipative Elements and the Pretension Elements.

The Internal Sliding Frame is positioned within the External Carter. The Carter presents guide elements allowing the Internal Sliding Frame to move only in the axial direction and, at the same time, serve as “stops” for the Endplates in the longitudinal direction. The Endplates are located in correspondence of the ends of the Internal Sliding Frame.

The Dissipative Elements, located within the skeleton, are made up of *dog bone shaped* steel elements linked to the Internal Carter and the Endplates. They are equipped with a lateral buckling restraining system. The Pretension Elements, made with Pre-Stressed cables, are located within the skeleton and are linked to the Endplates at both their extremities.

The elements are positioned and connected to each other in order to ensure the same global behaviour of the SSCD device both under tension and compression external forces.



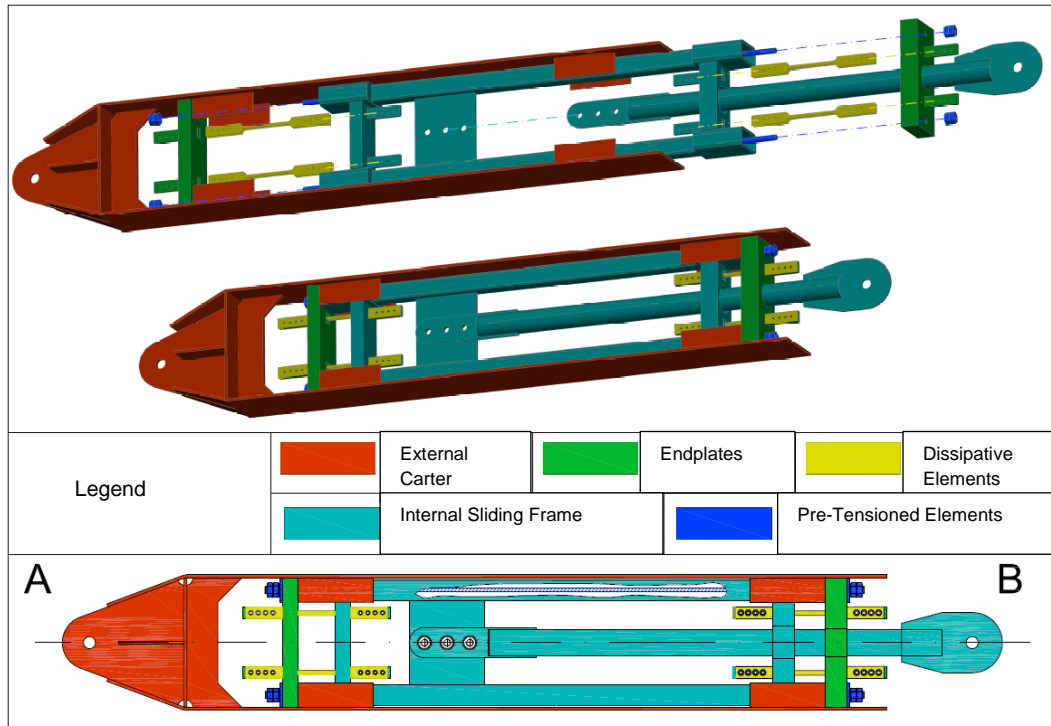


Fig. 10.3 Main components of the proposed system.

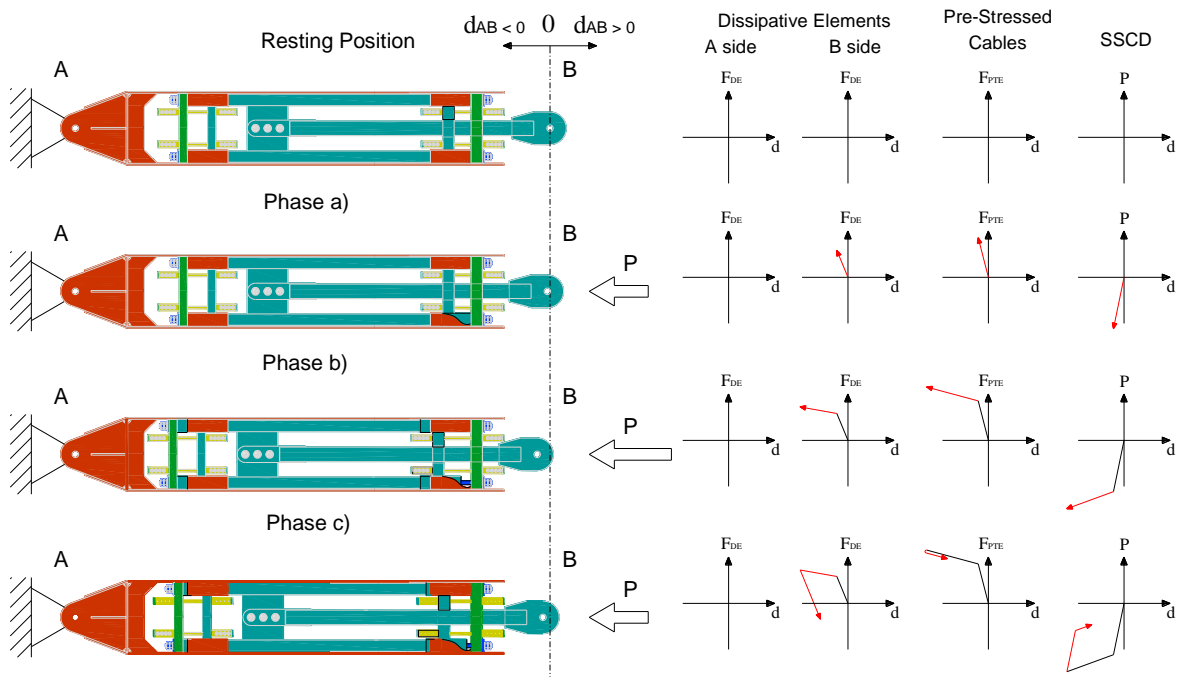


Fig. 10.4: Scheme of SSCD behaviour under external compression force.

Fig. 10.4 shows the behaviour of the SSCD system under an external compression force. Its overall behaviour can be divided into three main stages:

- loading stage with the external force  $P$  smaller than the pretension force  $P_{TE}$ ;
- loading stage with  $P$  greater than  $P_{TE}$ ;
- unloading stage.

In the first stage (*stage a*) the external compression force pushes the Internal Frame against Endplate A, but the pretension force does not allow any sliding of the Endplate itself. Thus, any relative movement between the Endplates and the Internal Frame is prevented and the Dissipative Elements are not activated. The loading force acting on the Internal Frame is transmitted from Endplate A to Endplate B and then to the Carter up to point A by means of the Pretension Elements. In this stage the overall behaviour of the SSCD is *linear elastic*.

When the value of the external force exceeds the one of the pretension force (*stage b*), Endplate A loses contact with the Stops on the External Carter and, pushed by the Internal Frame in the direction of the force, starts sliding. Thus, the Internal Frame and Endplate B move relatively to each other, and the corresponding Dissipative Elements are activated, experiencing a tensile deformation proportional to the value of the external force. At this stage, the external force is balanced by the elastic force in the Pre-Stressed Cables and by the force acting on the Dissipative Elements. The shift from stage (a) to the stage (b) is characterized by a sudden decrease in stiffness due to decompression of the Carter and the yielding of the Dissipative Elements.

When the external force decreases (*stage c*), the force transmitted by the Pre-Stressed Cables tends to bring Endplate A back to its original position, compressively deforming the Dissipative Elements, which are prevented from undergoing any buckling deformation thanks to the lateral restraining system. This stage is characterized by a sudden variation in stiffness due to yielding of the Dissipative Elements in compression. When the external force is equal to zero, if the initial pre-stress level is sufficiently high to cause the dissipative fuses to yield in compression, Endplate A is brought back in contact with the Internal Frame and the stops on the Carter.

Thus, the cyclic behaviour of the SSCD is characterized by a *flag-shaped* hysteretic curve with a residual displacement of zero.

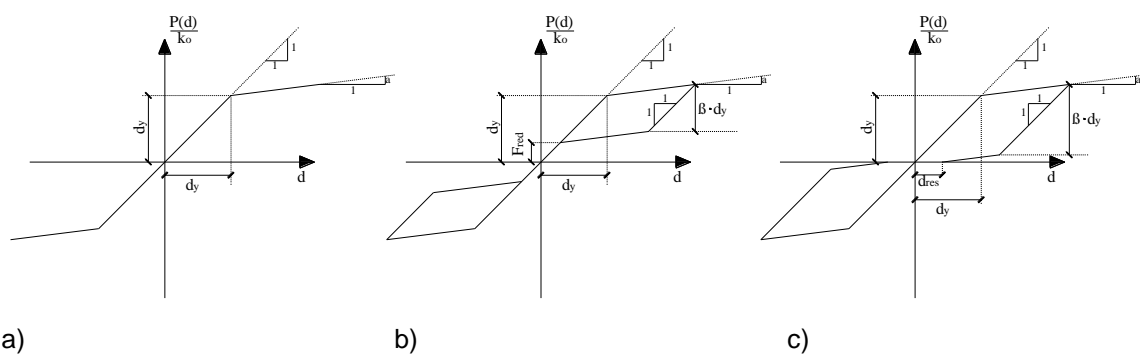


Fig. 10.5: Idealized flag-shaped hysteretic curve normalized by the initial stiffness  $k_0$  : (a)  $\beta=0$ ; (b)  $0<\beta<1$ ; (c)  $\beta>1$ .

Depending mainly on the value of the ratio between the initial pretension force and the yield strength of the Dissipative Elements, the hysteretic curve of the SSCD may present different shapes, each characterized by different values of the dissipated energy, residual displacement and residual re-centering force, as shown in Fig. 10.5. The shape of the hysteretic curve is determined by two parameters,  $\alpha$  and  $\beta$ , where  $\alpha$  is the ratio between the hardening and the initial stiffness, while  $\beta$  reflects the energy dissipation and the system's re-centering capacity (Christopoulos and Filiatrault 2006), which can be assumed equal to the ratio between the yield strength of the Dissipative Elements and the initial pretension force. A hysteretic curve with  $\beta = 0$  can be obtained by using the SSCD without any Dissipative Element, in which case the device exhibits non-linear elastic behaviour with great re-centering capacity, but no energy dissipation. On the other hand, values of  $\beta > 1$  lead to residual displacements (when the external force drops to zero) and a relatively "fat" hysteretic cycle: in this case the initial pretension force is not high enough to cause the Dissipative Elements to yield in compression completely, and the Endplate is not brought back into contact with the Internal Frame and the Carter stop. The descending branch of the flag-shaped curve intersects the displacement axis to identify the value of the residual displacement.

Values of  $\beta$  between 0 and 1 ensure suitable re-centering capacity of the device with a dissipative capacity that depends on the value of  $\beta$  itself (near zero: low energy dissipation, but great residual re-centering capacity; near one: great energy dissipation, but low residual re-centering force). In these cases, the descending branch of the flag-shaped curve intersects the elastic loading branch and the ordinate of the intersection point represents the device's residual re-centering capacity, which in the context of seismic design or retrofitting, can be assumed to be the force that the device is able to transmit to the structure when its residual displacement becomes minimum. As shown in Fig. 10.6, the SSCD exhibits similar behaviour when the external action is a tension force, the only difference being that, in this case, the Internal Frame pushes against Endplate B and the Dissipative Elements linked to Endplate A yield due to the tensile stress.

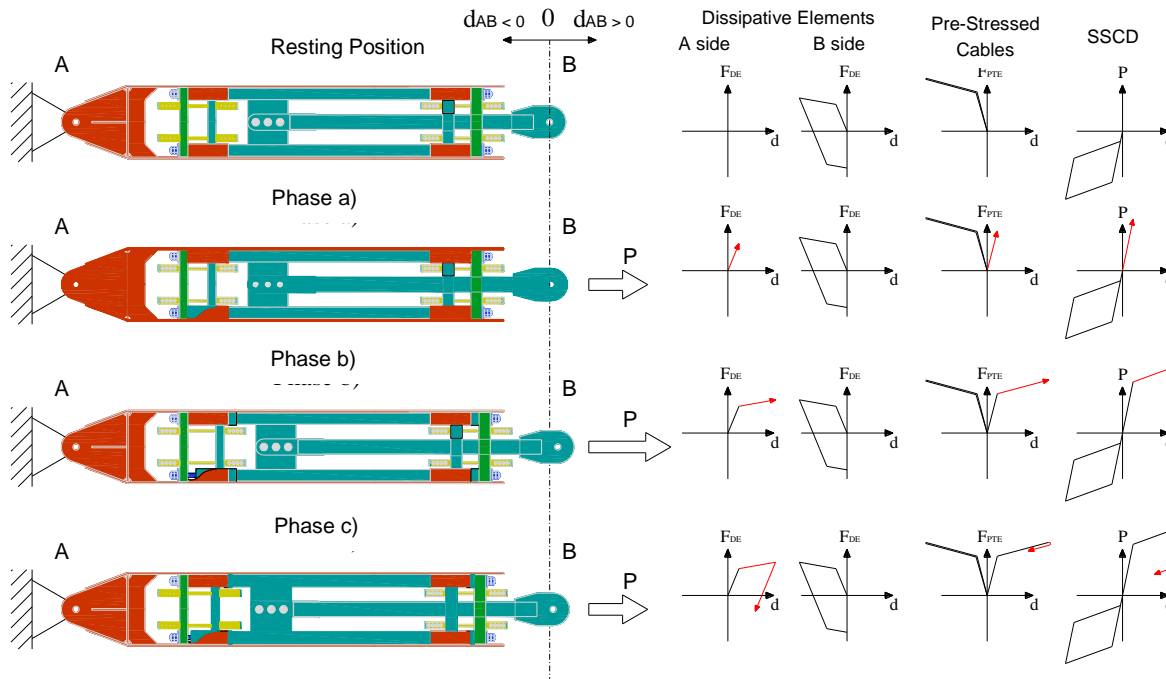


Fig. 10.6: Scheme of SSCD behaviour under external tension force.

### 10.3 MECHANICAL MODEL AND EXPERIMENTAL CHECK OF THE SSCD

#### 10.3.1 Theoretical formulation: semi-analytic model

A very detailed semi-analytic model of the adopted SSCD was proposed by Banushi (Banushi G. (2010)); simplified versions were then provided and simply adopted for the application of the device to different case study buildings.

In the mechanical behaviour of the SSCD, the main elements are schematized such as springs with a specific stiffness and constitutive relationship. The stiffness  $k_i$  of each single component can be evaluated on the base of the following equation:

$$k_i = \frac{EA_i}{L_i} \quad \text{Eq. (10.1)}$$

Being  $E$  the elastic modulus of the material,  $A_i$  the transversal section and  $L_i$  the length of the considered elements.

Table 10.1 presents the summary of the main components of the SSCD system with the corresponding assumed constitutive relationships.

**Table 10.1: Main components of the SSCD and constitutive relationship.**

Element		Constitutive law
Carter 1	C1	Linear Elastic
Carter 2	C2	Linear Elastic (no tension)
Sliding frame	TM	Linear Elastic
Piston	P	Linear Elastic
Endplate (left)	CT <sub>SX</sub>	$k=\infty$ (no tension)
Endplate (right)	CT <sub>DX</sub>	$k=\infty$ (no tension)
Pre-tensioned cables	PT	Bilinear Elastic
Dissipative element (left)	DE <sub>SX</sub>	Elastic perfectly plastic
Dissipative element (right)	DE <sub>DX</sub>	Elastic perfectly plastic

The carter can be schematically divided into two different sections, the first (C1) made up by the main part between the 8 flanges, the second (C2) made up by the remaining part up to the anchorage to the structure. This last one is schematized as characterized by  $k=\infty$  and consequently neglected in the calculations.

The determination of the constitutive laws of the different components allows to represent the SSCD as a *system of springs* opportunely connected to one another. Two main conditions (Fig. 10.7), in relation to the behaviour under compression or tension, can be determined; the difference in the tension/compression behaviour is related to the distribution of forces inside single components.

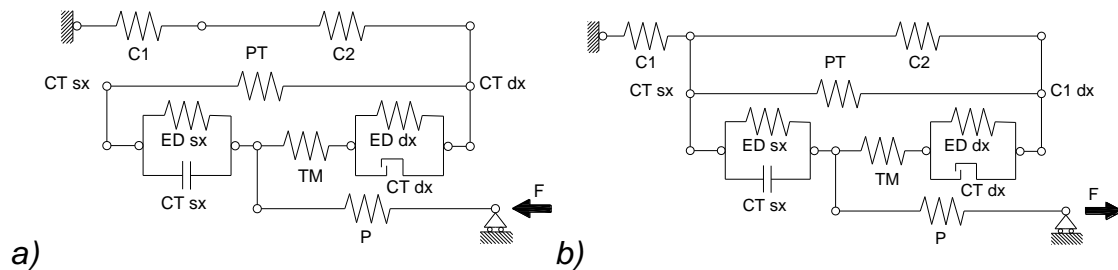


Fig. 10.7: a) Scheme for compression behaviour, b) scheme for the behaviour under tension.

The equivalent stiffness of the system can be evaluated according to the following equations:

$$\frac{1}{K_{eq}} = \sum_i \frac{1}{K_i} \text{ for springs in series} \quad \text{Eq. (10.2)}$$

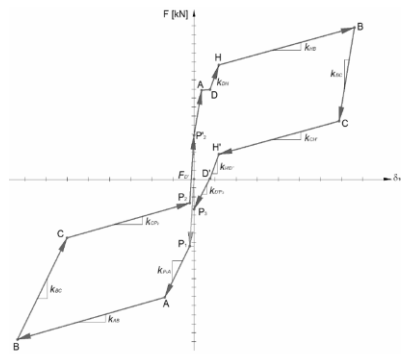
$$K_{eq} = \sum_i K_i \text{ for springs in parallel} \quad \text{Eq. (10.3)}$$

The detailed solution of the simplified schemes represented in Fig. 10.7 allows the elaboration of the semi-analytic model proposed by Banushi able to effectively represent the structural behaviour of the SSCD. Actually, the obtained

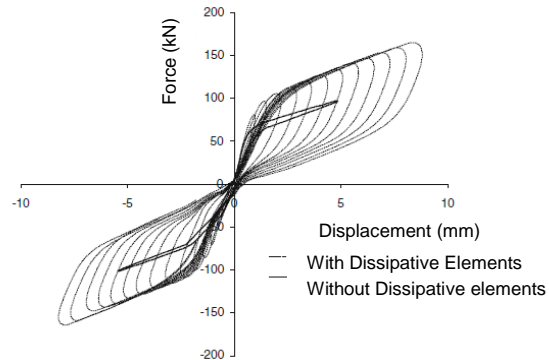
Force/Displacement curve is coherent with the flag-shaped one observed when the prototype has been experimentally tested (Fig. 10.8). The definition of the F/D curve is characterized by many parameters (Table 10.2), and this does not allow an easy application of the model to practical situations.

**Table 10.2: Parameters implicated in the definition of the F/d curve.**

Pre-tensioned cables		Dissipative elements	
$\phi$	diameter of the cables	$A_{DE}$	global section
$A_{PTE} = n \frac{\pi \phi^2}{4}$	global section	$f_{yDE}$	yielding strength
$f_{ypte}$	yielding strength	$f_{DE} = A_{DE} \cdot f_{yPTE}$	tensile force
$\rho_{PTE}$	pre-tension percentage	$L_{DE}$	length
$f_{PTE} = \rho_{PTE} \cdot f_{yPTE}$	pre-tension stress		
$F_{PTE} = A_{PTE} \cdot f_{PTE}$	pre-tension force		
$L_{PTE}$	length		
$E_{PTE}$	elastic modulus		
$d_{PTE} = \frac{f_{yPTE} \cdot (1 - \rho_{PTE})}{E_{PTE}} \cdot L_{PTE}$	displacement		



a)



b)

Fig. 10.8: a) Semi-analytic model according to Banushi and b) experimental F/D curve of the SSCD.

### 10.3.2 Simplified models for the SSCD

Since the definition of all the parameters involved (Table 10.2) is too much requiring, a *simplified model* has been elaborated taking into consideration equivalent stiffness of involved elements.

For the determination of the F/D simplified curve (Fig. 10.9), the pre-sizing of the significant components of the system is necessary. The transversal sections of the

carter, of the internal sliding frame and of the piston shall be evaluated in order to avoid buckling phenomena under seismic action, while pre-tensioned cables and dissipative elements are designed in order to satisfy the seismic demand. For the present SSCD system, the dimensions of the main components are summarized in Table 10.3.

**Table 10.3: Dimensional data of the elements constituting the SSCD system.**

Element	$A_i$ [mm <sup>2</sup> ]	$L_i$ [mm]	$k_i$ [kN/mm]	
Carter 1	11088	3700	$k_C$	629,32
Carter 2	-	690	$k_{C2}$	$\infty$
Sliding frame	1538,72	3500	$k_{TM}$	92,32
Piston	861,55	3500	$k_P$	51,69
Endplate (left)	66538	50	$k_{CT}$	$\infty$
Endplate (right)	60048	70		$\infty$
Pre-tensioned cables	226,19	3500	$k_{PT}$	12,67
Dissipative element (left)	320	170	$k_{DE}$	395,29
Dissipative element (right)				

The initial dimensions of elements shall be designed in relation to the definition of parameters  $k_{el}$ ,  $k_{pe}$ ,  $F_y$ ,  $F_u$ ,  $d_y$ ,  $d_u$ ,  $\alpha$  and  $\beta$ , determining the characteristic flag-shaped curve:

- $k_{el}$  Elastic stiffness
- $k_{pe}$  Post elastic stiffness
- $F_y$  Yielding force of the system
- $F_u$  Maximum force allowed by the system
- $d_y$  Yielding displacement
- $d_u$  Ultimate displacement
- $\alpha$  Post-elastic stiffness coefficient
- $\beta$  Energy dissipation coefficient

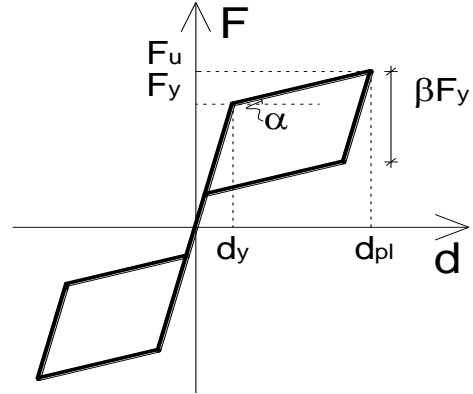
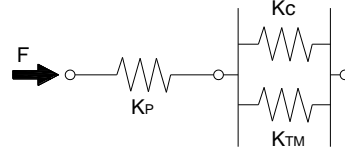


Fig. 10.9: Ideal force - displacement relationship for a hysteretic self-centering system.

The first branch of the curve is characterized by stiffness equal to  $k_{el}$ , determined considering the spring associated to the piston ( $k_P$ ) connected in parallel to the ones of the carter ( $k_C$ ) and of the sliding frame ( $k_{TM}$ ) according to the Eq. (10.4).

$$k_{el} = \frac{k_P(k_C + k_{TM})}{k_P + k_C + k_{TM}} \quad \text{Eq. (10.4)}$$



The post-elastic branch of the F/D curve, starting from the yielding point of the system, presents stiffness equal to  $k_{pe}$ . Two different schemes shall be adopted to determine this value in relation to the compression (Eq.(10.5)) or tension behaviour (Eq. (10.6)) of the system. In both of the two cases, the contribution of the dissipative elements, yielded after the first loading, is neglected.

$$k_{pec} = \frac{k_p \cdot k_{PT} \cdot k_C}{k_p k_{PT} + k_p k_C + k_{PT} k_C}$$

Eq.(10.5): Compression ( $k_{pec}$ ): springs associate to the piston ( $k_p$ ), pre-tensioned cables ( $k_{PT}$ ) and carter ( $k_C$ ) in series.

$$k_{pet} = \frac{k_p \cdot k_{TM} \cdot k_{PT}}{k_p k_{TM} + k_p k_{PT} + k_{PT} k_{TM}}$$

Eq. (10.6): Tension ( $k_{pet}$ ): springs associate to the piston ( $k_p$ ), sliding frame ( $k_{TM}$ ) and cables ( $k_{PT}$ ) in series.

Assuming that the behaviour of the SSCD system is exactly the same under tension and compression according to what previously discussed, the stiffness of the post-elastic branch can be adopted as the average between the two values obtained (Eq. (10.7)):

$$k_{pe} = \frac{k_{pet} + k_{pec}}{2} \quad \text{Eq. (10.7)}$$

where  $k_{pec}$  and  $k_{pet}$  only depends from the stiffness of the components of the system that always remain in the elastic field under seismic action.

The shape of the hysteretic curve is determined by the two parameters  $\alpha$  and  $\beta$  that can be defined as described in Eq. (10.8) and Eq. (10.9).

$$\alpha = \frac{k_{pe}}{k_{el}} \quad \text{post yielding stiffness coefficient} \quad \text{Eq. (10.8)}$$

$$\beta = \frac{F_{yDE}}{F_{PTE}} \quad \text{energy dissipation coefficient} \quad \text{Eq. (10.9)}$$



$F_{yDE}$  is the yielding force associated to dissipative elements and  $F_{PTE}$  the force of pre-tensioned elements. The coefficient  $\beta$  can be also expressed by the Eq. (10.10):

$$\beta = \frac{F_{yDE}}{F_{PTE}} = \frac{A_{DE} f_{yDE}}{A_{PTE} \rho_{PTE} f_{yPTE}} \quad \text{Eq. (10.10)}$$

being  $A_{PTE}$  and  $A_{DE}$  respectively the transversal sections of pre-tensioned elements and dissipative elements and  $\rho_{PTE}$  the pre-tension percentage.  $\beta$  is consequently dependent on the variation of the section, of the pre-tension of cables and on the transversal section of dissipative components.

A specific combination of the two parameters  $\alpha$  and  $\beta$  shall be provided for each designed system (Fig. 10.10)

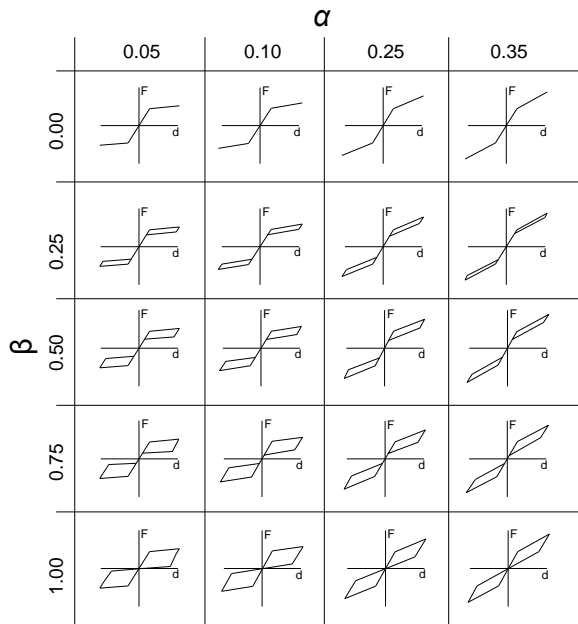


Fig. 10.10: Variation of the flag-shaped curve in relation to parameters  $\alpha$  and  $\beta$ .

Depending mainly on the value of the ratio between the initial pretension force and the yield strength of the dissipative elements, the hysteretic curve of the SSCD may present different shapes, each one characterized by different values of the dissipated energy, residual displacement and residual re-centering force, as pointed in Par. 10.2.

The yielding of the system, representing the limit in correspondence of which the stiffness shifts from the elastic to the post-elastic value, due to the overcoming of the pre-tensioning force of the cables. This force can be assumed consequently equal to:

$$F_y = F_{PTE} = A_{PTE} \cdot \rho_{PTE} \cdot f_{yPTE} \quad \text{Eq. (10.11)}$$

The displacement  $d_y$  in correspondence of  $F_y$  can be determined as:

$$d_y = \frac{F_y}{k_{el}} \quad \text{Eq. (10.12)}$$

The ultimate (maximum) displacement of the system  $d_u$ , assumed equal to the maximum deformation of pre-tensioned cables, is defined as:

$$d_u = d_{PTE} = \frac{F_{yPTE} \cdot (1 - \rho_{PTE})}{E_{PTE}} L_{PTE} \quad \text{Eq. (10.13)}$$

According to the above formulation, the displacement capacity can be increased or decreased acting on different parameters; if the mechanical properties of the materials are maintained constant ( $F_{yPTE}$  and  $E_{PTE}$ ), the maximum deformation is related to the length and to  $\rho_{PTE}$ . According to experimental test executed on a real-scale prototype (Braconi et al. (2012)), a value equal to 0.50 for such parameter is able to provide a good re-centering capacity of the system with good level of equivalent damping of the whole structure.

The maximum force of the system  $F_u$  can be finally expressed according to:

$$F_u = F_y + (d_u - d_y) \cdot k_{pe} \quad \text{Eq. (10.14)}$$

In the proposed design procedure, the transversal sections of the carter, sliding frame, piston and the global dimensions of the endplates have been kept constant. The mechanical properties of materials are the same for all the considered systems (for all the elements of the frame, the cables and the dissipative elements), according to what presented in Table 10.4.

In such a way, the number of parameters that shall be determined for the sizing of the SSCD system can be reduced according to what summarized in Table 10.5. Specific indications can be provided for the selection of the materials to be adopted for the realization of the dissipative SSCD device. The results obtained in the pre-design analyses showed that low yielding strength values of the dissipative elements provided a good global ductility and, at the same time, an effective re-centering capacity of the system once the external force drops to zero.

**Table 10.4: Fixed value assumed for the design of the SSCD system.**

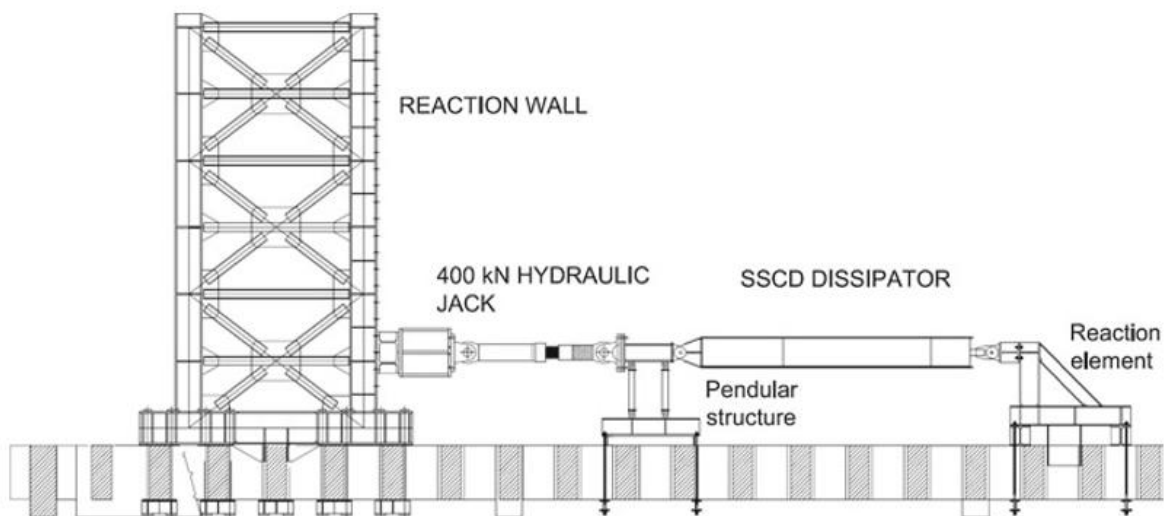
Parameter	Value	
$A_{c1}$	11088	mm <sup>2</sup>
$A_{TM}$	1539	mm <sup>2</sup>
$A_P$	862	mm <sup>2</sup>
$A_{CT}$	66538	mm <sup>2</sup>
$E$	210000	N/mm <sup>2</sup>
$f_{yPTE}$	1670	N/mm <sup>2</sup>
$E_{PTE}$	196000	N/mm <sup>2</sup>
$f_{yDE}$	240	N/mm <sup>2</sup>
$L_{DE}$	170	mm

**Table 10.5: Parameters modified during the design and influence on the parameters describing the force/displacement curve.**

Input parameter	Dependent
$L_{C1}$	$k_{el}, d_y$
$L_{TM}$	$k_{el}, d_y$
$L_P$	$k_{el}, d_y$
$L_{PTE}$	$k_{pe}, \alpha, d_u, F_u$
$\phi$	$k_{el}, k_{pe}, \alpha, d_u, F_u$
$\rho$	$F_u, d_y$
$A_{DE}$	$\beta$

### 10.3.3 Experimental check of the SSCD prototype

Two different tests were conducted on the SSCD prototype: preliminary tests on the SSCD without the Dissipative Elements, in order to evaluate the actual value of the re-centering force applied by the Pre-Stressed Cables, and final tests on the SSCD with the Dissipative Elements, in order to check the overall performance of the device. Different values of the initial pretension force and Dissipative Element cross-sections were considered in order to assess these factor's influence on the overall behaviour of the device. The experimental tests of the SSCD prototype were performed at the "Laboratorio Ufficiale per le Esperienze dei Materiali da Costruzione" of the University of Pisa. An overview of the test setup is shown in Fig. 10.11.

**Fig. 10.11: Test setup front view**

The external force was applied by means of a 400 kN hydraulic jack equipped with a loading cell and displacement sensor. The jack, horizontally positioned, was linked on one side to the reaction wall, and on the other to and a pendular steel structure providing for horizontal displacements. The SSCD prototype was linked via pinned joints at one end to the pendular steel structure (Fig. 10.12 a) and at the other to a steel reaction element that prevents any horizontal or vertical displacement of the device (Fig. 10.12 b). In order to measure and record the displacements, deformations and loads, the prototype was fitted with 8 LVDT displacement sensors, 20 strain gauges and a loading cell, arranged as shown in Fig. 10.13. The preliminary tests were executed by completing one loading-unloading cycle in both tension and compression, under controlled displacement amplitude up to a maximum/minimum value of  $\pm 5\text{mm}$ . The test results are shown in Fig. 10.14 for varying values of the pretension force fastening torque.

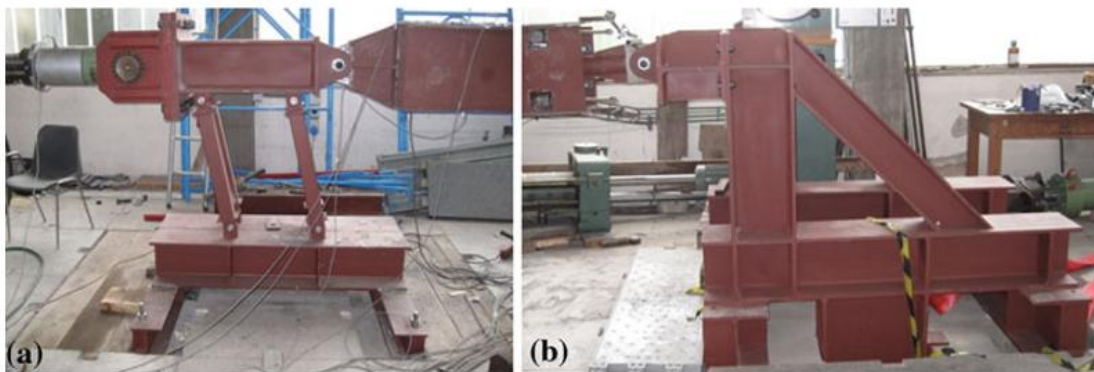


Fig. 10.12: a) Pendular steel structure; b) steel reaction element

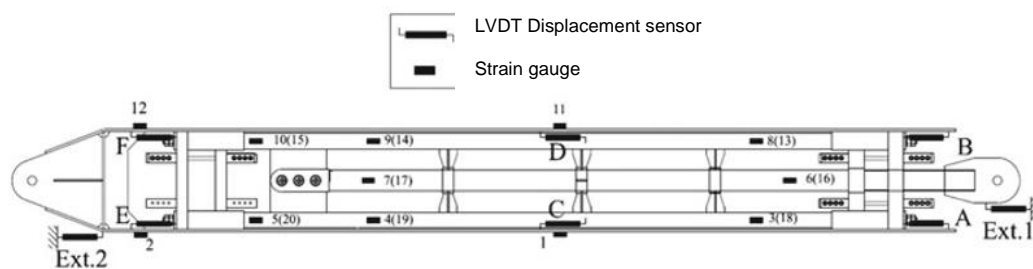


Fig. 10.13: Layout of displacement sensors (Ext.1, Ext.2 and A to F) and strain gauges (from 1 to 20, strain gauges placed on the opposite side of the SSCD are in brackets)

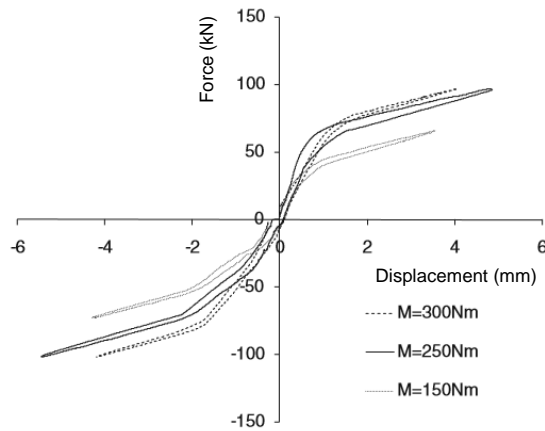


Fig. 10.14: F/D curve of the SSCD without dissipative elements

Fig. 10.14 plots the force applied by the jack as a function of the relative displacement between the External Carter and the Internal Sliding Frame, as recorded by the C and D LVDT displacement sensors (Fig. 10.13). The behaviour of the SSCD was modelled by a bilinear curve for each fastening torque value. The pretension force was evaluated as the value corresponding to the overall change in stiffness. The first branch of the bilinear model corresponds to the behaviour of the SSCD until the Endplates are forced into contact with the Internal Frame by the action of the Pre-Stressed Cables. When the external force exceeds the pre-stressing value, the Endplates lose contact with the Internal Frame, and the stiffness decreases. The results obtained for both tension and compression are reported in Table 10.6.

**Table 10.6: Pre-tension force for different values of fastening torque**

Pre-Stressed strand diameter (mm)	Fastening torque (Nm)	Pretension force (kN)	
		Tension	Compression
12	150	41	49
12	250	66	67
12	300	72	77

The final tests were carried out following the short testing procedure described by the ECCS group (ECCS TWG 1.3 1986). In the first stage of the test, small displacement increments (0.1mm) were used in order to execute at least 4 complete cycles before the Dissipative Elements yielded. Afterwards, the displacement increments were raised to 1mm and, for each successive displacement level, 3 complete cycles were performed. The velocity of the hydraulic actuator was set at 3mm/min and three cyclic tests were executed, varying the geometrical and mechanical characteristics of the Pre-Stressed Cables and Dissipative Elements., Fig. 10.15 and Fig. 10.16 show the cyclic behaviour of the SSCD prototype with

the Dissipative Elements for different values of the initial pretension force. It is evident that at the end of each loading-unloading cycle the residual displacement was practically nil (in any case, below 0.5mm): the SSCD exhibited optimal re-centering capacity. Moreover, for each maximum displacement level, the SSCD exhibited stable hysteretic loops, thereby ensuring a constant level of energy dissipation. Lastly, addition of the Dissipative Elements to the system significantly increased the area of the hysteretic loops, though the slope of the curve was practically the same as that of the SSCD without the Dissipative Elements.

The test results confirm the preliminary findings of the numerical parametric analyses. Fig. 10.17 a) shows a comparison of the hysteretic cycle of the SSCD with different cross-sectional area Dissipative Elements (tests 1 and 2), together with the results for the SSCD without the Dissipative Elements. The figure shows that the increase of the cross section leads to greater energy dissipation, but at the same time, more residual displacement. Fig. 10.17 b) plots the cyclic behaviour of the SSCD for two values of the fastening torque (tests 2 and 3). In both cases the energy dissipated is practically the same, though the SSCD yields greater force values for the higher fastening torque values.

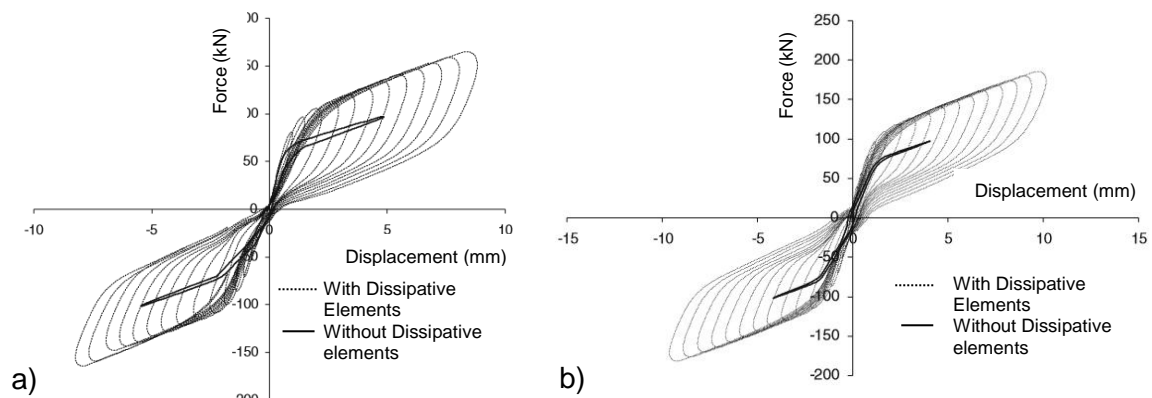


Fig. 10.15: F/D curve of the SSCD with dissipative elements: a) test 1; b) test 2.

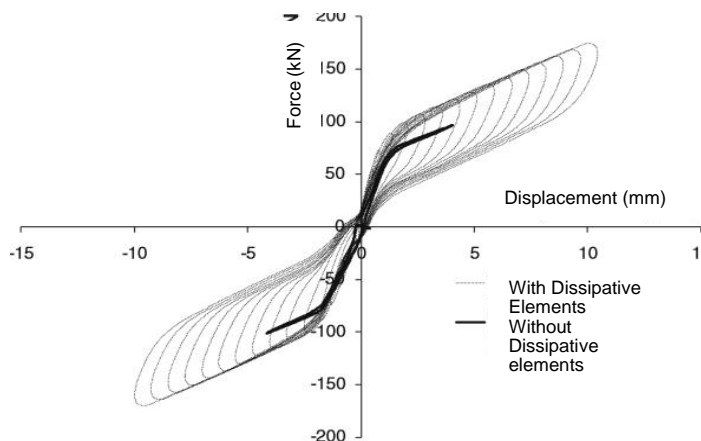


Fig. 10.16: F/D curve of the SSCD with dissipative elements, test 3

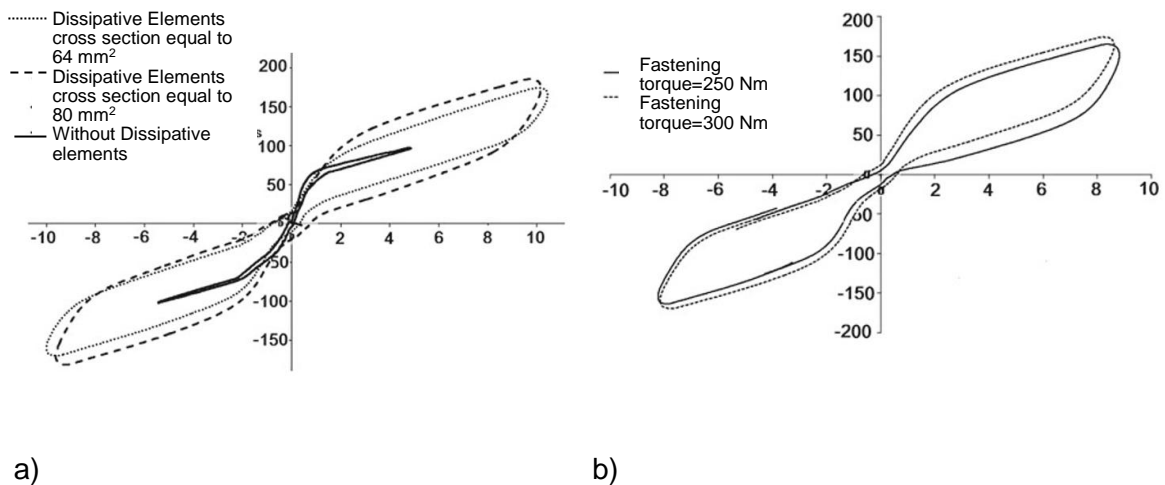


Fig. 10.17: F/D curve: a) test 1 and 2; b) test 2 and 3.

Once defined the mechanical behaviour of the system and made an experimental check of the prototype, the application to different case studies can be analysed. It's necessary to highlight that actually there are no specific standards to be followed in designing of structures with passive protection systems - for example, the absence of indications regarding *behaviour factor*  $q$  to be adopted for the element pre-sizing and so on.

## 10.4 APPLICATION TO THE DESIGN OF A COMMERCIAL BUILDING (A CASE STUDY)

### 10.4.1 General description of the case study building

The commercial building is located in Mirandola (Emilia-Romagna, MO). The building presents a hybrid structure characterized by the following main components (Fig. 10.18):

- **Reinforced Concrete walls** in the four corner of the building, carrying the horizontal seismic action;
- **internal steel pinned frames**, carrying vertical loads;
- **SSCD hysteretic systems** for the (horizontal) connection between R.C. walls and steel frames.

The design procedure adopted for these components is iterative and accurately carried out, because the mechanical and geometrical properties of the elements (especially the R.C. walls) strongly influence the stiffness and the global dynamic behaviour of the structure. Linear and nonlinear analyses have been executed on the three dimensional model realized using SAP2000 software: the latter to pre-size all the different components; the former to refine the design and verify the behaviour of the structure.

The building presents 4 storeys, characterized by a rectangular plant whose dimensions are 50x36 m. The inter-storey height is equal to 4.50 m. The 1<sup>st</sup> and 2<sup>nd</sup>

floors are destined for commercial use, while in the basement is used as a parking. Even though the four main stair cases are located in corners of the building, there are also internal ramps that imply some differences in the disposition of structural elements and of the slabs of the basement (level P1) and of the other floors (P2, P3 and P4), (Fig. 10.19). The slabs are all arranged in the same way with a maximum span of 6.0 m. Fig. 10.20 shows the typical section of the building.

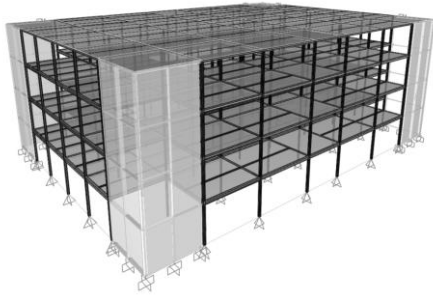


Fig. 10.18: Three dimensional schematization of the case study building.

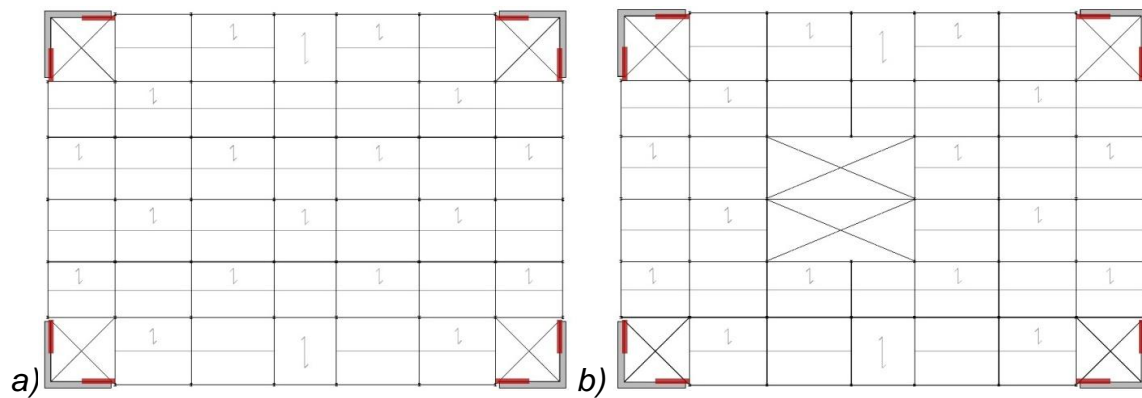


Fig. 10.19: Typical plan dispositions: a) P1, b) P2 and P3.

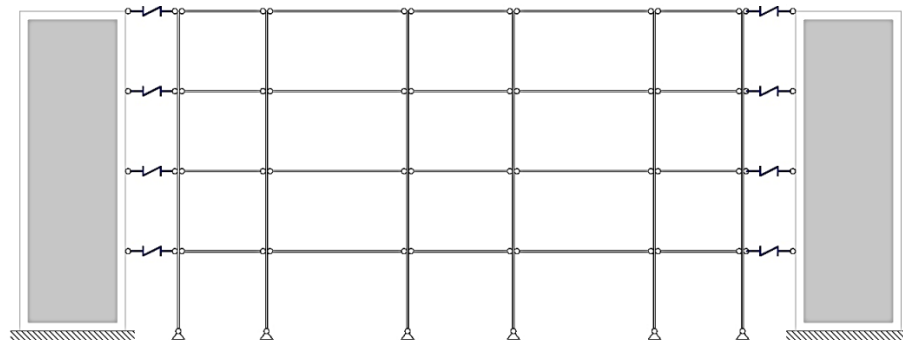


Fig. 10.20: Typical section of the designed system.

**The design strategy is based on make the R.C walls and the steel frames remain in the elastic field, while concentrate the non-linear behaviour in the SSCD device.**



The width of the steel frame is from 6.00 to 8.00 m and a steel grade S275 is used. In order to separate those close to the R.C. walls, 10 cm long gaps have been introduced in the model.

The R.C. walls have been designed, according to EN1998-1:2005, as large lightly reinforced walls, that in the present case have to carry the maximum reactions due to the connected SSCD. Concrete class C25/30 and steel reinforcing bars B450C have been adopted.

The SSCD systems have been introduced to adsorb and to dissipate the seismic energy, containing the displacements and the deformation of the building. They both connect and disconnect the R.C. walls from the frames. In fact, the SSCD devices geometrically joint them, but let them move independently of each other, and each device is activated by their relative displacement.

The initial length of the dissipative systems has been assumed equal to 3.5 m (corresponding to the one of the prototypes experimentally tested and presented in Braconi et al.); steel grade S355JR has been used for all the components of the SSCD except for the dissipative elements, characterized by low yield strength.

#### 10.4.2 Preliminary design of the case study

##### 10.4.2.1 Determination of actions

Static and seismic loads have been determined in relation to the actual Italian Standard for Constructions prescriptions (D.M.14/01/2008). Fig. 10.21 shows the response spectra adopted for linear analyses, while the permanent and the other static actions are listed below:

- $G_1 = 1,90 \text{ kN/m}^2$  Permanent load of the inter-storey floor slab (dead);
- $G_2 = 2,45 \text{ kN/m}^2$  Permanent load of the inter-storey floor slab;
- $G_1 = 0.15 \text{ kN/m}^2$  Permanent load of the roof slab (dead);
- $G_2 = 0.20 \text{ kN/m}^2$  Permanent load of the roof slab;
- $Q_k = 5,00 \text{ kN/m}^2$  Live load for commercial activities (inter-storey);
- $Q_k = 1.20 \text{ kN/m}^2$  Snow load (roof);
- $V_N = 50 \text{ years}$  Nominal life of the building;
- $C_U = 1,5$  "Coefficiente d'uso", equivalent to the "importance factor", as defined in par. 2.1(3) and 4.2.5, Eurocode 8, UNIEN 1998-1 (2004);
- $V_R = V_N C_U = 75$  Reference period;

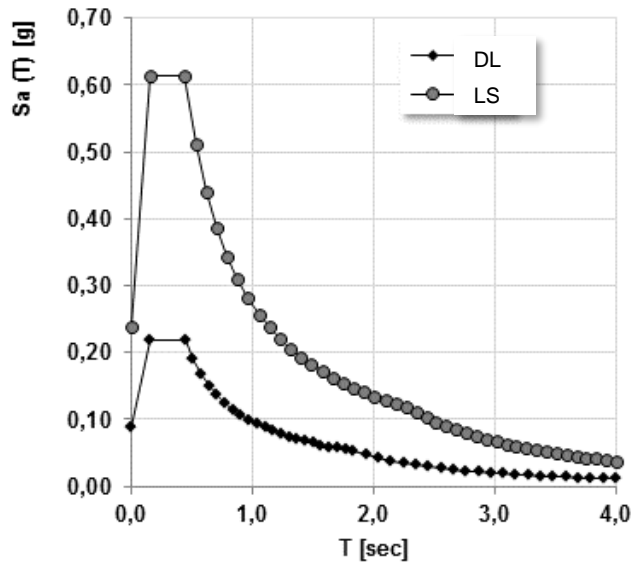


Fig. 10.21: Response spectra according to D.M.14/01/2008 for Life Safety and Damage Limitation limit state.

#### 10.4.2.2 Pre-sizing of structural elements – Gravity frames

The steel frames have been designed to sustain only vertical load, that has been evaluated using the Ultimate Limit State combination (Eq. ((10.15))).

$$q = \gamma_{G1}G_1 + \gamma_{G2}G_2 + \gamma_{Q1}Q_{k1} + \gamma_{Q2}\psi_{02}Q_{k2} \quad \text{Eq. (10.15)}$$

The prescriptions of D.M.14/01/2008 have been used to evaluate the minimum required section, both for beams and columns. The adopted profiles are summarized in Table 10.7.

**Table 10.7: Elements profiles for the steel frames.**

Element	L [m]	q [kN/m]	Profile
Inter-storey	6.0	40.94	HEB220
Inter-storey	8.0	40.94	HEB280
Roof beam	6.0	6.9	HEB160
Roof beam	8.0	6.9	HEB160
Columns			HEB220

#### 10.4.2.3 Pre-sizing of structural elements – SSCD

An initial length equal to 3.50 m has been adopted, based on the results of experimental investigations. The transversal sections of the carter, the piston, the sliding frame and the pre-tensioned elements has been then evaluated, considering that they contribute to the multi-linear elastic behaviour of the SSCD system and allow to determine the slope of the bilinear F/D curve. The parameters influencing

the dissipative behaviour have been initially neglected, introducing them only when the structure shifts in the nonlinear domain. In the first step, all the SSCD at different levels have been assumed to be equal. The data used for the determination of the F/D bilinear elastic curve are summarized in Table 10.8.

To introduce the dissipative systems in the SAP2000 model, a multilinear elastic schematization has been adopted Fig. 10.22.

**Table 10.8: Initial parameters of the F/d curve of the SSCD systems.**

$k_{el}$	144,658	kN/mm
$k_{pe}$	28,886	kN/mm
$F_y$	634,822	kN
$d_y$	4,388	mm
$F_u$	938,765	kN
$d_u$	14,911	mm

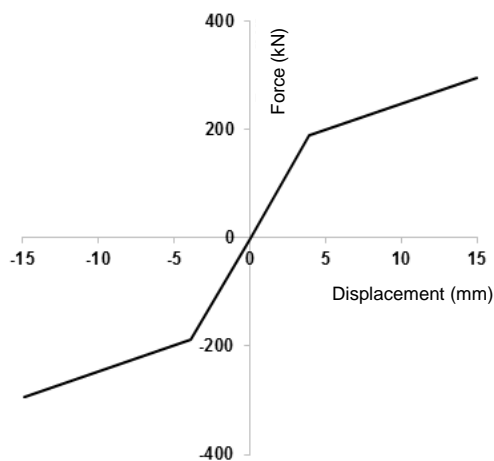


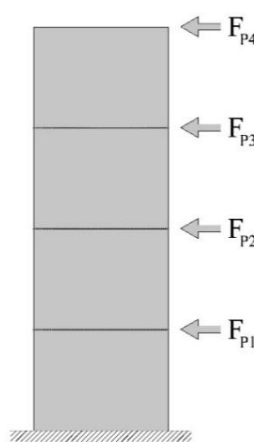
Fig. 10.22: Bilinear elastic curve of the SSCD

#### 10.4.2.4 Pre-sizing of structural elements – R.C. walls

The length of R.C. walls has been assumed equal to 6.0 m, according to the architectural design. A static equivalent analysis has been executed to preliminary determine their thickness, considering the R.C. wall as a cantilever with concentrated loads evaluated using a unitary behaviour factor. This means that the SSCD devices behave as “rigid components” that do not dissipate the seismic action but transfer it directly to the walls.

The design forces and resulting shear and bending actions are summarized in Table 10.9.

**Table 10.9: Static forces for  $q=1$ , resulting design actions and schematization adopted for the R.C. walls.**

	$F_h$ [kN]	Storey	$z_i$ [m]	Design actions	
	23838,1	P1	4,5	$V_{ed}$	4935 kN
		P2	9,00	$M_{ed}$	30964 kNm
		P3	13,5		
		P4	18,00		
$W_i$ [kN]	$F_i$ [kN]				
15449,74	$F_{P1}$	969,63			
13590,34	$F_{P2}$	1705,86			
14214,94	$F_{P3}$	2676,38			
2420,58	$F_{P4}$	607,66			

According to EN1998-1:2005 and D.M.14/01/2008 the following prescriptions shall be respected.

The thickness of the section  $b_w$  shall be higher than the maximum between 150 mm and  $h_s/20$ , being  $h_s$  the height of the inter-storey, shifting in the present case into:

$$b_w \geq 225 \text{ mm}$$

Longitudinal steel bars have to be placed maximum 300 mm apart along both sides of the wall and their diameter shall satisfy the relationship below (Eq. (10.16)):

$$\phi_l \leq \frac{b_w}{10} \quad \text{Eq. (10.16)}$$

The two extreme confined portions of the wall shall be long as prescribed in Eq. (10.18):

$$l_c = 0,20 l_w \geq 1,5 b_w = 1,20 \text{ m} \quad \text{Eq. (10.17)}$$

The vertical steel reinforcements in those zones shall satisfy the following equation (Eq. (10.18)):

$$1\% \leq \rho \leq 4\% \quad \text{Eq. (10.18)}$$

Considering all the prescriptions above listed, the wall thickness obtained was equal to 600 mm; in confined portions 24 mm diameter steel bars, placed 100 mm apart, must be used while in the other parts their spacing increase up to 250 mm.

#### 10.4.3 Modelling and structural analysis of the case study

##### 10.4.3.1 Linear model and analysis

As a result of the dynamic modal analysis (see Fig. 10.21 for the response spectra used), the structural behaviour of the building is similar in the two main directions X and Y (i.e. similar vibration periods, modal shapes), exhibiting a flexural behaviour and high participating mass (Fig. 10.23).

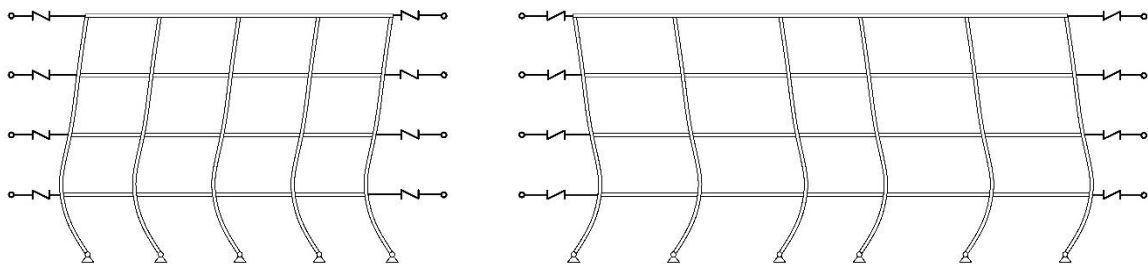


Fig. 10.23: First modal shape associated to Y and X directions.

The horizontal displacement of the building is directly related to the activation of the SSCD in the considered direction, with elastic forces proportional to the displacement of the different storeys.

In order to optimize the structural behaviour of the system, a modal deformed shape as much as possible *uniform*, aiming to remain more or less “vertical” above the first floor, has been pursued: in this way, all the SSCD system shall behave with the same level of forces and deformations, with related displacements near to zero for all the storeys above the first one (Fig. 10.24).

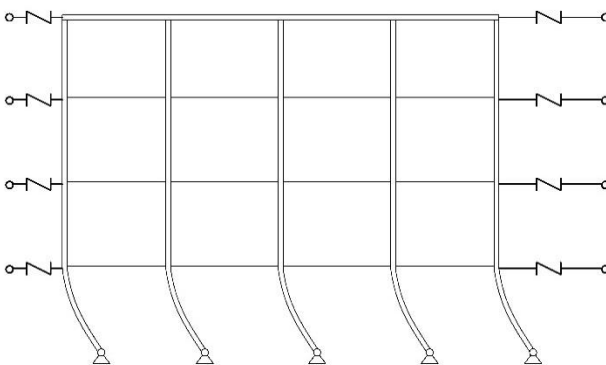


Fig. 10.24: Desired modal deformation.

The desired deformation has been obtained varying the elastic stiffness of the SSCD devices ( $k_{el}$ ), using as “control parameters” the displacements  $x_i$  of the building at SSCD of different levels ( $x_1, x_2, x_3, x_4$ ).

At first, the stiffness  $k_{el}$  has been modified only through the length of the piston  $L_P$ . This parameter has been iteratively changed until as a result of the linear modal analysis the desired configuration was obtained.

Due to the reduced stiffness of the columns, that is designed only to carry the gravity loads, they are not capable to realize a strong connection between different storeys. This implied that each floor behaves as independent (i.e. masses with independent behaviour). If each storey is independent from one another, the vibration period of the single mass of the generic  $i$ -th floor is provided by (Eq. (10.19)).

$$T_i = 2\pi \sqrt{\frac{m_i}{k_i}} \quad \text{Eq. (10.19)}$$

If all the storeys shall behave in a similar way (i.e. with the same displacement), it is necessary to impose them to have the same vibration period. Since the seismic mass of each floor is given, the different stiffness of the SSCD could be easily evaluated (Table 10.10).

**Table 10.10: Stiffness of the different SSCD in relation to the results of linear dynamic analysis.**

Storey	$z_i$ [m]	$m_i$ [kN]	$k_{el}$ SSCD
P1	4,50	15449,74	144,66
P2	9,00	13590,34	144,66
P3	13,50	14214,94	144,66
P4	18,00	2420,58	48,02

In the present case, considering that the seismic masses of the first three levels are about the same, the same SSCD devices are adopted for levels P1, P2 and P3, while different systems are only used for P4.

With the values of stiffness presented in Table 10.10 the modal deformed shape presented in Fig. 10.25 was obtained, very close to the desired “vertical configuration” (Fig. 10.24). Table 10.11 shows the results of linear modal analysis in the final selected configuration.

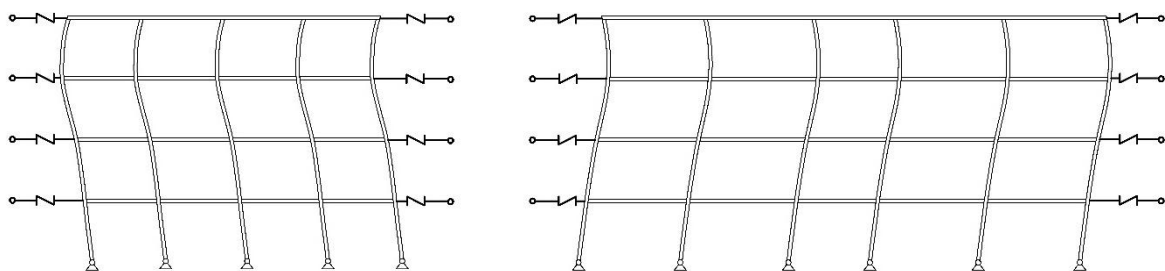


Fig. 10.25: Modal deformed shape corresponding to first modes in Y and X directions.

**Table 10.11: Modal analysis results.**

Mod	Period	% Mass	% Mass	% Mass	% Resulting	% Resulting
1	0,31512	0,00	81,36	0,00	0,00	81,36
2	0,31385	84,10	0,00	0,00	84,10	81,36
3	0,28409	0,00	17,47	0,00	84,10	98,82
4	0,27696	15,59	0,00	0,00	99,69	98,82

The actions on the SSCD during the elastic phase can be estimated considering seismic action for Damage Limitation limit state (DL), allowing to evaluate the maximum expected displacement for each one of the SSCD; base actions in the R.C. walls can be determined and compared to the ones initially considered, with the eventual optimization of the element's thickness.

The final design of SSCD can be then executed through the determination of the transversal area of the dissipative elements, previously neglected, directly influencing  $\beta$  parameter, the global dissipated energy and the shape of the F/D curve. The main characteristics of the designed SSCD applied to different levels are summarized in Table 10.12, and Table 10.14; and Fig. 10.26 shows the corresponding flag-shaped curves.

**Table 10.12: Geometrical and mechanical properties of pre-tensioned cables.**

Pre-tensioned cables		P1, P2, P3		P4	
Number of elements	n	2		2	
Diameter	$\phi$	22 mm		12 mm	
Transversal area	$A_{PTE}$	380,13 mm <sup>2</sup>		113,10 mm <sup>2</sup>	
Global transversal	$A_{PTE,tot}$	760,27 mm <sup>2</sup>		226,19 mm <sup>2</sup>	
Yielding strength	$f_{y,PTE}$	1670,00 N/mm <sup>2</sup>		1670,00 N/mm <sup>2</sup>	
Pre-tension	$\rho_{PTE}=f_{PTE}/f_{y,PTE}$	0,50		0,50	
Pre-tension strength	$f_{PTE}$	835,00 N/mm <sup>2</sup>		835,00 N/mm <sup>2</sup>	
Pre-tension force	$F_{PTE}$	634,82 kN		188,87 kN	
Length	$L_{PTE}$	3500 mm		3500 mm	
Elastic modulus	$E_{PTE}$	196000 N/mm <sup>2</sup>		196000 N/mm <sup>2</sup>	
Maximum elongation	$d_{PTE}$	14,91 mm		14,91 mm	

**Table 10.13: Geometrical and mechanical properties of dissipative elements.**

Dissipative Elements (Steel Grade BO40)			
		P1, P2, P3	P4
Number of elements	n	4	4
Transversal area	$A_{ED}$	120 mm	80 mm <sup>2</sup>
Global transversal area	$A_{ED,}$	480 mm	320 mm <sup>2</sup>
Yielding strength	$f_{y,ED}$	240 N/m	240 N/m
Yielding force	$F_{y,E}$	115 kN	76, kN
Ultimate elongation	$A_{gt,}$	24, %	24, %
Length of reduce	$L_{ED}$	170 mm	170 mm

**Table 10.14: Parameters of SSCD for levels P1, P2 and P3.**

Flag shaped F/D curve			
Parameters	P1, P2, P3		P4
$k_{el}$	144,658	kN/mm	48,237 kN/mm
$k_{pe}$	28,886	kN/mm	9,588 kN/mm
$F_y$	634,822	kN	188,873 kN
$d_y$	4,388	mm	3,9155 mm
$F_u$	938,765	kN	294,295 kN
$d_u$	14,911	mm	14,911 mm
$\alpha = k_{pe}/k_{el} =$	<b>0,200</b>		<b>0,199</b>
$\beta = F_{y,ED}/F_{PTE}$	<b>0,181</b>		<b>0,407</b>

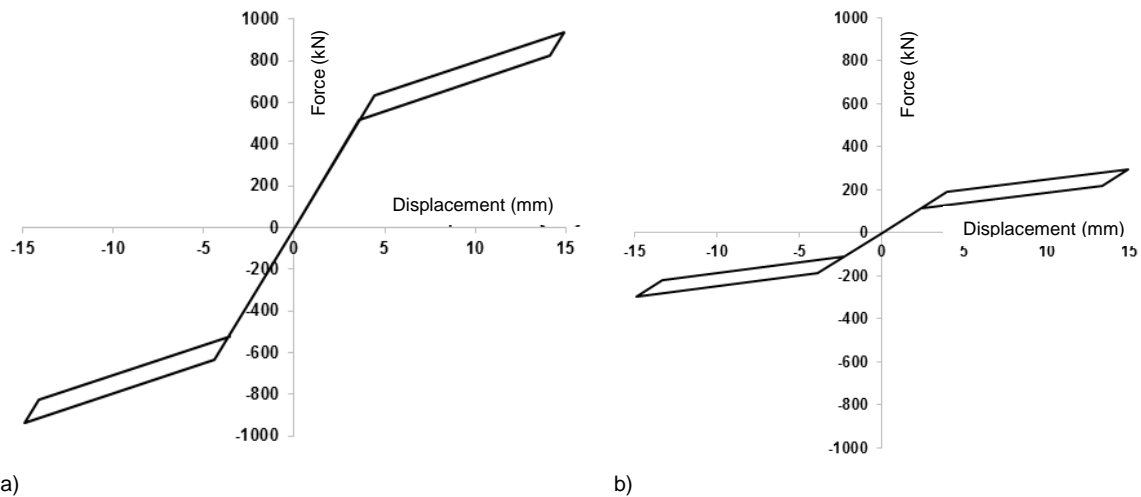


Fig. 10.26: Flag-shaped curves for SSCD of levels: a) P1, P2 and P3; b) P4.

In order to introduce the SSCD in the numerical model of the building, link elements with a specific flag-shaped constitutive relationship have been used.

The SSCD model is simulated by two different elements working in parallel (Fig. 10.27): the first one characterized by a “*multilinear elastic*” relationship defining the first two branches of the curve with stiffness equal to  $k_{el}$  and  $k_{pe}$ , yielding force  $F_y$  and maximum displacement  $d_u$  (Fig. 10.28a), the second one defined as “*plastic*”



characterizes the hysteretic cycles of dissipative elements through the parameter  $k_{DE}$  and the corresponding  $F_{yDE}$  (Fig. 10.28b).

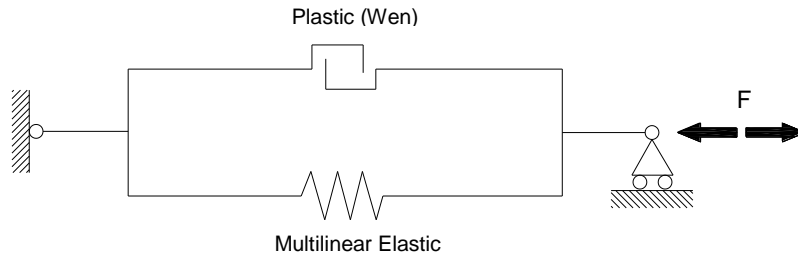


Fig. 10.27: Simplified model of the SSCD with two NL Link elements in parallel.

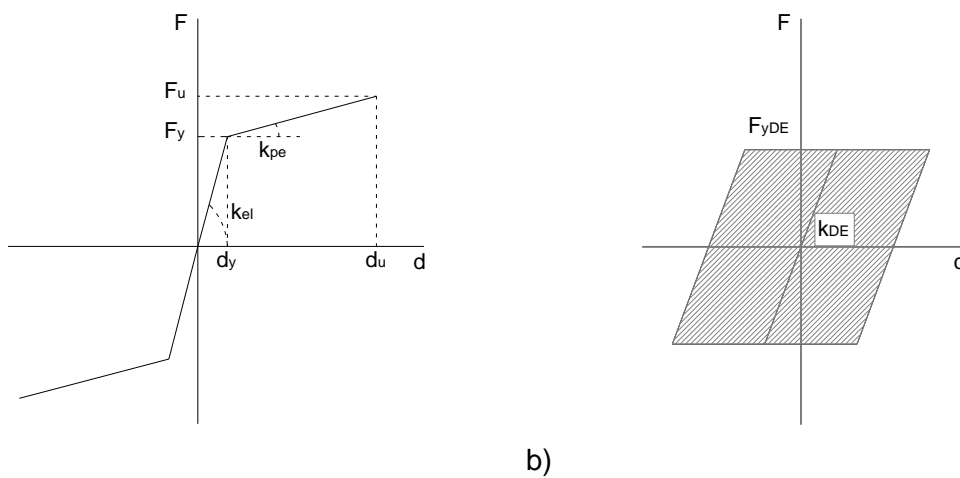


Fig. 10.28: a) Multilinear Elastic and b) Plastic constitutive laws.

#### 10.4.3.2 Nonlinear model and nonlinear dynamic analyses

Nonlinear dynamic analyses have been further executed to deeply investigate the structural behaviour of the building in the post-elastic domain. Incremental dynamic analyses (IDA) have been made according to the procedure proposed by Vamvatsikos and Cornell, based on the steps listed below:

1. determination of the unscaled accelerograms to be used:  $a_1(ti)$ ;
2. determination of the Scale Factor (SF) to be applied to the accelerogram:  
 $a_\lambda = \lambda a_1$ ;
3. determination of the Intensity Measure (IM), function of the unscaled accelerogram that monotonically increases with the scale factor  $\lambda$  (i.e. the PGA – peak ground acceleration, the Spectral Acceleration corresponding to the first period and so on);
4. determination of the Damage Measure (DM), parameter characterizing the structural response of the building during seismic events (for example the maximum base shear  $V_b$ , the maximum inter-storey drift, and so on);
5. determination of the IDA Curve, that is a graphical representation of the DM towards the parameter IM considered for the selected accelerogram.

In the present case, the PGA is selected as IM parameter.

Two DM are adopted: the maximum inter-storey drift  $d_{max}$  and the maximum displacement of the SSCD systems  $d_{dmax}$ . The reaching of the Damage Limitation limit state (DL) is associated to the achievement of the maximum inter-storey drift according to D.M. 14/01/2008 to guarantee the effective use of the building (Eq. (10.20)):

$$d_r \leq 0,01 h \quad \text{Eq. (10.20)}$$

being  $h$  the inter-storey heights. In this case, the relationship shifted into Eq. (10.21):

$$d_r \leq 45 \text{ mm} \quad \text{Eq. (10.21)}$$

The Life Safety limit state (LS) is associated to axial deformation of the SSCD systems higher than the maximum allowed elongation, corresponding to the yielding condition of pre-tensioned cables and the loss of re-centering capability. This limit could be imposed equal to (Eq. (10.22)):

$$d_{SSCD} \leq 14,91 \text{ mm} \quad \text{Eq. (10.22)}$$

It's necessary to highlight that such limitation does not perfectly correspond to the reaching of an "ultimate" collapse limit state, since, from a static point of view, the SSCDs are still able to provide to the structure with sufficient residual strength towards collapse. The problem mainly consists in the loss of the re-centering capability (a reduced dissipative capacity remains). Besides, the LS condition is not simultaneously reached by all the SSCD systems, with the subsequent loss of efficacy in only some of them.

Seven accelerograms have been used for the execution of IDA. The considered IM has been scaled considering different SF for the different accelerograms up to 0.40g (Table 10.15).

**Table 10.15: Scale factors adopted for the different accelerograms.**

Seismic	PGA <sub>ma</sub>	0,05	0,10	0,15	0,20	0,25	0,30	0,35	0,40
0520ME	0,2591	0,193	0,386	0,579	0,772	0,965	1,158	1,35	1,54
0529ME	0,2672	0,187	0,374	0,561	0,749	0,936	1,123	1,31	1,49
SPC1	0,3127	0,160	0,320	0,480	0,640	0,799	0,959	1,11	1,27
SPC2	0,2508	0,199	0,399	0,598	0,797	0,997	1,196	1,39	1,59
SPC3	0,2855	0,175	0,350	0,525	0,701	0,876	1,051	1,22	1,40
SPC4	0,3374	0,148	0,296	0,445	0,593	0,741	0,889	1,03	1,18
SPC5	0,2507	0,199	0,399	0,598	0,798	0,997	1,197	1,39	1,59

Fig. 10.29 and Fig. 10.30 represent the summary of the results of IDA executed adopting the 7 different accelerograms. Analysing the results coming from the IDAs, it is evident that the maximum elongation of dissipative devices ( $d_{dmax}$ ) is strongly influenced by the considered accelerograms: up to IM equal to 0.15g a similar behaviour is visible, while increasing levels of IM corresponded to increasing difference in the obtained results. Similar considerations can be executed also for the maximum inter-storey drift ( $d_{rmax}$ ), related to DL. To partially reduce this effects, the average results of the seven accelerograms, according to what is foreseen by D.M.14/01/2008, was considered. Average values of DM evidence the ability of the designed structure to highly satisfy the requirement imposed for DL for PGA up to 0.30g, while in the case of LS the maximum PGA is within the range 0.25g (satisfaction) and 0.30g (overcoming of LS limitation).

Residual displacements have been also evaluated to test the efficacy of the model (Table 10.16): residual displacements have resulted lower than 2% of the maximum exhibited inter-storey displacements, value that can be considered allowable to guarantee the re-centering capability of the system. As visible from Fig. 10.30, P1, P2 and P4 levels presented similar behaviour for increasing levels of PGA while P3 is characterized by higher displacement. The yielding limit of the four curves is, more or less, the same and within the range [0.10g; 0.15g], defining a quite regular behaviour of the building.

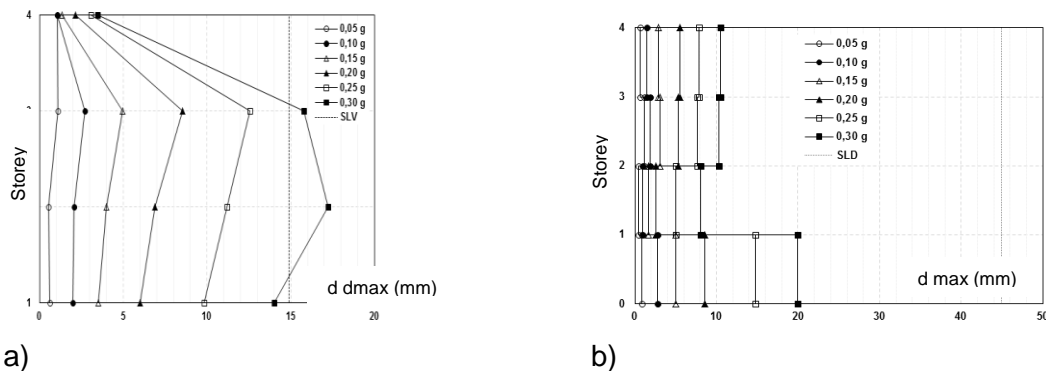


Fig. 10.29: Average results of 7 inputs: a) max displacement of SSCD (LS) and b) max inter-storey displacement (DL) .

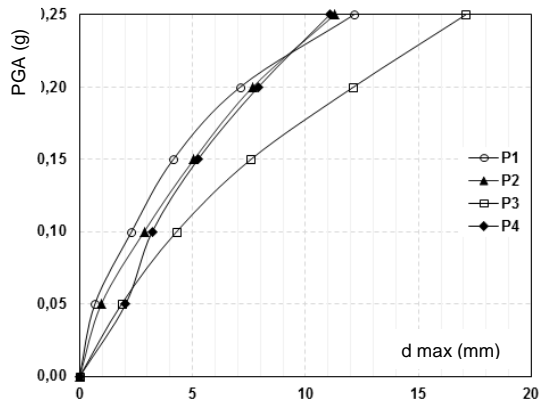


Fig. 10.30: Result of IDA in terms of displacement of different storeys towards PGA (average of 7 accelerograms).

**Table 10.16: Residual average displacements for the building (PGA equal to 0.25g).**

storey	$d_r$ [mm]	$d_{max}$ [mm]	$d_r$ [%]
P1	0,08	14,79	0,55
P2	0,09	5,03	1,89
P3	0,08	7,65	1,02
P4	0,16	7,90	2,07

The execution of safety checks for all the structural elements constituting the building, according to what is foreseen by actual standard and in correspondence of PGA equal to 0.25g for LS, has led to several modifications in the profiles of elements, according to what briefly summarized in Table 10.17 for steel sections. No changes have been otherwise required for the dimensions and the reinforcement of R.C. walls.

**Table 10.17: Modification needed for steel profiles according to the results of nonlinear analyses.**

Element	Preliminary profile	Modification	Reason
Inter-storey steel beams	HEB280	HEA340	Flexural behaviour
Roof steel beams	HEB160	HEB180	Flexural behaviour
Column	HEB220	HEB240	Buckling

#### 10.4.4 Optimization of proposed solution

Results of nonlinear analyses globally evidenced that the structural behaviour of the system is mainly influenced by the maximum elongation of SSCD, directly characterizing the achievement of LS, while inter-storey displacement, related to the satisfaction of DL condition, are usually well below the imposed limitation and do not represent a limit for the determination of the effective capacity of the system.

The modification of SSCD can be then executed in order to increase the structural capacity of the building for the satisfaction of LS limitation for IM higher than 0.25g,

directly acting on different parameters. The following possibilities have been taken into consideration.

#### 10.4.4.1 Case 1 - Increase of SSCD length

Several modifications have been introduced and tested modifying the SSCD length, finally adopting a 5.30 m external length device and 5.10 m long pre-tensioned cables, as opposed to the initial one equal to 3.50 m (resulted from experimental tests on the SSCD prototype) (Fig. 10.31). As a result (Fig. 10.32), the increase of the SSCD length do not significantly affect the behaviour of the structure, since the maximum allowable PGA remains equal to 0.25g. This is mainly due to the fact that the increase of the length is related to the decrease of the linear stiffness (Fig. 10.31).

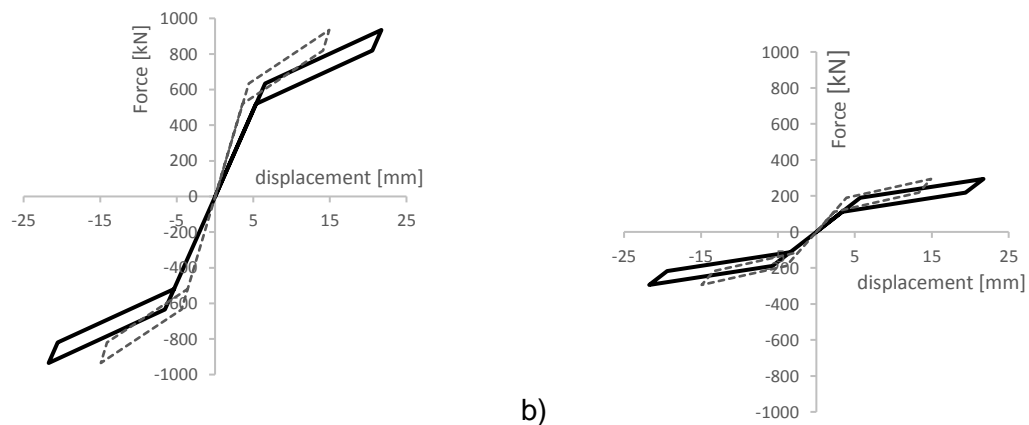


Fig. 10.31: First modification (SSCD length): modified flag-shaped curves for a) levels P1, P2 and P3, b) P4.

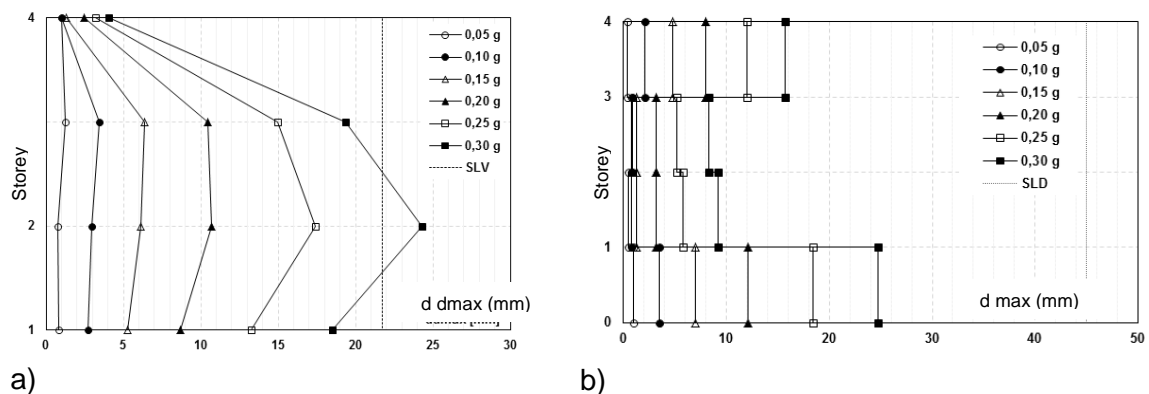


Fig. 10.32: Average results of IDA for a) maximum displacement of SSCD (LS) and b) inter-storey displacement (DL)

#### 10.4.4.2 Case 2 - Increase of pre-tensioned cables diameter

The second possibility consists in the modification of pre-tensioned cables diameter increasing them by 4.0 mm; the global length of the SSCD is, also in this case, increased with respect to the initial one up to 5.30 m. Since the diameter does not affect this parameter, the target LS displacement remains equal to 21.93 mm. The

modification of the cables diameter directly influences the yielding and ultimate forces, as well as the stiffness of both the elastic and post-elastic branches of the flag-shaped curve (Fig. 10.33).

As visible, the coupling of the modifications of SSCD length and cables diameter is able to increase the effective structural capacity of the system, with maximum allowable PGA equal to 0.30 g without the overcoming of LS. No modifications at DL can be observed.

The comparison between the 1<sup>st</sup> and the 2<sup>nd</sup> floors does not evidence significant differences for IM lower or equal to 0.15g: this means that below 0.15g the influence of pre-tensioned cable is not relevant. Increasing the PGA, the influence of cables becomes higher mostly on the post-elastic behaviour of SSCDs.

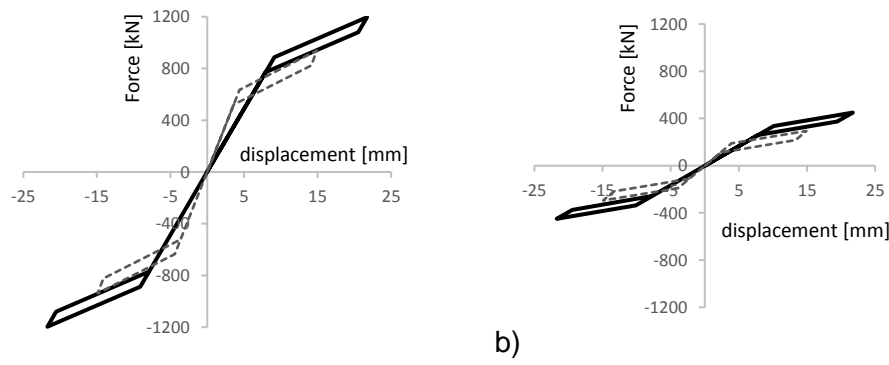


Fig. 10.33: 2<sup>nd</sup> modification (SSCD length and cables' diameter): flag-shaped curves for a) levels P1, P2 and P3, b) P4.

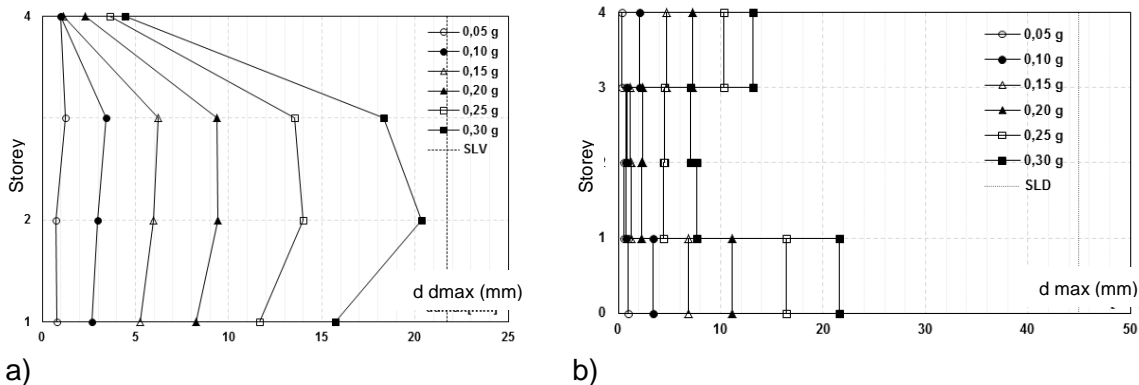


Fig. 10.34: Average results of IDA for a) maximum displacement of SSCD (LS) and b) inter-storey displacement (DL) – case 2.

#### 10.4.4.3 Case 3 - Increase of dissipative elements - $\beta=0,50$

The global capacity of the structure can be also increased enlarging the dissipative capacity of the SSCD devices. For the moment, the  $\beta$  coefficients that characterize the flag-shaped curves obtained are respectively equal to 0.18 for P1, P2 and P3 and to 0.40 for P4.

In this third case, to evaluate the efficacy of that parameter, the initial length of the SSCD (3.50 m) is adopted, increasing the dimension of dissipative elements up to achieve  $\beta=0.50$ , without modifying the other characteristics (Fig. 10.35).

As evidenced by Fig. 10.36, this solution has relevant efficacy, with maximum allowed PGA at LS equal to 0.35g and about 50% reduction of the maximum inter-storey displacement. Since the stiffness of the SSCD is not modified, inter-storey displacements are reduced, moreover the lower size of the device allows lower costs and more easiness in the assembly.

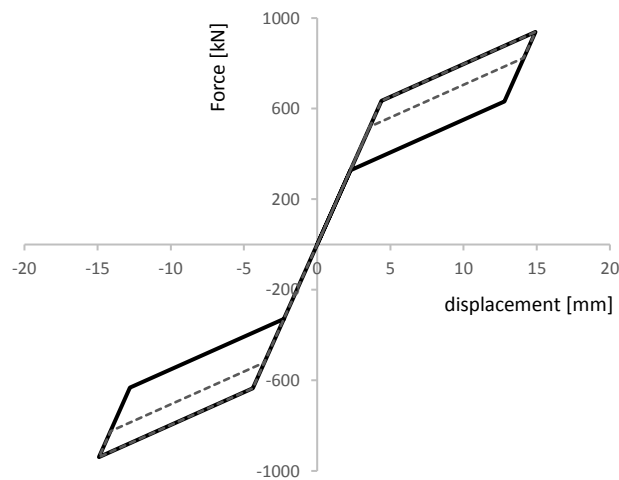


Fig. 10.35: 3<sup>rd</sup> modification ( $\beta=0.50$ ): flag-shaped curves for levels P1, P2 and P3.

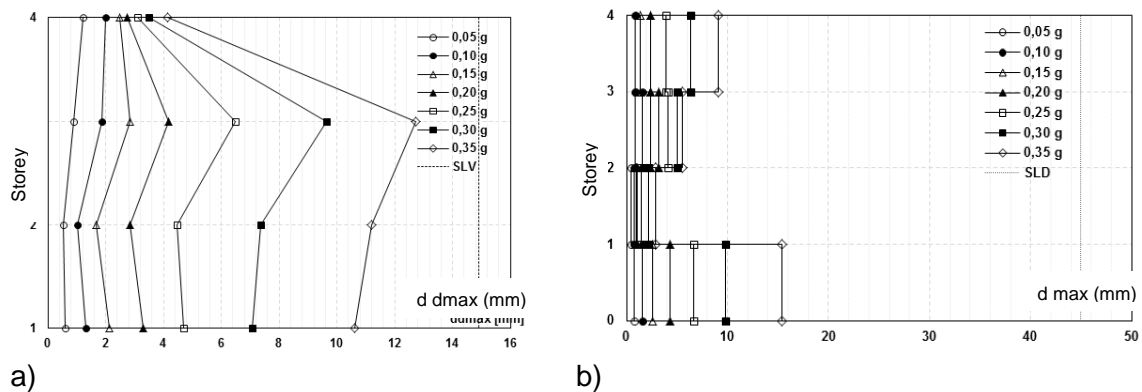


Fig. 10.36: Average results of IDA for a) maximum displacement of SSCD (LS) and b) inter-storey displacement (DL) – case 3.

#### 10.4.4.4 Case 4 - Increase of dissipative elements - $\beta=1,25$

The increase of  $\beta$  coefficient over 0.90 leads, according to experimental test results, to the loss of the typical flag-shaped behaviour of dissipative elements: as visible from Fig. 10.37, and also residual displacements in this case are relevant. The most evident result of IDA is that the increase of the dissipative elements section reduces the global capacity of the building, with maximum allowable PGA equal to 0.30g (Fig. 10.38): this means that, over a certain limit, the increase of the size of dissipative elements is not useful to improve the structural performance of the building.

The SSCD devices of P4 reach the higher elongations (in all the other considered cases, the P4 SSCD devices are the less affected by the variation of the parameters): this is responsible for the decrease of the global capacity at LS. This aspect is evidenced by the capacity curve of the different levels (Fig. 10.39): despite that the curve relative to P4 shows yielding at PGA equal to 0.10g, the curves for the other three levels exhibit a more or less linear behaviour. This means that the building reaches its maximum limit at level P4 with the other SSCD in the elastic range.

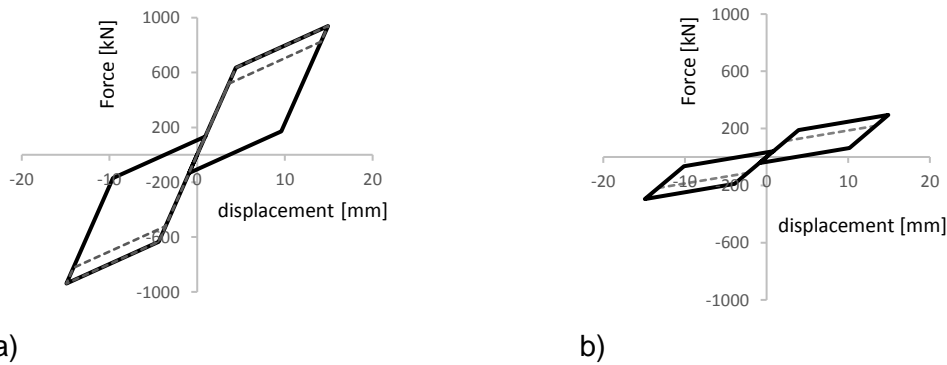


Fig. 10.37: 5<sup>th</sup> modification ( $\beta=1.25$ ): flag-shaped curves for levels a) P1, P2 and P3, b) P4.

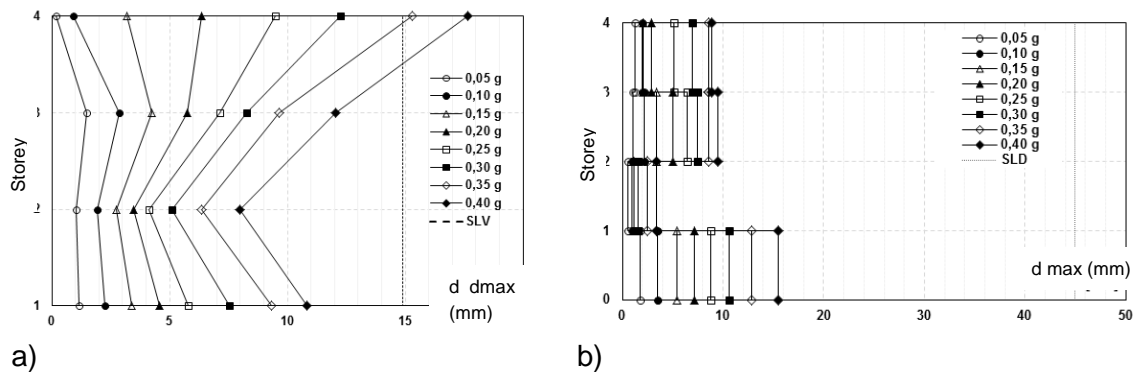


Fig. 10.38: Average results of IDA for a) maximum displacement of SSCD (LS) and b) inter-storey displacement (DL) – case 5.

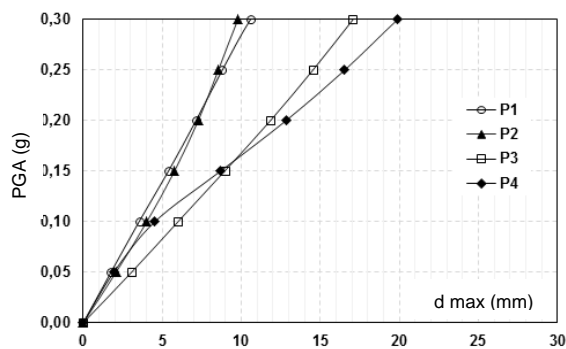


Fig. 10.39: Capacity curves for the different storeys – case 5.



Residual displacements have been finally evaluated: for  $\beta$  values higher than 1.0, the SSCD loss the re-centering capacity, leaving the building exposed to residual displacements. Their average values for PGA equal to 0.30g are summarized in Table 10.18.

**Table 10.18: Average residual values of the steel structure for PGA=0.30g.**

storey #	$\beta=1.25$			$\beta=2.00$		
	$d_r$ [mm]	$d_{rmax}$ [mm]	$d_r$ [%]	$d_r$ [mm]	$d_{rmax}$	$d_r$ [%]
P1	0,54	10,56	5,08	0,64	11,75	5,48
P2	0,40	1,54	25,85	0,76	1,61	47,26
P3	0,59	7,45	7,98	0,75	8,06	9,36
P4	0,24	6,93	3,41	0,37	9,53	3,87

Similar conclusions can be made in the case of  $\beta$  coefficient equal to 2.0, once again with the increase of the size of dissipative elements and the loss of flag-shaped behaviour.

## 10.5 CONCLUSIONS

The proposed SSCD system has been used for the design of a commercial hybrid R.C./steel commercial building. The design procedure, as widely presented, is iterative and includes both linear and nonlinear analyses.

The “original” prototype of the system, with mechanical and geometrical properties described in Braconi et al., allowed to design the building for seismic action with maximum PGA equal to 0.25g, in agreement with the requirements of actual standards for both the DL and LS and providing a good re-centering capacity, with very limited residual displacements.

The modification of parameters such as the length of the device, the diameter of the cables and the size of the dissipative elements of the SSCD allows to improve the structural performance of the building, as widely demonstrated.

The optimization of the system can be achieved through the application of parametric investigations aiming to determine the characteristics values of SSCD systems – mainly the length of pre-tensioned cables and the transversal area of dissipative elements – to be used in relation to the effective requirements of the building.

The horizontal location of the SSCD (as connection between R.C. walls and steel frames) allows the direct control of the structural behaviour of the building and the possibility to optimize the modal deformed shape in order to have, such as in the considered case, equal displacements in correspondence of all the storeys.

The comparison between the numerical results of the analyses and the data coming from the experimental tests evidence that the simplifications adopted in the model (such as, for example the neglecting of friction and of dissipative elements in the

determination of equivalent stiffness) leads to an error that mainly influences the quantity of dissipated energy. On the other hand, very low differences between analysis and experimental tests have been revealed for what concerns the estimation of residual displacements.

The most significant limit of the SSCD system is related to the reduced displacement capacity, able to sustain maximum 25 mm. The quantity of dissipated energy is related to the displacements and to the forces acting on the device: the displacement can be increased with the increase of the dimension of pre-tensioned cables or with the length of the device – the last one difficult to be applied. The dissipative capacity of the SSCD can be increased with higher size of the dissipative elements, keeping the  $\beta$  coefficient lower than 0.90.

It's moreover necessary to underline that the absence of specific standards determining the parameters needed for the characterization of the dissipative devices does not allow to directly compare the behaviour of a “traditional” system with the one of a building with dissipative protection system. The SSCD proposed device has been designed and checked considering both the static and the seismic condition, but the effective determination of performance levels according to IO, DL, LS and CP is not clear, as well as the definition of the effective behaviour factor  $q$ , assumed in the present case equal to 1.0.

## 10.6 FIELD OF APPLICATION

The Steel Self-Centering Device may be applied both to existing and new buildings. It is particularly fitted to be incorporated in steel or concrete frames.

## 10.7 PUBLICATIONS

Publications in international journals

1. Braconi A, Morelli F, Salvatore W (2012) *Seismic protection of structures through an innovative steel-based self-centering hysteretic device: numeric analysis and test*. In: Proceedings of the 15<sup>th</sup> world conference on earthquake engineering, Lisbon, Portugal, September 24–28.
2. Braconi A., Morelli F., Salvatore W. *Development, design and experimental validation of a steel self centering device (SSCD) for seismic protection of buildings*. Bulletin of Earthquake Engineering 10 (6), 1915-1941, 2012.
3. F. Morelli, A. Piscini, W. Salvatore, *Seismic retrofit of an industrial structure through an innovative self-centering hysteretic device: modelling, analysis, optimization*, Proceedings of the VII European Congress on Computational Methods in Applied Sciences and Engineering, ECCOMAS Congress 2016, Crete Island, Greece, 5–10 June 2016.
4. F. Morelli, A. Piscini, W. Salvatore, *Seismic behavior of an industrial steel structure retrofitted with self-centering hysteretic dampers*. Under preparation

## 10.8 BIBLIOGRAPHIC REFERENCES

- [1] Alderighi E, Bayo E, Bianco L, Braconi A, Coscetti C, Dall'Asta A, Filippuzzi P, Fulop L, Gracia J, Hoffmeister Hradil PB, Karamanos S, Leoni G, Mallardo R, Moller S, Osta A, Salvatore W, Tsintzos P, Varelis G, Vasilikis D (2010) *PREfabriCated STEEL structures for low-rise buildings in seismic areas*. RFSR-CT-2007-00038 project. Final report, European Commission, Brussels.

- 
- [2] Banushi G. Un modello semianalitico del comportamento meccanico di un dissipatore autocentrante per la protezione sismica delle strutture, Tesi di Laurea, Facoltà di Ingegneria, Università di Pisa, 2010.
- [3] Braconi A, Morelli F, Salvatore W (2012) *Seismic protection of structures through an innovative steel-based self-centering hysteretic device: numeric analysis and test*. In: Proceedings of the 15<sup>th</sup> world conference on earthquake engineering, Lisbon, Portugal, September 24–28.
- [4] Braconi A., Morelli F., Salvatore W. *Development, design and experimental validation of a steel self centering device (SSCD) for seismic protection of buildings*. Bulletin of Earthquake Engineering 10 (6), 1915-1941, 2012.
- [5] Christopoulos C, Filiatrault A, Folz B, Uang C-M (2002a) *Post-tensioned energy dissipating connections for moment-resisting steel frames*. ASCE J Struct Eng 128(9):1111–1120.
- [6] Christopoulos C, Filiatrault A, Folz B (2002b) *Seismic response of self-centering hysteretic SDOF systems*. Earthq Eng Struct Dyn 31(5):1131–1150.
- [7] Christopoulos C, Filiatrault A (2006) *Principles of supplemental damping and seismic isolation*. IUSS Press, Pavia.
- [8] Christopoulos C, Tremblay R, Kim HJ, Lacerte M (2008a) *Self-centering energy dissipative bracing system for the seismic resistance of structures: development and validation*. J Struct Eng 134(1): 96–107.
- [9] Christopoulos C, Choi H, Eronchko J (2008b) *Comparison of the seismic response of steel buildings incorporating self-centering energy dissipative braces, buckling restrained braces and moment resisting frames*.
- [10] Cormack LG (1988) *The design and construction of the major bridges on the mangaweka rail deviation*. Transaction of the Institute of Professional Engineers of New Zealand, vol 15. I/CE, pp 16–23.
- [11] Desroches R, Smith B (2004) *Shape memory alloy in seismic resistant design and retrofit: a critical review of their potential and limitations*. J Earthq Eng 8 (3):1–15.
- [12] EN1998-1:2005 - *Eurocode 8 –Design of structures for earthquake resistance, Part 1: General Rules, seismic action and rules for buildings*.
- [13] Filiatrault A, Tremblay R, Kar R (2000) *Performance evaluation of friction spring seismic damper*. ASCE J Struct Eng 126:491–499.
- [14] NTC (2008) Norme tecniche per le Costruzioni. Gazzetta Ufficiale n. 29, February 4, 2008, Suppl. Ordinario n.30, Italy (in Italian).
- [15] Priestley MJN, Sritharan S, Conley JR, Pampanin S (1999) *Preliminary results and conclusions from the PRESSS five-storey precast concrete test building*. PCI J 44(6):42–47.
- [16] Uang C.M., Bertero V.V. (1990) - *Evaluation of seismic energy in structures*, Earthquake Engineering & Structural Dynamics 19 (2), 77-90.
- [17] Vamvatsikos D., Cornell C.A. *Incremental dynamic analysis*, Earthquake Engineering and Structural Dynamics 31, 491-514, 2002-.



## 11 TRIANGLE STEEL HYSTERETIC DEVICE (TRSH)

### 11.1 INTRODUCTION

Within a joint research project “RISK MITIGATION FOR EARTHQUAKES AND LANDSLIDES” (acronym LESSLOSS, ID GOCE-CT-2003-505448) of the 6<sup>th</sup> framework European Research Program TRIangular Steel Hysteretic (TRSH) devices as complementary dissipative element in base-isolation systems were developed and tested with regard to their applicability [1, 2]. The research activities belonged to sub-project 6 “Development and manufacturing of energy dissipation devices and seismic isolators”.

Current report presents the results of the investigations on the seismic performance of TRSH devices and proposes a design procedure for steel and composite buildings, in which the TRSH device is used in hysteretic bracing systems.

### 11.2 DESCRIPTION OF THE TRIANGULAR STEEL HYSTERETIC BRACING SYSTEM

Steel Hysteretic Devices (SHD) represent an effective solution to increase the capability of structures to dissipate seismic energy. Among SHD devices, the TRIangular Steel Hysteretic (TRSH) device (see Fig. 11.1) is an effective element for the implementation into a structural bracing system, e.g.:

- the bending curvature produced by a transverse force applied at the end of the triangular plate is uniform over the full height of the plate (see Fig. 11.2),
- it can undergoes large inelastic deformations without curvature concentrations (see Fig. 11.2).

Fig. 11.3 illustrates two possible layout of the TRSH system: single element (left) or in series (right) with a coupling group connection.



Fig. 11.1: TRSH element with a half-moon head [1]

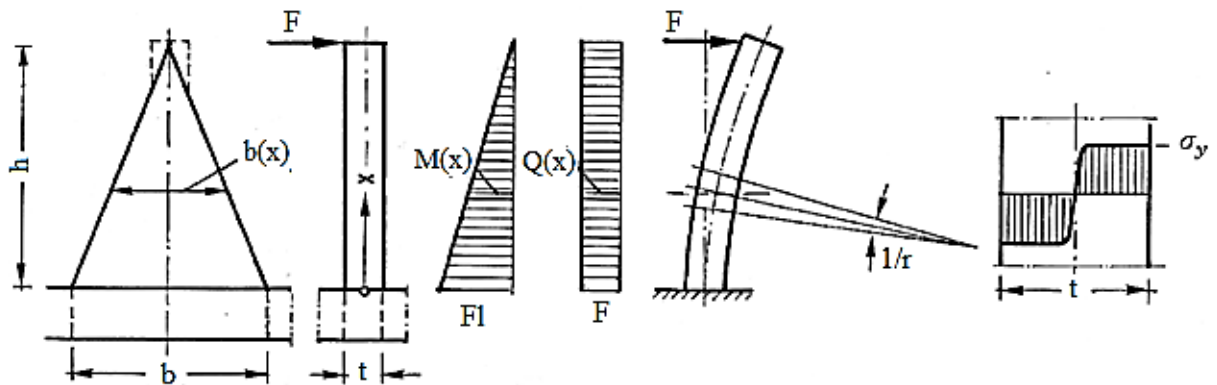


Fig. 11.2: Geometrical parameters and mechanical behavior of a TRSH element [1]

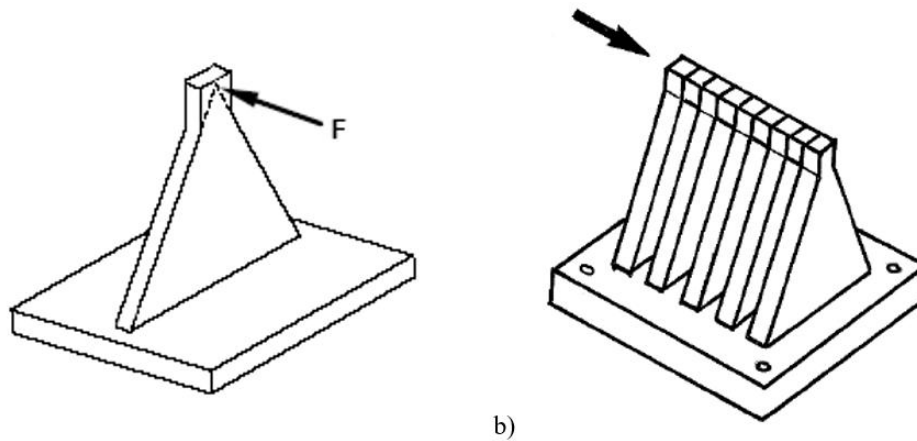


Fig. 11.3: TRSH element: a) single one, b) series connection [1]

The operational principle of a bracing system implementing TRSH devices and its qualitative kinematics are represented in Fig. 11.4. A possible layout of the connection of braces with a beam by means of a TRSH is shown in Fig. 11.5 and Fig. 11.6. The triangular plates dissipate seismic energy related to the horizontal components of the seismic action while the transmission of the braces vertical components is entrusted to a sliding guide.

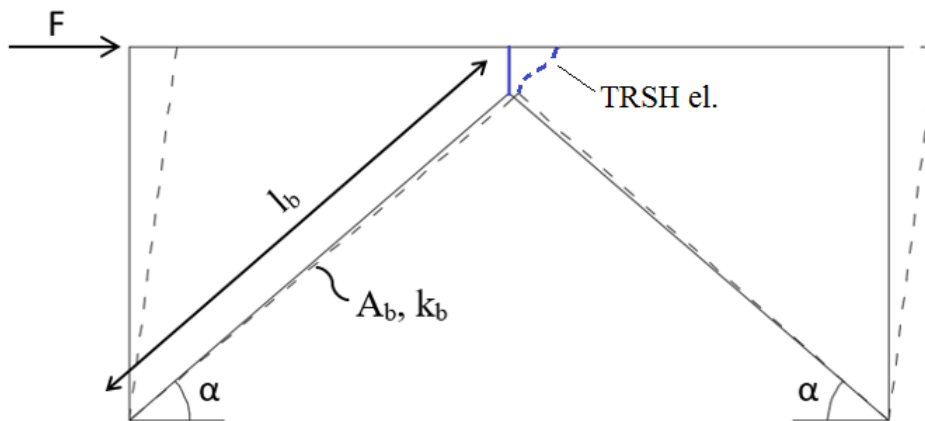


Fig. 11.4: Operational principle and qualitative kinematics of a TRSH bracing system

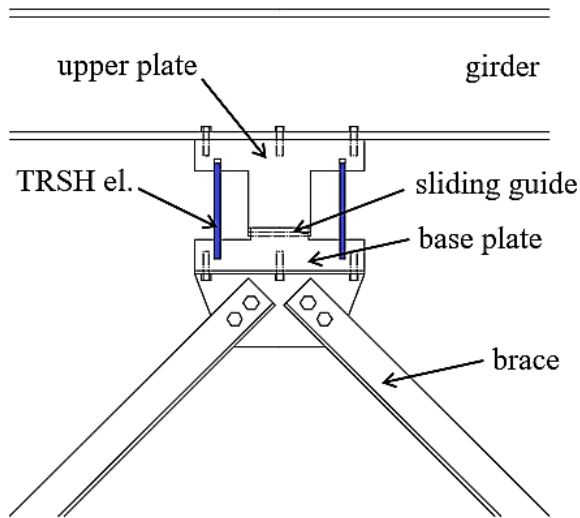


Fig. 11.5: Main components of a TRSH bracing system – side view

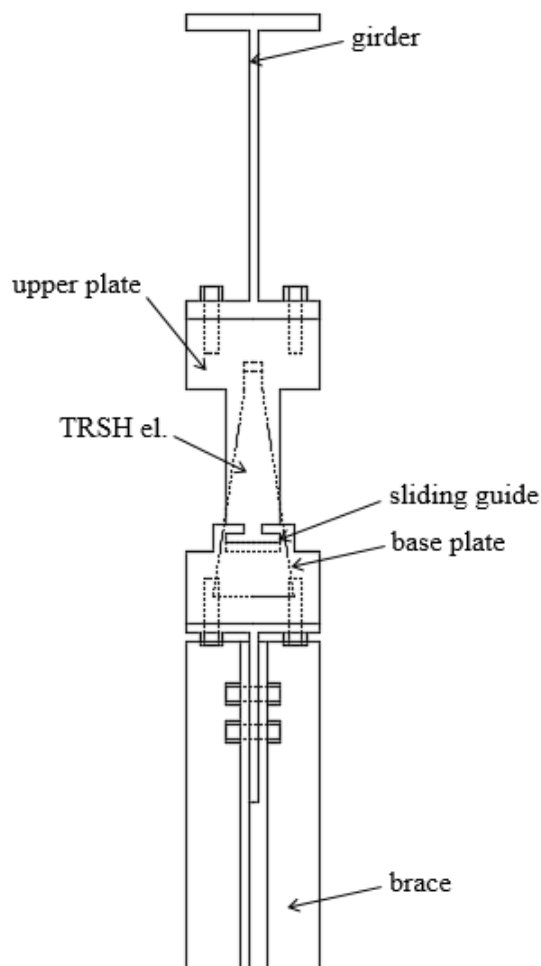


Fig. 11.6: Main components of a TRSH bracing system – section view

First numerical and experimental investigations related to the seismic response of structures implementing TRSH devices are dated back to the early 90's [3-8].

According to these studies, the elastic lateral stiffness  $k_{el,t}$ , the elastic curvature  $\chi_{el,t}$  (constant), the yielding force  $F_{y,t}$ , the ultimate strength  $F_{u,t}$ , and the yield displacement  $\Delta_{y,t}$  of a TRSH device can be calculated as follow [6]:

$$k_{el,t} = \frac{nEbt^3}{6h^3} \quad \text{Eq. (11.1)}$$

$$\chi_{el,t} = \frac{12Fh}{Ebt^3} \quad \text{Eq. (11.2)}$$

$$F_{y,t} = \frac{n\sigma_y bt^2}{6h} \quad \text{Eq. (11.3)}$$

$$F_{u,t} = \frac{n\sigma_y bt^2}{4h} \quad \text{Eq. (11.4)}$$

$$\Delta_{y,t} = \frac{F_{y,t}}{K_{el,t}} = \frac{\sigma_y h^2}{Et} \quad \text{Eq. (11.5)}$$

where  $b$ ,  $h$ , and  $t$  are the geometrical parameters represented in Fig. 11.2,  $n$ ,  $E$ , and  $\sigma_y$  are respectively the number, the elastic modulus and the yielding stress of TRSH steel.

It could be demonstrated that the overall elastic lateral stiffness  $k_{el,T+B}$  of a bracing system implementing the TRSH device is:

$$k_{el,t+b} = \frac{k_{el,t} \cdot k_{el,b}}{k_{el,t} + k_{el,b}} \quad \text{Eq. (11.6)}$$

where  $k_{el,b} = 2(EA_b/l_b) \cos^2 \alpha$  is the lateral stiffness of the braces without the dissipative elements.

### 11.3 ANALYTICAL MODEL

#### 11.3.1 Bilinear approximation of the force-displacement loop

For design purposes, the curved force-displacement loops are usually approximated by a bilinear hysteresis loops with an initial stiffness  $k_1$ , a yielded stiffness  $k_2$  and a yield force  $F_y$ . The method adopted hereafter for the bilinear approximation to a hysteresis loops is shown Fig. 11.7.



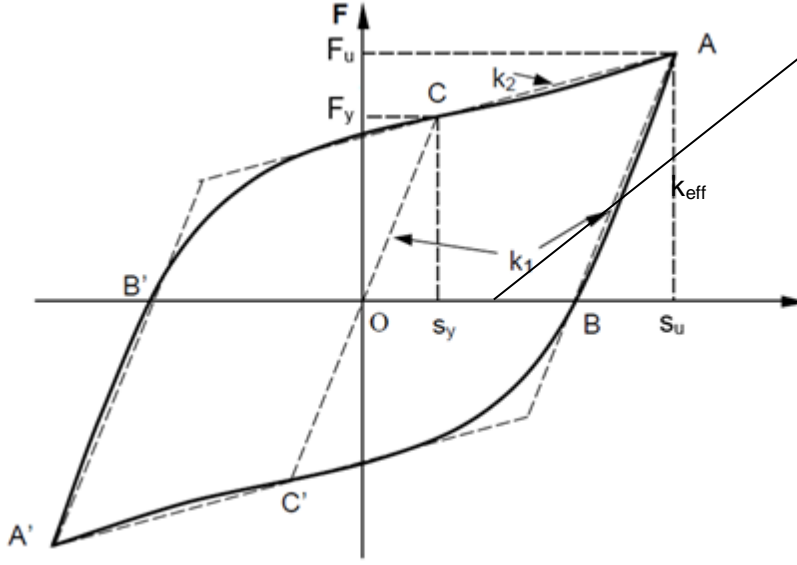


Fig. 11.7: Bilinear approximation to the hysteresis loop

The curved loop  $A'B'CABC'A'$  is not symmetric about the center  $O$ , and the coordinates of vertices  $A$  and  $A'$  are the maximum displacements  $\pm s_u$  and the maximum force  $\pm F_u$ .

The initial stiffness  $K_1$  is approximated by the slope of the parallel lines  $AB$  and  $A'B'$  where  $B$  and  $B'$  are the loop intercepts on the  $x$ -axis.

The yield stiffnesses  $K_2^+$  and  $K_2^-$  are approximated by the slope of the lines  $AC$  and  $A'C'$  where  $CC'$  is the line through  $O$  with slope  $K_1$ .

The coordinates of point  $C$  ( $s_y, F_y$ ) are the yield displacement and the yield force respectively for the approximation to the curved hysteresis loop.

The bilinear loop parameters change rapidly with the maximum strain amplitude  $\varepsilon_u$  at low strain, but more slowly at larger strain. In practice, these parameters changes do not introduce large errors to seismic based on bilinear loops, since seismic responses are dominated by relatively large strain, with slowly varying parameters. With fixed values of  $K_1$ ,  $K_2$  and  $F_y$  the bilinear loops nest on a two slope generating curve with a fixed starting point.

Often the bilinear behaviour is simplified by means of an equivalent stiffness  $k_{eff}$  and an equivalent damping  $\xi_{eff}$  as follows:

$$k_{eff} = \frac{F_y}{s_u} + k_2 \quad \text{Eq. (11.7)}$$

$$\xi_{eff} = \frac{4F_y \left( s_u - \frac{F_y}{k_1 - k_2} \right)}{2\pi \cdot k_{eff} \cdot s_u^2} \quad \text{Eq. (11.8)}$$

### 11.3.2 The “Scaling Factor Method”

The response of any metallic damper is a function of its geometry and the mechanical characteristics of the metal from which it is manufactured. In this regard, the “Scaling Factor Method” (SFM) is based on the assumption that the force-displacement response of a Steel Hysteretic Devices (SHD) can be obtained scaling the stress-strain ( $\sigma - \varepsilon$ ) curve (Fig. 11.8) of the used steel by means of proper “scaling factors”.

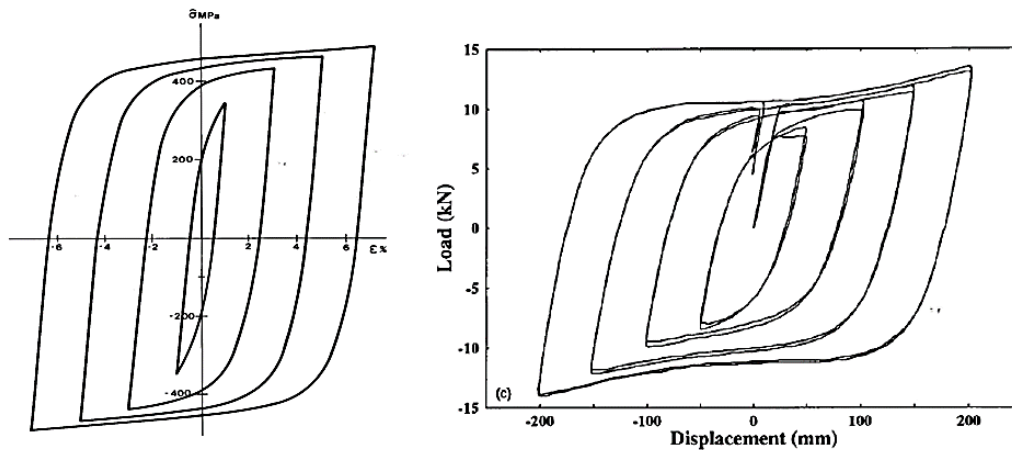


Fig. 11.8: Scaled stress-strain curves (left) and corresponding force-displacement loops of a TRSH device made of hot-rolled mild steel (right)

Let set the following variables:

$s$  device displacement

$F$  device damping force

$\varepsilon$  steel strain

$\sigma$  normal steel stress (assumed to be constant over the cross-section).

The following “scaling equations” can be written:

$$s = \delta \cdot \varepsilon \quad \text{Eq. (11.9)}$$

$$F = \varphi \cdot \sigma \cdot (1 + \alpha \cdot s^2) \quad \text{Eq. (11.10)}$$

where, for the TRSH device represented in Fig. 11.9, the force factor  $\varphi$ , displacement factor  $\delta$ , and the (large-displacement) correction  $\alpha$  factor are:

$$\varphi = \frac{b \cdot t^2}{4 \cdot h} \quad \text{Eq. (11.11)}$$

$$\delta = \frac{h^2 - c^2}{t} \quad \text{Eq. (11.12)}$$

$$\alpha = \frac{2}{(h+c)^2} \quad \text{Eq. (11.13)}$$

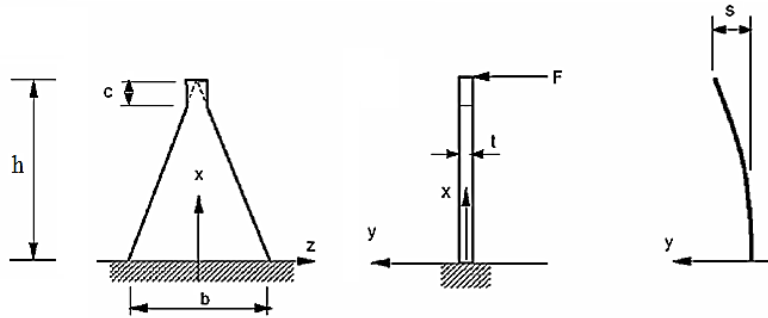


Fig. 11.9: geometrical parameters a TRSH element [9]

Given the results of a tensile test on a steel specimen of the TRSH (e.g. Table 11.1), the elastic  $k_1$  and post-yielding  $k_2$  stiffness can be calculated by applying the “*scaling factor method*”:

$$k_1 = \frac{\varphi}{\delta} E_1 \quad \text{Eq. (11.14)}$$

$$k_2 = \frac{\varphi}{\delta} E_2 + \alpha F_y s_u \left(1 + \frac{\varepsilon_y}{\varepsilon_u}\right) \quad \text{Eq. (11.15)}$$

These formulas may be found as follows:

$$\begin{aligned} k_1 &= \frac{F_y}{s_y} = \frac{\sigma_y \varphi}{\varepsilon_y \delta} = E_1 \frac{\varphi}{\delta} \\ k_2 &= \frac{F_u - F_y}{s_u - s_y} = \frac{\varphi \cdot \sigma_u + \varphi \cdot \sigma_u \cdot \alpha \cdot s_u^2 - \varphi \cdot \sigma_y}{s_u - s_y} = \frac{\varphi(\sigma_u - \sigma_y)}{\delta(\varepsilon_u - \varepsilon_y)} + \frac{\varphi \cdot \sigma_u \cdot \alpha \cdot s_u^2}{s_u(1 - s_y/s_u)} \\ &= E_2 \frac{\varphi}{\delta} + \frac{\varphi \cdot \sigma_u \cdot \alpha \cdot s_u}{(1 - \varepsilon_y/\varepsilon_u)} \cdot \frac{(1 + \varepsilon_y/\varepsilon_u)}{(1 + \varepsilon_y/\varepsilon_u)} = E_2 \frac{\varphi}{\delta} + \frac{\varphi \cdot \sigma_u \cdot \alpha \cdot s_u}{(1 - \varepsilon_y^2/\varepsilon_u^2)} \\ &\cdot \left(1 + \varepsilon_y/\varepsilon_u\right) \cong E_2 \frac{\varphi}{\delta} + \alpha F_y s_u \left(1 + \frac{\varepsilon_y}{\varepsilon_u}\right) \end{aligned}$$

where:  $E_1 = \sigma_y/\varepsilon_y$ ,  $E_2 = \sigma_u - \sigma_y/\varepsilon_u - \varepsilon_y$ , and  $\varepsilon_y^2/\varepsilon_u^2 \cong 0$ .

Table 11.1: SFM-parameters for TRSH device made of mild steel

$\varepsilon_u$ [-]	$\varepsilon_y$ [-]	$\sigma_y$ [N/mm <sup>2</sup> ]	$E_1$ [N/mm <sup>2</sup> ]	$E_2$ [N/mm <sup>2</sup> ]
0,01	0,0036	270	70000	12200
0,02	0,0055	370	70000	2560
0,03	0,0059	406	70000	1220
0,04	0,0061	424	70000	758
0,05	0,0063	442	70000	534
0,06	0,0065	452	70000	479
0,07	0,0066	458	70000	465

The scaling factor method includes 4 main inaccuracies:

1. Deviation of relevant real material properties (i.e. yield strength, elastic and plastic strain) of the TRSH device to be designed and the prototype from which the relevant design values are derived (see Table 11.1),
2. The elastic stiffness is strongly influenced by the stiffness of the clamping and the force application. A deviation of appr. 50% can occur,
3. Due to gradual change of the cross section at large deformation the strain hardening of the TRSH device can increase,
4. Other secondary effects might influence the hysteresis.

Strictly speaking the Scaling factor method leads to reliable prediction of the elastic-plastic behavior, if the TRSH elements are manufactured with steel from the the same material batch as the prototype element, from which the data in Table 11.1 is derived.

### 11.3.3 Design example

Let consider the TRSH element represented in Fig. 11.10 with relevant geometrical parameters reported in Table 11.2.

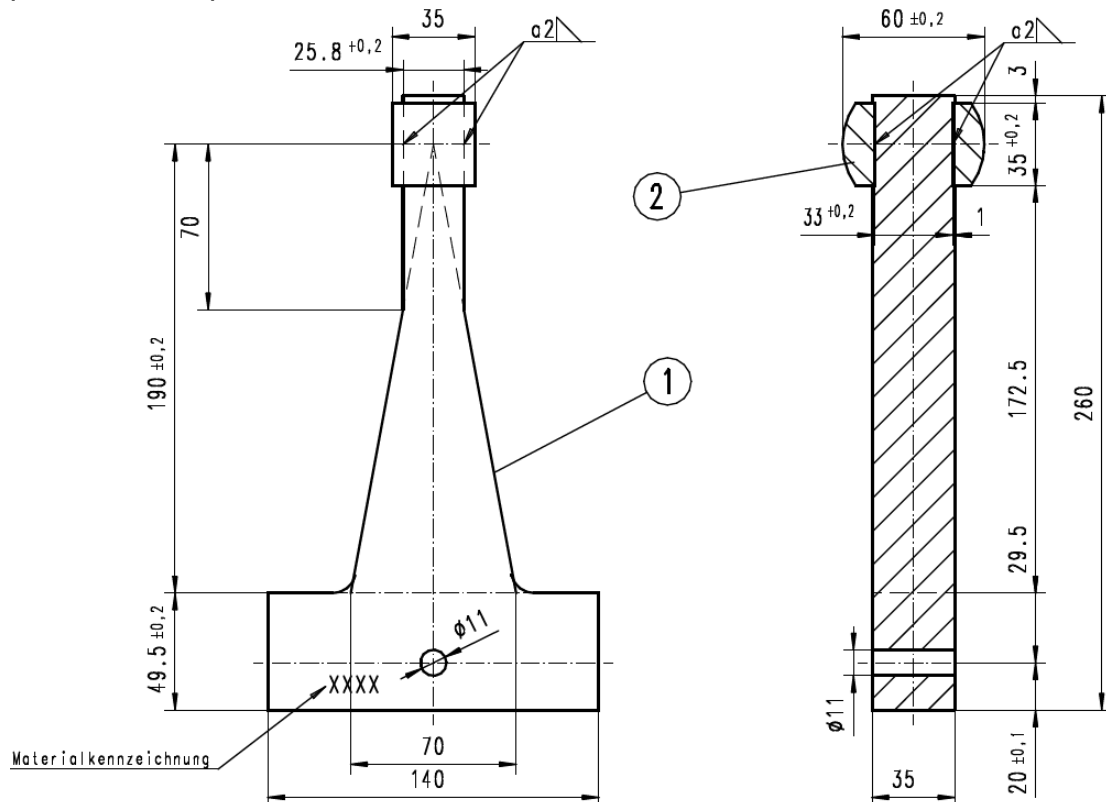


Fig. 11.10: Considered TRSH element

**Table 11.2: Geometrical parameters of the considered TRSH element**

h [mm]	b [mm]	c [mm]	t [mm]
190	70	70	35

Let assume a maximum strain  $\varepsilon_u = 0,04$ , the corresponding displacement  $s$  of the TRSH device can be calculated as:

$$s = \frac{h^2 - c^2}{t} \cdot \varepsilon_u = \frac{190^2 - 70^2}{35} \cdot 0,04 = 35,7 \text{ [mm]}$$

and the relevant yielding  $F_y$ , damping force  $F$ , elastic  $k_1$  and post yielding  $k_2$  stiffness are:

$$F_y = \frac{b \cdot t^2}{4 \cdot h} \cdot \sigma_y = \frac{70 \cdot 35^2}{4 \cdot 190} \cdot 424 = 47,8 \text{ [kN]}$$

$$F = \frac{b \cdot t^2}{4 \cdot h} \cdot \sigma \cdot \left(1 + \frac{2}{(h+c)^2} \cdot s\right) = \frac{70 \cdot 35^2}{4 \cdot 190} \cdot 424 \cdot \left(1 + \frac{2}{(190+70)^2} \cdot 35,7^2\right) \cdot 10^{-3} \\ = 49,6 \text{ [kN]}$$

$$k_1 = \frac{b \cdot t^3}{4 \cdot h \cdot (h^2 - c^2)} \cdot E_1 = \frac{70 \cdot 35^3}{4 \cdot 190 \cdot (190^2 - 50^2)} \cdot 70000 = 8227,1 \text{ [N/mm]}$$

$$k_2 = \frac{b \cdot t^3}{4 \cdot h \cdot (h^2 - c^2)} \cdot E_2 + \frac{2}{(h+c)^2} \cdot F_y \cdot s \cdot \left(1 + \frac{\varepsilon_y}{\varepsilon_u}\right) \\ = \frac{70 \cdot 35^3}{4 \cdot 190 \cdot (190^2 - 70^2)} \cdot 758 + \frac{2}{(190+70)^2} \cdot 47800 \cdot 35,7 \cdot \left(1 + \frac{0,0061}{0,04}\right) \\ = 107,6 \text{ [N/mm]}$$

## 11.4 EXPERIMENTAL INVESTIGATIONS

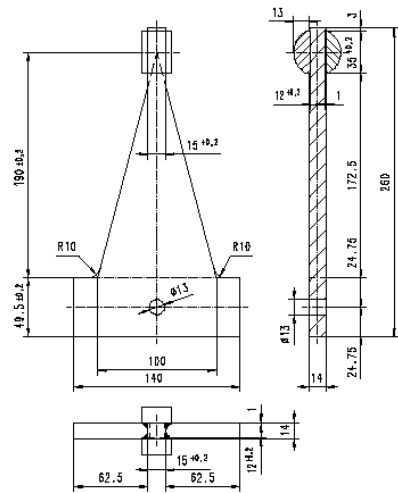
Within the framework of the LESSLOSS European research project [1], an extensive experimental campaign was conducted on TRSH devices. Their reliability for structural applications was indeed assessed in both displacement-controlled and shake table tests.

### 11.4.1 Displacement-controlled tests

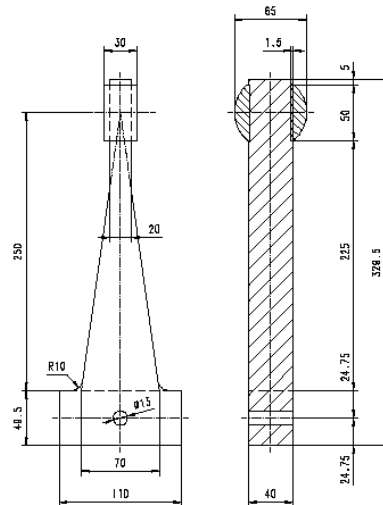
In order to investigate the actual response of TRSH devices, two different geometric prototypes of TRSH and different steel grades were tested. Their design parameters are reported in Table 11.3. Both TRSH devices were tested with specimens with half moon head and with a roller bearing to measure the behaviour without the parasitic effect of friction (see Fig. 11.11 and Fig. 11.12).

**Table 11.3: Geometrical parameters of the tested TRSH prototypes**

TRSH #	h [mm]	b [mm]	c [mm]	t [mm]	steel ID #
7	250	70	50	40	S355J2 (1.0570), X5CrNi18-10 (1.4301) X2CrNiMoN22-5-3 (1.4462)
13	190	100	50	14	



*TR-Damper 190x 100x 14*



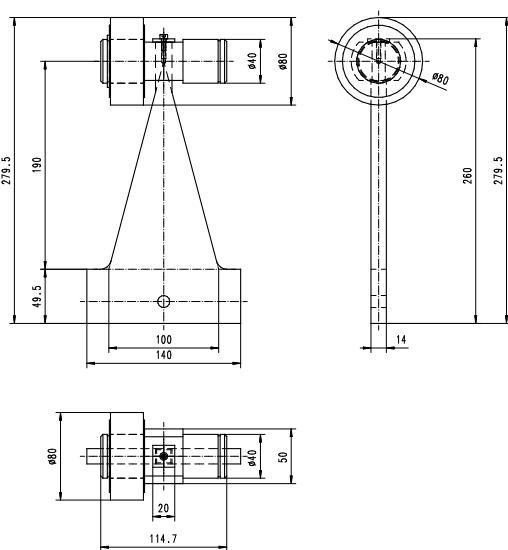
*TR-Damper 250x 70x 40*

Technical drawing of TRSH no. 13 (left) and no. 7 (right)



b) TRSH test specimen

Fig. 11.11 a)-b): Test specimen with half moon head [9]



a) Technical drawing



b) Test specimen

Fig. 11.12 a) –b): Test specimen with roller bearing [9]

The characterisation tests on each TRSH prototype were carried out at Universitaet der Bundeswehr in Munich.

Fig. 11.13 represents the test equipment: the top side of the TRSH element is clamped while at the bottom side a roller bearing head and the actuator apply the horizontal movement. The roller bearing head of the half-moon head of the TRSH-element rotates in the special linear movable sliding carriage. The horizontal actuator applies the desired displacement to the sliding carriage with a sinusoidal waveform. TRSH prototypes were tested in both static and dynamic conditions. The force-displacement loops were recorded. Additionally, a thermal camera recorded the temperature sequence during the dynamical tests.

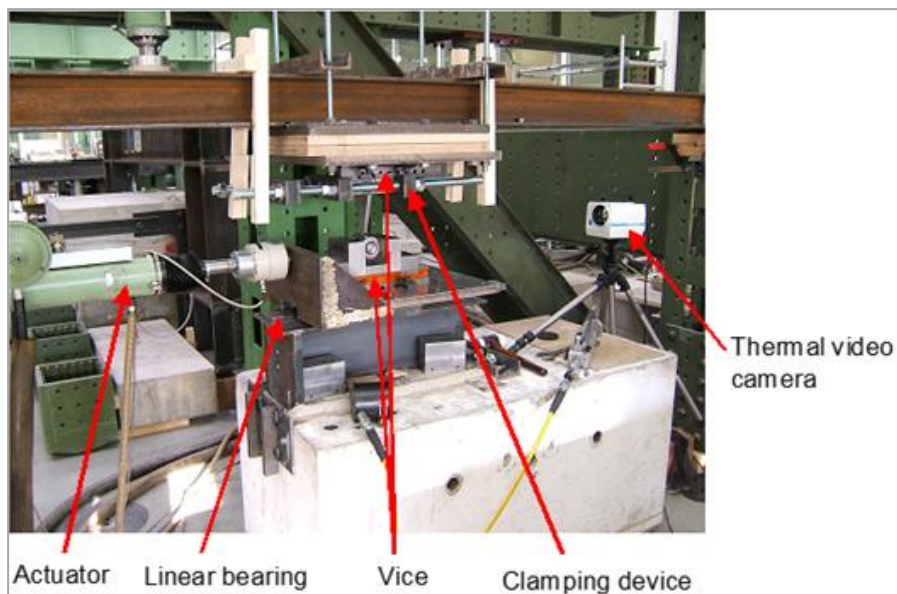


Fig. 11.13: Test set-up [9]

Fig. 11.14 shows the hysteretic loops obtained for the dynamic test of the TRSH - element 7 – steel 1.0570 (resp. S355J2).

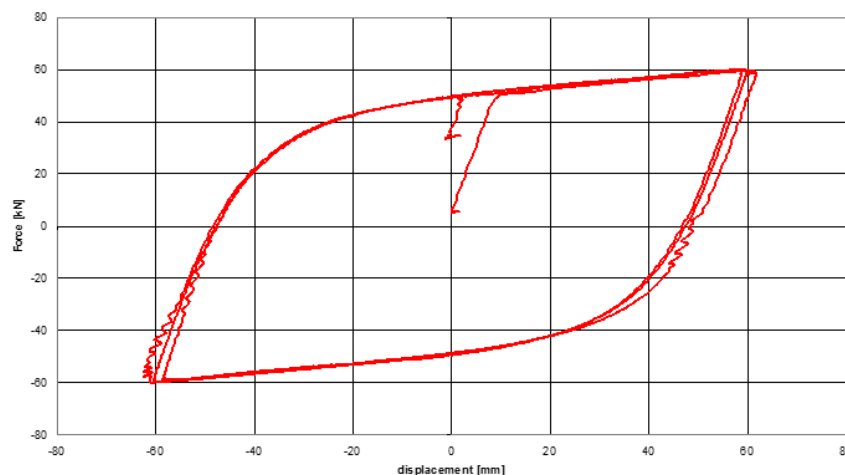


Fig. 11.14: Dynamic test TRSH no. 7 – 1.0570 (peak displacement 60mm) [10]

Fig. 11.15 shows the hysteretic loops obtained for the dynamic test of the TRSH - element 7 - steel 1.4301 (resp. X5CrNi18-10).

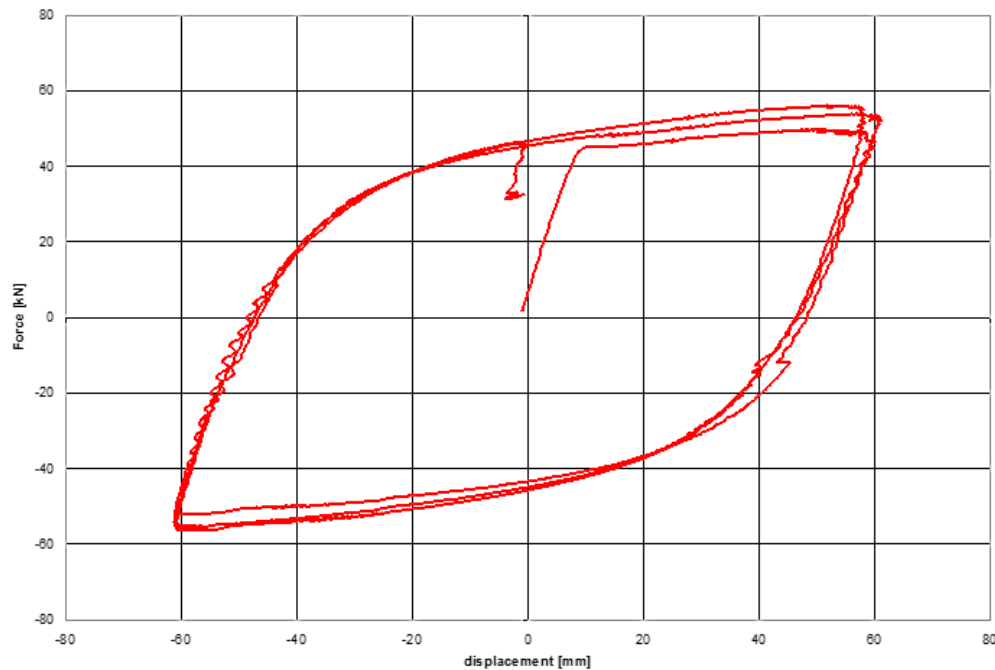


Fig. 11.15: Dynamic test TRSH no. 7 – 1.4301 (peak displacement 60mm) [10]

Fig. 11.16 and Fig. 11.17 show the hysteretic loops of the dynamic test on the TRSH- element 13 - steel 1.0570 (resp. S355J2).

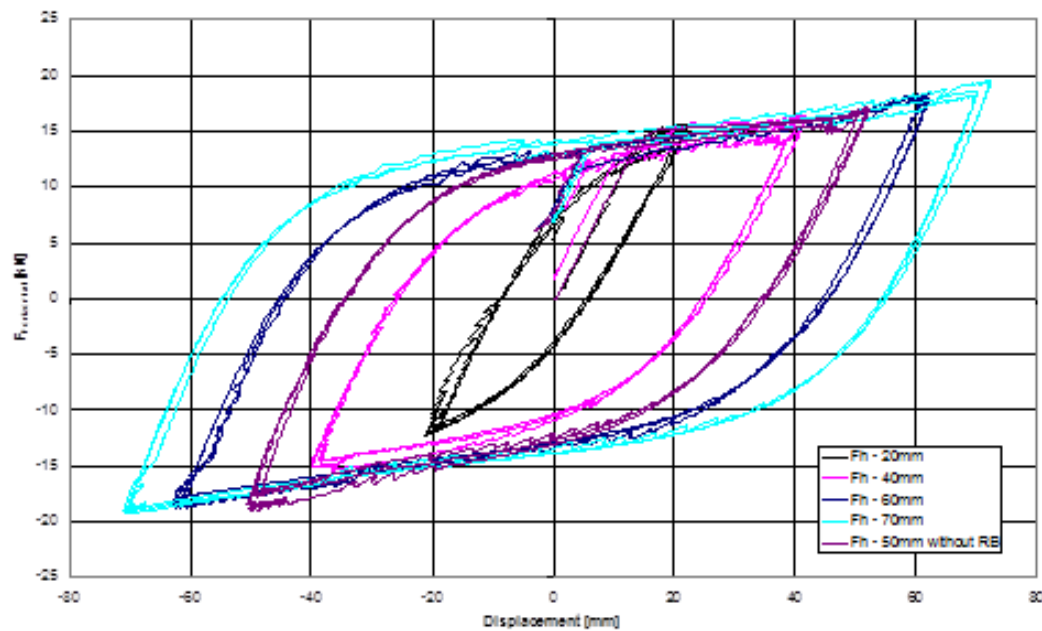


Fig. 11.16: Dynamic test TRSH 190 – 1.0570 (peak displacement 20-70mm) [10]



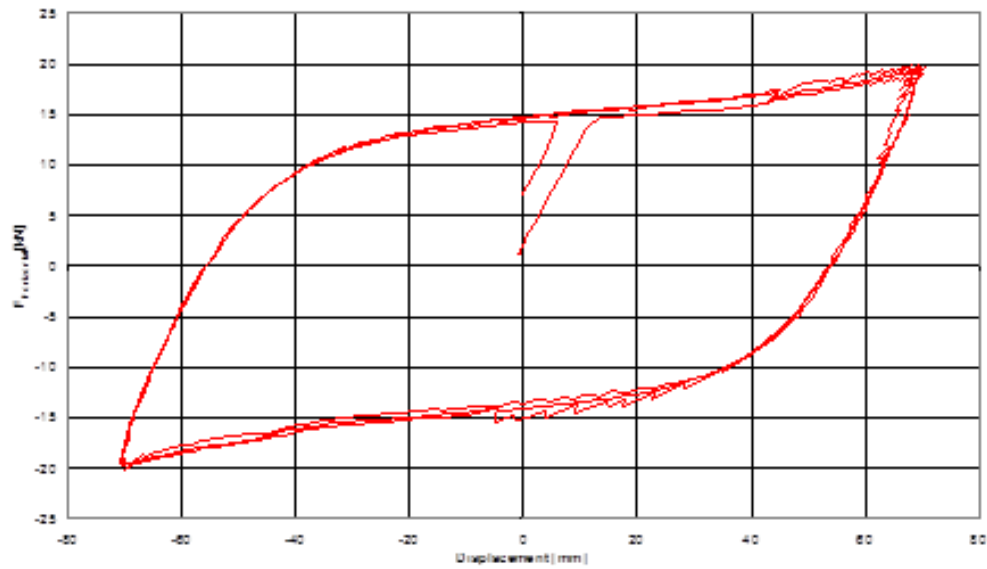


Fig. 11.17: Dynamic test TRSH 190 – 1.0570 (peak displacement 70mm) [10]

Fig. 11.18 shows the hysteretic loops of the dynamic test on the TRSH- element 190 - steel 1.4301.

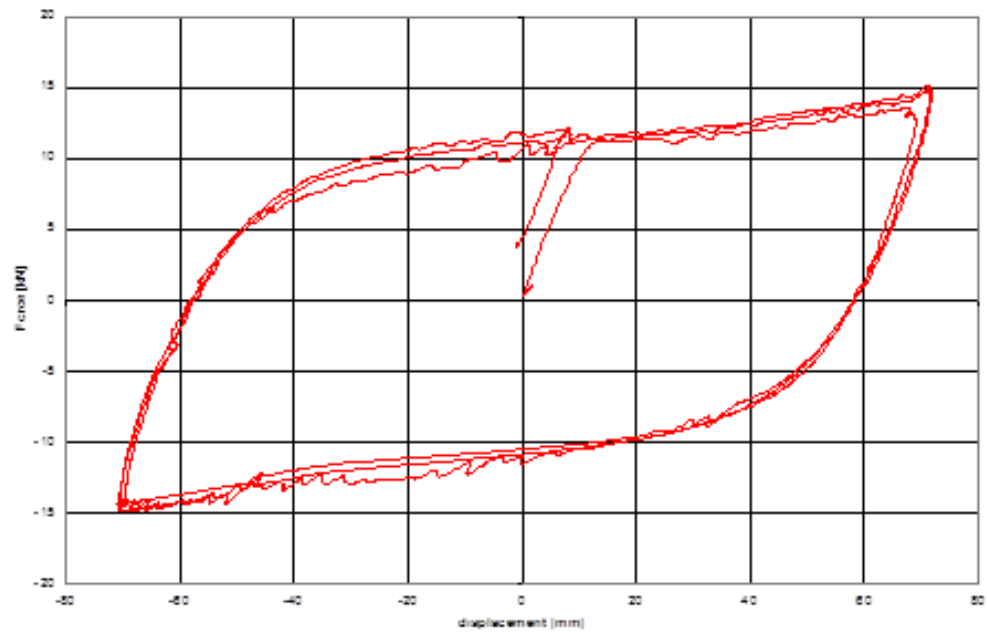


Fig. 11.18: Dynamic test TRSH 190 – 1.4301 (peak displacement 70mm) [10]

Test results, in terms of elastic  $k_1$  and post-yielding  $k_2$  stiffness, yielding force  $F_y$  and displacement  $s_y$ , and ultimate strength  $F_u$  and displacement  $s_u$  are reported in Table 11.4 for each TRSH prototype.

**Table 11.4: Test results for each type of TRSH prototype [10]**

Characteristic data	Elements 1.0570		Elements 1.4462		Elements 1.4301	
	TR 190 (13)	TR 250 (7)	TR 190 (13)	TR 250 (7)	TR 190 (13)	TR 250 (7)
$K_1$ [N/mm]	1100,00	5000,00	930,00	4850,00	670,00	4700,00
$K_2$ [N/mm]	80,00	180,00	82,00	(800)	72,00	160,00
$F_y$ [N]	12000,00	50000,00	13000,00	58000,00	8000,00	47000,00
$s_y$ [mm]	11,00	10,00	14,00	12,00	12,00	10,00
$F_u$ [N]	18000,00	59000,00	18000,00	63000,00	12500,00	55000,00
$S_u$ [mm]	85,00	60,00	75,00	18,00	75,00	60,00

### Comparison with the Scaling Factor Method

Fig. 11.19 shows two comparisons between the experimental results and the model prediction of the scaling factor method for TRSH no. 7 and TRSH no. 13.

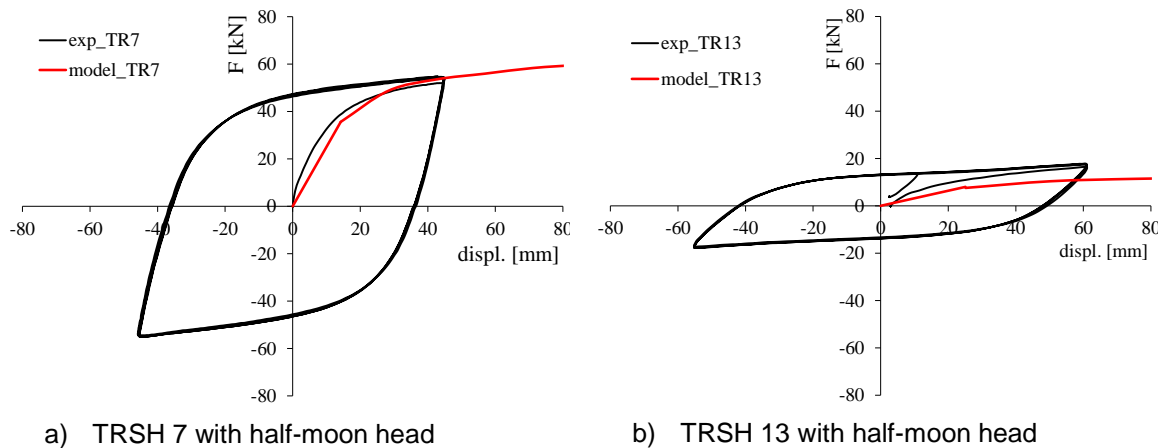


Fig. 11.19 a)-b): Comparison between experimental results and model prediction for TRSH devices made of S355J2

Experimental loops recorded in displacement-controlled tests on TRSH devices exhibits for the TRSH 7 element a good agreement with the ones predicted by means of the Scaling Factor Method, while for the more slender TRSH 13 the agreement is quite poor due to the reasons mentioned in section 11.3.2.

Comparisons of experimental loops for other materials lead to no agreement with the SFM based on the values given in Table 11.1. Other values have to be derived.

#### 11.4.2 Shake table tests

Within the LESSLOSS project [1], shake table tests were conducted on SDOF system composed of a massive slab implementing a base sliding isolation system with TRSH elements acting in parallel to the same [9]. The overall test mock-up is shown in Fig. 11.20 and comprises:

- a steel frame (Fig. 11.21);
- 4 PTFE flat sliding bearings (Fig. 11.22);
- from 1 up to 3 TRSH hysteretic elements (Fig. 11.23)
- a modular slab (from 12,2 up to 16,4 tons).

The testing ring is equipped with four guides that restrain the movement in one direction only, as well as other safety accessories.



Fig. 11.20: Test mock-up for shake table tests



Fig. 11.21: Detail of the steel frame with the TRSH element and its anchoring system



Fig. 11.22: Detail of the PTFE flat sliding bearing



Fig. 11.23: Test on three TRSH elements

Three TRSH prototypes were tested: TR(7) and TR(13) of S355J2. For each type of isolation layout, the following testing procedure was applied:

- a sine-sweep test was initially carried out in order to determine the elastic stiffness of the TRSH device;
- the isolation system was then subjected to a progressively increasing seismic input (e.g. Fig. 11.24) in order to obtain displacement time-histories with different ductility ratios (from 1 to 13).

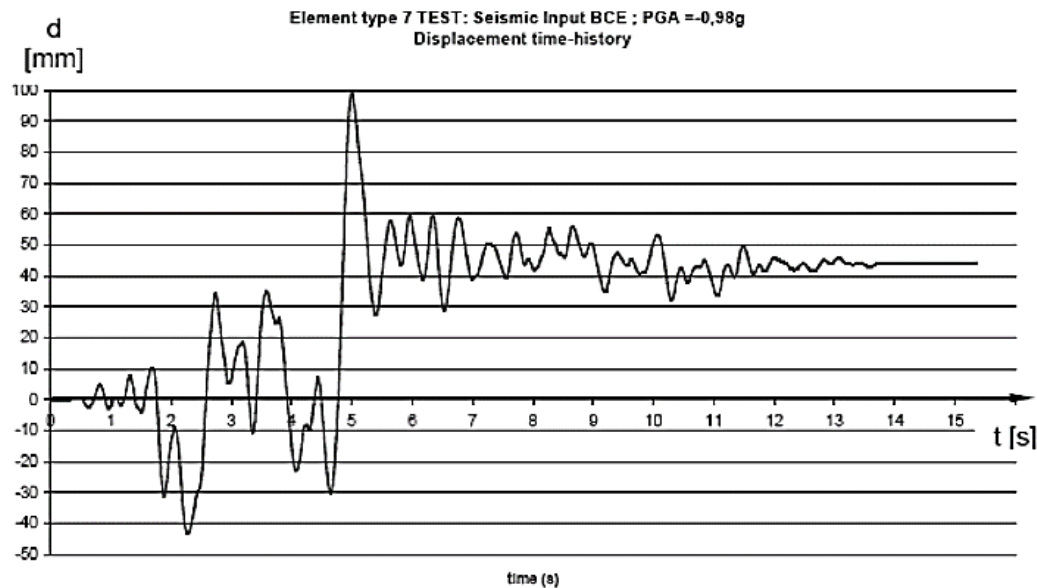


Fig. 11.24: Displacement time-history for TR(7) element subjected to a synthetic seismic input

Shake table tests proved that the TRSH devices even when subjected to strong seismic input (inducing high ductility ratios up to 13) exhibit a stable and repeatable behavior without any structural failure or significant deviations of the post-yielding stiffness.

#### 11.4.3 Final remarks

The robustness of TRSH devices as potential source of hysteretic structural damping has been proven in both displacement controlled and shake table tests. Even when subjected to large peak displacements (ductility ratios up to 13) the TRSH device exhibited a stable and repeatable dissipative behavior.

The SFM can be a reliable tool to design TRSH elements with other geometries than the tested prototype, if material properties and clamping behavior are very similar. It has to be taken into account that the SFM only gives representative values and does not give upper and lower boundary characteristics of the device neither tolerances, which is required according to EN 15129 [13] for a reliable application within structures. Before implementation into a structure, further tests according to the specifications given in EN 15129 [13] are recommended.

## 11.5 DESIGN RULES

### 11.5.1 General

The design methodology, described in the following, is based on the provisions of EN 1993-1 [11], EN 1998-1 [13] and EN 15129 [13]. Some clauses of EN 1998-1-1 were appropriately rearranged to cover the use of TRSH elements by the normal Code provisions and compared to the provisions given in EN 15129 [13].

For a preliminary design of a structure equipped with TRSH two different approaches exist:



1. Multimodal response spectrum analysis with consideration of the elastic stiffness  $k_1$  of the TRSH devices and an appropriate Q-factor
2. Multimodal response spectrum analysis with consideration of the equivalent stiffness  $k_{eff}$  of the TRSH devices with appropriate Q-factor.

In the following the structural design taken into account first approach is shown.

### 11.5.2 Preliminary Design

Assuming that the gravitational loads at Ultimate Limit States (ULS) combination ( $1.3G_1 + 1.5G_2 + 1.5Q$ ) are entrusted to the main frame (beams and columns), at each story level of the building, the TRSH bracing system is preliminary designed in order to withstand alone the overall lateral seismic load. In this regard, according to EN 1998-1 (§ 4.3.3.2.2 and 4.3.3.2.3), a rough approximation of the lateral seismic load (inertia force) acting at the  $i$ -th floor level  $F_i$  can be obtained as follow:

$$F_i = F_b \cdot \frac{z_i \cdot m_i}{\sum z_j \cdot m_j} \quad \text{Eq. (11.16)}$$

where:

$$\begin{aligned}
 F_b &= S_a(T_1) \cdot m \cdot \lambda && \text{seismic base-shear;} \\
 S_a(T_1) &= \left(\frac{1}{q}\right) \cdot S_{ae}(T_1) && \text{inelastic spectrum;} \\
 S_{ae}(T_1) &&& \text{reference elastic spectrum;} \\
 q &= 3.0 && \text{assumed behavior factor;} \\
 T_1 &= C_t \cdot H^{3/4} && \text{fundamental period of the building.}
 \end{aligned}$$

Once known the inertia forces  $F_i$ , the shear load acting at the base of column elements at each story level  $F_{b,i}$  can be calculated (sum of inertia forces at upper story levels) and the TRSH device shall be designed in order to accomplish the following verification:

$$F_{Rd,t,i} = n_i \cdot F_{y,t,i} \geq \gamma_x \cdot \gamma_b \cdot F_{b,i} \quad \text{Eq. (11.17)}$$

where  $F_{Rd,t,i} = n_i \cdot F_{y,t,i}$  is the design resisting force of the TRSH device (being  $F_{y,t,i}$ , and  $n_i$  respectively the yielding force, and the number of triangular elements composing the device).  $\gamma_x=1,2$  is the reliability factor and  $\gamma_b=1,1$  is the partial factor for the device acc. to EN 15129 [13].

In case of frame with V bracings, it is worth noting that both the tension and compression diagonals shall be taken into account and element cross-sections should be chosen in order fulfill the following checks:

$$N_{Ed,b,i} = \frac{F_{b,i} \cdot \cos \alpha}{2} \leq 0.5 \cdot N_{Rd,b,i} \quad \text{Eq. (11.18)}$$

$$\lambda_{b,i} = \sqrt{A_{b,i} \cdot f_y / N_{cr,b,i}} \leq 2.0 \quad \text{Eq. (11.19)}$$

where  $N_{Ed,b,i}$  is the axial action effect;  $N_{Rd,b,i}$ ,  $N_{cr,b,i}$  are respectively the design axial resisting force and the critical buckling load of brace the elements;  $\lambda_{b,i}$  is the a-dimensional slenderness of the same (2.0 is the limit for V bracing systems according to EN 1993-1 [11]).

### 11.5.3 Design for linear elastic analysis

#### Multi-modal response spectrum analysis

In the current state of the art, a building with TRSH bracing system may be simulated with linear-elastic elements with lateral stiffness calculated according to formula reported in Section 11.2.

Both dissipative and non-dissipative structural elements shall be verified with reference to the seismic load combination ( $G_1 + G_2 + \psi Q + E$ ). In this regard, the conventional method for the calculation of internal forces due to the seismic action ( $E$ ) is Multi-Modal Response Spectrum Analysis, where the number of modes of vibration considered in each direction is such that the sum of the effective mass is at least equal to 85% of the total mass and there are no modes with mass participating  $> 5\%$ . The design spectrum shall be defined with a maximum behavior factor equal  $q = 3.0$ , which was confirmed through non-linear static analyses (Pushover).

#### Limitation of interstory drift

Limitation of interstory drift ensures the protection of non-structural elements under seismic loading and consists a basic criterion for the design of TRSH devices. It provides an estimation of the damage for different performance levels and defines the distribution of stiffness within the structure and eventually the size and type of the cross sections applied on the system.

Assuming that the building has ductile non-structural elements the following verification relevant of the maximum interstorey  $d_r$  shall be fulfilled:

$$d_r \cdot v \leq 0.0075 \cdot h \quad \text{Eq. (11.20)}$$

where  $v = 0.5$  is a reduction factor on the design displacements due to the importance class of the building (ordinary buildings) and  $h$  is the story height.

In linear analysis the displacements induced by the design seismic action  $d_s$  shall be calculated on the basis of the elastic deformations  $d_e$  of the structural system through the expression:

$$d_s = q \cdot d_e \quad \text{Eq. (11.21)}$$

In case the capacity ratios of the dissipative elements ( $\Omega$ ) are low, the calculation of the design interstory drift based on  $d_s$  is conservative and a therefore reduction factor ( $q_\Omega$ ) equal to the capacity ratio of the devices may be employed as follows:

$$d_s = q \cdot q_\Omega \cdot d_e \quad \text{Eq. (11.22)}$$

The design interstory drift  $d_r$  is defined as the difference of the average lateral displacements at the top and bottom of the story under consideration. Depending on the type of the non – structural elements (brittle materials, ductile or not connected) and the importance class of the building, the design interstory drift  $d_r$  is compared to the corresponding values of the Code. The optimal design is achieved when the maximum interstory drifts of the structure are close to the limit values. Since the horizontal displacements are multiplied by the behavior factor the limitation of interstory drift does not depend on it.

#### 2<sup>nd</sup> order effects

The possible influence of 2<sup>nd</sup> order effects shall be controlled by the limitation of the interstory drift sensitivity coefficient  $\theta$  below the limit values of the Code. Coefficient  $\theta$  is calculated as:

$$\theta = \frac{P_{tot} \cdot d_r}{V_{tot} \cdot h_{story}} \quad \text{Eq. (11.23)}$$

where  $P_{tot}$  is the total gravity load at and above the considered story,  $V_{tot}$  is the seismic story shear,  $d_r$  is the interstorey drift, and  $h_{story}$  is the interstorey height.

Alternatively, the interstory drift sensitivity coefficient  $\theta$  may be calculated more accurately by a linear buckling analysis through the factor  $\alpha_{cr}$ , the factor by which the design loading would have to be increased to cause elastic instability in a global mode. The analysis is carried out under conditions of the constant gravity loads of the seismic combination ( $1,0 \cdot G + 0,3 \cdot \varphi \cdot Q$ ) and produces the buckling modes. The modes that move the building at x and y directions are chosen and the correspondent  $\alpha_{cr}$  values are calculated as follows:

$$\alpha_{cr} = \frac{1}{\theta} = \frac{F_{cr}}{F_{Ed}} \quad \text{Eq. (11.24)}$$

where  $F_{cr}$  is the elastic critical buckling load for global instability mode based on initial elastic stiffnesses and  $F_{Ed}$  is the design loading for the seismic combination.



To take into consideration the inelastic displacements of the building,  $\alpha_{cr}$  shall be divided by the  $q$  factor. The values of  $\theta$  in this case are:

$$\theta = \frac{q}{\alpha_{cr}} \quad \text{Eq. (11.25)}$$

The relevant EC3 [11] provisions require for buildings that the interstory drift sensitivity coefficient is limited to  $\theta \leq 0.1$ , if second order effects are ignored. If  $0.1 < \theta < 0.2$ , second-order effects may approximately be taken into account by multiplying the relevant seismic action effects by a factor equal to  $1/(1 - \theta)$ . If  $0.2 < \theta < 0.3$  a more accurate second order analysis applies. In any case it shall be  $\theta < 0.3$ .

#### Dissipative elements (TRSH devices)

At each generic  $i$ -th story level it shall be verified that the seismic action  $F_{Ed,i}$  with consideration of  $\gamma_x$  as reliability factor and  $\gamma_b$  as partial factor of the device on the TRSH damping device does not exceed its design resistance  $F_{Rd,t,i}$  (see EN 15129, section 4.1.2):

$$F_{Rd,t,i} = n_i \cdot F_{y,t,i} \geq \gamma_b \cdot \gamma_x \cdot F_{Ed,i} \quad \text{Eq. (11.26)}$$

Moreover, to achieve a uniform dissipative behavior at each storey level, it should be checked that the maximum over-strength ratio  $\Omega$  of TRSH elements over the entire structure do not differ from the minimum value  $\Omega$  more than 25%. In this check it is crucial to consider the upper and lower bound design properties given by the TRSH manufacturer:

$$\frac{\max \Omega_i}{\min \Omega_i} \leq 1.25 \quad \text{Eq. (11.27)}$$

where  $\Omega_i = (n_i \cdot F_{y,t,i})/F_{Ed,i}$

To be precise  $F_{y,t,i}$  has to be in agreement with lower and upper design properties of the TRSH devices, which are provided by the manufacturer. Hence, for both equation above design values and not representative values have to be taken into account.

#### Non-dissipative element verifications: braces, beams, and columns.

In order to ensure that plasticization occurs only in the TRSH elements, non-dissipative structural members (beams, columns and braces) shall be capacity designed for increased values of internal forces compared to the ones derived from the analyses with the most unfavourable seismic combination:

$$\begin{cases} N_{Rd} \geq N_{Ed,G} + 1,1 \cdot \gamma_{ov} \cdot \Omega \cdot N_{Ed,E} \\ M_{Rd} \geq M_{Ed,G} + 1,1 \cdot \gamma_{ov} \cdot \Omega \cdot M_{Ed,E} \\ V_{Rd} \geq V_{Ed,G} + 1,1 \cdot \gamma_{ov} \cdot \Omega \cdot V_{Ed,E} \end{cases} \quad \text{Eq. (11.28)}$$

where:

- $N_{Rd}$  ( $M_{Rd}$ ,  $V_{Rd}$ ) is the axial (bending or shear accordingly) design resistance of the structural element;
- $N_{Ed,G}$  ( $M_{Ed,G}$ ,  $V_{Ed,G}$ ) is the axial (bending or shear accordingly) force acting on the structural element due to the non-seismic actions;
- $N_{Ed,E}$  ( $M_{Ed,E}$ ,  $V_{Ed,E}$ ) is the axial (bending or shear accordingly) force acting on the structural element due to the design seismic action;
- $\gamma_{ov}$  is the overstrength factor ( $\gamma_{ov} = 1,25$  for steel S355);
- $\Omega = \min(N_{Rd,i}/N_{Ed,E,i})$  over all the bracing diagonals.

#### 11.5.4 Design for non-linear analysis (Pushover)

The structural model used for elastic analysis shall be extended to include the response of structural elements beyond the elastic state and estimate expected plastic mechanisms and the distribution of damage. Beam elements with a bilinear behavior of in horizontal shear direction are used to model the TRSH devices while linear elements are used for other structural members. Mechanical properties of TRSH elements shall be calculated according to the analytical models described in Section 11.3.1. Since a quasi-static analysis shall be carried out, the hysteresis of TRSH elements can be neglected in behavior-diagram (Fig. 11.25). On the contrary, the failure of the element due to the exceedance of the ultimate displacement is accounted for.

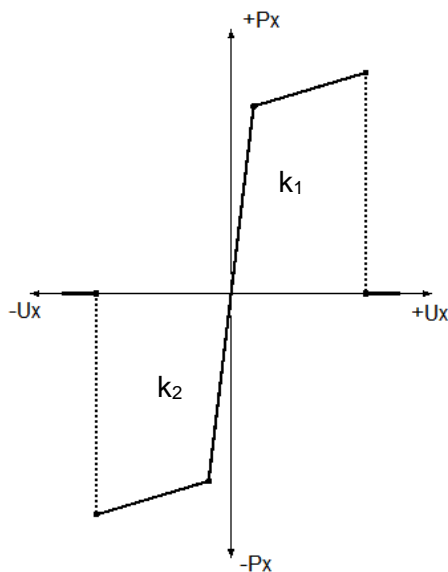


Fig. 11.25: Qualitative force-displacement diagram used for TRSH elements in Pushover analyses

## 11.6 2D CASE-STUDY FRAME

Equations, element properties, design recommendations, critical checks and proposed behaviour factor, included in the Design Guide, are verified hereafter through numerical analyses on a 2D case-study building equipped with the TRSH elements. At first, the frame is designed through an elastic analysis with equivalent lateral seismic loads applied to the structure. A nonlinear static analysis (Pushover) is eventually conducted in order to investigate the TRSH response beyond the elastic range and determine the overall behaviour factor  $q$ . All the analyses are carried out by means of the commercial software RFEM v5.08 [14].

### 11.6.1 Description of the considered building frame

#### Geometry

The 2D case study analysed hereafter is represented in Fig. 11.26. The width of the influence area of the frame in the transversal direction considered to calculate linear distributed loads is 8,0m.

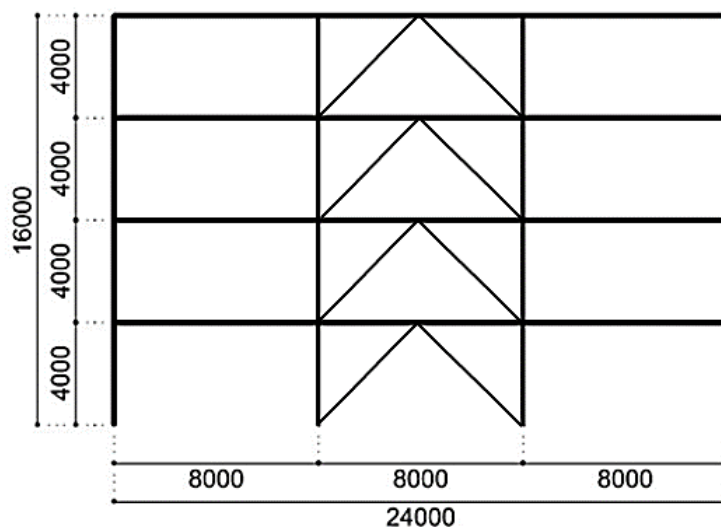


Fig. 11.26: Geometry of the considered frame

#### Loads

Dead Loads ( $G$ ):

Steel self-weight:  $78.5 \text{ kN/m}^3$

Composite slab:

Concrete self-weight:  $25.0 \text{ kN/m}^3$

Steel sheeting: height 73 mm, thickness 1 mm

Total slab thickness: 150 mm

Equivalent uniform slab thickness: 110 mm

$g_{2,c} = 2.75 \text{ kN/m}^2$  (including steel sheeting)

Services, ceilings, raised floors:

$g_{2,fl} = 0.70 \text{ kN/m}^2$  for intermediate floors

$$g_{2,rf} = 1.00 \text{ kN/m}^2 \text{ for top floor}$$

Perimeter walls ( $1.00 \text{ kN/m}^2$ ):

$$g_{2,per} = 4.00 \text{ kN/m}$$

Live Loads ( $q$ ) for offices (Class B):

$$q = 3.00 \text{ kN/m}^2$$

Movable partitions ( $\leq 2.00 \text{ kN/m}^2$ ):

$$q_{add} = 0.80 \text{ kN/m}^2$$

Total live load:

$$q_{add} = 3.80 \text{ kN/m}^2$$

Coefficient for the seismic combinations:  $\psi_2 = 0.6$

The roof is accessible

Snow load is ignored.

Seismic Load ( $E$ ):

Importance factor:  $\gamma_I = 1.0$

Peak ground acceleration:  $a_{gR} = 0.36g$

Ground Type B – Type 1 spectrum:

$$S = 1.2, S = 1.2, T_B = 0.15s, T_C = 0.50s, T_D = 2.00s$$

Vertical ground acceleration not accounted for.

### 11.6.2 Preliminary design

Each structural element of the main frame (beams and columns without bracings) is preliminary designed in order to withstand ( $N_{Rd} \geq N_{Ed}$ ,  $V_{Rd} \geq V_{Ed}$ , and  $M_{Rd} \geq M_{Ed}$ ) alone the gravitational loads at Ultimate Limit States (ULS) combination ( $1.3G_1 + 1.5G_2 + 1.5Q$ ). The columns are supposed completely restrained (encastre) at the base while beams hinged to the columns. The resulting cross-sections is IPE450 for beams and HEB280 for columns at all storey levels (Table 11.5).

**Table 11.5: Beam and column cross-section at each story level**

	column	beam	steel
1 <sup>st</sup> level	HEB 280	IPE 450	S 355
2 <sup>nd</sup> level	HEB 280	IPE 450	S 355
3 <sup>rd</sup> level	HEB 280	IPE 450	S 355
4 <sup>th</sup> level	HEB 280	IPE 450	S 355

The TRSH dissipative bracing system is then preliminary designed according to the procedure described in Section 11.5.2. Inertia and shear forces on column elements at each storey level are reported in Table 11.6.

$$T_1 = C_t \cdot H^{\frac{3}{4}} = 0.0075 \cdot 16^{\frac{3}{4}} = 0.14s$$

$q = 3.0$  behavior factor for buildings with TRSH devices (see Section 11.6.4)

$$S_a(T_1) = \frac{S_{ae}(T_1)}{q} = 0.35g$$

$$F_b(T_1) = m_{tot} \cdot \lambda \cdot S_a(T_1) \cong 868kN$$

$$F_i = F_b \cdot \frac{z_i \cdot m_i}{\sum z_j \cdot m_j}$$

**Table 11.6: Mass and inertia force distribution at each story level**

	$m_i$ [kg]	$F_i$ [kN]	$F_{b,i}$ [kN]
level 1	67635	98.5	867.9
level 2	67635	196.9	769.5
level 3	67635	295.4	572.5
level 4 (roof)	47595	277.2	277.2

The TRSH devices to be installed at each story level are chosen based on the real devices prototypes tested in LESSLOSS (see Table 11.4). The values given in Table 11.4 are assumed as representative values. Lower and upper bound design properties of the TRSH have to be provided by the manufacturer and shall be considered in design.

The number triangular dissipative elements has to be determined as follow:

$$n_i = \frac{\gamma_x \cdot \gamma_b \cdot F_{b,i}}{F_{y,LBDP,t,i}}$$

where  $F_{y,LBDP,t,i}$  is the **lower bound design property** of the yielding force of the single dissipative element ,  $\gamma_x$  is the reliability factor and  $\gamma_b$  the partial factor for the TRSH device given in the Codes.

As LBDP and UBDP are not known at this stage, the number of TRSH devices is calculated by neglecting  $\gamma_x$  and  $\gamma_b$ . Having more precise information about the TRSH these factors have to be considered.

Table 11.7 summarizes the obtained design parameters of the TRSH devices at each story level.

**Table 11.7: TRSH devices distribution at each story level**

	TRSH type	$F_{y,t,i}$ [kN]	$F_{u,t,i}$ [kN]	$n^\circ$ [-]	$n \cdot F_{y,t,i}$ [kN]	$n \cdot F_{u,t,i}$ [kN]
level 1	TR 250(7) - 1.0570	50	59	18	900	1062
level 2	TR 250(7) - 1.0570	50	59	16	800	944
level 3	TR 250(7) - 1.0570	50	59	12	600	708
level 4 (roof)	TR 250(7) - 1.0570	50	59	6	300	354

Finally, the cross-section of braces elements in order are chosen (Table 11.8) in order to fulfil the requirements relevant to both axial resistance and non-dimensional slenderness (see Section 11.5.2).

**Table 11.8: Cross section of brace elements at each story level**

	cross section	$N_{Ed,i}$ [kN]	$N_{Rd,i}$ [kN]	$l_0$ [m]	$N_{cr,i}$ [kN]	$\lambda_{b,i}$ [-]
level 1	2 UPN300	228.0	2x3795	5.26	2x943.5	2.0
level 2	2 UPN300	202.1	2x3795	5.26	2x943.5	2.0
level 3	2 UPN300	150.4	2x3795	5.26	2x943.5	2.0
level 4 (roof)	2 UPN300	72.8	2x3795	5.26	2x943.5	2.0

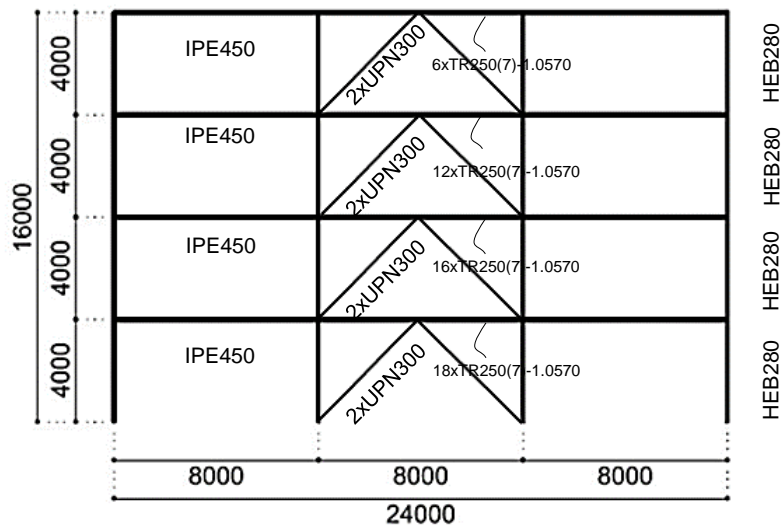


Fig. 11.27: Elements cross-section derived from the preliminary design

### 11.6.3 Linear elastic analysis

It is noted that for the seismic design following conditions were to be fulfilled in accordance with the design rules described in Section 11.5.3 and EN 1998-1-1 [11] rules. Both dissipative and non-dissipative structural elements are verified with reference to the seismic load combination ( $G_1 + G_2 + \psi Q + E$ ).

### Multi-modal response spectrum analysis

Multi-modal response spectrum analysis has been performed. Equivalent lateral seismic loads have been calculated considering only the first three modes since they activate the 97% of the total mass of the building (Table 11.9).

**Table 11.9: Participating mass ratio and periods**

Mode n°	Period [s]	Participating mass [%]	Total [%]
1	0.613	0.811	97.0
2	0.239	0.117	
3	0.147	0.042	

### Limitation of interstory drift

Assuming that the building has ductile non-structural elements the following verification relevant to the maximum interstorey  $d_r$  has been verified (see Section 11.5.3):

$$d_r \cdot v \leq 0.0075 \cdot h = 30\text{mm}$$

The check is satisfied at all storey levels with a peak value much lower than the limit value 30.0mm (Table 11.10).

**Table 11.10: Results of interstorey drift verifications**

Storey level	1	2	3	4
$d_{e,top}$ [mm]	8.8	19.6	29.2	37.9
$d_{e,bottom}$ [mm]	0.0	8.8	19.6	29.2
$d_r = q \cdot (d_{e,top} - d_{e,bottom})$ [mm]	26.4	32.4	28.8	26.1
$d_r \cdot v$ [mm]	13.2	16.2	14.4	13.05

### 2<sup>nd</sup> order effects

The possible influence of 2<sup>nd</sup> order effects has been controlled by the limitation of the interstory drift sensitivity coefficient  $\theta$  below the limit values of the Code (see Section 11.5.3):

$$\theta = \frac{P_{tot} \cdot d_r}{V_{tot} \cdot h_{story}}$$

Verification results are reported in Table 11.11; since for each storey level  $\theta < 0.1$ , 2<sup>nd</sup> order effects can be neglected.

**Table 11.11: Results of 2nd order effects verifications**

Storey level	$P_{tot}$ [kN]	$d_r$ [mm]	$V_{tot}$ [kN]	$h_{story}$ [mm]	$\theta$ [-]
1	2107.6	26.4	484.1	4000	0.03
2	1488.2	32.4	427.7	4000	0.03
3	887.8	28.8	303.3	4000	0.02
4	272.6	26.1	145.7	4000	0.01

**Dissipative elements (TRSH devices)**

It has been verified that, at each storey level, the seismic action  $\gamma_x \gamma_b F_{Ed,i}$  on the TRSH device has not exceeded the design resistance  $F_{Rd,t,i}$  of the element (see Section 11.5.3):

$$F_{Rd,t,i} = n_i \cdot F_{y,t,i} \geq \gamma_x \cdot \gamma_b \cdot F_{Ed,i}$$

Relevant results are reported in Table 11.12.

**Table 11.12: Resistance verification on TRSH elements at each storey level**

Storey level	TRSH type	$F_{y,t,i}$ [kN]	$F_{u,t,i}$ [kN]	$n^\circ$ [-]	$n \cdot F_{y,t,i}$ [kN]	$n \cdot F_{u,t,i}$ [kN]	$F_{Ed,i}$ [kN]	$\gamma_x \gamma_b F_{Ed,i,i}$ [kN]
level 1	TR 250(7) - 1.0570	50	59	18	900	1062	498.2	658
level 2	TR 250(7) - 1.0570	50	59	16	800	944	515.4	681
level 3	TR 250(7) - 1.0570	50	59	12	600	708	374.8	495
level 4 (roof)	TR 250(7) - 1.0570	50	59	6	300	354	195.6	258

Moreover, to achieve a uniform dissipative behavior at each storey level, the following requirement related to the distribution of the over-strength ratios  $\Omega$  of the TRSH elements over the entire structure has been verified (see Section 11.5.3):

$$\frac{\max \Omega_i}{\min \Omega_i} \leq 1.25$$

Here, it has to be kept in mind that lower or upper bound design properties of the TRSH devices are not known. In case of a real implementation in a structure, these properties have to be taken into account.

Relevant results are reported in Table 11.13.



**Table 11.13: Overstrength factor of TRSH elements at each storey level**

Storey level	$F_{Ed,i}$ [kN]	$(n_i \cdot F_{y,t,i})$ [kN]	$\Omega_i$ [-]	$\frac{\max \Omega_i}{\min \Omega_i}$ [-]
1	498.2	900	1.81	1.18
2	515.4	800	1.55	
3	374.8	600	1.60	
4	195.6	300	1.53	

**Non-dissipative element verifications: braces, beams, and columns**

In order to ensure that plasticization occurs only in the TRSH elements, non-dissipative structural members (beams, columns, and braces) have been verified according to capacity design requirements (see Section 11.5.3):

$$\begin{cases} N_{Rd} \geq N_{Ed,G} + 1,1 \cdot \gamma_{ov} \cdot \Omega \cdot N_{Ed,E} \\ M_{Rd} \geq M_{Ed,G} + 1,1 \cdot \gamma_{ov} \cdot \Omega \cdot M_{Ed,E} \\ V_{Rd} \geq V_{Ed,G} + 1,1 \cdot \gamma_{ov} \cdot \Omega \cdot V_{Ed,E} \end{cases}$$

Results relevant to most stressed structural elements are reported from Table 11.14 to Table 11.16.

**Table 11.14: Verifications of non-dissipative element subjected to axial loads**

element type	$N_{Rd}$ [kN]	$N_{Ed,G} + 1,1 \cdot \gamma_{ov} \cdot \Omega \cdot N_{Ed,E}$ [kN]
column - HEB280	4241.0	1233.0
beam – IPE450	n.a.	n.a.
brace – 2UPN300	3795.0	448.7

**Table 11.15: Verifications of non-dissipative element subjected to bending moments**

element type	$M_{Rd}$ [kNm]	$M_{Ed,G} + 1,1 \cdot \gamma_{ov} \cdot \Omega \cdot M_{Ed,E}$ [kNm]
column - HEB280	495.1	69.1
beam – IPE450	549.3	192.2
brace – 2UPN300	n.a.	n.a.

**Table 11.16: Verifications of non-dissipative element subjected to shear loads**

element type	$V_{Rd}$ [kN]	$V_{Ed,G} + 1,1 \cdot \gamma_{ov} \cdot \Omega \cdot V_{Ed,E}$ [kN]
column - HEB280	1878.0	19.7
beam – IPE450	1034.0	96.1
brace – 2UPN300	n.a.	n.a.

#### 11.6.4 Pushover analysis

##### Evaluation of the non-linear behaviour of the frames

A Static Pushover analysis (SPO) has been performed on the structure using two monolithically increasing patterns of lateral load. According to EC8 [13], as shown in Fig. 11.28, the Pushover analyses has been carried out considering both uniform and modal distribution of lateral loads. The TRSH devices are modelled according to Fig. 11.25 and Table 11.7. Obviously, since applied load are different, the resulting capacity curves exhibit the different trends represented in Fig. 11.29.

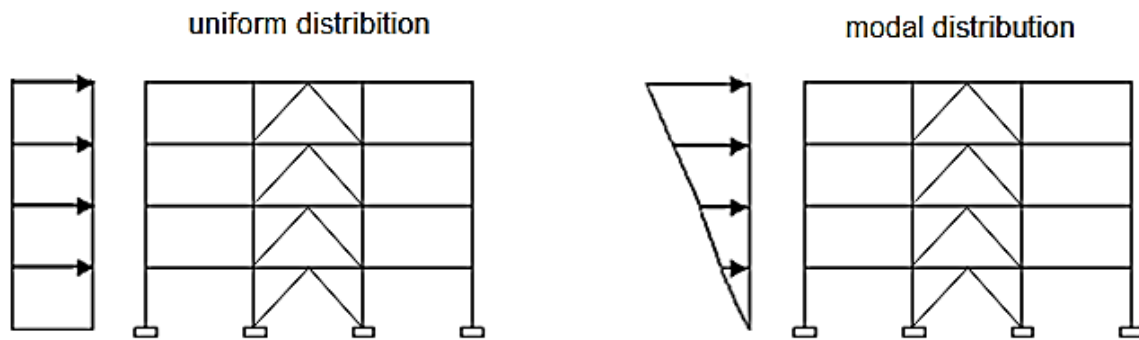


Fig. 11.28: Uniform and modal lateral load distribution

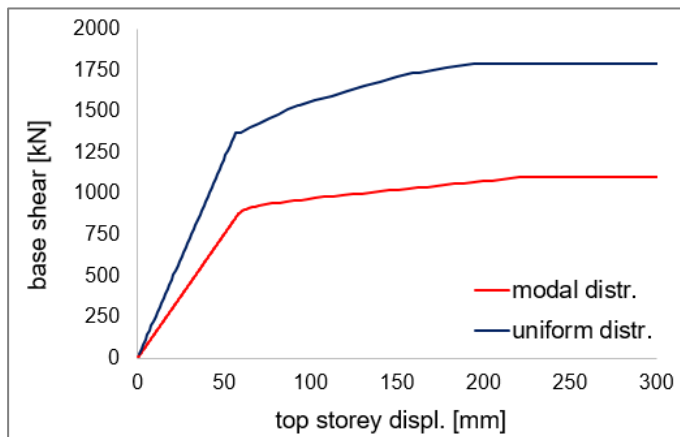


Fig. 11.29: Capacity curves calculated for both uniform and modal distributions

##### Evaluation of the behaviour factor $q$

In order to evaluate the structural ductility, the behaviour factor  $q$  is calculated according to the FEMA P695 [23] provisions (Fig. 11.30). According to this methodology, the overstrength factor  $\Omega$  is hence defined as the ratio between the maximum base shear resistance  $V_{max}$  and the yield base shear  $V$ . The period-based ductility  $\mu$  is defined as the ratio between the ultimate roof drift displacement  $d_u$  and the effective yield roof drift displacement  $d_{y,eff}$ .

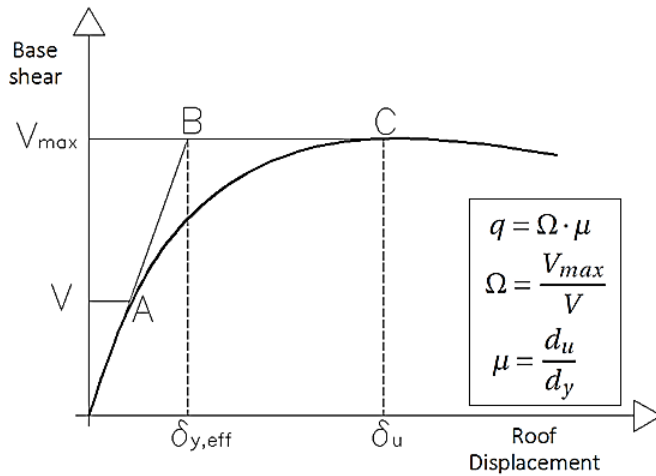


Fig. 11.30: Behaviour factor  $q$  calculation method according to FEMA 695

The resulting behaviour factors  $q$  for both modal and uniform lateral load distributions are given in Table 11.17.

**Table 11.17: Behaviour factors for both modal and uniform distributions**

distribution	$V_{max}$ [kN]	$V$ [kN]	$\Omega$ [-]	$d_u$ [mm]	$d_{y,eff}$ [mm]	$\mu$ [-]	$q$ [-]
modal	1092	894	1.22	216	74	2.92	3.57
uniform	1792	1372	1.31	194	76	2.55	3.33

The recommended  $q$  factor is the lower among the obtained ones; in this case  $q = 3.3$ .

## 11.7 CONCLUSIONS

In the present study, results of experimental tests on the TRSH device are presented showing that the element exhibit a stable and repeatable non-linear behaviour even when subjected to large peak displacements (ductility ratios up to 13. Furthermore, a design procedure for the implementation of TRSH devices in V bracing systems of multi-story steel structures is proposed and applied to a 2D case-study building. A linear static analysis with equivalent seismic lateral loads estimated with Multi-Modal Response Spectrum Analysis is carried out and relevant structural verifications on both dissipative (TRSH devices) and non-dissipative structural elements are executed. A non-linear static analysis (Pushover) has been carried out in order to evaluate the behaviour factor  $q$ . Even if further investigations are suggested, this preliminary assessment allows to have a rough estimation ( $q=3.0\div3.5$ ) of the dissipative behaviour of steel structures implementing TRSH devices in V bracing systems.

It should be noticed that the properties of the TRSH devices are based on a prototype tests. These properties are taken as characteristic values. Before implementation in a structure further data is necessary, e.g. lower and upper bound

design properties, which has to be considered in the design of the structure, and further tests have to be performed (see EN 15129 [13]).

## 11.8 FIELD OF APPLICATION

The innovative TRSH device may be applied in V bracing systems of multi-story steel buildings in order to achieve a significant increase of the dissipative capacity of the structure by combining ductility and architectural transparency with stiffness.

## 11.9 REFERENCES

1. LESSLOSS 2007/03 – Innovative Anti-Seismic Systems Users Manual. Available online at <http://elsa.jrc.ec.europa.eu/events.php?id=4#reports>.
2. Medeot, R. – Re-centring capability of seismic isolation systems based on energy concepts. Proceedings of the 13<sup>th</sup> World Conference on Earthquake Engineering, Vancouver 2004.
3. Tsai, K.C., Hong, C.P. and Su, Y.F. – Experimental study of steel triangular plate energy absorbing device for seismic-resistant structures. Report No CEER/R81-08, Center for Earthquake Engineering Research, National Taiwan University, Taipei 1992.
4. Tsai, K.C. and Chen, H.W. – Seismic response of building structures using steel triangular plate energy dissipators. Report No CEER/R81-09, Center for Earthquake Engineering Research, National Taiwan University, Taipei 1992.
5. Tsai, K.C. – Steel triangular plate energy absorber for earthquake-resistant buildings. Proceedings of the First World Conference on Constructional Steel Design, Mexico, Acapulco 1992. Earthquake Spectra, Vol. 9(3): 505-528, 1993(a).
6. Tsai, K.C., Chen, H.W., Hong, C.P. and Su, Y.F. – Design of steel triangular plate energy absorbers for seismic-resistant construction.
7. Tsai, K.C., Li, J.W., Hong, C.P., Chen, H.W. and Su, Y.F. – Welded steel triangular plate device for seismic energy dissipation. Proceedings of the ATC-17-1 Seminar on Seismic Isolation, Passive Energy Dissipation, and Active Control, California, San Francisco 1993(b).
8. Tsai, K.C., Chen, H.W., Hong, C.P., and Wang, T.F. – Steel plate energy absorbers for improved earthquake resistance. Proceedings of the ASCE Structures Congress, California, Irvine 1993(c).
9. LESSLOSS - Deliverable D36 - Analysis of shake table test SHS. 2007.
10. LESSLOSS - Deliverable D31 – Characterisation tests of SH elements. 2007.
11. EN1993-1-1, Eurocode 3: Design of steel structures - Part 1-1: General rules and rules for buildings. Brussels: Comitee Europeen de Normalisation (CEN); 2003.
12. EN1998-1-1, Eurocode 8: Design of structures for earthquake resistance – Part 1-1: General rules, seismic actions and rules for buildings. Brussels: Comitee Europeen de Normalisation (CEN); 2003.
13. EN 15129: Anti-seismic devices, Brussels: Comitee Europeen de Normalisation (CEN); 2010.
14. RFEM 5 – Reference Manual. Dlubal.
15. FEMA – P695: Quantification of building seismic performance factors, Washington; 2009.

## 12 MOON-SHAPED STEEL HYSTERETIC DEVICE (MSSH)

### 12.1 INTRODUCTION

Steel Hysteretic Devices (SHD) are anti-seismic devices and represent an effective solution to increase the capability of structures to dissipate seismic energy by plastic deformation resp. yielding. Yield may be obtained through uniaxial tension (or compression), shear, torsion and bending.

Among SHD the Moon Shaped Steel Hysteretic (MSSH) device, shown in Fig. 12.1, was developed as damper for base isolated structures. The isolator consists of a flat surface slider resp. elastomeric bearing and MSSH devices (see Fig. 12.2).

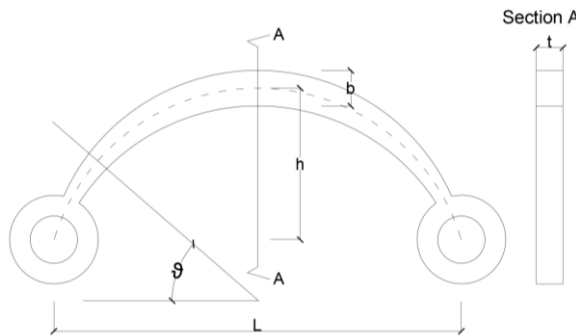


Fig. 12.1: General Geometry of the Moon Shaped Steel Hysteretic Device



Fig. 12.2: Moon Shaped Steel Hysteretic Devices combined with a Lead Rubber Bearing as isolator unit

For dampers as part of isolators it was supposed to be able of great displacements with a low to moderate force resistance. The purpose within INNOSEIS is to insert the MSSH devices into dissipative bracing systems and outline a design guideline for application in structures regarding the relevant Codes and Standards.

### 12.2 DESCRIPTION OF THE MOON SHAPED STEEL HYSTERETIC DEVICE

The sketches in Fig. 12.3 show a Moon Shaped Hysteretic (MSSH) device that is exposed first to a horizontal tension force,  $F_1$ , and then to a horizontal compression force,  $F_2$ . The device is symmetric in respect to the Y-axis. The bending moment  $M(\theta)$  and the axial force  $N(\theta)$  are variable with the sinus, while the shear force  $Q(\theta)$  is variable with the cosine.

Looking at the different deformed shape in Fig. 12.3 for tension and compression forces applied it may be deduced that the behaviour is not symmetric, at least in the plastic field where the deformations are unneglectable (Fig. 12.4). In the elastic field, where the deformations are neglectable, the behaviour it is almost symmetric. In case of tension the element is lowered (i.e. the lever arm decreases), therefore it will need a bigger applied force to reach the maximum allowed displacement for the

device, and instead in case of compression the element raises (h, i.e. the lever arm h, increases) therefore a lower force is needed to reach the maximum allowed displacement.

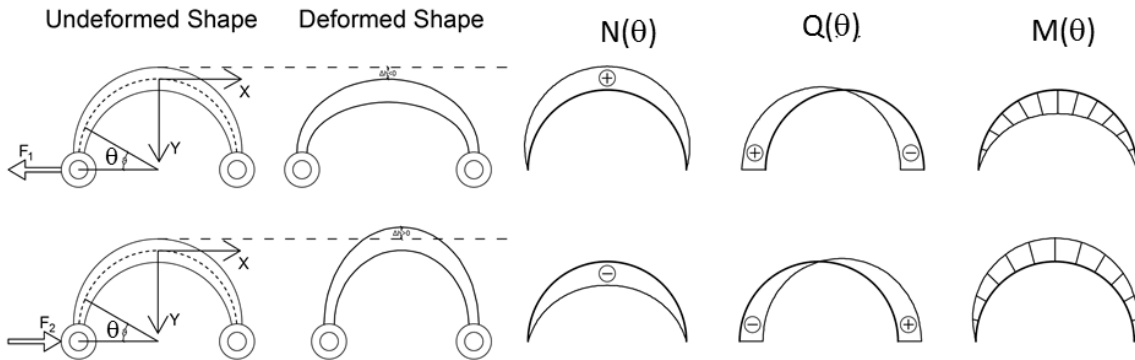


Fig. 12.3: Undeformed and Deformed shape, Bending, Shear and Axial effects on MSSH element exposed to a horizontal tension and compression force.

To reach a high strain for the MSSH device without material failure, the utilized steel has to possess the characteristics of very distinctive flow behaviour. The curved hysteretic gradient of the steel hysteretic dampers is influenced through the element design. In Fig. 12.4 it shows the force-displacement diagram of a MSSH element developed and tested as base isolation damper.

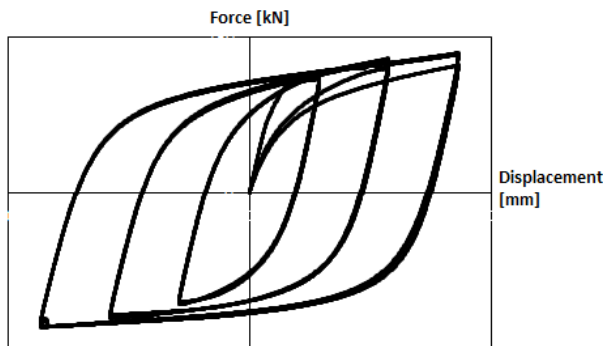


Fig. 12.4: Force displacement curves of a MSSH Device

The innovative seismic resistant system with MSSH devices consists in the introduction of these devices at every storey of a building: considering a concentric bracing system, the devices are introduced at the end of every brace element. Under strong seismic motion inelastic deformations are restricted to the MSSH devices, which dissipate a large amount of input energy, leaving the rest of the structure elastic and undamaged.

Repair works are easy, since they are restricted to the MSSH devices which are not subjected to vertical loads, as they are placed between storey levels.

The devices are easy to replace and manufacture, offering a cost-effective solution.

## 12.3 STRUCTURAL MODELS

### 12.3.1 Constitutive Model for MSSH Device

#### 12.3.1.1 Bilinear Force-Displacement loop based on test data

The response of any metallic damper is a function of its geometry and the mechanical characteristics of the metal from which it is manufactured. The best approximation of the nonlinear behaviour of steel hysteretic devices is to use experimental data obtained from component testing according to EN 15129 [1], section 12.6.

For incorporating a nonlinear displacement dependent device (see [1]) into a numerical structural model, the measured curved force-displacement loops of steel hysteretic devices are usually approximated by a bilinear hysteresis loops with an initial stiffness  $K_1$ , a post elastic stiffness  $K_2$  and a yield force  $F_y$ . The method adopted here for selecting a bilinear approximation to a hysteresis loops is shown in Fig. 12.5.

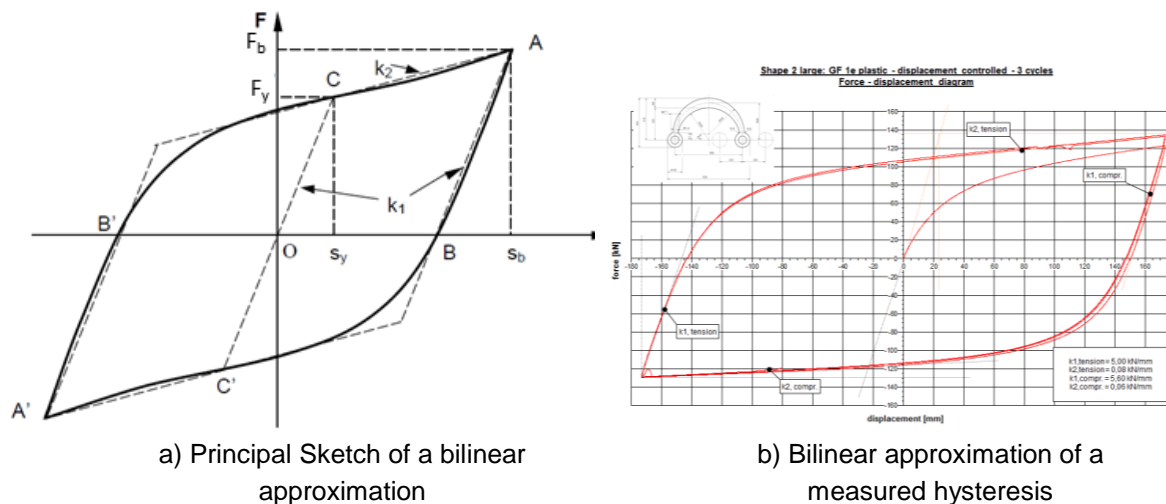


Fig. 12.5 a)-b): Bilinear approximation to a curved hysteresis loop.

The curved loop  $A'B'CABC'A'$  might be not symmetric about the centre  $O$ , and the coordinates of vertices  $A$  and  $A'$  are the maximum displacements  $\pm s_b$  and the maximum force  $\pm F_b$ .

- The initial stiffness  $k_1$  is approximated by the slope of the parallel lines  $AB$  and  $A'B'$  where  $B$  and  $B'$  are the loop intercepts on the x-axis.
- The yield stiffness  $k_2^+$  and  $k_2^-$  are approximated by the slope of the lines  $AC$  and  $A'C'$  where  $CC'$  is the line through  $O$  with slope  $k_1$ .
- The coordinates of point  $C$  ( $s_y, F_y$ ) are the yield displacement and the yield force respectively for the approximation to the curved hysteresis loop.

The bilinear loop parameters change rapidly with the maximum strain amplitude  $\epsilon_m$  at low strain, but more slowly at larger strain. In practice, these parameters changes do not introduce large errors to seismic based on bilinear loops, since seismic responses are dominated by relatively large strain, with slowly varying parameters.

With fixed values of  $k_1$ ,  $k_2$  and  $F_y$  the bilinear loops nest on a two slope generating curve with a fixed starting point.

### 12.3.1.2 Bilinear Force-Displacement loop based on Scaling Factor Method

The response of any metallic damper is a function of its geometry and the mechanical characteristics of the metal from which it is manufactured and the fixing resp. the clamping conditions.

The family of force-displacement loops for a bending-beam damper can be scaled on the basis of a simple model, to give a set of stress-strain curves. Approximate force-displacement loops for a wide range of steel-beam dampers can then be obtained from the scaled stress-strain curves.

The scaling factors  $\varphi$  and  $\delta$  are based on a greatly simplified but effective model of the yielding beam. The extreme-fibre strains  $\varepsilon_{SC}$  are based on the shape which the beam would assume if it remained fully elastic. The nominal stresses  $\sigma_{SC}$  are related to the force-scaling factor  $\varphi$  on the assumption that they remain constant over a beam section (as they would for a rigid-plastic beam material). The index SC is introduced to emphasize the nominal nature of the stresses and moduli derived using the uniform-stress assumption.

The relevant properties of a bilinear approximation of the force-displacement loop can be determined:

$$k_1 \approx \frac{\varphi}{\delta} \cdot E_{1,SC} \quad \text{Eq. (12.1)}$$

$$k_2 \approx \frac{\varphi}{\delta} \cdot E_{2,SC} + \alpha \cdot F_y \cdot s_b \cdot \left(1 + \frac{\varepsilon_{y,SC}}{\varepsilon_{b,SC}}\right) \quad \text{Eq. (12.2)}$$

$$F_y \approx \varphi \cdot \sigma_{SC} \quad \text{Eq. (12.3)}$$

$$s_u \approx \delta \cdot \varepsilon_{b,SC} \quad \text{Eq. (12.4)}$$

$$s_y \approx k_1 \cdot F_y \quad \text{Eq. (12.5)}$$

$$F_b \approx F_y + k_2 \cdot (s_u - s_y) \quad \text{Eq. (12.6)}$$

The derivation of scaled stress-strain properties are described in section 12.4.4.

The scaling factors  $\varphi$ ,  $\alpha$  and  $\delta$  depend on the geometry of the MSSH device.

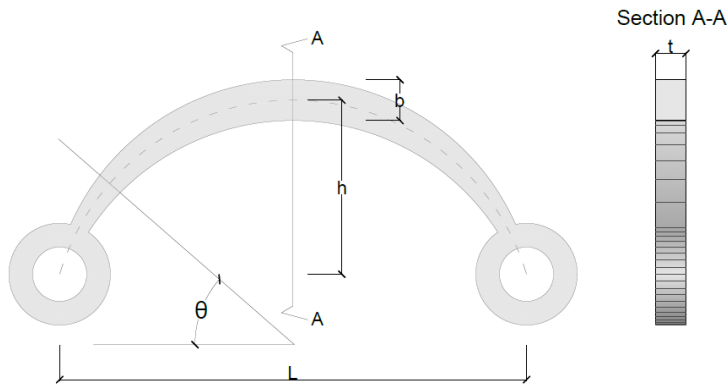


Fig. 12.6: Parametric dimensions of a MSSH element



Parameters  $t$ ,  $b$ ,  $h$ ,  $L$ , and the curved outlines (contour) of the hysteretic element define the geometry of the reference prototype. The outlines can be parabolic, elliptic or circular, the latter being the simplest and thus the most commonly used.

Force scaling factor for a rectangular section with height  $b/t$  and lever arm  $h$ :

$$\varphi = \frac{tb^2}{6h} \quad \text{Eq. (12.7)}$$

Displacement scaling factor:

$$\delta(\theta) = 2 \cdot \frac{h^2}{b} \cdot 1,32 \cdot \sin(\theta) \quad \text{Eq. (12.8)}$$

Large deflection correcting factor:

Another factor has to be considered in order to take into account the variation in the slope of the force – displacement loop for large yield displacements. This element has a symmetric behaviour in the elastic field but not symmetric above the yielding point. For large yield displacements, the second order effects cannot be neglected, for the MSSH device the changing of the parameter  $h$  during the load cycle is the most important effect to be considered.

$$\alpha = \begin{cases} \frac{+1}{|s|(2h-s)} & \text{Tension} \\ \frac{-1}{|s|(2h-s)} & \text{Compression} \end{cases} \quad \text{Eq. (12.9)}$$

It should be noted that here are four main sources of error in the damper loops and parameters:

- Differences between the material properties of the hysteretic beam used to generate the stress-strain loops and the material properties of the hysteretic beam in the prototype.
- End-effects and non-beam deformations. End-effects usually reduce the initial stiffness by about 50%.
- Alteration of loop loads, for a given displacement, by changes in the shape of the damper under large deflections. Shape changes can reduce or increase the post-yield or plastic stiffness.
- Small changes in the damper loops caused by secondary forces.

If damper loops are derived from models of similar proportions and exactly the same material (same batch), the scale-model method partially eliminates the four sources of error given above. In this case, the scaling factor method can be handsome to

reduce testing. Nevertheless, before implementing MSSH devices into a structure, the testing procedure according to EN 15129 [1] have to be considered.

### 12.3.2 Modelling system with MSSH bracings

The dissipative parts of the system are the MSSH devices. They are designed to deform and, by deformation, to dissipate energy. The other parts of the structure shall remain elastic. To understand what happens in the ultimate limit state of the system only one frame is taking into account and the behavior is studied (see Fig. 12.7).

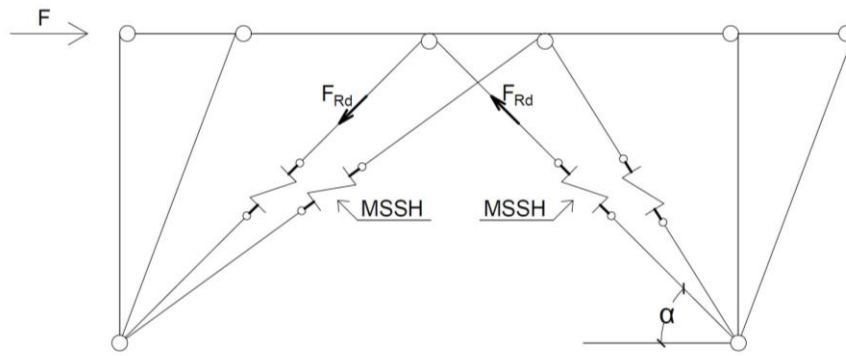


Fig. 12.7: Sketch of the behaviour of the structure.

The braces are directly connected to the hysteretic devices, their axial force, in the ultimate state limit, is equal to the  $F_{Rd}$  of the MSSH device.

$$N_{Ed,Brace} = N_{Rd,MSSH} \quad \text{Eq. (12.10)}$$

The braces transmit to the beam a vertical force resp. shear, that can be calculated using  $N_{pl,Rd,MSSH}$  for the brace in tension and  $0.3 \cdot N_{pl,Rd,MSSH}$  for the brace in compression. The factor 0.3 is suggested by EN1998-1-1 [2] and used for the estimation of the post buckling resistance of diagonals in compression.

$$V_{Ed,Beam} = \frac{0.7}{\sin(\alpha)} N_{Rd,MSSH} \quad \text{Eq. (12.11)}$$

The stresses in columns can be calculated doing a global equilibrium using the symmetry of the system:

$$N_{Ed,Columns} = \frac{Fh}{L} - \frac{N_{Rd,MSSH}}{\sin(\alpha)} \quad \text{Eq. (12.12)}$$

Where:

- h is the interstorey height;
- L is the span between two columns;
- F is the external load applied, as in Fig. 12.7
- $\alpha$  is the inclination of the braces.

## 12.4 EXPERIMENTAL INVESTIGATIONS ON MSSH DEVICES

### 12.4.1 General

The MSSH steel hysteretic element uses following physical properties to disappear energy:

- yield of the steel material as a consequence of high bending strain and
- to transform movement energy to thermal and deformation energy.

One type of a MSSH is shown in Fig. 12.8 and Fig. 12.9, which is designed like a moon shape and it uses bending to obtain the yielding. Bending is the most commonly used way to stress the dissipating elements in MSSH and damping devices which rely on the plastic deformation of metals have been found to be very economic and reliable.

### 12.4.2 Test specimen and loading protocol

Two different test specimen (see Fig. 12.8 and Fig. 12.9) made from the two different steel plates with steel grade S355J2+N were loaded cyclically in tension and compression. The loading protocol is given in Table 12.1.

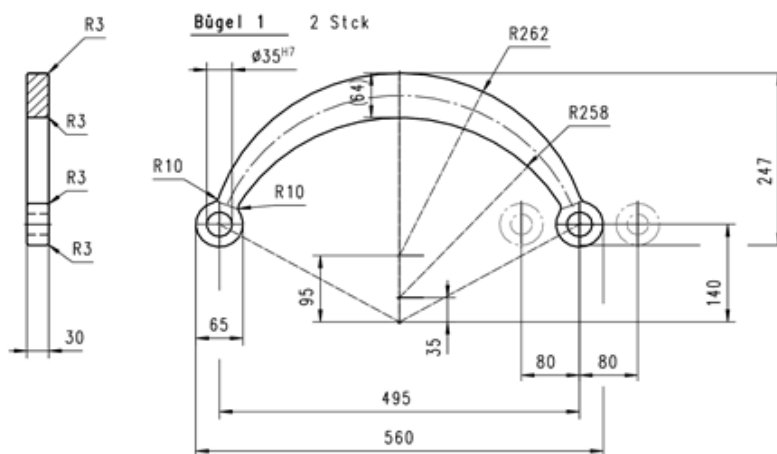


Fig. 12.8: Geometry of the MSSH device “Small” tested.

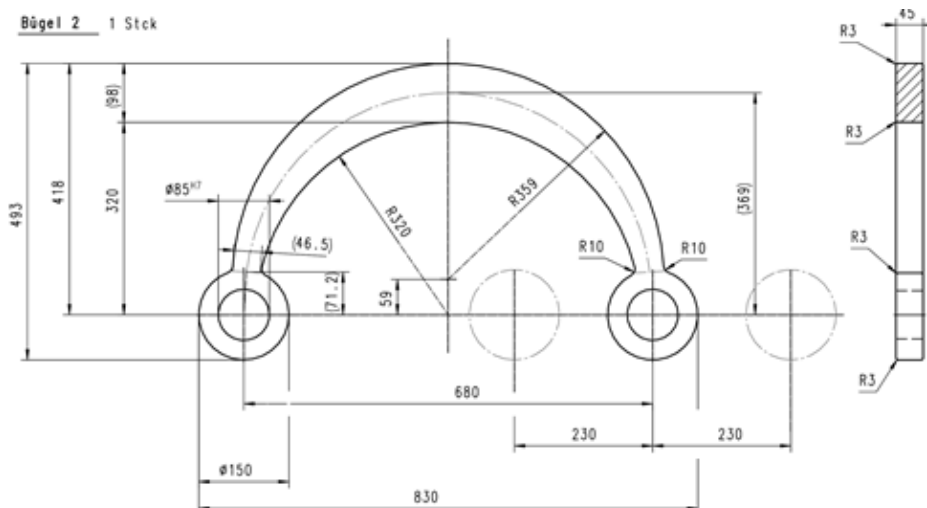


Fig. 12.9: Geometry of the MSSH device “Large” tested

**Table 12.1: Loading protocol of the MSSH tests**

No. of cycles	MSSH device “small”		MSSH device “large”	
	Amplitude [mm]	Velocity [mm/s]	Amplitude [mm]	Velocity [mm/s]
3	$\pm 3$	4		
	$\pm 5$		$\pm 15$	10
	$\pm 20$	10	$\pm 60$	
	$\pm 40$		$\pm 115$	25
	$\pm 60$		$\pm 175$	
9	$\pm 80$		$\pm 230$	

The tests were conducted with a Zwick servo-hydraulic Universal Testing Machine at Materials Testing Institute for Civil Engineering at Technical University Munich (see Fig. 12.10).



a) Test Specimen “Large”



b) Test specimens “Small” and “Large”

Fig. 12.10a)-b): Tested MSSH devices

### 12.4.3 Test Results

Tests show a stable and very high post-elastic stiffness (Fig. 12.11) with a significant inelastic plateau, indicative of good seismic behaviour.

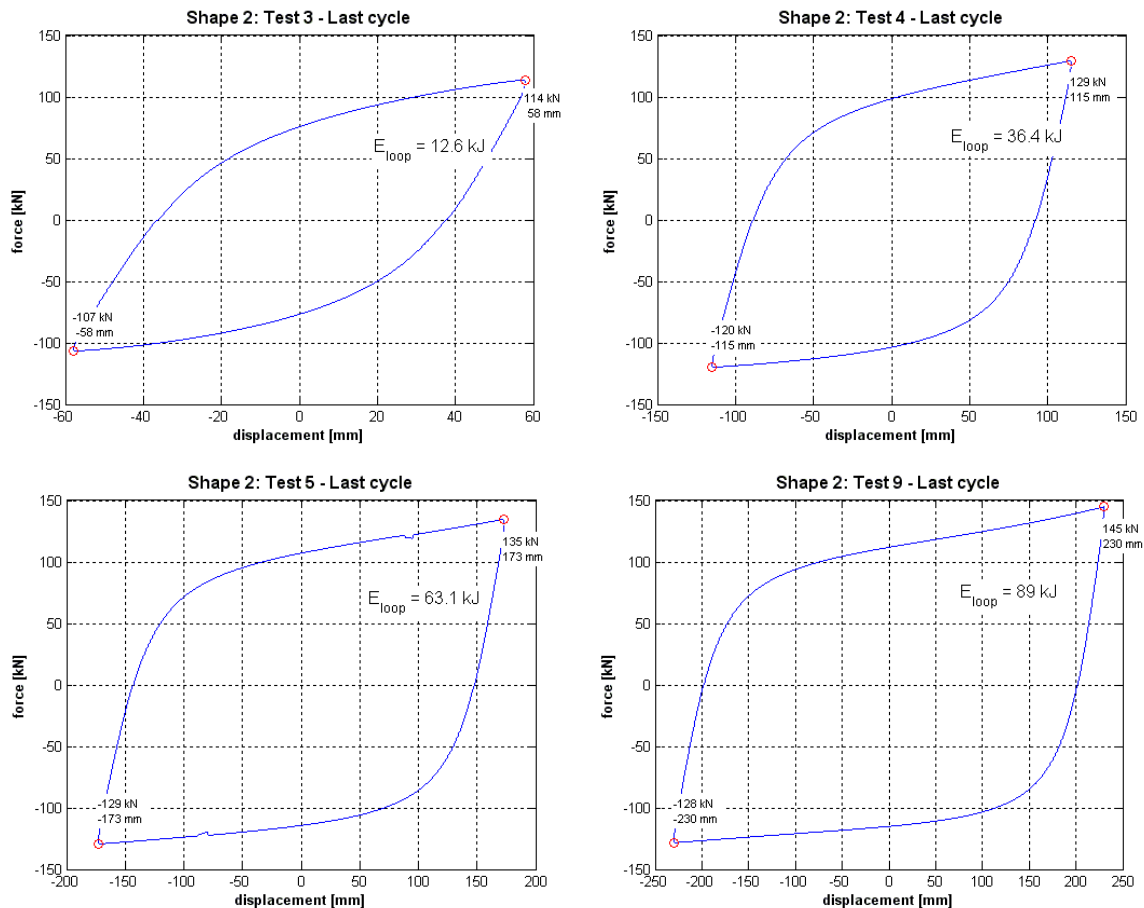


Fig. 12.11: Different Experimental Force – Displacement Diagrams of a MSSH Device “Large” (3<sup>rd</sup> cycle)

The main requirement for the functionality of a steel hysteresis damper is a satisfactory plastic ductility during the violent phase of an earthquake. For this reason, it is very important that alternating plasticizing must not lead to low cycle fatigue or brittle failure. As indicated in Fig. 12.12, mild steel is able to withstand high plastic energy dissipation for a certain period of time. The number of acceptable cycles depends on the strain rate (Note the logarithmic scale on the abscissa).

It is therefore essential to know the height of amplitudes particularly at critical locations of the device to check functionality and reliability. Time history analysis with several, natural or artificial accelerograms are necessary to evaluate the load impact on the MSSH.

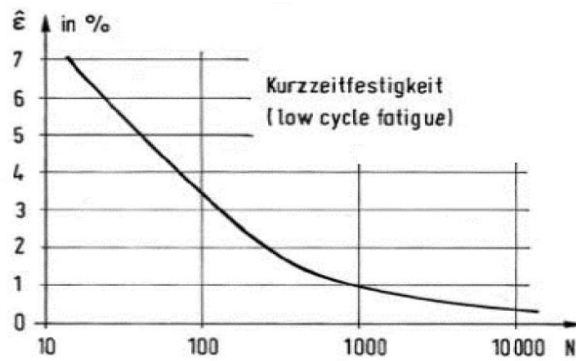


Fig. 12.12: A characteristic low cycle fatigue curve of mild steel (The strain amplitude versus the number of cycles to failure)

#### 12.4.4 Experiment based Modelling using Scaling Factors

The experimental force-displacement loops of MSSH device “small” and “large” are used to derive scaled stress strain curves (see Fig. 12.13 and Fig. 12.14) using the scaling factors  $\alpha$ ,  $\delta$  and  $\varphi$  given in section 12.3.1.2. The results in terms of elastic and plastic moduli, yield stress and yield strain for strains up to 9% are given in Table 12.2 and Table 12.3.

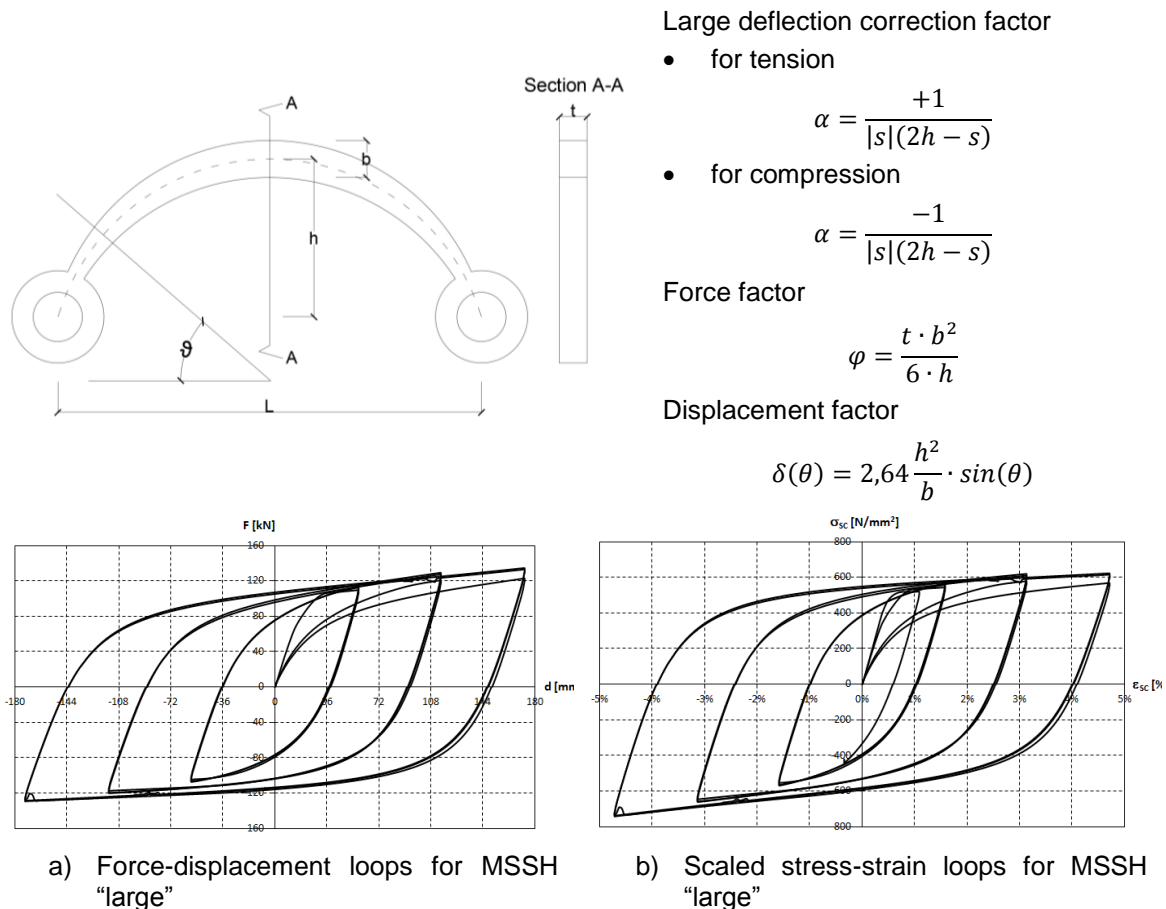
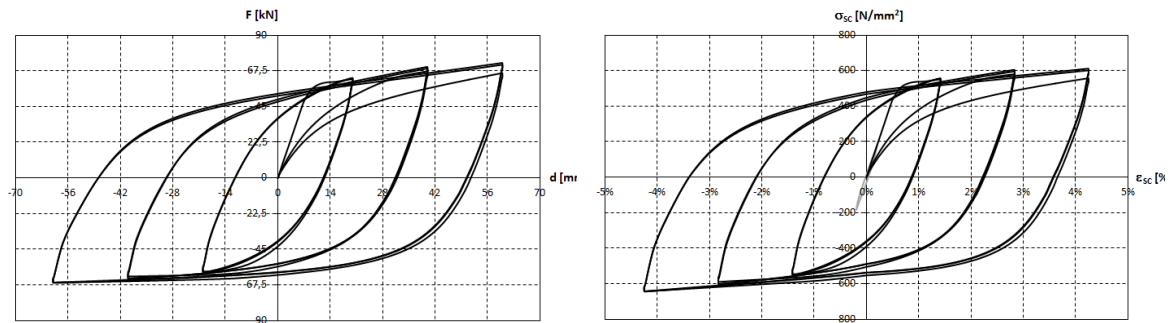


Fig 12.13: Force-Displacement and Scaled stress-strain loops for the small and large MSSH devices



c) Force-displacement loops for MSSH „small“

d) Scaled stress-strain loops for MSSH „small“

Fig. 12.13: Force-Displacement and Scaled stress-strain loops for the small and large MSSH devices (continuation)

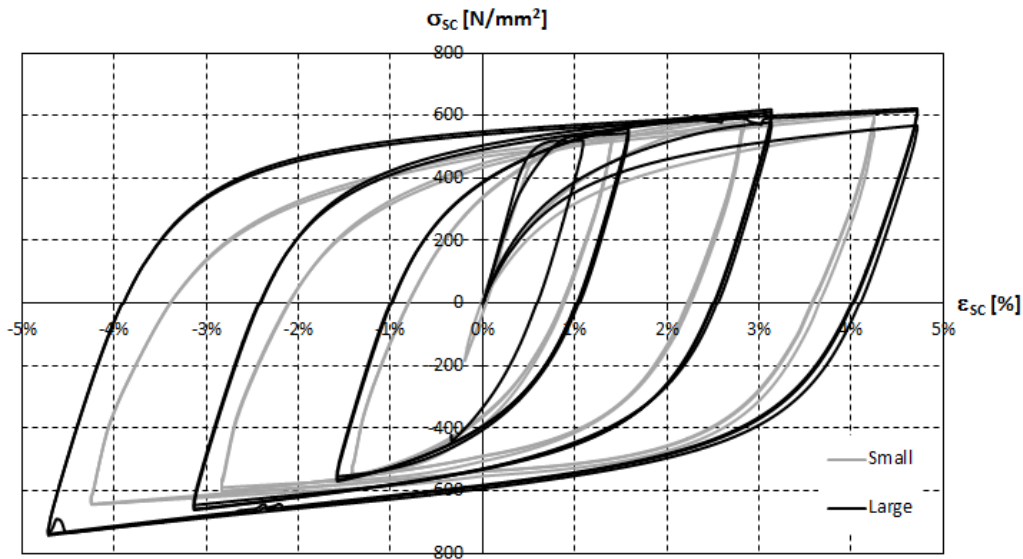


Fig. 12.14: Scaled stress-strain loops for the small and large MSSH device

Table 12.2: Approximated moduli, stress and strain up to strain amplitude of 9% in section A.

Section A ( $\theta = 90^\circ$ ; $\epsilon_{\min}$ )					
$\epsilon_{SC}$ [%]	$E_{1,SC}$ [N/mm <sup>2</sup> ]	$E_{2,SC}^+$ [N/mm <sup>2</sup> ]	$E_{2,SC}^-$ [N/mm <sup>2</sup> ]	$\sigma_{y,SC}$ [N/mm <sup>2</sup> ]	$\epsilon_{y,SC}$ [%]
1	103667	25769	17201	394	0,38
2		8740	7039	436	0,42
3		4643	4174	477	0,46
4		2964	2881	519	0,50
5		2093	2161	560	0,54
6		1575	1708	602	0,58
7		1238	1400	643	0,62
8		1005	1179	685	0,66
9		837	1013	727	0,70

**Table 12.3: Approximated moduli, stress and strain up to strain amplitude of 9% in section B.**

Section B ( $\theta = \theta_0; \varepsilon_{\max}$ )					
$\varepsilon_{SC}$ [%]	$E_{1,SC}$ [N/mm <sup>2</sup> ]	$E_{2,SC}^+$ [N/mm <sup>2</sup> ]	$E_2^-$ [N/mm <sup>2</sup> ]	$\sigma_{y,SC}$ [N/mm <sup>2</sup> ]	$\varepsilon_{y,SC}$ [%]
1	44527	32738	18110	316	0,71
2		11095	7406	334	0,75
3		5892	4390	352	0,79
4		3760	3029	370	0,83
5		2654	2271	388	0,87
6		1997	1795	405	0,91
7		1570	1471	423	0,95
8		1274	1239	441	0,99
9		1060	1064	459	1,03

When these equations are used to generate scaled stress-strain loops from force displacement loops they eliminate the large displacement increases in nominal stress, as it is evident from comparison of Fig. 12.13 a) and b) resp. c) and d).

The diagrams F-s for every cycle are shown in Fig. 12.15 and Fig. 12.16. In each diagram are shown the test results and the results derived with the scaling factor method.

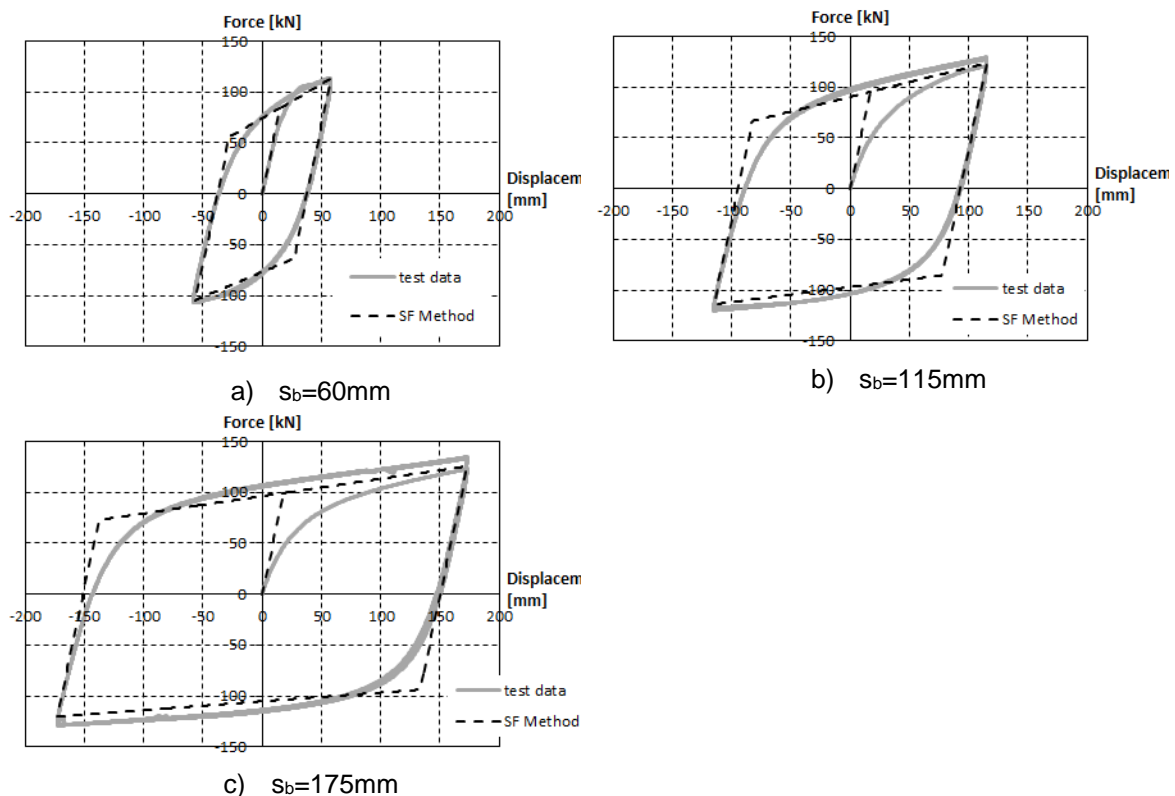


Fig. 12.15a)-c): Force-displacement diagrams of the large MSSH device and comparison with SF Method



It should be noted that the derived values given in Table 12.2 and Table 12.3 can be used for preliminary design of MSSH devices with similar material characteristics and same fixing conditions. A preliminary design of MSSH devices based on the Scaling Factor Method is not sufficient guaranteeing reliable behaviour of the device. It is only helpful for a predimensioning. Prototype tests and factory production control tests acc. EN 15129 [1] are strongly recommended, when implementing MSSH devices into a structure.

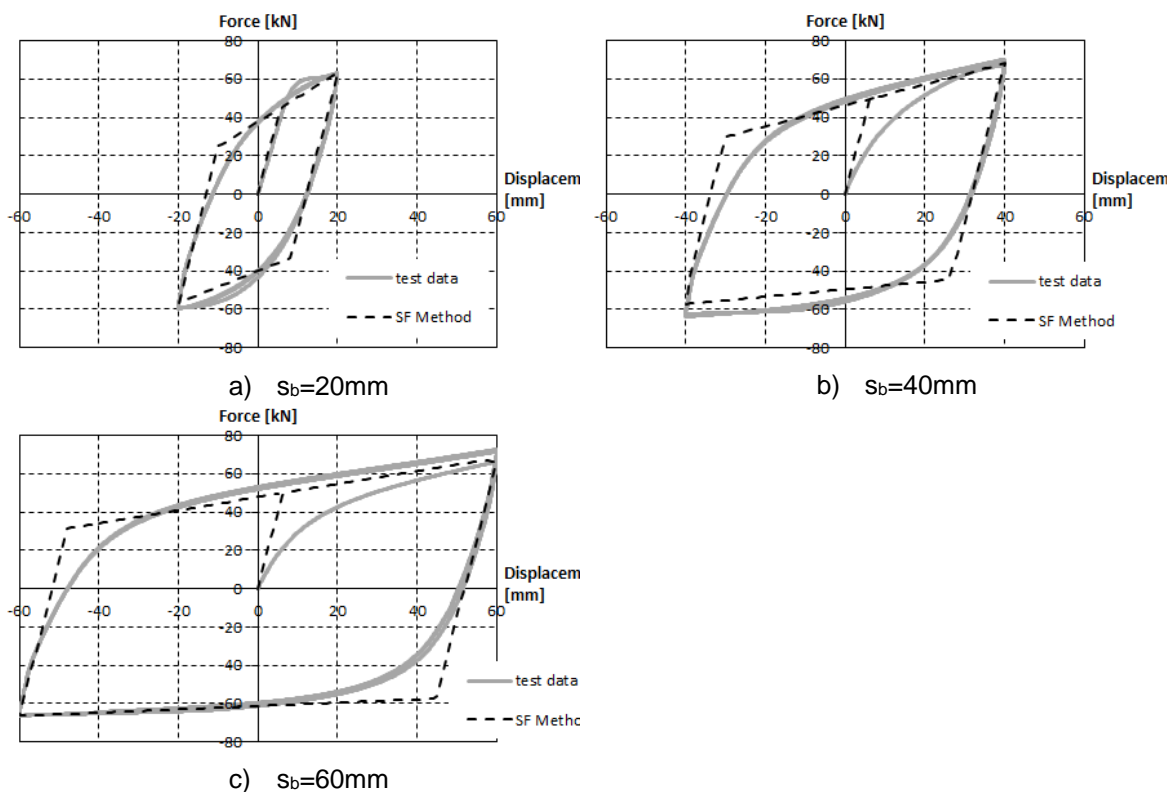


Fig. 12.16a)-c): Force-displacement diagrams of the small element and comparison with SF Method

## 12.5 DESIGN RULES

### 12.5.1 General

When the MSSH devices are used as dampers in base isolated structures, they need a low elastic resistance to increase the natural period of the isolated structure as much as possible. The MSSH devices are now applied to braced structures. Precisely, they are put in series with the braces. This location allows the devices to work properly, when the braces are subjected to axial force. Compared to the MSSH devices for base isolation the MSSH devices for structural braces have to dissipate energy at rather moderate displacements to keep the threshold of the allowable interstorey displacements resp. the stresses in the adjacent members within elastic region. To reach this goal the geometry of the test specimen shown in section 12.4

is not appropriate. Thus, the geometry is changed and several devices are put in parallel in order to increase resistance and stiffness of the “joints”.

These changes improve the mechanical characteristics without reducing the ductility and the area of the hysteretic cycle. Ductility and damping are the crucial properties for base isolation and are still necessary in the new damping system. The shape of the hysteretic cycle is now changed, in fact the displacements are reduced but the resistance is increased, thus the dissipation of energy is still present and copious enough to satisfy the structure requirements.

Conclusions from the analytical and numerical studies are summarized in a design guide for practical applications. The design methodology is based on the provisions of EN 1993-1-1 [17], EN 1998-1-1 [2] and EN15129 [1]. Some clauses of EN 1998-1-1 are appropriately rearranged to cover the use of the MSSH elements by the normal Code provisions.

#### 12.5.2 Preliminary Design of MSSH devices

As previously mentioned the MSSH system works as a brace system. Considering that the MSSH devices resist alone the lateral loads of the structure, a rough estimation of the required number of MSSH device for a building in each direction and the type of their cross sections can be made from the theoretical limit state model of the system. This calculation is based on the assumption that at the ultimate limit state all MSSH devices reach, as the dissipative elements of the system, their axial force capacity.

$$N_{Ed} \leq N_{Rd} \geq \gamma_x \cdot \gamma_b \cdot F_i \cdot \frac{\sin(\alpha)}{4} \quad \text{Eq. (12.13)}$$

Where:

- $F_i$  is the horizontal force acting on storey  $i$  calculated according to EN1998-1-1, section 4.3.3.2.3 [2]
- 4 is the number of groups of MSSH element of every storey
- $\alpha$  is the inclination of the braces ( $45^\circ$  in the case study).

$$F_{Rd,t,i} = n_i \cdot F_{y,t,i} \geq \gamma_x \cdot \gamma_b \cdot F_{b,i} \quad \text{Eq. (12.14)}$$

$\gamma_x=1,2$  is the reliability factor and  $\gamma_b=1,1$  is the partial factor for the device acc. to EN 15129 [13].

#### 12.5.3 Design for linear elastic analysis

The design rules are intended to ensure that yielding, will take place in the hysteretic devices prior to any yielding or failure elsewhere. Therefore, the design of buildings with MSSH devices is based on the assumption that these devices are able to dissipate energy by the formation of plastic bending mechanisms. The following

design methodology may be applied:

### 1) Simulation

In the current state of the art, a building with MSSH device may be simulated with a linear-elastic model by appropriate brace elements. The brace elements containing and representing the MSSH devices are divided in two parts, with the same cross sections, connected in the middle with an appropriate hinge that represent the MSSH device. That hinge does not allow the rotations and the shear deformation, but as the real MSSH devices allowed the axial deformation reacting like a linear spring. The brace elements, because they must stay in the elastic field without being damaged during the earthquake, have to be projected over strength to the MSSH devices.

### 2) Analysis

Static linear analysis is performed under dead and live loads and the members of the main frame are dimensioned according to the provisions of EN1993-1-1 [17] at ULS and SLS. The conventional method for the calculation of internal forces under seismic loading is Multi-Modal Response Spectrum Analysis, where the number of modes of vibration considered in each direction is such that the sum of the effective mass is at least equal to 85% of the total mass and there are no modes with mass participating > 5%. The design spectrum shall be defined with a maximum behavior factor equal to 3, which was confirmed through non-linear static analyses (Pushover).

### 3) Limitation of interstorey drift

Limitation of interstorey drift ensures the protection of non-structural elements under seismic loading and consists a basic criterion for the design of MSSH devices. It provides an estimation of the damage for different performance levels and defines the distribution of stiffness within the structure and eventually the size and type of the cross sections applied to the system.

In linear analysis, the displacements induced by the design seismic action  $d_s$  shall be calculated on the basis of the elastic deformations  $d_e$  of the structural system through the expression:

$$d_s = q \cdot d_e \quad \text{Eq. (12.15)}$$

The design interstorey drift  $d_r$  is defined as the difference of the average lateral displacements at the top and bottom of the story under consideration. Depending on the type of the non – structural elements (brittle materials, ductile or not connected) and the importance class of the building, the design interstorey drift  $d_r$  is compared to the corresponding values of the FEMA. The optimal design is achieved when the maximum interstorey drifts of every storey is almost constant in all the structure.

Since the horizontal displacements are multiplied by the behaviour factor the limitation of interstorey drift does not depend on it.

#### 4) 2<sup>nd</sup> order effects

The possible influence of 2<sup>nd</sup> order effects shall be controlled by the limitation of the interstorey drift sensitivity coefficient  $\theta$  below the limit values of the EN1998-1-1. Coefficient  $\theta$  is calculated from Equation (12.16) for each floor at x and y directions of the building.

$$\theta = \frac{P_{tot} \cdot d_r}{V_{tot} \cdot h_{story}} \quad \text{Eq. (12.16)}$$

Where  $P_{tot}$  is the total gravity load at and above the story considered in the seismic design situation and  $V_{tot}$  is the seismic storey shear.

Alternatively, the interstorey drift sensitivity coefficient  $\theta$  may be calculated more accurately by a linear buckling analysis through the factor  $\alpha_{cr}$ , the factor by which the design loading would have to be increased to cause elastic instability in a global mode. The analysis is carried out under conditions of the constant gravity loads of the seismic combination  $(1,0 \cdot G + 0,3 \cdot \varphi \cdot Q)$  and produces the buckling modes. The modes that move the building at x and y directions are chosen and the correspondent  $\alpha_{cr}$  values are calculated as follows:

$$\alpha_{cr} = \frac{1}{\theta} = \frac{F_{cr}}{F_{Ed}} \quad \text{Eq. (12.17)}$$

Where  $F_{cr}$  is the elastic critical buckling load for global instability mode based on initial elastic stiffness and  $F_{Ed}$  is the design loading for the seismic combination.

To take into consideration the inelastic displacements of the building,  $\alpha_{cr}$  shall be divided by the q factor. The values of  $\theta$  in this case are given by Equation (12.18).

$$\theta = \frac{q}{\alpha_{cr}} \quad \text{Eq. (12.18)}$$

The relevant EN1998-1-1 provisions require for buildings that the interstorey drift sensitivity coefficient is limited to  $\theta \leq 0.1$ , if second order effects are ignored. If  $0.1 < \theta < 0.2$ , second-order effects may approximately be taken into account by multiplying the relevant seismic action effects by a factor equal to  $1/(1 - \theta)$ . If  $0.2 < \theta < 0.3$  a more accurate second order analysis applies. In any case, it shall be  $\theta < 0.3$ .

### 5) Dissipative devices and braces verifications

The MSSH devices and the braces shall be verified to resist the internal forces of the most unfavourable seismic combination and fulfil the following conditions:

#### f) Slenderness

In frames with V bracings, the non-dimensional slenderness  $\lambda$  should be less than or equal to 2,0.

$$\lambda = \sqrt{\frac{A \cdot f_y}{N_{cr}}} \quad \text{Eq. (12.19)}$$

#### g) Axial Force

The non-dissipative brace elements shall be capacity designed for increased values of internal forces compared to the ones derived from the analyses with the most unfavourable seismic combination, to ensure that the failure of the dissipative elements occurs first. The yield resistance  $N_{pl,Rd}$  of the cross-section of the diagonals should be such that:

$$N_{Pl,Rd,brace} \geq 1.1 \cdot \gamma_{ov} \cdot N_{pl,Rd,MSSH} \quad \text{Eq. (12.20)}$$

Where:

- $\gamma_{ov}$  is the over strength factor,  $\gamma_{ov} = 1,25$  for steel S355
- $N_{pl,Rd,MSSH}$  is the ultimate resistance of the MSSH device connected.

#### h) Dissipative behaviour constant in height

To achieve a distributed dissipative behaviour in the structure, it should be checked that the maximum ratios  $\Omega$  over the entire structure does not differ from the minimum value  $\Omega$  by more than 25%.

$$\frac{\max \Omega}{\min \Omega} \leq 1.25 \quad \text{Eq. (12.21)}$$

### 6) Non-dissipative elements verifications: columns.

The non-dissipative elements, the system columns, the beams and their connections, shall be capacity designed for increased values of internal forces compared to the ones derived from the analyses with the most unfavourable seismic combination, to ensure that the failure of the dissipative elements occurs first.

- g) The columns shall be verified to resist the capacity design action effects as following:

$$N_{Pl,Rd}(M_{Ed}) \geq N_{Ed,G} + 1,1 \cdot \gamma_{ov} \cdot \Omega \cdot N_{Ed,E} \quad \text{Eq. (12.22)}$$

Where:

- $N_{pl,Rd(MEd)}$  is the design buckling resistance of the beam or the column in accordance with EN 1993, taking into account the interaction of the buckling resistance with the bending moment  $M_{Ed}$ , defined as its design value in the seismic design situation;
- $N_{Ed,G}$  is the axial force in the beam or in the column due to the non-seismic actions included in the combination of actions for the seismic design situation;
- $N_{Ed,E}$  is the axial force in the beam or in the column due to the design seismic action;
- $\gamma_{ov}$  is the over strength factor,  $\gamma_{ov} = 1,25$  for steel S355
- $\Omega$  is the minimum value of  $\Omega_i = N_{pl,Rd,i} / N_{Ed,i}$  over all the MSSH devices of the braced frame system; where
  - $N_{pl,Rd,i}$  is the design resistance of MSSH device  $i$ ;
  - $N_{Ed,i}$  is the design value of the axial force in the same MSSH device  $i$  in the seismic design situation.

7) Non-dissipative elements verifications: beams.

- The beams have been considered as composite beam concrete – steel, using the collaboration of the slab. The resistant mechanism is the one shown in Fig. 12.17.

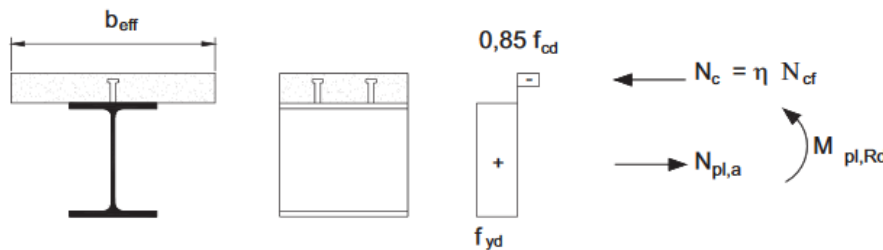


Fig. 12.17: Plastic strain distribution at ULS in order to calculate the  $M_{pl,Rd}$  positive.

The unbalanced vertical seismic action effect applied to the beam by the braces after buckling of the compression diagonal. This action effect is calculated using  $N_{pl,Rd,MSSH}$  for the brace in tension and  $\gamma_{pb} \cdot N_{pl,Rd,MSSH}$  for the brace in compression:

$$V_{Ed} = 1.1 \cdot \gamma_{ov} \cdot N_{pl,Rd,MSSH} \cdot \frac{1-\gamma_{pb}}{\sin(\alpha)} \quad \text{Eq. (12.23)}$$

#### 12.5.4 Design for non-linear analysis (Pushover)

1) The structural model used for elastic analysis shall be extended to include the response of structural elements beyond the elastic state and estimate expected plastic mechanisms and the distribution of damage.

2) Pushover analysis was carried out with RFEM v5.07.11 by Dlubal . The non-linearity has been considered only for the MSSH element, the other elements have

been considered perfectly elastic. The behaviour diagram of the MSSH does not take into account of the hysteresis, because a quasi-static analysis has been carried out.

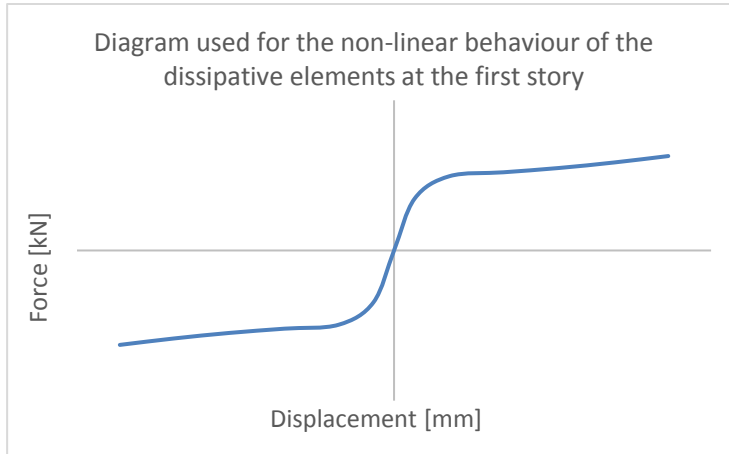


Fig. 12.18: Qualitative diagram used for the non-linear behaviour of the dissipative elements

**Table 12.4: Values used for the non-linear behaviour of the dissipative elements at every storey.**

Displacement [mm]	Force [kN]			
	first storey	second storey	third storey	fourth storey
-0,173	-1509	-1132	-755	-377
-0,139	-1407	-1055	-704	-352
-0,104	-1318	-989	-659	-330
-0,069	-1250	-937	-625	-312
-0,035	-1187	-890	-594	-297
-0,013	-829	-622	-415	-207
0	0	0	0	0
0,013	829	622	415	207
0,035	1187	890	594	297
0,069	1250	937	625	312
0,104	1318	989	659	330
0,139	1407	1055	704	352
0,173	1509	1132	755	377

## 12.6 ANALYSES OF A 2D BUILDING FRAME

Equations, element properties, design recommendations, critical checks and proposed behaviour factor, included in the Design Guide, are verified through numerical analyses on real 2D building frames with MSSH devices with the use of the software RFEM v.5.07.11 by Dlubal. Initially the frames are designed through elastic analysis at ULS and SLS. Nonlinear static analyses followed to investigate their behaviour beyond the elastic range and confirm the behaviour factor  $q=3$ .

## 12.6.1 Description of examined building frames

### 12.6.1.1 Geometry and assumptions

The case study presented hereafter is based on the extraction of a plane frame from a four-story building, see Fig. 12.19. The columns have rectangular hollow sections (SHS 200x200x16 for the first and the second floors and SHS 180x180x16 for the third and fourth floors) and the floor beams are composed of steel beams with wide flange I-sections (IPE400) that act compositely with the concrete slabs (C20/25, B450C). The braces have double UPN300 sections.

The columns are hinged at the base and the beams are hinged to the columns. The braces are also hinged to the frames. The structure has steel grade S355 and the MSSH devices have the same characteristic of the devices tested in section 12.4, the used steel is S355J2+N. The tests assure to know accurately the behaviour and the characteristics of the steel used for the applied devices.

Table 6.1 and

Table 12.6 summarize the geometric characteristics of the MSSH device.

**Table 12.5: Geometry of the used MSSH elements**

	b [mm]	h [mm]	t [mm]
MSSH	110	390	60

**Table 12.6: Number of MSSH used at every storey and resultant stiffness**

Number of MSSH at every storey		$K_{el}$ [kN/m]
4 <sup>th</sup>	2 MSSH	15138
3 <sup>rd</sup>	4 MSSH	30276
2 <sup>nd</sup>	6 MSSH	45414
1 <sup>st</sup>	8 MSSH	60551

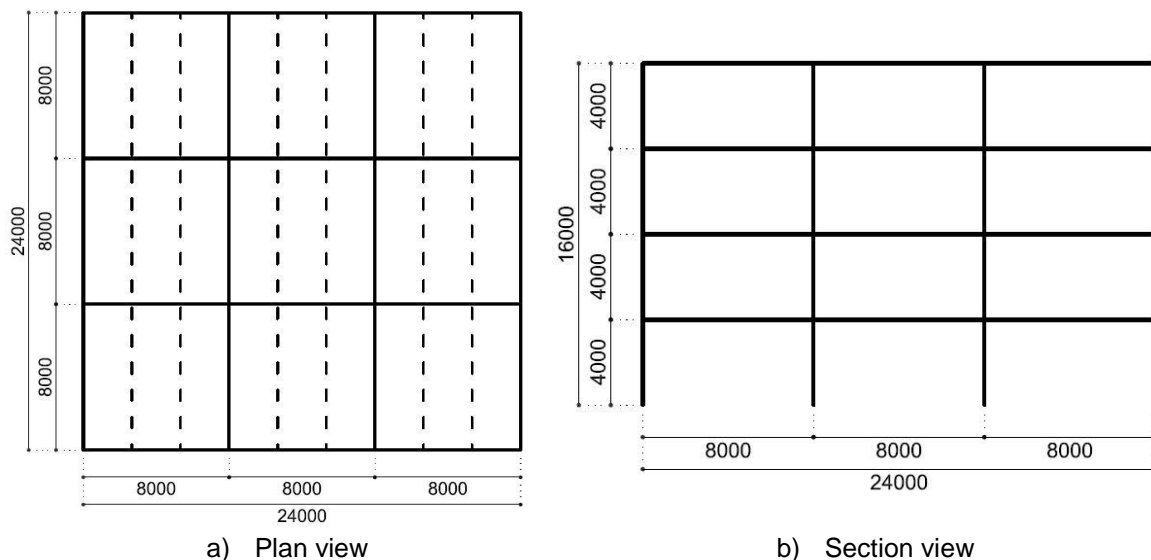


Fig. 12.19: Plane geometry and 2D building frame



### 12.6.1.2 Loads

Dead Loads ( $G$ ):

Steel self-weight:  $78.5 \text{ kN/m}^3$

Composite slab:

Concrete self-weight:  $25.0 \text{ kN/m}^3$

Steel sheeting: height 73 mm, thickness 1 mm

Total slab thickness: 150 mm

Equivalent uniform slab thickness: 110 mm

$g_{2,c} = 2.75 \text{ kN/m}^2$  (including steel sheeting)

Services, ceilings, raised floors:

$g_{2,fl} = 0.70 \text{ kN/m}^2$  for intermediate floors

$g_{2,rf} = 1.00 \text{ kN/m}^2$  for top floor

Perimeter walls ( $1.00 \text{ kN/m}^2$ ):

$g_{2,per} = 4.00 \text{ kN/m}$

Live Loads ( $q$ ) for offices (Class B):

$q = 3.00 \text{ kN/m}^2$

Movable partitions ( $\leq 2.00 \text{ kN/m}^2$ ):

$q_{add} = 0.80 \text{ kN/m}^2$

Total live load:

$q_{add} = 3.80 \text{ kN/m}^2$

Coefficient for the seismic combinations:  $\psi_2 = 0.6$

The roof is accessible

Snow load is ignored.

Seismic Load ( $E$ ):

Importance factor:  $\gamma_I = 1.0$

Peak ground acceleration:  $a_{gR} = 0.36g$

Ground Type B – Type 1 spectrum:

$S = 1.2, S = 1.2, T_B = 0.15s, T_C = 0.50s, T_D = 2.00s$

Vertical ground acceleration not accounted for.

### 12.6.2 Response spectrum analysis

Multi-modal response spectrum analysis is performed and the results are summarized in Table 12.7. The first three modes, which are translational, activated more than 95% of the mass, this assure there are not Eigen's Mode with participating mass  $> 5\%$  that have been not considered.

**Table 12.7: Participating mass ratio and periods**

Mode No	Eigen Period [s]	Participating mass ratio [%]	Total [%]
1	0.781	77.6	97.4
2	0.325	14.5	
3	0.200	5.3	

### 12.6.3 Seismic design

It is noted that for the seismic design following conditions are to be fulfilled in accordance with the design rules described in Section 5.2 and EN 1998-1-1 [13] rules.

#### 12.6.3.1 Limitation of interstorey drift

Considering that the building has ductile non-structural elements the following Equation (12.24) is checked.

$$d_r \cdot v \leq 0.0075 \cdot h = 30 \text{ [mm]} \quad \text{Eq. (12.24)}$$

Where  $v = 0.5$  is a reduction factor on the design displacements due to the importance class of the building (ordinary buildings) and  $h$  is the story height. Table 12.8 includes the results of the analysis; the check is verified for all storeys with values much lower than the limit value 30mm. The selection of the columns' and the receptacle beams' sections was defined by this check.

**Table 12.8: Limitation of interstorey drift.**

Storey	1	2	3	4
$d_{e,top}$ [mm]	9.5	21	34.1	48.6
$d_{e,bottom}$ [mm]	0.00	9.5	21	34.1
$d_r = (d_{e,top} - d_{e,bottom}) \cdot q$ [mm]	28.5	34.5	39.3	43.5
$d_r \cdot v$ [mm]	14.25	17.25	19.65	28.2

#### 12.6.3.2 2<sup>nd</sup> order effects

A linear buckling analysis for the seismic combination is carried out in order to control 2<sup>nd</sup> order effects. From this analysis, the critical buckling modes and the corresponding buckling factors derived.

The values of  $\theta$  were calculated from the critical buckling factors and it was checked whether 2<sup>nd</sup> order effects should be taken into account (Table 12.9). Since  $\theta < 0.1$ , 2<sup>nd</sup> order effects are neglected.

**Table 12.9: 2<sup>nd</sup> order effect: results.**

Storey	P [kN]	d <sub>r</sub> [mm]	V [kN]	h [mm]	θ [adm]	α [adm]
1	3769	28.5	525	4000	0.05	1
2	2698	34.5	462	4000	0.05	1
3	1670	39.3	365	4000	0.04	1
4	734	43.5	226	4000	0.04	1

### MSSH Devices and Braces

The MSSH devices are designed to resist the forces of the most unfavourable seismic combination  $1.0 \cdot G + 0.3 \cdot \phi \cdot Q + Ex$ . Table 12.10,

Table 12.11 and

Table 12.12 summarize the results of the braces and the MSSH devices verifications. Table 12.12 also includes the MSSH over strength values  $\Omega$  used to check the global dissipative behaviour of the system which is ensured when the  $\Omega$  values of all the MSSH in all stories differ no more than 25% of its minimum value.

**Table 12.10: Check of the slenderness of the braces.**

	A [cm <sup>2</sup> ]	f <sub>y</sub> [kN/cm <sup>2</sup> ]	EI [kNcm <sup>2</sup> ]	l <sub>o</sub> [cm]	N <sub>cr</sub> [kN]	λ [adm]
2UPN 300	117.6	30,87	56700000 0	565.7	1887	2

**Table 12.11: Check of the over strength of the Braces compared to the MSSH devices.**

	A [cm <sup>2</sup> ]	f <sub>y</sub> [kN/cm <sup>2</sup> ]	N <sub>Rd,B</sub> [kN]	N <sub>Rd,MSSH,max</sub> [kN]	N <sub>Rd,MSSH,max</sub> /N <sub>Rd,B</sub> [adm]
2UPN 300	117.6	30,87	3630.3	1509	0.42

**Table 12.12: Check of axial forces and overstrenght factor of the MSSH.**

Storey	N <sub>Ed,C</sub>   =  N <sub>Ed,T</sub>   [kN]	N <sub>Rd,C</sub> = N <sub>Rd,T</sub> [kN]	N <sub>Ed</sub> / N <sub>Rd</sub> [adm]	Ω [adm]
1	371	829	0.48	2.2
2	326	622	0.52	1.9
3	258	415	0.62	1.6
4	160	207	0.77	1.3

#### 12.6.3.3 Non-dissipative element: Columns

The columns shall be verified to resist the capacity design action effects as following:

$$N_{Pl,Rd}(M_{Ed}) \geq N_{Ed,G} + 1,1 \cdot \gamma_{ov} \cdot \Omega \cdot N_{Ed,E} \quad \text{Eq. (12.25)}$$

In the model, there are two kind of cross section, the most stressed have been checked:

1<sup>st</sup> and 2<sup>nd</sup> storey: SHS 200x200x16:

$$\begin{aligned}
 N_{Ed,G} &= 688 \text{ [kN]} \\
 N_{Ed,E} &= 507 \text{ [kN]} \\
 N_{Ed} &= 688 + 1.1 \cdot 1.25 \cdot 1.3 \cdot 507 = 1594 \text{ [kN]} \\
 N_{Pl,Rd}(M_{Ed}) &= 3550 \text{ [kN]} \\
 \frac{N_{Ed}}{N_{Pl,Rd}(M_{Ed})} &= \frac{1594}{3550} = 0.45
 \end{aligned}$$

3<sup>rd</sup> and 4<sup>th</sup> storey: SHS 180x180x16:

$$\begin{aligned}
 N_{Ed,G} &= 307 \text{ [kN]} \\
 N_{Ed,E} &= 113 \text{ [kN]} \\
 N_{Ed} &= 307 + 1.1 \cdot 1.25 \cdot 1.3 \cdot 113 = 509 \text{ [kN]} \\
 N_{Pl,Rd}(M_{Ed}) &= 3149 \text{ [kN]} \\
 \frac{N_{Ed}}{N_{Pl,Rd}(M_{Ed})} &= \frac{509}{3149} = 0.16
 \end{aligned}$$

#### 12.6.3.4 Non-dissipative element: Beams

##### Vertical loads:

The beams have been considered as composite beam concrete – steel, using the collaboration of the slab, the resistance to vertical loads has been checked for the most stressed beam as follow:

Principal beam (IPE400):

$$b_{eff} = \min(L_e/8; b_i) = \min(1000; 2000) = 1000 \text{ [mm]}$$

neutral axis (cut the steel profile) (y):

$$A_{concrete} \cdot f_{cd} + t_{wIPE400} \cdot f_{yd} \cdot y = (400-y) \cdot t_{wIPE400} \cdot f_{yd}$$

$$y = 0 \text{ [mm]}$$

$$M_{pl,Rd} = N_c \cdot b = N_{pl,a} \cdot b = 949,2 \text{ [kNm]}$$

$$M_{Ed,max} = 621 \text{ [kNm]}$$

$$\frac{M_{Ed,max}}{M_{pl,Rd}} = 0,65$$

##### Seismic Load:

The unbalanced vertical seismic action effect applied to the beam by the braces after buckling of the compression diagonal. This action effect is calculated using  $N_{pl,Rd,MSSH}$  for the brace in tension and  $\gamma_{pb} \cdot N_{pl,Rd,MSSH}$  for the brace in compression.

The factor  $\gamma_{pb}$  is used for the estimation of the post buckling resistance of diagonals in compression. The recommended value is 0,3.

**Table 12.13: Check of the maximum shear in the beams.**

Number MSSH	$N_{pl,Rd}$ [kN]	$V_{Ed} = N_{pl,Rd} \cdot \frac{0,7}{\sin(\alpha)}$ [kN]	Cross Section	$V_{Rd}$ [kN]	$V_{Ed} / V_{Rd}$
4	1509	746	IPE400	761	0.98

#### 12.6.4 Non-linear static analyses (Pushover)

##### 12.6.4.1 Evaluation of the non-linear behavior of the frames

Static Pushover analysis (SPO) is performed on the structure using two monolithically increasing patterns of lateral load. The lateral loads are applied monolithically in a step by step non-linear static analysis.

As far as lateral load distributions are concerned, EN1998-1-1 suggests to take into account both uniform and modal distribution, as shown in Fig. 12.20. Obviously, since the load resultant is different, the curves show different shapes; both can represent the structural real response.

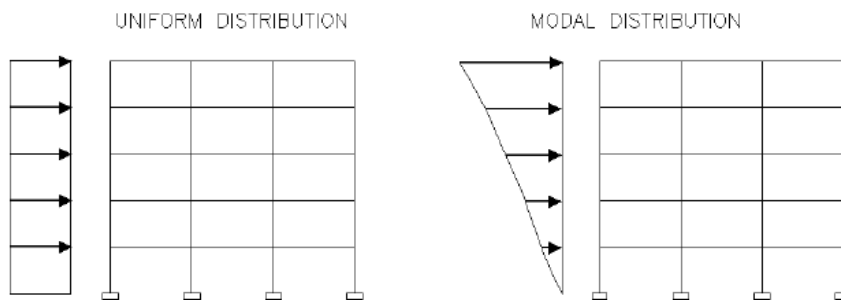


Fig. 12.20: Uniform and Modal lateral load distribution.

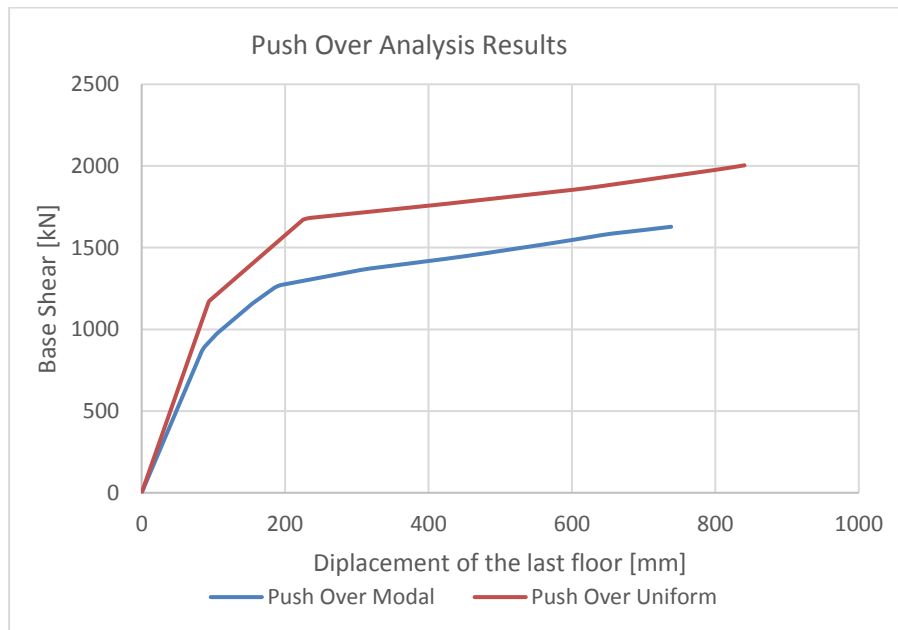


Fig. 12.21: Push Over Analysis Results.

The limit of the ultimate state has been chosen according to FEMA, that for structures with bracing recommend a maximum interstorey drift of 2% of the interstorey height, in this case  $d_{\max} = 0.02 \cdot 4000 = 80$  [mm]. In order to evaluate this limit, the capacity curve of every storey for both, uniform and modal, distribution have been plotted and are show in Fig. 12.22 and Fig. 12.23

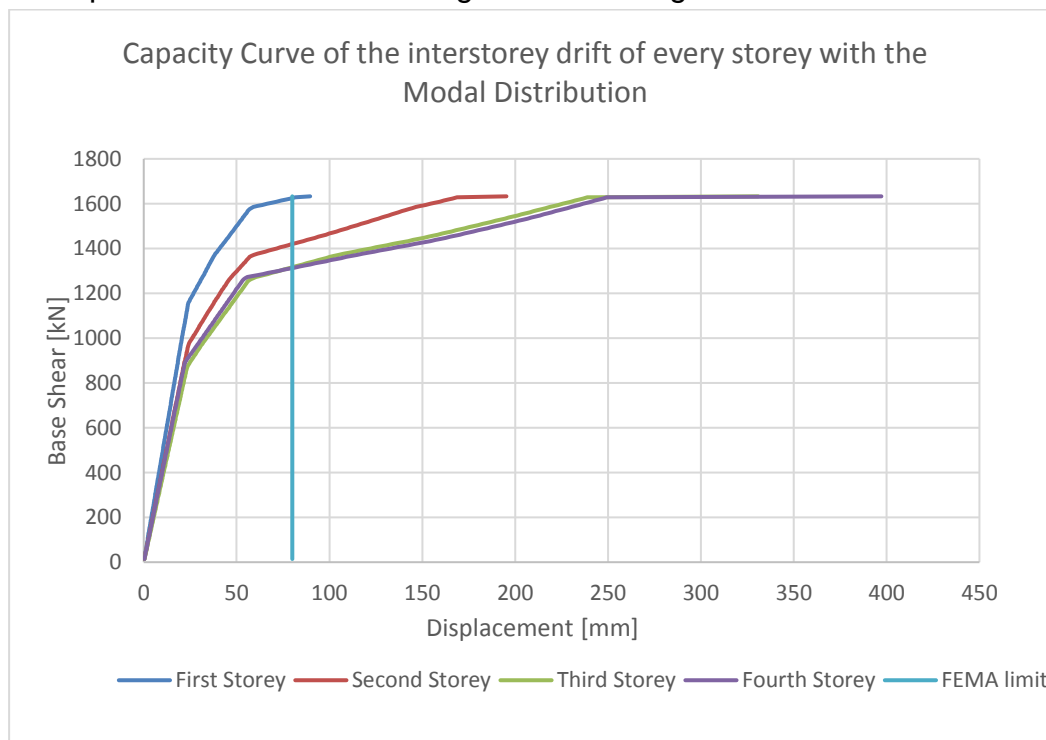


Fig. 12.22: Capacity Curve of the interstorey drift of every storey with the Modal Distribution.

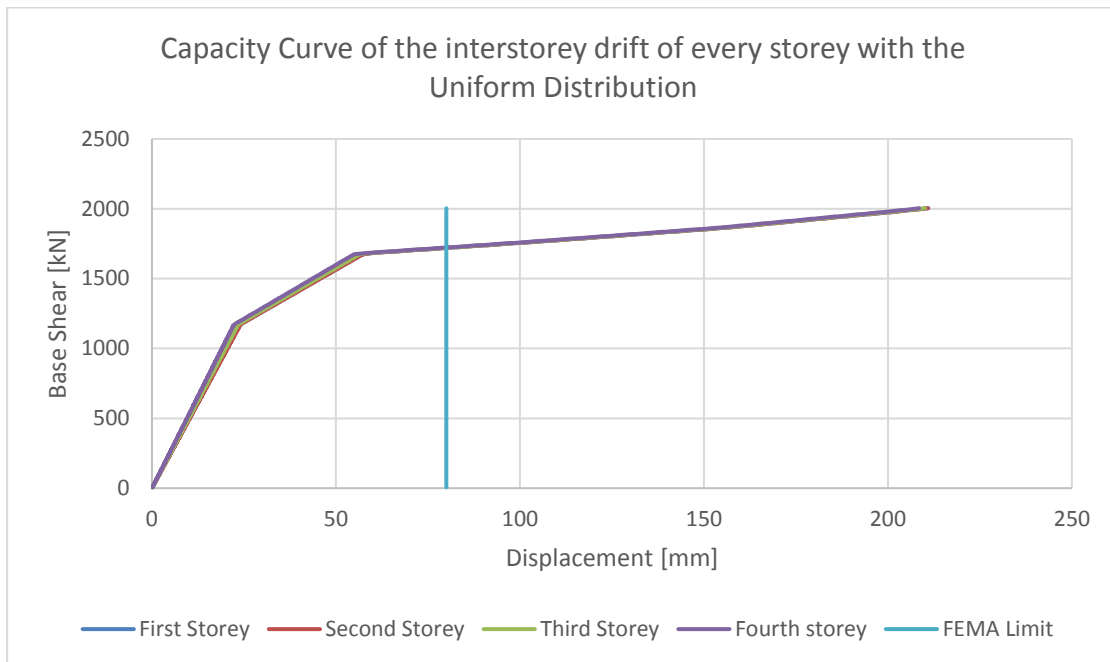


Fig. 12.23: Capacity Curve of the interstorey drift of every storey with the Uniform Distribution.

The base shear corresponding to the maximum displacement has been plotted on the Push Over Curve Diagram in order to find the ultimate state limit, see Fig. 12.24.

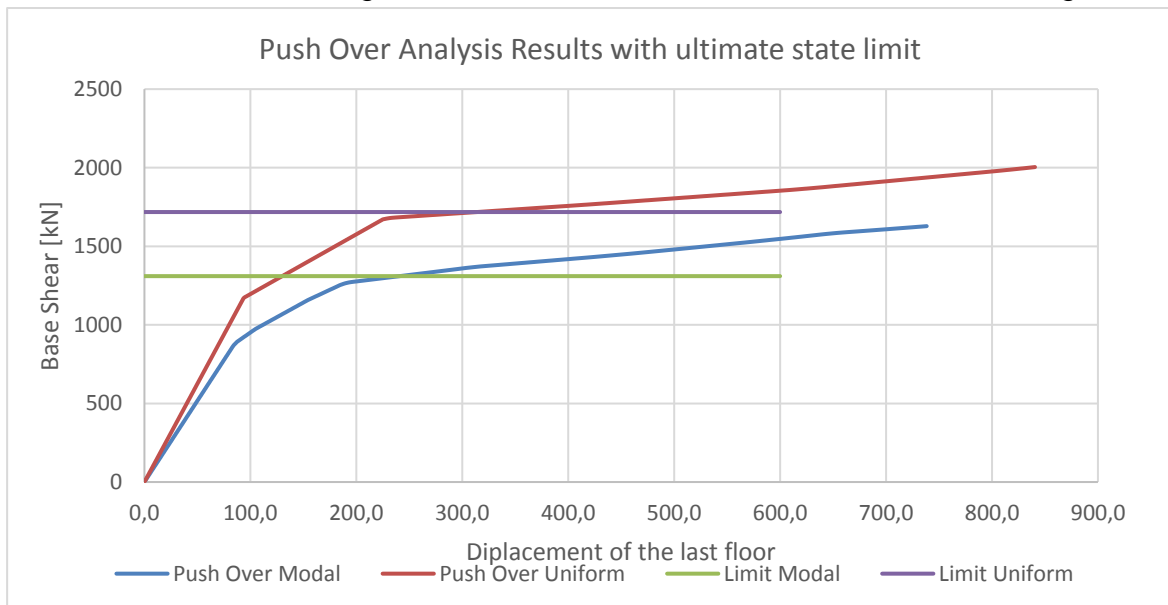


Fig. 12.24: Push Over Analysis Results with ultimate state limit.

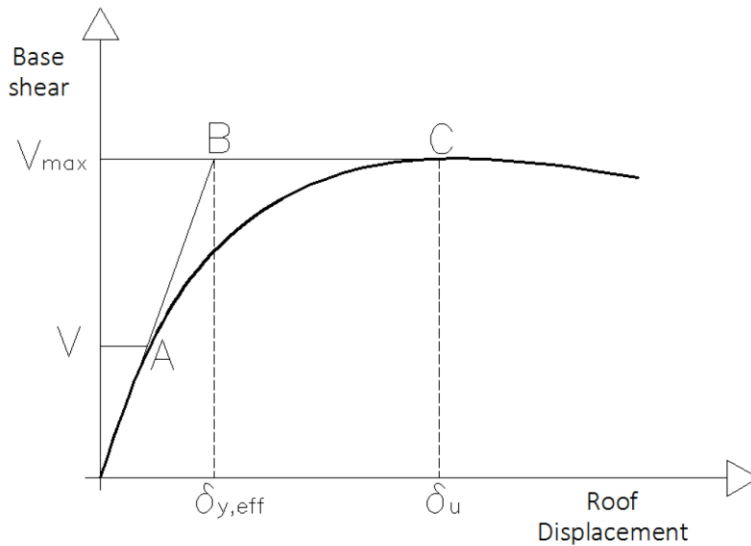
#### 12.6.4.2 Evaluation of the behavior factor $q$

In order to evaluate the structural ductility, the behaviour factor  $q$  is calculated, as suggested FEMA 695, [23]. According FEMA 695, the over-strength factor - is defined as the ratio of the maximum base shear resistance  $V_{max}$ , to the yield base

shear,  $V$ . The period-based ductility is defined as the ratio of ultimate roof drift displacement,  $d_u$ , to the effective yield roof drift displacement  $d_{y,eff}$ , Fig. 12.25.

Fig. 12.25: Method to calculate the behaviour factor  $q$  suggested by FEMA 695

The factor  $q$  has been calculated with the modal and the uniform distribution. The results are shown in Table 12.14.



$$q = \Omega \cdot \mu;$$

$$\Omega = \frac{V_{max}}{V}$$

$$\mu = \frac{d_u}{d_y}$$

**Table 12.14: Calculated behaviour factor  $q$ .**

Distribution	$q_\mu$	$\Omega$	$q$
Modal	1.51	1.88	2.83
Uniform	1.47	2.29	3.37

In the most cases the recommended  $q$  factor is the lower one, in this case  $q=2.8$ , but, also if Nonlinear Dynamic Analysis have been not performed the expected behaviour, taking into account the hysteresis effect is closer to the behaviour with the uniform distribution. The dissipation effect is expected to raise both the push over curves, thus the chosen value  $q = 3$  can be considered confirmed and on the safe side.

## 12.7 CONCLUSIONS

The above study introduces the MSSH devices as dissipative brace elements. The following observations are worth noting:

- The system exhibits a very good behaviour under seismic loading: strong, stiff, large capacity of energy absorption. The seismic resistance of a building may be obtained by appropriate provision of a number of systems in the relevant directions.
- It may be designed as more flexible/rigid depending on the section types and their distribution between floor levels.



- c) Inelastic deformations are strictly limited to the dissipative devices preventing the spreading of damage into the rest of the structural members. The MSSH devices are easily fabricated, installed and replaced, if they are damaged after a strong seismic event.
- d) Code relevant design rules for the seismic design of braced frames with MSSH devices, including practical recommendations on the selection of the appropriate fuses and member verifications, have been formulated in a Design Guide.
- e) The devices offer a cost-effective solution even for seismic retrofitting of structures.

## 12.8 FIELD OF APPLICATION

The MSSH devices can easily applied to multi-story steel buildings and substitute the conventional systems used worldwide (such as concentric and eccentric braced frames, moment resisting frames etc.) by combining elastic resistance for wind loads and distinct plastic energy dissipation for seismic loads. The devices are easy to replace and manufacture, offering a cost-effective solution.

## 12.9 BIBLIOGRAPHIC REFERENCES

1. EN15129: Anti-seismic Devices. Brussels: Comitee Europeen de Normalisation (CEN); 2003.
2. EN1998-1-1, Eurocode 8: Design of structures for earthquake resistance – Part 1-1: General rules, seismic actions and rules for buildings. Brussels: Comitee Europeen de Normalisation (CEN); 2003.
3. ECCS document: Recommended testing procedure for assessing the behavior of structural steel elements under cyclic loads, Technical committee 1: structural safety and loadings, Technical working group 1.3: seismic design; 1986.
4. DIN 50125: Testing of metallic materials - Tensile test pieces; 2009.
5. EN1993-1-1, Eurocode 3: Design of steel structures - Part 1-1: General rules and rules for buildings. Brussels: Comitee Europeen de Normalisation (CEN); 2003.
6. FEMA – 356: Prestandard and Commentary for the seismic rehabilitation of Buildings. Washington; 2000.
7. EN1993-1-9, Eurocode 3: Design of steel structures – Part 1-9: General – Fatigue strength. CEN. 2005
8. SAP2000, CSI, Computers and Structures Inc., [www.csiberkeley.com](http://www.csiberkeley.com).
9. EN1994-1-1: Eurocode 4: Design of composite steel and concrete structures. Part 1-1: General rules and rules for buildings. Brussels: Comité Européen de Normalisation (CEN); 2005.
10. EN 1993-1-8: Eurocode 3: Design of steel structures. Part 1-8: Design of joints. Brussels: Comité Européen de Normalisation (CEN); 2004.
11. FEMA – P695: Quantification of building seismic performance factors, Washington; 2009.
12. Seismomatch v.2.1.0, Seismosoft, [www.seismosoft.com](http://www.seismosoft.com).